

**NONLINEAR DRILLSTRING MODELING WITH APPLICATIONS TO
INDUCED VIBRATIONS IN UNCONVENTIONAL HORIZONTAL WELLS**

A Dissertation

by

JOSHUA KYLE WILSON

Submitted to the Office of Graduate and Professional Studies of
Texas A&M University
in partial fulfillment of the requirements for the degree of

DOCTOR OF PHILOSOPHY

Chair of Committee, Committee Members,	Sam Noynaert Jerome Schubert Eduardo Gildin Alan Palazzolo
Head of Department,	A. Dan Hill

May 2017

(Last Corrected: May 2021)

Major Subject: Petroleum Engineering

Copyright 2017 Joshua Kyle Wilson

ABSTRACT

A new mathematical model is developed for the nonlinear-static, linearized-dynamic, and fully nonlinear-dynamic behavior of drillstrings in arbitrary wellbore profiles. The formulation is based on a three-dimensional nonlinear finite beam element and accounts for the fully coupled flexibility of the drillstring, geometric nonlinearity (large displacement, small strain), automatic determination of wellbore contact points, friction acting between the drillstring and the wellbore, stabilizer clearance, three-dimensional wellbore profiles, added fluid mass and damping effects from the hydrodynamic forces generated between the drillstring and surrounding fluid, complex tool geometry (including steerable mud motors, rotary steerable systems, and eccentric stabilizers/components), shear beam deformations, lateral rotary inertias, and gyroscopic effects. The resulting model is numerically validated through comparisons with analytical formulas and previous nonlinear models, showing that it can readily be applied to a wide range of drilling engineering problems and used for practical analysis. Additionally, individual contributions of shear deformations, lateral rotary inertias, and gyroscopic effects are definitively shown to be insignificant when calculating the static and dynamic behavior of horizontal drilling assemblies within the rotational speed range of most drilling applications. An initial comparison with field data is also provided, which shows the practicality of the developed algorithms in predicting the characteristics of real drilling scenarios.

The model is then adjusted and applied to the specific case of inducing lateral vibrations in unconventional horizontal wells. It is proposed that exciting a lateral resonance in the drill pipe lying on the low side of a horizontal wellbore can induce enough movement to help overcome parasitic axial drag acting on a drillstring. This, in turn, would help to increase weight transfer to the bit while slide-drilling with a steerable mud motor in long lateral sections of a wellbore. The change in this lateral resonant behavior due to variations in weight-on-bit (WOB), inclination, well path curvature, wellbore diameter, fluid properties, and tubular dimensions are clearly shown through linearized-dynamic sensitivity studies. Nonlinear time-domain simulations are also performed to better understand the limitations of linearized-dynamic modeling and to provide a more detailed assessment of how inducing lateral vibration influences the WOB while drilling. It is shown that induced lateral vibrations provide a noticeable dynamic WOB of up to $\pm 250 \text{ lbf}$ about the static value, and a slight increase in the average WOB value of up to 150 lbf . The effects on WOB are dependent on the excitation frequency of the induced lateral vibrations, with the greatest benefits being seen at resonant conditions.

DEDICATION

To my Father in Heaven...I may never know where you are leading me, but I trust that it is in the right direction.

ACKNOWLEDGEMENTS

I would like to thank Dr. Sam Noynaert for his support through the entire “Doctoral Process”, and his willingness to accommodate unique situations; his enthusiasm and readiness to help was greatly appreciated throughout this project. I would also like to express gratitude to Dr. Jerome Schubert and Dr. Eduardo Gildin, of the Petroleum Engineering Department, and Dr. Alan Palazzolo, of the Mechanical Engineering Department, for serving as members of my advisory committee.

Appreciation is also well deserved to the management of Scientific Drilling International, Inc., for their unwavering support of this research. A special acknowledgement must also be given to Dr. Gerald Heisig; I am immeasurably grateful for his guidance, advice, and friendship over the last three and a half years. He has been a tremendous influence on my work and has expressed nothing but support for both my career and my education.

And finally, above all, I want to thank my wife Brandi; you have shared the burden of this work over the last two years, often times more than you would have preferred. I cannot say thank you enough for the love and support that you have shown on a daily basis and I am eternally grateful to have you as a partner in life.

CONTRIBUTORS AND FUNDING SOURCES

Contributors

This work was supervised by a dissertation committee consisting of Dr. Sam Noynaert (Chair), Dr. Jerome Schubert, and Dr. Eduardo Gildin of the Petroleum Engineering Department, as well as Dr. Alan Palazzolo of the Mechanical Engineering Department.

All work conducted for this dissertation was completed independently by the student.

Funding Sources

Financial support for this course of study, in its entirety, was provided by Scientific Drilling International, Inc. Its contents are solely the responsibility of the author and do not necessarily represent the official views of Scientific Drilling International or its employees.

NOMENCLATURE

x^t	value of x at time t
$x^{t+\Delta t}$	value of x at time $t + \Delta t$
\vec{x}	x is a vector
\underline{x}	x is a column vector
$\{x\}$	x is a column vector
\hat{x}	x is a unit vector
$\hat{\underline{x}}$	x is a column vector of unit vectors, i.e. x is a matrix
$\underline{\underline{x}}$	x is a matrix
$[x]$	x is a matrix
x'	derivative of x with respect to the well path coordinate, s
x''	derivative of x' with respect to the well path coordinate, s
x'''	derivative of x'' with respect to the well path coordinate, s
\dot{x}	derivative of x with respect to time
\ddot{x}	derivative of \dot{x} with respect to time
\vec{x}^T	transpose of the vector x
\underline{x}^T	transpose of the column vector x
a	fluid-damping parameter
A	cross-sectional area
A_o	area calculated from outer diameter
AET	axial excitation tool
b	parameter for velocity-dependent friction model
BA	bend angle
BHA	bottom-hole assembly
c	wave speed
c_{f_A}	linearized axial fluid-damping coefficient
$c_{f_{lat}}$	linearized lateral fluid-damping coefficient
c_{f_T}	linearized torsional fluid-damping coefficient
$\underline{\underline{C}}$	proportional damping matrix
$\underline{\underline{C}}_F$	linearized fluid-damping matrix
C_f	nonlinear fluid-damping coefficient
CPU	central processing unit

D_{ch}	diameter of wellbore
D_i	inner diameter of tubular
D_o	outer diameter of tubular
\underline{D}_v	derivative matrix of wellbore basis vectors
\underline{D}_1	transformation matrix about axis-1
\underline{D}_2	transformation matrix about axis-2
\underline{D}_3	transformation matrix about axis-3
DC	drill collar
DOC	depth of cut
DP	drill pipe
e	eccentricity
\hat{e}_N	normal contact vector
\hat{e}_T	tangential contact vector
$\hat{\underline{e}}$	deformed drillstring vector basis
\hat{e}_1	deformed unit vector of axis-1
\hat{e}_2	deformed unit vector of axis-2
\hat{e}_3	tangent vector of deformed drillstring
E	Young's modulus
EB	Euler-Bernoulli
ECD	equivalent circulating density
ERD	extended-reach-drilling
f	frequency
f_f	fluid friction coefficient
f_{exc}	excitation frequency
F	axial force
\underline{F}_B	internal force vector of beam
\underline{F}_{Exc}	excitation force vector
\underline{F}_{E_c}	cosinusoidal excitation force vector
\underline{F}_{E_s}	sinusoidal excitation force vector
F_{f_1}	lateral fluid force along axis-1
\underline{F}_{f_1}	lateral fluid force vector along axis-1
F_{f_2}	lateral fluid force along axis-2
\underline{F}_{f_2}	lateral fluid force vector along axis-2

F_{f_3}	axial fluid force
\underline{F}_{f_3}	axial fluid force vector
$\underline{F}_{M_{gyro}}$	gyroscopic moment vector
\underline{F}_W	wall contact force vector
F_{W_A}	axial friction force
\underline{F}_{W_A}	axial friction force vector
F_{W_M}	torsional friction moment
\underline{F}_{W_M}	torsional friction moment vector
F_{W_N}	normal contact force
\underline{F}_{W_N}	normal contact force vector
F_{W_T}	tangential friction force
\underline{F}_{W_T}	tangential friction force vector
FEM	finite element method
FFR	forced-frequency response
g_i	gravity component along i-th axis
G	shear modulus
GPM	gallons per minute
GPU	graphics processing unit
$\underline{h}_1 - \underline{h}_6$	shape function column vectors
H_1, H_2	scalar parameters for beam model
HWDP	heavy-weight drill pipe
\hat{i}	unit vector along global x-direction (North)
I	area moment of inertia
ID	inner diameter
\hat{j}	unit vector along global y-direction (East)
J	polar moment of inertia
k	consistency index of YPL fluid
k_f	fluid-damping parameter
k_w	wellbore wall stiffness
\hat{k}	unit vector along global z-direction (TVD)
$\underline{\underline{K}}$	tangent stiffness matrix
$\underline{\underline{K}}_{eff}$	effective tangent stiffness matrix
K_s	shear-correction factor

l, L	length
LET	lateral excitation tool
LIH	lost-in-hole
m	linear mass
m_{ecc}	linear eccentric mass
m_{fax}	added fluid mass in axial direction
m_{flat}	added fluid mass in lateral direction
\tilde{m}_{flat}	simplified added fluid mass in lateral direction
m_{fT}	added fluid mass in torsion
M	mass
M_B	bending moment
$\underline{\underline{M}}_o$	mass matrix of drillstring
$\underline{\underline{M}}_f$	fluid mass matrix
$\tilde{\underline{\underline{M}}}_f$	simplified fluid mass matrix
MD	measured depth
MWD	measurement-while-drilling
n	node number
n_f	flow behavior index of YPL fluid
N_{lobes}	number of lobes on rotor of power section
N_s	Stokes number
$N_1 - N_{10}$	shape functions
OD	outer diameter
ppf	pound per foot
ppg	pound per gallon
psi	pound per square inch
PU	pick-up
q	linear weight
\tilde{q}	buoyed linear weight
$\underline{\underline{Q}}$	external load vector
$\underline{\underline{Q}}_{eff}$	effective external load vector
r	radial clearance
\vec{r}	position vector of drillstring axis
\vec{r}_o	position vector of “shear-free” drillstring axis

\vec{r}_w	position vector of the wellbore axis
\underline{R}	residual force vector
$\underline{\underline{R}}$	transformation matrix from the wellbore basis, to the deformed drillstring basis
ROB	rotating-off-bottom
ROP	rate of penetration
rpg	revolutions per gallon
RPM	rotations per minute
RSS	rotary steerable system
s	coordinate along central axis of the wellbore/drillstring
S	shear load
SG _f	specific gravity of fluid
SO	slack-off
t	time
\hat{t}	tangent unit vector of the drillstring's central axis
\vec{t}	tangent vector of the drillstring's central axis
\vec{t}_o	tangent vector of the "shear free" drillstring's central axis
T	torque
\underline{T}_{D1}	transformation matrix about axis-1
\underline{T}_{D3}	transformation matrix about axis-2
T_f	fluid torque
\underline{T}_f	fluid torque vector
T _k	kinetic energy
\underline{T}_γ	tool face transformation matrix
$\underline{\underline{T}}_{\Delta\gamma}$	change in tool face transformation matrix
T&D	torque and drag
TD	total depth
TDA	torque and drag analysis
TFO	tool face orientation
TIH	trip-in-hole
TOB	torque on bit
TOOH	trip-out-of-hole
TVD	true vertical depth
\vec{u}	displacement vector of beam
\underline{u}_{ele}^A	6x1 column vector of displacements at the first node of an element

\underline{u}_{ele}^B	6x1 column vector of displacements at the second node of an element
\vec{u}_n	6x1 column vector of nodal displacements
\vec{u}_o	displacement vector of “shear-free” beam
u_1	lateral displacement along \hat{v}_1 axis
u_2	lateral displacement along \hat{v}_2 axis
u_3	axial displacement along \hat{v}_3 axis
U	internal strain energy of beam
$\underline{\hat{v}}$	wellbore basis vectors
\hat{v}_1	bi-normal vector of wellbore
\hat{v}_2	normal vector of wellbore
\hat{v}_3	tangent vector of the wellbore
V_{flow}	effective flow velocity
V_∞	bulk flow velocity
VARD	vibration-assisted rotary drilling
VID	vibration inducing device
W	WOB
WOB	weight-on-bit
x	northern coordinate
y	eastern coordinate
YPL	yield-plastic-law
z	true vertical depth coordinate
α	azimuth
α_N	Newmark integration parameter
β	parameter for velocity-dependent friction model
β_D	proportional damping parameter
β_{DL}	dog-leg angle
γ	tool face angle
γ_D	proportional damping parameter
γ_1	shear rotation about axis-1
γ_2	shear rotation about axis-2
δ	variational operator
δ_{bl}	boundary layer thickness
δ_N	Newmark integration parameter
δT_K	variation of kinetic energy

δT_{K_b}	boundary terms of the variation of kinetic energy
δU	virtual strain energy of beam
δW_e	virtual work due to external forces
$\delta \alpha_1$	virtual rotation about the \hat{e}_1 axis
$\delta \alpha_2$	virtual rotation about the \hat{e}_2 axis
$\delta \alpha_3$	virtual rotation about the \hat{e}_3 axis
$\delta \theta_1$	virtual rotation about the \hat{v}_1 axis
$\delta \theta_2$	virtual rotation about the \hat{v}_2 axis
$\delta \theta_3$	virtual rotation about the \hat{v}_3 axis
Δr	deflection of wellbore wall
$\underline{\Delta u}$	incremental displacement vector
$\Delta \gamma$	change in tool face angle between two nodes of a beam
ϵ	generalized axial strain
η	effective tool face angle
θ	dummy angle
θ_{span}	span angle of eccentric stabilizer
θ_1	rotation angle about axis-1
θ_2	rotation angle about axis-2
θ_3	rotation angle about axis-3
κ	generalized bending strain
κ_o	wellbore curvature
κ_1	generalized bending strain along axis-1
κ_2	generalized bending strain along axis-2
λ	magnitude parameter
λ_L	wavelength
Λ	shape factor parameter
μ	friction coefficient
μ_A	effective axial friction coefficient
μ_D	dynamic friction coefficient
μ_M	distributed fluid mass
μ_o	velocity-dependent friction coefficient
μ_s	static friction coefficient
μ_t	effective tangential friction coefficient
ν	Poisson's ratio
ν_f	kinematic fluid viscosity

v_o	smoothing parameter
ξ	non-dimensional length along element
ρ	density
ρ_f	fluid density
σ	stress
τ	generalized torsional strain
τ_o	wellbore torsion
τ_y	fluid yield point
ϕ	inclination
ϕ_1	tilting angle along axis-1 (about axis-2)
ϕ_2	tilting angle along axis-2 (about axis-1)
$\underline{\Psi}$	linearized-displacement vector
$\hat{\underline{\Psi}}$	linearized modal displacement vector
$\underline{\Psi}_c$	cosinusoidal modal displacement vector
$\hat{\underline{\Psi}}_s$	sinusoidal modal displacement vector
ω	circular frequency
ω_{ds}	drillstring rotation speed
ω_{em}	rotation speed of the eccentric mass
ω_{rot}	rotation speed of the rotor within a power section
ω_1	rotational velocity about the \hat{e}_1 axis
ω_2	rotational velocity about the \hat{e}_2 axis
ω_3	rotational velocity about the \hat{e}_3 axis
Ω	circular frequency of excitation
$\underline{\Omega}$	rotational velocity matrix

TABLE OF CONTENTS

	Page
ABSTRACT	ii
DEDICATION	iii
ACKNOWLEDGEMENTS	iv
CONTRIBUTORS AND FUNDING SOURCES.....	v
NOMENCLATURE.....	vi
TABLE OF CONTENTS.....	xiv
LIST OF FIGURES.....	xvi
LIST OF TABLES	xxii
1. INTRODUCTION	1
1.1 Background.....	2
1.2 Problems Associated with Horizontal Drilling	11
1.3 Literature Review	15
1.4 Statement of Purpose	26
2. DERIVATION OF DRILLSTRING MECHANICS	29
2.1 Wellbore Geometry.....	32
2.2 Drillstring Kinematics.....	34
2.3 Frictional Wall Contact.....	44
2.4 Nonlinear Fluid Forces	50
3. NONLINEAR FINITE ELEMENT FORMULATION	52
3.1 Hamilton's Principal of Virtual Work	52
3.2 Element Discretization.....	55
3.3 Complete Drillstring Equations	61
3.4 Further Considerations for Drilling Systems	69
4. NUMERICAL VALIDATION AND INITIAL FIELD TRIALS.....	72
4.1 Nonlinear-Static/Quasi-Static Analysis	72
4.2 Linearized-Dynamic Analysis	94
4.3 Nonlinear-Dynamic Analysis.....	101
4.4 Initial Field Trials	106
4.5 Summary of Numerical Validation and Comparative Analysis.....	116
5. A LINEARIZED APPROACH TO INDUCED LATERAL VIBRATIONS	117

5.1 Free Vibration	120
5.2 Forced Vibration	124
5.3 Practical Considerations for Operations and Analysis	143
6. NONLINEAR SIMULATIONS OF INDUCED LATERAL VIBRATIONS	147
6.1 Nonlinear Modeling Considerations	147
6.2 Nonlinear Simulation Results and Discussion	153
7. CONCLUSIONS AND FUTURE WORK	183
7.1 Conclusions.....	183
7.2 Future Work.....	187
REFERENCES.....	190
APPENDIX A. MINIMUM CURVATURE RELATIONSHIPS AND TRAJECTORY CALCULATIONS	201
APPENDIX B. DERIVATION OF TIME-INTEGRATION EQUATIONS.....	205
APPENDIX C. SURVEY DATA FROM NORTHEAST WELL	208
APPENDIX D. FREE VIBRATION PLOTS FOR SECTION 5.....	215
APPENDIX E. FORCED VIBRATION PLOTS FOR SECTION 5	225

LIST OF FIGURES

	Page
Figure 1.1: Generic Layout of a Drilling System [13]	3
Figure 1.2: Visual Comparison of Drill Pipe, Heavy-Weight Drill Pipe, and Drill Collars [14]	4
Figure 1.3: Various Types of Drill Bits [15-18].....	5
Figure 1.4: General Layout of a Modern Horizontal Well	7
Figure 1.5: Visualization of the Inner Workings of a Point-the-Bit RSS (From [32])	9
Figure 1.6: Cross-Section of Actuated Pads on a Push-the-Bit RSS (From [33])	9
Figure 1.7: Down-Hole Steerable Mud Motor (Courtesy of Scientific Drilling International, Inc.)	10
Figure 1.8: Cross-Section of a 5/6 Power Section, Looking Down-Hole Towards the Bit (From [34]) ...	10
Figure 1.9: Illustration Showing the Difference between Rotary and Slide Drilling with a Steerable Mud Motor [35].....	11
Figure 1.10: Moderate Buckling in an 8 ½" Horizontal Well with 4 ½" Drill Pipe (WOB = 30 klb _f).....	14
Figure 1.11: Severe Buckling in an 8 ½" Horizontal Well with 4 ½" Drill Pipe (WOB = 60 klb _f)	14
Figure 1.12: Field Observation of the Static/Dynamic Friction Concept (From [62])	17
Figure 1.13: Example of Dynamic WOB from an AET (From [63])	18
Figure 1.14: Example of Dynamic WOB from an AET (From [64])	18
Figure 1.15: Coiled Tubing Axial Force Transfer Experiment – No AET (From [65])	19
Figure 1.16: Coiled Tubing Axial Force Transfer Experiment – With AET (From [65])	19
Figure 1.17: Experimental Axial Force Transfer While using an AET (From [7]).....	20
Figure 2.1: Well Path in the Global Coordinate System	33
Figure 2.2: Illustration of Drillstring/Wellbore Contact.....	44
Figure 2.3: Broom Plot Generated for Permian Basin Well using Commercial T&D Software	48
Figure 2.4: Absolute Coefficient of Friction as a Function of Slip-Velocity	49
Figure 3.1: Finite Element Representation of the Drillstring	56
Figure 3.2: Diagram of Eccentric Stabilizer/Component	71

Figure 4.1: Comparison of Different Beam Models for the Deflection of a Cantilevered Beam	73
Figure 4.2: 3D Mechanics Plot of BHA Deflection, Contact Forces, and Bending Moments	75
Figure 4.3: Comparison of Calculated High-Side BHA Deflection	75
Figure 4.4: Comparison of Calculated High-Side BHA Sag (Rotation Angle).....	75
Figure 4.5: Comparison of Calculated High-Side BHA Bending Moment	76
Figure 4.6: Comparison of Calculated High-Side BHA Contact Forces	76
Figure 4.7: 3D Mechanics Plot Output from Commercial Software	78
Figure 4.8: 3D Mechanics Plot Output from MADSim Code	79
Figure 4.9: Total Contact Force Comparison for Full Test Well – No Friction	80
Figure 4.10: Total Bending Moment Comparison for Full Test Well – No Friction.....	81
Figure 4.11: Drillstring Torque Comparison for Full Test Well – No Friction.....	82
Figure 4.12: Axial Force Comparison for Full Test Well – No Friction.....	83
Figure 4.13: Drillstring Torque Comparison for Full Test Well – With Friction.....	85
Figure 4.14: Axial Force Comparison for Full Test Well – With Friction	86
Figure 4.15: Axial Force Comparison for Full Test Well – With Friction, Enlarged.....	87
Figure 4.16: Comparison of Steering Mechanism between an RSS and a Steerable Mud Motor	89
Figure 4.17: Sliding Motor Yield Comparison with Commercial Software.....	90
Figure 4.18: Rotational Motor Yield Comparison with Commercial Software	90
Figure 4.19: RSS Yield Comparison with Commercial Software	92
Figure 4.20: RSS Steering Force Comparison with Commercial Software	92
Figure 4.21: Total Shear Load along BHA Calculated from MADSim	93
Figure 4.22: Contact Force Distribution with Changing Active Pad Eccentricity	94
Figure 4.23: Natural Frequency Comparison between Beam Models, Length = 30 ft	96
Figure 4.24: Natural Frequency Comparison between Beam Models, Length = 15 ft	96
Figure 4.25: Natural Frequency Comparison between Beam Models, Length = 10 ft	97
Figure 4.26: Linearized Natural Frequencies and Mode Shapes of Horizontal Drillstring	99

Figure 4.27: Linearized Natural Frequency Comparison of Horizontal Drillstring	101
Figure 4.28: Linearized Natural Frequency Comparison of Horizontal Drillstring, Zoom-In	101
Figure 4.29: Rotational Speed Applied at the “Top” of the Drilling Assembly for Time-Domain Simulations	102
Figure 4.30: Nonlinear Simulation Results using Heisig’s [34] Model (Does not Include Shear Deformation, Lateral Rotary Inertias, or Gyroscopic Effects).....	104
Figure 4.31: Nonlinear Simulation Results using Current Model (Includes Shear Deformation, Lateral Rotary Inertias, but not Gyroscopic Effects)	105
Figure 4.32: Nonlinear Simulation Results using Current Model (Includes Shear Deformation, Lateral Rotary Inertias, and Gyroscopic Effects).....	106
Figure 4.33: Surface Parameters and MWD Vibration Data for Marcellus Well, while Back-Reaming near 14,300 ft MD	110
Figure 4.34: Static Deflection of BHA in Marcellus Well (MD = 14,300 ft)	111
Figure 4.35: Critical RPM Analysis of BHA in Marcellus Well (MD = 14,300 ft)	111
Figure 4.36: Marcellus BHA in a Perfectly Straight, Horizontal Well at a TFO of 0°.....	113
Figure 4.37: Marcellus BHA in a Perfectly Straight Horizontal Well at a TFO of 180°.....	113
Figure 4.38: Surface Parameters and MWD Vibration Data for Eagle Ford Well 1, while Back-Reaming near TD.....	114
Figure 4.39: Static Deflection of BHA in Eagle Ford Well 1 at TD	115
Figure 4.40: Critical RPM Analysis of BHA in Eagle Ford Well 1 at TD	115
Figure 4.41: Surface Parameters and MWD Vibration Data for Eagle Ford Well 2, while Back-Reaming near TD.....	116
Figure 5.1: 3D Mechanics Plot of Drilling Assembly in a Perfectly Straight, Horizontal Wellbore (Diameters are not Drawn to Scale).....	118
Figure 5.2: Mechanical Layout of the LET (Courtesy of Scientific Drilling International, Inc.).....	119
Figure 5.3: Internal Excitation Mechanism of the LET (slightly modified from [47])	119
Figure 5.4: Lateral (Right-Side) Forced-Frequency Displacement Response due to the LET Excitation	126
Figure 5.5: Lateral (Right-Side) Forced-Frequency Displacement Response due to LET Excitation, with Frequency Markers	128
Figure 5.6: Lateral (Right-Side) Forced-Frequency Velocity Response due to LET Excitation	130
Figure 5.7: Lateral (Right-Side) Forced-Frequency Acceleration Response due to LET Excitation	130

Figure 5.8: Lateral (Right-Side) Forced-Frequency Displacement Response due to LET Rotor Excitation.....	131
Figure 5.9: Lateral (Right-Side) Forced-Frequency Velocity Response due to LET Rotor Excitation... ..	131
Figure 5.10: Lateral (Right-Side) Forced-Frequency Acceleration Response due to LET Rotor Excitation.....	132
Figure 5.11: Diagram of Quantities used for the Sensitivity Analysis	133
Figure 5.12: Contact Force along the Drillstring for Varying Wellbore Curvatures	137
Figure 5.13: Contact Force Distribution near the LET for a DLS of 0°/100ft (Straight Wellbore)	138
Figure 5.14: Contact Force Distribution near the LET for a DLS of 5°/100ft	139
Figure 5.15: Contact Force Distribution near the LET for a DLS of 10°/100ft	139
Figure 5.16: Mechanics Plot of Drillstring in an “Ideal” Horizontal Wellbore.....	141
Figure 5.17: Mechanics Plot of Drillstring in a “Realistic” Horizontal Wellbore.....	141
Figure 5.18: Forced-Frequency Response with LET in “Ideal” Horizontal Wellbore	142
Figure 5.19: Forced-Frequency Response with LET in Realistic Horizontal Wellbore	143
Figure 5.20: Analysis of Figure 5.4 Performed with a Coarser Element Mesh.....	145
Figure 6.1: Quasi-Static Deflection of Drillstring (Diameters are not Drawn to Scale).....	149
Figure 6.2: Quasi-Static Axial Force and Contact Force along the Drillstring	149
Figure 6.3: Forced-Frequency Response of Shortened Assembly due to LET Excitation	150
Figure 6.4: Forced-Frequency Response of Shortened Assembly due to Power Section Excitation	151
Figure 6.5: Time History of Excitation Frequency for Nonlinear “Frequency Sweep” Simulations	152
Figure 6.6: Results of Original Nonlinear Simulation.....	154
Figure 6.7: Animation “Snap-Shot” of Original Simulation near 1.4 Hz Excitation Frequency	155
Figure 6.8: Animation “Snap-Shot” of Original Simulation near 1.5 Hz Excitation Frequency	155
Figure 6.9: Animation “Snap-Shot” of Original Simulation near 1.8 Hz Excitation Frequency	156
Figure 6.10: Animation “Snap-Shot” of Original Simulation near 1.9-2.0 Hz Excitation Frequency	156
Figure 6.11: Axial Shortening of the Drillstring due to Lateral Displacement (From [47]).....	157
Figure 6.12: WOB Fluctuation in Original Assembly, near 1.8 Hz Excitation Frequency	158

Figure 6.13: Results of Constant Excitation Frequency at 1.8 Hz.....	159
Figure 6.14: Time Stamps of Primary Excitation in WOB Data for 1.8 Hz Excitation Frequency	160
Figure 6.15: Time Stamps of Secondary Excitation in WOB Data for 1.8 Hz Excitation Frequency	160
Figure 6.16: WOB Fluctuations near 1.9-2.0 Hz Excitation Frequency for Original Simulation	161
Figure 6.17: Axial and Rotational Velocities from Original Simulation.....	162
Figure 6.18: Axial and Rotational Velocities from Constant Frequency Simulation (1.8 Hz).....	162
Figure 6.19: Summation of Contact Forces for Original Simulation	163
Figure 6.20: Summation of Contact Forces for Original Simulation, near 1.4 Hz Excitation	163
Figure 6.21: Summation of Contact Forces for Original Simulation, near 1.8 Hz Excitation	163
Figure 6.22: Summation of Contact Forces for Constant Excitation Simulation (1.8 Hz)	164
Figure 6.23: Results of Simulation with Alternative Friction Model	165
Figure 6.24: Results of Constant Excitation Frequency at 1.9 Hz.....	167
Figure 6.25: Axial and Rotational Velocities, and Summation of Contact Forces for Constant Excitation Simulation (1.9 Hz)	168
Figure 6.26: Results of Constant Excitation Frequency at 2.0 Hz.....	169
Figure 6.27: Axial and Rotational Velocities, and Summation of Contact Forces for Constant Excitation Simulation (2.0Hz)	170
Figure 6.28: Original Simulation with Fluid Damping	172
Figure 6.29: Results of Constant Excitation Frequency at 1.8 Hz, with Fluid Damping	173
Figure 6.30: Results of Constant Excitation Frequency at 1.9 Hz, with Fluid Damping	174
Figure 6.31: Results of Constant Excitation Frequency at 2.0 Hz, with Fluid Damping	175
Figure 6.32: Results of Constant Excitation Frequency at 12 Hz, with Fluid Damping	177
Figure 6.33: WOB Fluctuation of 12 Hz Excitation, between 10 and 11 Seconds Simulation Time	178
Figure 6.34: Orbital Displacement of Cross-Section for Constant Excitation (12 Hz) Simulation	178
Figure 6.35: Axial and Rotational Velocities, and Summation of Contact Forces for Constant Excitation Simulation (12 Hz)	179
Figure 6.36: Forced-Frequency Response of Assembly with Multiple LETs	181
Figure 6.37: Results of Simulation with Multiple LETs in the Drillstring	181

Figure 6.38: Rotational Velocity, Axial Velocity, and the Summation of Contact Forces for the Case of using Multiple LETs in the Drillstring 182

LIST OF TABLES

	Page
Table 4.1: Input Data for Cantilevered Beam Deflection Comparison	73
Table 4.2: Assembly for Static BHA Comparison	74
Table 4.3: Drilling Assembly for Full Well Comparison	77
Table 4.4: BHA Layout for Motor Yield Comparison	89
Table 4.5: BHA Layout for Push-the-Bit RSS Yield Comparison	91
Table 4.6: Beam Comparison Data	95
Table 4.7: Dimensions of Compressive Service Drill Pipe	98
Table 4.8: Lateral BHA, Marcellus Well	111
Table 4.9: Lateral BHA, Eagle Ford Well.....	114
Table 5.1: Assembly for LET Analysis	121
Table 5.2: Operational Parameters for LET Analysis	121
Table 5.3: Linearized Lateral Natural Frequencies of the Drillstring.....	122
Table 5.4: Forced Vibration Response Sensitivity Results	134
Table 6.1: Boundary Conditions for Nonlinear Simulations	148
Table 6.2: Dynamic Analysis Parameters	152
Table 6.3: Comparison Summary of Simulations with, and without, Fluid Damping	175

1. INTRODUCTION¹

Directional and horizontal wells have become an integral part of modern oil and gas operations. They have allowed for the economic development of unconventional hydrocarbon plays and have changed not only the way engineers think about developing reservoir deposits, but the petroleum industry as a whole. These types of wells have tapped a whole new volume of global reserves that was previously thought to be non-existent, effectively destroying the concept of “peak oil” proposed in the 1950’s [1]. While it has become more prominent over the last couple of decades, and is even thought to be a fairly recent advancement by some, directional drilling has actually been around since the late 1920s [2]. The first directional wells were certainly not as complex as they can be today, but the available technology has greatly expanded over the years which has enabled a cost-effective approach of executing these types of projects on a routine basis. However, even with the technological advancements of the 21st century, several challenges remain in terms of operational limitations when drilling these horizontal wells. One of the most prevalent of these limiting factors is the frictional resistance along the wellbore. Several techniques have been developed over the years that help to minimize this restriction, but even the greatest approaches still have their limits. As the envelope is continually pushed to exceed these physical boundaries, groundbreaking methods and technology will be at the forefront of success in these horizontal drilling applications.

This dissertation explores a new method of reducing the effects of frictional resistance in the wellbore by instigating lateral vibrations in sections of the drillstring that are in contact with the wellbore wall. Inducing lateral vibrations in this way, say with a down-hole tool containing some type of rotating eccentric mass, is not an original concept in of itself and has been used in the past as a way to increase drilling performance [3]. Axially vibrations are also commonly utilized, probably more often than their lateral counterpart, in order to achieve similar, if not better, results [4-9]. However, of the available lateral vibration inducing devices (VIDs) on the market, and even among commercial axial VIDs, none consider the excitation frequency of the tool as a parameter that should be matched to the application. This seems neglectful, as anyone with experience in dealing with dynamic systems will immediately wonder about the potential resonance of the system. When drilling with an axial VID, for example, it would be wise to wonder if, and at what frequency, this type of tool might instigate excessively large axial vibrations that could either interfere with the measurement-while-drilling (MWD) tools or cause premature wear of the bit.

1. Portions of Section 1 have been presented previously, and have been reprinted here with the permission from The Society of Petroleum Engineers: Wilson, J.K., Noynaert, S.F. (2017) “Inducing Axial Vibrations in Unconventional Wells: New Insights through Comprehensive Modeling” (SPE 184635). SPE/IADC Drilling Conference and Exhibition. The Hague, The Netherlands. Copyright holder: The Society of Petroleum Engineers.

Alternatively, because lateral waves are known to travel less efficiently through beams [10-12], one may wonder about the effectiveness of lateral VIDs outside of a resonant frequency, i.e. resonance may be required for lateral VIDs to provide a noticeable benefit.

The novelty of this work coincides with the reliable determination of the resonant behavior associated with vibration inducing devices, as well as attempting to quantify the increase in axial force transfer during their use. Specific attention is given to the operation of lateral VIDs, in unconventional horizontal wellbores, while “slide drilling” with steerable mud motors. Through the development of a new comprehensive drillstring model, the effect of various operational parameters on the dynamic behavior of the drillstring, when using lateral VIDs, is explored in great detail. The modeling results also provide insights into the practical implementation of these types of tools. This section lays the foundation for this in-depth study by providing a background of modern horizontal drilling and presenting a literature review of previous research efforts dealing with vibration inducing devices. The current applications and limitations of contemporary drillstring models are also explored in order to determine the best approach for estimating the dynamic behavior of the drillstring when using lateral VIDs.

1.1 Background

The basic components of any drilling operation are the derrick, the rotary drive system, the mud circulation equipment, the drillstring, and the bit (Figure 1.1). The derrick provides structural support for the weight of the drillstring and the rotary drive system. The rotary system is usually an electric driven top drive, but can also be a powered turn-table that is built into the rig floor. The latter is more common on older, smaller, rigs with the majority of modern rigs running some type of top drive system. Torque and fluid is supplied to the drillstring, through the rotary drive system, and is then transmitted down-hole via the various drillstring components. In its simplest form, the drillstring can be divided into two primary sections: the drill pipe, and the bottom-hole-assembly (BHA). The drill pipe is actually an assembly of several hundred “joints”, or individual lengths usually ranging from 30-40 ft, of drill pipe. These tubular components can have a broad range of sizes but generally have the same physical attributes, with the majority of the pipe consisting of a single OD and a single ID and the ends of the drill pipe (roughly 1-2 ft on each end) are usually of a larger OD and a slightly smaller ID. These “Tool Joints” allow for rotary shouldered connections to be machined into the ends of the pipe so that each joint can be sufficiently connected to the next. Located at the bottom of the drillstring, just above the bit, is the BHA. This section of the drilling assembly can additionally be subdivided into three generalized components: the steering mechanism (down-hole mud motor or rotary steerable system (RSS)), the MWD system, and an assembly of drill collars or heavy-weight drill pipe (HWDP) if they are needed.

The steering mechanism is a rather important component of the BHA, but will be discussed later. MWD tools are measurement sensors that record, among a variety of other things, the position of the wellbore through an inclination and azimuth measurement. The inclination is an angle measurement indicating the degree of deflection from a hypothetical vertical line, extending straight down from the surface location. Technically the inclination measurement can range from 0-180°, but very rarely will it ever exceed 100°. The azimuth is a measure of the direction of the wellbore in the North-South, East-West geographic plane. This measurement is always a positive number ranging between 0-360°, with 0° being oriented along the Northern direction. Usually these MWD sensors are run directly above, or relatively close to, the top of the steering component.

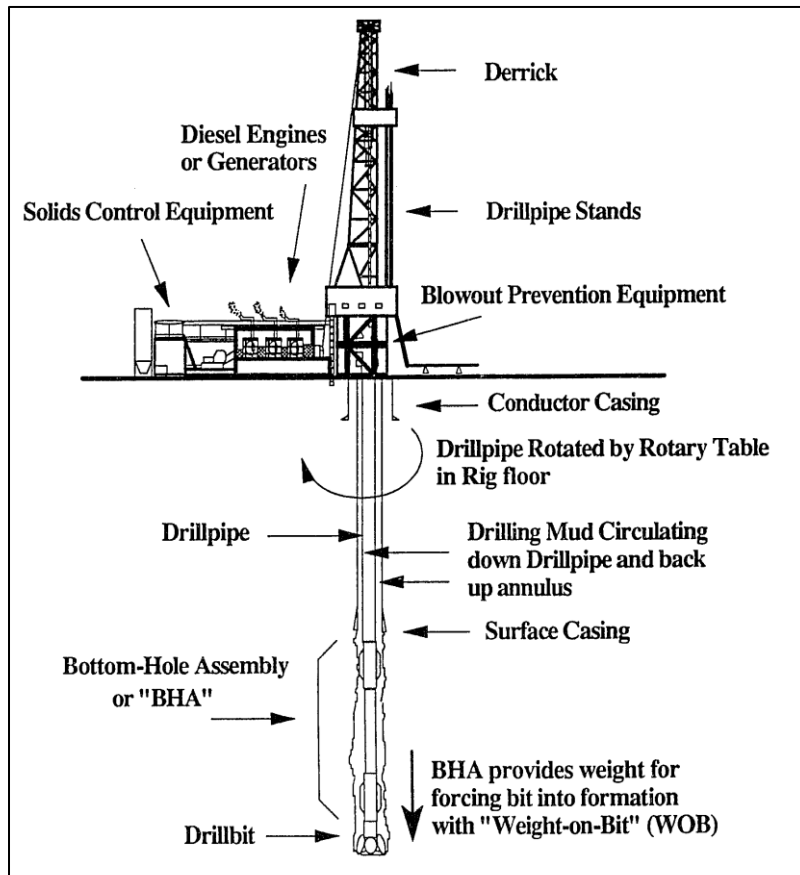


Figure 1.1: Generic Layout of a Drilling System [13]

Above the MWD system are the drill collars and/or HWDP. Drill collars are relatively thick tubulars which generally have constant outer and inner diameters along their length. However slight variations also exists; these include components such as flexible drill collars (“flex collars”), which are primarily used to more easily drill directional portions of the well, or spiraled drill collars, which are thought to help alleviate

differential sticking and help to stir up formation cuttings. HWDP can be thought of as a “hybrid combination” of drill collars and drill pipe. Usually these tubulars have a thicker wall as compared to drill pipe, but are substantially lighter than drill collars; they add some flexibility to an assembly that would otherwise be utilizing drill collars, but still provide a strong resistance to buckling. HWDP also tends to have additional wear pads at their mid-span in order to add more weight without largely affecting the stiffness, as well as provide an additional wear spot. The differences between drill collars, HWDP, and drill pipe are more easily visualized in Figure 1.2.

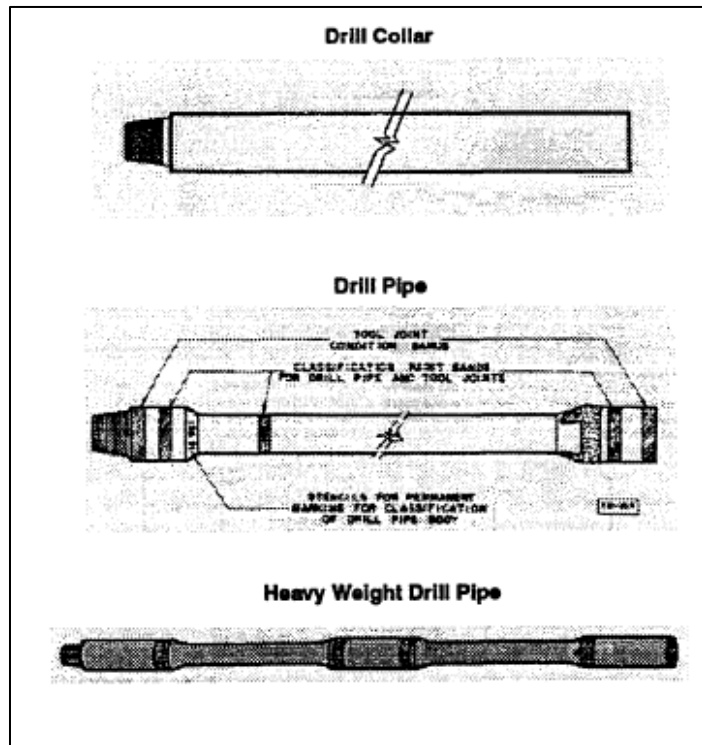


Figure 1.2: Visual Comparison of Drill Pipe, Heavy-Weight Drill Pipe, and Drill Collars [14]

And, of course, at the very bottom of the drilling assembly, is the bit. This component is what physically destroys the formation, via a crushing and/or shearing action, in order to create the wellbore. The exact rock-failure mechanism that occurs will be dependent on the specific bit being used, as well as the environment in which it is drilling. Unfortunately, throughout the course of a well, the formations encountered can vary significantly and homogeneity within a rock is a rarity. For this reason, many types of bits have been developed over the years in order to provide the most efficient cutting structure for a given application. A brief synopsis of these variations can be seen in Figure 1.3. Due to these broad variances, not all bits will behave the same way with respect to dynamic and/or directional characteristics. Therefore, care must be taken to ensure that the bit is matched to the goals of the well and to minimize the risk of premature failure

or under-performance. Polycrystalline diamond compact (PDC) are generally the most common type of bit used for drilling modern horizontal wells. Some common characteristics to consider among PDC bits are aggressiveness/steerability, active/passive gauge length, cutter size, back-rake angle, number/size of nozzles, depth-of-cut (DOC), and number of blades. This is certainly not an exhaustive list, but merely provides an idea of the different considerations that go into the bit selection/design process.



Figure 1.3: Various Types of Drill Bits [15-18]

The aforementioned drilling configurations are rather generalized but are fairly consistent across most operations, with slight variations being made depending on the particular project (for an introduction on the variability of rig operations and drilling assemblies, the reader is referred to several books that provide general knowledge on the subject [19-21]). While the overall layout may be similar across a broad range of jobs, the quality and capability of the various drilling components can vary significantly depending on the geographic location or the financial support of the project. Obviously with larger amounts of monetary

backing, one would be inherently more capable of drilling the “record wells” with state of the art equipment, such as those completed by Exxon in the Chayvo Field [22] or Maersk Oil in offshore Qatar [23]. Unfortunately, most operators are on tighter budget constraints and must often times sacrifice in some areas in order to maximize in others. The success rate of these various optimization efforts will, in large part, depend on the complexity of the wellbore and how well the engineers and field personnel adjust to the challenge.

Traditional oil and gas wells have been drilled in a, relatively simple, vertical orientation. Of course, “simple” should not imply that these wells were not without their own difficulties. One of these challenges, which was a significant problem in the early days of drilling, came to be referred to as the “crooked-hole problem” [24]. Prior to 1927, the only aim of drilling a well was to create the straightest, and most vertical, hole possible. Unfortunately, as surveying methods began to emerge as a standard practice for quantifying and recording hole-deviation in the late 1920s, it became quite apparent that the term “vertical” was being applied more loosely than intended. Anderson [25] surveyed several wells that had already been drilled in order to understand the severity of hole-deviation within the industry. His work demonstrated that “vertical” wells could be substantially deviated from their intended trajectories, with some instances of wells that had drifted to inclinations in excess of 65° . As can be imagined, that much drift from vertical can certainly lead to a missed bottom-hole target.

Clearly this “crooked-hole problem” was a significant issue for wells whose primary intent was to connect a sub-surface location to the surface directly above it. However, it was realized by some that there were potential benefits to intentionally steering the hole away from a vertical configuration. Weaver[2] noted that the first deliberate use of this intentional directional drilling was within the Signal Hill Field in California in 1927, and came about as a means to access oil reserves whose location would have been too expensive for conventional vertical wells. Six years later, in 1933, directional wells began to gain significant notoriety as both a commercially viable alternative to purely vertical wells in Huntington Beach, California [2], and as a valuable tool for relief well drilling, as was seen in Conroe, TX [26]. Since then, directional drilling slowly became a valuable method of reservoir development [27-29]; allowing for course corrections, side-tracking lost tools or collapsed wells, and even avoiding troublesome formations. Yet, it wasn’t until the 1980s that large scale directional drilling began to emerge. This was initially brought about as a means to reduce cost in offshore environments by drilling multiple wells that all originated from the same surface location, with true horizontal wells ($\text{Inclination} \approx 90^\circ$) sprouting up later that decade as a way to increase production from low permeability formations like the Barnett and Eagle Ford shales. Towards the latter half of the decade “conference chatter” was full of examples of success in drilling these intentionally deviated

wellbores. Joshi [30] provides a broad list of references which illustrate this “explosion” of the modern directional and horizontal well.

As the end of 2016 approaches, contemporary horizontal wells have become a standard across the United States. These wells largely have a familiar layout, which can be seen in Figure 1.4, with three primary intervals: the vertical or “surface/intermediate” section, the curve or “build” section, and the horizontal or “lateral” section. The vertical sections are not necessarily purely up-and-down and can actually have a slight inclination to them. Ultimately this portion of the well is not all that different from the conventional vertical wells of the “pre-directional” era, however their direction is much better controlled thanks to the available surveying and drilling technology of the modern day. The drill pipe used in these wellbore sections consists of heavier tubular components which are usually a combination of larger diameter drill pipe, heavy-weight drill pipe, or even drill collars. Most of the axial force transmitted to the bit originates from the pipe in this section of the hole. Apart from the required weight transfer, the size of the drill pipe in this section may also be selected based on strength and buckling criteria as the tubulars may be under considerable tension closer to the surface and significant compression towards the bottom. In these modern wells it is virtually impossible to avoid some degree of buckling within the tubulars contained in the vertical section of the well, but the severity of the buckling can be minimized through proper selection of drill pipe and/or HWDP [31].

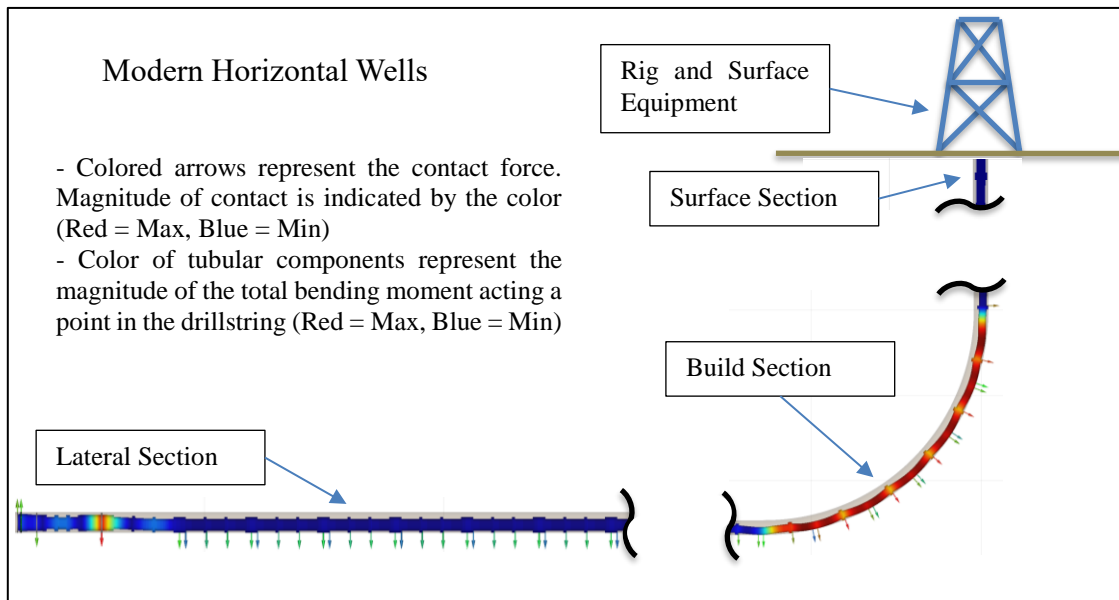


Figure 1.4: General Layout of a Modern Horizontal Well

Conversely, the curved section of the well typically consist of lighter weight drill pipe, in order to minimize the frictional resistance due to the contact forces that occur between the pipe and the wellbore wall. The

buckling in this portion of the well is less of a concern, due to the stress-stiffening effect of the pipe being forced to curve with the wellbore and/or added contact at the mid-span of the pipe's body, but still should be considered as a criteria when selecting drill pipe. Similarly, the portion of drill pipe in the horizontal section of the wellbore is usually lighter in weight, but large enough to minimize the potential for buckling and to support the various loads in which it is subjected to. Buckling in the horizontal section of the well is of less concern than in the vertical portion, due to the added stability from the increased contact force between the drillstring and the wellbore, but is of higher importance than in the curved section because of the general absence of stress-stiffening. In some cases compressive service drill pipe (CSDP) or flexible "flex" collars may also be used in portions of the drillstring, especially closer to the BHA, in order to increase the resistance to buckling while also minimizing the contact force between the pipe and the wellbore wall.

In addition to the three primary wellbore intervals, there can also be intermediate well sections between the vertical and curve, or the curve and lateral portions of the well. These sections are usually straight, with a constant inclination, and are commonly referred to as "tangents". The inclusion of tangent sections in the wellbore's design will be dependent on weight transfer requirements, formation characteristics, or can even depend on how close a well is being drilled to a neighboring well. Drilling tangents can be particularly tricky, in terms of directional control, simply due to the inherent mechanical interaction between the BHA, bit, and the formation; this can be especially true at lower inclinations. Again, proper consideration must be given to the strength and buckling characteristics of the drill pipe used in these sections of a well.

Regardless of the wellbore interval being excavated, all of the aforementioned wellbore sections are usually drilled with some sort of directional control system. The most common of these systems are steerable mud motors and rotary steerable systems. The latter typically comes in two types: a point-the-bit system, or a push-the-bit system. A point-the-bit system (Figure 1.5) tilts the bit in a specified direction in order to steer the well, while a push-the-bit system (Figure 1.6) physically pushes the bit into the formation via actuated pads that are usually mounted within 2-4 ft of the bit. The direction in which the BHA is "steered" is called the tool-face orientation, or TFO for short. The TFO, or simply the "Tool Face" as it is often referred to, is an angle measurement, with respect to the high-side of the wellbore, and is always a positive number ranging between 0° and 360°. Generally an RSS has a "non-rotating" outer housing (this component actually does rotate, only at a much slower rate than the drillstring ≈ 1 revolution per hour) which allows it to be actively controlled along a specified TFO while the drillstring, and the internal drive shaft of the RSS, is continuously rotated. Continuous string rotation is required in order to drill with an RSS, much like conventional "non-steerable" assemblies. This turns out to be particularly beneficial in terms of reducing frictional drag and/or improving hole-cleaning. However, RSS can be rather expensive to operate due to their intricate designs and advanced technology.

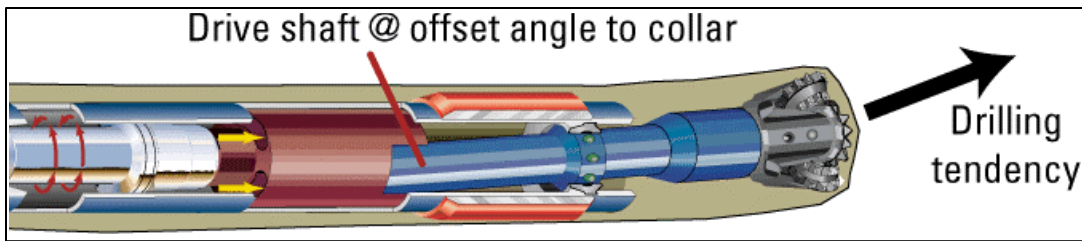


Figure 1.5: Visualization of the Inner Workings of a Point-the-Bit RSS (From [32])

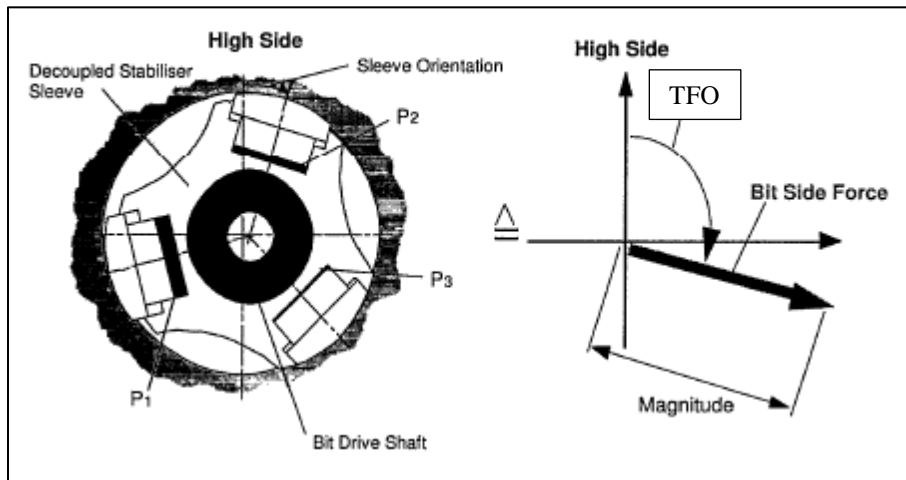


Figure 1.6: Cross-Section of Actuated Pads on a Push-the-Bit RSS (From [33])

The more cost-effective method to directional drilling is the use of steerable mud motors. A typical steerable mud motor can be seen in Figure 1.7, where three distinct sections are noticed: the power section, the bent housing containing the drive train (labeled as “Ti-Flex” in the figure), and the bearing section. The bearing section merely provides the axial support to accommodate the longitudinal force that is applied to the bit, while also providing radial support for the internal drivetrain components. The drive train is the assembly of internal components that transmits torque from the power section to the bit, through the bent housing of the motor. The power section converts hydraulic energy (fluid flow) into additional mechanical rotational energy at the bit via progressive cavities within the tool. Figure 1.8 provides a cross-section of a typical power section to help outline the mechanics of this component. Essentially, these mud motor power sections are just progressive cavity pumps that work in reverse.



Figure 1.7: Down-Hole Steerable Mud Motor (Courtesy of Scientific Drilling International, Inc.)

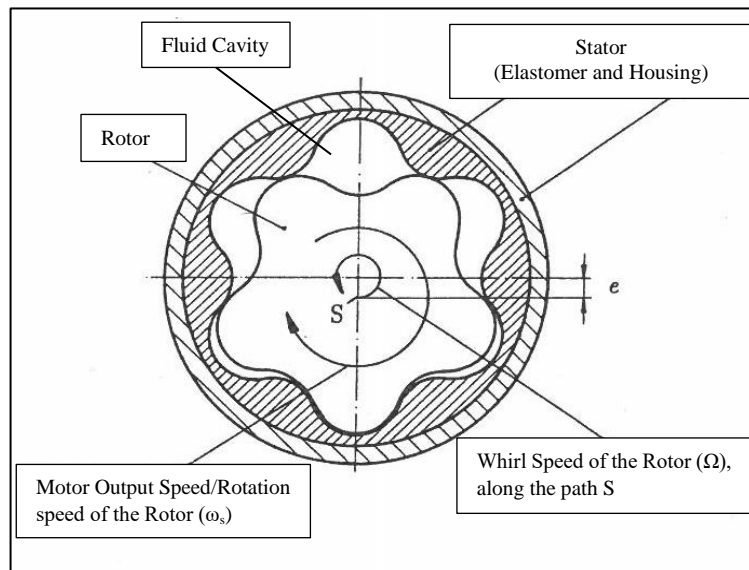


Figure 1.8: Cross-Section of a 5/6 Power Section, Looking Down-Hole Towards the Bit (From [34])

In the above figure, it can be seen that the power section consists of a rotor and a stator. The stator is made of a metallic outer housing with a contoured rubber elastomer lining. The lobe pattern of this elastomer is designed to coincide with that of the rotor and is helically twisted along the length of the power section. These power sections are typically referenced by the ratio of the lobes on the rotor to the lobes on the stator, such as the 5/6 power section shown in Figure 1.8. As fluid flows through the open cavities, the rotor is forced to whirl around within the stator in a counter-clockwise direction (when looking down-hole, towards the bit), which is indicated as path S in the figure. Because the contours of the rotor-stator interface prevent any slippage, the rotor is also forced to rotate clockwise, about its center of gravity, as this whirling occurs. The rotation speed of the rotor about its center of gravity (ω_s) is what provides the additional rotation to the bit. Furthermore, because the motor provides power to the bit via hydraulic means, it allows for the bit to be rotated without drillstring rotation. Drilling ahead in this manner, without string rotation, is known as “slide drilling”. This operation, coupled with the bend in the motor, is what allows these down-hole tools to be directionally controlled. Using the MWD system above the motor, the bend can be oriented during a “slide” in any desired TFO.

The difference between rotary drilling and slide drilling, with a steerable mud motor, can be visualized via the simplified representation in Figure 1.9. When rotary drilling (top of Figure 1.9), generally a larger diameter wellbore will be created because the bend in the motor instigates an off-center rotational motion of the bit about the central axis of the well. A wellbore drilled in this fashion will be straight, or at least straighter, than one that is drilled while slide drilling. When slide drilling (bottom of Figure 1.9) it can be seen how the bit only rotates about its own axis, which is collinear with the wellbore's axis, creating a borehole whose diameter is approximately the same size as the bit. The trajectory created when slide drilling generally follows a curved path whose curvature is dictated by the degree in which the motor is deflected, i.e. the motor "bend angle". It should be noted that the illustrations in Figure 1.9 are very generalized and do not capture the full mechanics of how a steerable mud motor deflects within a wellbore, they merely help to describe the difference between rotary and slide drilling. In reality, the flexibility of the various motor components, as well as the applied torque and WOB, will dictate how the assembly deflects within the wellbore which, in turn, will contribute to the directional tendencies of the motor as well as the diameter of the wellbore that is created.

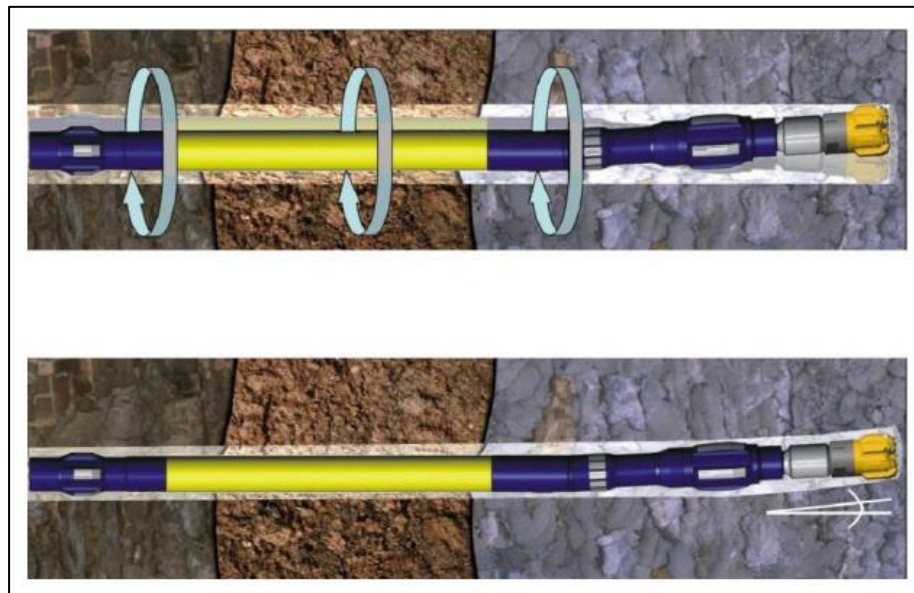


Figure 1.9: Illustration Showing the Difference between Rotary and Slide Drilling with a Steerable Mud Motor [35]

1.2 Problems Associated with Horizontal Drilling

Regardless of the specific tool being utilized for a given operation, or the wellbore section being drilled, care must always be given to the proper planning and execution of each job. In order to provide the greatest chance of success in this planning stage, the pertinent issues associated with these types of wells should be

reasonably understood. Additionally, it is useful to recognize how these problems originate and the potential solutions that can be applied in order to overcome them. One of the principal limiting factors of horizontal drilling is an inherent inefficiency in hole-cleaning. Hole-cleaning is the process in which fluid, flowing back to the surface through the annulus, removes the formation cuttings from the wellbore. Without adequate hole-cleaning the cuttings can overload the wellbore and lead to increased equivalent circulating densities (ECDs) or even pack-offs, where the BHA or drillstring can become physically entrapped in a bed of cuttings. Hole-cleaning for vertical wells is not usually an issue because the annular fluid flow is acting in the opposite direction of the gravitational forces that pull the cuttings back down the wellbore. However, this is not the case for directional wells as the fluid generally flows at some angle with respect to the pull of gravity. Additionally, the drill pipe tends to rest on the low-side of the hole in directional wellbores, which generates an eccentric annular passage on the high-side of the wellbore. This ultimately creates areas of low fluid velocity towards the low-side of the borehole; lower fluid velocities inevitably lead to less “carrying capacity” within the fluid. Because of this, the formation cuttings have a natural tendency to fall out of the higher flow velocities in the upper portion of the eccentric annuli created by high angle wells, and thus are not moved as easily along the well path [36, 37]. This, in turn, leads to the need for higher flow rates in order to compensate for this “settling” behavior of the cuttings. Hole-cleaning issues are particularly troublesome at inclinations above 50°-60° [38], with the worst condition being observed between 65° and 67°[20] due to the “avalanching effect”. Avalanching is exactly what it sounds like; where the cuttings fall out of the higher velocity flow on the high-side of the hole, begin to pile up on the low-side of the wellbore, and then start to topple over each other and tumble back down the well. Inclinations above this 65°-67° range are still inefficient in terms of hole-cleaning, but the “avalanching” of cuttings usually subsides at higher angles.

From a purely hydraulic perspective, the higher flow rates required to make-up for the inefficiency in cuttings transport can lead to an increase in the pressure required to displace the fluid through the system. This situation can be troublesome if the required flowing pressure exceeds the capabilities of the mud circulation equipment or, even worse, if the pressure in the annulus begins to approach the fracture pressure of the formation, i.e. the pressure within the wellbore required to break the surrounding rock. This is especially true in extended reach drilling (ERD) operations where the horizontal displacement of the well path can be larger than the vertical depth of the well by factors of 2 or more [39]. Because confining/pore pressure is largely dictated by the overburden pressure (the pressure generated from the weight of the rock layers above a point in the earth) of the formation, the relatively shallow depth of the wells in ERD operations correlates to a smaller pressure being exerted on the wellbore from the surrounding formation (confining pressure). When higher flow rates are required for hole-cleaning purposes in these types of wells, the increase in hydraulic pressure within the annulus is not counter-balanced by an increase in this confining

pressure, and thus can exceed the formation fracture pressure more easily. This situation can lead to fluid losses to the formation or wellbore stability issues. Additional string rotation is often used in lieu of excessive flow rates to assist in hole-cleaning, but there is also a limit to how fast a drillstring can be rotated due to dynamic concerns [14, 34, 40].

Aside from the reduced effectiveness of hole-cleaning, horizontal wells are also notorious for their increased frictional drag. As can be imagined with long lateral well sections, the numerous contact points within the assembly can lead to a significant reduction in axial force transfer to the bit. This ultimately leads to a lower rate of penetration (ROP). However, it is known that increased rotation rates tend to increase the allowable WOB when drilling these types of wells, which leads to the desire to rotate the drillstring as fast as possible within the dynamic limits of the system. While this is certainly convenient when rotary drilling, it has already been established that directional control sometimes requires slide-drilling with a steerable mud motor. Unfortunately when slide-drilling is required, either for building a curve or making a course correction in the vertical or lateral sections of the well, the ROP is generally reduced not only by the lower WOB that can be applied, but the reduced rotation speed of the bit itself ($RPM_{Bit} = RPM_{Drillstring} + RPM_{Motor\ Output}$). Lower ROP leads to longer drilling times which, in turn, leads to increased costs.

Increased friction in the wellbore can also lead to an increased risk of buckling. Buckling is a phenomenon that occurs when a tubular component loses its ability to support a compressive axial load. When a flexible member reaches its buckling limit, it loses lateral stability and will begin to deflect in an adjacent direction to the applied load. Because drillstrings are confined within wellbores, this lateral deflection is eventually stopped by the borehole, thus generating a new contact point with the wellbore wall. This, in turn, adds another frictional force that opposes the motion of the drillstring. A visualization of buckling in the horizontal section of a well can be seen in Figure 1.10 and Figure 1.11, where the bottom 1,000 ft of drillstring is shown at the total depth (TD) of a horizontal well that was drilled in the northeastern United States. The axis coordinates in the illustrations are in reference to the surface-hole location of the well. In the diagrams, contact forces are represented by colored arrows, with red being a maximum and blue being a minimum. The color of the tubulars represent the magnitude of the total bending moment along the drillstring. Examination of these figures makes it easy to see why buckling can be detrimental to operations, and should be avoided whenever possible; not only does the number of contact points increase along the well, but the bending moments increase significantly along the length of the drillstring. Increased bending loads can lead to accelerated fatigue of down-hole components while, as stated previously, contact forces contribute to diminished weight transfer to the bit. The case of applying 30 klf WOB (Figure 1.10) is certainly more realistic in terms of the target WOB that would be seen during horizontal drilling operations. However, the case of applying 60 klf (Figure 1.11) is shown to illustrate the impact of further exceeding

buckling limits. This illustrates why it is not normally advisable to keep “pushing” on the drillstring when it is suspected that the WOB is inadequate, unless it can be determined that buckling is not the issue.

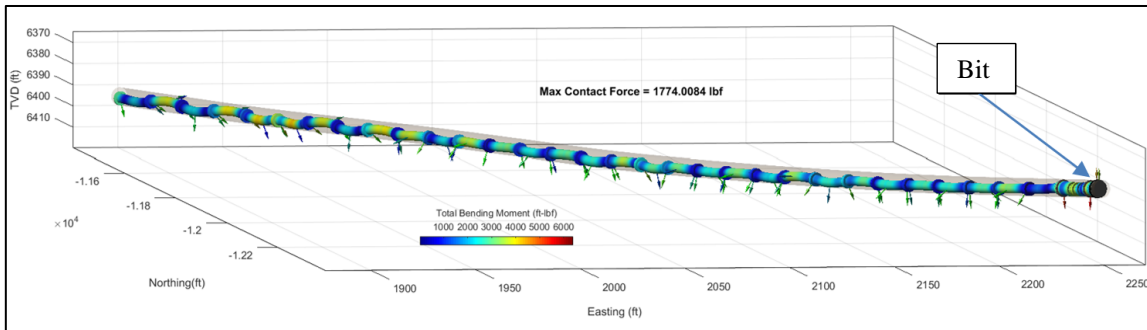


Figure 1.10: Moderate Buckling in an 8 ½" Horizontal Well with 4 ½" Drill Pipe (WOB = 30 klf)

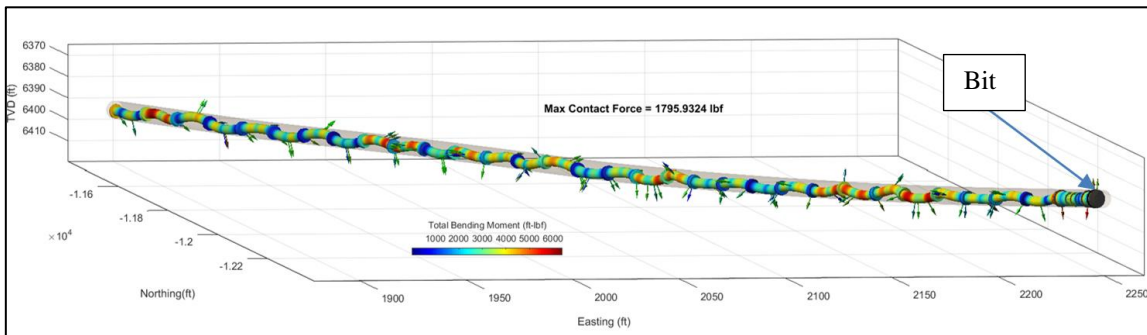


Figure 1.11: Severe Buckling in an 8 ½" Horizontal Well with 4 ½" Drill Pipe (WOB = 60 klf)

It is worth mentioning that WOB is typically a surface measurement that is calculated from a reduction in a “base-level” hook-load value (weight measurement of the drillstring at the surface), which is supposed to be recalibrated periodically throughout the course of drilling a well. While this is a reasonable indicator to the driller of what is going on, this measurement approach will always show a WOB value higher than what is actually being seen at the bit in directional wells; this is a direct consequence of friction in the wellbore. Therefore, the surface WOB measurement should be considered a combination of the actual WOB and the frictional resistance while moving the drillstring. This excess WOB reading, generated from the frictional resistance, is commonly referred to as “weight stacking”. Generally this creates a scenario in which the portion of the drill pipe closer to the vertical section of the well will be under higher compression than the portion of the drill pipe closer to the bit. Because of this, the buckling situations depicted Figure 1.10 and Figure 1.11 are more likely to occur further away from the bit. Irrespective of where the buckling occurs, it is never ideal to have this behavior in the drillstring. Of course, any buckling or post-buckling behavior will

be greatly dependent on the type of drill pipe being used, as well as the curvature and inclination variations of the wellbore. Heisig [41] provides a useful overview of buckling in vertical and horizontal wellbores.

Over the years several methods have been proposed to help alleviate this frictional resistance, such as using fluid additives to help lubricate contact points [42, 43] or lighter drill pipe materials [44, 45]. Unfortunately, the price tag associated with these methods can either be quite costly, at which point it may be more prudent to use a rotary steerable system that can constantly be rotated, or the methods can be time consuming to implement. One of the more recent trends in alleviating the effects of drag within the drillstring has been the use of Vibration Inducing Devices (VIDs). These types of tools are thought to help overcome the effects of static friction by instigating a controlled vibration within the drillstring. The most common type of VIDs are ones that produce axial vibrations [8], as these waves tend to travel more efficiently within the drillstring. However, lateral [3] and torsional [46] VIDs are also seen in drilling operations across the globe. Additionally, it has also been suggested that the pure radial motion of a lateral vibration excitation may serve an additional benefit with respect to hole-cleaning in highly inclined wellbores [47].

1.3 Literature Review

The focus of this study deals with modeling the effects of induced vibrations on the drillstring. In order to adequately explore this scenario, it is important to understand the current state of research with respect to the development and application of VIDs. Additionally, for theoretical investigations, it is imperative to develop a robust drillstring model that can sufficiently capture the intricacies associated with the dynamics of these tools. For this reason, the applications and limitations of modern drillstring models must also be examined in great detail.

1.3.1 Vibration Inducing Devices

Using vibration as a tool for efficiency is not a new concept, and has actually been utilized as early as the 1950's [48] with the development of percussion-like tools that were run directly above the bit. These components provided a hammering effect on the bit which helped to breakdown the formation more efficiently, similar in concept to how vibrations are used for general machining and finishing applications [49-52]. Over the years these methods have received notable attention [53-57] and have come to be referred to as hammer drilling, percussion drilling, or even "vibration assisted rotary drilling" (VARD). While these approaches have certainly shown some benefit, they are not often used for directional applications due to the concern of reduced steering capabilities. Additionally, percussion drilling tools only address the limitations of the bit, i.e. they provide more energy to the bit in order to more effectively breakdown harder formations but, they still require adequate WOB in order to be effective. VIDs, on the other hand, work to overcome/bypass the parasitic drag along the length of the drillstring, which then allows for more WOB to

effectively be applied in long lateral wellbore sections and thus removing the need for any hammering action.

Possibly the first concept of a VID-like device was seen in the 1960's when Angona [10] suggested to produce a dynamic WOB by generating axial vibrations at the surface. This was not directly intended to overcome axial drag in the wellbore, as the concept was not discussed in terms of directional drilling, but was the first notion that generating vibrations in one section of the well (the surface, in this case) could have a positive impact on a different part of the drillstring (the efficiency of the bit). He even hinted at the idea of intentionally inducing axial resonance of the drillstring for the method to be even more effective. While this work could be considered a link between the percussion-like VARD tools and modern VIDs, the latter are intentionally developed to "reduce friction", as is commonly stated, along the length of the drillstring in directional applications.

The idea of "friction reduction", via induced vibrations, is based on the concept of a velocity-dependent friction relationship. Within the context of drilling a well, velocity-dependence can be understood as a combination of two components: a true velocity-weakening effect in which the coefficient of friction decreases with an increase in velocity, and a change in the direction the frictional force is acting. The latter is consistently observed via real-time friction factor monitoring through recording the hook-load at the surface during pick-up, slack-off, and rotating-off-bottom operations (an example is provided in Section 2), and has been presented by several authors over the years [58, 59]. Essentially this can be summarized by the fact that increased rotation speeds will generally decrease the longitudinal drag along the drillstring, and the greatest resistance to axial movement occurs when the drillstring is not being rotated (i.e. sliding). The former case of velocity dependence has been observed in bit studies [60] by noticing a nonlinear relationship between rotation speed and reactive torque, as well as in a study related to metal-to-metal contact [61] which illustrated that both axial (along the movement direction) as well as lateral (perpendicular to the direction of movement) vibrations provided a decrease in the required force to move an object. Additionally this velocity weakening has also been observed in field tests, albeit without measured data to support the observation, by Dykstra [14] who noticed a reduction in surface torque with increasing drillstring rotation speed. Assuming Dykstra's observation was supported by reasonable data, it is likely that this reduction in friction was not related to the reduction in bit-torque with increasing rotary speed, as was the case in Brett's study [60], because his experiments utilized a bull-nose (a non-cutting "dummy" bit that is usually reserved hole-opening operations) instead of a real bit. Mason and Chen [62] presented data that also supports this velocity dependence of torque, clearly illustrating the static/dynamic friction concept; this is shown in Figure 1.12, where the surface torque and rotation speed are both plotted as a function of time. Here it is quite apparent

that a threshold torque exists which must be overcome in order to get the drillstring to rotate. After reaching this threshold value, the drillstring begins to rotate and the required torque greatly diminishes.

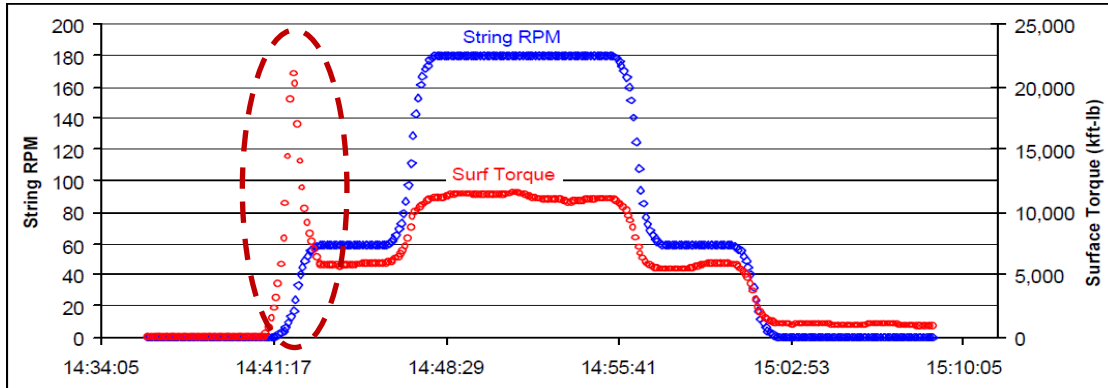


Figure 1.12: Field Observation of the Static/Dynamic Friction Concept (From [62])

Clearly these observations suggest that a velocity-dependent friction relationship does indeed exist, and it is this concept that is generally thought to be the reason why induced vibrations provide a “friction reduction” when drilling. However, when thinking about how VIDs actually function, this idea may be an overly generalized view of what is actually taking place down-hole. For example, axial excitation tools (AETs) are designed to instigate an oscillating axial motion that produces a cyclical velocity along the length of the drillstring, which switches between positive and negative values. Therefore, the net velocity increase with these tools is theoretically zero (i.e. there is no net increase in velocity to provide an overall decrease in the friction coefficient). Intuitively, it would be thought that this might result in a dynamic WOB rather than a net increase in axial force transfer. This is supported by down-hole WOB data that has been recorded while using these types of devices [63, 64], as can be seen in Figure 1.14 and Figure 1.13. Obviously this is not the standard “friction reduction” behavior that is typically quoted as the tool’s primary method of operation. However, this cyclical axial force behavior most likely helps the drillstring to “break free” from ledges and stuck-points along the length of the assembly which, in turn, would give the impression of less resistance to axial movement (i.e. lower effective friction coefficients). This “axial agitation” may also help to explain how these types of tool aid in mitigating friction-induced stick-slip fluctuations as well; although stick-slip caused by depth-of-cut (DOC) variations could still potentially be a risk. Furthermore, the induced dynamic WOB (soft hammering) may serve to increase the effectiveness of the bit, which would directly contribute to an apparent increase in ROP.

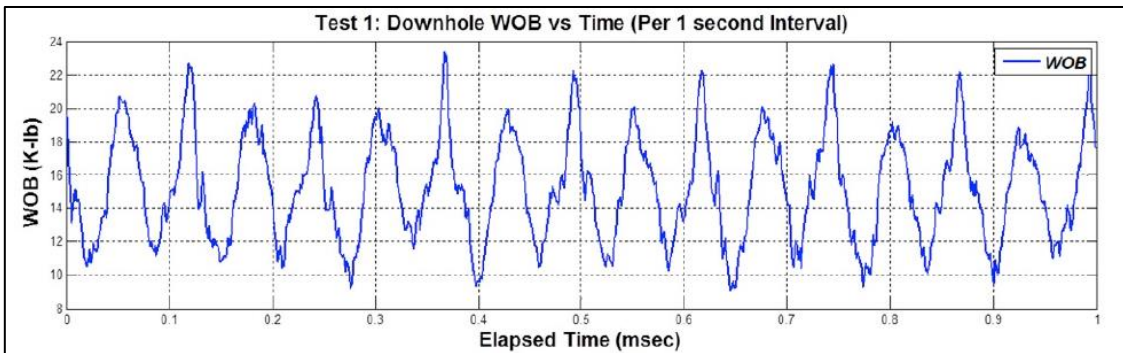


Figure 1.13: Example of Dynamic WOB from an AET (From [63])

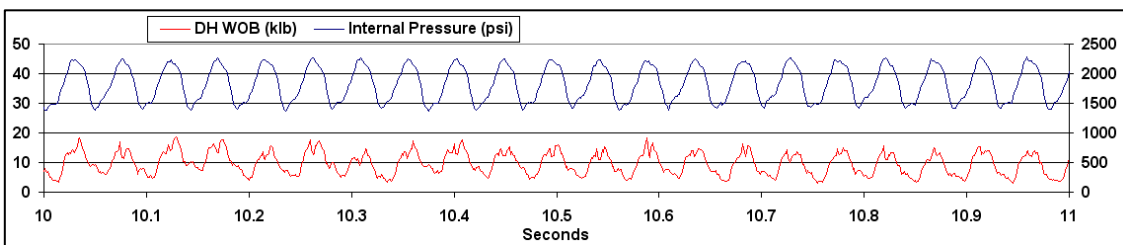


Figure 1.14: Example of Dynamic WOB from an AET (From [64])

A few authors, which were more adamantly convinced about the “friction reduction” provided from axial oscillations, have attempted to measure the increase in axial force transfer through tubing when using these axial vibration tools. However, it appears that their data isn’t necessarily “concrete”. Robertson et al. [65] experimentally measured the input and transfer forces through coiled tubing with, and without, axial vibrations in the system. While an initial look at the data may be convincing (Figure 1.15 and Figure 1.16), the experiments do not appear to have been well controlled, so it is difficult to say if the increase in force transfer was actually due to the induced axial vibration or an artifact of how the input load was applied. For example, for the case without using an AET (Figure 1.15), it can be seen that the applied force (blue line) is increased in incremental steps, with little change in the transferred force (pink line). Although, a slight dynamic force event, occurring slightly after 410 seconds, seemed to minimally increase the transferred force. Alternatively, the test performed with the AET (Figure 1.16) showed a significant increase in transferred force, but with a vastly different applied force history. Instead of increasing the applied force in a step-wise manner, as was done in the case of Figure 1.15, it appears that the applied force was repetitively increased and decreased until the transferred force achieved an acceptable value. This inconsistency in testing procedures certainly raises questions about the integrity and reliability of the results. It would have been far more favorable for the authors to present data that showed consistency and repeatability in the experiment. Newman [7] performed a similar experiment (Figure 1.17), again with coiled tubing, and developed an adjusted Torque and Drag model that matched the data well. However, the specifics of the

experiment and the model were not discussed in much detail and thus are not particularly useful for a theoretical understanding of how these tools actually work.

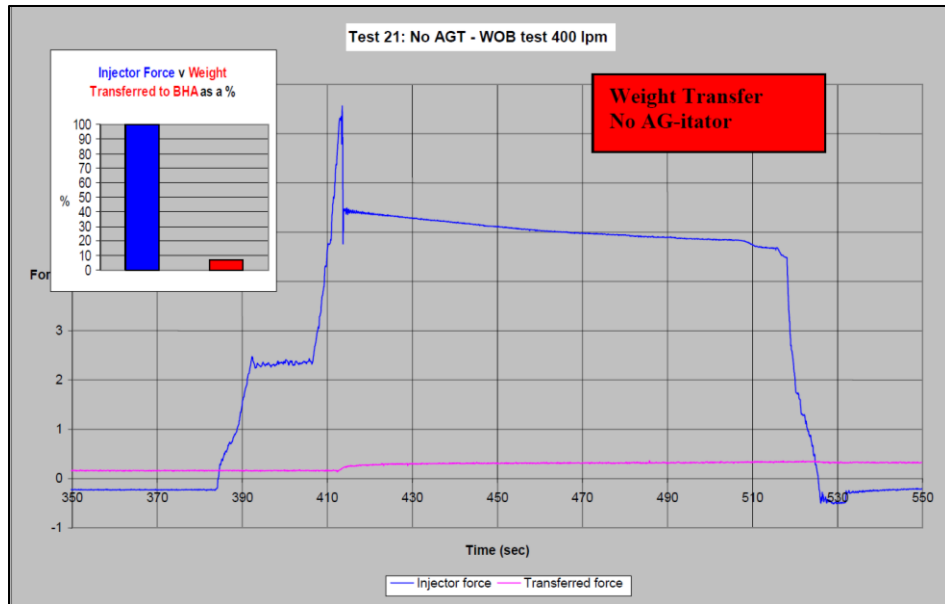


Figure 1.15: Coiled Tubing Axial Force Transfer Experiment – No AET (From [65])

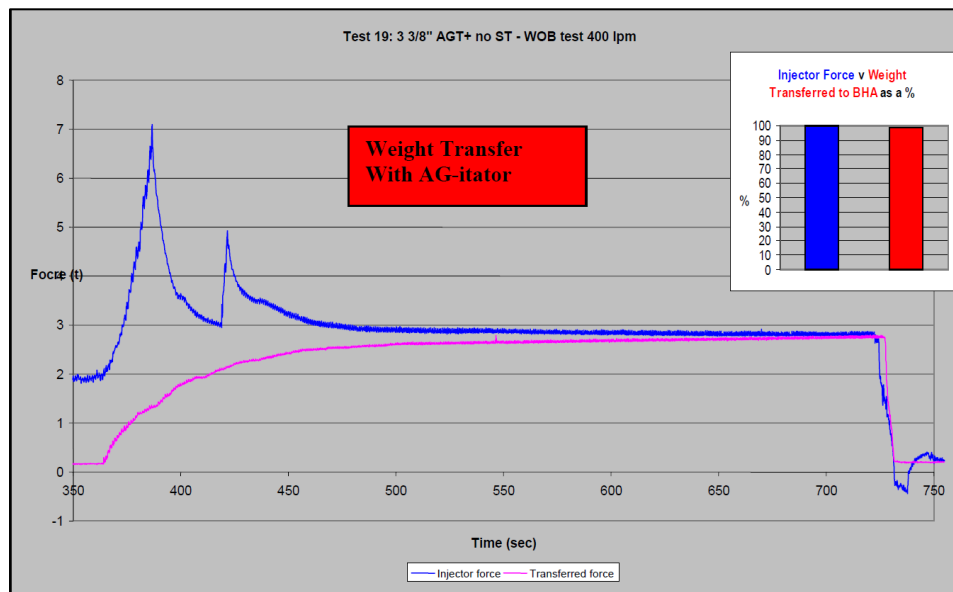


Figure 1.16: Coiled Tubing Axial Force Transfer Experiment – With AET (From [65])

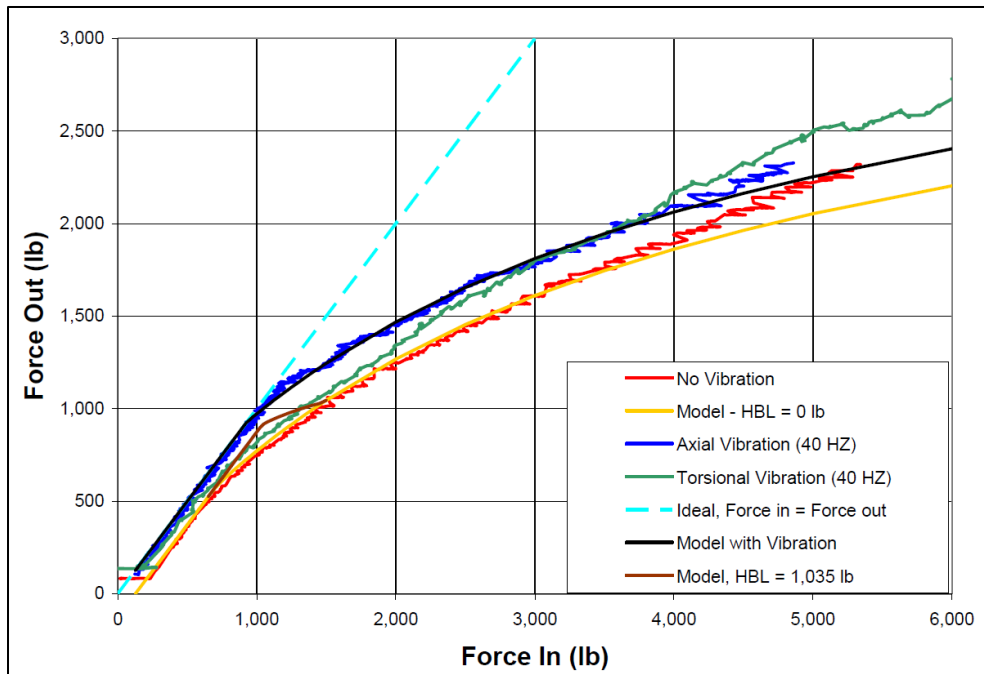


Figure 1.17: Experimental Axial Force Transfer While using an AET (From [7])

Despite these somewhat uncertain results, the usefulness of the tool cannot be discredited due to the positive field trials that have been run over the years, especially with axial vibration tools [4-9, 66]. However, as already mentioned, a fundamental understanding, of exactly how these tools work, is lacking. There have been a few crude attempts at modeling these tools with either a simplified mass-spring system [63, 67, 68] or a modified torque and drag model [69], and an even fewer number of true theoretical studies [70-72]. Of these limited references, none have explored the possibility of inadvertently exciting an axial resonance within the drillstring. Although, the possibility of resonance with these tools is acknowledged via applications to fishing operations [67, 73] and is even suggested as a possible way to help improve the effectiveness of such a tool [63] when drilling. In part, this lack of analysis, regarding the resonant behavior of the system, may be due to a deficiency in the available modeling techniques for examining the nonlinear dynamics associated with drilling.

Lateral excitation tools (LETs) have also been shown to be effective at improving drilling efficiency [3], albeit to a far lesser extent. This could be due to previous observations that lateral vibrations are less effective than their axial counterparts [7], however, just as the case with axial vibration tools, consideration has never been given to the frequency in which these systems were excited (except in a paper that was published as a result of the initial work done for this study by Wilson and Heisig [47]). Axial waves are known to travel more efficiently throughout the drillstring than lateral waves [10-12], therefore it may be crucial for the

lateral excitations to induce a resonance within the drillstring in order to be most effective. Axial vibrations may be effective outside of resonance due to their propagation efficiency, however this may also lead to adverse dynamic effects on the BHA if care is not taken to avoid resonance with axial vibration tools. Or perhaps, as mentioned earlier, operation within an axial resonance range would also increase the efficiency of an AET; that has yet to be determined.

1.3.2 Drillstring Dynamics Modeling

The general absence of adequate analysis of VIDs, their potential resonant behavior, and the lack of understanding of the underlying physics, perpetuates the idea that sufficient modeling is unavailable to researchers exploring the concept of inducing vibrations while drilling. Therefore it becomes necessary to understand what limitations exist on current modeling approaches and how these limitations would prevent proper modeling of vibration inducing devices. In order to fully understand the current state of drillstring modeling it is important to recognize the foundation of dynamic drillstring analysis.

Pioneering in this field began with the work of Bailey and Finnie in 1960 [74, 75] who investigated the axial and torsional natural frequencies of an “ideal” (no tool joints) drillstring using an analytical technique, and attempted to correlate their model with field measurements. However, they noted that the field measurements did not necessarily match their predictions. This could have been either a limitation in their modeling approach or a limitation in their measurement capabilities, and it very well could have been a limitation of both. It was recognized that the measurement device that was used for the tests was of “*questionable accuracy*” and they additionally noted that the data suggested a coupling between axial and torsional dynamics which was not accounted for in their analytical model. Although, the coupling observation may have been related to the excitation from the bit [76] rather than the inherent coupling of the tubular components.

The decade following Bailey’s and Finnie’s publications, several analytical/semi-analytical studies were presented. Bradbury and Wilhoit [77] verified that modeling the drillstring as “ideal”, with no tool joints, was sufficient for analyzing longitudinal and torsional vibrations, except at high-frequencies. They analyzed both a simplified tool joint, which was represented via a sudden change in OD and ID, and a realistic tool joint, which has a more gradual transition in diameters. It was determined that the simplified tool joint had a rather small effect on the axial and torsional wave propagation throughout the drillstring, and the actual tool joints had even less of an effect. This result was also determined to be independent of drillstring length. Paslay and Bogy [76] first explored the effects of axial bit excitation on the dynamic response of the drillstring and concluded that surface boundary conditions did not significantly influence the system’s response near the bit, which might even contradict Angona’s [10] vibration tool concept discussed earlier.

They also suggested that axial vibration generated at the bit could be comparable in magnitude to that of the applied WOB of the system. Grahm et al. [78], and Frost and Wilhoit [79], were the first to investigate lateral dynamics and its effect on bending stress. Hsu and Wilhoit [80] also explored lateral vibrations, but with the addition of wellbore contact considerations. Probably the most interesting conclusion from their study was the observation that the normal (axial-acting) stresses in the drillstring, which could be due to axial or bending loads, are of much greater significance to the overall stress field than shear forces; in a sense, this was supported by claims made several years afterwards that bending loads/vibrations are a significant form of failure for down-hole components [81]. Huang and Dareing [82] looked at the dynamic stability of vertical drillstrings with fluid effects; their work suggested that the viscous fluid forces could have a stabilizing effect on the system. Frohrib and Plunkett [83] determined that the effect of curvature had an effect on the lateral dynamics of the drillstring via a stress-stiffening behavior. Dareing and Livesay [84] later determined that friction effects were also important in the modeling of axial and torsional dynamics, and were able to obtain reasonable agreement between modeling predictions and field measurements.

While all of the above mentioned works were certainly notable contributions to drillstring dynamics research, and really embody the first decade of this type of study, none can be directly applied to induced vibrations in horizontal wellbores. Exploring the mechanics and dynamics associated with modern unconventional wells generally requires a modeling approach that goes beyond these semi-analytical methods. This is primarily because of the frictional wellbore contact, geometric nonlinearity (large displacements, small strains), and the known elastic coupling between the various degrees of freedom of the drillstring. Understanding these general requirements for modeling, researchers have greatly expanded the volume of literature available on the topic of drillstring dynamics since the 1960's and, as a result, the "database" on drillstring dynamics has become rather immense and somewhat over-whelming. However, it has been noticed that a large portion of "drillstring modeling" endeavors focus on very case-specific formulations that cannot be applied outside of a particular scenario. Because of this it would be impractical, and rather pointless, to attempt and summarize each individual model that has been developed over the last 40 years within this manuscript. Therefore, in investigating the post-1960s drillstring dynamics studies, the review is limited to the discussion of works deemed most significant for modeling induced drillstring vibrations under realistic conditions, or notable (novel) contributions to the field of drillstring mechanics and dynamics modeling. The main qualification for a "significant model", in the author's opinion, is the ability of the model to represent the actual drilling environment, to a reasonable degree, and subsequently capture how changes in this environment will affect the static and dynamic response of the drillstring. This equates to the incorporation of specific considerations within the model such as applied WOB, torque-on-bit (TOB), rotary RPM, elastic coupling, wellbore contact, 3D wellbore trajectories, friction, and fluid

contributions. This brief list is by no means exhaustive, but provides some guidelines for consideration in determining what constitutes a useable model for general drillstring analysis.

Nicholson, Jr. [85] provided the first numerical study of drillstrings by using the finite element method. This approach greatly expanded the applicability of drillstring modeling because it allowed for a discontinuous drillstring, i.e. the model did not have to be simplified to a constant outer and inner diameter configuration along the length of the drillstring. Nicholson's approach examined the static deflection of drillstrings in straight wellbore sections, of varying inclinations. He accounted for the contact between the drillstring and the wellbore using a penalty approach, which has been shown to be a valuable method of accounting for this source of nonlinearity over the years. The penalty approach for modeling wellbore contact iteratively determines if the drillstring comes into contact with the borehole; if contact is detected, then a restorative (contact) force is activated to keep the drillstring confined within the wellbore. While this model was relatively robust, it did not account for any torsional coupling and it was limited to purely static analysis. However, this work showed the value of the finite element method for analyzing drillstrings. Eronini [86] went a step beyond Nicholson Jr. and provided the first time-domain analysis of drilling assemblies by exploring the surface- and bottom-hole dynamics of drillstrings in straight and deviated wellbores. His model was rather broad and included a bit/formation interaction model, viscous fluid forces, and elastic coupling. Eronini was able to quantify a nonlinear relationship between WOB and ROP and additionally noted that mud pressure variations had a noticeable effect on the WOB and torque fluctuations. One of his more subtle conclusions was that, "*bending signals have frequencies about the same as the rotating speed*", which fully supports conclusions made by Dykstra over 20 years later that mass imbalances were a major source of down-hole vibration [87].

In 1978, Millheim et al. [88] used a commercial finite element software to examine the directional tendencies of BHAs via static analysis. The guiding principle behind this approach was that the lateral bit force, generated by the deflection of the BHA, provided the potential for the assembly to drill directionally. This work was later expanded [89] to explore the effect of BHA dynamics on the directional tendencies of the bit. Through their studies the authors were able to identify different forms of rolling friction behavior: low energy stable, moderate energy unstable, high energy stable, high energy unstable; these would later become known, in the present industry vernacular, as "snaking", whirl-transition with slight impacts, whirl-transition with large impacts, and full-whirl. While the approach is fairly reliable, it would not be very practical to rely on a commercial finite element software for analyzing the static and dynamic behavior of drillstrings. This is primarily due to a lack of visibility behind the underlying equations, but also because the setup of such an analysis could be quite involved. Brakel [90] also explored dynamic BHA behavior and its effect on the directional characteristics of the bit, through the development of a new finite element model built specifically

for analyzing drillstrings; he additionally incorporated a bit/formation interface relationship that had not been done previously. This type of approach, one “built from scratch”, would certainly be more promising for future research since it allows for the complete control of the computational algorithms.

The first application of advanced modeling to the lateral dynamics of BHAs came via Burgess et al. [81], where natural frequencies and mode shapes were calculated in order to reduce MWD and drilling tool failures that were suspected of being related to transverse dynamics. His model indirectly coupled axial and lateral displacements through an added axial force term in the drillstring’s stiffness matrix. Shyu [91] expanded on this axial-lateral coupling by thoroughly examining its effect in stabilized drill collars. Additionally, Shyu was the first to account for added fluid mass within the drillstring as well as the hydrodynamic mass of the drilling mud surrounding the pipe. Noting this observation of fluid effects, Apostal et al. [92] examined how the fluid might influence the lateral damping characteristics of BHAs using a forced-frequency approach. This investigation was very insightful as the authors examined experimentally derived fluid damping, and were able to consider arbitrary wellbore shapes. Payne [13] explored similar forced-frequency computations to a greater degree, but ultimately reached similar conclusions which showed the practicality of a forced-frequency approach to drillstring/BHA dynamics.

In 1993, Jansen [93] extensively examined the nonlinear dynamics of drill collars via analytical techniques, similar to the previous efforts of Shyu [91], but also developed a full-string finite element model to analyze the dynamic characteristics of various drillstring components within the wellbore. However, he noted some computational limitations to his full-string modeling such as a lack of Eigen-value analysis capabilities and insufficiencies in analyzing higher degrees of nonlinearity. Due to his analytical model being of limited usefulness to general scenarios, Jansen’s modeling approach would be insufficient for analyzing the present problem of induced vibrations.

Within that same year a thesis was published by Heisig [34] which derived a new drillstring model based on nonlinear, spatially-curved, finite-beam elements. The mathematical approach behind this study was quite clever, and incorporated all of the effects that had previously been investigated: geometric nonlinearity (large displacement-small strain), a penalty approach for frictional contact, three-dimensional wellbores, and the added mass and damping due to hydro-dynamic effects from the drilling fluid. Additionally, he incorporated the fully-coupled elastic displacement within the derived beam model. This lead to a rather robust computational tool that could predict the nonlinear-static and linearized-dynamic behavior of drillstrings in three-dimensional wellbore profiles. However, Heisig was limited to the “standard drillstring assumptions” of the day which stated that shear beam deformations, gyroscopic effects, and lateral rotary inertias are all considered negligible.

Dykstra [14] briefly examined the applicability of ignoring gyroscopic effects and lateral rotary inertias, in his study of lateral BHA dynamics and its effect on down-hole tool failure, and concluded that these are sufficiently valid assumptions. However, his results may not necessarily apply to all well configurations. The primary reasoning for ignoring gyroscopic effects is the fact that the drillstring is confined within the wellbore and, therefore, is not physically able to deflect far enough in a lateral direction for gyroscopic effects to provide much of an effect at the low rotary speeds typically seen in drilling applications. Based on this reasoning it can be understood how the lack of gyroscopic effects may be considered more appropriate within smaller wellbore diameters with low radial clearance values, and the applicability of the assumption may change depending on the drillstring-to-wellbore diameter ratio. Unfortunately Dykstra did not examine such an effect on the gyroscopic characteristics of the drillstring. Regardless of the applicability of the results, Dykstra's model was rather robust and he was able to draw an interesting conclusion about rotational resonance. This observation, which has practical implications when attempting to optimize field operations, showed that lateral vibrations can be decreased by increasing the rotational speed above a resonant range, at low rotation speeds. However, at higher rotation speeds he noted that the opposite holds true and an increase in rotation speed will only further increase the vibration response. This conclusion is likely related to the onset of whirl-like behavior; if whirling is induced, then continued increases in rotation speed will only exacerbate the problem. While these were interesting results, Dykstra's work still left the question open as to if shear beam deformations were necessary to include within a drillstring model. This was probably not done out of negligence, it simply was not clear how to apply proper shape functions of a Timoshenko-like finite element model at the time. Most likely, this is why shear beam deformations had not been examined up to this point in the literature.

Belaid [94], in 2005, appears to be the first to have considered shear-deformations as a necessity for modeling drillstrings. Although his investigation was limited to torque and drag (static/quasi-static) studies, it was still based on a method that somewhat resembles the finite element approach through its segmentation of the drillstring's domain. It wasn't until four years later that this Timoshenko-like beam assumption was incorporated into a fully dynamic model [95] for investigating the dynamics of BHAs, albeit this study was limited to a drill collar section in between two stabilizers in a vertical well. Ritto [96] later expanded the shear-deformation assumption to a full-string model through an investigation of the stochastic dynamics associated with drilling in a vertical well. Since then, several studies have been published that incorporate shear beam deformations for general static and dynamics analysis of BHAs and drillstrings [97-100], which suggests a sense of necessity among researchers in this field to include these effects. However, there hasn't been a strong justification as to why this sudden interest in shear deformations has occurred. Realizing this, Al Dushaishi [101] developed both an Euler-Bernoulli-like drillstring model (without shear deformations) and a Timoshenko-like drillstring model (with shear deformations) and directly compared the two with

respect to dynamics in a vertical wellbore. He noted that, within the range of typical drillstring rotation speeds, shear-deformations are completely negligible in vertical wells. Again, this is attributed to the relatively long unsupported length of drillstrings, and thus the large length-to-thickness ratio of the beam. It would be interesting, and somewhat necessary for the sake of completeness, to perform a similar study for horizontal wells as significant contact occurs along the drillstring's length which can result in a "simply supported" scenario, or even more of a "fixed-simply supported" scenario, of relatively short beam sections ($\approx 5\text{-}10$ ft).

Of the published literature to date, Heisig's model appears to be the most robust in terms of what it accounts for and how it can be applied. Additionally, it is worth noting that, his is the only model that has been routinely validated through various researchers from both a mechanical loading [102, 103] and a dynamic perspective [104, 105]. Heisig's model was even later expanded, using a modified Newmark approach, to simulate the fully nonlinear-dynamics of drillstrings in horizontal wells [40]. However, as powerful as this tool seems to be, there are still limitations that prevent it from being directly applied to modern drilling operations without some sort of adjustment. Predominantly these limitations include the incorporation of complex drilling tools such as steerable mud motors, RSSs, and eccentric stabilizers. Also, as already discussed, it would be rather interesting to understand if shear deformations, gyroscopic effects, and lateral rotary inertias can truly be neglected in horizontal wellbores.

1.4 Statement of Purpose

The proposed research aims to examine the dynamics associated with lateral vibration inducing devices, or lateral excitation tools (LETs), in horizontal wellbores. Through this effort, a comprehensive drillstring model is developed to fully analyze the problem. Apart from the detailed analysis of LETs, the new drillstring model is intended to provide definitive clarity on whether or not the "standard drillstring assumptions" are sufficient for modeling the nonlinear behavior of drilling assemblies in horizontal wellbores. These traditional assumptions are: neglecting the shear deformation of beams, ignoring gyroscopic effects, and disregarding lateral rotary inertias. It is further intended that the developed drillstring model will be robust enough to analyze problems outside of the scope of induced drillstring vibrations.

In order to gain confidence in the model, it is numerically validated through comparisons to analytical formulations, commercial software, and previous nonlinear models. Once the model is developed, and computational confidence has been established, the algorithms are expanded in order to fully examine the dynamics associated with the operation of an LET. Linearized dynamic computations are analyzed to understand how various operational conditions (WOB, wellbore diameter, mud properties, inclination, well path curvature, trajectory variations, and drill pipe dimensions) affect the resonant behavior of a drilling

assembly using this type of tool. Nonlinear simulations are then performed in order to more completely understand how an LET impacts the drillstring. The major benefit to examining the nonlinear behavior is understanding how well the linearized analysis represents the nonlinear system, as well as how using these types of tools affects the WOB. The latter is critical in understanding the potential change in ROP while using LETs.

The primary novel contribution of this work is the reliable and effective method of predicting the resonant behavior of the drillstring when using LETs. This resonant behavior may, or may not, result in an increased benefit to “friction reduction” along the length of the drillstring. In the pursuit of this steadfast resonant frequency prediction, a secondary novel contribution is provided through the development of a comprehensive drillstring model which combines all considerations from previous studies in order to provide the most robust model to date. This model accounts for the fully coupled flexibility of the drillstring, geometric nonlinearity (large displacement, small strain), automatic determination of wellbore contact points, friction acting between the drillstring and the wellbore, stabilizer clearance, three-dimensional wellbore profiles, added fluid mass and damping effects from the hydrodynamic forces generated between the drillstring and surrounding fluid, complex tool geometry (including steerable mud motors, rotary steerable systems, and eccentric stabilizers/components), shear beam deformations, lateral rotary inertias, and gyroscopic effects. Additionally, the progression of the research has led to the development of a new nonlinear fluid-damping model which is utilized to examine the potential impact of fluid forces on the overall response of the drillstring due to the use of LETs.

The sections of this dissertation are organized in such a way so that the reader can follow the development process of the research. Section 1, obviously, provides a background to directional drilling and the thought process which has led to the desire to explore the concept of VIDs. Due to the lack of available modeling for properly analyzing these types of tools, which became apparent through the literature review in Section 1, Section 2 outlines the derivation of a theoretical nonlinear drillstring mechanics model capable of analyzing such scenarios. Section 3 then utilizes a nonlinear finite element approach in order to solve these equations for the nonlinear-static, linearized-dynamic, and fully nonlinear-dynamic scenarios of the “drillstring problem”. Section 4 provides detailed validation examples which illustrate that the developed equations, and associated coding algorithms, are producing accurate and reliable results. Once computational confidence has been established through the analysis contained within Section 4, the model is slightly adjusted to properly analyze the dynamics of the drillstring under the action of induced lateral vibrations in a horizontal wellbore. A thorough sensitivity study of these tools is presented in Section 5 via a forced-frequency, linearized-dynamic, approach. Section 6 then takes the analysis a step further by examining the fully nonlinear-dynamics associated with LETs in order to quantify their effect on the WOB.

In closing, Section 7 provides a synopsis of the conclusions drawn through the various studies and presents thoughts on potential future research based on the current results.

2. DERIVATION OF DRILLSTRING MECHANICS

Proper simulation of the down-hole environment requires a robust model that can account for the various intricacies of the drillstring, the wellbore, the drilling fluid, and how these three interact with each other. Of the models found in the literature, Heisig [34] presents the most practical in terms of modeling real world applications. In his thesis, he derives a drillstring model based on a geometrically nonlinear beam element. The resulting finite element formulation led to a computational tool capable of calculating the nonlinear-static and linearized-dynamic behavior of drillstrings, and has been shown to be effective for estimating the general dynamics of a drilling system [105]. Heisig's equations were later expanded [40] to perform time-domain simulations which offered a way of analyzing the complex nonlinear-dynamics associated with the down-hole environment. While these works have led to a rather impressive model that has served the industry well over the past couple of decades [41, 102, 104, 106-109], there is still room for expansion in the mathematical formulation.

The assumptions behind Heisig's model have neglected three main aspects of beam mechanics. These simplifications are stated as follows:

- 1) Gyroscopic effects are considered negligible
- 2) Rotational inertias about the lateral axes are considered negligible
- 3) Infinite Shear Stiffness. This "Kirchhoff Rod" approach can be thought of as the three-dimensional equivalent to the traditional Euler-Bernoulli assumption for planar beams, which ignores shear beam deformations.

These characteristics, which have been considered "standard assumptions" in a majority of early works on drillstring modeling [13, 14, 90, 93], have in part been removed in more recent studies [94-96, 100]. However, as alluded to earlier, the more recent models are not of practical use for real world applications due to their lack of detail with respect to nonlinearities and/or variations in well path trajectory.

The first two assumptions listed above have been investigated previously [14] in limited nonlinear-dynamic studies, leading to the conclusion that they are sufficiently valid for rotary speeds of up to 90 RPM. However, speeds above this threshold were not examined. Similar conclusions can also be observed in general rotor dynamics studies [110] at some threshold rotation speed, the magnitude of which will be dependent on the beam or rotor being investigated, after which these effects can play a significant role. In general, these types of studies make it apparent that gyroscopic effects are indeed negligible if operating below a few thousand RPM. However, there are some authors [111] who feel that gyroscopic effects are necessary for proper

rotational dynamic analysis of beams, but the speed in which the beam is rotated will still dictate how severe these contributions are. Because the maximum rotation speed that can reasonably be applied to a drillstring is about 200 RPM, and even then it is a rare occurrence in modern drilling applications, it is rational to assume that gyroscopic effects can be ignored. Regardless of this reasoning, the gyroscopic contributions will be included in the present formulation in order to provide a definitive comparison between the dynamics with, and without, the effects of gyroscopic moments in horizontal wellbores.

Shear beam deformations are typically left out of drillstring models simply due to the, rather large, length-to-thickness ratio associated with drilling assemblies. However, it is important to note that neglecting shear deformations in beam modeling has been known to lead to improper coupling between lateral and torsional displacements [112], although this concern may be more important when dealing with the warping characteristics of noncircular beam cross-sections. Furthermore, a growing number of drillstring studies are incorporating shear deformations within their beam models [94-96, 100] which suggests that there is a sense of necessity, among the researchers in this field, to account for these types of lateral rotations. For this reason it is desired to compare the simulated dynamics of drillstrings with, and without, shear deformations. Al Dushaishi [101] provided a comparison of modeling shear deformations in vertical wells, leading to the conclusion that they can be ignored for drillstring dynamics modeling. However, as mentioned in the previous section, it is necessary to test this theory in horizontal wells due to the increase distribution of contact points which ultimately leads to smaller effective length-to-thickness ratios in the drillstring. Additionally, including shear deformations within the beam model does not restrict the length of individual beam elements, which was suggested to be necessary when ignoring these effects [14].

While it is suspected that all three of the “standard assumptions” are fairly reasonable for the present problem of inducing lateral vibrations in modern horizontal wells (Wellbore Diameter $\approx 8 \frac{3}{4}''$, Drillstring OD $\approx 4 \frac{1}{2}''$), all of the previous assumptions are neglected. This leads to a more comprehensive model that can be compared directly to previous efforts in order to fully understand the applicability of the traditional simplifications. With this understanding a drillstring model is derived with assumptions based only on mathematical justification or practical implementation. These are listed below:

- 1) Each beam has a hollow circular cross-section. This is the standard configuration for any tool that goes down-hole. Occasionally there are special-purpose tools that have unique cross-sectional configurations, however they are still circular in nature. Reductions in stiffness of components, due to geometry variations, can be captured by determining an equivalent ID of the cross-section based on the area moment of inertia.

- 2) The drillstring/BHA material behaves elastically (i.e. no plastic deformation). Once a component has plastically deformed it is considered damaged. Continued operation of damaged components is not a recommended practice and, therefore plastic deformation is not of interest in the present study.
- 3) Beam cross-sections remain plane, but not necessarily perpendicular to the central axis of the beam (i.e. cross-sections do not warp under torsional loading). This can be mathematically proven for the elastic deformation of hollow circular cross-sections [113].
- 4) Each beam has constant cross-sectional properties (E , ρ , I , A , m). This makes it fairly simple to create complex drilling assemblies as a linkage of multiple beams with different characteristics.
- 5) A beam may lie in a constant curvature section of the wellbore whose trajectory can be estimated by the “Minimum Curvature Method” [21]. This method has become the standard approach to well path planning and trajectory calculations within the drilling industry, thus using this approach makes it relatively simple to incorporate arbitrary wellbore profiles from actual survey data. It should be noted that there are some who feel the minimum curvature method is outdated and have suggested alternatives to this approach [114], however these methods have not gained any real traction within the industry as of yet.
- 6) Drillstring components will rotate about their geometric center, not necessarily the center of the wellbore.
- 7) Any reduction in displacement magnitudes (e.g. small angle assumptions) will be based on a mathematical foundation.

These assumptions do not reduce the problem to a linear representation of the system, nor do they limit the application of the model to simple wellbore shapes or rudimentary drillstring assemblies. The resulting mathematics provides the most comprehensive drillstring model to date, and thus will be the most appropriate tool for analyzing, among a variety of other applications, the dynamics associated with inducing vibrations while drilling.

A realistic damping model will also be critical for understanding the complexities associated with drilling dynamics. Drillstring damping arises from four primary sources: structural damping from the drillstring itself, frictional contact between the drillstring and the wellbore, fluid forces acting on the drillstring, and formation cuttings lying on the low-side of the wellbore in cases of inefficient hole-cleaning. Structural damping of the drillstring is almost exclusively captured with a proportional, or Rayleigh, damping model for nonlinear simulations, which will also be applied for the present study. Damping due to friction is fairly straight forward to model and will be captured in the present study by implementing a Stribeck-type (velocity dependent) friction relationship within the wellbore contact model. The other two scenarios however, are

much more complex. Drillstring damping due to a buildup of cuttings in the wellbore requires a comprehensive description of the formation particles and how they travel through the annulus as fluid is pumped throughout the system. Such a model would necessitate a numerical approach that would require a coupling between the dynamics of individual rock particles and the intricate fluid dynamics of eccentric annular flow. Attempting to model this would be impractical in terms of computational costs and therefore will be neglected in the present study. It will simply be assumed that the wellbore remains sufficiently clean such that any damping due to cuttings loading is negligible. Fluid damping, on the other-hand, cannot be neglected as drilling mud is always present during normal drilling operations and has been known to be a significant factor in drillstring dynamics [86, 101, 115, 116].

This section outlines the detailed derivation of the mechanics of the drillstring described above. This is done by following, and expanding upon, an approach similar to the one taken by Heisig [34]. The key differences between the two models will be the inclusion of shear deformations, lateral rotational inertias, gyroscopic effects (to be introduced in Section 3), axially-acting friction, and a new nonlinear fluid-drillstring interaction model. This section first presents a mathematical description of the well path trajectory, after which the kinematics of a nonlinear beam are described within the context of the wellbore geometry. The nonlinear beam equations are then reduced through a scientific examination of displacement magnitudes. Once the equations for the beam have been established, a frictional contact formulation is presented that includes contributions along the axial, lateral, and rotational degrees of freedom. Lastly, a nonlinear fluid-drillstring interaction model is described which accounts for the effects of pipe eccentricity, lateral drillstring velocity, drillstring rotation, fluid rheology, and confined annular flow of Yield-Plastic Law (YPL) fluids.

2.1 Wellbore Geometry

Assuming that the wellbore trajectory can be represented as a continuous curve in space, then the vector describing the location of a point along the drillstring can be expressed with (2.1). This vector representation can be visualized by Figure 2.1.

$$\vec{r}_w(s) = x\hat{i} + y\hat{j} + z\hat{k} \quad (2.1)$$

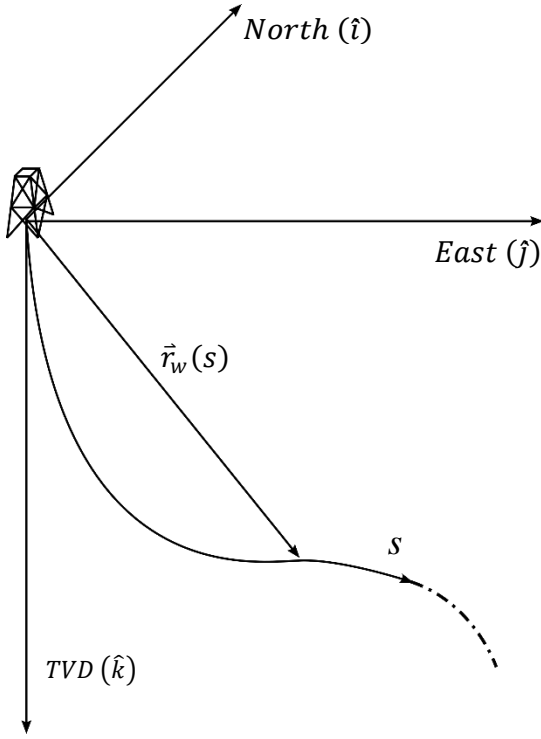


Figure 2.1: Well Path in the Global Coordinate System

Here x , y , and z are the global coordinates of the wellbore with respect to the surface hole location, \hat{i} , \hat{j} , and \hat{k} are the unit vectors corresponding to the global North, East and True Vertical Depth (TVD) directions, and s is the curvilinear coordinate along the well path (For simplicity in this text, once a variable has been defined as a function of other variables, it will simply be referenced by itself, i.e. $\vec{r}_w(s) = \vec{r}_w$).

The orientation of a wellbore cross-section along the length of the trajectory can be defined by a basis of three unit vectors which are listed below

$$\hat{v}_3(s) = \vec{r}'_w \quad (2.2)$$

$$\hat{v}_2(s) = \frac{\vec{r}''_w}{|\vec{r}''_w|} \quad (2.3)$$

$$\hat{v}_1(s) = \hat{v}_2 \times \hat{v}_3 \quad (2.4)$$

Where \hat{v}_3 is the unit tangent vector of the centerline of the wellbore, \hat{v}_2 is the unit normal vector (which is always pointed towards the center of the curve for the Minimum Curvature Trajectory, see Appendix A), and \hat{v}_1 is the bi-normal unit vector. The “primes” (‘) in the previous equations represent the derivative with

respect to the well path coordinate s . Because the well path is assumed to be a continuous curve in space, its derivative can be expressed using the well-known Frenet-Serret formulas [117], which are written in matrix form as

$$\hat{\underline{v}}' = \frac{\partial \hat{\underline{v}}}{\partial s} = \underline{\underline{D}}_v \hat{\underline{v}} \quad (2.5)$$

$$\begin{aligned} \hat{\underline{v}} &= \begin{pmatrix} \hat{v}_1 \\ \hat{v}_2 \\ \hat{v}_3 \end{pmatrix} \\ \underline{\underline{D}}_v &= \begin{bmatrix} 0 & -\tau_o & 0 \\ \tau_o & 0 & -\kappa_o \\ 0 & \kappa_o & 0 \end{bmatrix} \end{aligned} \quad (2.6)$$

Where κ_o is the curvature at a point along the well path

$$\kappa_o = |\vec{r}_w''| \quad (2.7)$$

And τ_o is the torsion of a point along the well path

$$\tau_o = \frac{\hat{v}_1 \cdot \vec{r}_w'''}{\kappa_o} \quad (2.8)$$

2.2 Drillstring Kinematics

The goal of deriving kinematic relationships for the present beam, is to define the generalized strain-displacement and velocity relationships associated with the structure. Once the equations are defined, they are reduced into a usable format through an examination of displacement magnitudes. In order to derive the shear deformable beam model, it is first assumed that the beam deforms without consideration of the shear strains (This was the basis of the model presented by Heisig [34]). From this initial deformation configuration, the shear distortions are then considered through a transformation, via the shear rotation angles, from the “shear-free” configuration to the “shear-corrected” configuration. In this way, the generalized strain components of the beam can be defined without prior knowledge of the total displacement field of the shear-deformable body. The final equations provide a basis from which a drillstring model can be implemented.

2.2.1 Generalized Strain Components

It is assumed that the drillstring’s initial position corresponds to the centerline of the wellbore, from which the drillstring will deflect. Thus, initially assuming a “shear-free” deformation, the position of any point in the drilling assembly can be defined as

$$\vec{r}_o(s, t) = \vec{r}_w + \vec{u}_o(s, t) \quad (2.9)$$

Where \vec{u}_o is the initial displacement vector, before considering shear deformations of the drillstring's cross-sections, that can be defined by three independent deflection variables as

$$\vec{u}_o = u_1(s, t)\hat{v}_1 + u_2(s, t)\hat{v}_2 + u_3(s, t)\hat{v}_3 \quad (2.10)$$

Where u_1 and u_2 are the lateral displacements along the transverse directions (\hat{v}_1, \hat{v}_2), and u_3 is the longitudinal displacement along the tangent direction to the central axis of the wellbore (\hat{v}_3).

Let it be kept in mind that the goal is to determine the deflection of the drillstring, from the wellbore basis \hat{v} to a deformed drillstring basis \hat{e} . If the following transformation matrices are defined

$$\underline{\underline{D}}_1(\theta) = \begin{bmatrix} 1 & 0 & 0 \\ 0 & \cos \theta & \sin \theta \\ 0 & -\sin \theta & \cos \theta \end{bmatrix} \quad (2.11)$$

$$\underline{\underline{D}}_2(\theta) = \begin{bmatrix} \cos \theta & 0 & -\sin \theta \\ 0 & 1 & 0 \\ \sin \theta & 0 & \cos \theta \end{bmatrix} \quad (2.12)$$

$$\underline{\underline{D}}_3(\theta) = \begin{bmatrix} \cos \theta & \sin \theta & 0 \\ -\sin \theta & \cos \theta & 0 \\ 0 & 0 & 1 \end{bmatrix} \quad (2.13)$$

Then a complete transformation between the basis \hat{v} and the basis \hat{e} , which includes shear deformations, can be defined through rotations (θ_1, θ_2 , and θ_3) about the local axes of a point in the drillstring. The angles θ_1, θ_2 , and θ_3 correspond to the rotation angles about the \hat{v}_1, \hat{v}_2 , and \hat{v}_3 axes respectively.

$$\hat{e} = \underline{\underline{D}}_3(\theta_3)\underline{\underline{D}}_2(\theta_2)\underline{\underline{D}}_1(\theta_1)\hat{v} = \underline{\underline{R}}\hat{v} \quad (2.14)$$

$$\underline{\underline{R}} = \begin{bmatrix} \cos \theta_2 \cos \theta_3 & \cos \theta_1 \sin \theta_3 + \sin \theta_1 \sin \theta_2 \cos \theta_3 & \sin \theta_1 \sin \theta_3 - \cos \theta_1 \sin \theta_2 \cos \theta_3 \\ -\cos \theta_2 \sin \theta_3 & \cos \theta_1 \cos \theta_3 - \sin \theta_1 \sin \theta_2 \sin \theta_3 & \sin \theta_1 \cos \theta_3 + \cos \theta_1 \sin \theta_2 \sin \theta_3 \\ \sin \theta_2 & -\sin \theta_1 \cos \theta_2 & \cos \theta_1 \cos \theta_2 \end{bmatrix} \quad (2.15)$$

From this relation, the deformed unit tangent vector of the drillstring can be written as

$$\hat{e}_3 = \sin \theta_2 \hat{v}_1 - \sin \theta_1 \cos \theta_2 \hat{v}_2 + \cos \theta_1 \cos \theta_2 \hat{v}_3 \quad (2.16)$$

This equation will later be used for determining a relationship between the beam displacements and the deformation rotation angles ($\theta_1, \theta_2, \theta_3$).

In order to relate the “shear-free” configuration to the final “shear-corrected” configuration, consider the tangent vector of the “shear-free” deformed cross-section. In a manner consistent with (2.2), this can be expressed as

$$\vec{t}_o = \vec{r}'_o = \vec{r}'_w + \vec{u}'_o = \hat{v}_3 + \frac{\partial}{\partial s} (u_1 \hat{v}_1 + u_2 \hat{v}_2 + u_3 \hat{v}_3) \quad (2.17)$$

Differentiating (2.17) using the chain rule and (2.5), the “shear-free” tangent vector can be written as a function of displacements

$$\vec{t}_o = (u'_1 + u_2 \tau_o) \hat{v}_1 + (u'_2 - u_1 \tau_o + u_3 \kappa_o) \hat{v}_2 + (1 + u'_3 - u_2 \kappa_o) \hat{v}_3 \quad (2.18)$$

If the shear deformation rotations about \hat{v}_1 and \hat{v}_2 are then accounted for via the transformation matrices (2.11) and (2.12), then the “shear-corrected” deformed unit tangent vector can be expressed as

$$\hat{t} = \frac{\vec{t}}{|\vec{t}|} = \frac{\underline{\underline{D}}_2(\gamma_2) \underline{\underline{D}}_1(\gamma_1) \vec{t}_o}{|\vec{t}|} \quad (2.19)$$

$$\begin{aligned} \hat{t} &= \frac{1}{|\vec{t}|} \{ \cos \gamma_2 (u'_1 + u_2 \tau_o) + \sin \gamma_1 \sin \gamma_2 (u'_2 - u_1 \tau_o + u_3 \kappa_o) - \cos \gamma_1 \sin \gamma_2 (1 + u'_3 - u_2 \kappa_o) \} \hat{v}_1 \\ &\quad + \frac{1}{|\vec{t}|} \{ \cos \gamma_1 (u'_2 - u_1 \tau_o + u_3 \kappa_o) + \sin \gamma_1 (1 + u'_3 - u_2 \kappa_o) \} \hat{v}_2 \\ &\quad + \frac{1}{|\vec{t}|} \{ \sin \gamma_2 (u'_1 + u_2 \tau_o) - \cos \gamma_2 \sin \gamma_1 (u'_2 - u_1 \tau_o + u_3 \kappa_o) + \cos \gamma_1 \cos \gamma_2 (1 + u'_3 - u_2 \kappa_o) \} \hat{v}_3 \end{aligned} \quad (2.20)$$

Where γ_1 and γ_2 are the shear rotations about the \hat{v}_1 and \hat{v}_2 axes respectively, and $|\vec{t}|$ is the magnitude of the tangent vector \vec{t}

$$|\vec{t}| = \sqrt{\frac{\{ \cos \gamma_2 (u'_1 + u_2 \tau_o) + \sin \gamma_1 \sin \gamma_2 (u'_2 - u_1 \tau_o + u_3 \kappa_o) - \cos \gamma_1 \sin \gamma_2 (1 + u'_3 - u_2 \kappa_o) \}^2}{+ \{ \cos \gamma_1 (u'_2 - u_1 \tau_o + u_3 \kappa_o) + \sin \gamma_1 (1 + u'_3 - u_2 \kappa_o) \}^2} + \{ \sin \gamma_2 (u'_1 + u_2 \tau_o) - \cos \gamma_2 \sin \gamma_1 (u'_2 - u_1 \tau_o + u_3 \kappa_o) + \cos \gamma_1 \cos \gamma_2 (1 + u'_3 - u_2 \kappa_o) \}^2} \quad (2.21)$$

Now it can be realized that the axial strain of the beam, as defined from nonlinear elasticity theory [118], can be written as

$$\epsilon = \frac{\partial u_3}{\partial s} + \frac{1}{2} \left(\left(\frac{\partial u_3}{\partial s} \right)^2 + \left(\frac{\partial u_2}{\partial s} \right)^2 + \left(\frac{\partial u_1}{\partial s} \right)^2 \right) \quad (2.22)$$

Because the displacement field of a shear deformable beam cannot be fully defined by only three independent variables, as it was in (2.10) for the “shear-free” beam, the derivatives in (2.22) cannot be determined unless the complete displacement field has already been properly defined as a function of all of the displacement variables (u_1 , u_2 , u_3 , γ_1 , and γ_2). However, by applying the relationship in (2.17) to the “shear-corrected” tangent vector given by (2.20), the necessary derivatives can be determined without initial knowledge of the shear-deformed displacement field. This approach leads to

$$\vec{u}' = \vec{t} - \vec{r}'_w = \vec{t} - \hat{v}_3 \quad (2.23)$$

Where \vec{u} is the total deformation vector of a point along the drillstring, including shear rotations. From this it can be determined that

$$\frac{\partial u_3}{\partial s} = \sin \gamma_2 (u'_1 + u_2 \tau_o) - \cos \gamma_2 \sin \gamma_1 (u'_2 - u_1 \tau_o + u_3 \kappa_o) + \cos \gamma_1 \cos \gamma_2 (1 + u'_3 - u_2 \kappa_o) - 1 \quad (2.24)$$

$$\frac{\partial u_2}{\partial s} = \cos \gamma_1 (u'_2 - u_1 \tau_o + u_3 \kappa_o) + \sin \gamma_1 (1 + u'_3 - u_2 \kappa_o) \quad (2.25)$$

$$\frac{\partial u_1}{\partial s} = \cos \gamma_2 (u'_1 + u_2 \tau_o) + \sin \gamma_1 \sin \gamma_2 (u'_2 - u_1 \tau_o + u_3 \kappa_o) - \cos \gamma_1 \sin \gamma_2 (1 + u'_3 - u_2 \kappa_o) \quad (2.26)$$

These equations are reduced, and combined with (2.22), in a later section to give a simple expression for the generalized axial strain. It is worth noting that the generalized axial strain represented by (2.22) and (2.24) – (2.26) is equivalent to a previous expression for the extension of nonlinear beams, $\epsilon = |\vec{t}| - 1$ [119].

Returning to the deformed tangent vector of the beam’s cross-section, recall that this vector was previously defined by (2.16), setting this equal to (2.20) leads to the following relationships

$$\sin \theta_2 = \frac{1}{|\vec{t}|} \{ \cos \gamma_2 (u'_1 + u_2 \tau_o) + \sin \gamma_1 \sin \gamma_2 (u'_2 - u_1 \tau_o + u_3 \kappa_o) - \cos \gamma_1 \sin \gamma_2 (1 + u'_3 - u_2 \kappa_o) \} \quad (2.27)$$

$$-\sin \theta_1 \cos \theta_2 = \frac{1}{|\vec{t}|} \{ \cos \gamma_1 (u'_2 - u_1 \tau_o + u_3 \kappa_o) + \sin \gamma_1 (1 + u'_3 - u_2 \kappa_o) \} \quad (2.28)$$

$$\cos \theta_1 \cos \theta_2 = \frac{1}{|\hat{\epsilon}|} \{ \sin \gamma_2 (u'_1 + u_2 \tau_o) - \cos \gamma_2 \sin \gamma_1 (u'_2 - u_1 \tau_o + u_3 \kappa_o) + \cos \gamma_1 \cos \gamma_2 (1 + u'_3 - u_2 \kappa_o) \} \quad (2.29)$$

After some slight trigonometric algebra (2.27), (2.28), and (2.29) can be combined to give expressions for θ_1 and θ_2

$$\tan \theta_1 = - \frac{\cos \gamma_1 (u'_2 - u_1 \tau_o + u_3 \kappa_o) - \sin \gamma_1 (1 + u'_3 - u_2 \kappa_o)}{\sin \gamma_2 (u'_1 + u_2 \tau_o) - \cos \gamma_2 \sin \gamma_1 (u'_2 - u_1 \tau_o + u_3 \kappa_o) + \cos \gamma_1 \cos \gamma_2 (1 + u'_3 - u_2 \kappa_o)} \quad (2.30)$$

$$\tan \theta_2 = \frac{\cos \gamma_2 (u'_1 + u_2 \tau_o) + \sin \gamma_1 \sin \gamma_2 (u'_2 - u_1 \tau_o + u_3 \kappa_o) - \cos \gamma_1 \sin \gamma_2 (1 + u'_3 - u_2 \kappa_o)}{\sqrt{\{ \sin \gamma_2 (u'_1 + u_2 \tau_o) - \cos \gamma_2 \sin \gamma_1 (u'_2 - u_1 \tau_o + u_3 \kappa_o) + \cos \gamma_1 \cos \gamma_2 (1 + u'_3 - u_2 \kappa_o) \}^2 + \{ \cos \gamma_1 (u'_2 - u_1 \tau_o + u_3 \kappa_o) + \sin \gamma_1 (1 + u'_3 - u_2 \kappa_o) \}^2}} \quad (2.31)$$

In order to take advantage of equations (2.30) and (2.31), it is beneficial to understand how the vector orientation of the cross-section changes along the length of the beam. This correlates to a derivative of the basis $\hat{\epsilon}$, with respect to s . Thus the derivative of the directional unit vectors of the deformed cross-section can be written as

$$\begin{aligned} \hat{\epsilon}' &= \frac{\partial}{\partial s} (\underline{\underline{R}} \hat{\underline{\nu}}) \\ &= (\underline{\underline{R}}' \hat{\underline{\nu}} + \underline{\underline{R}} \hat{\underline{\nu}}') \\ &= (\underline{\underline{R}}' + \underline{\underline{R}} \underline{\underline{D}}_{\nu}) \hat{\underline{\nu}} \\ &= (\underline{\underline{R}}' \underline{\underline{R}}^T + \underline{\underline{R}} \underline{\underline{D}}_{\nu} \underline{\underline{R}}^T) \hat{\underline{\epsilon}} \end{aligned} \quad (2.32)$$

Again, because the drillstring is a continuous curve in space, the derivative expressed by (2.32) can also be written as

$$\hat{\epsilon}' = \underline{\underline{D}}_{\rho} \hat{\underline{\epsilon}} \quad (2.33)$$

$$\underline{\underline{D}}_{\rho} = \begin{bmatrix} 0 & \tau & -\kappa_2 \\ -\tau & 0 & \kappa_1 \\ \kappa_2 & -\kappa_1 & 0 \end{bmatrix} \quad (2.34)$$

Where κ_1 and κ_2 are the deformation curvatures (generalized bending strains) of the beam along the lateral axes, and τ is the generalized torsional strain of the beam's central axis. From (2.32) - (2.34) it can be determined that

$$\kappa_1 = \theta'_1 \cos \theta_2 \cos \theta_3 + \theta'_2 \sin \theta_3 - \kappa_o \cos \theta_2 \cos \theta_3 + \tau_o (\cos \theta_1 \sin \theta_2 \cos \theta_3 - \sin \theta_1 \sin \theta_3) \quad (2.35)$$

$$\kappa_2 = -\theta'_1 \cos \theta_2 \sin \theta_3 + \theta'_2 \cos \theta_3 + \kappa_o \cos \theta_2 \sin \theta_3 - \tau_o (\cos \theta_1 \sin \theta_2 \sin \theta_3 + \sin \theta_1 \cos \theta_3) \quad (2.36)$$

$$\tau = \theta'_3 + \theta'_1 \sin \theta_2 - \kappa_o \sin \theta_2 - \tau_o \cos \theta_1 \cos \theta_2 \quad (2.37)$$

The variables defined by (2.22), (2.35)-(2.37), and the shear strains γ_1 and γ_2 , together fully describe the generalized strain field of a point along the central axis of the beam confined within a wellbore.

2.2.2 Components of Rotational Drillstring Velocity

Rotational velocities of the drillstring are defined with respect to the deformed configuration. This serves a practical benefit when describing rotations about the “current” orientation of the drillstring’s axes (Assumption 6). The velocity of a point on the drillstring can be defined by taking the derivative, with respect to time, of the deformed basis \hat{e} . This is expressed by (2.38)

$$\begin{aligned} \dot{\hat{e}} &= \underline{\underline{\dot{R}}} \underline{\hat{v}} \\ &= \underline{\underline{\dot{R}}} \underline{\underline{R}}^T \underline{\hat{e}} \\ &= \underline{\underline{\Omega}} \underline{\hat{e}} \end{aligned} \quad (2.38)$$

This can also be represented in a similar fashion as (2.33), by defining a rotational velocity matrix as

$$\underline{\underline{\Omega}} = \begin{bmatrix} 0 & \omega_3 & -\omega_2 \\ -\omega_3 & 0 & \omega_1 \\ \omega_2 & -\omega_1 & 0 \end{bmatrix} \quad (2.39)$$

Where ω_1 , ω_2 , and ω_3 are the rotational velocities about the e_1 , e_2 , and e_3 axes respectively. Using (2.38) and (2.39) leads to the following relationships.

$$\begin{aligned} \omega_1 &= \dot{\theta}_1 \cos \theta_2 \cos \theta_3 + \dot{\theta}_2 \sin \theta_3 \\ \omega_2 &= -\dot{\theta}_1 \cos \theta_2 \sin \theta_3 + \dot{\theta}_2 \cos \theta_3 \\ \omega_3 &= \dot{\theta}_3 + \dot{\theta}_1 \sin \theta_2 \end{aligned} \quad (2.40)$$

$$\vec{\omega} = \omega_1 \hat{e}_1 + \omega_2 \hat{e}_2 + \omega_3 \hat{e}_3 \quad (2.41)$$

As shown by Heisig [34], the total rotational velocity vector (2.41) of the drillstring also leads to an expression for the virtual rotations of the drillstring

$$\delta\vec{\alpha} = \delta\alpha_1\hat{e}_1 + \delta\alpha_2\hat{e}_2 + \delta\alpha_3\hat{e}_3 \quad (2.42)$$

$$\begin{aligned}\delta\alpha_1 &= \delta\theta_1 \cos \theta_2 \cos \theta_3 + \delta\theta_2 \sin \theta_3 \\ \delta\alpha_2 &= -\delta\theta_1 \cos \theta_2 \sin \theta_3 + \delta\theta_2 \cos \theta_3 \\ \delta\alpha_3 &= \delta\theta_3 + \delta\theta_1 \sin \theta_2\end{aligned} \quad (2.43)$$

Where $\delta\alpha_i$ corresponds to the virtual rotation about the \hat{e}_{i-th} axis. These relationships will become important when developing the contact force equations.

2.2.3 Examination of Displacement Magnitudes

The equations derived, up to this point, are represented in a highly nonlinear generalized form and would be rather cumbersome to solve. In order to arrive at a practical set of equations that are more suitable for obtaining approximate solutions, the magnitudes of the displacement variables are examined.

2.2.3.1 Radial Displacement and Lateral Rotation

If a magnitude parameter (λ) is defined such that

$$\lambda = \frac{r}{L} \quad (2.44)$$

Where r is the radial clearance between the drillstring and the wellbore, and L is an arbitrary length that results in a small value of the magnitude parameter.

For example: 4 ½ " Drill Pipe in a 12 ¼ " Wellbore with $L = 10 \text{ ft}$

$$\lambda = \frac{0.3229 \text{ ft}}{10 \text{ ft}} = 3.22 \cdot 10^{-2}$$

**Note: A length (L) of 10 feet was chosen as it is the shortest length of a drillstring that would intentionally be suspended off the wellbore wall in a horizontal well. For example, a “Pony Collar” (short drill collar, $L \approx 10 \text{ ft}$) could be run between two stabilizers in a Bottom Hole Assembly (BHA).*

Because r is the maximum value that could be reached for the lateral displacements, the following holds true

$$\left| \frac{u_1}{L} \right| \leq \lambda \quad \left| \frac{u_2}{L} \right| \leq \lambda \quad (2.45)$$

Where the general statement $|x| \leq \lambda$ says that the quantity x , at its maximum, is of the same order of magnitude as λ , i.e. a first order approximation. Therefore an equation representing x only needs to include first order terms, and higher-order terms can be dropped. Similarly, if $|x| \leq \lambda^2$ then an equation representing x would only need to include second-order terms. Under an Euler-Bernoulli assumption, the rotation of the beam's cross-section can be approximated as

$$\frac{u_1}{L} \approx \theta_2 \quad \frac{u_2}{L} \approx \theta_1$$

Knowing that, in the present case, the rotation about the lateral axes of the beam is a combination of the Euler-Bernoulli assumption and the added rotation due to shear deformation, in a general sense, θ_1 and θ_2 are written as

$$\theta_1 = \gamma_1 + \frac{u_2}{L} \quad \theta_2 = \gamma_2 + \frac{u_1}{L}$$

From this it can be reasoned that θ_1 , θ_2 , γ_1 , γ_2 , u_1/L , and u_2/L are of similar magnitudes, thus

$$|\gamma_1| \leq \lambda, \quad |\gamma_2| \leq \lambda, \quad |\theta_1| \leq \lambda, \quad |\theta_2| \leq \lambda \quad (2.46)$$

2.2.3.2 Curvature and Lateral Displacement

If a general wellbore curvature is selected as $\kappa_o = 15^\circ/100\text{ft} = 0.002618 \text{ rad/ft}$, then

$$|\kappa_o L| = 0.02618 \leq \lambda$$

**Note: A wellbore curvature (κ_o) of 15 °/100 ft was chosen as this is typically the largest curve that would be planned for a modern unconventional well in North America.*

Combining this with (2.45) yields the following

$$|\kappa_o L| \left| \frac{u_1}{L} \right| = |\kappa_o u_1| \leq \lambda^2 \leftrightarrow |\kappa_o u_2| \leq \lambda^2 \quad (2.47)$$

2.2.3.3 Axial Strain and Displacement

It is worth noting that the maximum bending stress in a beam can be expressed as a function of its deformation curvature

$$\sigma_{bending_{max}} = E\kappa \frac{D_o}{2} \quad (2.48)$$

For example: 4 ½" Drill Pipe in a 15°/100ft curve

$$\sigma_{bending_{max}} = 14,726 \text{ psi}$$

If it is assumed that the axial stress is of the same order of magnitude as the bending stress, then it can be written that

$$\sigma_{axial} = E\epsilon = \sigma_{bending_{max}} = E\kappa \frac{D_o}{2} \quad (2.49)$$

$$\epsilon = \kappa \frac{D_o}{2} = |\kappa L| \frac{D_o}{2L} \quad \leftrightarrow \quad \epsilon = |\kappa L| \left| \frac{r}{L} \right| \leq \lambda^2 \quad (2.50)$$

While it has been assumed that the beam can undergo large displacements, it is required that the strains remain small in order to limit the deformation to the elastic limits of the material. Consequently, from a purely linear theory of elasticity, the axial strain is approximated as $\epsilon \approx u'_3$, thus

$$|u'_3| \leq \lambda^2 \quad (2.51)$$

In a “worse case” scenario let it be assumed that a drillstring consisting of 4 ½" 16.6 ppf ($D_i = 3.826"$) S-135 drill pipe, with an NC50 connection (adjusted weight = 18.63 ppf) is suspended in a perfectly vertical hole. If the length of the suspended string is assumed to be 5,000ft, then the maximum axial elongation can be written as

$$u_{3_{max}} = \frac{(ppf \cdot l)l}{EA} = 3.5225 \text{ ft}$$

Which, again, using a curvature of 15°/100ft, leads to the observation that

$$|\kappa_o u_3| \leq \lambda \quad (2.52)$$

2.2.3.4 Torsional Strain and Displacement

The stress in a circular beam under pure shear (torsion) can be expressed as

$$\sigma_{torsion} = \frac{TD_o}{2J} = G\tau \frac{D_o}{2} \quad (2.53)$$

If the output from a down-hole mud motor is considered to be the lower limit of applied torque (Average torque output from a 6 ½" mud motor $\approx 3,000$ ft-lb_f) then the following can be determined

For example: 4.5" Drill Pipe ($D_i = 3.826"$) with an applied torque of 3,000 ft-lb_f

$$\sigma_{torsion} = 4,214 \text{ psi}$$

Thus it can been seen that the lower limit of torsional stress is typically an order of magnitude lower than the bending stress. With this understanding, a comparison of (2.48) and (2.53) leads to

$$|\tau L| \approx \lambda |\kappa L| \leq \lambda^2 \quad (2.54)$$

And again, because the strain of the drillstring is limited to elastic behavior, a purely linear assumption of torsional strain ($\tau \approx \theta'_3$) leads to the simplification

$$|\theta'_3| \leq \lambda^2 \quad (2.55)$$

2.2.3.5 Reduced Nonlinear String Equations

With the magnitude considerations in the previous section, the nonlinear beam equations can be written in a simpler, more concise form. Recalling that the well path is assumed to follow a minimum curvature trajectory ($\kappa_o = \text{constant}$ between survey points, $\tau_o = 0$), (2.30) and (2.31) can be reduced, through the use of (2.46), to

$$\theta_1 = -(u'_2 + \gamma_1 + \kappa_o u_3) \quad (2.56)$$

$$\theta_2 = u'_1 - \gamma_2 \quad (2.57)$$

(2.22) and (2.24) - (2.26), with (2.46) and (2.50), can be combined to obtain an expression for the generalized axial strain

$$\epsilon = u'_3 - \kappa_o u_2 + u'_1 \gamma_2 - \gamma_1 (u'_2 + \kappa_o u_3) + \frac{1}{2} (u'_1 - \gamma_2)^2 + \frac{1}{2} (u'_2 + \gamma_1 \kappa_o u_3)^2 \quad (2.58)$$

And (2.35) - (2.37) can be reduced to

$$\kappa_1 = -(u''_2 + \gamma'_1) \cos \theta_3 + (u''_1 - \gamma'_2) \sin \theta_3 - \kappa_o \cos \theta_3 \quad (2.59)$$

$$\kappa_2 = (u''_2 + \gamma'_1) \sin \theta_3 + (u''_1 - \gamma'_2) \cos \theta_3 + \kappa_o \sin \theta_3 \quad (2.60)$$

$$\tau = \theta'_3 - (u''_2 + \gamma'_1)(u'_1 - \gamma'_2) - \kappa_o(u'_1 - \gamma'_2) \quad (2.61)$$

Equations (2.58) – (2.61), and the shear deformations (γ_1 and γ_2), are the reduced-form equations describing the generalized strain of a point along the central axis of the drillstring.

2.3 Frictional Wall Contact

For the “drillstring problem” to be fully addressed, the lateral confinement of the wellbore must be accounted for. Heisig [34] outlined this drillstring-wellbore interaction by introducing a quasi-static frictional contact model. The model assumes that, during rotation, the drillstring will “roll up” the side of the wellbore due to the frictional contact between the wellbore wall and the rotating drillstring. This can be better understood by an examination of Figure 2.2.

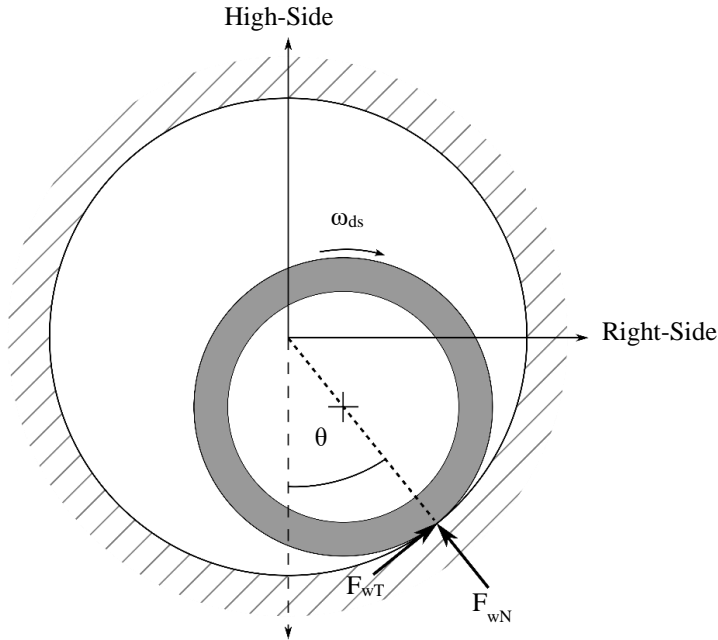


Figure 2.2: Illustration of Drillstring/Wellbore Contact

In the figure, the normal (F_{wN}) and the tangential (F_{wT}) components of the contact force can be seen. The tangential force created by the friction between the drillstring and wellbore also generates a torsional

moment about the central axis of drillstring. In a quasi-static state, the rotating drillstring will reach an equilibrium angle (θ) based on the magnitude of the friction coefficient (μ). Heisig's contact formulation, which only considers the lateral frictional forces acting on the drillstring, is presented here for reference.

2.3.1 Normal “Wellbore Confinement” Force

$$\underline{F}_{wN} = k_w \Delta r \hat{e}_N \quad (2.62)$$

$$\hat{e}_N = \frac{1}{\sqrt{u_1^2 + u_2^2}} (u_1 \hat{v}_1 + u_2 \hat{v}_2) \quad (2.63)$$

Where \hat{e}_N is the unit normal vector acting at the point of contact between the drillstring and the wellbore, and k_w is the radial stiffness of the wellbore wall. It can be noted that the value of the wellbore wall stiffness is such that it results in a very small wellbore penetration ($\Delta r \ll 1$).

$$\Delta r = \sqrt{u_1^2 + u_2^2} - r \quad (2.64)$$

r in the above equation is the radial clearance between the drillstring and the wellbore.

$$r = \frac{D_{ch} - D_o}{2} \quad (2.65)$$

Where D_{ch} is the diameter of the wellbore and D_o is the outer diameter of the drillstring.

2.3.2 Tangential Friction Force

The tangential, or transverse, frictional force is written as

$$\underline{F}_{wT} = \mu_T k_w \Delta r \hat{e}_T \quad (2.66)$$

Where μ_T is the tangential friction coefficient and the tangential contact vector, \hat{e}_T , is defined as

$$\hat{e}_T = \hat{e}_3 \times \hat{e}_N \quad (2.67)$$

2.3.3 Torsional Friction Moment

The torsional moment induced by the tangential friction is expressed as

$$\underline{F}_{wM} = \mu_T k_w \Delta r \frac{D_o}{2} \hat{\alpha}_3 \quad (2.68)$$

2.3.4 Axial Friction Force

In addition to the lateral frictional forces described by Heisig, there will also be an axial frictional force acting on the drillstring which can be described as

$$\underline{F}_{wA} = \mu_A k_w \Delta r \hat{e}_3 \quad (2.69)$$

Here μ_A is the axial coefficient of friction. The nature of equations (2.66) – (2.69) ensure that the frictional forces act along the axes of the drillstring and not just the axes of the wellbore.

From the previous equations, it is noticed that there exist two distinct friction coefficients: one for the lateral (tangential) direction and one for the axial direction. This is due to the fact that the resultant of the frictional force acts along the direction of the total slip-velocity at the point of contact. Equations describing this behavior have been presented, among other authors, by Samuel [58] and can be written as

$$\mu_T = \frac{\omega_3 D_o}{2\sqrt{\dot{u}_3^2 + (\omega_3 \frac{D_o}{2})^2}} \mu_o \quad (2.70)$$

$$\mu_A = \frac{\dot{u}_3}{\sqrt{\dot{u}_3^2 + (\omega_3 \frac{D_o}{2})^2}} \mu_o \quad (2.71)$$

Where μ_o is the absolute friction coefficient and the term, $\sqrt{\dot{u}_3^2 + (\omega_3 \frac{D_o}{2})^2}$, is the absolute slip-velocity at the contact point between the drillstring and the wellbore. Thus, with (2.70) and (2.71), the frictional forces and moments are applied based on the direction (+/-) and the magnitude of the drillstring velocity.

This directional friction behavior is observed in the field when monitoring hook-loads while tripping-in-hole (TIH)/slackening-off (SO), tripping-out-of-hole (TOOH)/picking-up (PU), and rotating-off-bottom (ROB). During TIH/SO operations, the hook load will be the lowest. This occurs because friction is acting in the opposite direction of the pipe movement and thus is helping to support the weight of the drillstring. While TOOH/PU the hook load will be the greatest because friction is “holding on” to the drillstring as the rig is trying to pull the pipe out of the well. During these two operations there is generally no string rotation and friction, according to (2.70) and (2.71), would only act in the axial direction along the length of the drillstring. When ROB however, the hook load will be independent of the friction coefficient because there is no axial velocity and all of the friction resistance would be acting in the lateral direction of the drillstring, thus contributing to an increased torque resistance at the surface. These operations can be visualized through the use of a broom plot. A broom plot shows the hook-load during these three different surface operations, as a function of the measured depth of the bit, for different friction coefficient values. Broom plots can be

generated with commercial Torque and Drag (T&D) software, which typically utilize the friction relationship shown by (2.70) and (2.71).

Figure 2.3 is a practical field example, showing one way a broom plot can be used, illustrating this “directional friction” relationship. In this case, the purpose was to track the friction coefficients, in real-time, in order to monitor hole-cleaning. The well depicted in the chart was a horizontal well drilled in the Permian Basin during September, 2014. The solid and dashed lines represent the PU, SO, and ROB hook-load values calculated with commercial T&D software using friction coefficients of 0.1, 0.2, and 0.3. ROB generated a hook-load that is independent of the coefficient of friction and thus only one curve represents this operation. The colored squares, triangles, and diamonds represent the actual hook-load recorded by the directional driller for PU, SO, and ROB operations respectively. From the recorded data, it can be noticed that when drilling from about 8,800 ft to around 12,200 ft, the hook-loads indicated a friction coefficient of around 0.2. After 12,200 ft, the ROB weight began to shift to the left, while the PU and SO weight started to move outward indicating a transition towards a friction coefficient of 0.3. The cause of this hook-load shift was excessive cutting-loading in the wellbore. As the volume of cuttings increase along the wellbore, the effective density of the fluid surrounding the drill pipe is increased. This adds more buoyancy to the drillstring making it appear lighter at the surface, and thus the ROB weight is decreased. Increased cutting’s loading also makes it more difficult to move the drillstring in and out of the wellbore, which in turn increases the effective friction coefficient. Noticing this trend in shifting friction coefficients, the drilling team stopped at around 13,300 ft for a dedicated clean-up cycle in which the driller continues to circulate fluid, usually at a higher flow rate, while rotating off bottom. This helps to remove the excessive amount of cuttings that have accumulated in the wellbore. Again, looking at the figure, after the dedicated clean-up cycle at 13,300 ft the friction coefficient came back down to around 0.2 and the drilling team continued to drill-ahead.

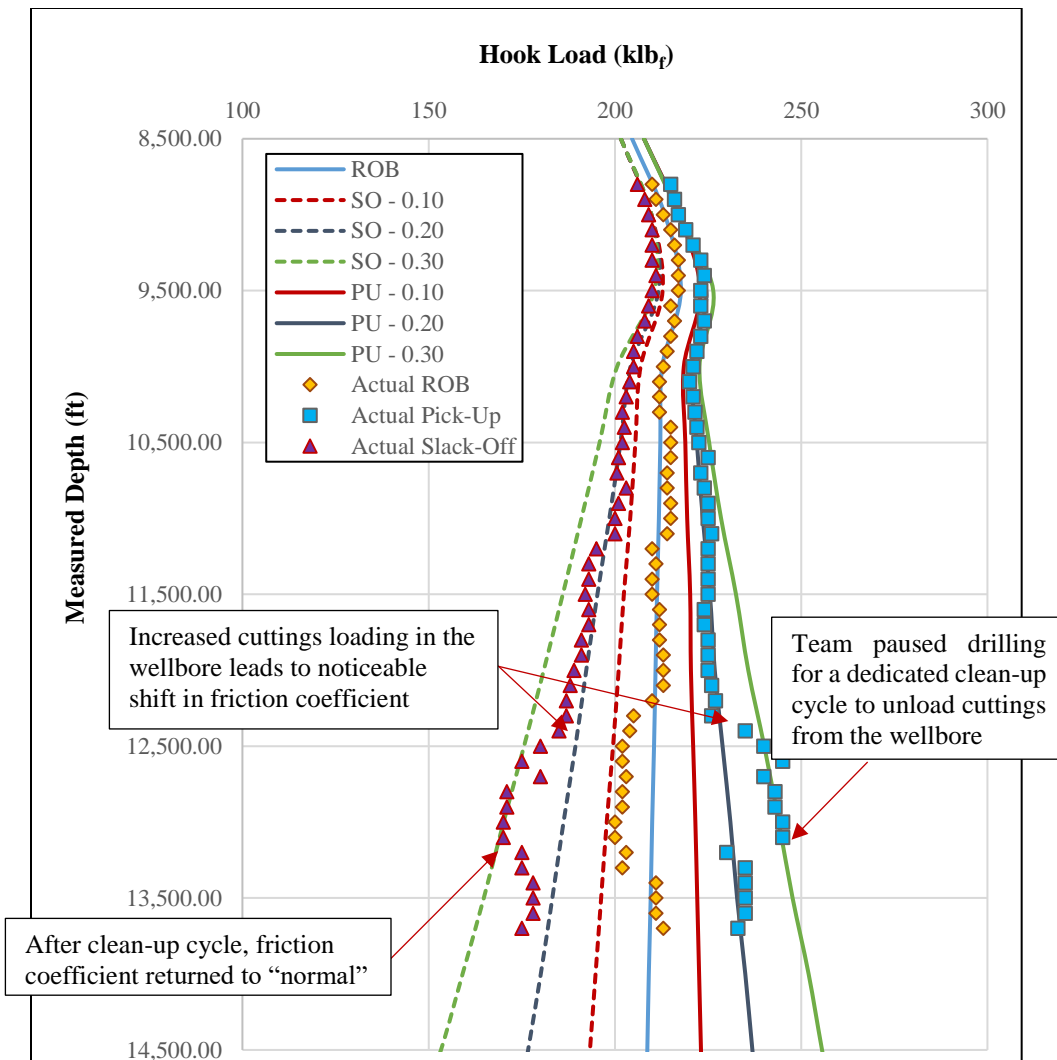


Figure 2.3: Broom Plot Generated for Permian Basin Well using Commercial T&D Software

This example not only shows the usefulness of broom plots, but also illustrates the practicality of the friction relationship provided by (2.70) and (2.71). However it must be realized that when capturing the field data to plot on these types of charts, the same operational parameters need to be used every time a data point is recorded, i.e. the same rotation speed for every ROB data point, and the same trip speed for every PU/SO data point. If care is not taken to maintain this consistency, then the data points may not necessarily follow the anticipated curves on the broom plot. This implies a “velocity weakening” effect of the friction coefficient with respect to the velocity of the drillstring, which suggests the need to incorporate a velocity-dependence within the absolute friction coefficient.

This “velocity weakening” behavior is not a new concept and, as discussed in Section 1, has been reported by several authors [60, 62]. Dykstra [14] noted this effect through monitoring the surface torque while increasing the rotation speed of the drillstring. Through this, he was able to quantify the change in friction coefficients with increasing drillstring rotation speed which can be depicted by the linear, piece-wise, dashed lines in Figure 2.4.

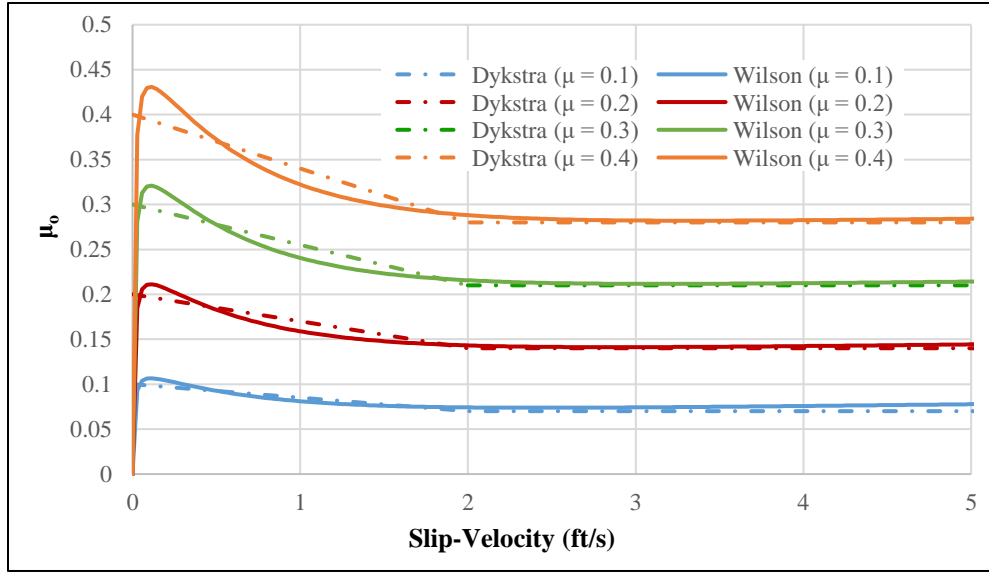


Figure 2.4: Absolute Coefficient of Friction as a Function of Slip-Velocity

For computational purposes it is beneficial to obtain smooth curves that represent this “Stribeck-like” velocity relationship within the friction coefficient. The model used in the present work is a combination of the friction coefficient presented by Jeffreys [120] and the “smoothing function” given by Gorelik et al. [121], and is shown via (2.72).

$$\mu_o = \frac{2}{\pi} \operatorname{atan} \left(\frac{\sqrt{u_3^2 + (\omega \frac{D_o}{2})^2}}{v_o} \right) \left(\mu_D + (\mu_S - \mu_D) e^{-\log(2)\beta \sqrt{u_3^2 + (\omega \frac{D_o}{2})^2}} + b \sqrt{u_3^2 + (\omega \frac{D_o}{2})^2} \right) \quad (2.72)$$

Here μ_S is the static coefficient of friction (value presented by Dykstra at zero slip-velocity), μ_D is the dynamic coefficient of friction (value presented by Dykstra at high slip-velocities), b and β are both calibration parameters, and v_o is a reference velocity which acts as a smoothing parameter. In order to maintain a level of confidence in the model, the above friction coefficient is calibrated to match the observed field data presented by Dykstra [14]. This “curve-match” is shown as the solid colored curves in Figure 2.4.

2.4 Nonlinear Fluid Forces

As mentioned previously, the fluid filling the annulus (“Drilling Mud”) will generate hydrodynamic forces on the drillstring as the various tubular components are moving around within the wellbore. While this is an understood concept within the drilling industry, clearly defining these forces in an efficient manner remains somewhat elusive. Wilson and Noynaert [122] attempt to provide a general formulation for this fluid-drillstring interface that can be readily applied to nonlinear finite element simulations. Their paper presents a nonlinear semi-analytical fluid-force model that accounts for drillstring eccentricity, drillstring velocity, flow rate, and fluid rheology. The equations of this formulation are presented below

$$F_{f_1} = \frac{1}{2} C_f \rho_f D_o V_{\text{flow}} (\dot{u}_1 - V_{\text{flow}} \varphi_1) + k_f \dot{u}_1 \quad (2.73)$$

$$F_{f_2} = \frac{1}{2} C_f \rho_f D_o V_{\text{flow}} (\dot{u}_2 - V_{\text{flow}} \varphi_2) + k_f \dot{u}_2 \quad (2.74)$$

$$F_{f_3} = \frac{1}{2} C_f \rho_f D_o V_{\text{flow}}^2 \quad (2.75)$$

$$T_f = \frac{\pi D_o^2}{2} \left(\tau_y + k \left(\frac{4\pi D_{ch}^2}{D_{ch}^2 - D_o^2} \omega_{ds} \right)^{n_f} \right) \quad (2.76)$$

Here F_{f_1} and F_{f_2} are the lateral fluid forces, F_{f_3} is the axial fluid force, and T_f is the fluid torque acting on the drillstring. φ_1 and φ_2 are the lateral tilting angles along the first and second axes of the beam, D_{ch} is the diameter of the wellbore, ρ_f is the density of the drilling fluid, τ_y is the yield point of the fluid, k is the consistency index associated with Yield-Plastic Law (YPL) fluids, and n_f is the flow behavior index of the fluid. The bulk flow velocity (V_{flow}) of the fluid in the annulus is a combination of the flow velocity (V_∞) and the axial drillstring velocity (\dot{u}_3).

$$V_{\text{flow}} = V_\infty + \dot{u}_3 \quad (2.77)$$

k_f is a damping parameter that is defined as [123]

$$k_f = \frac{2\sqrt{2}}{\sqrt{N_s}} \frac{1 + \left(\frac{D_o}{D_{ch}}\right)^3}{\left(1 - \left(\frac{D_o}{D_{ch}}\right)^2\right)^2} \rho_f A_o \Omega \quad (2.78)$$

Where A_o is the cross-sectional area of the outer diameter of the drillstring ($A_o = \pi D_o/4$), and Ω is the oscillating circular frequency (taken to be the rotation speed for a rotating drillstring or the lateral excitation frequency when simulating slide drilling with an LET). N_s is the stokes number, which is defined as

$$N_s = \frac{\Omega D_o^2}{4\nu_f} \quad (2.79)$$

Where ν_f is the kinematic viscosity of the drilling fluid. The novel contribution of this fluid model is the introduction of a dynamic fluid-damping parameter, C_f .

$$C_f = af_f \quad (2.80)$$

Here f_f is the Yield-Plastic Law fluid friction coefficient calculated via the approach taken by Erge et. al. [124] and a is an empirical factor that must be calibrated based on experimental data.

It should be noted that this drillstring-fluid interaction is not intended to provide definitive solutions to the nonlinear problem of drillstring dynamics, it is merely examined as a possibility of the fluid-damping mechanisms taking place down-hole. Any analysis conducted with this fluid force model is only meant to provide a comparison with traditional proportional damping (commonly used for nonlinear finite element simulation models) in order to better understand the potential range of behaviors associated with nonlinear drillstring dynamics.

3. NONLINEAR FINITE ELEMENT FORMULATION

The equations developed thus far have been for a single point on the central axis of a beam, with a constant cross-section, constrained within a wellbore of constant curvature. Keeping in mind the nature of the “drillstring problem”, cross-sectional properties are never constant along the length of the drilling assembly and curvatures can vary considerably over the course of a wellbore’s trajectory. Because of this, it is necessary to solve the nonlinear equations in such a way that allows the drillstring to be divided into separate sections. On top of this, it will be necessary to be able to apply force and/or displacement boundary conditions at arbitrary points along the drillstring. With the above considerations in mind, the Finite Element Method (FEM) was chosen as the best fit approach to analyze the problem.

This section outlines the derivation of the nonlinear finite element model based on the equations presented in Section 2. The principal of virtual work is first applied, which transforms the beam equations into a “weak form” [125] with relaxed continuity requirements. From this weak form, the drillstring is sectioned into elements, and the displacement vectors of each node are defined. Interpolation functions, or shape functions, are then applied directly to the weak form of the beam equations in order to provide descriptions of how the displacement variables change over the length of each beam. This discretization approach is then also applied to the external force functions. Once the elemental and nodal vectors have been defined by this procedure, the complete equations for static, linearized-dynamic, and fully nonlinear-dynamic analysis are presented. In addition, considerations for modeling specific aspects of the drillstring such as rotary steerable systems, steerable mud motors, and eccentric/concentric stabilizers are provided.

3.1 Hamilton’s Principal of Virtual Work

Derivation of a finite element model begins with Hamilton’s extended Principle of Virtual Work for a deformable body [126], which can be expressed as

$$\int_t (\delta T_K - \delta U + \delta W_e) dt = 0 \quad (3.1)$$

Where T_K is the kinetic energy, U is the strain energy, W_e is the contribution of external forces acting on the body of interest, and the δ operator corresponds to the first variation of a function with respect to virtual displacement. Thus, the above equation states that the virtual strain energy (δU), subtracted from the summation of the variation of the kinetic energy (δT_K) and the external virtual work (δW_e), remains unchanged in time and equal to zero. The following sections outline the derivation of the terms in (3.1), then discretizes the equations into a usable form for nonlinear finite element analysis.

3.1.1 Variation of Kinetic Energy

The kinetic energy of the beam can be represented in the same manner as presented by Heisig [34].

$$T_K = \frac{1}{2} \int_0^L \{\rho A(\dot{u}_1^2 + \dot{u}_2^2 + \dot{u}_3^2) + \rho I(\omega_1^2 + \omega_2^2) + \rho J\omega_3^2\} ds \quad (3.2)$$

Where (\cdot) represents a derivative with respect to time. Thus, \dot{u}_i is the translational velocity in the i -th direction and the rotational velocities, ω_i , are the same as defined by (2.40). Taking the first variation of (3.2) and integrating by parts leads to

$$\int_{t_2}^{t_2} \delta T_K dt = \delta T_{K_b} - \int_{t_2}^{t_1} \left\{ \begin{array}{l} \int_0^L \{\rho A[\delta u_1 \ddot{u}_1 + \delta u_2 \ddot{u}_2 + \delta u_3 \ddot{u}_3] \\ + \rho I[\delta \tilde{\varphi}_2 \ddot{\tilde{\varphi}}_2 + \delta \varphi_1 \ddot{\varphi}_1] + \rho J \delta \theta_3 \ddot{\theta}_3\} ds \\ + \int_0^L \{\rho J[-\delta \tilde{\varphi}_2(-\varphi_1^2 \ddot{\tilde{\varphi}}_2 + \varphi_1 \ddot{\theta}_3) - \delta \theta_3 \varphi_1 \ddot{\tilde{\varphi}}_2 \\ + \delta \tilde{\varphi}_2(2\varphi_1 \ddot{\tilde{\varphi}}_2 - \dot{\theta}_3)\dot{\varphi}_1 \\ + \delta \varphi_1(\varphi_1 \ddot{\tilde{\varphi}}_2 - \dot{\theta}_3)\dot{\tilde{\varphi}}_2 - \delta \theta_3 \dot{\tilde{\varphi}}_2 \dot{\varphi}_1]\} ds \end{array} \right\} dt \quad (3.3)$$

Where the boundary terms, δT_{K_b} , will vanish and go to zero [127]. It can be noticed that the first group of spatial integral terms in (3.3) is representative of the drillstring's mass, including rotary inertias. The second group of spatial integral terms is associated with the gyroscopic moments acting on the system. This latter term was neglected in Heisig's formulation. The tilting angles introduced in (3.3) are defined as

$$\begin{aligned} \varphi_1 &= u'_1 - \gamma_2 \\ \varphi_2 &= u'_2 + \gamma_1 \end{aligned} \quad (3.4)$$

And the effective tilting angle along the beam's second axis is defined such that

$$\tilde{\varphi}_2 = \varphi_2 + \kappa_o u_3 \quad (3.5)$$

3.1.2 External Virtual Work

The external virtual work acting on the beam suspended in drilling fluid is identical to that presented by Heisig [34]

$$\delta W_e = \int_0^L \tilde{q}(g_1 \delta u_1 + g_2 \delta u_2 + g_3 \delta u_3) ds \quad (3.6)$$

$$\tilde{q} = q S G_f \quad (3.7)$$

Where q is the linear weight of the drillstring, \tilde{q} is the effective buoyed weight of the drillstring, SG_f if the specific gravity of the drilling fluid, and g_i is the gravity component acting along the i -th axis and represents the scalar projection of the vector \hat{v}_i ($i = 1, 2$, and 3) onto the principal z-axis (\hat{k}). In mathematical terms this is the dot product of \hat{v}_i and \hat{k} .

$$g_i = \hat{v}_i \cdot \hat{k} \quad (i = 1, 2, 3) \quad (3.8)$$

3.1.3 Virtual Strain Energy

Nachbagauer [128] outlines the structural mechanics based formulation of the internal strain energy of a shear deformable beam as

$$U = \frac{1}{2} \int_0^L \{EI\kappa^2 + GAK_s(\gamma_1^2 + \gamma_2^2) + EA\epsilon^2 + GJ\tau^2\} ds \quad (3.9)$$

Where E is the Young's Modulus of the material, G is the shear modulus (for elastic materials this is related to Young's Modulus through Poisson's ratio, ν , as $G = E/2(1 + \nu)$), A is the cross-sectional area, I is the area moment of inertia, J is the polar area moment of inertia (for circular cross-section $J = 2I$), κ is the total deformation curvature of the central axis of the beam, γ_1 and γ_2 are the shear deformation rotations about the first and second axes respectively, ϵ is the generalized axial strain, τ is the generalized torsional strain, L is the length of the beam, and K_s is the shear correction factor. For a hollow circular cross-section the shear correction factor is provided by equation (3.10) [129].

$$K_s = \frac{6(1+\nu)\left(1+\left(\frac{D_i}{D_o}\right)^2\right)^2}{(7+6\nu)\left(1+\left(\frac{D_i}{D_o}\right)^2\right)^2 + 4(5+3\nu)\left(\frac{D_i}{D_o}\right)^2} \quad (3.10)$$

Noting that $\kappa^2 = \kappa_1^2 + \kappa_2^2$, the total deformation curvature of the beam's central axis can be expressed as

$$\kappa^2 = \varphi'_1^2 + (\varphi'_2 + \kappa_o)^2 \quad (3.11)$$

Now taking (2.58), (2.61), (3.11), and putting them into (3.9), then taking the first variation, leads to an expression for the virtual strain energy of the beam.

$$\delta U = \int_0^L \left\{ \begin{array}{l} EI[\delta\varphi'_1\varphi'_1 + \delta\varphi'_2(\varphi'_2 + \kappa_o)] \\ + GAK_S[\delta\gamma_1\gamma_1 + \delta\gamma_2\gamma_2] \\ + EAH_1[\delta\tilde{u}'_3 + \delta u'_1\gamma_2 + \delta\gamma_2 u'_1 - \delta\tilde{u}'_2\gamma_1 \\ \quad - \delta\gamma_1\tilde{u}'_2 + \delta\varphi_1\varphi_1 + \delta\tilde{\varphi}_2\tilde{\varphi}_2] \\ + GJH_2[\delta\theta'_3 - \delta\varphi_1\varphi'_2 - \delta\varphi'_2\varphi_1] \end{array} \right\} ds \quad (3.12)$$

Where,

$$\begin{aligned} H_1 &= \tilde{u}'_3 + u'_1\gamma_2 - \tilde{u}'_2\gamma_1 + \frac{1}{2}\varphi_1^2 + \frac{1}{2}\tilde{\varphi}_2^2 \\ H_2 &= \tilde{\theta}'_3 - \varphi'_2\varphi_1 \end{aligned} \quad (3.13)$$

And,

$$\begin{aligned} \tilde{u}'_2 &= u'_2 + \kappa_o u_3 \\ \tilde{u}'_3 &= u'_3 - \kappa_o u_2 \\ \tilde{\theta}'_3 &= \theta'_3 - \kappa_o \gamma_1 \end{aligned} \quad (3.14)$$

Equations (3.12)-(3.14) represents the weak form of the internal forces developed within the drillstring as it deflects in the wellbore. The weak form relaxes the continuity requirement of the system which allows for a segmentation of the domain.

3.2 Element Discretization

The drillstring is represented as a flexible curve whose displacement is dictated by the equations presented by (3.1), (3.3), (3.6), and (3.12). If the drillstring is broken down into sections, as shown in Figure 3.1, then each section will have two end points, A and B. The individual drillstring sections are referred to as elements, while the end points are referred to as nodes. Each node has six degrees of freedom and is restricted in the lateral directions by the radial clearance between the drillstring and the wellbore wall.

The degrees of freedom correspond to two lateral deflections (u_1 and u_2), two lateral rotations (φ_1 and φ_2), an axial deflection (u_3), and a rotation about the centerline of the drillstring (θ_3). For each element the displacement, velocity, and acceleration vectors can be expressed by

$$\begin{aligned} \underline{u} &= (u_1^A, \varphi_1^A, u_2^A, \varphi_2^A, u_3^A, \theta_3^A, u_1^B, \varphi_1^B, u_2^B, \varphi_2^B, u_3^B, \theta_3^B)^T \\ \underline{\dot{u}} &= (\dot{u}_1^A, \dot{\varphi}_1^A, \dot{u}_2^A, \dot{\varphi}_2^A, \dot{u}_3^A, \dot{\theta}_3^A, \dot{u}_1^B, \dot{\varphi}_1^B, \dot{u}_2^B, \dot{\varphi}_2^B, \dot{u}_3^B, \dot{\theta}_3^B)^T \\ \underline{\ddot{u}} &= (\ddot{u}_1^A, \ddot{\varphi}_1^A, \ddot{u}_2^A, \ddot{\varphi}_2^A, \ddot{u}_3^A, \ddot{\theta}_3^A, \ddot{u}_1^B, \ddot{\varphi}_1^B, \ddot{u}_2^B, \ddot{\varphi}_2^B, \ddot{u}_3^B, \ddot{\theta}_3^B)^T \end{aligned} \quad (3.15)$$

It can be noted that the definition of the above vectors is completely arbitrary. This means that the order in which the variables are presented within the vectors could be changed if desired.

3.2.1 Shape Functions

With the previous definition of elemental displacements, the various deflections along the length of a beam can be expressed as a function of a local beam coordinate ξ .

$$\xi = \frac{s - s_n}{l} \quad (3.16)$$

Where n is the 1st node (Node A) of the n -th element. With this definition the length-wise derivatives along the beam can be expressed as

$$()' = \frac{\partial()}{\partial s} = \frac{1}{l} \frac{\partial()}{\partial \xi} \quad (3.17)$$

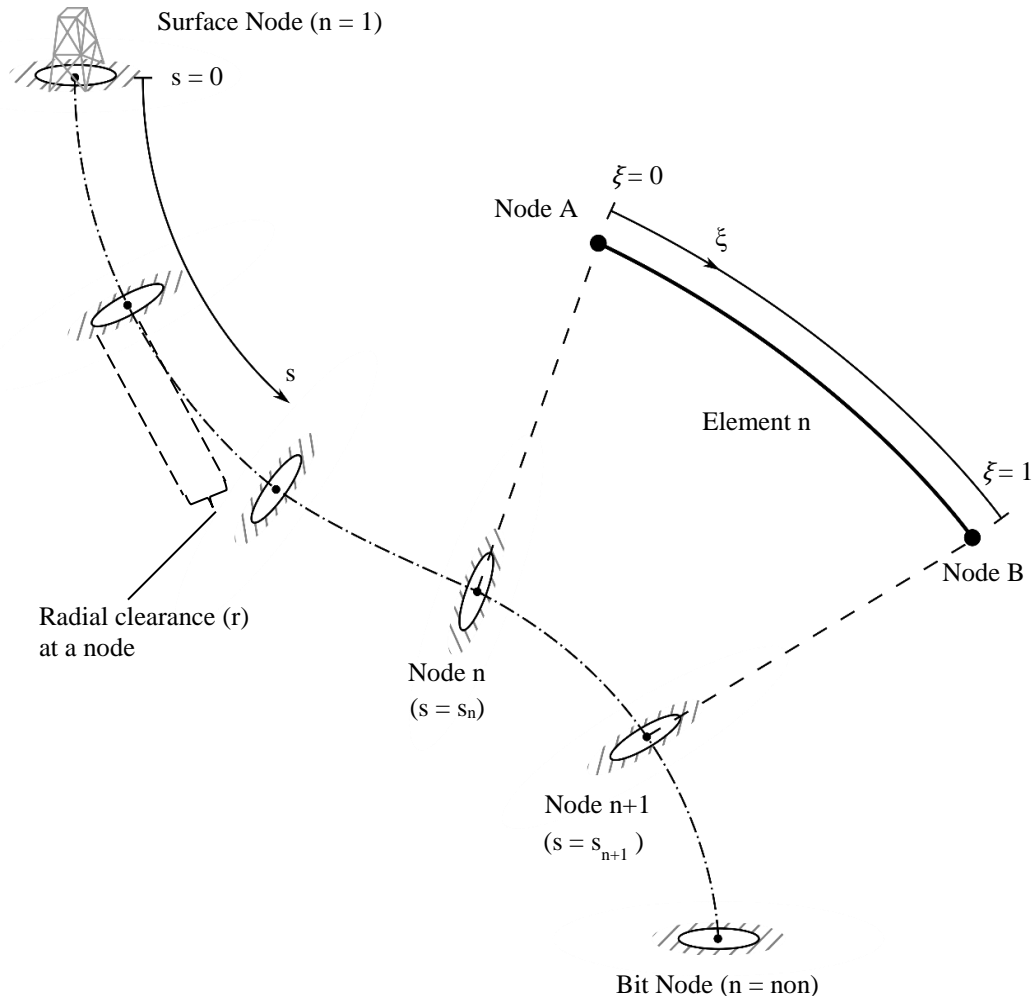


Figure 3.1: Finite Element Representation of the Drillstring

Using the local coordinate, displacements and virtual displacements along the length of an element are written as

$$\begin{aligned}
u_1 &= \underline{h}_1^T(\xi) \underline{u} & \delta u_1 &= \underline{\delta u} \underline{h}_1^T(\xi) \\
\varphi_1 &= \underline{h}_2^T(\xi) \underline{u} & \delta \varphi_1 &= \underline{\delta u} \underline{h}_2^T(\xi) \\
\gamma_1 &= \left(\underline{h}_4^T(\xi) - \underline{h}_3'^T(\xi) \right) \underline{u} & \delta \gamma_1 &= \underline{\delta u} \left(\underline{h}_4^T(\xi) - \underline{h}_3'^T(\xi) \right) \\
u_2 &= \underline{h}_3^T(\xi) \underline{u} & \delta u_2 &= \underline{\delta u} \underline{h}_3^T(\xi) \\
\varphi_2 &= \underline{h}_4^T(\xi) \underline{u} & \delta \varphi_2 &= \underline{\delta u} \underline{h}_4^T(\xi) \\
\gamma_2 &= \left(\underline{h}_1'^T(\xi) - \underline{h}_2^T(\xi) \right) \underline{u} & \delta \gamma_2 &= \underline{\delta u} \left(\underline{h}_1'^T(\xi) - \underline{h}_2^T(\xi) \right) \\
u_3 &= \underline{h}_5^T(\xi) \underline{u} & \delta u_3 &= \underline{\delta u} \underline{h}_5^T(\xi) \\
\theta_3 &= \underline{h}_6^T(\xi) \underline{u} & \delta \theta_3 &= \underline{\delta u} \underline{h}_6^T(\xi)
\end{aligned}
\quad (3.18) \quad (3.19)$$

Where the \underline{h} vectors are made up of interpolation functions, or shape functions, that relate the nodal displacements to displacements throughout the beam.

$$\begin{aligned}
\underline{h}_1 &= (N_1, N_2, 0, 0, 0, 0, N_3, N_4, 0, 0, 0, 0)^T \\
\underline{h}_2 &= (N_5, N_6, 0, 0, 0, 0, N_7, N_8, 0, 0, 0, 0)^T \\
\underline{h}_3 &= (0, 0, N_1, N_2, 0, 0, 0, 0, N_3, N_4, 0, 0)^T \\
\underline{h}_4 &= (0, 0, N_5, N_6, 0, 0, 0, 0, N_7, N_8, 0, 0)^T \\
\underline{h}_5 &= (0, 0, 0, 0, N_9, 0, 0, 0, 0, 0, N_{10}, 0)^T \\
\underline{h}_6 &= (0, 0, 0, 0, 0, N_9, 0, 0, 0, 0, 0, N_{10})^T
\end{aligned}
\quad (3.20)$$

In order to avoid the “shear-locking” phenomena typically associated with shear deformable beam models, the “consistent shape functions” derived by Luo [130] are incorporated into (3.20). These shape functions are shown by

$$\begin{aligned}
N_1 &= \frac{1}{1-\Lambda}(2\xi^3 - 3\xi^2 + \Lambda\xi + 1 - \Lambda) & N_6 &= \frac{1}{1-\Lambda}(3\xi^2 + \xi(\Lambda - 4) + 1 - \Lambda) \\
N_2 &= \frac{l}{1-\Lambda}\left(\xi^3 + \xi^2\left(\frac{\Lambda}{2} - 2\right) + \xi\left(1 - \frac{\Lambda}{2}\right)\right) & N_7 &= \frac{6}{l(1-\Lambda)}(-\xi^2 + \xi) \\
N_3 &= \frac{1}{1-\Lambda}(-2\xi^3 + 3\xi^2 - \Lambda\xi) & N_8 &= \frac{1}{1-\Lambda}(3\xi^2 - \xi(\Lambda + 2)) \\
N_4 &= \frac{l}{1-\Lambda}\left(\xi^3 - \xi^2\left(1 + \frac{\Lambda}{2}\right) + \frac{\Lambda}{2}\xi\right) & N_9 &= 1 - \xi \\
N_5 &= \frac{6}{l(1-\Lambda)}(\xi^2 - \xi) & N_{10} &= \xi
\end{aligned}
\quad (3.21)$$

$$\Lambda = \frac{12EI}{K_s G A l^2} \quad (3.22)$$

3.2.2 Internal Forces, Moments, and Inertia of the Drillstring

With the shape functions described in the previous section, definitions of the elemental equations can readily be extracted from the relationships in Section 3.1. Based on the principle of virtual work, the elemental mass matrix and gyroscopic moment vector are determined from (3.3), where the mass matrix is expressed as

$$\underline{\underline{M}}_\rho = \int_0^1 \{ \rho A (\underline{h}_1 \underline{h}_1^T + \underline{h}_3 \underline{h}_3^T + \underline{h}_5 \underline{h}_5^T) + \rho I (\tilde{\underline{h}}_4 \tilde{\underline{h}}_4^T + \underline{h}_2 \underline{h}_2^T) + \rho J (\underline{h}_6 \underline{h}_6^T) \} l d\xi \quad (3.23)$$

And the gyroscopic moment vector is

$$\underline{F}_{M_{gyro}} = \rho J \int_0^1 \left\{ \begin{array}{l} \tilde{\underline{h}}_4 [(\underline{h}_2^T \underline{u})^2 (\tilde{\underline{h}}_4^T \dot{\underline{u}}) - (\underline{h}_2^T \underline{u})(\underline{h}_6^T \dot{\underline{u}})] \\ -\underline{h}_6 [(\underline{h}_2^T \underline{u})(\tilde{\underline{h}}_4^T \dot{\underline{u}})] \\ +\underline{h}_2 [(\underline{h}_2^T \underline{u})(\tilde{\underline{h}}_4^T \dot{\underline{u}})^2 - (\tilde{\underline{h}}_4^T \dot{\underline{u}})(\underline{h}_6^T \dot{\underline{u}})] \\ -\tilde{\underline{h}}_4 [(\underline{h}_2^T \underline{u})(\underline{h}_6^T \dot{\underline{u}}) - 2(\underline{h}_2^T \underline{u})(\underline{h}_2^T \dot{\underline{u}})(\tilde{\underline{h}}_4^T \dot{\underline{u}})] \\ -\underline{h}_6 [(\underline{h}_2^T \underline{u})(\tilde{\underline{h}}_4^T \dot{\underline{u}})] \end{array} \right\} l d\xi \quad (3.24)$$

It can be noted that (3.23) and (3.24) are elemental quantities, meaning that they will produce values for both nodes of an element. As such, the mass matrix in (3.23) is a 12x12 array while the gyroscopic moment vector of (3.24) is a 12x1 array.

The beam's internal force vector is determined from (3.12) and is written as

$$\underline{F}_B = \int_0^1 \left\{ \begin{array}{l} EI [h'_2 (\underline{h}_2'^T \underline{u}) + h'_4 ((\underline{h}_4'^T \underline{u}) + \kappa_o)] \\ + GAK_S [\tilde{h}_{43} (\tilde{\underline{h}}_{43}^T \underline{u}) + \tilde{h}_{12} (\tilde{\underline{h}}_{12}^T \underline{u})] \\ + EAH_1 [\tilde{h}'_5 + \underline{h}_2 (\underline{h}_2^T \underline{u}) + h'_1 (\tilde{\underline{h}}_{12}^T \underline{u}) + \tilde{h}_{12} (\underline{h}_1^T \underline{u}) \\ \quad + \tilde{h}_4 (\tilde{\underline{h}}_4^T \underline{u}) - \tilde{h}'_3 (\tilde{\underline{h}}_{43}^T \underline{u}) - \tilde{h}_{43} (\tilde{\underline{h}}_3^T \underline{u})] \\ + GJH_2 [\tilde{h}'_6 - \underline{h}_2 (\underline{h}_4'^T \underline{u}) - h'_4 (\underline{h}_2^T \underline{u})] \end{array} \right\} l d\xi \quad (3.25)$$

Where the scalar quantities H_1 and H_2 are

$$\begin{aligned} H_1 &= (\tilde{\underline{h}}_5'^T \underline{u}) + \frac{1}{2} (\underline{h}_2^T \underline{u})^2 + \frac{1}{2} (\tilde{\underline{h}}_4^T \underline{u})^2 + (\underline{h}_1'^T \underline{u})(\tilde{\underline{h}}_{12}^T \underline{u}) - (\tilde{\underline{h}}_{43}^T \underline{u})(\tilde{\underline{h}}_3'^T \underline{u}) \\ H_2 &= (\tilde{\underline{h}}_6'^T \underline{u}) - (\underline{h}_4'^T \underline{u})(\underline{h}_2^T \underline{u}) \end{aligned} \quad (3.26)$$

The effective shape functions used in (3.23)-(3.26) are listed below

$$\begin{aligned}
 \tilde{h}'_3 &= \underline{h}'_3 + \kappa_o \underline{h}_5 \\
 \tilde{h}'_5 &= \underline{h}'_5 - \kappa_o \underline{h}_3 \\
 \tilde{h}'_6 &= \underline{h}'_6 - \kappa_o \underline{h}_2 \\
 \tilde{h}_4 &= \underline{h}_4 + \kappa_o \underline{h}_5 \\
 \tilde{h}_{43} &= \underline{h}_4 - \underline{h}'_3 \\
 \tilde{h}_{12} &= \underline{h}'_1 - \underline{h}_2
 \end{aligned} \tag{3.27}$$

Similar to (3.24), (3.25) will be a 12x1 vector with values corresponding to the internal shear forces (S), bending moments (M_B), axial forces (F), and torque (T) values associated with each beam. This is expressed by (3.28).

$$F_B = (S_1^A, M_{B1}^A, S_2^A, M_{B2}^A, F_3^A, T_3^A, S_1^B, M_{B1}^B, S_2^B, M_{B2}^B, F_3^B, T_3^B)^T \tag{3.28}$$

With this understanding, it can be seen how internal drillstring forces can be extracted from the drillstring model. If one wishes to determine the shear loads, bending moments, axial forces, or torque at a given point in the drillstring, then (3.25) can be used to calculate these internal force components. Note that the external force vector (3.29) must be subtracted from (3.28) in order to determine the proper internal loads on the beam.

3.2.3 External Forces Acting on the Drillstring

The external forces acting on the drillstring consist of gravitational forces, frictional contact between the drillstring and the wellbore, and the fluid forces being exerted on the drillstring as it moves within the confines of the wellbore.

3.2.3.1 Gravitational Forces

The gravitational forces acting on an element are determined from (3.6) as

$$\underline{Q} = \int_0^1 \{\tilde{q}(g_1 \underline{h}_1^T + g_2 \underline{h}_3^T + g_3 \underline{h}_5^T)\} l d\xi \tag{3.29}$$

For practical analysis, the static WOB and TOB are added to this force vector at the appropriate node.

3.2.3.2 Frictional Wall Contact

Frictional wall contact is a nodal quantity, thus the forces and moments acting on the drillstring at a particular node can be written as a 6x1 vector. As discussed in Section 2, Heisig [34] presented a frictional contact model based on the quasi-static state of a rotating drillstring. These equations can be expressed in terms of the current finite element model as

$$\underline{F}_{wN} = k_w \frac{\sqrt{u_1^2 + u_2^2} - r}{\sqrt{u_1^2 + u_2^2}} (u_1, 0, u_2, 0, 0, 0)^T \quad (3.30)$$

$$\underline{F}_{wT} = \mu_T k_w \frac{\sqrt{u_1^2 + u_2^2} - r}{\sqrt{u_1^2 + u_2^2}} (-u_2, 0, u_1, 0, \varphi_1 u_2 - (\varphi_2 + \kappa_o u_3) u_1, 0)^T \quad (3.31)$$

$$\underline{F}_{wM} = \frac{D_o \mu_T k_w}{2} \left(\sqrt{u_1^2 + u_2^2} - r \right) (0, 0, 0, -\varphi_1, -\kappa_o \varphi_1, 1)^T \quad (3.32)$$

However, equations (3.30)-(3.32) only account for lateral acting friction. The axial friction (2.69) can also be incorporated as

$$\underline{F}_{wA} = \mu_A k_w \left(\sqrt{u_1^2 + u_2^2} - r \right) (\varphi_1, 0, \varphi_2 + \kappa_o u_3, 0, 1, 0)^T \quad (3.33)$$

Of course the frictional contact forces will only be present if the drillstring, at a particular node, has come into contact with the wellbore wall. Therefore the forces will only “activate” within the model if the drillstring deflects beyond the boundary of the wellbore. This is quantified by the following rule.

$$\underline{F}_w = \begin{cases} 0 & \text{for } \sqrt{u_1^2 + u_2^2} \leq r \\ \underline{F}_{wN} + \underline{F}_T + \underline{F}_{wM} + \underline{F}_{wA} & \text{for } \sqrt{u_1^2 + u_2^2} > r \end{cases} \quad (3.34)$$

Based on (3.34), if the radial clearance is exceeded within the model, then a restoring force will be applied to keep the drillstring confined within the wellbore. This is known as a penalty approach for imposing a contact restriction within a finite element model. Also, if the friction is non-existent, all of the frictional forces will vanish due to their dependence on a friction coefficient.

3.2.3.3 Fluid-Drillstring Interaction

Incorporating the element discretization described in this section, (2.73) – (2.76) can be written as

$$F_{f1} = \int_0^1 \left\{ \frac{1}{2} C_f \rho_f D_o (V_\infty + \underline{h}_5^T \dot{\underline{u}}) \left((\underline{h}_1^T \dot{\underline{u}}) - (V_\infty + (\underline{h}_5^T \dot{\underline{u}})) \underline{h}_2^T \underline{u} \right) \underline{h}_1 + k_f (\underline{h}_1^T \dot{\underline{u}}) \underline{h}_1 \right\} l d\xi \quad (3.35)$$

$$\underline{F}_{f_2} = \int_0^1 \left\{ \frac{1}{2} C_f \rho_f D_o (V_\infty + \underline{h}_5^T \dot{\underline{u}}) \left((\underline{h}_3^T \dot{\underline{u}}) - (V_\infty + (\underline{h}_5^T \dot{\underline{u}})) \underline{h}_4^T \underline{u} \right) \underline{h}_3 + k_f (\underline{h}_3^T \dot{\underline{u}}) \underline{h}_3 \right\} l d\xi \quad (3.36)$$

$$\underline{F}_{f_3} = \int_0^1 \left\{ \frac{1}{2} C_f \rho_f D_o (V_\infty + \underline{h}_5^T \dot{\underline{u}})^2 \underline{h}_5 \right\} l d\xi \quad (3.37)$$

$$\underline{T}_f = \int_0^1 \left\{ \frac{\pi D_o^2}{2} \left(\tau_y + k \left(\frac{4\pi D_{ch}^2}{D_{ch}^2 - D_o^2} (\underline{h}_6^T \dot{\underline{u}}) \right)^n \right) \left(-(\underline{h}_2^T \underline{u}) \underline{h}_4 - \kappa_o (\underline{h}_2^T \underline{u}) \underline{h}_5 + \underline{h}_6 \right) \right\} l d\xi \quad (3.38)$$

$$\underline{F}_f = \underline{F}_{f_1} + \underline{F}_{f_2} + \underline{F}_{f_3} + \underline{T}_f \quad (3.39)$$

Again, because the fluid forces act over the length of the element, (3.39) will be 12x1 vector.

3.3 Complete Drillstring Equations

The complete nonlinear system of equations, originally represented by (3.1), can now be expressed as

$$[\underline{\underline{M}}_o + \underline{\underline{M}}_F] \ddot{\underline{u}} + [C] \dot{\underline{u}} + \underline{F}_{M_{Gyro}}(\underline{u}, \dot{\underline{u}}, \ddot{\underline{u}}) + \underline{F}_w(\underline{u}, \dot{\underline{u}}) + \underline{F}_B(\underline{u}) + \underline{F}_f(\underline{u}, \dot{\underline{u}}) = \underline{Q} + \underline{F}_{Exc}(t) \quad (3.40)$$

An additional mass term ($\underline{\underline{M}}_F$) can be noticed in (3.40). This represents the added fluid mass of the drilling mud surrounding the drillstring, and will be described in the following sections. A damping term ([C]) is also present in the above equation, which is representative of the structural damping of the system and will also be discussed shortly. Solving (3.40) cannot be done directly as it is a nonlinear equation that depends on the displacement, velocity, and acceleration of the drillstring. The specific approach to solving (3.40) will depend on the type of result desired. Specifically, three types of analyses are possible: nonlinear-static deflection, linearized-dynamic vibration, and fully nonlinear-dynamic behavior. Each approach requires a unique method of calculation.

3.3.1 Nonlinear-Static Equations

For the case of a static drillstring, all velocities and accelerations are zero. Thus (3.40) reduces to

$$\underline{F}_w(\underline{u}) + \underline{F}_B(\underline{u}) = \underline{Q} \quad (3.41)$$

Again, this is a nonlinear equation and cannot be solved directly; an iterative approach must be taken. Employing the Newton-Raphson method [125], (3.41) can be expressed as

$$\begin{aligned} \underline{K}_i \Delta \underline{u}_i &= \underline{Q} - \underline{F}_B(\underline{u}_i) - \underline{F}_w(\underline{u}_i) \\ \underline{u}_{i+1} &= \underline{u}_{i-1} + \Delta \underline{u}_i \end{aligned} \quad (3.42)$$

*Note: The summation of the terms on the right hand side of (3.42) is sometimes referred to as the “Residual Force Vector” ($\underline{R} = \underline{Q} - \underline{F}_B(\underline{u}_i) - \underline{F}_W(\underline{u}_i)$)

Where \underline{K}_i is known as the “tangent stiffness” matrix that is generated through the linearization procedure of (3.41). This matrix is written as

$$[K]_i = \left[\frac{\partial F_B}{\partial \underline{u}} (\underline{u}_i) + \frac{\partial F_W}{\partial \underline{u}} (\underline{u}_i) \right] \quad (3.43)$$

The system represented by (3.42) is continuously solved for each i -th iteration until $\Delta \underline{u}_i$ becomes so small that it provides a negligible contribution to the overall solution.

The linearization of the internal force vector of the beam requires a derivative, with respect to displacement, of (3.25). This is fairly straight forward to calculate and is provided below for reference.

$$\begin{aligned} \frac{\partial F_B}{\partial \underline{u}} &= \int_0^1 \left\{ \begin{array}{l} EI[h'_2 h'_2^T + h'_4 h'_4^T] \\ + GAK_S[\tilde{h}_{43} \tilde{h}_{43}^T + \tilde{h}_{12} \tilde{h}_{12}^T] \\ + EA[(\tilde{h}'_5 + \underline{h}_2(h'_2 \underline{u}) + \underline{h}'_1(\tilde{h}_{12}^T \underline{u}) + \tilde{h}_{12}(h'_1 \underline{u}) \\ \quad + \tilde{h}_4(\tilde{h}_4^T \underline{u}) - \tilde{h}'_3(\tilde{h}_{43}^T \underline{u}) - \tilde{h}_{43}(\tilde{h}_3^T \underline{u})) \frac{\partial H_1}{\partial \underline{u}} \\ \quad + H_1(\tilde{h}'_5 + \underline{h}_2 h'_2 + \underline{h}'_1 \tilde{h}_{12}^T + \tilde{h}_{12} h'_1^T \\ \quad \quad + \tilde{h}_4 \tilde{h}_4^T - \tilde{h}'_3 \tilde{h}_{43}^T - \tilde{h}_{43} \tilde{h}_3^T)] \\ + GJ[(\tilde{h}'_6 - \underline{h}_2(h'_4 \underline{u}) - \underline{h}'_4(h'_2 \underline{u})) \frac{\partial H_2}{\partial \underline{u}} \\ \quad + H_2(-\underline{h}_2 h'_4^T - \underline{h}'_4 \underline{h}_2^T)] \end{array} \right\} d\xi \\ \frac{\partial H_1}{\partial \underline{u}} &= \tilde{h}'_5^T + (\underline{h}_2^T \underline{u}) h'_2^T + (\tilde{h}_4^T \underline{u}) \tilde{h}_4^T + (\tilde{h}_{12}^T \underline{u}) \underline{h}'_1^T + (h'_1^T \underline{u}) \tilde{h}_{12}^T - (\tilde{h}_3^T \underline{u}) \tilde{h}_{43}^T - (\tilde{h}_{43}^T \underline{u}) \tilde{h}_3^T \\ \frac{\partial H_2}{\partial \underline{u}} &= \tilde{h}'_6^T - (\underline{h}_2^T \underline{u}) h'_4^T - (\underline{h}'_4^T \underline{u}) h'_2^T \end{aligned} \quad (3.44)$$

The linearization of the wall contact force vector is a little more complicated because it is not written as an exact function of the displacement vector, \underline{u} . The derivative of (3.34) can be determined by calculating the Jacobian Matrix of the wall contact force vector. Determining the Jacobian of a vector can be described in the following way: If \underline{F} is a vector with m components, and is a function of n variables, then the Jacobian Matrix of \underline{F} , with respect to the vector of n variables (\underline{x}), can be expressed by (3.45).

$$\frac{\partial \underline{F}}{\partial \underline{x}} = \begin{bmatrix} \frac{\partial F_1}{\partial x_1} & \dots & \frac{\partial F_1}{\partial x_n} \\ \vdots & \ddots & \vdots \\ \frac{\partial F_m}{\partial x_1} & \dots & \frac{\partial F_m}{\partial x_n} \end{bmatrix} \quad (3.45)$$

As an example, the non-zero components of the Jacobian Matrix of (3.30), which yields a 6x6 array, is written as

$$\begin{aligned} \frac{\partial E_{vN}}{\partial \underline{u}}(1,1) &= \frac{k_w}{\sqrt{u_1^2+u_2^2}} \left(\sqrt{u_1^2+u_2^2}^3 - ru_2^2 \right) \\ \frac{\partial E_{vN}}{\partial \underline{u}}(1,3) &= \frac{k_w}{\sqrt{u_1^2+u_2^2}} u_1 u_2 r \\ \frac{\partial E_{vN}}{\partial \underline{u}}(3,1) &= \frac{k_w}{\sqrt{u_1^2+u_2^2}} u_1 u_2 r \\ \frac{\partial E_{vN}}{\partial \underline{u}}(3,3) &= \frac{k_w}{\sqrt{u_1^2+u_2^2}} \left(\sqrt{u_1^2+u_2^2}^3 - ru_1^2 \right) \end{aligned} \quad (3.46)$$

The same approach can be taken for the frictional components of the wall contact force vector. However, it must be remembered that the friction coefficients defined by (2.70)-(2.72) are a function of the axial and rotational velocities of the drillstring. Therefore, frictional effects are only present if the string is rotating and/or moving axially in the wellbore. Knowing this, it is possible to examine a quasi-static case assuming a constant rotation speed (drillstring RPM) and/or a constant axial speed (ROP/trip speed).

At this point it must be noted that the orientation of the normal (\hat{v}_2) and tangent (\hat{v}_3) unit vectors will not necessarily be constant over a given curved wellbore section. This is due to how the basis vectors are defined in (2.2)-(2.4). According to the Minimum Curvature Method for calculating wellbore trajectories (see Appendix A), the curvature of a wellbore segment (between two survey points for example) will lie in a single plane. This plane will contain the normal and tangential vectors of the well path within the curved wellbore segment. The bi-normal vector (\hat{v}_1) of the well path will be constant over the course of a curved wellbore segment, and will be perpendicular to the plane containing the curve. The normal unit vector will always be oriented towards the center of the wellbore curvature. This means that the relative gravity components in (3.6) may not be constant values over the length of an element, if that element is lying in a curved section of the wellbore. Again, this change in orientation can be quantified through the tool face angle (Appendix A), γ , which should not be confused with the tool face orientation (TFO) of a down-hole steering tool (see Section 1). The tool face angle can be utilized to address the problem of the changing

vector orientation over the length of an element. In order to properly account for the change in the relative gravities (\underline{g}_i) acting along the wellbore basis ($\hat{\nu}$), the following transformation is applied over an element.

$$\underline{\underline{T}}_{\Delta\gamma} = \begin{bmatrix} \cos(\Delta\gamma) & 0 & -\sin(\Delta\gamma) & 0 & 0 & 0 \\ 0 & \cos(\Delta\gamma) & 0 & -\sin(\Delta\gamma) & 0 & 0 \\ \sin(\Delta\gamma) & 0 & \cos(\Delta\gamma) & 0 & 0 & 0 \\ 0 & \sin(\Delta\gamma) & 0 & \cos(\Delta\gamma) & 0 & 0 \\ 0 & 0 & 0 & 0 & 1 & 0 \\ 0 & 0 & 0 & 0 & 0 & 1 \end{bmatrix} \quad (3.47)$$

Where the change in the tool face angle, $\Delta\gamma$, is the difference in the tool face angles of the two nodes on either end of the element.

$$\Delta\gamma = \gamma_{n+1} - \gamma_n \quad (3.48)$$

Here, node n would be associated with the top node of the element (closest to the surface, Node A), while node $n + 1$ would be associated with the bottom node of the element (closest to the bit, Node B). (3.47) can be applied directly to the global displacement vector of the element via

$$\begin{Bmatrix} \underline{u}_{ele}^A \\ \underline{u}_{ele}^B \end{Bmatrix} = \begin{bmatrix} \underline{\underline{1}} & \underline{\underline{0}} \\ \underline{\underline{0}} & \underline{\underline{T}}_{\Delta\gamma} \end{bmatrix} \begin{Bmatrix} \underline{u}_n \\ \underline{u}_{n+1} \end{Bmatrix} \quad (3.49)$$

where $\underline{u}_{ele}^{A/B}$ represent the local nodal deflections of the beam in the rotated reference frame (see Figure A.1), and \underline{u}_n represents that global nodal displacement values. The element transformation, expressed by (3.49), can then be used directly with elemental vectors and matrices such as (3.24), (3.25), (3.39), and (3.44). Nodal quantities, such as the wall contact forces, do not require this transformation as they are calculated directly from global/nodal displacements.

**Note: The matrix represented by $\underline{\underline{1}}$ indicates a square matrix of zeros, whose diagonal is populated with ones.*

Another practical aspect of the static analysis represented in (3.42) is the incorporation of “Soft-Spring Stabilization”. Because the governing equations of the system are highly-nonlinear it becomes beneficial, in terms of solution convergence, to incorporate this soft-spring for the first few iterations or so. Essentially, a very soft spring is applied to each node at the start of the iterative procedure. As the iteration advances, the stiffness of the springs is gradually decreased until a specified iteration number. Once the iteration count

reaches this specified limit, the springs are removed and the final solution is determined from continued iteration past this point. It should be noted that the number of iterations that require a soft-spring generally depends on the analysis, but care should be taken that the soft-springs are removed from the system prior to reaching a final solution.

3.3.2 Linearized-Dynamic Equations

Once a static solution has been determined, a linearized vibrational analysis can be conducted. Linearized-dynamic analysis of drillstrings can be done in one of two ways: a free vibration response, or a forced-frequency response; both of which estimate the tendency of a drillstring to have a larger response at a certain frequency. These types of analyses are limited to “continuous contact” dynamics. This means that the drillstring cannot lift off of the wellbore wall while it is oscillating, which is not the case in almost all occurrences of resonant dynamics. However, even in the absence of this complex behavior, linearized analysis has been shown to be effective for anticipating the critical frequencies associated with the fully nonlinear behavior of the drillstring [40, 122].

The linearized-dynamic system, neglecting gyroscopic effects, can be represented by (3.50)

$$[\underline{\underline{M}} + \underline{\underline{M}_F}(\omega)]\ddot{\underline{\psi}} + \underline{\underline{C}_F}(\omega)\dot{\underline{\psi}} + \underline{\underline{K}}\underline{\psi} = \underline{\underline{F}_{Ec}} \cos(\omega t) + \underline{\underline{F}_{Es}} \sin(\omega t) \quad (3.50)$$

Here, $\underline{\psi}$ represents the small perturbation displacements about the system’s equilibrium (static/quasi-static) position, $\underline{\underline{F}_E}$ is the vector of excitation force amplitudes, the subscripts s and c correspond to sinusoidal and cosinusoidal components respectively, ω is the circular excitation frequency ($\omega = 2\pi f$), $\underline{\underline{M}_F}(\omega)$ and $\underline{\underline{C}_F}(\omega)$ are the frequency-dependent added mass and damping due to the fluid surrounding the drillstring, and t is time.

3.3.2.1 Free Vibration

The free vibration response is associated with linearized natural frequencies, or normal modes, of the system. In this type of computation the undamped ($\underline{\underline{C}_F}(\omega) = 0$), unforced ($\underline{\underline{F}_{Ec}} = \underline{\underline{F}_{Es}} = 0$), system is examined. Thus (3.50) reduces to

$$[\underline{\underline{M}} + \underline{\underline{\tilde{M}}_F}]\ddot{\underline{\psi}} + \underline{\underline{K}}\underline{\psi} = 0 \quad (3.51)$$

Inserting an assumed displacement, $\underline{\psi} = \hat{\underline{\psi}}e^{-i\omega t}$, into (3.51) leads to the well-known Eigen-Value problem

$$\left[\underline{\underline{K}} - \omega^2 \left[\underline{\underline{M}} + \underline{\underline{\tilde{M}_F}} \right] \right] \hat{\underline{\psi}} = \underline{0} \quad (3.52)$$

Here, the tangent stiffness matrix is evaluated at the static position of the drillstring and $\hat{\underline{\psi}}$ is the eigenvector (non-dimensional displacement vector, or mode shape) associated with a specific eigenvalue (ω^2). $\underline{\underline{\tilde{M}_F}}$ is the added fluid mass due to the hydrodynamic effects generated from the lateral displacement of a fluid-filled drillstring, confined within a fluid-filled annulus. Heisig [34] presents a simplified formula for this added mass as

$$\begin{aligned} \underline{\underline{\tilde{M}_F}} &= \int_0^1 \{ \tilde{m}_{f_{lat}} (\underline{h}_1 \underline{h}_1^T + \underline{h}_3 \underline{h}_3^T) \} l d\xi \\ \tilde{m}_{f_{lat}} &= \rho_f \frac{\pi}{4} \left(D_o^2 \frac{D_{ch}^2 + D_o^2}{D_{ch}^2 - D_o^2} + D_i^2 \right) \end{aligned} \quad (3.53)$$

In which ρ_f is the density of the fluid, D_{ch} is the diameter of the wellbore, D_o is the outer diameter of the drillstring component, and D_i is the inner diameter. While it is believed that the added fluid mass is dependent on vibrational frequency [13, 34, 92], this simplified formula has proven to be effective [103, 105] for the calculation of normal modes.

The purpose of a free vibration study is to understand the inherent vibrational characteristics of a drillstring, namely the frequencies that have the potential of leading to higher levels of vibration (natural/resonant frequencies), and the vibrational patterns (mode shapes) associated with those frequencies. A common use of this type of analysis in the drilling industry is a “Critical RPM” calculation [40], in which the calculated frequency is expressed as a rotation speed ($RPM_{crit} = \frac{\omega}{2\pi} * 60$). This rotation speed would then be avoided in order to evade a resonant behavior in the drillstring due to unavoidable mass imbalances [87] along the length of the drilling assembly. While this is a reasonable analysis for examining the potential negative effects of string rotation, a free vibration analysis is not necessarily appropriate for localized excitations from things like bits, stabilizers, or vibration inducing devices. The reason behind this will be described in Section 5, but for now it can be stated that a forced-frequency analysis will more appropriately address these types of dynamic events.

3.3.2.2 Forced Vibration

Forced-frequency response (FFR) analysis determines the linearized (small displacement) response due to a harmonic (sine/cosine) excitation. These excitations can be applied at any point in the string, as well as any direction (axial, lateral, or torsional). The general form of this type of analysis is easily determined from (3.50) by assuming a displacement of the form

$$\underline{\psi} = \hat{\psi}_c \cos(\omega t) + \hat{\psi}_s \sin(\omega t) \quad (3.54)$$

Which leads to the linear system

$$\begin{bmatrix} \underline{\underline{K}} - \omega^2 [\underline{\underline{M}} + \underline{\underline{M}}_F(\omega)] & \omega \underline{\underline{C}}_F(\omega) \\ -\omega \underline{\underline{C}}_F(\omega) & \underline{\underline{K}} - \omega^2 [\underline{\underline{M}} + \underline{\underline{M}}_F(\omega)] \end{bmatrix} \begin{Bmatrix} \hat{\psi}_c \\ \hat{\psi}_s \end{Bmatrix} = \begin{Bmatrix} F_{Ec} \\ F_{Es} \end{Bmatrix} \quad (3.55)$$

The equations for the frequency-dependent fluid mass and fluid-damping, originally presented by Heisig [34], are listed below for reference.

$$\begin{aligned} \underline{\underline{M}}_F(\omega) &= \int_0^1 \{m_{f_{lat}}(\underline{h}_1 \underline{h}_1^T + \underline{h}_3 \underline{h}_3^T) + m_{fA}(\underline{h}_5 \underline{h}_5^T) + m_{fT}(\underline{h}_6 \underline{h}_6^T)\} l d\xi \\ m_{f_{lat}} &= \rho_f \frac{\pi}{4} \left((D_o - \delta_{bl})^2 \frac{(D_{ch} - \delta_{bl})^2 + (D_o + \delta_{bl})^2}{(D_{ch} - \delta_{bl})^2 - (D_o + \delta_{bl})^2} + 2D_o \delta_{bl} + D_i^2 \right) \\ m_{fA} &= \frac{\pi \rho_f \delta_{bl}}{2} (D_o + D_i) \\ m_{fT} &= \frac{\pi \rho_f \delta_{bl}}{2} \left(D_o \left(\frac{D_o}{2}\right)^2 + D_i \left(\frac{D_i}{2}\right)^2 \right) \end{aligned} \quad (3.56)$$

$$\begin{aligned} \underline{\underline{C}}_F(\omega) &= \int_0^1 \{c_{f_{lat}}(\underline{h}_1 \underline{h}_1^T + \underline{h}_3 \underline{h}_3^T) + c_{fA}(\underline{h}_5 \underline{h}_5^T) + c_{fT}(\underline{h}_6 \underline{h}_6^T)\} l d\xi \\ c_{f_{lat}} &= \frac{2\pi\rho_f v_f}{\delta_{bl}} D_o \frac{D_{ch}^4 + D_o^3 D_{ch}}{(D_{ch}^2 - D_o^2)^2} \\ c_{fA} &= \frac{2\pi\rho_f v_f}{\delta_{bl}} \left(\frac{D_o}{2} + \frac{D_i}{2} \right) \\ c_{fT} &= \frac{2\pi\rho_f v_f}{\delta_{bl}} \left(\left(\frac{D_o}{2}\right)^3 + \left(\frac{D_i}{2}\right)^3 \right) \end{aligned} \quad (3.57)$$

The added mass and damping in the above equations are a function of the boundary layer surrounding the drillstring ($\delta_{bl} = \sqrt{\frac{2v_f}{\omega}}$). It can be noticed that (3.55) will be twice the size of the static system in (3.42) and, depending on the range of frequencies desired for the solution, can take more time to calculate.

3.3.3 Nonlinear-Dynamic Equations

The analysis of nonlinear drillstring dynamics is the most complex and computationally intensive of the methods described here. However, when performed correctly, nonlinear-dynamic simulations can provide significant insight into the intricate dynamic behavior of drillstrings. The well-known method of Newmark [131], as applied to nonlinear problems [125], is utilized to numerically solve (3.40) at incremental time-

steps. This technique is summarized by equations (3.58)-(3.66). A full derivation of these equations is provided in Appendix B.

$$[K_{eff}]^{t+\Delta t} \underline{\Delta u}^{t+\Delta t} = \underline{Q}_{eff}^{t+\Delta t} \quad (3.58)$$

Here, $t+\Delta t$, represents the current time-step being solved for. $[K_{eff}]^{t+\Delta t}$, $\underline{\Delta u}^{t+\Delta t}$, and $\underline{Q}_{eff}^{t+\Delta t}$ are the effective stiffness matrix, incremental displacement vector, and the effective force vector for the current time-step respectively.

$$[K_{eff}]^{t+\Delta t} = \frac{1}{\alpha_N \Delta t^2} [M] + \frac{\delta_N}{\alpha_N \Delta t} [C]^{t+\Delta t} + [K]^{t+\Delta t} \quad (3.59)$$

$$\begin{aligned} \underline{Q}_{eff}^{t+\Delta t} = & \underline{Q} + \underline{F}_{exc}^t - \underline{F}_{M_{gyro}}^{t+\Delta t} - \underline{F}_B^{t+\Delta t} - \underline{F}_W^{t+\Delta t} - \underline{F}_f^{t+\Delta t} + [M] \left\{ \frac{1}{\alpha_N \Delta t} \underline{\dot{u}}^t + \left(\frac{1}{2\alpha_N} - 1 \right) \underline{\ddot{u}}^t \right\} + \\ & [C]^{t+\Delta t} \left\{ \left(\frac{\delta_N}{\alpha_N} - 1 \right) \underline{\dot{u}}^t + \Delta t \left(\frac{\delta_N}{2\alpha_N} - 1 \right) \underline{\ddot{u}}^t \right\} \end{aligned} \quad (3.60)$$

The mass matrix is constant for all time-steps, and is a combination of the mass of the drillstring and the added hydrodynamic mass of the surrounding drilling fluid (3.53), and can be expressed by (3.61)

$$[M] = [M_o] + [\tilde{M}_F] \quad (3.61)$$

The structural damping ($[C]$) is represented by (3.62).

$$[C] = \beta_D [M] + \gamma_D [K]^{t+\Delta t} \quad (3.62)$$

β_D and γ_D are structural damping parameters that can be determined based on the damping ratio of a given component. A practical method for calculating these values for various drillstring components is described by Dykstra [14]. For all analysis contained within this study it is assumed that each drillstring component has 1% damping associated with it.

The stiffness of the system at each time-step contains contributions from the beam, the wellbore wall, the gyroscopic moments, and the fluid surrounding the drillstring as shown by (3.63)

$$[K]^{t+\Delta t} = \left[\frac{\partial \underline{F}_{M_{gyro}}}{\partial \underline{u}} \right]^{t+\Delta t} + \left[\frac{\partial \underline{F}_B}{\partial \underline{u}} \right]^{t+\Delta t} + \left[\frac{\partial \underline{F}_W}{\partial \underline{u}} \right]^{t+\Delta t} + \left[\frac{\partial \underline{F}_f}{\partial \underline{u}} \right]^{t+\Delta t} \quad (3.63)$$

The system represented by equations (3.58)-(3.63) can be solved using an algorithm similar to the one outlined by Subbaraj and Dokainish [132]. After solving (3.58) at each time-step, the displacements, velocities and accelerations are updated via (3.64)-(3.66). For the initial time step ($t = 0$) the displacement should be taken as the static deflection calculation via Section 3.3.1.

$$\underline{u}^{t+\Delta t} = \underline{u}^t + \underline{\Delta u}^{t+\Delta t} \quad (3.64)$$

$$\underline{\dot{u}}^{t+\Delta t} = \frac{\delta_N}{\alpha_N \Delta t} \underline{\Delta u}^{t+\Delta t} + \left(1 - \frac{\delta_N}{\alpha_N}\right) \underline{\dot{u}}^t + \Delta t \left(1 - \frac{\delta_N}{2\alpha_N}\right) \underline{\ddot{u}}^t \quad (3.65)$$

$$\underline{\ddot{u}}^{t+\Delta t} = \frac{1}{\alpha_N \Delta t^2} \underline{\Delta u}^{t+\Delta t} - \frac{1}{\alpha_N \Delta t} \underline{\dot{u}}^t + \left(1 - \frac{1}{2\alpha_N}\right) \underline{\ddot{u}}^t \quad (3.66)$$

δ_N and α_N in the above equations are constants that indicate the integration scheme being used. For linear structural dynamic problems, a constant-average acceleration scheme ($\delta_N = 1/2$, $\alpha_N = 1/4$) generally provides an unconditionally stable solution and will be used for the nonlinear analysis within this study. However, it should be noted that this “unconditionally stable” characteristic does not necessarily apply to nonlinear problems. For nonlinear structural dynamics, the stability and accuracy of the solution is generally limited by the size of the time-step being used. For this reason an automated time-increment control algorithm, similar to the one presented by Zhang and Hisada [133], has been implemented within the model.

3.4 Further Considerations for Drilling Systems

Apart from the equations described in the previous sections, there are modeling aspects specific to drillstrings that must be addressed. Of particular interest is the consideration of steerable mud motors, rotary steerable systems, and concentric or eccentric stabilizers. These aspects of the drillstring assembly must be accounted for in order to apply the presently derived model to realistic drilling engineering problems.

3.4.1 Steerable Mud Motors

Steerable mud motors allow for the intentional deviation of a well path by orienting a bent section of a mud motor, just above the bit, in a certain radial direction with respect to the high-side of the wellbore. In order to account for this an initial lateral displacement, proportional to the motor bend angle, is specified along the section of the motor between the bend and the bit. This initial displacement must be directed along the tool face orientation (TFO) of the motor. The TFO is defined as the angle between the high-side of the wellbore and the direction that the bit is deflected towards (see Appendix A).

Additionally, because the section of pipe is deflected at a certain angle (motor bend angle, BA) with relation to the centerline of the wellbore, the global (wellbore coordinate frame) stiffness will be different than the local (initial drillstring coordinate frame). To correct for this, a transformation must be applied to the

tangent-stiffness matrix and internal force vector of every beam element on the bent section of the motor. This is a requirement for proper determination of shear forces, bending moments, and wellbore contact forces near the bit. The appropriate transformation is described by (3.67)-(3.69).

$$\underline{\underline{T}}_{D1} = \begin{bmatrix} 1 & 0 & 0 & 0 & 0 & 0 \\ 0 & 1 & 0 & 0 & 0 & 0 \\ 0 & 0 & \cos(BA) & 0 & \sin(BA) & 0 \\ 0 & 0 & 0 & \cos(BA) & 0 & 0 \\ 0 & 0 & -\sin(BA) & 0 & \cos(BA) & 0 \\ 0 & 0 & 0 & 0 & 0 & 1 \end{bmatrix} \quad (3.67)$$

$$\underline{\underline{T}}_{D3} = \begin{bmatrix} \cos(\eta) & 0 & \sin(\eta) & 0 & 0 & 0 \\ 0 & \cos(\eta) & 0 & \sin(\eta) & 0 & 0 \\ -\sin(\eta) & 0 & \cos(\eta) & 0 & 0 & 0 \\ 0 & -\sin(\eta) & 0 & \cos(\eta) & 0 & 0 \\ 0 & 0 & 0 & 0 & 1 & 0 \\ 0 & 0 & 0 & 0 & 0 & 1 \end{bmatrix} \quad (3.68)$$

$$\eta = \gamma - TFO$$

$$\begin{Bmatrix} \underline{u}_{ele}^A \\ \underline{u}_{ele}^B \end{Bmatrix} = \begin{bmatrix} \left(\underline{\underline{T}}_{D1} \right)^T \left(\underline{\underline{T}}_{D3}^A \right)^T & \underline{0} \\ \underline{0} & \left(\underline{\underline{T}}_{D1} \right)^T \left(\underline{\underline{T}}_{D3}^B \right)^T \end{bmatrix} \begin{Bmatrix} \underline{u}_n \\ \underline{u}_{n+1} \end{Bmatrix} \quad (3.69)$$

This transformation will only affect the portion of the BHA that is below a bent sub, or the bend in a steerable mud motor, however it must be pointed out that this transformation is necessary for the accurate determination of BHA build rates/motor yields (see Section 4). Additionally, when applying (3.69) to the elements below the bend on a steerable mud motor, the transformation given by (3.47) can be ignored. The curvature term (κ_o) in (3.25) – (3.27) must also be set to zero for the elements below the bend, regardless of the shape of the wellbore. The above-mentioned method is only one way of determining the deflection of bent mud motors, and not without its limitations. For example, the proposed method proves difficult for nonlinear time-domain simulations. The reader is encouraged to explore more efficient methods.

3.4.2 Rotary Steerable Systems

The increasing use of rotary steerable systems in modern operations dictates the need to account for their behavior within drillstring/BHA models. As was described in Section 1, there are generally two types of rotary steerable systems: point-the-bit, and push-the-bit. The former provides a means to adjust the tilt direction of the bit down-hole. These types of systems can be modeled in a similar manner as steerable mud motors. The latter, a push-the-bit system, works in a significantly different way and consideration must be

given to its method of steering. A push-the-bit system applies a lateral force, via a grouping of actuated pads, near the bit. The applied force from the active pad pushes the bit into the formation at a certain steering direction, thus causing a change in the wellbore trajectory.

In terms of modeling, a push-the-bit system is incorporated either by applying a specified force at the location of the active pad, or by specifying an eccentricity at the active pad. In each case, a check must be made at the end of the analysis to verify that the required eccentricity (for an applied steer force), or the required steer force (for an applied eccentricity) has not exceeded the realistic limit of the tool.

3.4.3 Concentric/Eccentric Stabilizers

Within the proposed drillstring model, stabilizers and variations in outer diameters can be modeled either by creating a larger element with the appropriate effective stiffness properties or by specifying a reduction in the clearance between the components and the wellbore wall. It is usually sufficient to pursue the latter option. When considering a stabilizer, one can simply change the allowable clearance between a specific node (the location of the stabilizer) in order to limit the lateral displacement of the drillstring at that point. However, in some cases it is necessary to consider eccentric stabilizers, or components that have asymmetrical protrusions. This scenario can be seen in Figure 3.2 where an eccentric component is shown on the outer diameter of a drillstring component. Modeling this scenario equates to specifying a reduction in the radial clearance over only a portion of the component annotated by the span angle, θ_{span} .

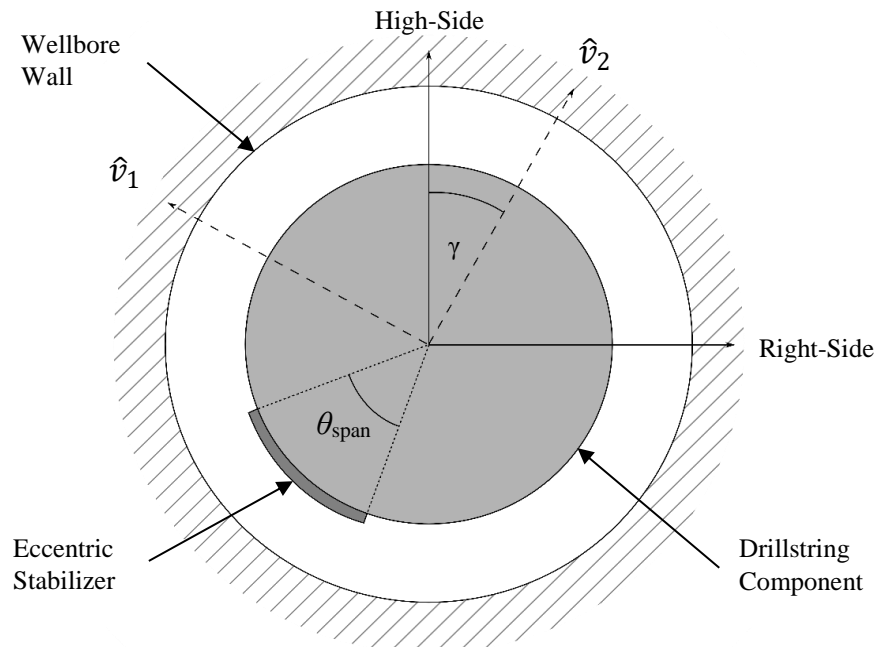


Figure 3.2: Diagram of Eccentric Stabilizer/Component

4. NUMERICAL VALIDATION AND INITIAL FIELD TRIALS

The nonlinear finite element model presented in Section 3 was coded via MatLab [134], which contains a large library of build in matrix manipulation functions making it a very helpful tool for general engineering programming. The collective assembly of MatLab scripts written in this course of study has come to be referred to as the drillstring mechanics and dynamics simulator, or MADSIm for short. With the algorithms of MADSIm established, it becomes necessary to validate the mathematics behind the code. Through this validation process it is hoped that specific questions can be answered, namely:

- 1) Can the model reliably predict appropriate solutions? This includes determining solutions to the simple problems that are governed by analytical formulas, as well as determining reasonable solutions to more advanced problems.
- 2) Do shear deformations provide any significant contribution to the static or dynamic behavior of drillstrings in horizontal wellbores?
- 3) Are gyroscopic effects truly negligible when considering the relatively low rotation speeds of drillstrings?
- 4) How does this model compare to the most advanced commercial software?

To explore these questions, comparisons are conducted for nonlinear-static, linearized-dynamic, and nonlinear-dynamic calculations. For the “simple problems” (i.e. beam deflections and natural frequencies, as well as the natural frequencies of a drillstring lying in a horizontal well) direct comparisons are provided between the developed model, MADSIm, and analytical formulas presented in the literature. As the drilling scenarios increase in complexity (i.e. realistic wellbore geometries with full length drillstrings), comparisons are carried out between MADSIm and two previous nonlinear drillstring models: that of Heisig [34], and a commercial software [135] that was based on the work of Belaid [94]. Apart from validating the mathematics behind the present model, the results, for the first time, provide a direct comparison between the two types of beam models (Euler-Bernoulli and Timoshenko) within the context of analyzing the static and dynamic behavior of drillstrings in horizontal wellbores, as well as a quantification of the effects of gyroscopic moments when simulating a rotating drillstring in the lateral section of a well.

4.1 Nonlinear-Static/Quasi-Static Analysis

Static calculations are the starting point for any structural analysis validation process. Without confidence in the static solution, by default, there will be no confidence in the dynamic solution. All static analysis is conducted in the manner outlined in Section 3.3.1.

4.1.1 Cantilevered Beam Deflection

Initially, the case of static beam deflection is examined. This is done via a comparison of simple cantilevered beam formulae. The equation for the deflection of a cantilevered beam, subjected to an end point load, is easily obtained from the basic theory of elasticity and can be expressed by (4.1) [136].

$$u = \underbrace{-\frac{Px}{K_s GA} - \frac{PL}{EI} \left(\frac{x^2}{2L} - \frac{x^3}{6L} \right)}_{T} \quad (4.1)$$

The first term in equation (4.1) represents the deflection attributed to the shear deformation (Timoshenko assumption) of the beam while the second term is associated with the classic Euler-Bernoulli assumption. This equation is compared directly with the numerical beam model presented by Heisig [34], and the current beam model described in Sections 2 and 3. It should be noted that the beam deflections represented by (4.1) are a linear approximation of the elastic behavior of a beam. Therefore, in order to provide an adequate comparison between the nonlinear numerical models, all parameters must be such that the deflections of the beam remain relatively small (i.e. $\ll 1$). All of the necessary comparative parameters are listed in Table 4.1. The results of this comparison are graphically illustrated in Figure 4.1.

Table 4.1: Input Data for Cantilevered Beam Deflection Comparison

Parameter	E (psi)	ν	OD (in)	ID (in)	L (in)	P (lb_f)
Value	30×10^6	0.3	6.5	2.5	24	1,000

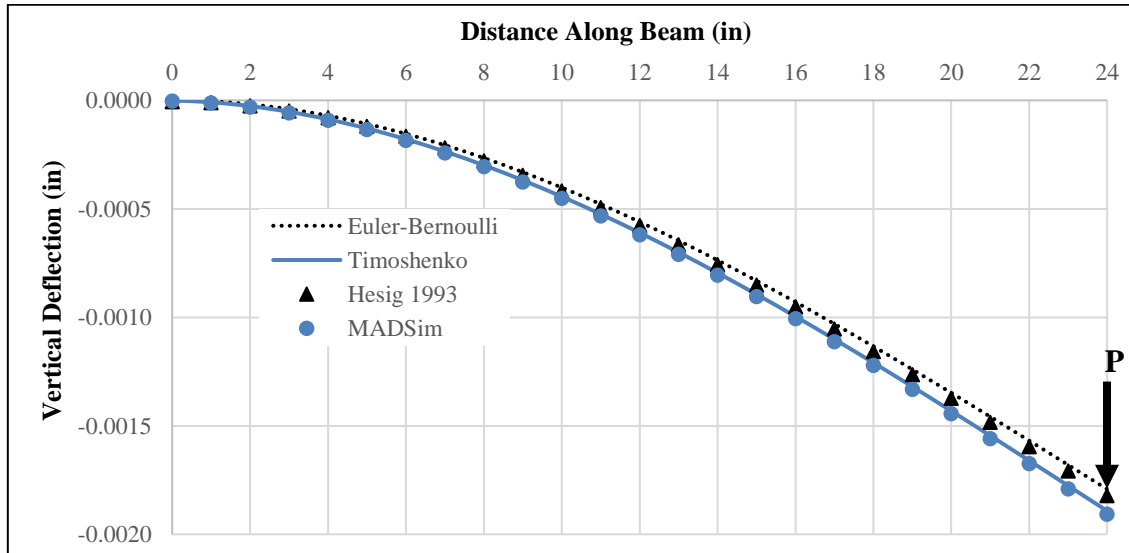


Figure 4.1: Comparison of Different Beam Models for the Deflection of a Cantilevered Beam

It is seen in the previous figure that, while both nonlinear beam models compare favorably with their respective linear counterparts, MADSim provides a closer approximation to its corresponding analytical formula. It can further be noticed that MADSim and the Timoshenko beam formula predict a slightly larger deflection than Heisig's model and the Euler-Bernoulli beam equation. This makes since due to the fact that the added shear deformation allows for more lateral flexibility of the beam, and thus more lateral deflection to an applied load.

4.1.2 BHA Deflection

The second static comparison examines the deflection of a BHA in a perfectly straight horizontal wellbore. The assembly used for the comparison consists of a push-the-bit RSS, MWD flex collar assembly, and a joint of CSDP as described in Table 4.2. Typical horizontal drilling operation parameters are used: WOB = 20 klf, TOB = 3500 ft-lbf, MW = 11ppg, Hole Size = 8.5 in. Elastic material properties are assumed to be comparable to common steel ($E = 30 \times 10^6$ psi, $v = 0.3$). The assembly is divided into 85 elements and friction is taken to be zero. The boundary conditions for the model are such that the WOB and TOB are applied directly to the bit, axial and torsional displacements are fixed at the opposite end. The bit itself is not allowed to move radially but can tilt freely, and the far end of the drillstring (opposite the bit) is free to move laterally within the confines of the wellbore but is forced to stay parallel to the central axis of the hole.

Table 4.2: Assembly for Static BHA Comparison

Sec No.	Component Description	OD (in)	ID (in)	L (ft)
1	8 1/2" Bit	8.500		0.83
2	6 3/4" RSS - Active Steering Pad @ 2.41 ft from Bit - 8.25" Stabilizer @ 9.02 ft from Bit	6.750	Variable	10.65
3	MWD Flex Assembly - Body OD = 5", Wear Knot OD = 6.75"	6.750	2.739	22.2
4	String Stabilizer (8.25" Blade OD)	6.750	3.250	5.00
5	Compressive Service Drill Pipe - Body OD = 5", Wear Knot OD = 6.5"	6.500	3.000	30.12

Using these parameters, a direct comparison between Heisig's model and the current model is presented by Figure 4.2-Figure 4.6. Figure 4.2 displays a 3-D mechanics plot of the BHA, generated with MADSim. The colored arrows indicate the magnitude and direction of contact forces, with red being a maximum and blue being a minimum. The color of the tubulars corresponds to the magnitude of the total bending moment along the length of the BHA. Stabilizers are shown as gray disks and the active pad of the RSS is shown as a green

disk. Figure 4.3-Figure 4.6 depict the comparative loading values, along the BHA, between the two models; examination of the results indicates an indistinguishable difference in the solution. This suggests that the “typical assumption” of infinite shear stiffness (Euler-Bernoulli beam), while theoretically less accurate, is sufficiently valid for the static analysis of drillstrings and BHAs.

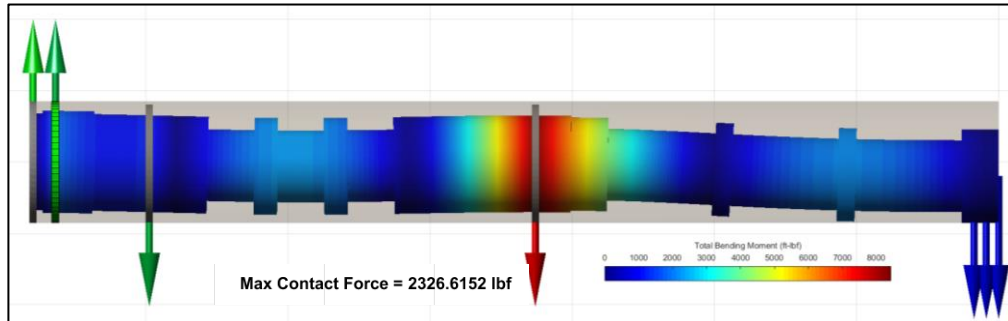


Figure 4.2: 3D Mechanics Plot of BHA Deflection, Contact Forces, and Bending Moments

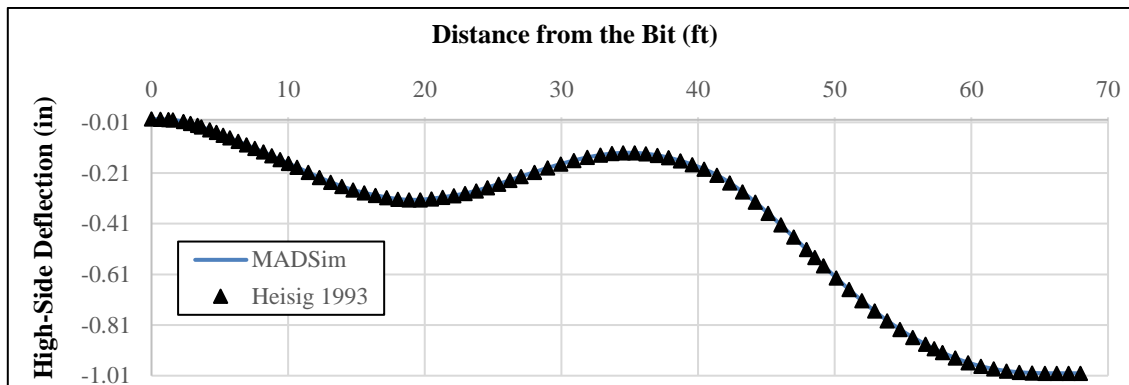


Figure 4.3: Comparison of Calculated High-Side BHA Deflection

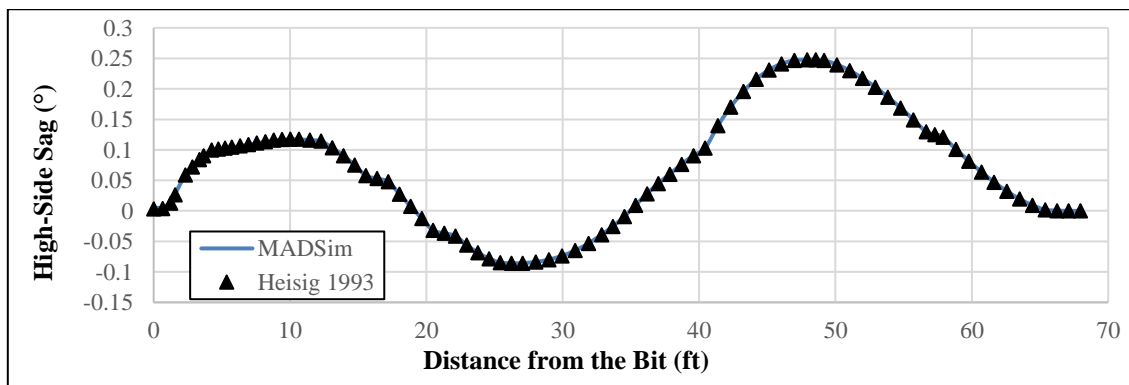


Figure 4.4: Comparison of Calculated High-Side BHA Sag (Rotation Angle)

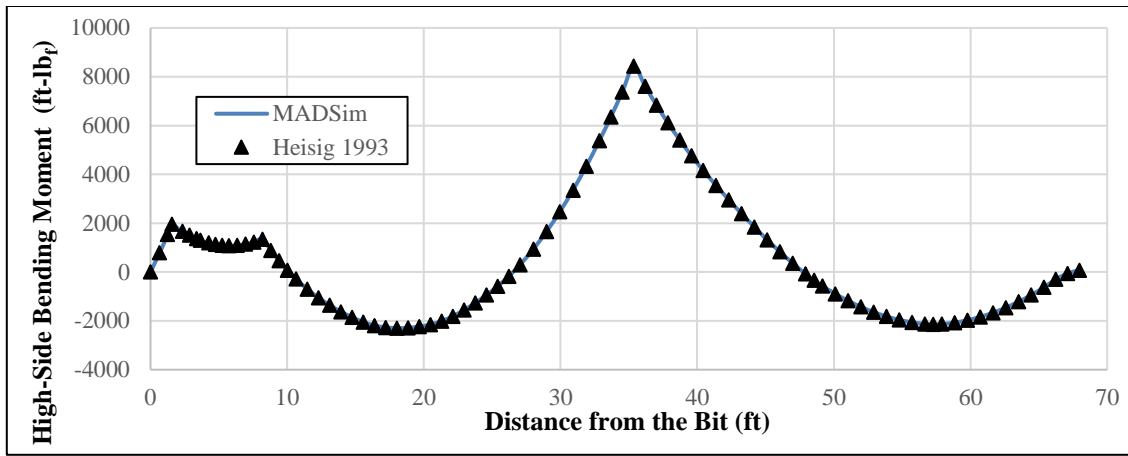


Figure 4.5: Comparison of Calculated High-Side BHA Bending Moment

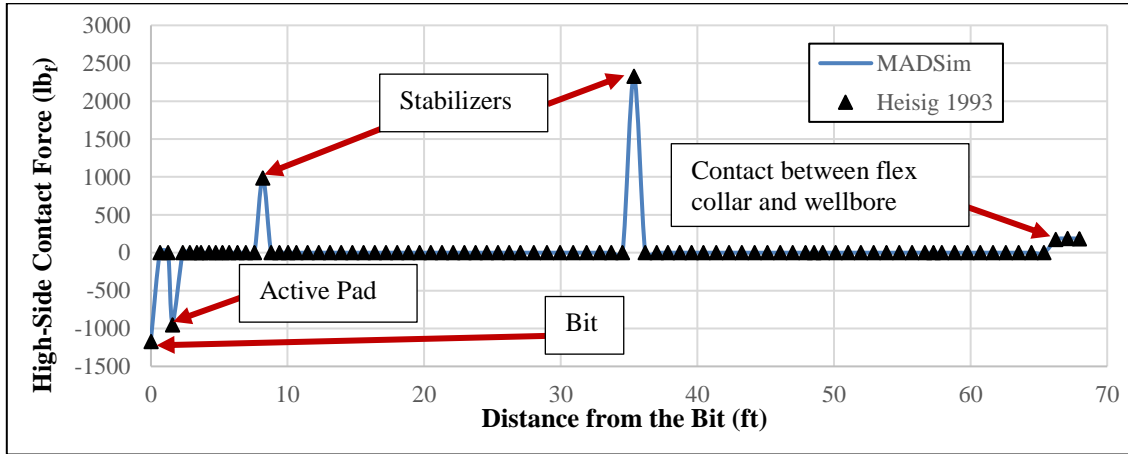


Figure 4.6: Comparison of Calculated High-Side BHA Contact Forces

4.1.3 Full Drillstring Deflection

Seeing the similarities in the static analysis between the two models, and considering that both models were implemented as part of this study, it is important to consider the numerical reliability of the developed code. This is to ensure that the 5,000+ lines of code within MADSim are free of errors. In order to accomplish this verification, various comparisons are made with a commercial drillstring analysis software. The commercial software employs a nonlinear drillstring model [94] and, thus, makes it a useful tool for static/quasi-static drillstring comparison. The term “quasi-static” is intended to imply that the friction coefficient used within the model is a function of, both axial and rotational, steady-state velocities.

For the comparison, data was gathered from an actual well drilled in the north eastern United States. The well had a total measured depth of 19,277 ft, with roughly 12,000 ft of lateral section (Inclination $\approx 90^\circ$).

The complete, “as-drilled”, survey for this well can be found in Appendix C. The drilling assembly, described in Table 4.3, is placed in this well with the bit at TD. In this configuration, the following parameters are applied: WOB = 10 klb_f, TOB = 2,500 ft-lb_f, Mud Weight = 11 ppg, Hole Size = 8.5 in, μ_s = 0.2 (solid green line in Figure 4.2). These parameters are not necessarily reflective of the actual parameters used while drilling the well and are simply provided for the sake of comparison. A constant axial velocity (ROP = 35 ft/hr) and a constant rotary speed (60 RPM) are applied to the quasi-static model. As discussed in Section 2, when applied to the static model, these steady-state velocities only affect the friction coefficients within the model as represented by (2.70)-(2.72), which offers a quasi-static representation of the drillstring. Within MADSim the drilling assembly is divided into 3,055 elements.

Table 4.3: Drilling Assembly for Full Well Comparison

<i>Sec</i>	<i>Component Description</i>	<i>OD (in)</i>	<i>ID (in)</i>	<i>L (ft)</i>
1	8 1/2" Bit	8.500		0.83
2	6 1/2" Mud Motor	6.500	5.500	25.83
3	Non-Mag Pony Collar	6.438	3.250	9.54
4	Non-Mag MWD Collar	6.188	3.250	27.39
5	Non-Mag MWD Pulser Sub	6.500	3.250	6.18
6	Non-Mag Drill Collar	6.250	3.250	28.49
7	Non-Mag Drill Collar	6.188	3.250	28.27
8	Cross-Over Sub	6.500	2.500	2.61
9	5" DP NC50 (4 1/2" IF) 19.50 ppf	5.000	4.276	To Surface

For the analysis, two comparisons are presented: one with friction, and one without friction. This is done in order to fully understand the differences between the present model (MADSim) and the commercial static analysis software. Without friction, the applied ROP and string RPM do not influence the calculation. It is only when friction is included that the steady-state velocities contribute to the solution of the problem.

Figure 4.7 and Figure 4.8 provide a visual “snap-shot” comparison between the two models. In each figure, contact forces are shown distributed along the length of the drillstring within the wellbore. Again, the coloring of the arrows represents the relative magnitude of the contact force, with red indicating a maximum and blue representing a minimum. Ignoring the discrepancies in graphics rendering between the two figures, the visual outputs are essentially identical. A more quantitative comparison between the results are shown in Figure 4.9-Figure 4.12, in which the total contact force, total bending moment, torque value, and tension are shown as a function of measured depth (MD) along the drillstring.

With the exception of torque, the loading values along the length of the string are, for all practical purposes, the same. It should be noted that any contact force of zero (no contact with the wellbore at that node), predicted within MADSim, has been omitted from the plots shown here. This is done purely for the sake of visualization. Additionally, it can be noticed that there are slight differences in the way the contact force is presented between the two models (Figure 4.9). This could be due to the “continuous contact” model [94] utilized within the commercial package, which is a fundamental requirement of the “iterative contact point calculation” method used to perform calculations within the software, or it could simply be a preference of the software company to present the data that way. Regardless of the reasoning, it can be seen that the peak contact force values calculated within MADSim match well with the values estimated with the commercial software. Furthermore, as will be shown later, the torque values and axial tension along the length of the drillstring are very close in magnitude regardless of whether friction is included in the analysis. Because friction will affect the axial force and torque distribution based on the magnitude of the contact forces, these results suggest that both models are predicting similar contact forces. With this understanding it would seem more plausible that the commercial software simply processes the contact force data and presents it in a way which is dictated by preference.

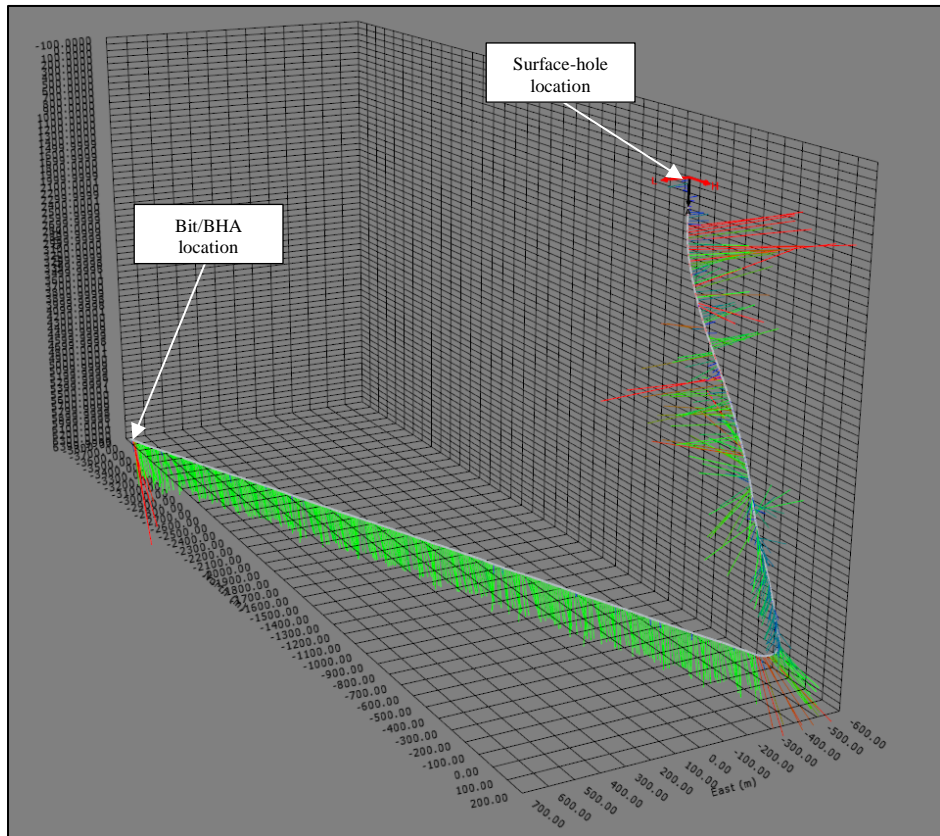


Figure 4.7: 3D Mechanics Plot Output from Commercial Software

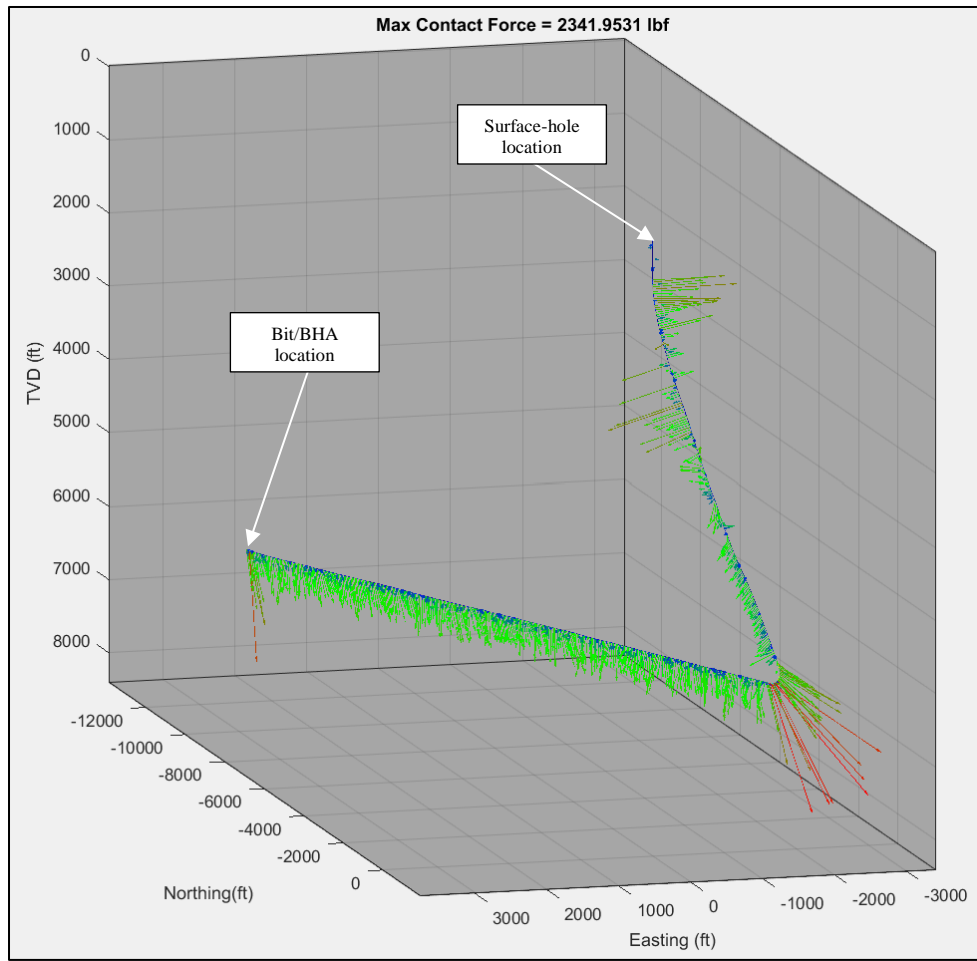


Figure 4.8: 3D Mechanics Plot Output from MADSim Code

The more peculiar result is the torque distribution along the drillstring, as is shown in Figure 4.11. When ignoring friction, whatever torque is applied at one end of the drillstring (say bit torque) should be seen at the other end of the drillstring since there is theoretically no additional torque being applied anywhere in the assembly; this is observed from the results generated via MADSim. However, when looking at the values calculated within the commercial software it is clear that there is some erratic behavior going on. It is uncertain what is causing this inconsistent torque variation along the length of the drillstring as the specific algorithms and mathematics behind the software are unknown. Based on this result it is concluded that, while the commercial software has advantages in computational efficiency, MADSim provides more reliable results. Although, it can be pointed out that this “apparent error” within the commercial software is relatively small (< 60 ft-lbf difference) and would still be considered valuable for any practical Torque and Drag analysis (TDA).

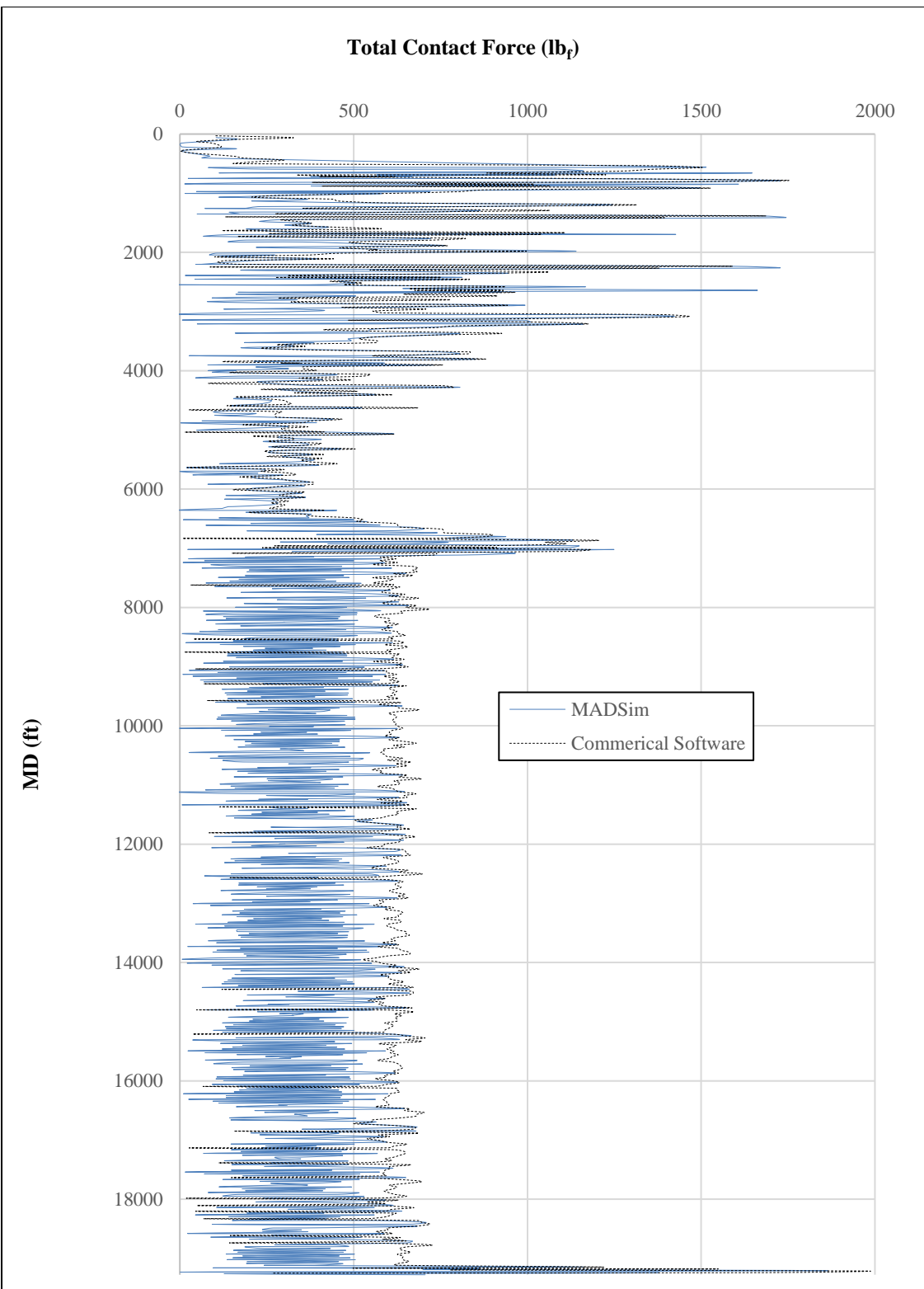


Figure 4.9: Total Contact Force Comparison for Full Test Well – No Friction

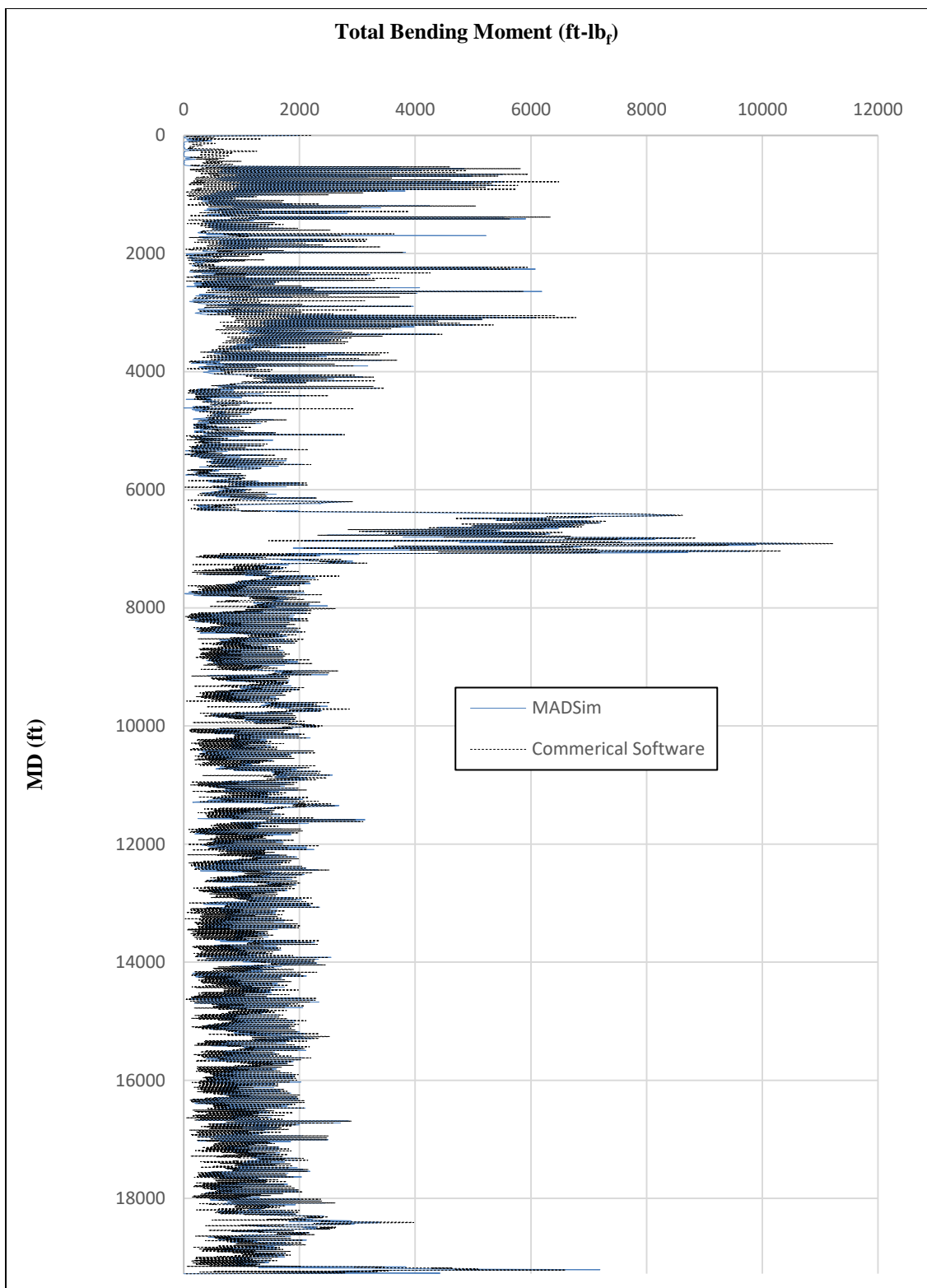


Figure 4.10: Total Bending Moment Comparison for Full Test Well – No Friction

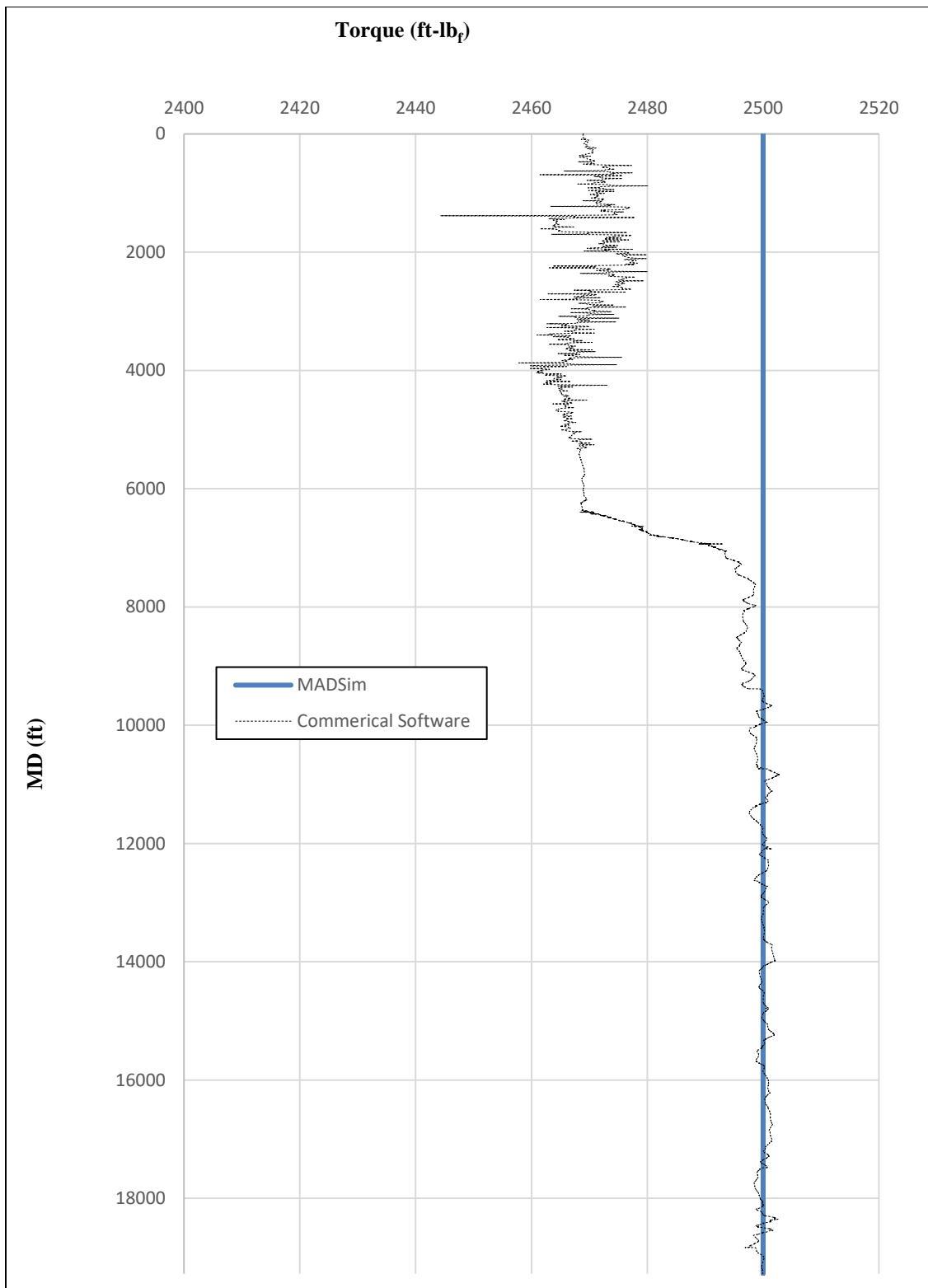


Figure 4.11: Drillstring Torque Comparison for Full Test Well – No Friction

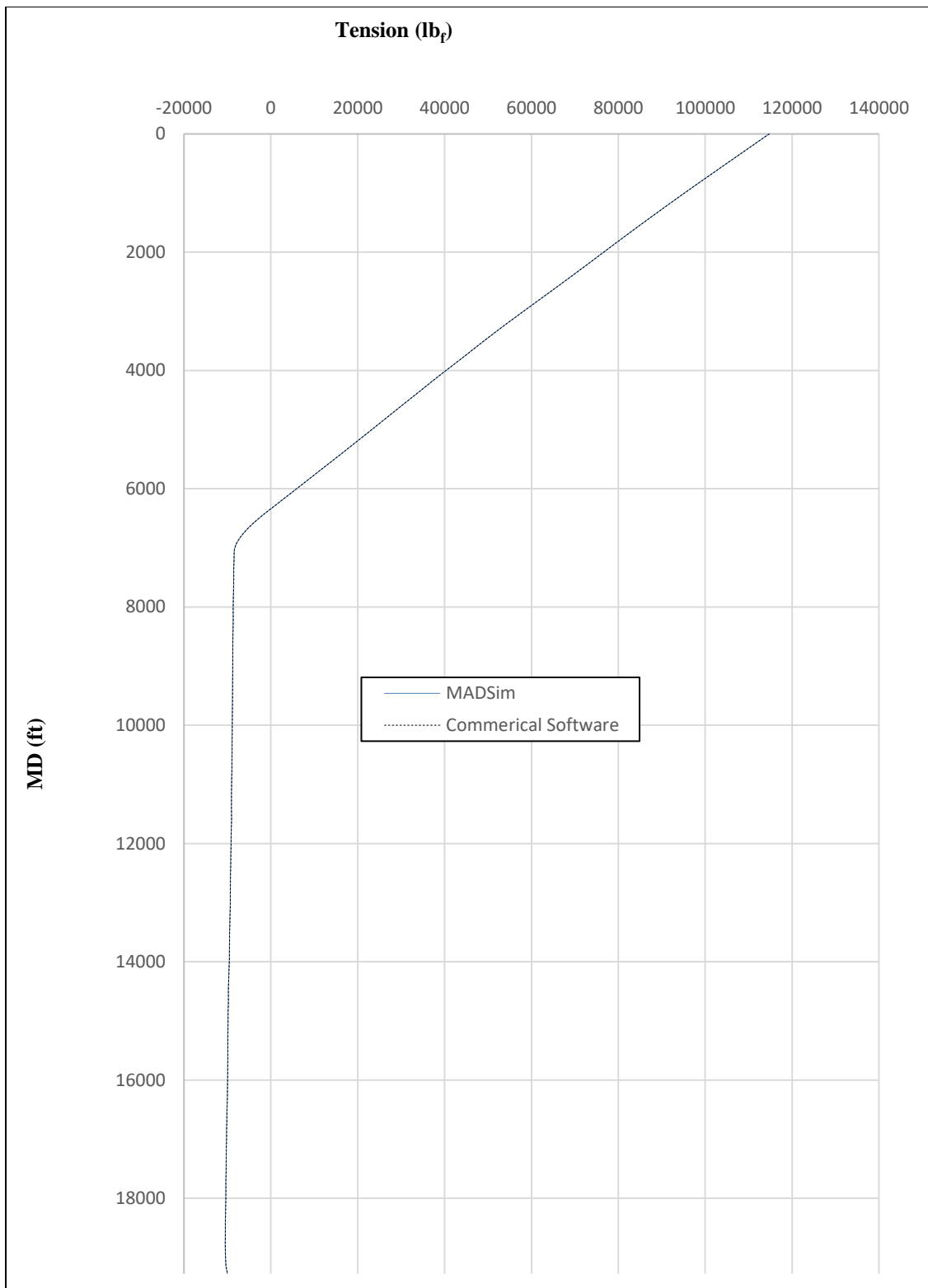


Figure 4.12: Axial Force Comparison for Full Test Well – No Friction

A comparison between the models, including the effects of friction, is also presented in Figure 4.13–Figure 4.15. The contact forces and bending moments are the same as they were in the case of no friction, and therefore have not been shown. This makes sense as lateral/axial acting friction will not change the magnitude of the normal contact forces (assuming no buckling is occurring), but will only slightly alter the direction in which they are acting. Furthermore, because the contact distribution is not changing significantly, the bending moments along the length of the string should not change either. This, of course, would be very different if buckling was involved.

Using the friction model presented in Section 2, Figure 4.13 shows a significant difference in estimated torque along the length of the drillstring when compared to the commercial software. This is a direct result of the definition of the friction coefficient defined by (2.70) – (2.72). It becomes apparent that the friction model used within the commercial software is defined purely by (2.70) and (2.71), with the absolute friction coefficient (μ_o) simply being a constant static value, which in this case is equal to 0.2. This is the typical approach to friction coefficient modeling within Torque and Drag software. If the friction coefficients used within MADSim are adjusted in a similar way, then there is a much more agreeable comparison between the two models. This adjustment is illustrated by the green line labeled “MADSim Adjusted” in Figure 4.13. Slight differences between the solutions are still noticed but this could, again, be a result of the erratic behavior of the torque calculation shown via the no-friction case (Figure 4.11). Initially, examining Figure 4.14, the tension along the string looks identical for both models. However, when the graph is enlarged, as it is in Figure 4.15, a clearer distinction between the two models is seen. While there are slight differences in the values calculated, the overall deviation is negligible for all practical purposes.

It is worth noting that the commercial software used for the comparative study, while somewhat less reliable, is more efficient than MADSim in terms of computational cost. For example, in the comparison shown in Figure 4.7–Figure 4.15, the calculation times varied significantly between the two models. Each static calculation of the 19,277 ft drilling assembly takes roughly 10 – 15 minutes to compute with the commercial software, while MADSim (using 3,055 elements) required 50 minutes to an hour to perform the calculations. This is why MADSim is not necessarily intended to be a “full-string” analysis tool, rather it is intended to be primarily a BHA analysis tool. For static/linearized-dynamic calculation of BHAs, and relatively short lengths of drillstring (\approx 3,000 ft), MADSim has much more manageable calculation times. In general the greater number of finite elements contained within the model, the longer the calculation will take. For most practical analyses of BHAs, the number of elements is less than 200. This results in computation times for static analysis, and subsequent linearized-dynamic calculations, of less than 30 seconds.

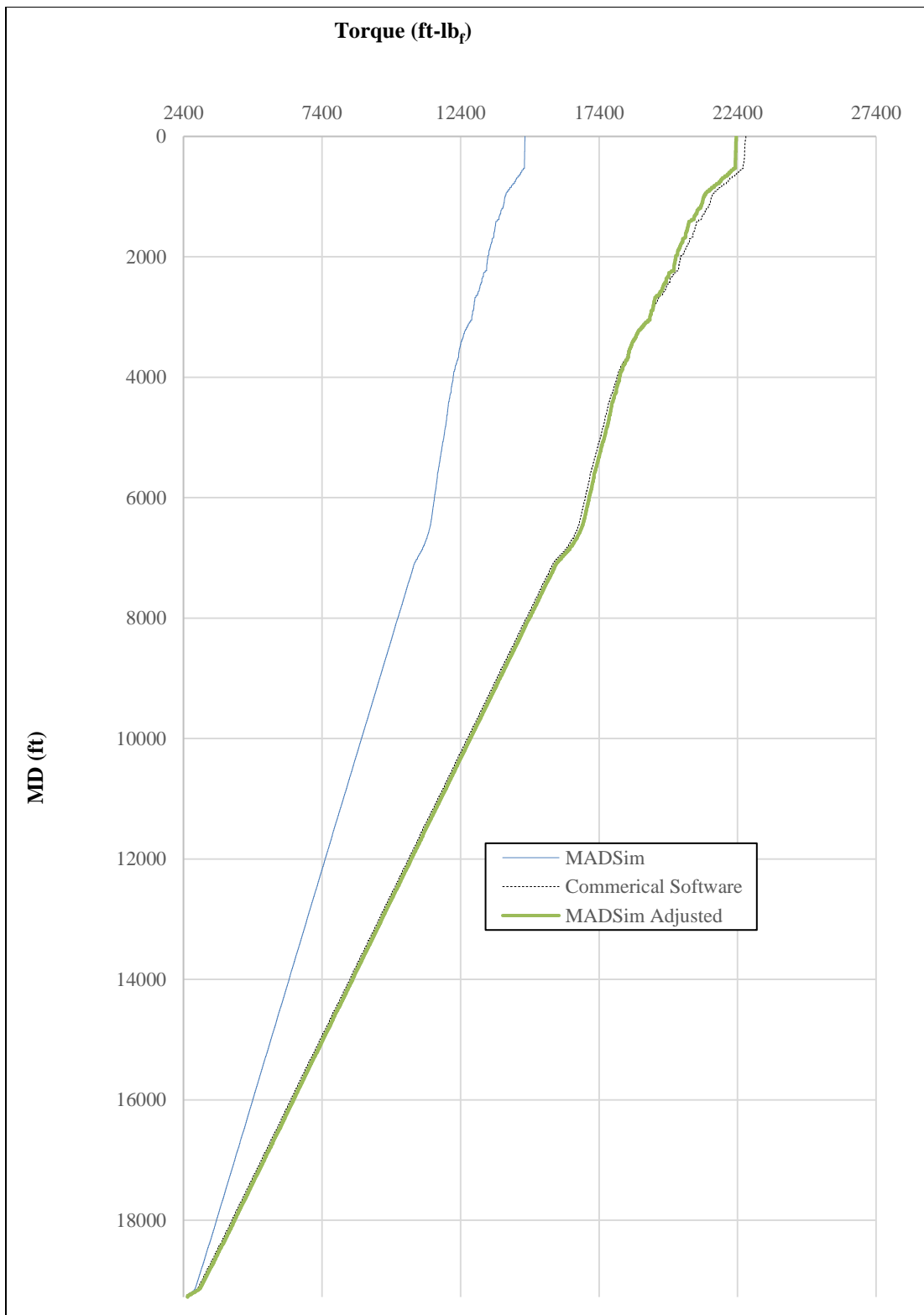


Figure 4.13: Drillstring Torque Comparison for Full Test Well – With Friction

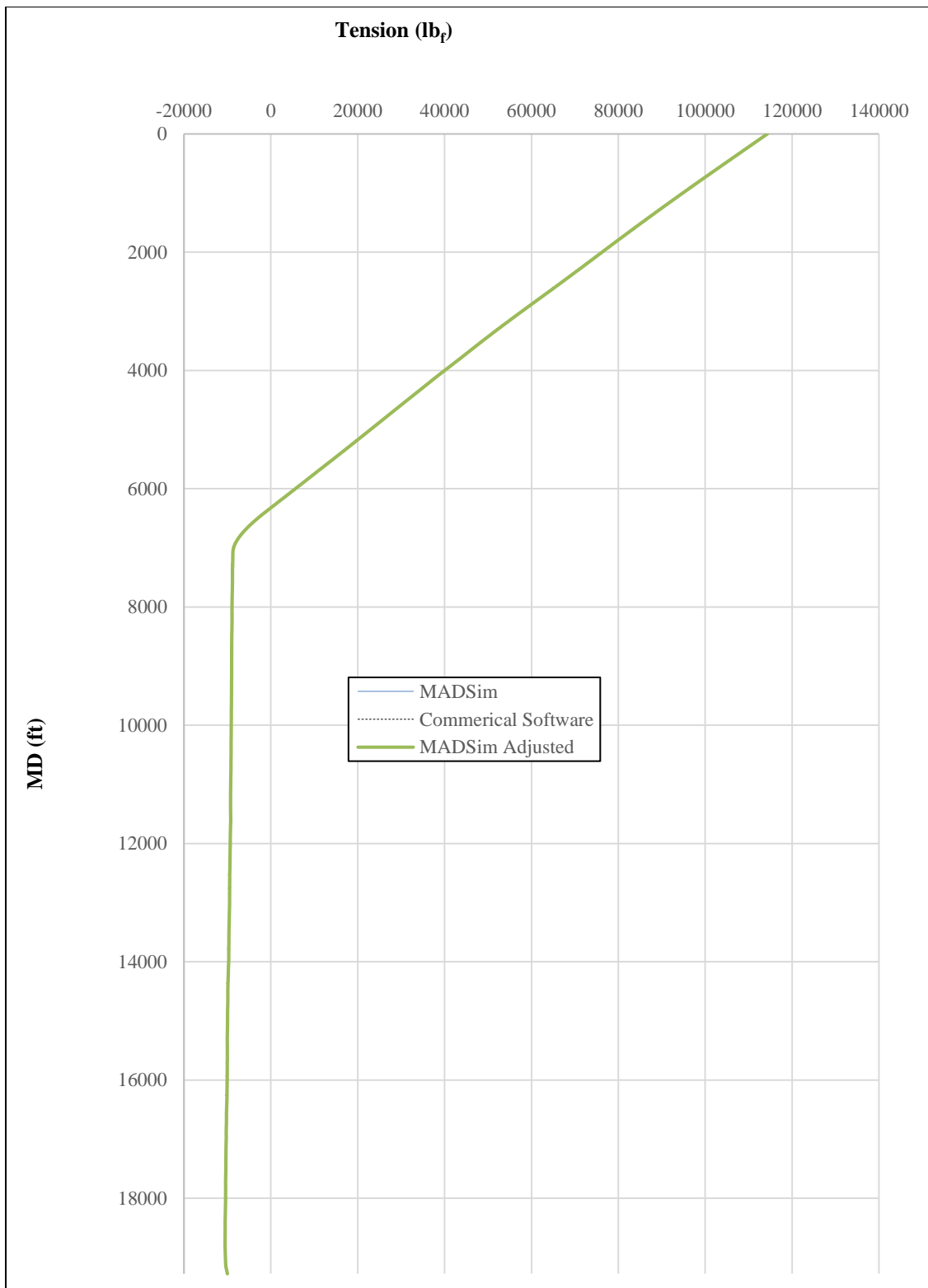


Figure 4.14: Axial Force Comparison for Full Test Well – With Friction

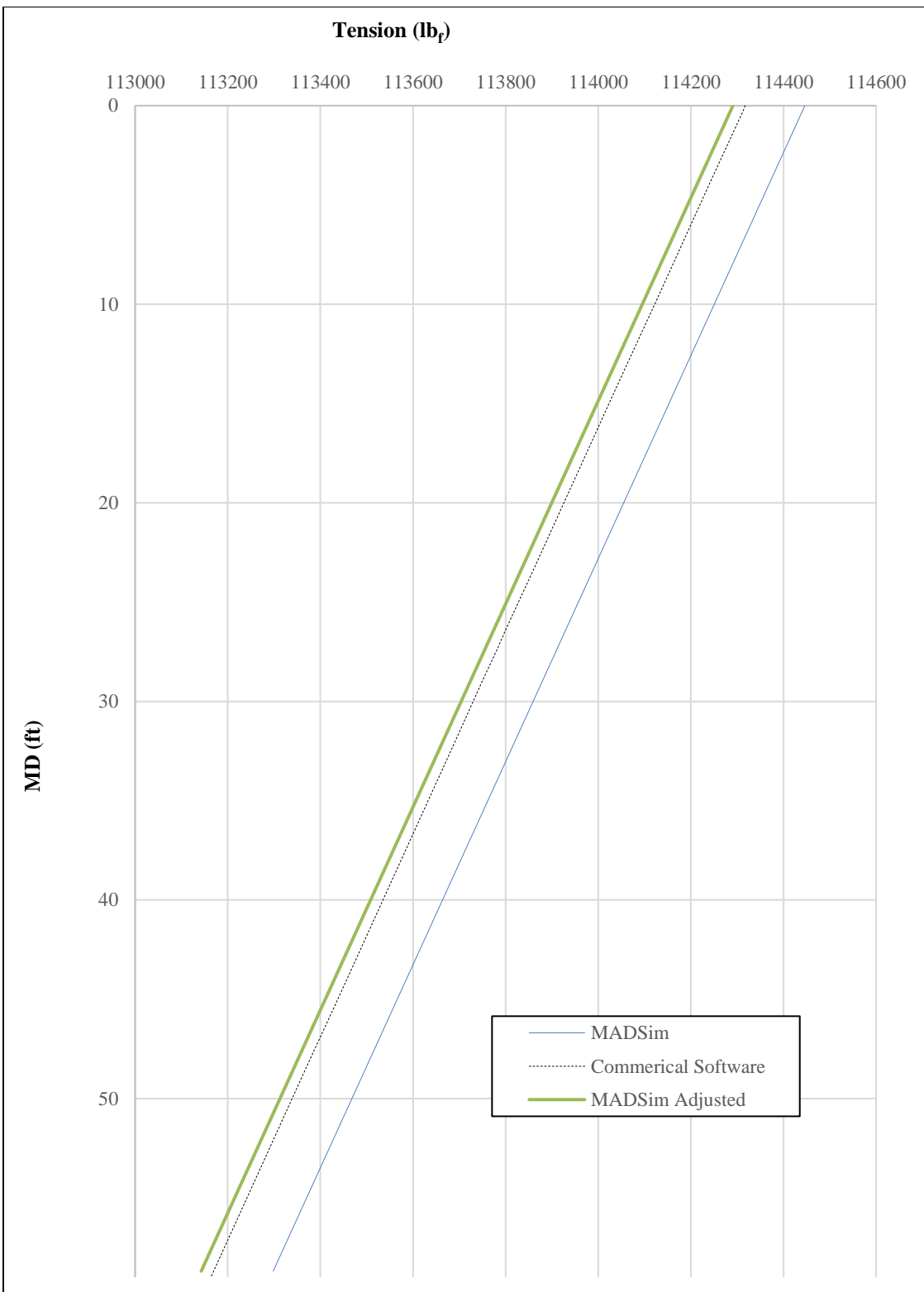


Figure 4.15: Axial Force Comparison for Full Test Well – With Friction, Enlarged

4.1.4 Motor/RSS Yield Estimation

Static/quasi-static analysis can also be used for the estimation of the directional behavior of BHAs [137]; this is often referred to as a directional yield analysis. The major assumption behind these motor/RSS yield analyses is that the side force generated at the bit provides the potential for the BHA to drill in a lateral direction. With this assumption, the basic procedure to this type of calculation can be described by three simple steps. First, the BHA is placed in a constant curvature wellbore section and the side force at the bit is calculated. Next, the change in bit side force, due to the change in wellbore curvature, is examined. Finally, based on the degree of change in the side force at the bit, the curvature of the wellbore section is adjusted and a new bit side force is computed. This iterative process continues until the side force at the bit is minimized. The final curvature estimated by the procedure is termed the “Equilibrium Curvature”, or Motor/RSS Yield. In general, there are ways of accounting for the steering characteristics of the bit [138, 139] within this analysis, however, for the sake of simplicity, the comparisons shown here are examined without consideration of individual bit characteristics.

The same iterative process applies to both RSS assemblies and steerable mud motors, however the method in which the bit side force is generated is fundamentally different for these two scenarios. As described in Sections 1 and 3, a push-the-bit rotary steerable system applies a controlled force via an actuated stabilizer (“active pad”) near the bit. Alternatively, a steerable mud motor and point-the-bit rotary steerable systems provide a bit side force via a “kink” (motor bend) in the motor/RSS. The distinction between these two types of steering mechanisms is shown in Figure 4.16. In the figure, the RSS is directionally controlled by applying a force at the location of the active pad (green disk). This generates an opposing force at the bit. The steerable mud motor is directionally controlled by orienting the motor’s bend in the desired steering direction, in this case at TFO = 0° (pointed towards the high-side of the hole).

In general, the motor/RSS yield will depend on the orientation of the bend/applied pad force. This orientation, with respect to the high-side of the wellbore, is referred to as the Tool Face Orientation (TFO) and is always a positive value that ranges between 0 and 360°. Typically, for a steerable mud motor, a “sliding motor yield” is calculated for a TFO of 0° and a “rotational motor yield” is the average of motor yields at TFOs of 0° and 180°. A push-the-bit RSS will only have a one type of yield since these tools require constant string rotation in order to drill ahead in the formation.

Motor and RSS yields should not be confused with build rates. A build rate is a change in inclination over a certain course length in a well, and is a property of the wellbore. Motor/RSS yields are the wellbore curvatures obtained during a full “slide” of the BHA, and is a property of the drilling assembly and the bit’s interaction with the formation. In terms of well planning, a build rate can be thought of at a planned curve

while a motor/RSS yields can be thought of as the Dog-Legs that occur over the course of drilling the planned curve. Both, build rates and motor/RSS yields, are commonly presented in a normalized fashion as a degree change per 100 ft ($^{\circ}/100\text{ft}$).

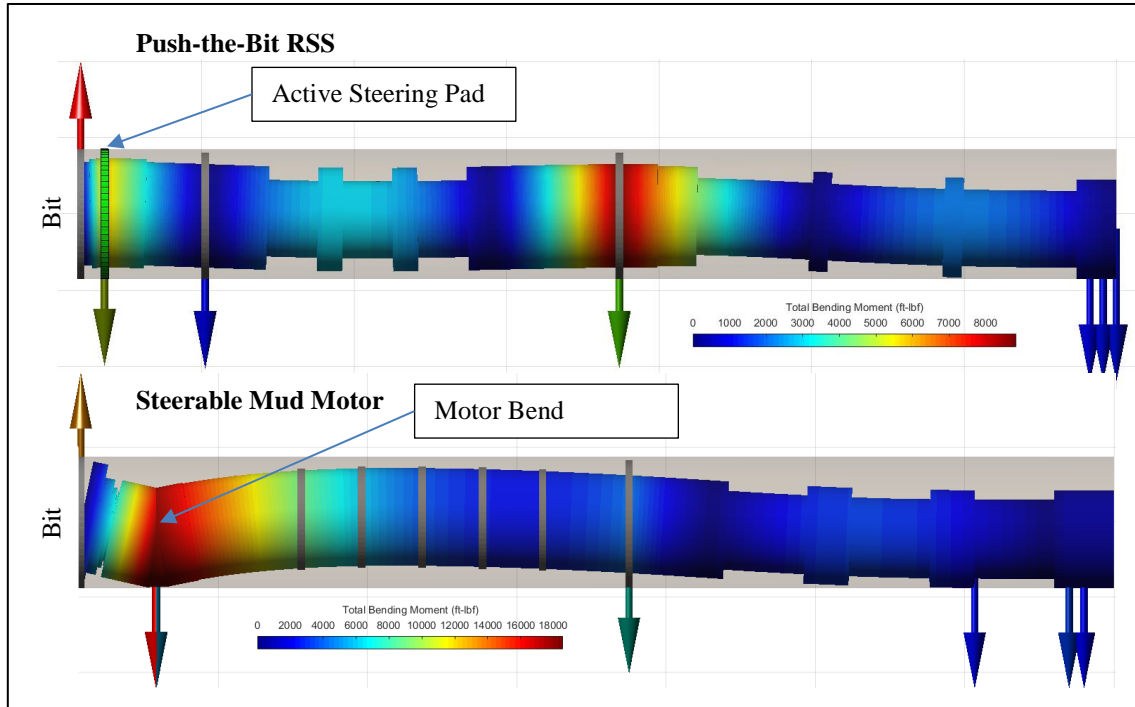


Figure 4.16: Comparison of Steering Mechanism between an RSS and a Steerable Mud Motor

The first build rate comparison is for a steerable mud motor BHA, whose layout is described in Table 4.4. As discussed previously, the sliding motor yield is calculated at a TFO of 0° while the rotational motor yield is calculated as an average for TFOs of 0° and 180° . The outer and inner diameters of the motor are listed as a single value for the sake of comparison. In reality, the inner and outer diameters of a motor can vary considerably along its length, thus leading to discontinuous stiffness and mass characteristics.

Table 4.4: BHA Layout for Motor Yield Comparison

<i>Sec No.</i>	<i>Component Description</i>	<i>OD (in)</i>	<i>ID (in)</i>	<i>L (ft)</i>
1	8 3/4" Bit	8.750		1.00
2	Mud Motor - "Bit to Bend" = 4 ft	6.500	5.000	21.00
3	Non-Mag Flex Collar - Body OD = 5.25", Wear OD = 6.5"	6.500	3.250	30.00

Figure 4.17 and Figure 4.18 display the results of the comparative motor yield study using the following operational parameters: WOB = 30 klb_f, TOB = 3,000 ft-lb_f, MW = 10 ppg, Hole Size = 8.75", E = 30x10⁶ psi, $\nu = 0.3$, and the initial inclination of the wellbore curvature = 60°. The assembly is sectioned into 55 elements within MADSim.

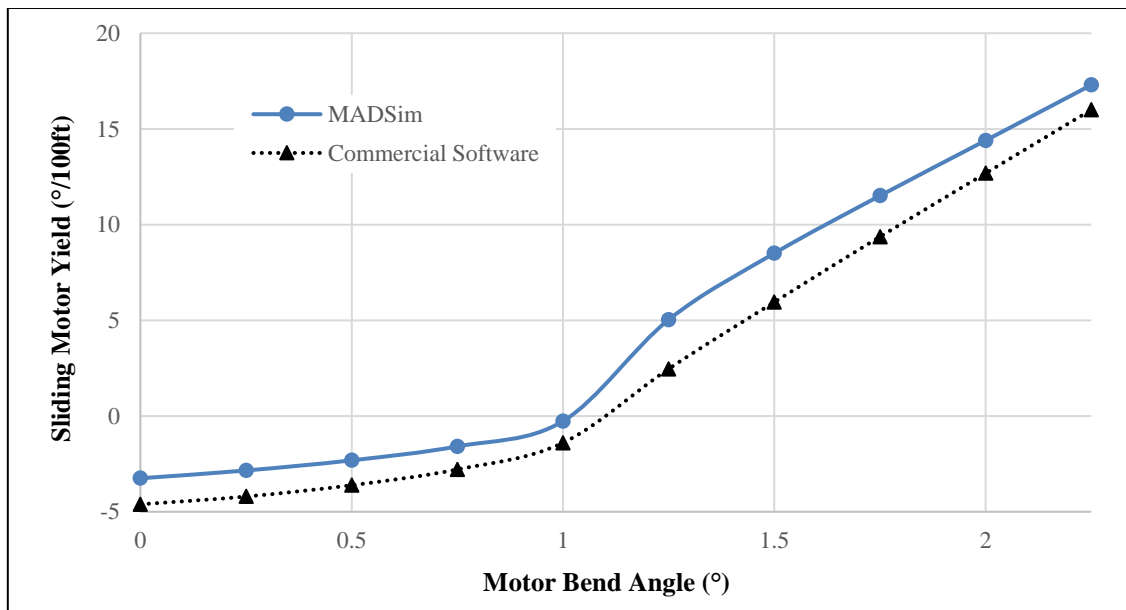


Figure 4.17: Sliding Motor Yield Comparison with Commercial Software

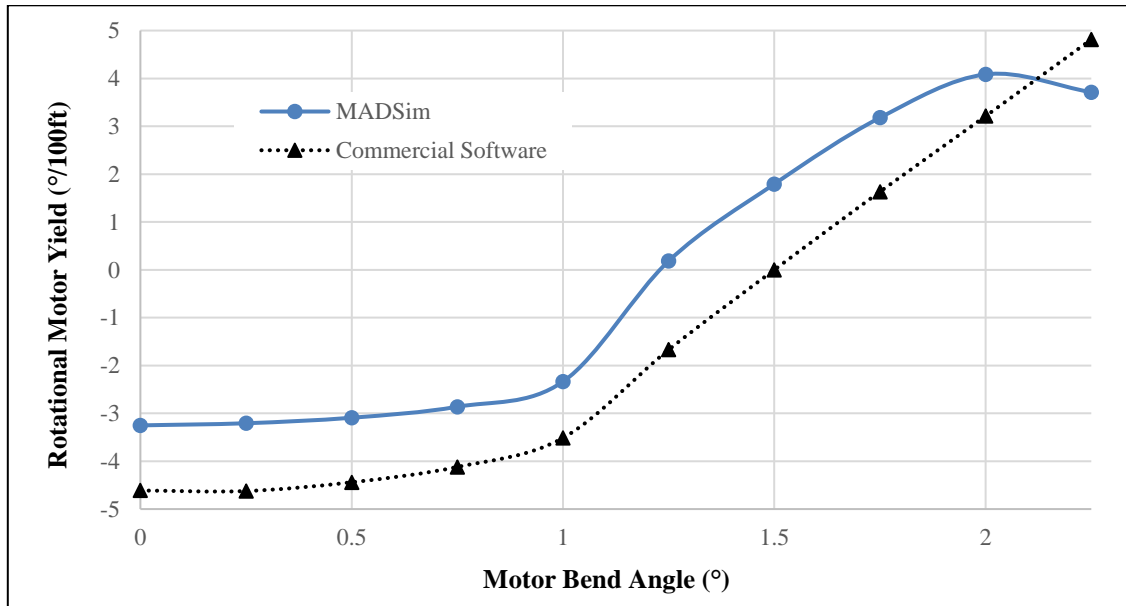


Figure 4.18: Rotational Motor Yield Comparison with Commercial Software

It is seen from the figures that, while the numbers do not match exactly, the trends with changing motor bend angle are similar. The difference in the solutions are attributed to variances in the numerical models, in terms of how the bend in the motor is dealt with, as well as the algorithms that dictate the solution. Because the specifics of the mathematics and the solution algorithms within the commercial software are not available, it is impossible to say exactly what the fundamental differences are that result in the variation of the solutions.

A comparison between RSS yields calculated between MADSim and the commercial software is also provided. The Push-the-Bit RSS assembly is described in Table 4.5, and was visualized previously in Figure 4.16. The operational parameters are: WOB = 10 klb_f, TOB = 2,500 ft-lb_f, MW = 10 ppg, Hole Size = 8.75", E = 30x10⁶ psi, v = 0.3, and the BHA is sectioned into 165 elements. The analysis is done by adjusting the eccentricity generated at the active pad through its physical range (Eccentricity = 0.00 – 0.30 in) at a TFO of 0°.

Table 4.5: BHA Layout for Push-the-Bit RSS Yield Comparison

<i>Sec No.</i>	<i>Component Description</i>	<i>OD (in)</i>	<i>ID (in)</i>	<i>L (ft)</i>
1	8 1/2" Bit	8.500		0.83
2	6 3/4" RSS	6.750	Variable	10.65
	- Active Steering Pad @ 2.41 ft from Bit			
	- 8.25" Stabilizer @ 9.02 ft from Bit			
3	MWD "Flex" Collar	6.750	2.739	16.40
	- Body OD = 5", Wear Knot OD = 6.75"			
4	MWD Pulser Housing	6.750	3.214	5.80
5	String Stabilizer (8.25" Blade OD)	6.750	3.250	5.00
6	Compressive Service Drill Pipe	6.500	3.000	30.12
	- Body OD = 5", Wear Knot OD = 6.5"			
7	6 1/2" Steerable Mud Motor	6.500	Variable	29.00
8	Filter Sub	6.500	3.250	3.00
9	1 Joint HWDP	5.000	3.000	30.50
	- Tool Joint OD = 6.5", Mid-Span OD = 5.5"			

Figure 4.19 shows the results of the RSS yield comparison. Again, the two models correlate well, with minor variations being attributed to the differences in the specific mathematics and respective solution algorithms. Because push-the-bit rotary steerable systems are not only limited by the amount of eccentricity that can be achieved at the active pad but also by the amount of steering force that the active pad can produce, it is

necessary to also examine the force required to achieve the desired eccentricity within the model. Figure 4.20 illustrates this steering force variation with changing eccentricity. Here it is seen that the trends are similar, but the steering force values differ by up to 1,000 lb_f. This may be due to a combination of how the steering force is extracted from the model within the commercial software, as well as the software's contact force algorithm. Again, it's difficult to tell exactly where the discrepancy is due to a lack of transparency in the commercial software. With that said, it is appropriate to describe how the steering force is extracted within MADSim. This can be illustrated by Figure 4.21.

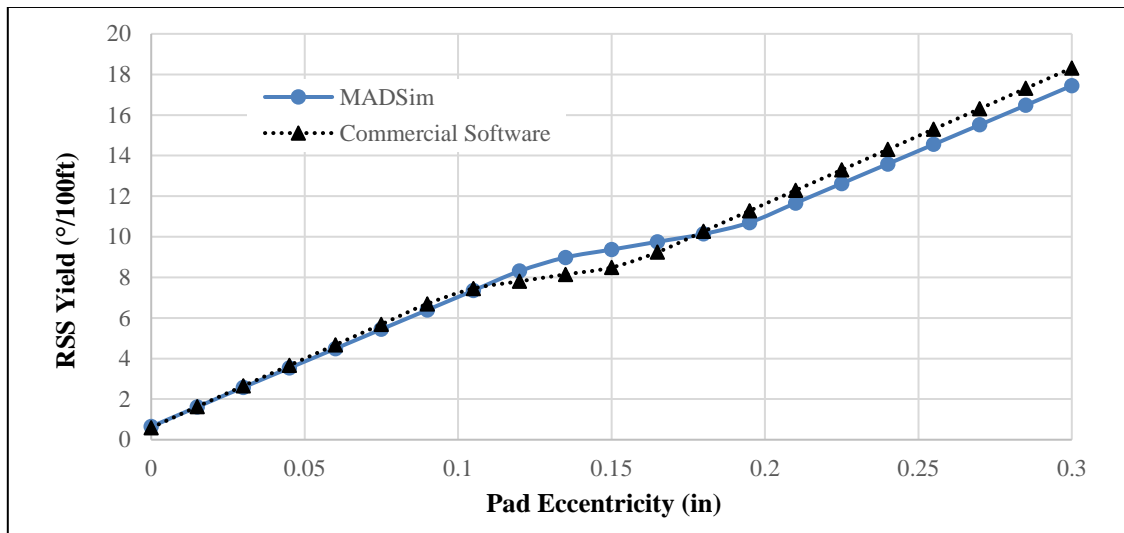


Figure 4.19: RSS Yield Comparison with Commercial Software

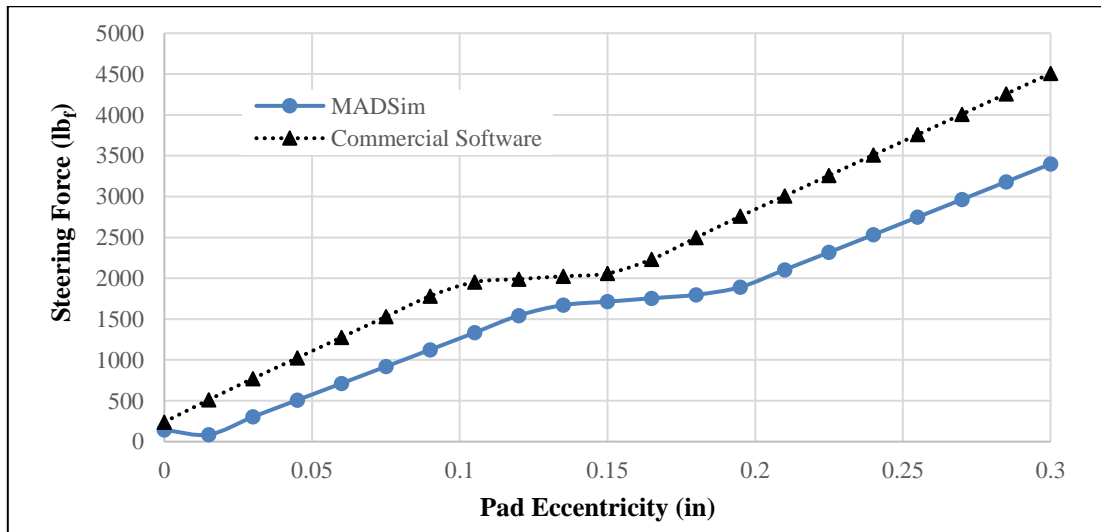


Figure 4.20: RSS Steering Force Comparison with Commercial Software

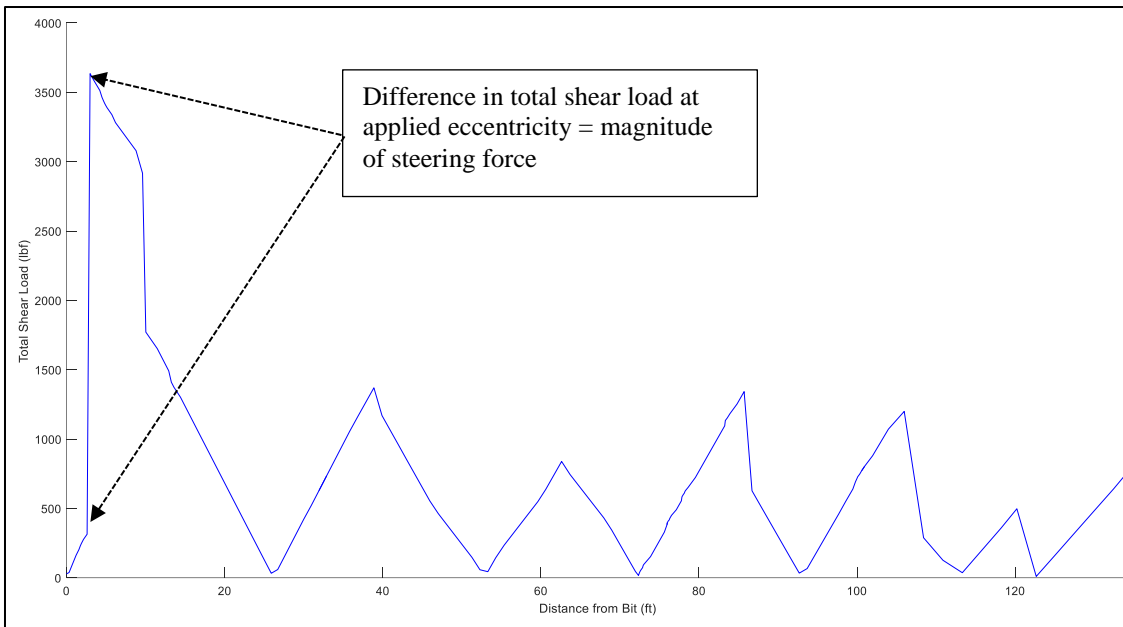


Figure 4.21: Total Shear Load along BHA Calculated from MADSim

In the above figure, the total shear load along the length of the RSS assembly, placed in a 17.4415 °/100ft curved wellbore with an active pad eccentricity of 0.30in, is determined. This shear load is calculated by simply subtracting the gravitational force vector (3.29) from the beam's internal force vector (3.25) for each element. The resulting vector will take on a similar form as (3.28). The total shear load at each end of the element can then be determined from the square-root, of the sum of squares, of the shear components at either end of the beam. Keeping in mind that, for the RSS yield analysis, an eccentricity (radial displacement) was specified at the location of the active pad. The force required to achieve that eccentricity (RSS steering force) is determined by the difference in shear forces between adjacent beams at the location of the applied eccentricity.

Additionally, it is worth pointing out that both the estimated RSS yield and the required active pad force have a very distinct change in slope between eccentricities of 0.1 and 0.2 inches. This is a direct result of a shift in stabilizer contact with applied eccentricity. This can be visualized in Figure 4.22 where three different eccentricities are applied to the RSS assembly in a perfectly horizontal wellbore section. At the top of the figure the eccentricity is 0.00 inches. This correlates to the active pad being perfectly centered in the wellbore. In this configuration, the stabilizer above the active pad (circled in a dashed-red line) is resting on the low-side of the hole. This contact point acts a fulcrum to give a steeper slope on the Yield vs. Eccentricity curve (Figure 4.19). At an eccentricity of 0.15 inches, the upper stabilizer is theoretically no longer in contact with the wellbore and the fulcrum effect is lost; this leads to a reduced slope on the RSS yield plot. At higher

eccentricities the upper stabilizer regains contact with the wellbore, this time being pushed against the high-side of the hole, and the fulcrum effect is again seen in the increased slope of the yield curve in Figure 4.19.

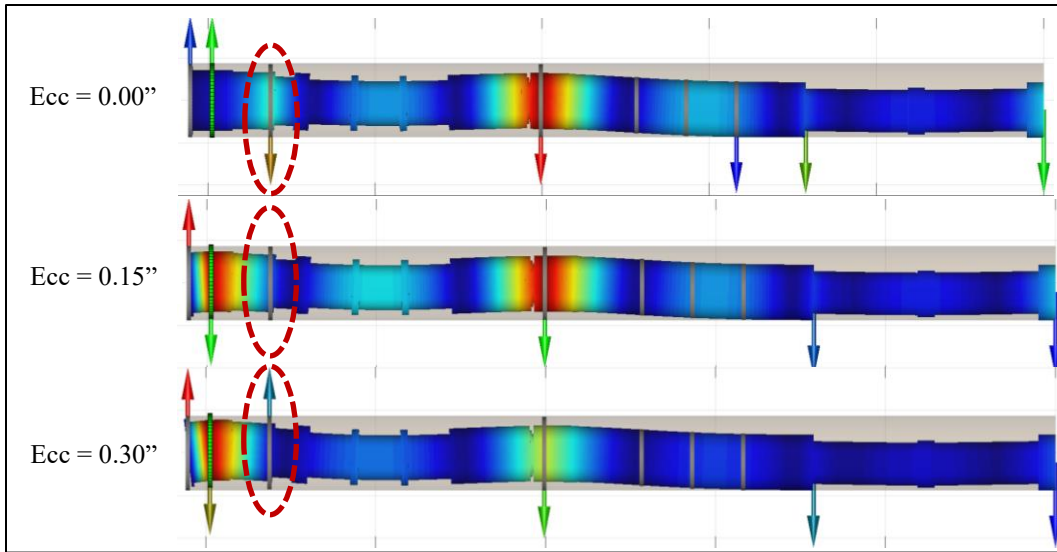


Figure 4.22: Contact Force Distribution with Changing Active Pad Eccentricity

It should be noted that motor/RSS yield calculations are considered “ideal” scenarios. This means that the results should not be taken as exact values of what would actually occur down-hole, but rather as a reasonable comparison between different configurations and/or operational parameters. Typically yield calculations, which assume the side force at the bit is the limiting factor in the directional characteristics of a BHA, such as the previous comparison, will overestimate what is actually seen in the field. Additionally, as stated before, the steering characteristics of the bit will play a significant role in the directional behavior of the BHA. For more advanced yield analyses, the bit steerability [138, 139] can be incorporated in the calculation algorithms.

4.2 Linearized-Dynamic Analysis

Results, to this point, have shown that MADSim produces reliable results when dealing with the nonlinear static/quasi-static behavior of drillstrings. However, considering the present interest in studying induced lateral vibrations while drilling, it is necessary to validate the dynamic analysis capabilities of the developed MatLab code. Initially this validation considers the linearized-dynamic behavior of beams, and then examines lateral drilling assemblies in a horizontal wellbore. Linearized-dynamics comparisons are performed via a free vibration approach as outlined in Section 3.3.2.1.

4.2.1 Pinned-Pinned Beam

Similar to the static analysis, the starting point for linearized-dynamics is an examination of the beam model within MADSim. For this, the lateral natural frequencies of a “pinned-pinned”, or simply-supported, beam are calculated using the developed model as well as Heisig’s previous model [34]. Both of the numerical models are compared to their analytical counterpart. The equation representing the natural frequency of a pinned-pinned Euler-Bernoulli beam is well known and can readily be found. This equation, as presented by NCEES [140], is expressed by (4.2).

$$f_n = \frac{\pi n^2}{2L^2} \sqrt{\frac{EI}{\rho A}} \quad (4.2)$$

Where n is the mode number. Examining the work of Timoshenko [141] it is seen that this is only a portion of the full representation of a beam, as shown by (4.3).

$$f_n = \frac{\pi n^2}{2L^2} \sqrt{\frac{EI}{\rho A}} \left[1 - \frac{1}{2} \left(n \frac{\pi \kappa}{L} \right)^2 \left(1 + \frac{E}{K_s G} \right) \right]$$

$$\kappa = \sqrt{\frac{I}{A}} \quad (4.3)$$

Using the above equations, direct comparisons are shown for the present model (MADSim) and Heisig’s model [34] using different beam lengths. The different lengths of beams are meant to represent the possible lengths of BHA sections that could be supported between two stabilizers: 30 ft (Drill Collar), 15 ft (10 ft Pony Collar + 5 ft tool/sub), and 10 ft (Pony Collar). The beam parameters are listed in Table 4.6.

Table 4.6: Beam Comparison Data

Parameter	E (psi)	ν	OD (in)	ID (in)	L (in)	ρ (lb _m /in ³)
Value	30x10 ⁶	0.3	6.5	3.25	120, 180, 360	0.286

Figure 4.23 shows the first 10 natural frequencies estimated by the 4 different models (2 numeric, 2 analytic) for the 30 ft (360 in) simply supported beam. The dotted black line and the smooth blue line are determined from equations (4.2) and (4.3) respectively, while the blue circles are from MADSim and the black triangles are calculated using Heisig’s model. It is clear from the results that both numerical models match their respective analytical beam formulae. The two beam models are almost identical to each other at lower modes and begin to differentiate at frequencies above 150 Hz. Figure 4.24 and Figure 4.25 display the results for a similar study using beam lengths of 15ft and 10ft respectively. In each case the Euler-Bernoulli model appears to match very well to the corresponding numerical model, while the numerical and analytical results

for the Timoshenko-type beam begin to significantly differentiate from one another at frequencies above 1,000 Hz. This leads to a “leveling-off” of the analytical solution with increasing mode number, while the numerical model continues to rise with increasing mode number. The “leveling-off” occurs due to the nonlinear term, $-\frac{1}{2} \left(n \frac{\pi \kappa}{L} \right)^2 \left(1 + \frac{E}{K_s G} \right)$, in (4.3). The present numerical model cannot account for this simply due to the nature of the Eigen-Value analysis. Linearized-dynamics of beams, using finite element analysis, is essentially limited to solving (3.52) or (3.55). Using this approach, natural frequencies can only increase with increasing mode number. Fortunately, the frequencies in which this nonlinear effect begins to become dominant (≈ 1 KHz) is well above the frequency range of interest for BHAs and drillstrings.

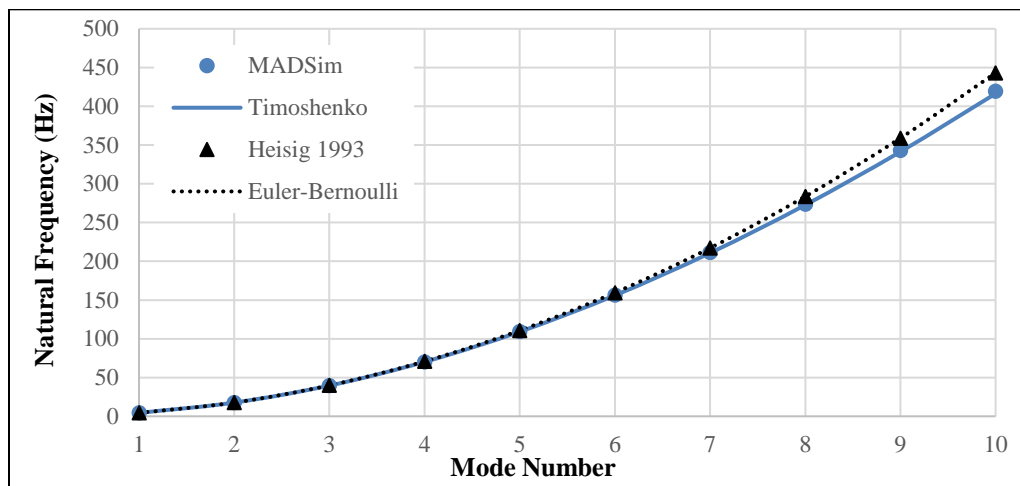


Figure 4.23: Natural Frequency Comparison between Beam Models, Length = 30 ft

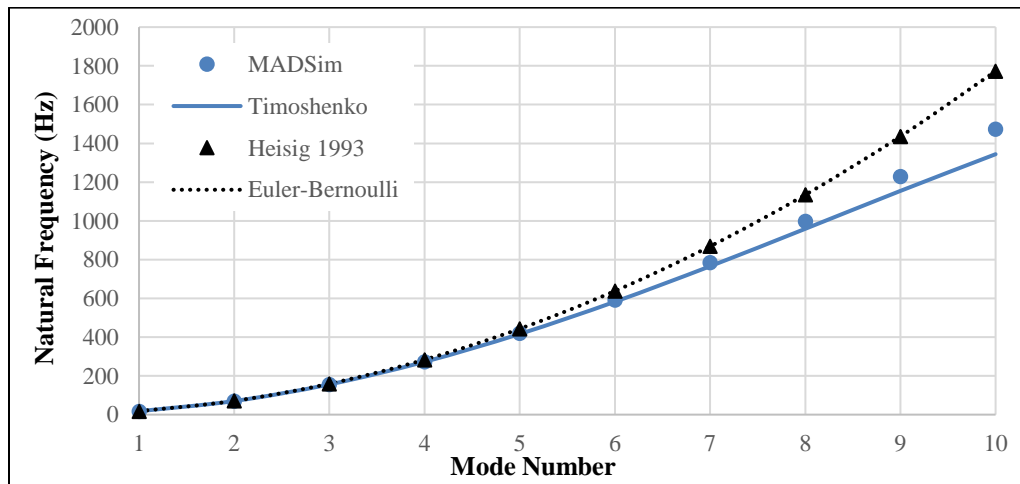


Figure 4.24: Natural Frequency Comparison between Beam Models, Length = 15 ft

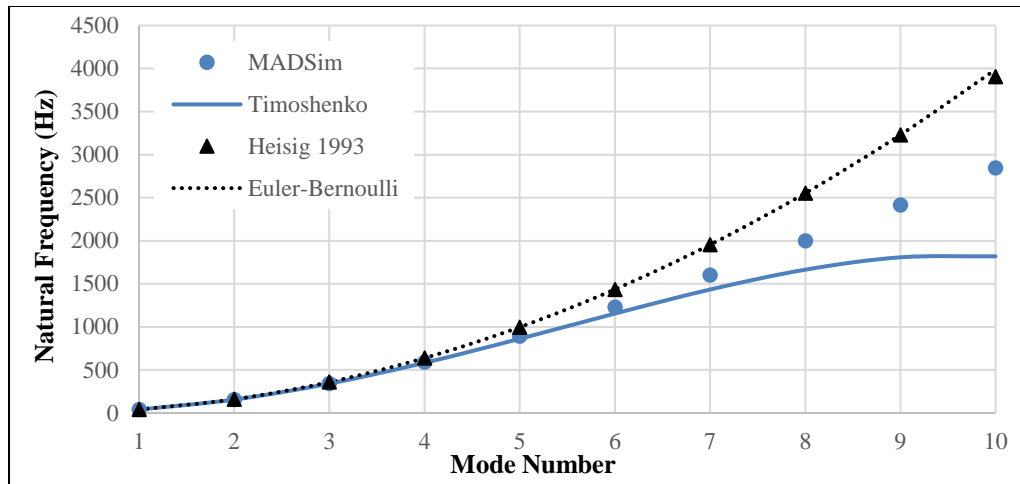


Figure 4.25: Natural Frequency Comparison between Beam Models, Length = 10 ft

4.2.2 Horizontal Drilling Assembly

At this point, it should be fairly obvious that the developed beam model is numerically sound. The next logical approach is to verify that the model can adequately represent the dynamic behavior of a BHA confined within a wellbore. For linearized-dynamics, this can be done with a comparison of the data presented by Heisig and Neubert [40]. In their paper, they examine the lateral dynamics of drillstrings in horizontal wellbores. Within the scope of their work, they present an analytical formula for predicting the lowest natural frequency of CSDP, or “Flex Collars”, in a horizontal well. This equation, derived from an EB-like beam, is shown in a slightly altered form by Equation (4.4).

$$f_{min} = \frac{1}{\pi} \sqrt{\frac{3}{\mu_m} \left(\frac{\tilde{q}}{r} - \frac{W^2}{4EI} \right)} \quad (4.4)$$

Where μ_m is the distributed mass of the CSDP and added fluid mass [slugs/in], \tilde{q} is the distributed buoyed weight of the CSDP [lb_f/in], r is the radial clearance between the wellbore and the largest section OD of the CSDP [in], W is the axial force [lb_f], E is the Young’s Modulus [psi], and I is the area moment of inertia of the smaller cross-section of the CSDP [in⁴]. The CSDP used for this analysis is described in Table 4.7, and was the same CSDP used in the assembly described by Table 4.2.

Table 4.7: Dimensions of Compressive Service Drill Pipe

<i>Sec Description</i>	<i>OD (in)</i>	<i>ID (in)</i>	<i>L (ft)</i>
<i>Tool Joint</i>	6.500	3.000	2.59
<i>Body</i>	5.000	3.000	7.48
<i>Wear Knot</i>	6.500	3.000	1.25
<i>Body</i>	5.000	3.000	7.48
<i>Wear Knot</i>	6.500	3.000	1.25
<i>Body</i>	5.000	3.000	7.48
<i>Tool Joint</i>	6.500	3.000	2.59

The CSDP is placed in 11 ppg drilling mud, within an 8 ½" wellbore, and an axial force of 20 klb_f is applied. With this scenario, (4.4) predicts the lowest natural frequency of the CSDP to be 2.1350 Hz. To validate this solution with MADSim, the same assembly outlined in Table 4.2 is utilized, with an additional 15 joints of CSDP (16 Jts of CSDP total). Applying a TOB of 3,500 ft-lbf to this assembly, and setting friction equal to zero, the lowest 12 linearized natural frequencies are calculated with MADSim.

The mode shapes corresponding to each of the 12 linearized natural frequencies are displayed in Figure 4.26. In a similar manner to the results presented by Heisig and Neubert [40], the lowest linearized natural frequency of the drilling assembly is associated with the transition between the MWD Collar and the CSDP at a value of 2.0451 Hz. The next lowest linearized natural frequency of the drilling assembly is associated with the CSDP and, at a value of 2.1393 Hz, corresponds well with the analytical solution of 2.1350 Hz. Considering the assumptions that went into the derivation of (4.4), the small difference in these solutions further illustrates that ignoring shear deformations and lateral rotary inertias is a sufficiently valid assumption when modeling drillstrings.

A similarity can also be noticed between the mode shapes in Figure 4.26, and the mode shapes calculated via Heisig and Neubert [40]. This is to be expected as the two assemblies are very similar in structure, and provides further evidence that the coding within MADSim is producing accurate and reliable results. Examining the mode shape plots, it is apparent that these vibrational patterns are not ones that could easily be predicted by analytical solutions. Bearing in mind that the response of a mechanical system is not only dependent on the frequency in which it is excited but also how similar the excitation is to a particular modal pattern [142], this further suggests the need for this type of advanced modeling when dealing with drillstring dynamics.

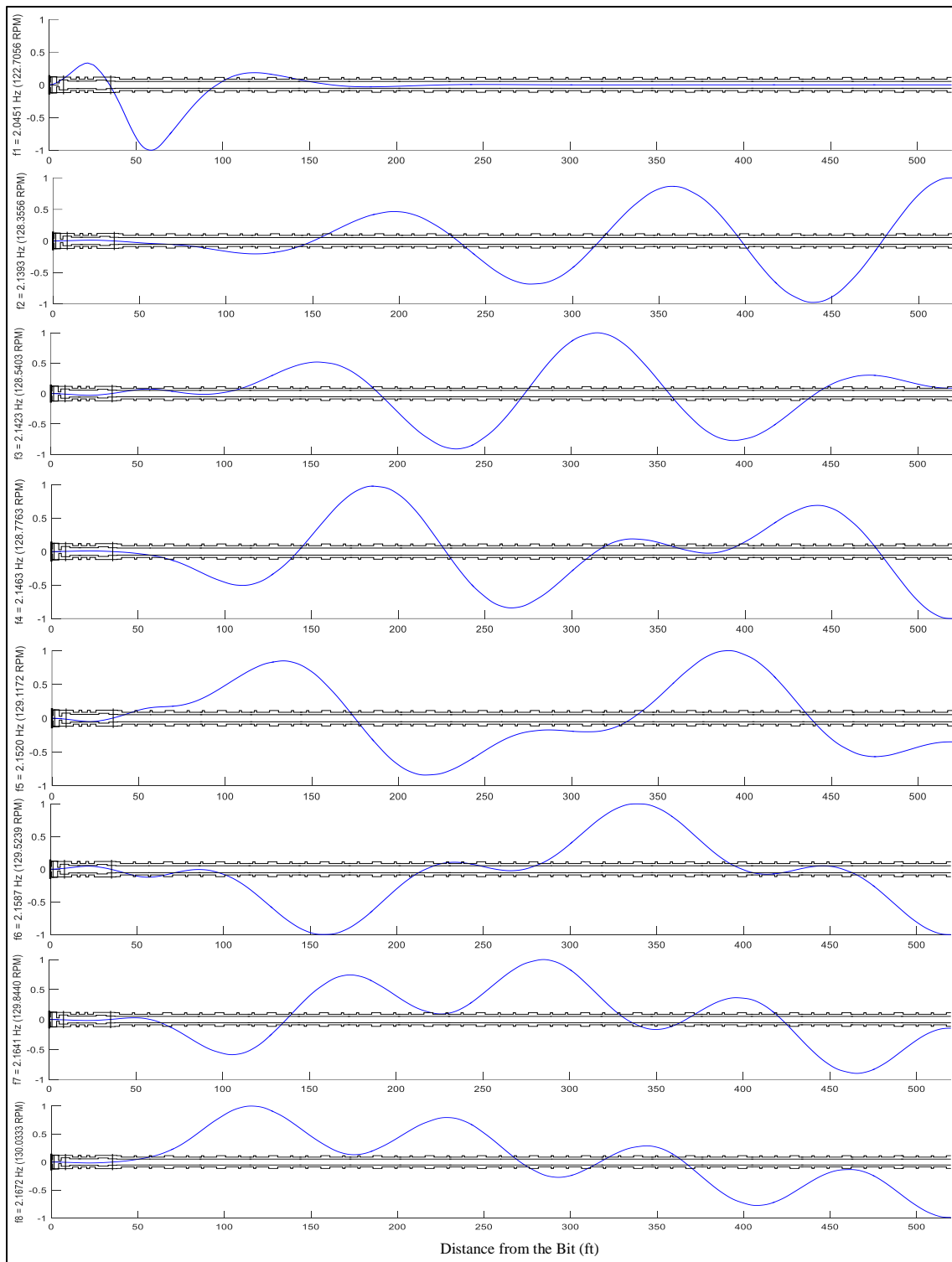


Figure 4.26: Linearized Natural Frequencies and Mode Shapes of Horizontal Drillstring

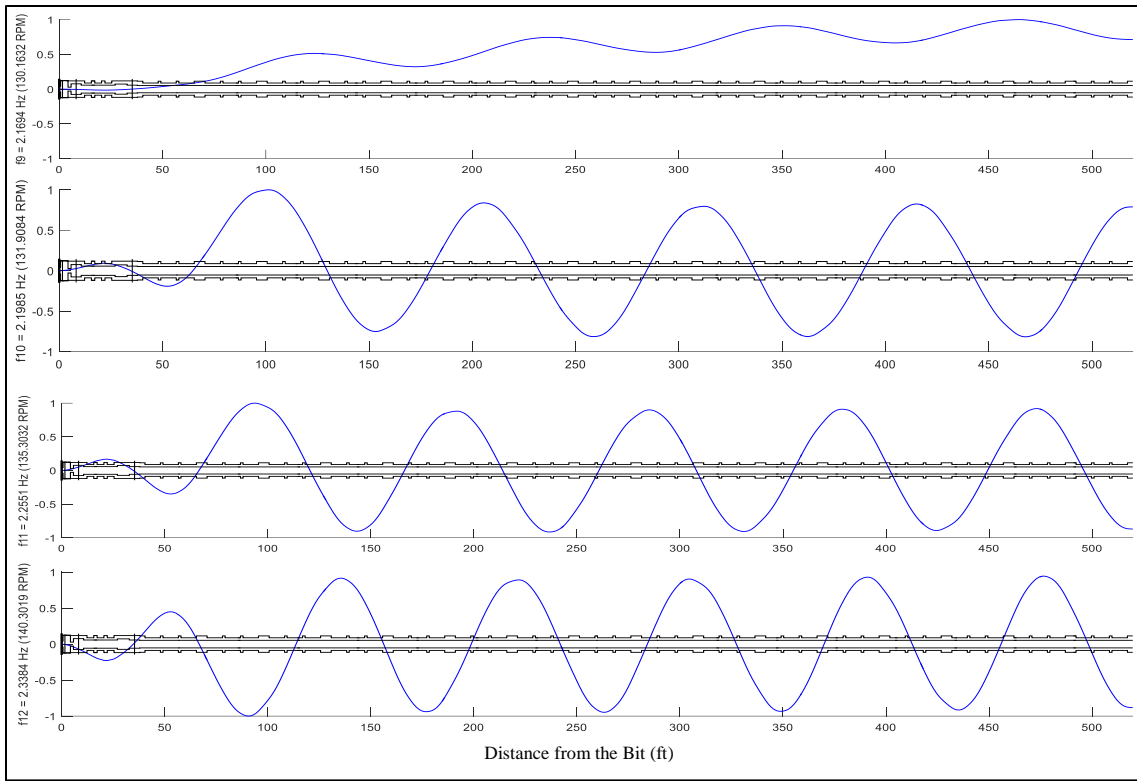


Figure 4.26 Continued

Of course, a comparison of the linearized natural frequencies predicted by MADSsim and Heisig's Model [34] is also provided in Figure 4.27 and Figure 4.28. Here it is seen that, even up to 100 Hz, the difference in solution is less than 2.5 %. This percentage is even smaller within the frequency range that would typically be of interest for drillstring dynamics optimization, with a maximum difference of less than 0.06 % across the lowest 12 modes.

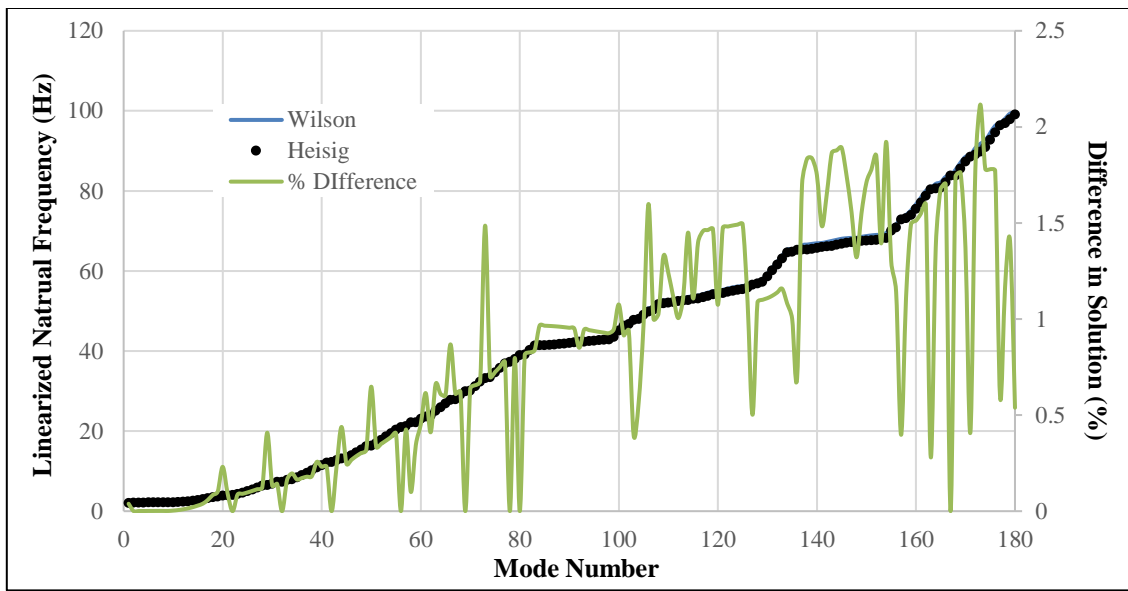


Figure 4.27: Linearized Natural Frequency Comparison of Horizontal Drillstring

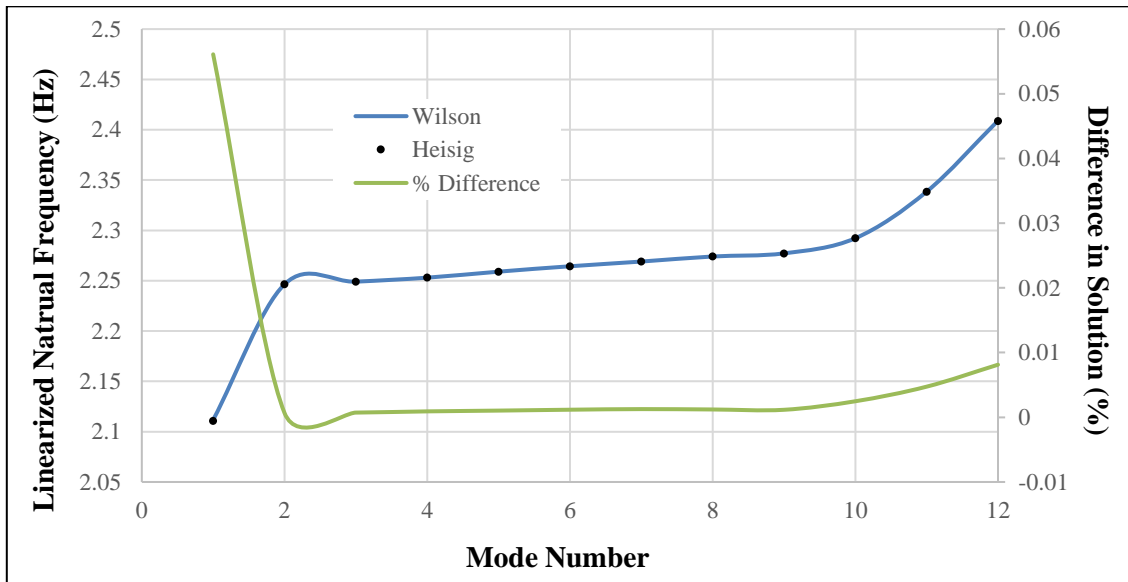


Figure 4.28: Linearized Natural Frequency Comparison of Horizontal Drillstring, Zoom-In

4.3 Nonlinear-Dynamic Analysis

The previous sections have numerically validated the nonlinear-static and linearized-dynamic solutions produced by MADSim. The validation process has also revealed that ignoring the shear deformations of beams, as well as the lateral rotary inertias of the cross-sections, are sufficiently valid assumptions within the realm of drillstring mechanics and linearized-dynamics. This is simply a function of the relatively large

aspect ratios of drillstrings and the relatively low frequency range of drilling operations. With this reasoning, as well as the fact that drillstrings are relatively confined within the wellbore, gyroscopic effects are generally thought to be negligible. However, for the sake of completeness, that statement is tested via nonlinear time-domain simulations. This numerical testing also allows for a direct comparison between a drillstring model based on the “standard assumptions” described in Section 2 [34], and the present model that makes no simplifying assumptions with regards to shear deformations, lateral rotary inertias, or gyroscopic effects.

For the numerical test, the same RSS assembly used for the analysis in Section 4.2.2 is utilized. Again, this is the same rotary steerable BHA described in Table 4.2 with 15 additional joints of CSDP. All of the same parameters are used, except for the friction coefficient. For the nonlinear simulation a friction coefficient of 0.4 is used. This correlates to the solid orange line in Figure 2.4. Mathematically, the time-domain analysis is carried out following the approach outlined in Section 3.3.3 and Appendix B.

In order to fully observe the dynamics of the system, the rotational speed of the drilling assembly is slowly increased through the critical range predicted in Figure 4.26, following the trend line shown in Figure 4.29. The boundary conditions for the simulation restrict the lateral displacement of the bit, but allow it to tilt freely; WOB and TOB are applied at this node. At the “top” of the drillstring, opposite the bit, the cross-section is allowed to move freely within the wellbore but is forced to remain parallel to the wellbore at all times; the rotational speed is applied here and displacement is fixed in the axial direction at this point. As a source of excitation within the simulations, mass eccentricities are prescribed along the length of the drilling assembly. These eccentricities are constant per joint of CSDP, but randomly distributed in terms of magnitude and circumferential direction. The eccentricities are limited to a maximum of 0.25 inches.

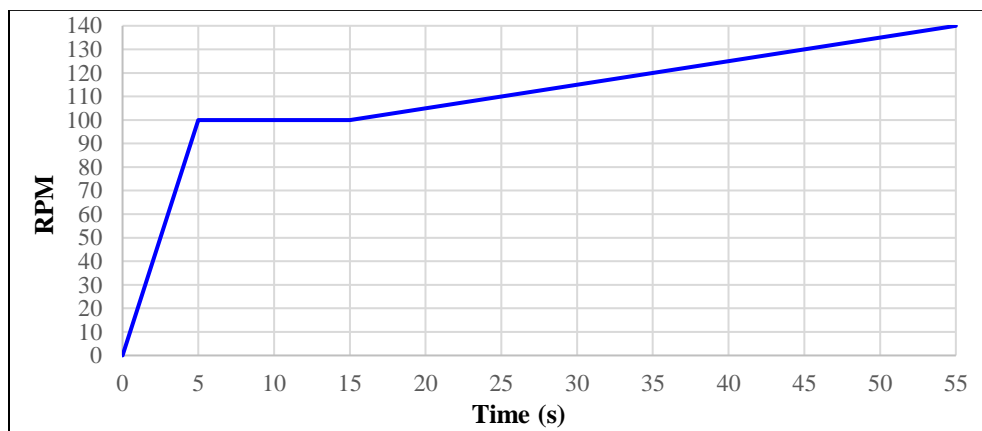


Figure 4.29: Rotational Speed Applied at the “Top” of the Drilling Assembly for Time-Domain Simulations

With the prescribed rotation speed in the previous figure, three individual simulation cases are performed:

- 1) Using Heisig's model [34] which neglects shear-deformations, lateral rotary inertias, and gyroscopic effects
- 2) Using the present model, but ignoring gyroscopic effects. This corresponds to removing (3.24) from (3.40) and, consequently, removing (3.24) from (3.60) as well as removing the $\left[\frac{\partial E_{M_{Gyro}}}{\partial \underline{u}} \right]$ term from (3.63).
- 3) Using the present model, in its entirety. This includes the effects of shear deformations, lateral rotary inertias of the cross-sections, and the gyroscopic moments acting within the system.

In all of the cases, any damping due to the fluid-drillstring interaction has been ignored. With the frequencies associated with the simulation, and an assumed 1% damping ratio, the damping parameters are calculated [14] to be $\beta_D = 0.1257$ and $\gamma_D = 7.6394 \times 10^{-4}$.

Figure 4.30-Figure 4.32 provide a snapshot of the results for each simulation case. In the figures, orbital plots (left-hand side) and lateral acceleration plots (right-hand side) are shown for two nodes in the drillstring, 188 ft and 399 ft behind the bit. The orbital plots display the high-side and right-side displacements of the cross-sections, with the thick black curve representing the wellbore wall, the thick blue curves representing the OD and ID of the drillstring at each node, the blue asterisk is a string rotation indicator for animated plots, and the red curve outlines the path traveled by the centerline of the cross-section over the course of the simulation. The lateral acceleration plots, on the right, show the absolute lateral acceleration of the corresponding cross-section as a function of string rotation speed. From Figure 4.30 it can be seen that the lateral acceleration values remain relatively low at rotation speeds below 123 RPM. The lateral displacement up to this rotation speed is a relatively benign “snaking” motion that gently rocks the drillstring back and forth. Once the rotation speed reaches the resonance range, as predicted by the linearized analysis in Figure 4.26, the lateral acceleration increases dramatically and the displacement becomes highly erratic. As the rotation speeds increases through this resonant frequency range, the drillstring attempts to transition from a “snaking” motion to a whirling motion. This leads to the “lift off” behavior and subsequent impact with the wellbore wall. It would be expected that maintained operation within this resonant range would result in full whirl behavior of the drillstring. This result not only shows why resonant frequencies (Critical RPMs) should be avoided, but also provides validation that the nonlinear simulation algorithms are producing reliable results that make sense from an engineering perspective.

Comparing all three of the figures, it is also quite apparent that the inclusion of shear deformations, rotary inertias, and gyroscopic effects add little value to the overall solution. Of course this conclusion has been

suggested by previous authors [14, 34, 90, 143], but with no direct evidence that it was a valid assumption within horizontal wellbores. It can further be noticed that the shear deformation considerations have a greater influence on the drillstring's response than do the gyroscopic effects. This is seen through minor differences in the acceleration values and displacement patterns between Figure 4.30 and Figure 4.31, while no difference is seen when comparing Figure 4.31 and Figure 4.32. In order to properly investigate nonlinear drillstring dynamics, it is imperative to provide proof of these simplifying assumptions; this study provides the definitive evidence necessary in order to justify the use of the “standard assumptions”, discussed in Section 2, when modeling the dynamics associated with drilling horizontal wells.

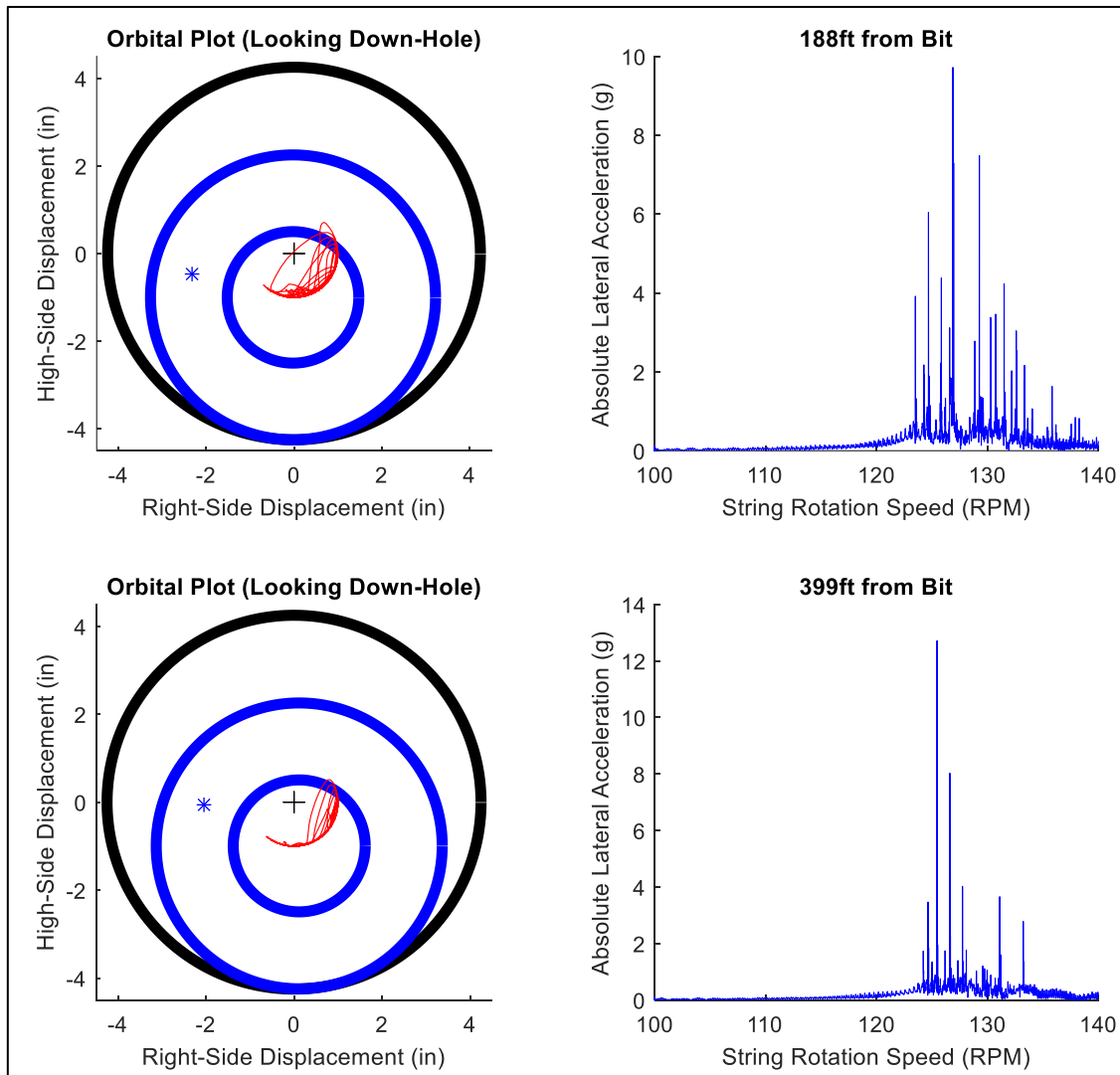


Figure 4.30: Nonlinear Simulation Results using Heisig's [34] Model (Does not Include Shear Deformation, Lateral Rotary Inertias, or Gyroscopic Effects)

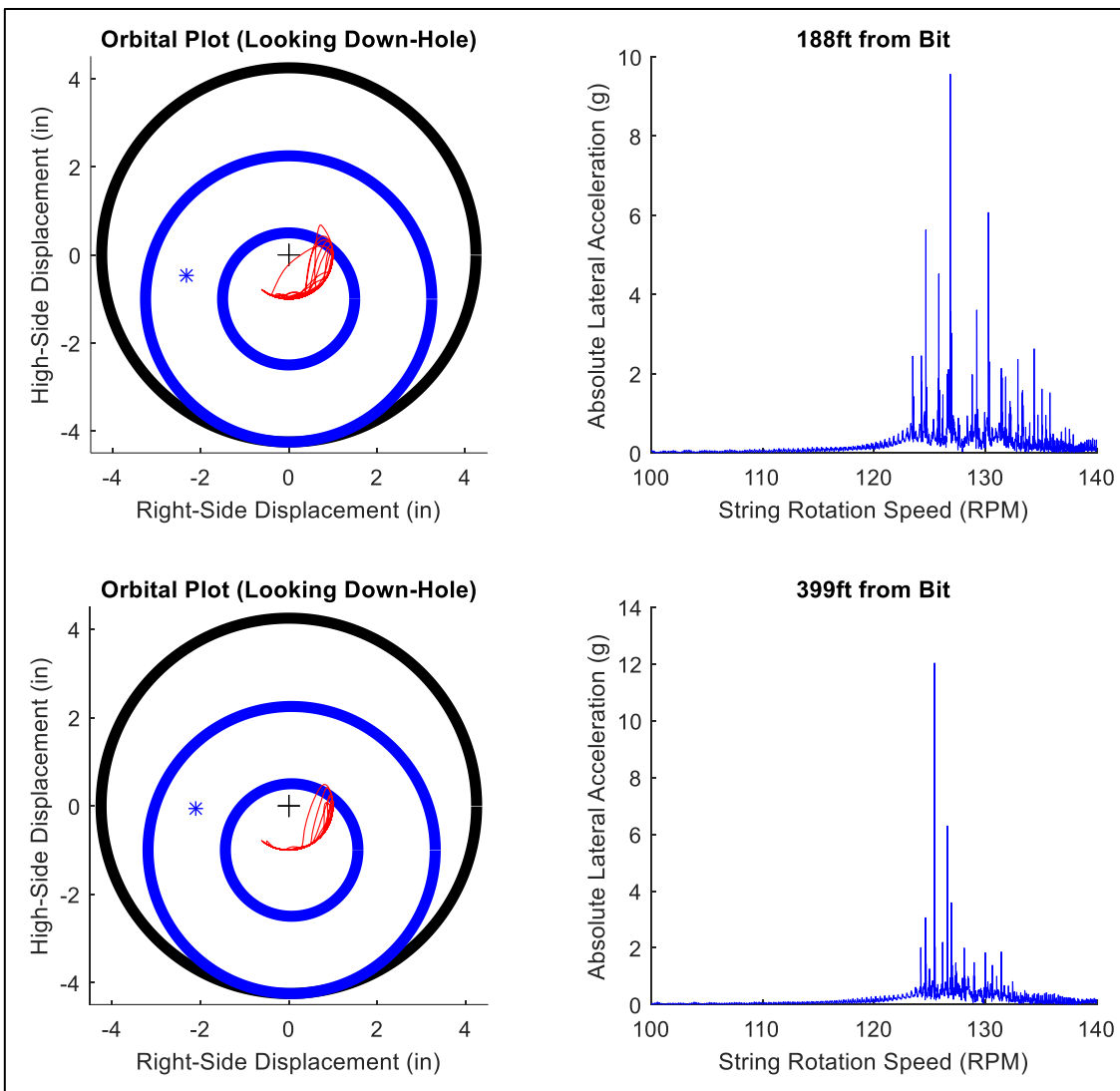


Figure 4.31: Nonlinear Simulation Results using Current Model (Includes Shear Deformation, Lateral Rotary Inertias, but not Gyroscopic Effects)

*Note: Acceleration values are periodically averaged for the sake of presentation

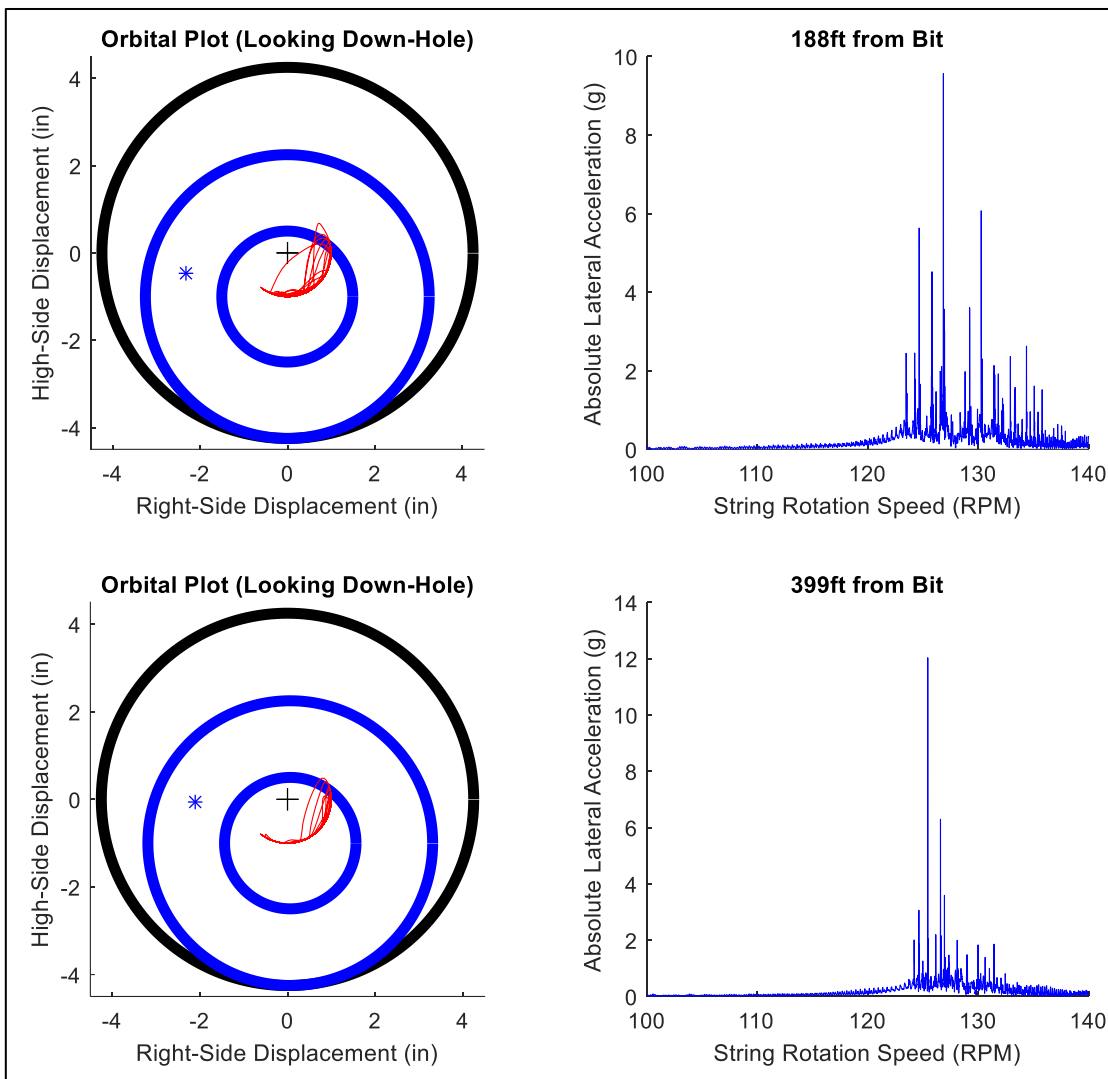


Figure 4.32: Nonlinear Simulation Results using Current Model (Includes Shear Deformation, Lateral Rotary Inertias, and Gyroscopic Effects)

4.4 Initial Field Trials

While numerical validation is a key process to assuring that an algorithm is generating appropriate results, it simply remains “only a model” until it can be proven to represent the reality of the environment in which it was designed to mimic. As an initial attempt to provide a true validation with field data, a comparison is made between MADSIM and recorded vibration data from Scientific Drilling’s MWD tool. However, before an evaluation of the modeling is performed, certain aspects of field data need to be discussed.

First, there is generally a discrepancy between the surface-measured WOB and what is actually seen at the bit. As discussed in Section 1, surface-measured WOB is actually a calculated value based on a reduction in the measured hook-load as the drillstring is advanced along the wellbore. After adding each stand of drill pipe to the drilling assembly, the entire drillstring is lifted off bottom and a “base-line” hook-load value is recorded. The WOB value is then “zeroed” before the driller tags bottom. As the top-drive lowers the drillstring, and the bottom of the hole begins to support the weight of the assembly, the hook-load is reduced by an equivalent amount. This reduction in hook-load is then taken as the WOB. However, apart from the axial force being supported by the bottom of the well, there will be frictional drag along the length of the drillstring that is not generally accounted for in the “zeroing” process. Therefore, the surface-measured WOB will contain the true axial force that is seen at the bit as well as the axial resistance due to friction along the length of the drillstring. When modeling a BHA, if the WOB is taken as what has been measured from the surface, then the axial force applied to the model may be excessive and lateral natural frequencies may be under-predicted (increased WOB decreases lateral resonant frequencies). This isn’t necessarily a bad thing since it would likely lead to more conservative, and safer, operational limitations; i.e., by staying below a lateral resonant frequency (critical RPM) predicted by a larger WOB value than what is actually being applied to the bit, the operational frequency is only going to be further below what the true lateral resonant frequency is. For a validation study, however, this is not an ideal scenario since it would be necessary to show that the model is predicting appropriate frequencies associated with the drilling system, which in turn depend on an accurate determination of WOB.

Secondly, the vibration sensors in MWD tools are not generally considered ideal for experimental purposes; typically recording vibration data every 1 or 2 seconds. While this is generally sufficient for basic monitoring and post-run analysis, such a low frequency of vibration data cannot identify the excitation frequencies present at the measurement point, which is crucial for understanding the source of down-hole vibrations. Additionally, the location of the measurement point is not always positioned well enough to detect potentially damaging vibrations of the components above or below the MWD. This can be understood by referring back to Figure 4.26; when looking at the first resonant frequency of this assembly ($f_1 = 2.0451$ Hz), the mode shape suggests that the maximum displacement response occurs in the joint of drill pipe directly on top of the last stabilizer in the BHA, while remaining relatively flat along the rest of the drillstring. This explains why the vibration data recorded at two points along the drillstring, that were not in the proximity of the 2.0451 Hz peak above the stabilizer (188 ft and 399 ft from the bit, Figure 4.30-Figure 4.32), did not show the largest response at this frequency; instead, these “measurement points” indicate a peak response at about 128 RPM, which correlates to larger lobe patterns at these locations in Figure 4.26. Therefore, in order to properly detect down-hole resonance, vibration sensors ought to be relatively close to a peak within a given mode.

Based on the aforementioned discussion, it can be understood how obtaining a proper validation with basic drilling tools can be somewhat of a challenge. There are tools available that overcome these limitations, like high-frequency vibration recorders with down-hole WOB measurement devices [144], but these are generally rather expensive additions to a BHA; financial limitations at the time of this research prevented any dedicated validation field tests from being conducted with these types of tools. However, by considering the limitations previously discussed, an initial attempt at validating the model can be performed solely from the surface and MWD data.

Because the WOB data from the rig is generally inaccurate due to the friction along the wellbore while drilling, comparisons can only be made in situations where the surface-measured WOB is considered a true reading of the down-hole value. The only scenario where this is applicable is during off-bottom rotation operations, i.e. back-reaming or performing clean-up cycles. Although not generally a recommended practice, back-reaming is often done periodically along the course of a well by rotating the drillstring and moving the assembly up and down through a given section. This, in theory, removes ledges and “tight-spots” along the wellbore, although the true advantages/dis-advantages are an ongoing topic of debate amongst field personnel and engineers. A dedicated clean-up cycle is similar to back-reaming in that the drillstring is continuously rotated and it is done periodically along the course of drilling a well, but generally the drillstring is not moved back and forth along the wellbore during the operation. Both of these procedures require the bit to be lifted off the bottom of the wellbore, and therefore the bit cannot be supporting any axial force during these practices. From a modeling perspective, knowing that the WOB is zero in these scenarios removes uncertainty in the analysis. Additionally, with no WOB applied to the BHA, there is generally no bit torque either which further removes loading uncertainty from the model. From this, the resonant behavior of a BHA can be estimated without external loading; the predicted linearized natural frequencies and mode shapes can then be used to examine if the MWD sensor in a particular BHA would be able to detect the vibration from operating within a resonant frequency range.

With the awareness of these limitations, two case studies are presented which provide a suggestive validation of the proposed model. The first is from a well drilled by an operator in the Marcellus shale in the north eastern United States. Field personnel reported damages to the top of the steerable mud motor after several runs in the lateral section of this well. No catastrophic failure was indicated (i.e. the tools survived the well), however the damage to the motor suggested that further operation of the tool may have resulted in a lost-in-hole (LIH) scenario. Examining surface and MWD data from the run, it was apparent that the MWD was detecting high vibration levels during back-reaming operations. A screen-shot of the field data can be seen in Figure 4.33. Here three data tracks are shown near a MD of 14,300 ft containing the bit depth, hole depth, block position, WOB, surface torque, surface rotary speed, stick-slip indicator, axial RMS vibrations, lateral

RMS vibrations, down-hole rotation speed, and peak vibration levels. At the top of the interval, as the assembly is drilling ahead at a WOB of 30 klf (marker 1), the vibration levels are relatively low (RMS = 1 g, peak = 2 gs). As the WOB is taken off and back-reaming begins (marker 2), the lateral and axial vibration see a prominent increase. In general, this increase in vibration is to be expected due to the fact that the bit is no longer engaged with the formation and there less resistance to lateral vibration at the face of the bit, which then allows lateral waves to travel more freely through the BHA. While continuously back-reaming, the surface rotation speed is increased in a step-wise manner from 70 RPM (marker 2), to 80 RPM (marker 3), to 90 RPM (marker 4), and finally to 100 RPM (marker 5). The increase in rotation speed from 70 to 80 RPM seems to further increase the peak vibration levels. In general, this behavior makes sense as a bent motor inherently induces a whirling behavior in the BHA. This whirling may be localized to the motor or, under higher RPM values and decreased lateral bit stability (non-engaged bit), could potentially spread out across the BHA. The erratic spikes in the peak vibration data above 80 RPM (marker 3) suggest that impact loading is occurring. Very similar behavior was seen at every back-reaming interval along the well, which totaled 7 intervals (about 25 hrs) throughout the lateral section.

It was decided to explore this incident with the model developed in this work. Investigating the specific interval associated with Figure 4.33, with a mud weight of 14 ppg, the static deflection of the BHA (outlined in Table 4.8) is determined at a MD of 14,300 ft. A mechanics plot, indicating the contact forces and bending moments calculated via this static analysis, is shown in Figure 4.34. From the static deflection, the system is linearized and the lowest four critical RPM values (critical RPM = [resonant frequency]*60) of the BHA are determined, which are shown in Figure 4.35. Each colored line in the figure represents the mode shape (vibrational pattern) associated with a specific RPM value, the red dot indicates the approximate location of the vibration sensor in the MWD tool, and the black outline shows the outer and inner diameter distribution along the BHA. It should be kept in mind that mode shapes do not represent actual displacement values, and merely show relative displacement severity along the BHA at a given resonant frequency.

It should be clear from the results in Figure 4.35 that the lowest critical RPM value, which is well within the operation range seen from the data in Figure 4.33, is associated the top of the motor, the “flex pony”, a “pony” collar, and the very bottom of the MWD collar. This is generally the case with steerable motor assemblies due to the fact that the bend in the motor causes a portion of the motor, directly behind the bend, to be lifted off of the wellbore wall. This behavior can be seen via the bowing behavior of the motor in Figure 4.34; notice the distance between the red contact force arrow at the bend and the blue contact forces on the MWD collar. Of course, this is only a scenario representing a TFO = 0°, i.e. the motor bend is oriented towards the high-side of the wellbore. When the bend is rotated, the contact force distribution along the BHA will change and will almost always result a larger resonant speed of the BHA at other tool face

orientation angles. Therefore, determining the critical RPM values at a TFO of 0° provides the lowest resonant limit of steerable motor BHAs.

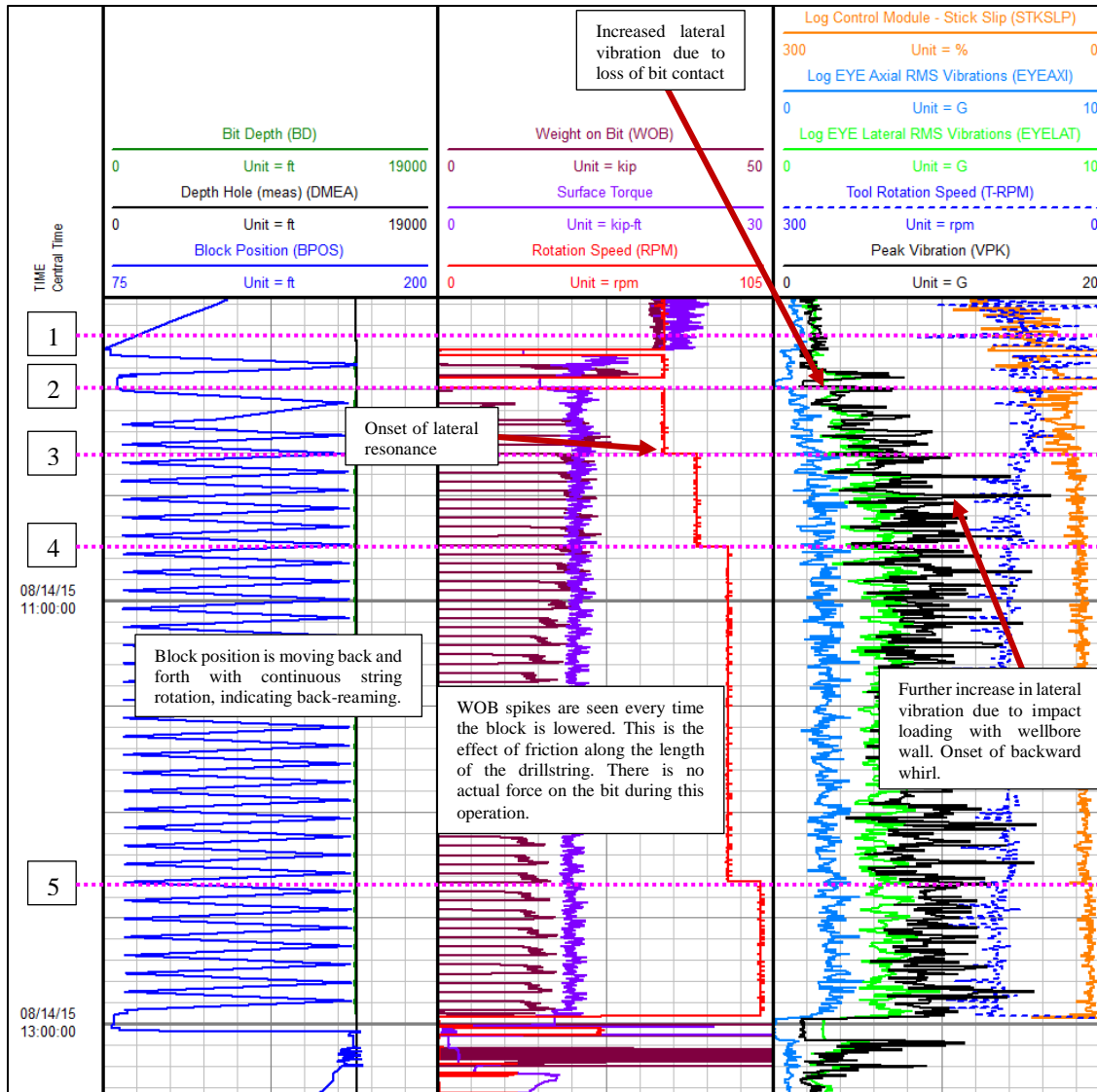


Figure 4.33: Surface Parameters and MWD Vibration Data for Marcellus Well, while Back-Reaming near 14,300 ft MD

Table 4.8: Lateral BHA, Marcellus Well

Sec No.	Component Description	OD (in)	ID (in)	L (ft)
1	8 3/4" PDC Bit	8.750	-	1.00
2	SDI 6 1/2" Titan 2 Drilling Motor (7/8-3.3), 1.75° Bend	6.500	Variable	28.93
3	Non-Mag "Flex Pony" Collar	6.500	3.250	10.05
4	Non-Mag "Pony" Collar	6.500	3.250	9.96
5	MWD Collar	6.500	3.250	30.61
6	MWD Pulser Sub	6.500	3.125	1.85
7	Gap Sub	6.500	2.813	4.60
8	Non-Mag Drill Collar	6.500	3.250	27.01
9	Non-Mag "Flex Collar"	6.500	3.250	31.10
10	6" Drill Collar (x2)	6.000	3.250	60.00

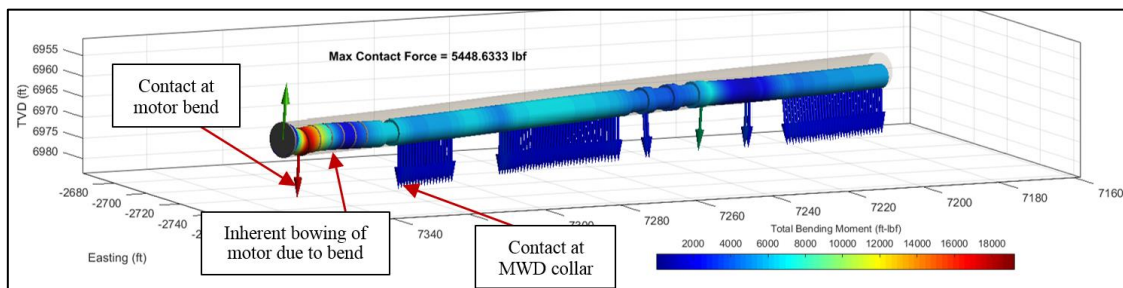


Figure 4.34: Static Deflection of BHA in Marcellus Well (MD = 14,300 ft)

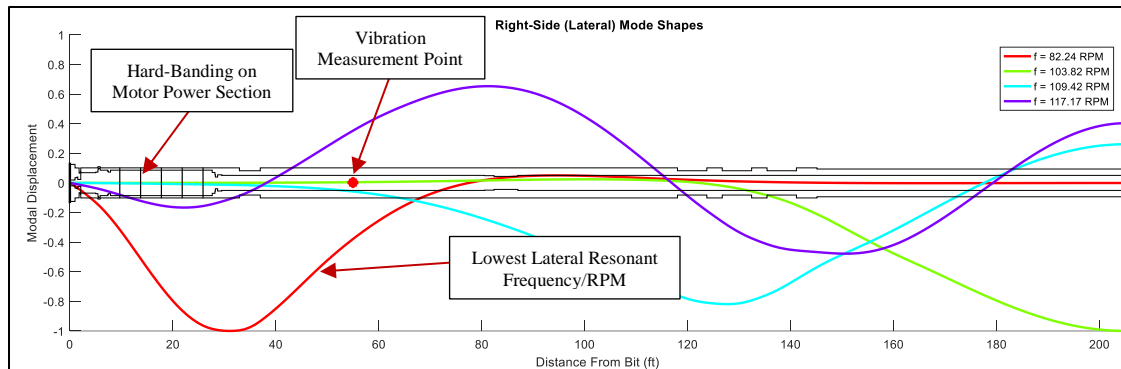


Figure 4.35: Critical RPM Analysis of BHA in Marcellus Well (MD = 14,300 ft)

Additionally it can be noticed that the vibration measurement point in the MWD collar is not directly centered on the lobe of the lowest estimated critical RPM. Depending on the lateral damping of the system, this may result in the vibration measurement not necessarily being able to detect the resonant vibration of this mode; this was the basis of the “measurement proximity” issue discussed previously. That’s not to say that the vibration sensor is not able to detect larger vibration levels at that mode (similar to the vibration

patterns in Figure 4.30-Figure 4.32), but there is certainly the potential for a lack of adequate detection. For the current example, the vibration sensors in the MWD appear to slightly detect the resonant behavior of the system. Looking back at Figure 4.33, between markers 3 and 4, the rotation speed at the surface (red trace in the second data track) is held constant at 80 RPM; this is nearly the value of the lowest critical RPM estimated in Figure 4.35. This portion of the data plot also indicates the onset of high, erratic, lateral vibrations, with the average values (green trace in data track 3) hovering around 4 gs RMS and the peak values (black trace in data track 3) reaching 16.5 gs. These magnitudes are not particularly troublesome for the MWD itself, but could have been an early indication that higher vibration levels were being seen below the measurement point at the motor.

It is interesting to note that the vibration levels do not appear to decrease as the rotation speed is increased passed the lowest critical value; this may be counter-intuitive when thinking about general resonance behavior in which increasing the excitation frequency past a resonant value typically reduces the response of the system [142]. However, it has been observed through previous numerical studies [14] that if a resonant rotation speed induces whirl in the drillstring, which then induces intermittent contact or backward whirl, further increasing the rotation speed will either sustain the vibration level or make it more severe. Due to the nature of how steerable mud motors interact with the wellbore (the bowing of the power section discussed previously), the possibility of this type of intermittent-contact/backward-whirl behavior seems likely, especially under resonant conditions. This induced whirling behavior can more easily be understood by Figure 4.36 and Figure 4.37. Figure 4.36 shows the same Marcellus BHA in an idealized (straight) wellbore, at a TFO of 0° . In this configuration the bend is shown to induce a bowing behavior of the section of the motor behind the bend, which subsequently separates this section of the motor from the wellbore wall. As the motor is rotated, and the TFO moves from 0° to 180° (Figure 4.37), the deflection of the motor changes substantially and the upper section of the motor is now bowing in the opposite direction. This “reverse bowing” inherently induces a whirling behavior of the motor as it is rotated during normal operation, which would likely generate intermittent contact or full backward whirl at a resonant frequency. From this understanding, the data presented in Figure 4.33 certainly suggests that the model is predicting the appropriate resonant characteristics of the system, however this cannot be validated from only one example. It can be noted that after these results were discussed with the operator, they agreed to reduce their off-bottom rotation speeds and keep them below the values predicated from the modeling. This resulted in an overall improvement in tool reliability. Before the BHA study the operator had 14 failures out of 35 wells; and after rotations speeds were reduced as a result of the critical RPM analysis, that failure rate had shrunk to 2 failures out of 28 wells. Of the two failures reported, neither was related to vibration issues; one was associated with the electronics in the MWD system, and the other was a faulty rubber lining within the motor.

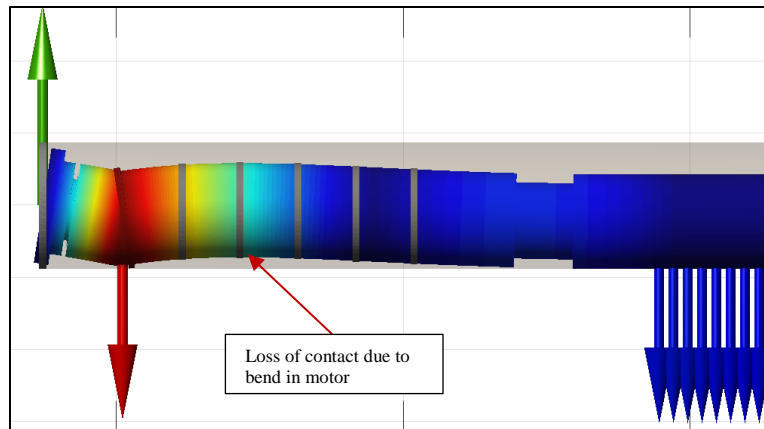


Figure 4.36: Marcellus BHA in a Perfectly Straight, Horizontal Well at a TFO of 0°

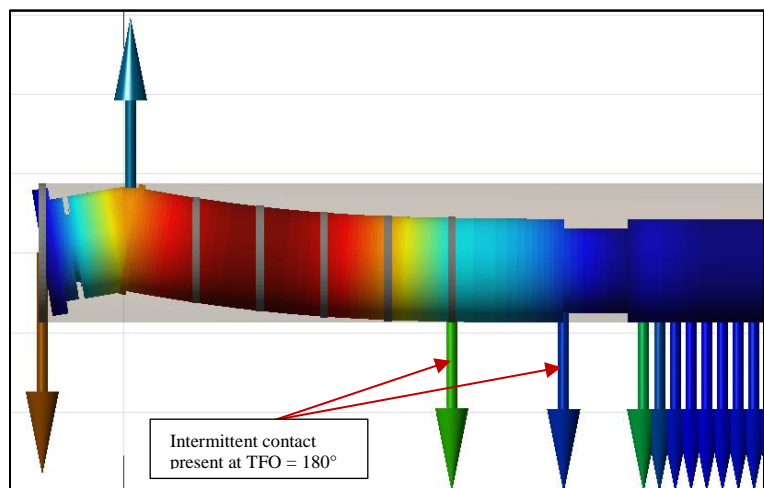


Figure 4.37: Marcellus BHA in a Perfectly Straight Horizontal Well at a TFO of 180°

The second case study is from a horizontal well drilled in the Eagle Ford shale play in south Texas. The situation was very similar to the previous run in the Marcellus; the field personnel were reporting unexplained damages to the motor. Examination of the field data (Figure 4.38) showed the familiar trend of high vibration levels occurring while rotating off-bottom, with average values reaching 10 gs RMS and peak values showing a maximum of about 35 gs. A similar BHA analysis was performed with the drilling assembly used for that particular run (Table 4.9), and the static deflection (Figure 4.39) and lowest four critical RPM values (Figure 4.40) were determined. Just as before, the lowest critical rotation speed (93 RPM) is associated with the top of the motor and the lower portion of the MWD collar. Based on this calculation, the rotation speed being used during back-reaming operations (100 RPM) was certainly in excess of the lowest critical rotation speed of the BHA (93 RPM) and, as discussed earlier, simply exceeding the lowest critical RPM will not always result in lower vibrations levels and may actually be making matters

worse, especially when considering the dynamic behavior of steerable mud motors. The analysis for that particular well was presented to the operator and it was agreed to reduce the off-bottom rotation speed to 80 RPM in future wells, which was sufficiently below the lowest critical speed of 93 RPM.

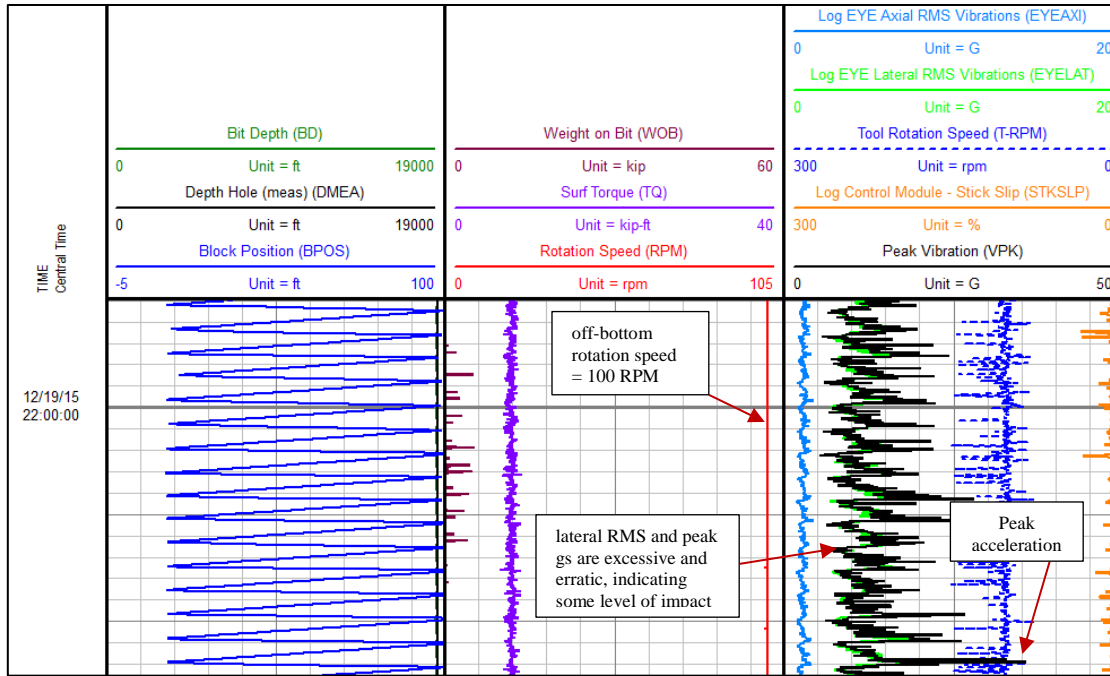


Figure 4.38: Surface Parameters and MWD Vibration Data for Eagle Ford Well 1, while Back-Reaming near TD

Table 4.9: Lateral BHA, Eagle Ford Well

Sec No.	Component Description	OD (in)	ID (in)	L (ft)
1	8 3/4" Bit	8.750	-	0.83
2	SDI 7" Titan 22 (5/6-10.8), 2.12° Bend, 8 1/4" Near-bit-stabilizer	6.465	variable	35.71
3	Cross Over Sub	6.875	2.875	2.65
4	MWD Collar	6.563	3.625	28.85
5	MWD Pulser Sub	6.875	3.500	6.14
6	Non-Mag Crossover Sub	6.750	3.563	2.69
7	Non-Mag "Flex" Collar	6.500	3.250	30.05
8	Filter Sub	6.500	3.250	3.17
9	Crossover Sub	7.000	3.313	4.13
10	5 1/2" Drill Pipe (HT55 conn, 21.9 ppf) (x2)	5.500	4.778	63.00

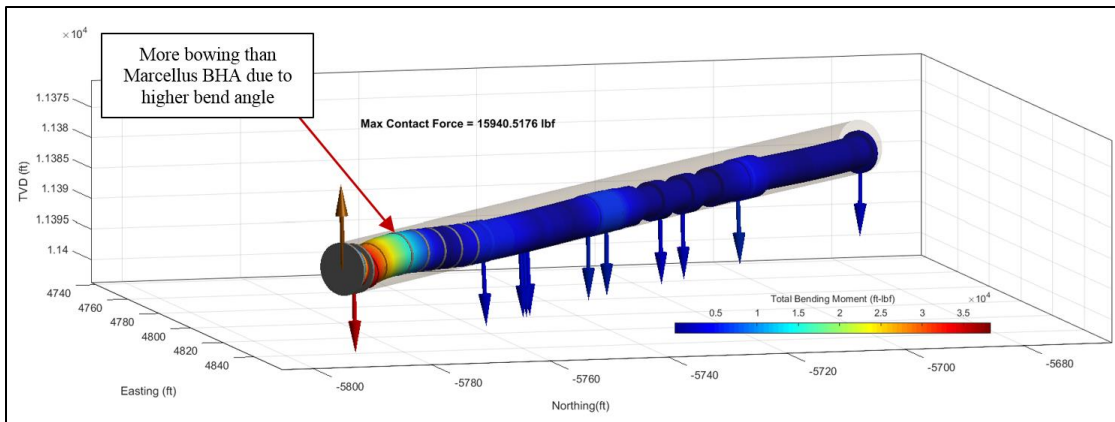


Figure 4.39: Static Deflection of BHA in Eagle Ford Well 1 at TD

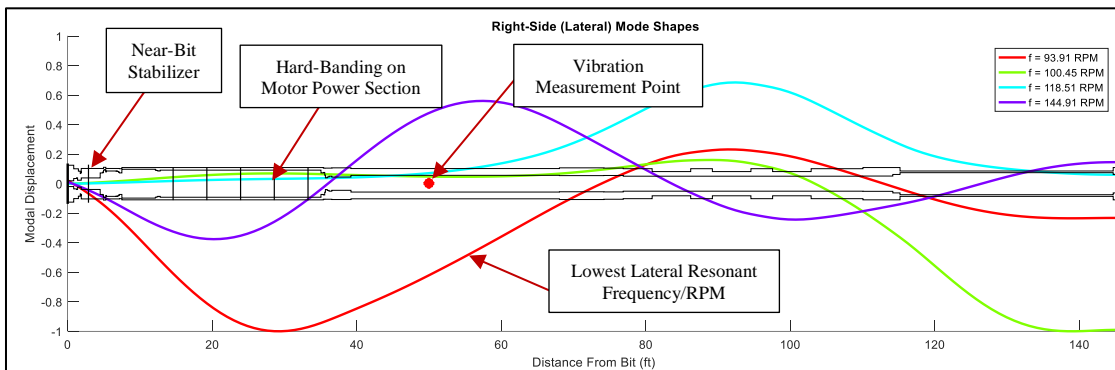


Figure 4.40: Critical RPM Analysis of BHA in Eagle Ford Well 1 at TD

With the recommended practice of maintaining the off-bottom rotation speed to a maximum of 80 RPM, using the same BHA configuration, data from the next well (Figure 4.41) revealed a significant reduction in the lateral vibration levels, with average values of 4 gs RMS and peak values ranging between 15 and 20 gs. It was also noted by field personnel that tools quit coming out of the hole damaged after the reduced rotation speeds were established. This improvement certainly suggests that the situation was related to the resonant frequencies predicted by the developed model. However, as discussed previously, these case studies cannot be considered concrete evidence that the model is accurate. This is primarily due to the fact that the whirling behavior of the motor may be making it difficult to identify a resonant vibration peak in the data. While these cases provide initial confidence in the model, it would be worthwhile to explore dedicated tests with straight BHA assemblies that wouldn't necessarily induce whirl at a resonant frequency in a horizontal wellbore.

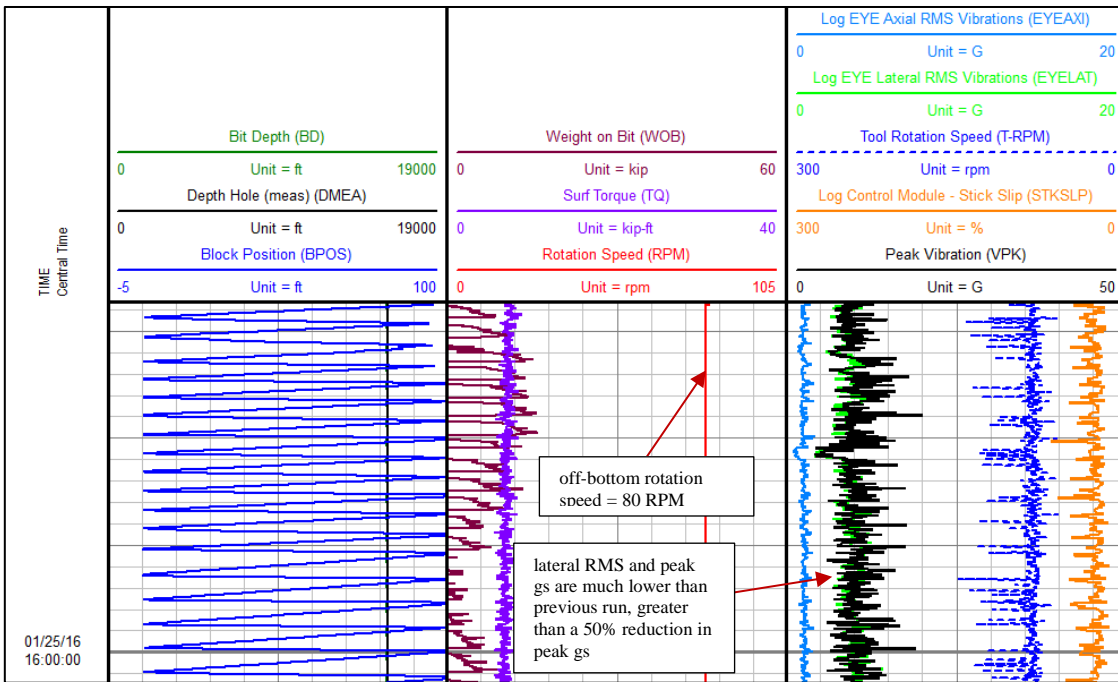


Figure 4.41: Surface Parameters and MWD Vibration Data for Eagle Ford Well 2, while Backreaming near TD

4.5 Summary of Numerical Validation and Comparative Analysis

While the results of this section have explicitly shown that the inclusion of shear deformations, lateral rotary inertias, and gyroscopic effects within drillstring models yield different results, the change in solution is negligible within the operating range of modern drillstrings and BHAs in horizontal wellbores. From a practical standpoint this means that these beam characteristics can safely be ignored which, in turn, results in simplified equations that require less computation time to solve. Additionally, the results have shown that the developed mathematics and coding algorithms produce theoretically accurate and reliable results. This is a required attribute of any numerical modeling that is to be used in practical, real-world, applications. An initial validation study, based on field data, has also been presented which provides further evidence that the model is a robust tool that can be used in a practical manner. Furthermore, this validation is supported by the fact that the present model (MADSim) shows remarkable agreement to Heisig's original model, which has been tested and validated on multiple occasions [102-105].

5. A LINEARIZED APPROACH TO INDUCED LATERAL VIBRATIONS

The idea of instigating vibrations in the drillstring, in order to reduce the effects of static friction, stems from the understanding of the frictional behavior between the drillstring and the wellbore wall. Referring back to (2.70) – (2.72), as well as the discussion in Section 1, a relationship between frictional forces and drillstring velocity is known to exist. Thus, if the rotational velocity of the drillstring is increased, the axial drag effects of friction are reduced, which is an observable behavior when rotating the drillstring in the field. However, during modern drilling operations, the drillstring is not always being rotated. With the advent of steerable mud motors, it is possible to drill ahead with a “stationary” drillstring. During this “sliding” operation, the bit continues to rotate as long as there is adequate fluid flow through the down-hole mud motor. This gives the directional driller the ability to steer the BHA in a desired direction. Unfortunately, during these course-correction operations, the axial drag along the drillstring is increased due to the lack of rotational drillstring velocity and thus it is more challenging to maintain adequate WOB. Lower WOB inevitably leads to lower ROP which means that, in long lateral wellbore sections, there will be a limit to how far the drillstring can be pushed in a horizontal direction while sliding. Once this limit is reached, the trajectory of the well can no longer be controlled because no axial force can be supplied to the bit during slide-drilling operations.

In order to increase the axial force transfer during these sliding operations, it is proposed to induce lateral vibrations in sections of the drill pipe that are in contact with the wellbore wall. Induced lateral vibration in a stationary drillstring should gently rock the drill pipe back and forth, thus generating an oscillating rotational velocity. The resulting rotation should not only decrease the overall friction coefficient, as was shown via equation (2.72), but should also change the direction in which the friction is acting and reduce the effective axial friction according to equation (2.71); at least this is the current understanding of how these tools function. The scenario in which these induced vibrations would be beneficial can be visualized in Figure 5.1, where roughly 730 ft of drillstring is shown in a perfectly straight, horizontal, wellbore. The colored arrows represent the magnitude and direction of the contact forces, with red being a maximum and blue being a minimum. The color of the tubular components indicates the magnitude of the bending moment along the length of the drillstring. This configuration is representative of slide-drilling with a steerable mud motor. The motor, and other BHA components, are seen on the left side of the figure, followed by several joints of 4 ½” drill pipe. The induced lateral vibrations are generated via the lateral excitation tool (LET), seen in the middle of the drill pipe in Figure 5.1. It is intended to induce a lateral resonant behavior in the drillstring in order to generate larger lateral displacements, and thus a greater increase in axial force transfer along the wellbore.

Wilson and Heisig [47] performed an initial assessment of LETs and presented a method of introducing these lateral vibrations down-hole. Their technique relies on rotating an eccentric mass within a metal housing. The rotation rate of the mass is controlled directly through the flow rate via a mud motor power section, which is essentially a progressive cavity pump that works in reverse. Additionally, they offered two different mass eccentricity configurations: an “in-phase” excitation in which the eccentric mass component is oriented in one direction along its length, and an “out-of-phase” excitation where two eccentric masses would be mounted 180° circumferentially offset from one another. Linearized, forced-frequency, modeling of the two configurations showed that doing this did have a significant impact on the effective resonant frequency. As such, it was suggested that the eccentric mass configuration could be changed, based on flow rate limitations, in order to assure that a lateral resonance could be achieved. However, from a design perspective, implementing off-set eccentric masses is not all that practical. Therefore, the primary focus of the present analysis will be on the “in-phase” excitation; Figure 5.2 and Figure 5.3 help to illustrate this configuration.

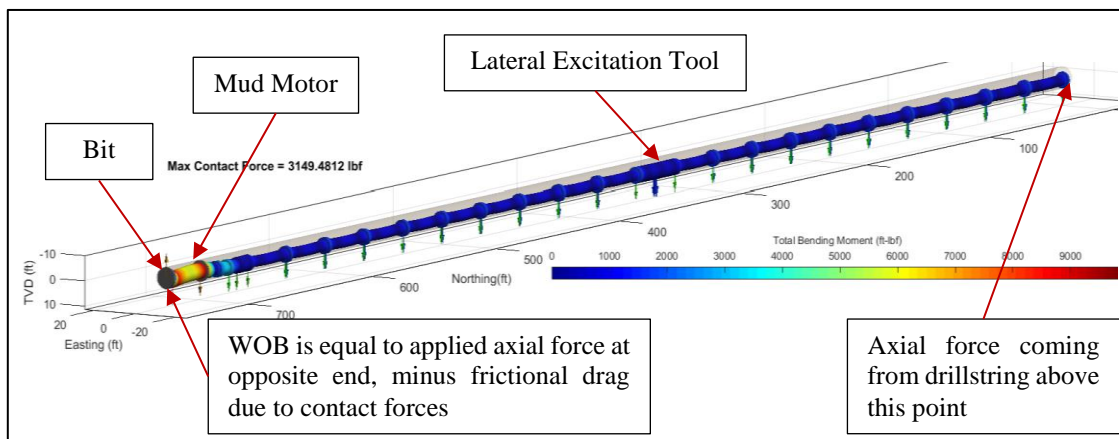


Figure 5.1: 3D Mechanics Plot of Drilling Assembly in a Perfectly Straight, Horizontal Wellbore
(Diameters are not Drawn to Scale)

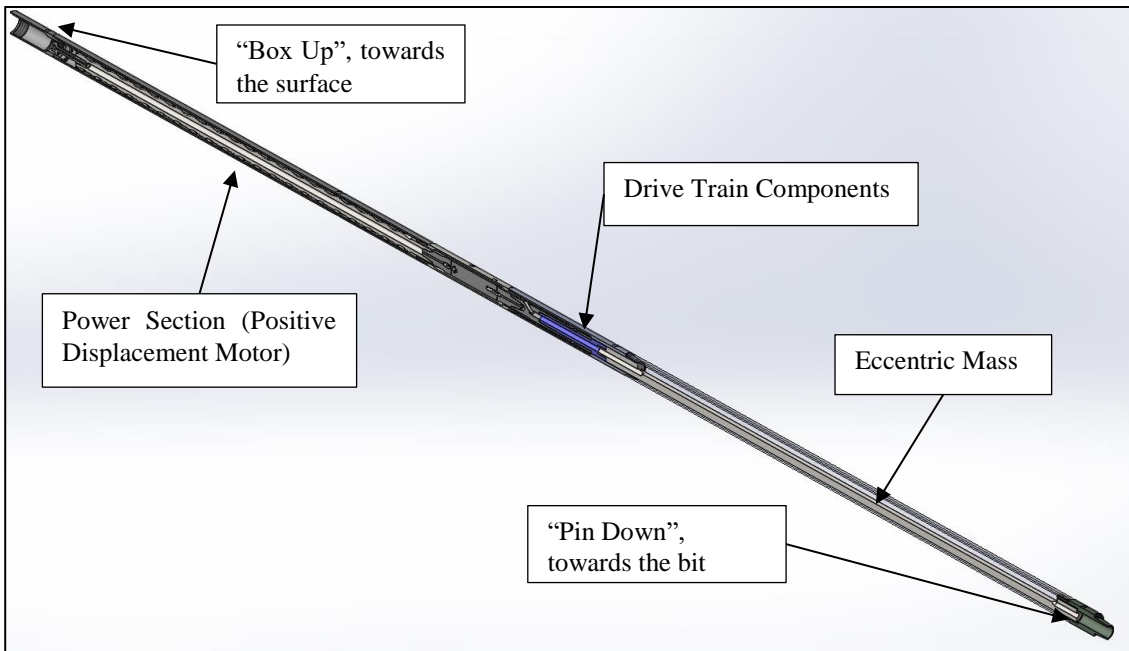


Figure 5.2: Mechanical Layout of the LET (Courtesy of Scientific Drilling International, Inc.)

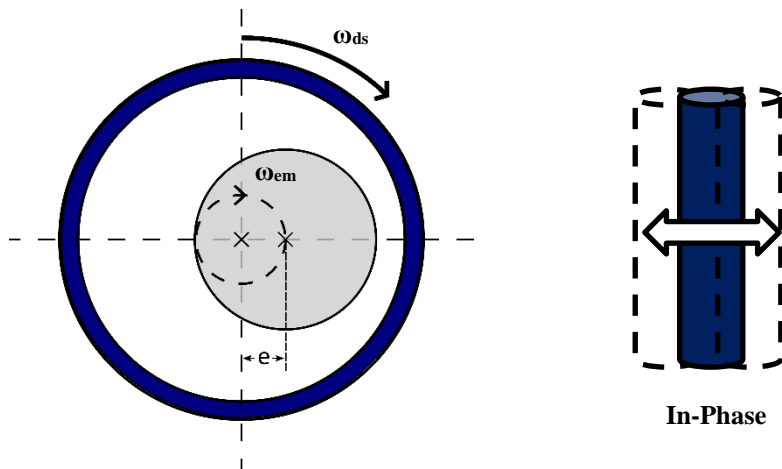


Figure 5.3: Internal Excitation Mechanism of the LET (slightly modified from [47])

Figure 5.2 shows a cut-away view of the LET; the device consists of a power section, a drive-train, and the rotating eccentric mass; it is a relatively simple design which makes it easy to assembly, break-down, and repair. Figure 5.3, which is not drawn to scale, illustrates the functionality of the eccentric mass component within the tool. The mass, which has a known linear distribution (m_{ecc}), is offset by a known eccentricity value (e) and will rotate at a known speed (ω_{em}) that is directly proportional to the volumetric flow rate

through the tool. Therefore, the resulting centripetal (lateral) force can be calculated via the following equations.

$$F_1 = F_o \sin((\omega_{em} + \omega_{ds})t) \quad (5.1)$$

$$F_2 = -F_o \cos((\omega_{em} + \omega_{ds})t) \quad (5.2)$$

$$F_o = m_{ecc}e(\omega_{em} + \omega_{ds})^2 \quad (5.3)$$

It is clear from (5.1) – (5.3) that the rotation speed of the drillstring (ω_{ds}) will alter the effective excitation frequency, however when slide-drilling the rotation speed of the drillstring will be zero and will not have an effect. The rotation speed of the eccentric mass can be determined using the following relationship.

$$\omega_{em} = \frac{2\pi}{60}(rpg)GPM \quad (5.4)$$

Where the output speed of the tool, rev-per-gallon (rpg), should be known based on the power section being used to drive the tool. Because the LET produces an “in-phase” excitation, these forces will be oriented in the same circumferential direction along the length of the eccentric mass.

Of course, as mentioned previously, for the lateral vibrations to be effective in reducing axial drag, the tool needs to induce movement across several contact points; not just the localized region around the tool. Due to the nature of lateral vibrations, namely the fact that transverse waves are heavily damped by wellbore contact and fluid interactions [12, 122], it is crucial to excite these tools at a resonant frequency in order to generate movement over a large span of drill pipe. The first step in being able to do this is developing a way to reliably predict the resonant frequency of the assembly. The drillstring model that has been developed through the previous sections is ideally suited to handle this type of problem.

5.1 Free Vibration

A free vibration analysis is the appropriate starting point for examining the dynamics of the system. Because it is planned to excite the drillstring at a resonant frequency when using an LET, the goal is to determine the lowest resonant frequency of the drill pipe assembly. The lowest resonant frequency, or fundamental frequency, is thought to result in the highest amplitude of vibration which, in turn, would result in the greatest effect on the drillstring. This thinking is based on the fact that higher modes tend to be damped-out to a greater extent than lower modes, but ultimately the amplitude of vibration will be dictated by the magnitude of the excitation source and damping present in the system. Specific damping considerations are explored in a forced-frequency analysis or a nonlinear time-domain simulation, which are shown in later sections. The free-vibration approach can only estimate the value of the natural frequency; it cannot predict the

response amplitude. However, the natural frequencies are predictors of large-amplitude vibration “zones” and therefore are a useful starting point. The assembly being investigated here is outlined in Table 5.1, with the operational parameters specified in Table 5.2. It should be noted that the linear weight (ppf) of the drill pipe listed in the table is a nominal value; the actual linear weight will depend on the specific connection dimensions.

Table 5.1: Assembly for LET Analysis

<i>Sec No.</i>	<i>Component Description</i>	<i>OD (in)</i>	<i>ID (in)</i>	<i>L (ft)</i>
1	8 3/4" PDC Bit	8.750	-	0.83
2	Mud Motor (Bend Angle = 1.75°) Bend @ 4.83 ft from face of the bit	6.500 -	Variable -	24.00 -
3	1/4" Under-gauge Stabilizer	6.500	3.250	5.00
4	MWD “Flex” Collar Body OD = 5", Wear Knot OD = 6.5"	6.500 5.000	2.875 2.875	30.00 -
5	MWD Pulser Sub	6.500	3.250	5.00
6	10 joints of 4 1/2" DP (S-135, 20 ppf, NC50/IF) Tool Joint	4.500 6.625	3.640 3.500	315.00 -
7	Lateral Excitation Tool (LET)	6.500	Variable	30.37
8	10 joints of 4 1/2" DP (S-135, 20 ppf, NC50/IF) Tool Joint	4.500 6.625	3.640 3.500	315.00 -

Table 5.2: Operational Parameters for LET Analysis

<i>Parameter</i>	<i>Value</i>
<i>WOB (klbf)</i>	20
<i>TOB (ft-lbf)</i>	2500
<i>MW (ppg)</i>	11
<i>Hole Size (in)</i>	8.75
<i>E (psi)</i>	30000000
<i>v</i>	0.3

The boundary conditions applied to the model are considered to be the same as they were for the free vibration analysis in Section 4, and the drillstring is segmented into 447 elements. For the free vibration response, and all linearized-dynamic computations contained within this section, the friction is set to zero. Following the methodology of Section 3.3.2.1, the linearized natural frequencies of the system are estimated, along with their respective mode shapes, for the lowest 28 modes. The values of these frequencies are provided in Table 5.3, with their corresponding mode shapes listed Appendix D. Examination of the mode

shapes reveals that the lowest modes are associated with the sections of drill pipe between the tool joints. These “pipe-body” cross-sections are unsupported by the wellbore and, as a result, are prone to vibration at lower frequencies. In the context of the current analysis, these modes are not particularly useful since the goal is to induce motion at the contact points along the drillstring. Inducing motion at the contact points correlates to modes that suggest a dynamic displacement at the tool joints. With this idea in mind, the mode shapes can more closely be examined to determine at what frequency there could potentially be larger lateral movement at the contact points. In the author’s opinion, based only on the free vibration analysis (Appendix D), the lowest resonant frequency that should be excited using the LET would be around 1.6188 Hz. This is the 12th lowest linearized natural frequency of the system and its mode shape shows a vibrational pattern that suggests lateral motion of the tool joints. However, an operational recommendation for induced vibrations while drilling, based solely on a free vibration analysis, would be misguided.

Table 5.3: Linearized Lateral Natural Frequencies of the Drillstring

<i>Mode Number</i>	<i>Linearized Natural Frequency</i>	<i>Mode Number</i>	<i>Linearized Natural Frequency</i>
1	0.9021	15	1.7467
2	0.9053	16	1.7708
3	1.0329	17	1.7914
4	1.0431	18	1.8065
5	1.1910	19	1.8131
6	1.2086	20	1.8250
7	1.3438	21	1.8981
8	1.3670	22	2.1935
9	1.4779	23	2.3172
10	1.5049	24	2.7329
11	1.5898	25	2.7626
12	1.6188	26	2.8233
13	1.6795	27	2.9103
14	1.7077	28	3.0113

As explained by Ginsberg [142], when performing modal analysis, a system’s physical response will be inter-dependent upon three things: the degree to which the excitation force is proportional to a particular mode shape, how close the excitation frequency is to a natural frequency, and the relative contribution from each mode. In more relatable terms this means that the drillstring’s lateral dynamic response will be dictated by how much the excitation force resembles a particular mode shape, how precise a rig crew can operate an

LET at a specified frequency, and how large certain modes are in relation to one another. The first of these considerations can be understood by thinking about how the LET would generate vibrations. The tool itself rotates a long eccentric mass, which produces a revolving centripetal force over a span of about 10 feet. Because this excitation only spans a relatively short section of the drillstring, and the force is always oriented in the same direction, a proportional mode shape would be one that has a lobe, or peak, over the span of the eccentric mass while remaining relatively flat along the rest of the assembly. It can be noticed that the 21st mode (Appendix D) of this assembly has a strong similarity to this hypothetical mode pattern representing the excitation source. Based on that observation one could argue that 1.8981 Hz would be the optimum frequency in which to excite the drillstring. However, it is also apparent that the 21st mode only spans approximately 175 feet of the drillstring, which may be less than ideal when trying to increase the axial force transfer over a large section of drillstring.

So, from free vibration analysis and an understanding of how the drillstring is to be excited, two possible choices of excitation frequencies exist (1.62 Hz and 1.90 Hz), but again it is difficult to say which one would be more appropriate. To help pin-point the “optimum” frequency of the LET, Equation (4.4) can be utilized. Recall that this equation was derived for the purpose of estimating the lowest natural frequency of drill pipe lying on the low-side of a horizontal wellbore. A major assumption with this equation is that continuous contact exist between the drill pipe and the wellbore wall, i.e. there are no tool joints that provide periodic support along the length of the drillstring. Therefore, as shown by Wilson and Heisig [47], it would not be expected that this formula would predict the lower modes associated with the drill pipe body supported between the tool joints (Table 5.3 and Appendix D), but could provide insight into the lowest frequency that would result in lateral movement of the contact points. Using this equation, the lowest natural frequency of the drill pipe is anticipated to be 1.9032 Hz. Obviously this is closer to the 21st mode in Table 5.3, which suggests that this would be the more appropriate excitation frequency. However, the amplitude of the vibration is still unknown and 1.9 Hz is only a “best estimate”, albeit it is better than blindly exciting the drillstring at a random frequency. In order for these types of tools to be successfully deployed for practical operations, there needs to be greater confidence on what this excitation frequency should be as well as what the relative dynamic response will be between different modes. Additionally, from this brief review of the results, it is quite apparent that selecting an appropriate operational frequency based solely on the linearized natural frequencies and mode shapes can be quite cumbersome; not an ideal situations for an engineer trying to make these decisions “on-the-fly”. A forced-frequency approach can help to simplify this analysis process as well as increase the objectivity of the results.

5.2 Forced Vibration

Forced-frequency analysis (Section 3.3.2.2) allows for the estimation of the linearized-dynamic response of a system that is subjected to a specified harmonic excitation. Therefore instead of combing through mode shape plots and trying to find one that seems like it would be the most appropriate frequency in which to excite the drillstring, which was shown to be a rather subjective process in the previous section, the excitation from the LET is applied directly to the system and the resulting steady-state response is calculated. This helps to make the analysis more objective and provide a clearer understanding of how the drillstring will behave when subjected to induced lateral vibrations.

The key concept to keep in mind when performing these types of analyses is the process of linearization. In the context of nonlinear finite element modeling of drillstrings, “linearized” refers to small displacements about an equilibrium position. Essentially, for a forced-frequency analysis, this means that the solutions can only predict the vibrational behavior that occurs about the static equilibrium position (Section 3.3.1 and Figure 5.1). Therefore, by its very nature, linearized-dynamic analysis cannot predict if, or when, contact points between the drillstring and the wellbore wall will separate and lead to impact dynamics. Consequently, this also means that any displacements, velocities, or accelerations calculated should be interpreted carefully as these values would likely not represent exact magnitudes of down-hole dynamics, but rather relative severity between different configurations, excitations, or frequencies.

Implementing the LET excitation into the forced-frequency equations is a relatively straight forward process. Because the excitation source is a rotating eccentric mass it is, by default, a harmonic excitation source. Therefore, the centripetal force of the revolving eccentric mass can be inserted directly into the right-hand side of (3.55) for each element in the model containing the eccentric mass. The elemental force vectors due to this lateral excitation, are expressed by (5.5) and (5.6).

$$\underline{F}_{exc\sin} = F_o \left(\frac{l}{2}, \frac{l^2}{12}, 0, 0, 0, 0, \frac{l}{2}, \frac{-l^2}{12}, 0, 0, 0, 0 \right)^T \quad (5.5)$$

$$\underline{F}_{exc\cos} = F_o \left(0, 0, \frac{-l}{2}, \frac{-l^2}{12}, 0, 0, 0, 0, \frac{-l}{2}, \frac{l^2}{12}, 0, 0 \right)^T \quad (5.6)$$

Here l is the length of the element, the $l/2$ terms represent the lateral force of the rotating eccentric mass, and the $l^2/12$ terms represent the induced bending moment due to the lateral force being distributed over the length of the element. It must also be kept in mind that the wellbore section being investigated will not always be of a constant inclination and could contain variations in the tool face angle (see Appendix A) along the length of the tool; this is the same thinking that required the transformation of (3.47). In order to accommodate a realistic well path, the following transformation should be applied to each elemental

excitation force vector, (5.5) and (5.6), before they are assembled into the global forced-frequency equations (3.55).

$$\underline{\underline{T}}_{\gamma} = \begin{bmatrix} \cos(\gamma) & 0 & -\sin(\gamma) & 0 & 0 & 0 \\ 0 & \cos(\gamma) & 0 & -\sin(\gamma) & 0 & 0 \\ \sin(\gamma) & 0 & \cos(\gamma) & 0 & 0 & 0 \\ 0 & \sin(\gamma) & 0 & \cos(\gamma) & 0 & 0 \\ 0 & 0 & 0 & 0 & 1 & 0 \\ 0 & 0 & 0 & 0 & 0 & 1 \end{bmatrix} \quad (5.7)$$

$$\underline{F}_{exe_corrected} = \begin{bmatrix} \underline{\underline{T}}_{\gamma}^A & \underline{0} \\ \underline{0} & \underline{\underline{T}}_{\gamma}^B \end{bmatrix} \underline{F}_{exe} \quad (5.8)$$

Where γ is the tool face angle of one node of an element, and A or B refers to the first or second node of an element.

Additionally, the power section that drives the eccentric mass will also generate a lateral excitation. The resulting forces from the rotor within the power section are quite similar to those of the rotating eccentric mass, with the primary difference being the “effective excitation frequency”. Since the rotor whirls within the stator in the opposite direction as the string rotation (see Section 1), the rotation speed of the drillstring actually decreases the excitation frequency from the power section. This can be shown through equations (5.9)-(5.11).

$$F_{1rot} = -F_{o_{rot}} \cos((\omega_{rot} - \omega_{ds})t) \quad (5.9)$$

$$F_{2rot} = -F_{o_{rot}} \sin((\omega_{rot} - \omega_{ds})t) \quad (5.10)$$

$$F_{o_{rot}} = m_{rot} e (\omega_{rot} - \omega_{ds})^2 \quad (5.11)$$

The rotation speed of the rotor (ω_{rot}) can be determined by multiplying the output speed of the power section, (5.4), by the number lobes on the rotor. This is shown via (5.12).

$$\omega_{rot} = N_{lobes} \frac{2\pi}{60} (rpg) GPM \quad (5.12)$$

The linearized-dynamic response of the drillstring, due to excitations generated from both the rotating eccentric mass and the LET power section, can be determined individually via separate computations. Due to the linearized nature of the analysis, it would be incorrect to attempt to analyze both of these excitations simultaneously since they operate at different frequencies. However, because the excitation frequency from

both the LET and the mud motor are controlled directly through volumetric flow rate, the solutions obtained from the separate analyses could be superimposed on one another based on a corresponding flow rate. For the sake of clarity, they will be shown as separate analyses here.

5.2.1 Initial Analysis

The equations presented in the previous section can be applied directly to (3.55), in order to solve for the linearized displacements ($\hat{\psi}_c$ and $\hat{\psi}_s$). To present these results in a meaningful way it is beneficial to plot the magnitude of the displacements as a function of excitation frequency and distance from the bit. The magnitude of the linearized-dynamic displacements can be determined via

$$|\underline{\psi}| = \sqrt{\hat{\psi}_c^2 + \hat{\psi}_s^2} \quad (5.13)$$

Applying an eccentricity (e) of 1.05", and a distributed mass (m_{ecc}) of 2 lb_m/in, to the 10 ft of eccentric mass contained within the LET, the lateral response magnitude (5.13) of the drillstring can be plotted as a function of increasing excitation frequency, using frequency steps of 0.1 Hz. This result is shown as a contour plot in Figure 5.4, with excitation frequencies ranging from 0 to 3 Hz (spanning the frequency range predicted via the free-vibration response). It should be noted that this frequency range was chosen because it encompasses the practical frequency range output from the tool. The coloring of the plot indicates the lateral displacement magnitude at a given excitation frequency (x-axis) and distance from the bit (y-axis).

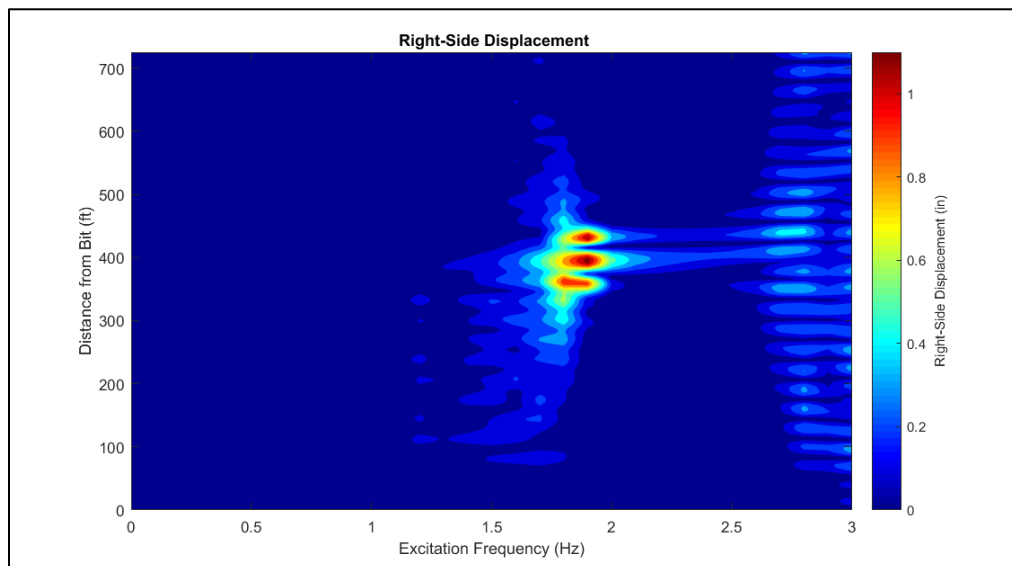


Figure 5.4: Lateral (Right-Side) Forced-Frequency Displacement Response due to the LET Excitation

The primary result from Figure 5.4 is the identification of the “critical frequency”, or the frequency which is likely to induce lateral motion over the largest length of drill pipe. From the figure, a maximum displacement magnitude of 1.16” is seen at an excitation frequency of 1.9 Hz. This is certainly near the natural frequency that was predicted by both the 21st mode of the free vibration analysis, as well as the value predicted by the analytical formula. However, further inspection of the displacement contours in Figure 5.4 suggests that this large response amplitude is only limited to about 110 ft of drill pipe surrounding the LET at 1.9 Hz. This “localized LET resonance” should come as no surprise considering the similarity between the excitation source and the mode shape of the 21st lowest linearized natural frequency. As was discussed in the previous section, the 21st mode (1.8981 Hz) is most similar in shape to the excitation source, thus it would be expected to produce the greatest response to that specific excitation. Additionally, because the shape of the 21st mode has a localized vibration pattern which is isolated to only the drill pipe adjacent to the LET, it would not be expected for the induced lateral vibration to travel very far along the drillstring. This is verified through the forced-frequency analysis shown in Figure 5.4.

Figure 5.5 displays the same contour plot, but with markers indicating the frequency and displacement magnitudes at specific points on the figure. It can be seen that the lateral response of the drillstring is relatively flat until the excitation frequency reaches 1.4 Hz. After which, the response gradually increases in both displacement magnitude and length of the drillstring that is affected by the LET. It is apparent that the frequency that results in displacement over the largest section of drill pipe is 1.8 Hz, with roughly 400 ft of drill pipe being affected. This falls between the two frequencies predicted from the analytical and free-vibration solutions, and would be considered the “optimum” frequency in which to excite the system. It can further be noticed that the BHA (bottom 65 ft of drillstring) is unaffected by the LET at all frequencies, which suggests that the LET can be intentionally positioned far enough away from MWD components in order to avoid any lateral dynamic interference with the measurement tools.

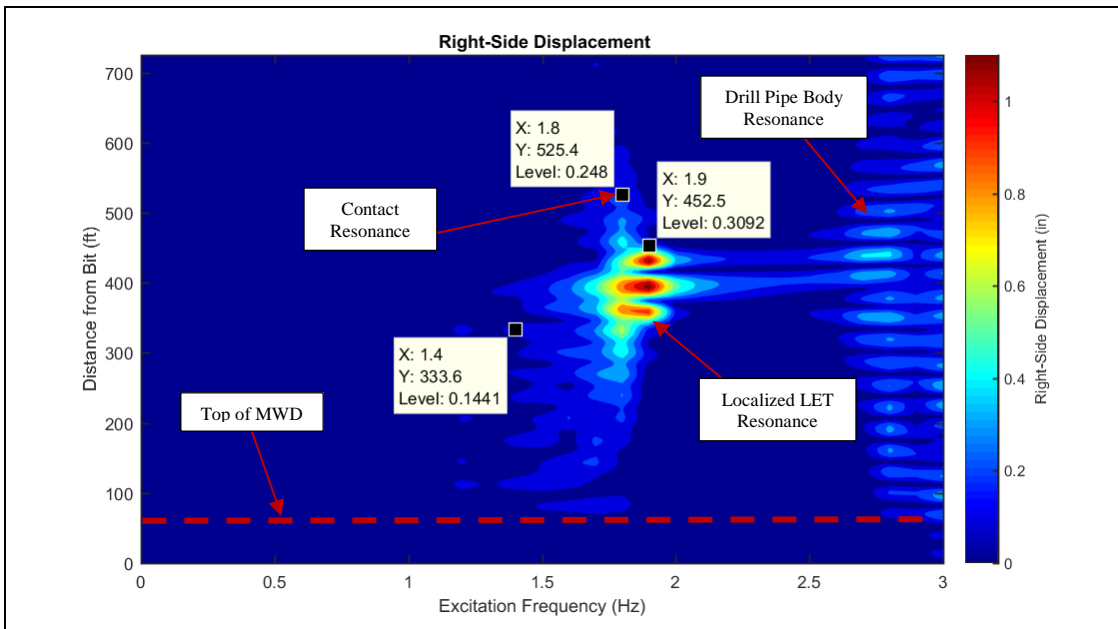


Figure 5.5: Lateral (Right-Side) Forced-Frequency Displacement Response due to LET Excitation, with Frequency Markers

Aside from the “primary resonance” zone, centered at 1.8 Hz in Figure 5.4 and Figure 5.5, an additional frequency range from 2.5Hz to 3 Hz appears to excite a less prominent response throughout the drillstring. However, this “secondary resonance” range is distinctly different from the primary resonant range. The primary resonant zone shows a maximum, or peak, behavior across the two primary axes of the chart; this is illustrated via the gradual change, from blue to red, from left to right across the 1.8 Hz frequency, as well as along the length of the drillstring from top to bottom. This suggests that there is lateral movement along the entire section of drill pipe contained within this peak, including the contact points. Therefore, this type of resonance peak is referred to as a “Contact Resonance”, and is the desired dynamic behavior when using an LET. When examining the secondary resonant zone, it can be noticed that the displacement pattern is periodic in nature, with a magnitude of zero occurring every 31.5 ft above the BHA. Upon further inspection, it is realized that these “troughs” of zero magnitude are associated with the contact points generated between the tool joints of the drill pipe and the wellbore wall. This means that the vibration patterns seen in the 2.5 Hz to 3 Hz range are associated primarily with the drill pipe body supported between tool joints. For this reason, this type of resonant behavior is called a “Pipe-Body Resonance”. Again, keep in mind that this is a linearized representation of a nonlinear system. Thus, even though zero displacement may be indicated at different points along the drillstring in the pipe-body resonance zone, there may still be slight movement of the drillstring at these locations under actual operating conditions. The linearized analysis simply suggests

that the displacement pattern associated with these frequencies is predominantly related to the movement of the pipe-body.

By taking derivatives of (3.54) with respect to time, the magnitudes of the velocities and accelerations along the length of the drillstring can also be determined. These are expressed as

$$|\underline{\dot{\psi}}| = \omega \sqrt{\hat{\psi}_c^2 + \hat{\psi}_s^2} \quad (5.14)$$

$$|\underline{\ddot{\psi}}| = \omega^2 \sqrt{\hat{\psi}_c^2 + \hat{\psi}_s^2} \quad (5.15)$$

Similar to Figure 5.4 and Figure 5.5, contour plots can be generated for these values to more clearly see the dynamic spectrum associated with inducing vibrations with the LET. These velocity and acceleration plots are shown in Figure 5.6 and Figure 5.7. It can be noticed that the dominant response in both plots occurs at the same frequency that it did in the displacement plot (1.8 Hz). This should not be surprising considering the nature of equations (5.14) and (5.15), as well as the relatively low excitation frequencies. The velocity shown in Figure 5.6 is not particularly useful in most applications due to the fact that velocity itself is not a particularly good indicator of potential damage from dynamic events. The more important quantity to investigate is the change in velocity over time, or acceleration, which is usually measured with MWD tools.

A plot of the linearized acceleration can be seen in Figure 5.7. Again, the calculated values are linearized representations of a nonlinear system and, thus, would not be expected to represent exact values that would be seen down-hole. What they do represent, however, is the relative severity of acceleration along the string that would be seen at different frequencies. This plot would not be expected to provide any additional information, apart from what has been determined by the linearized-displacement plot, simply because the frequencies being examined are relatively low. Although, relative low acceleration values are seen, which hints at a very small risk of potentially damaging dynamic behavior. It can be noted that if higher frequencies were of interest then more of a difference would be noticed between the linearized displacement plot and the linearized acceleration plot. This is an important concept to keep in mind if applying this calculation approach to other vibration-related scenarios, such as the case of the excitation generated from the power section within the LET.

As discussed earlier, these LETs are driven by a mud motor power section which generates an additional excitation source. Because a forced-frequency analysis is a linear computation, the response due this excitation cannot be calculated simultaneously with the response from the rotating eccentric mass within the tool. Applying only the excitation forces provided by (5.9) – (5.11) to the static drillstring, the linearized

vibrational response due to the rotor excitation within the LET can be computed. These results are illustrated in Figure 5.8-Figure 5.10.

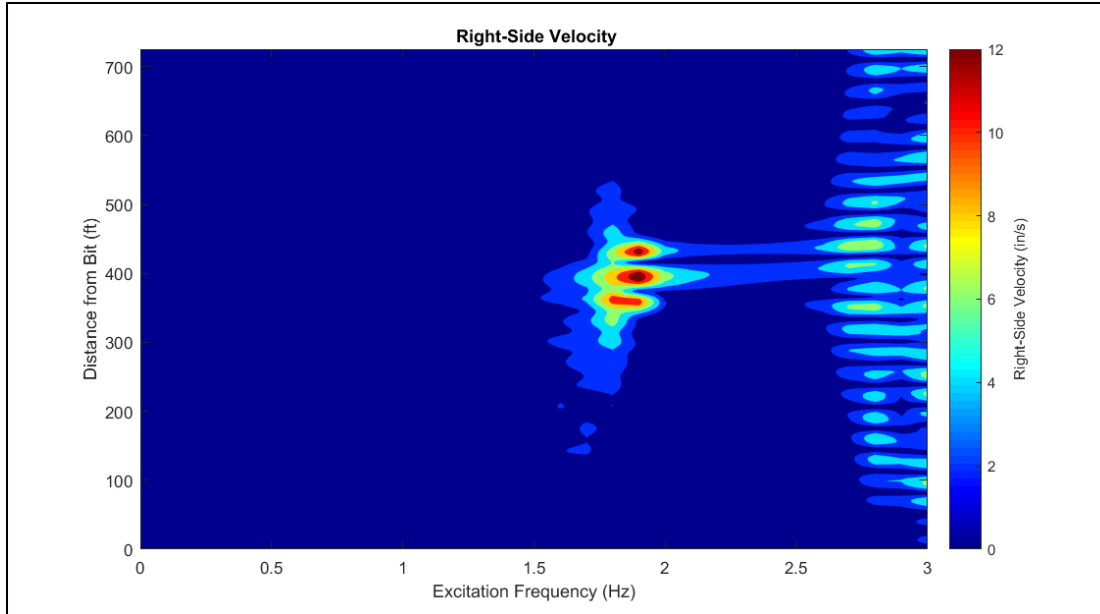


Figure 5.6: Lateral (Right-Side) Forced-Frequency Velocity Response due to LET Excitation

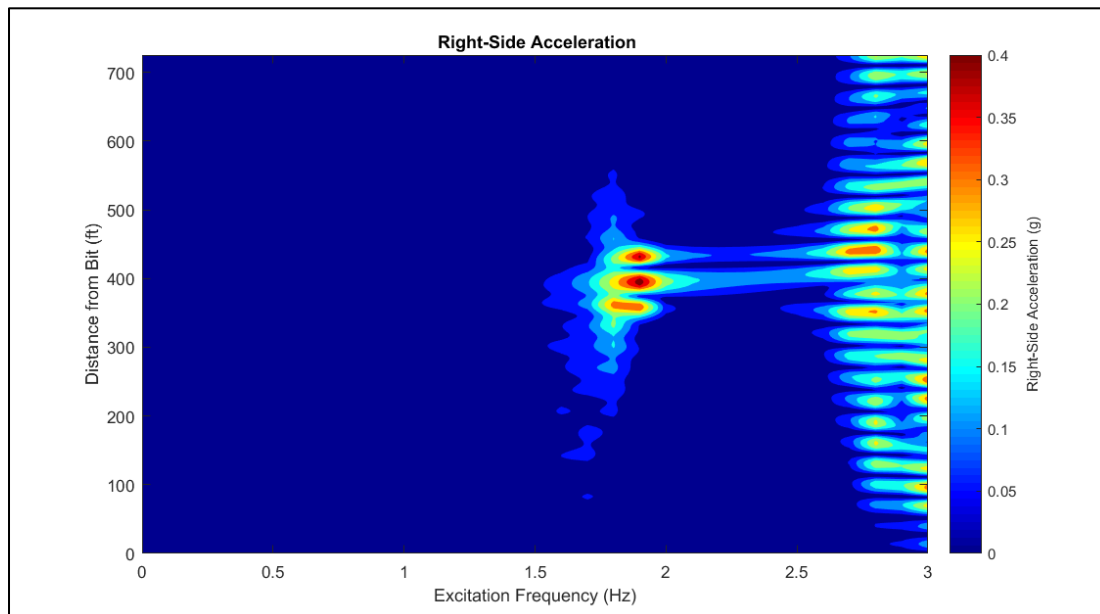


Figure 5.7: Lateral (Right-Side) Forced-Frequency Acceleration Response due to LET Excitation

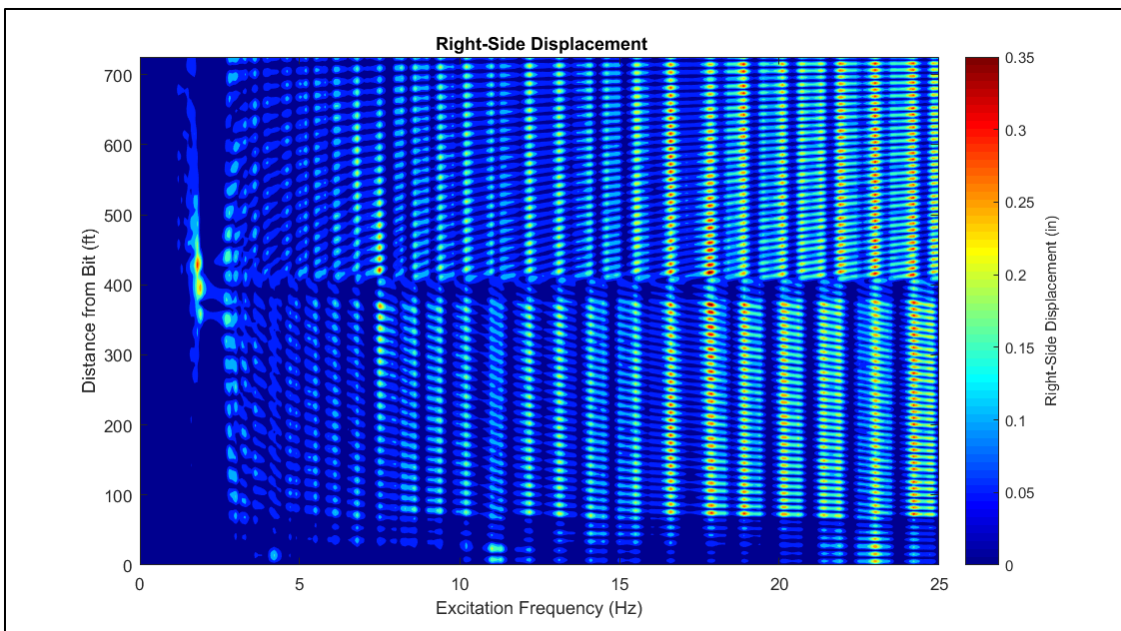


Figure 5.8: Lateral (Right-Side) Forced-Frequency Displacement Response due to LET Rotor Excitation

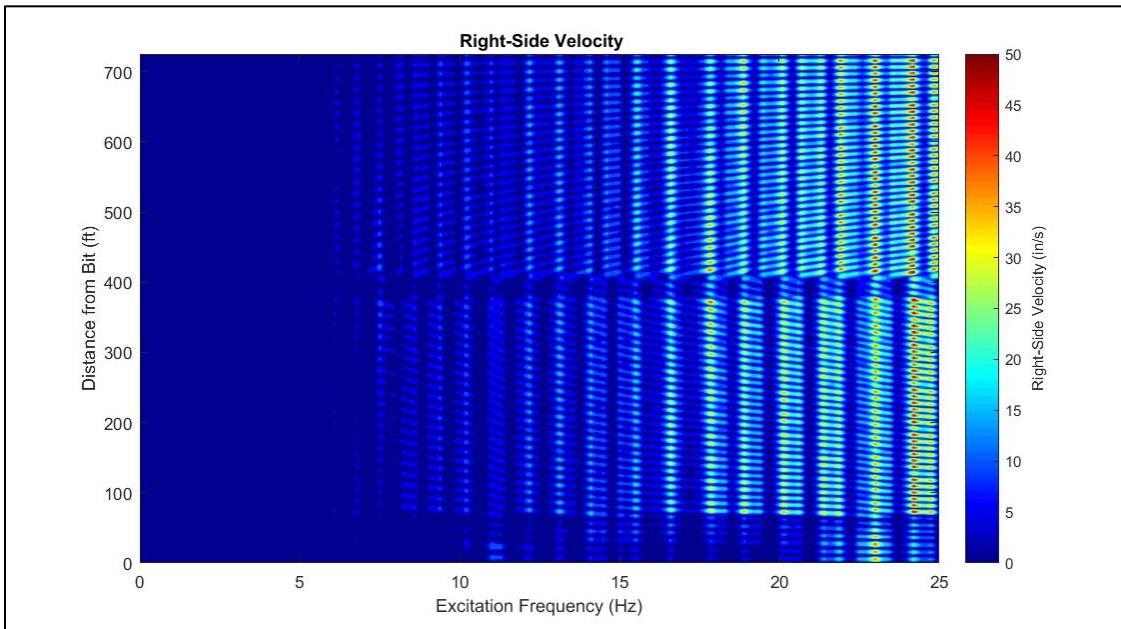


Figure 5.9: Lateral (Right-Side) Forced-Frequency Velocity Response due to LET Rotor Excitation

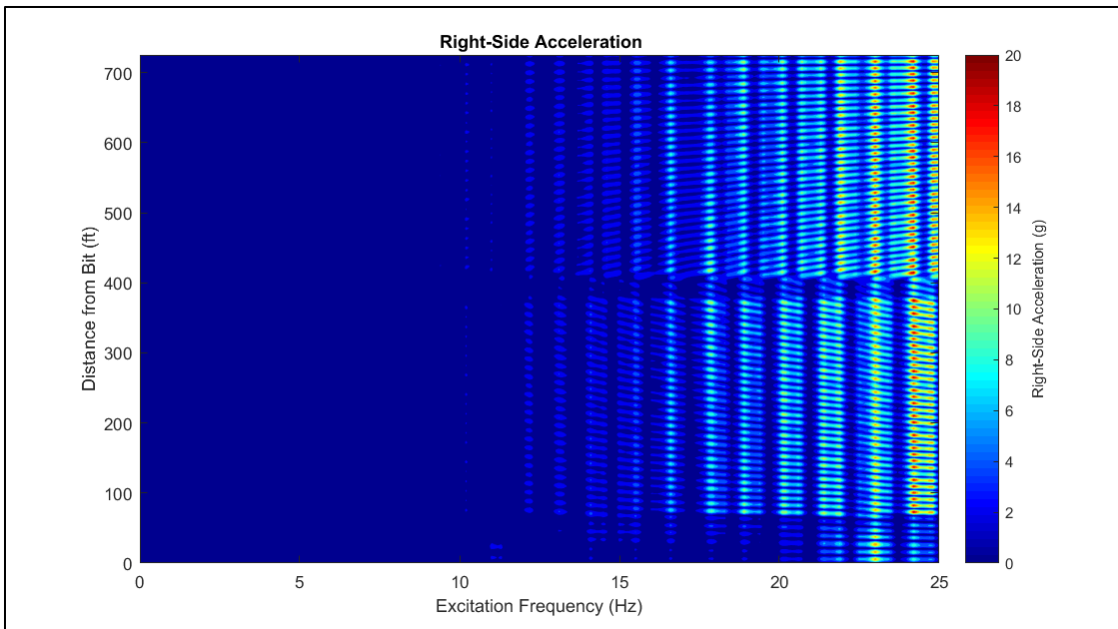


Figure 5.10: Lateral (Right-Side) Forced-Frequency Acceleration Response due to LET Rotor Excitation

It is clear from the contour plots in Figure 5.8–Figure 5.10 that the rotor within the LET will have an effect along the length of the drilling assembly over a broad range of frequencies. Of course, based on (5.12), the specific frequency range output from this excitation source will be dependent on the speed rating of the power section (rpg) and the volumetric flow rate going through the tool. Typical power sections that would be run as part of this LET would likely provide excitation frequencies of between 10 Hz and 15 Hz. Within this frequency range, fairly moderate dynamic responses are seen from the rotor excitation. Again, it should be reiterated that the displacement, velocity, and acceleration values calculated as part of the linearized analysis should not be taken as exact; at best, these calculated values provide a general understanding of the relative response between different points in the drillstring and different excitation frequencies. Therefore, when examining Figure 5.8–Figure 5.10, it would be unwise to state that these would be the expected dynamic magnitudes that would be seen during operation. Instead, the most that these plots indicate is that the lateral excitation from the rotor within the LET may be felt throughout the length of the drillstring. Additionally, these results suggest that the greatest velocity and acceleration responses will occur at the higher end of the frequency spectrum. In terms of optimization, there is little that can be done with regard to minimizing the response due to the rotor excitation. Fortunately, the displacement response due to this excitation is expected to be relatively small in comparison to the eccentric mass component of the LET, and would not be likely to result in significant dynamics loading on the system. It can also be noted, via Figure

5.8, that the higher frequencies appear to only induce a pipe body resonance, while contact resonance seems to only occur at lower frequencies (< 2.5 Hz).

5.2.2 Sensitivity Studies

It should be clear from the previous section that LETs do indeed instigate a noticeable response in the drillstring. However, as with most nonlinear systems, various parameters will alter this behavior and result in a change to this response. For operational purposes it becomes important to understand how these different factors will affect the overall dynamics of the system. Of particular interest are the parameters that can be adjusted in the planning stage of the well, as these could readily be altered in order to achieve a desired outcome based on the specific limitations of the job. The parameters to be investigated are the wellbore diameter, the applied WOB, the density and plastic viscosity of the drilling fluid, the inclination of the well, and the curvature of the wellbore. In comparing the effects of these changing variables, the quantities that are used as a means of assessment are the longitudinal reach of the tool, the “contact resonant frequency”, and the “pipe body resonant frequency”. The longitudinal reach is simply the length of the drillstring that is affected by the operation of the LET at an optimum frequency, while the two resonant frequency terms, as discussed previously, describe frequencies that result in a different displacement response behavior along the drillstring. These comparative values are illustrated in Figure 5.11 for reference.

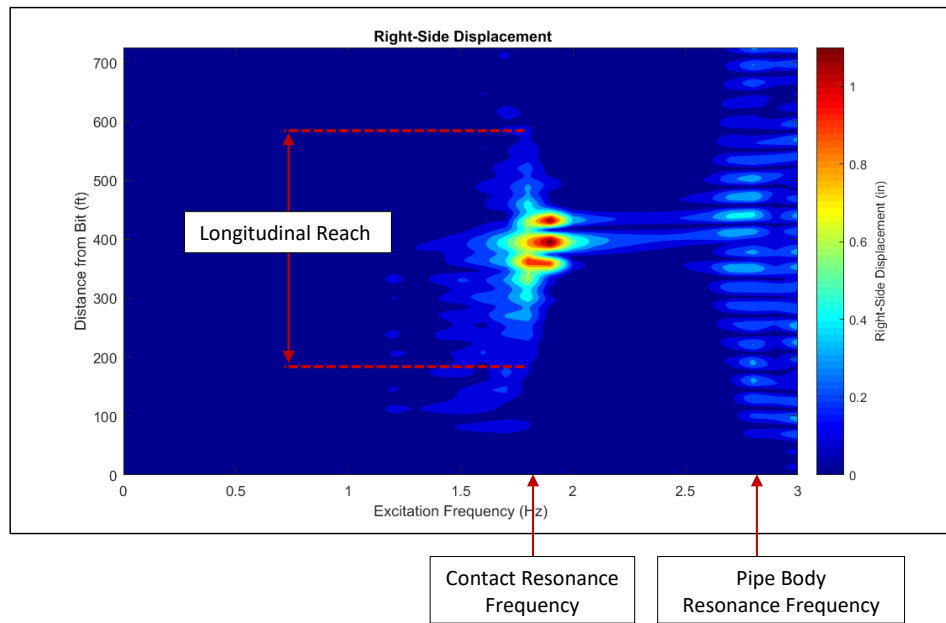


Figure 5.11: Diagram of Quantities used for the Sensitivity Analysis

The maximum response magnitudes of the drillstring's lateral displacement, velocity, and acceleration will also be valuable to look at throughout the comparative analysis, as they indicate the relative severity of response between the different parameter adjustments. Using the assembly in Table 5.1, these response quantities are tabulated in Table 5.4 as a function of the various operational parameters described previously. Again, the boundary conditions and operational parameters (except where indicated) are the same as they were for the free vibration analysis described in Section 4.2 and 5.1. The contour plots generated via the forced-frequency analysis, from which the data in Table 5.4 is generated, are provided in Appendix E.

Table 5.4: Forced Vibration Response Sensitivity Results

Peak Values at Contact Resonance						
	Contact Resonance Frequency (Hz)	Pipe-Body Resonance Frequency (Hz)	Longitudinal Reach (ft)	Displacement (in)	Velocity (in/s)	Accel. (g)
<i>Wellbore Diameter (in)</i>						
7 7/8"	2.1	≥ 3	190	0.78	10.06	0.33
8 1/2"	1.9	2.9	318	0.94	11.20	0.32
8 3/4"	1.8	2.8	412	1.16	13.88	0.43
<i>WOB (klb)</i>						
5	1.8	≥ 3	148	1.43	16.21	0.47
10	1.8	≥ 3	251	1.20	13.51	0.40
15	1.8	2.9	337	1.03	11.64	0.34
<i>Mud Weight (ppg)</i>						
8	2	≥ 3	298	1.54	20.38	0.70
10	1.85	2.9	215	1.27	15.13	0.47
12	1.7	2.7	473	1.19	13.49	0.40
<i>PV (cp)</i>						
12	1.8	2.8	422	1.83	21.51	0.67
24	1.8	2.8	305	1.29	15.43	0.48
36	1.8	2.8	371	1.06	12.71	0.39
<i>Inclination (°)</i>						
30	1.3	2.5	343	0.81	6.64	0.13
45	1.5	2.65	316	0.90	8.44	0.21
60	1.65	2.8	269	0.97	10.31	0.29
<i>DLS (°/100ft)</i>						
5	2.3	≥ 3	367	0.57	8.67	0.34
10	2.6	≥ 3	174	0.65	10.64	0.45

The results presented in the above table show distinct patterns with changing parameters, all of which inherently make sense when considering the physics behind each scenario. As the wellbore diameter is increased, both the contact resonance and the pipe body resonance decrease. Referring back to equation (4.4), the natural frequency of the drillstring is inversely proportional to the radial clearance between the drillstring and the wellbore, which is clearly demonstrated with the variation of the resonance behavior with increasing hole size. As the hole diameter increases, it is also apparent that the system has larger dynamic response with the reach, displacement, velocity, and acceleration all increasing. This can be understood by the fact that a smaller wellbore will better confine the drillstring, thus limiting the lateral dynamic response of the system. Additionally, the nature of the linearized damping model utilized in this analysis, (3.57), results in lighter damping at lower frequencies which may also be contributing to the increased response as the wellbore diameter increases.

The applied WOB is an important factor to consider since it is actively controlled at the surface by the driller. In Figures E.10-E.12 the lateral forced-frequency response is shown for a WOB value of 5,000 lbf, where both the contact resonance band and the localized LET resonance band are seen. As the WOB is increased, the localized LET resonance band shifts downward to a lower frequency, while the contact resonance band stays fixed at 1.8 Hz. At a WOB of 10 klf (Figures E.13-E.15) a pipe-body resonance appears right around the 3 Hz cut-off frequency for the analysis, which indicates that it follows a similar pattern to the localized LET resonance; shifting downwards with increased WOB. This behavior is expected as increased compressive loads tend to destabilize pipe. This can also be explained via (4.4), where increased axial force further contributes to a reduction in the minimum lateral natural frequency of the drillstring. The contact resonance band is not shifting because the contact forces at the tool joints are not changing with increased WOB. Therefore it would be expected that, as long as the drill pipe is not buckling, and creating larger forces at the contact points, the contact resonance should remain at a constant frequency for a given wellbore configuration. As the WOB is increased to 15 klf (Figures E.16-E.18), the localized LET resonance begins to “merge” with the contact resonance which seems to increase the frequency span and the longitudinal reach for which the LET affects the drillstring. However, this apparent increase in reach is an artifact of the plotting scale rather than an actual phenomenon; as the maximum response value reduces, the coloring of the contours shift and lower values may be seen. Therefore, the longitudinal reach used in Table 5.4 should not be considered a definitive measurement. It is simply used as a relative metric to better understand the behavior of the system and, as shown by this example, can generate misleading conclusions if care is not taken to acknowledge this. As the WOB is further increased to 20 klf (Figure 5.4) the contact resonance and the localized LET resonance are nearly identical, generating a more continuous response within the 1.8-1.9 Hz frequency range.

With regard to the dynamic response amplitudes, the WOB is proportional to the reach of the tool. This behavior is similar in concept to the buckling phenomenon where increasing the compressive load results in a drillstring that is more susceptible to lateral inputs. Additionally, as the reach increases, the maximum response amplitudes decrease in magnitude. This is merely a result of the energy from the LET being distributed over a greater distance. When the lateral response of the drillstring is localized near the LET, as was the case for $WOB = 5 \text{ klb}_f$, it results in a higher displacement amplitude within a localized region. As the response distribution along the drillstring increases (i.e. the reach of the tool increases), the dynamic response is also distributed resulting in a lower peak response.

Variations in mud density, as well as viscosity, affect the response of the drillstring in the “usual” ways. As the density goes up, the resonant frequencies go down. This is due to the surrounding fluid effectively adding mass to the system, as quantified by (3.56). The dynamic response magnitudes of the drillstring also decrease as the density increases due to the increased damping associated with heavier fluids, as seen by (3.57). Viscosity, on the other hand, only affects the dynamic response magnitudes of the system, with smaller amplitudes being seen at increased viscosity values. This is to be expected from the damping relationship described by Equation (3.57). In both cases (density and viscosity variations) the longitudinal reach shows a peculiar trend, with a minimum occurring at the central density/viscosity values. This suggests a nonlinear trend with changing fluid parameters. However, the larger reach seen at the higher density/viscosity values may, again, be an artifact of the plot generation with regard to the color-scale. That is to say that as the peak response values decrease, more visibility of the response along the drillstring is seen. This, in turn, leads to the apparent reach in the contour plots being larger when the peak value is smaller.

Changes in inclination directly affect the contact forces between the drillstring and the wellbore. As the inclination increases, the contact forces at the tool joints also increase due to gravity pulling the drillstring towards the low-side of the wellbore. This, of course, creates a maximum contact force at an inclination of 90° . As the contact forces increase along the drillstring, so does the “stabilization effect” due to the contact. This is reflected in the results shown in Table 5.4, with both the contact resonance and the pipe body resonance increasing as the inclination gets larger. Referring back to Section 3, increasing the contact forces at the tool joints, increases the “confinement” of the system, which is demonstrated through an increase in the contact force component of the stiffness matrix, (3.43) and (3.46). This obviously explains the increase in the contact resonance, but, perhaps less clearly, explains the increase in the pipe body resonance. As the tool joints become more “confined” due to the increase in the contact forces, it generates a “nodal point”, or a restriction, for the lateral waves traveling through the drillstring. In turn, the additional nodal points prevent longer wave lengths from freely passing through the assembly. This reduction in allowable wavelength is what causes the increase in frequency. The reach of the LET appears to decrease with increasing inclination

while the peak dynamic response amplitudes increase, which is an effect of the “energy distribution” effect described previously. It should be noted that the “decreasing reach, with increasing inclination” trend is contradictory to the original calculation that was performed at an inclination of 90° (Figure 5.4), which showed a reach of around 400 ft. According to the results in Table 5.4, the reach should have been less than what was predicted at an inclination of 60°. However, again, it appears that the plotting scale shifted slightly and thus skewed the visualization of the tool’s reach.

Adjusting the wellbore curvature provides an interesting observation. In contrast to every other calculation, adding curvature to the wellbore causes a “swap” between the contact resonance and the localized LET resonance. Not only is the localized LET resonance at a lower frequency, but it also induces more vibration along the length of the drillstring which makes it appear more as a pipe body resonance (Figures E.47-E.49). The contact resonance shifts upwards due to an increase in the contact forces surrounding the LET, which is illustrated in Figure 5.12. A closer examination of these variations in contact forces also helps to explain why there is a downward shift in the localized LET resonance. At a DLS of 0°/100ft there is contact at the mid-span of the LET which is not present at the higher curvature values of 5 and 10°/100ft. This reduction in contact effectively reduces the “stiffness” of the system which, in turn, shifts the resonant frequency to a lower value. This scenario also causes a change in how vibrations generated from the LET propagate throughout the drillstring. Because the contact at the mid-span of the LET is removed, it now more closely resembles the “simply-supported” contact that is associated with the joints of drill pipe (i.e., it is only supported by contact on either end of the tool). Therefore, there is less of a discontinuity in the stiffness through that point in the drillstring. This makes it easier for vibrations to propagate outwards from this excitation source. The changes in contact force distributions near the LET tool can more clearly be seen in Figure 5.13-Figure 5.15.

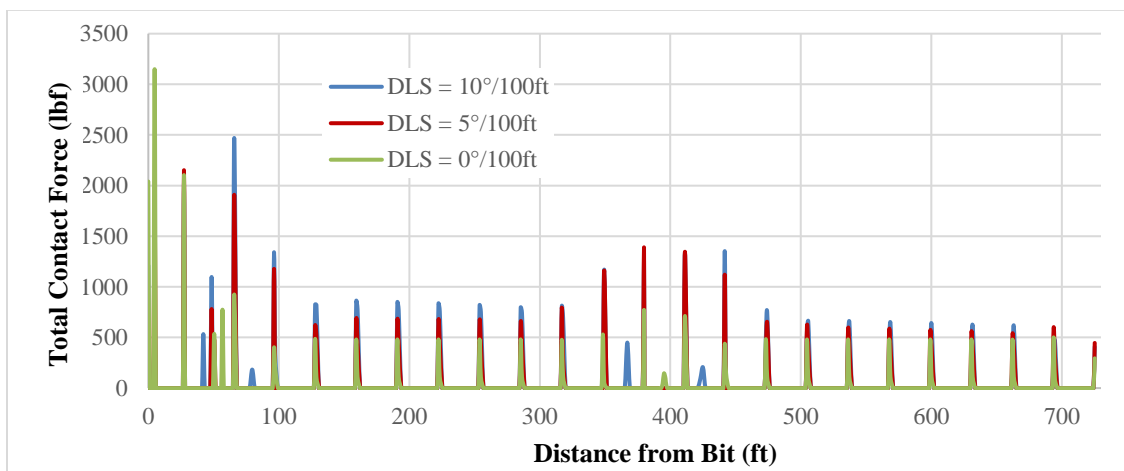


Figure 5.12: Contact Force along the Drillstring for Varying Wellbore Curvatures

Figure 5.13 shows the contact force distribution around the LET in a straight, horizontal wellbore. Here it can be noticed that a single contact point exists on either end of the LET. Because the tool joint OD (6.625") of the adjacent drill pipe is slightly larger than the OD of the LET (6.5"), these contact forces are actually acting on the tool joints and not the LET. As a result, the LET is somewhat "simply-supported" and slightly sags at its midpoint, which is why there are small contact forces in the middle of the tool. It should be kept in mind that this is a highly-idealized situation with perfect wellbore geometry, i.e. the borehole is a constant diameter along its length. In reality, there could be minor variations to this and more contact may be present over the length of the tool.

As the curvature of the well is increased to $5^\circ/100\text{ft}$ (Figure 5.14), the contact at the middle of the LET is removed. This, according to (3.43), reduces the effective stiffness of the system and subsequently results in lower resonant frequencies, which was indicated by the results in Table 5.4. It should be noted that the apparent curvature of the LET shown in Figure 5.14 should be interpreted very carefully. The nature of the calculation, and the associated scaling within the plotting algorithms, inherently distorts the displacements within the 3D mechanics plots of curved wellbore sections. This does not mean that incorrect results have been obtained, it is merely an optical illusion due to the distortion created by the scaling within the plotting algorithms. The true displacement of the LET in Figure 5.14 is actually bent slightly in the opposite direction that is depicted in the figure, i.e. the tool is slightly curved in the same direction as the wellbore.

Further increasing the curvature of the well appears to greatly diminish the response of the drillstring. This is actually caused by an "induced stabilization" effect on the adjacent drill pipe. Figure 5.15 shows the contact distribution near the LET in a curvature of $10^\circ/100\text{ft}$. From this illustration it is instantly apparent that the curvature has generated contact along the body of the drill pipe that is adjacent to the LET. This added contact isolates the vibration from the tool which not only decreases its effectiveness, but increases the localized dynamic response amplitude surrounding the tool.

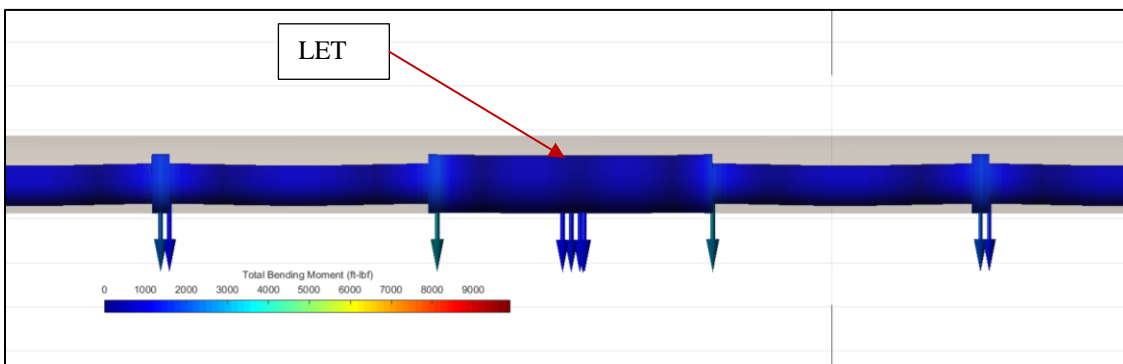


Figure 5.13: Contact Force Distribution near the LET for a DLS of $0^\circ/100\text{ft}$ (Straight Wellbore)

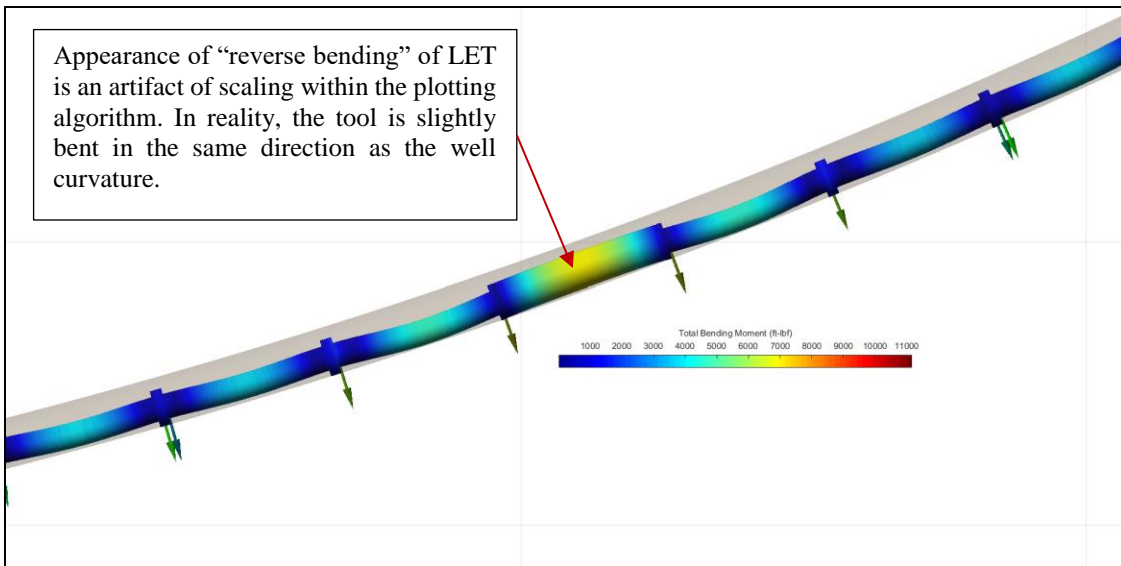


Figure 5.14: Contact Force Distribution near the LET for a DLS of 5°/100ft

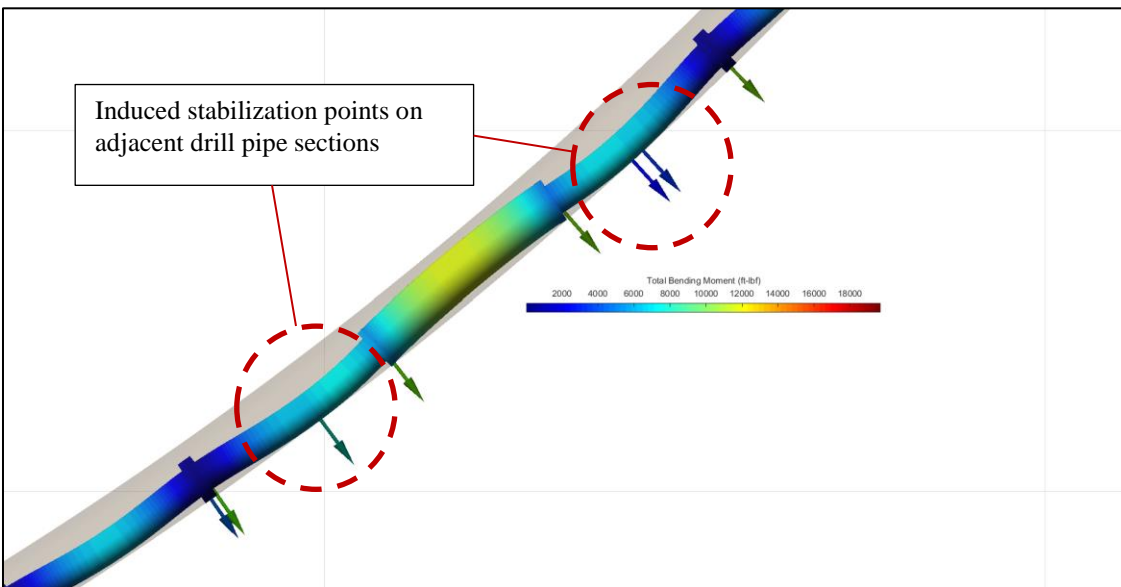


Figure 5.15: Contact Force Distribution near the LET for a DLS of 10°/100ft

*Note: The pip-body resonance for the curvature sensitivity studies (Figure E.47 – E.53) cannot be seen in the forced-frequency response plots. Because of the induced curvature of the drill pipe caused by the curvature of the well bore, a stress-stiffening effect is seen and the pipe-body resonance range is actually in the 4-5 Hz range.

*Note: Torque has been noticed to provide no influence on the lateral response of the drilling assembly and, therefore, is not considered an interesting quantity to examine within the sensitivity study presented here.

Additionally, the size of the drill pipe will also play a role in the dynamics of the drillstring. While modern horizontal drilling in 8 ½” and 8 ¾” wellbores is typically done with 4 ½” or 5” drill pipe, these components can vary in wall thickness as well as tool joint dimensions. These variations will change the stiffness and mass of the system, which will directly influence its dynamic characteristics. Section E.7 (of Appendix E) provides an overview of the forced-frequency responses calculated for a variety of common drill pipe sizes and tool joint connection types [145]. In general, it would seem that the drill pipe body predominately dictates the resonant frequency values, while the tool joint dimensions have more of an effect on the amplitude response at the contact resonance. For example, when going from a 4 ½” 20 ppf drill pipe with an NC50 connection (Figure 5.4-Figure 5.7) to 5” 19.5 ppf drill pipe with an NC50 connection (Figure E.75 – E.77), the contact resonance shifts from 1.8 Hz to 1.7 Hz. Then, going from the same 5” drill pipe with an NC 50 connection to a 5 ½” FH connection (Figures E.78-E.80), which alters the OD and ID of the tool joints, the response amplitude along the drillstring changes significantly, but the contact resonance frequency remains relatively fixed. Ultimately, all of the variations in drill pipe dimensions that were examined showed a resonant response generally in the same frequency range of 1.6 Hz – 1.8 Hz. This suggest that, although minor differences occur, a relatively narrow frequency window exists for a given well configuration. That is to say that, once a response has been determined with a given set of parameters values (such as those presented in Table 5.4), the “optimum frequency” (contact frequency) is not expected to shift drastically if 4 ½” drill pipe were to be swapped out with 5” Drill Pipe. However, the predicted amplitude response distribution may increase, or decrease, depending on the situation. And perhaps moving to even larger drill pipe, such as 5”-25.6 ppf or 5 ½”-21.9 ppf drill pipe, may more significantly impact the resonant behavior of the system. Of course if larger, or heavier, drill pipe is to be used, then that may negatively impact the Torque and Drag acting on the system.

Up to this point, all of the parameters that can reasonably be adjusted by the rig personnel have been examined. Using this analysis approach, a drilling engineer could determine the most appropriate parameters for a given well in order to maximize the response from the LET. However, what is somewhat out of the engineer’s control, is how the trajectory of the well evolves while drilling. Yes, it is true that BHAs can be designed to better meet directional requirements of a well, as was shown through some of the numerical validation cases found in Section 4, but analyses such as these cannot reasonably account for the influence that the formation has on the directional characteristics of the bit. There have been a few studies that show how advanced bit models can better estimate the directional tendencies of bits and BHAs based on known formation properties [138, 139], but rarely are adequate formation properties known as, or before, a particular well is being drilled. Even if the appropriate formation properties are determined with a “high level” of certainty, the model will not be able to predict the exact directional behavior of the BHA. In reality, the path of the wellbore will drift “off-course” to some degree and will require periodic course corrections.

This is why it is vitally important to maintain directional control throughout the course of the well, not just in the sections of the well that were intended to be “steered” (i.e. build or curve sections).

With this understanding, it is important to determine how the drillstring will respond to the LET excitations in a realistic wellbore, as compared to the ideal wellbore which has been modeled as a straight section with a constant inclination. The realistic wellbore will generally follow the same path as the planned (ideal) wellbore, assuming the driller is competent in his art, but will always have slight variations in inclination, azimuth, and curvature. This variation is very clearly seen via Figure 5.16 and Figure 5.17, where a comparison is made between a planned wellbore and the “as drilled” trajectory for the same well. The assembly used for this calculation is the same as it was in the previous section, only with a longer span of drill pipe (~ 2,000 ft) and the LET is shifted further from the bit (~ 1,000 ft from the bit). The ideal well (Figure 5.16) is shown as a smooth straight line, with the contact forces all pointing in the same direction. This is usually the picture that develops in the head of an inexperienced drilling engineer. As an engineer becomes more exposed to the intricacies of operations, and the challenges that drillers must overcome, their understanding of a “horizontal” wellbore becomes more solidified and representative of reality (Figure 5.17). The realistic well path does not look quite as well-ordered as the ideal case, with contact forces changing direction along the length of the drilling assembly and higher bending moments developing within the body of the drill pipe in various locations, but this is the nature of horizontal wells; imperfection. It can be noted that the actual well path in Figure 5.17 is the bottom 2,000 ft of the well path used for the comparative Torque and Drag analysis in Section 4 (See Appendix C). The planned inclination for the horizontal section of this well was 91°.

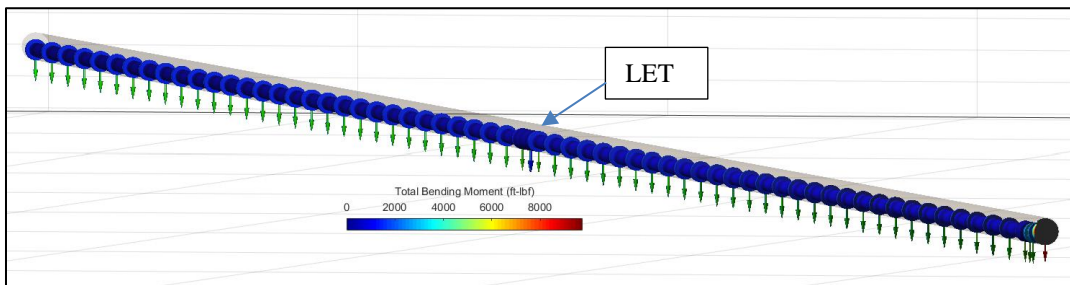


Figure 5.16: Mechanics Plot of Drillstring in an “Ideal” Horizontal Wellbore

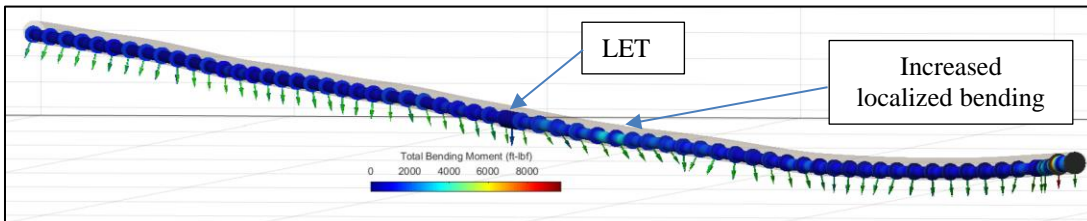


Figure 5.17: Mechanics Plot of Drillstring in a “Realistic” Horizontal Wellbore

Because of this inherent behavior, it is imperative to understand how the realistic well path alters the “ideal” behavior of LETs. Figure 5.18 and Figure 5.19 display the results of a comparative forced-frequency response analysis between the two wellbore trajectories, with the extended assembly shown in Figure 5.16 and Figure 5.17. Again, the same parameters used in the previous analysis (Table 5.2) are used here. Figure 5.18 shows an identical response to that predicted by the initial analysis in Figure 5.4, with the primary contact resonance occurring around 1.8 Hz and the secondary drill pipe resonance showing up around 2.75 Hz. This should not be surprising since, based on the equation presented by Heisig and Neubert [40], (4.4), the lateral natural frequencies of the system are not affected by the length of the assembly due to the periodic nature of the contact in a horizontal wellbore. Moving to the realistic wellbore (Figure 5.19), it is noticed that the frequency response is not quite as “clean” as it was for the ideal case. However, the contact resonance frequency remained relatively stationary. The primary displacement pattern still occurs at 1.8 Hz with a slight increase in displacement occurring in the 1.5 – 1.6 Hz range. This makes sense due to the fact that the magnitude of the contact forces, and thus the magnitude of the “stabilizing” force, are not changing; only the directions of the contact forces are changing. The variability of the contact force orientation, specifically near the LET (Figure 5.17), is what creates the more erratic displacement pattern in the realistic wellbore. The pipe-body resonance, on the other hand, shows a slight increase from 2.75 Hz, to 2.9 Hz. This makes sense as the curvature of the wellbore induces a stress-stiffening effect in the body of the drill pipe, which ultimately increases the natural frequencies of the unsupported tubular sections.

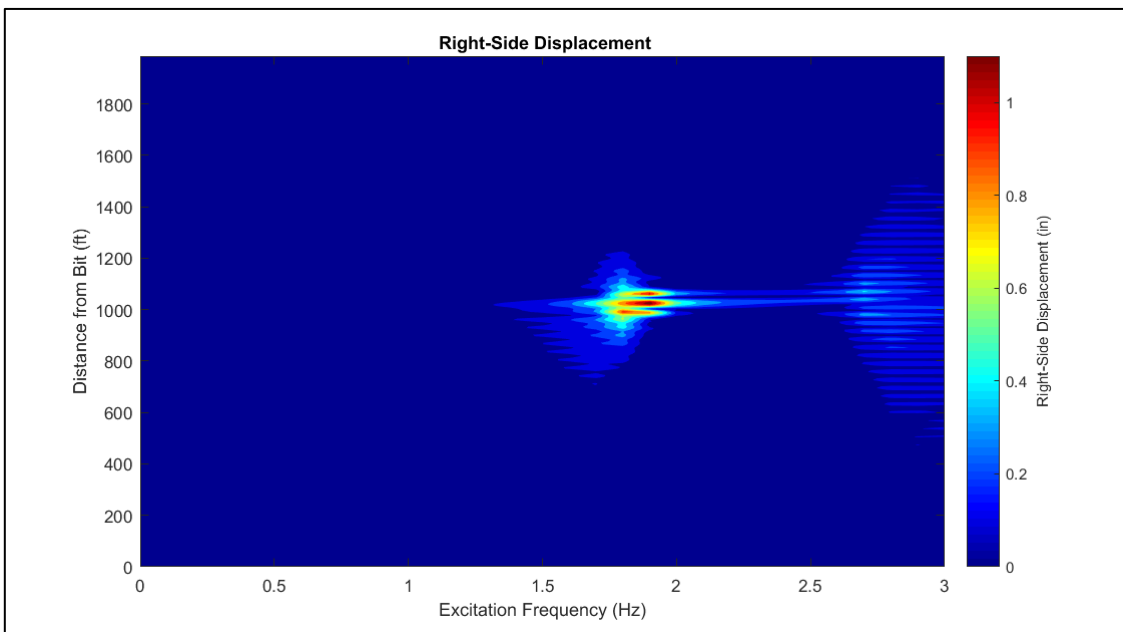


Figure 5.18: Forced-Frequency Response with LET in “Ideal” Horizontal Wellbore

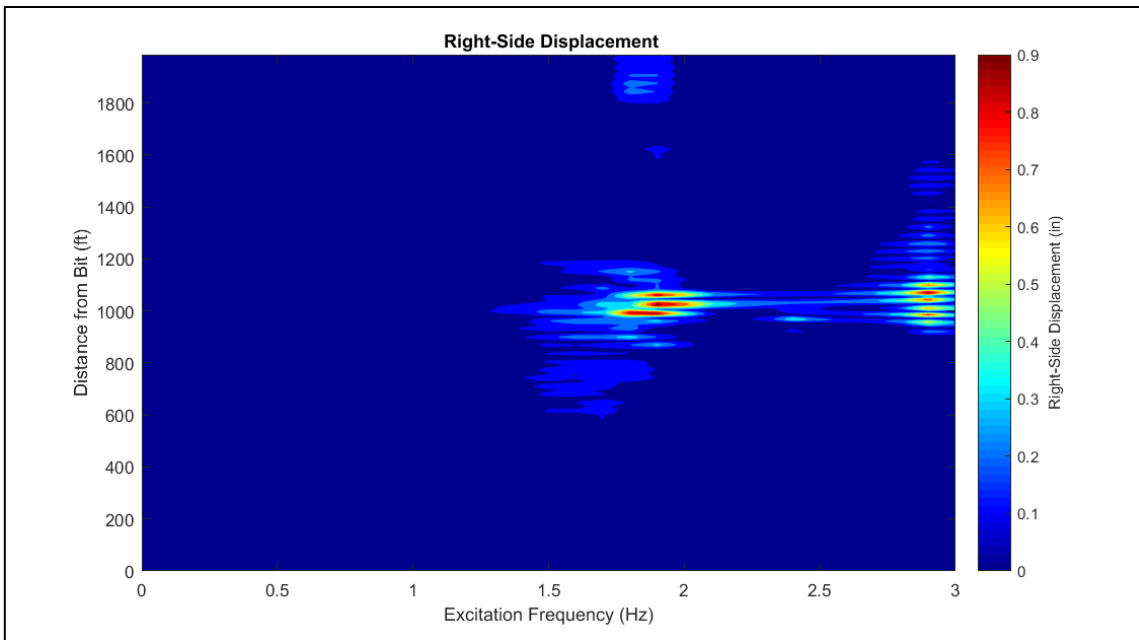


Figure 5.19: Forced-Frequency Response with LET in Realistic Horizontal Wellbore

The results depicted in Figure 5.18 and Figure 5.19 illustrate the practicality of pre-job planning when using LETs, such as the one described in this Section. So long as the “as-drilled” well path is reasonably on target, then the primary frequency response (the frequency that induces lateral motion of the contact points in the drillstring) should remain close to that predicted by the planned (“ideal”) case. Alternatively, if there is a great concern of the driller deviating off course, the analysis is efficient enough that the computation could be periodically updated with new survey information as the well is being drilled.

5.3 Practical Considerations for Operations and Analysis

The previous sections outline how the various details of the drilling operation can be captured through the linearized forced-frequency analysis, and subsequently can be utilized to help better plan the execution of a drilling project when using LETs. At first glance, this seems like a straight forward approach and one would think to simply excite the drillstring at the contact resonance frequency in order to achieve the best result. Unfortunately, it is not as simple as “locking in” a frequency and drilling ahead; thought must be given to the means in which the excitation frequency is reached. As discussed earlier in this section, when slide drilling with a LET, the excitation frequency is directly controlled via the volumetric flow rate through the tool. However, the flow rate is generally dictated by other aspects of the drilling operation. In the modern horizontal wells of North America, for example, the flow rate will usually be set to the maximum allowed by the down-hole mud motor and/or the ECD limits imposed by the formation that is being drilled. Maximum allowable flow rates are desirable because they not only help to keep the hole free of formation

cuttings, but also generate higher motor output speeds (i.e. higher bit rotation speeds). In this case, the operator may be reluctant to change the flow rate and, as a result, the “optimum” excitation frequency from the LET may not be ideally suited for that particular well. For a scenario like this it would be important to have a way of adjusting the frequency output of the tool based on the desired flow rate.

Recall that the excitation frequency of the LET is dependent on the output speed of the power section used to drive the eccentric mass (5.4). With this in mind, a target power section speed (revolutions per gallon, *rpg*) can be determined with the following relationship

$$rpg = 60 \frac{f_{exc}}{GPM} \quad (5.16)$$

Therefore, if the target excitation frequency output from the tool was 1.8Hz (as it was in Figure 5.4) and the desired flow rate is 600 GPM (a common maximum flow rate for 6 ½” down-hole mud motor power sections), then a power section output speed can be calculated to be 0.18 rev/gal. A power section with this output speed, or close to it, could then be selected to rotate the eccentric mass within the LET. This, of course, would require a “reserve” of power sections that can readily be utilized as needed.

Apart from frequency output, there are also computational aspects to keep in mind. As with any finite element analysis, the accuracy and reliability of the results can depend on the mesh size, or element density. For dynamic analysis, the mesh size will influence the frequency output of the model. More specifically, if the length of the element is shorter than about ¼ of the wavelength associated with a given frequency, then the model may not be able to capture the correct dynamic response. Even at ¼ the wavelength, the dynamic response can appear “jagged” with sharp changes in direction. This can be seen in Figure 5.20 where the same analysis, done for Figure 5.4 (15 elements per drill pipe body), is performed using a much larger element size (2 elements per drill pipe body). Clearly, the finer the mesh the more accurate and reliable the results will be. However, it can be noticed that the results provided by Figure 5.20 are still sufficient for identifying the optimum excitation frequency and could certainly be used for a “quick and dirty” analysis.

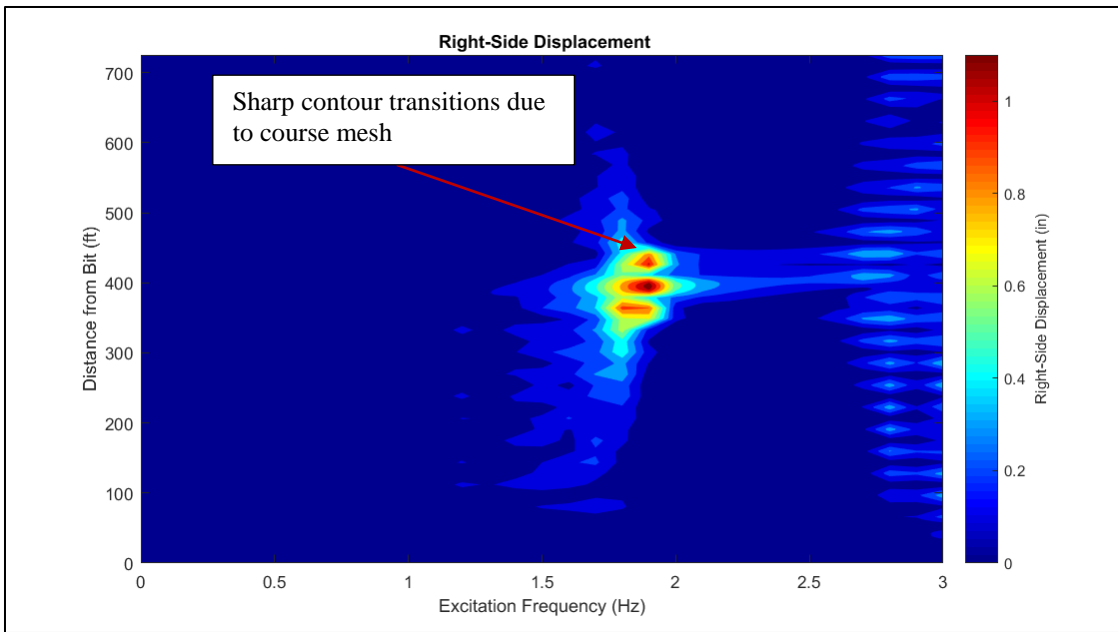


Figure 5.20: Analysis of Figure 5.4 Performed with a Coarser Element Mesh

Of course, due to computational constraints (i.e. time and computer hardware) there will be a practical limit on how short the elements within a model can be. Ideally the elements should be short enough so as to provide sufficient accuracy, but not so short that excessive computation time is required to reach a solution. In order to avoid having to run sensitivity studies for every analysis, the “1/4 wavelength approximation” can be used as a guideline. Knowing that the wavelength (λ_L) is related to the frequency (f) via,

$$\lambda_L = \frac{c}{f} \quad (5.17)$$

Where c is the wave speed, which for transverse waves in beams can be calculated as [146]

$$c = \left(\frac{EI}{\rho A} \omega^2 \right)^{\frac{1}{4}} \quad (5.18)$$

Then, 1/4 of the wavelength can be estimated as

$$L_{min} = \frac{\sqrt{2\pi}}{48\sqrt{f}} \left(386.088 \frac{EI}{\rho A} \right)^{\frac{1}{4}} \quad (5.19)$$

Where f is the maximum operational frequency of the LET in Hertz, E is the Young's Modulus in psi, I as the area moment of inertia of the pipe body in in^4 , and ρ is the density in lb_m/in^3 . (5.19) can be used as a guideline for estimating how short the elements within the model need to be. If the solutions appears to be "jagged" when using this element length, it can be further reduced from there as necessary.

6. NONLINEAR SIMULATIONS OF INDUCED LATERAL VIBRATIONS

The previous section examined the resonant behavior of lateral excitation tools in horizontal wellbores by using a linearized forced-frequency calculation method. While this provided valuable insights of how various parameters affect the steady-state response of the drillstring when using these types of tools, it is only a small-displacement approximation of a nonlinear-dynamic system. This essentially means that the previous analyses can only estimate the initial tendency of the system to oscillate about a stationary position. Additionally, the linearized analysis only showed how various parameters affect the lateral resonant response of the drillstring which, unfortunately, is not directly related to an improvement in axial force transfer. Referring back to Equations (2.70) - (2.72), any improvement in the axial force transfer should theoretically come from an increase in either the axial or rotational velocities. Based on the frictional interaction between the drillstring and the wellbore (see Figure 2.2), the lateral displacement generated by the LET should instigate a gentle rocking motion back and forth along the wellbore wall. As discussed in Section 5, this rocking motion should subsequently induce a rotational velocity. According to equation (2.71), this rotation should not only decrease the overall coefficient of friction, but should also change the direction in which the friction is acting and reduce the effective axial frictional resistance. Time-domain simulations (Section 3.3.3 and Appendix B) can be performed to directly quantify this lateral-torsional friction effect and determine the impact of induced lateral vibrations on the WOB. In turn, it is assumed that any change in WOB would be a direct indicator of how the ROP will change.

6.1 Nonlinear Modeling Considerations

In order to properly analyze the nonlinear dynamics associated with lateral excitation tools, several aspects of the drilling system must be examined in greater detail. Specifically, the linearized vibration analysis did not account for friction and, as a result, was not able to capture the induced torsional motion caused by the lateral displacement from the LET. Consequently, this approach cannot adequately determine how the induced lateral vibration will affect the WOB either. This section outlines the necessary adjustments that are required to overcome this limitation of the linearized analysis.

6.1.1 Friction and Axial Drag

According to (2.70) – (2.72), there will be no frictional resistance along a certain direction unless there is a component of velocity acting in that direction. Therefore, to simulate the axial drag acting on a “sliding” drillstring, a steady-state axial velocity must be assumed, and applied to Equations (2.70) – (2.72), within the initial quasi-static analysis. As a result, the axial velocity will be a combination of this steady-state axial velocity, taken to be the sliding ROP for the present case, and the transient axial velocity.

$$\dot{u}_3 = ROP + \dot{u}_{transient} \quad (6.1)$$

In Equation (6.1), the ROP represents the steady-state axial velocity that is applied to the initial quasi-static deflection of the drillstring, and the transient velocity ($\dot{u}_{transient}$) is the additional velocity that is calculated during the course of a nonlinear simulation. This velocity term is used within the coefficient of friction relationship developed for a dynamic value of 0.3, which is represented by the solid green line in Figure 2.4 ($\beta=5$, $b=0.002$, $v_o=0.01$, $\mu_s=0.365$, $\mu_D=0.56\mu_s$). The base ROP prescribed for all simulations is 50 ft/hr.

6.1.2 Boundary Conditions

Recall that all previous analyses within this study have applied the axial force (WOB) directly to the bit and fixed the opposite end of the drillstring in the axial direction. For the purposes of determining the effect that LETs have on the WOB, it would seem inappropriate to apply these same boundary conditions. A more realistic approach, and beneficial for the current investigation, would be to apply the axial compressive force at the “top” of the drillstring and fix the bit in the axial direction. In doing this, the reduction in axial force along the drillstring can be calculated directly from a quasi-static analysis and the dynamic simulation. The lateral and torsional boundary conditions will be similar to what they were in Section 5 and are summarized in Table 6.1 for reference.

Table 6.1: Boundary Conditions for Nonlinear Simulations

<i>Boundary Conditions</i>	<i>@ Bit</i>	<i>@ "Top"</i>
<i>Axial</i>	Fixed	$F_{axial} = 20 \text{ klb}_f$
<i>Torsional</i>	$TOB = 2,500 \text{ ft-lbf}$	Fixed
<i>Lateral (Radial)</i>	Fixed	Free
<i>Bending</i>	Free	Fixed

6.1.3 Initial Quasi-Static Analysis and Linearized-Dynamic Estimate

In the interest of computational efficiency, the nonlinear simulations are performed using a shortened version of the drilling assembly that was analyzed in Section 5 (Table 5.1 and Table 5.2). The total length of the drillstring for the nonlinear simulations is roughly 536 ft, with the LET located 285 ft from the bit. With this configuration (broken down into 188 elements), an initial quasi-static analysis is performed to determine the reduction in axial force between the “top” end of the drillstring and the bit. The deflection of the drillstring can be seen in Figure 6.1 and the magnitude of contact and axial forces (negative values represent compression) along the drillstring are shown in Figure 6.2.

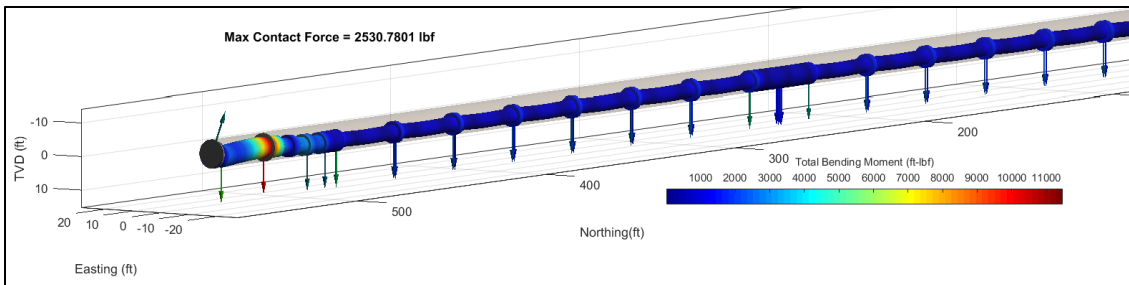


Figure 6.1: Quasi-Static Deflection of Drillstring (Diameters are not Drawn to Scale)

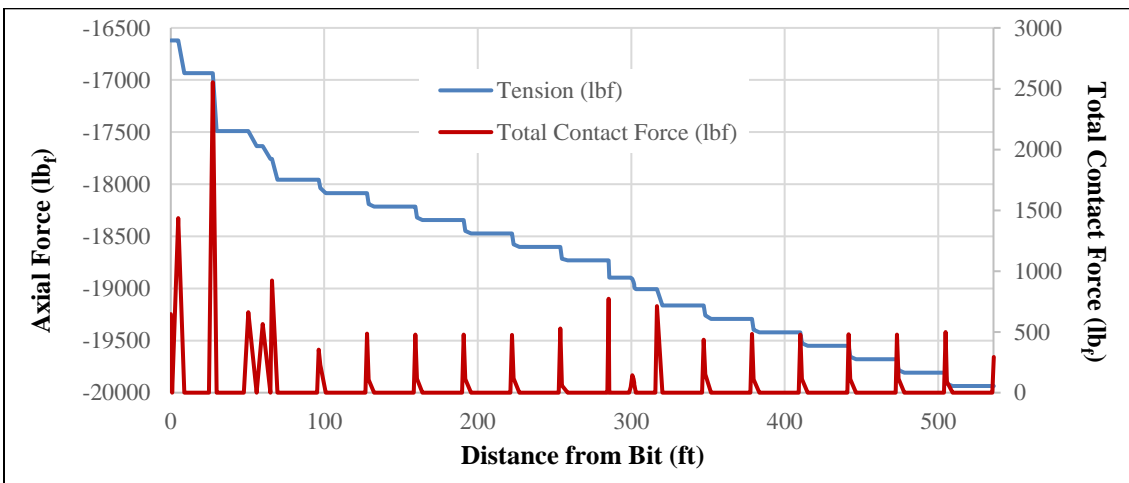


Figure 6.2: Quasi-Static Axial Force and Contact Force along the Drillstring

From the quasi-static results, it is clear how the contact in the wellbore is directly related to the transfer of axial force along the drillstring. At each contact point the axial force is reduced by an amount that is proportional to the coefficient of friction. This configuration is taken as the “base-line” from which the change in WOB will be measured through the nonlinear simulations. The quasi-static WOB is determined to be 16,620 lb_f. This is a 3,380 lb_f reduction in axial force transfer over only 536 ft! This may not seem like a significant amount, but when thinking about how long modern horizontal wells can get ($\approx 10,000$ ft), one can imagine how crippling frictional resistance like this can be.

Apart from the “base-line” WOB, it is also important to have an idea of the frequency response that is expected during the nonlinear simulation. Figure 6.3 displays a forced-frequency response plot of the shortened drillstring, due to the excitation from the LET (keep in mind that all linearized dynamic analyses are performed without friction). Again, it should not be surprising that the resonance response is the same as it was for the longer drillstring in Section 5, with the primary lateral response occurring at 1.8 Hz. As explained by Heisig and Neubert [40], so long as an assembly of tubulars is of sufficient length, the minimum

lateral natural frequency of tubulars confined within a wellbore will not depend on the overall length of the assembly, but merely the mechanical characteristics of the drillstring.

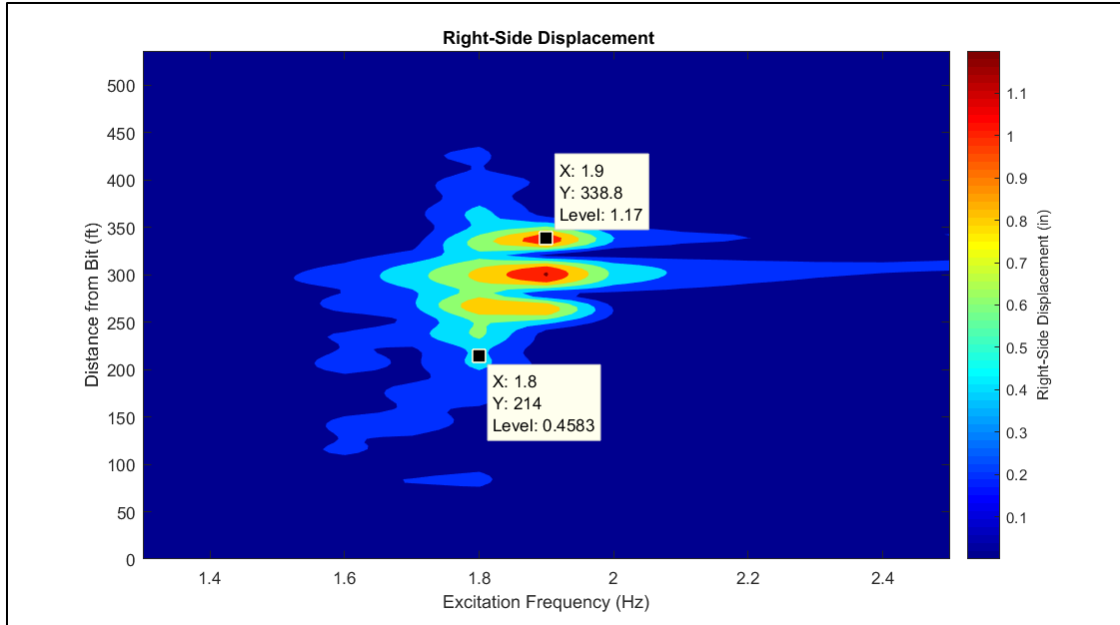


Figure 6.3: Forced-Frequency Response of Shortened Assembly due to LET Excitation

In addition to the excitation provided from the eccentric mass within the LET, as discussed in Section 5, the tool also generates a higher frequency excitation from the rotor within the power section. In order to understand the range of frequency output from this component, it is important to know how fast the eccentric mass within the tool rotates based on the flow rate of the drilling fluid. For the analysis, it is assumed that the power section attached to the LET has an output speed of 0.2 rev/gal. It is further assumed that the flow rate of interest for this configuration will be between 400 and 600 gpm, as this is a typical flow rate range for 6 ½" mud motors. Therefore, based on equations (5.4) and (5.12), the excitation frequency from the eccentric mass should range between 1.33 - 2.00 Hz and, with a 7/8 lobe configuration, 9.33-14 Hz for the rotor within the LET's power section. The linearized response for the higher frequency excitation from the power section can be seen in Figure 6.4. Because of the linearized nature of the frequency response shown in both Figure 6.3 and Figure 6.4, it can be expected that the true response will be a superposition of both of these dynamic behavior patterns. Thus, it would be likely that the eccentric mass within the LET will provide the primary excitation in the system with the rotor in the power section providing a secondary, less prominent, vibration in the drillstring.

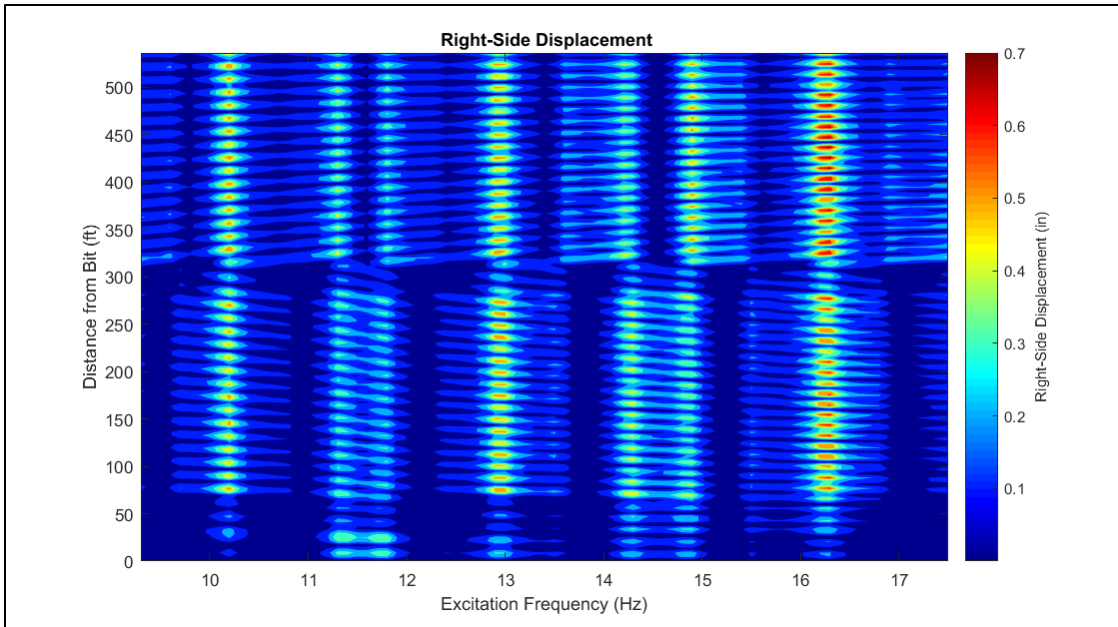


Figure 6.4: Forced-Frequency Response of Shortened Assembly due to Power Section Excitation

6.1.4 Nonlinear Simulation Analysis Parameters

Using the quasi-static deflection as an initial starting point, the system of equations can be integrated in time following the approach outlined in Section 3.3.3 and Appendix B. However, consideration of the damping and the time-increment must be dealt with prior to running any simulation. As discussed in Section 2, there are three sources of damping that are accounted for within the present model: wellbore contact, structural damping, and the fluid-drillstring interaction. Damping due to wellbore contact is captured entirely through the wellbore contact force vector outlined in Sections 2 and 3. Structural damping is assumed to follow a proportional damping model, as shown in Equation (3.62), whose coefficients can be determined with the method outlined by Dykstra [14]. Fluid damping is captured via the new fluid-drillstring interaction relationship described in Sections 2.4 and 3.2.3.3. The parameters for the damping models, as well as the other pertinent values for the nonlinear dynamic analysis, are listed in Table 6.2. It is also important to note that the time increment used for nonlinear analysis will have a significant impact on the accuracy and stability of the solution. For this reason, an automated time-control algorithm, similar to that presented by Zhang and Hisada [133], has been implemented here. The time-control algorithm automatically adjusts the initial time-step in order to reach a specific convergence criteria within the nonlinear calculation, and will attempt to move back to the original time-step when possible.

Table 6.2: Dynamic Analysis Parameters

Parameter	Value
a	1
τ_y (lbf/100ft ²)	16
β_D	0.1004
γ_D	9.5589×10^{-4}
Δt_0 (sec)	0.00005

Recall that there are two primary goals with the nonlinear simulation: to verify that the linearized analysis can predict the nonlinear resonant behavior of the system, and to quantify the effect that induced lateral vibrations have on the WOB. As a starting point to help answer these questions, it is desired to obtain a simulation that would yield a similar result to Figure 6.3. Based on the assumed output speed of the LET (0.2 rpg), and the typical flow rate range of a 6 ½" mud motor (400-600 gpm), the excitation frequency generated by the eccentric mass will range between 1.33 Hz and 2.0 Hz. In an attempt to generate an equivalent result, as depicted in Figure 6.3, the excitation frequency from the eccentric mass is slowly increased through this frequency range following the trend shown in Figure 6.5. The excitation frequency of the eccentric mass is quickly increased from 0 to 1.33 Hz in the first five seconds of the simulation, then it is held constant for five seconds in order for the system to stabilize at this frequency. At ten seconds, the excitation frequency is then gently increased through the frequency range of interest over the course of 50 seconds. The secondary excitation from the power section within the LET is also incorporated into the model in a consistent manner with (5.12). The power section in the LET has a 7:8 rotor-stator lobe configuration and, as a result, will generate an excitation frequency ranging from 9.33 Hz to 14 Hz throughout the simulation between 10 and 60 seconds.

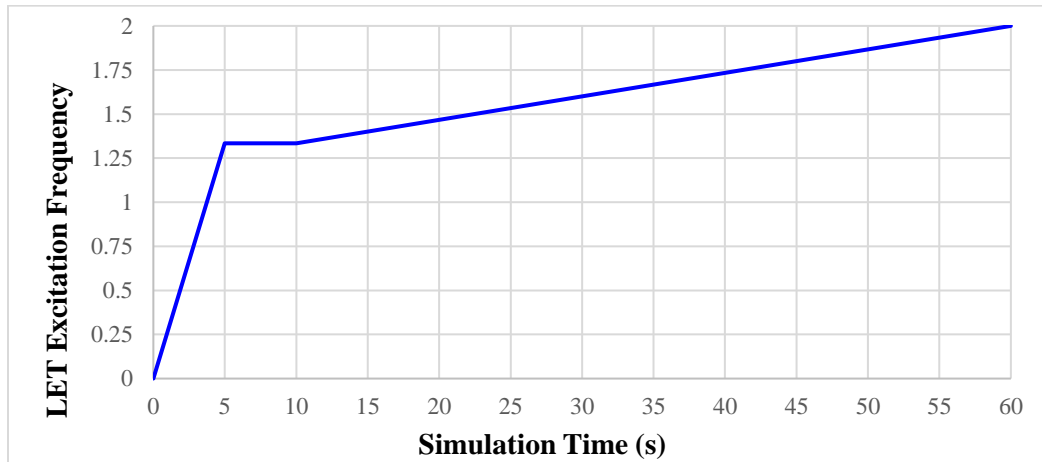


Figure 6.5: Time History of Excitation Frequency for Nonlinear “Frequency Sweep” Simulations

6.2 Nonlinear Simulation Results and Discussion

6.2.1 Initial Simulations, No Fluid Damping

The results of the initial simulation are shown in Figure 6.6. The upper left portion of the figure shows an orbital plot of a cross-section located 291 ft from the bit, which is a cross-section of the LET housing containing the eccentric mass. The black circle represents the wellbore wall, the blue contours represent the outer and inner diameters of the housing in this part of the tool, and the red curve represents the path traveled by the center point of the cross-section throughout the course of the simulation. The upper right section of the figure shows the absolute lateral (radial) acceleration, of the aforementioned cross-section, as a function of excitation frequency of the rotating eccentric mass. The bottom portion of the figure shows the WOB as a function of the LET's excitation frequency, with the static WOB shown in red as a reference.

In examining the figure it is immediately clear that there is a resonant behavior at 1.8 Hz, just as was predicted by the linearized analysis. This suggests that the linearized forced-frequency analysis associated with LETs can effectively predict the generalized nonlinear resonant behavior of drillstrings. Additionally, this lateral resonance is associated with a rocking-like motion of the LET, which was the anticipated behavior and is depicted by the crescent-shaped curve generated by the path of the cross-section in the orbital plot. This result also indicates that friction is not a crucial factor for estimating the lateral resonance of drillstrings in directional wellbores due to the fact that the linearized analysis was performed while ignoring frictional effects. Technically, including friction within the model adds stiffness to the system (see Section 3.3.1), but this contribution is relatively small and does not greatly affect the natural response (i.e. the Eigen-Values) of the drillstring.

While the dynamics associated with this specific cross-section certainly suggests that a resonant event is occurring, it does not indicate how far along the drillstring such a response is being felt. This is the concept of the tool's "reach" that was discussed in Section 5, and must be understood from a nonlinear perspective in order to verify that linearized analysis is sufficient for modeling the response of the system. Snap-shots of an animation can more clearly illustrate this reach. Figure 6.7 shows the displacement pattern, and bending severity (blue = minimum, red = maximum), of the drillstring around the time the eccentric mass is providing a 1.4 Hz lateral excitation (note that the bottom portion of the figure is not drawn to scale and, subsequently, results in a slight distortion of the tubular diameters). Clearly this excitation frequency is not generating a significant response in the drillstring, although a small wave pattern is noticed along the length of the assembly. This small response is due to the excitation, which would be about 9.8 Hz at this point, from the power section in the LET. As the eccentric mass excitation is increased past 1.5 Hz (Figure 6.8), the displacement pattern begins to resemble the lateral mode shapes of similar frequencies that were predicted in Section 5 (Appendix D), where a slight response becomes apparent in the portion of the

drillstring between the LET and the bit. This was also indicated from the forced-frequency response in Figure 6.3.

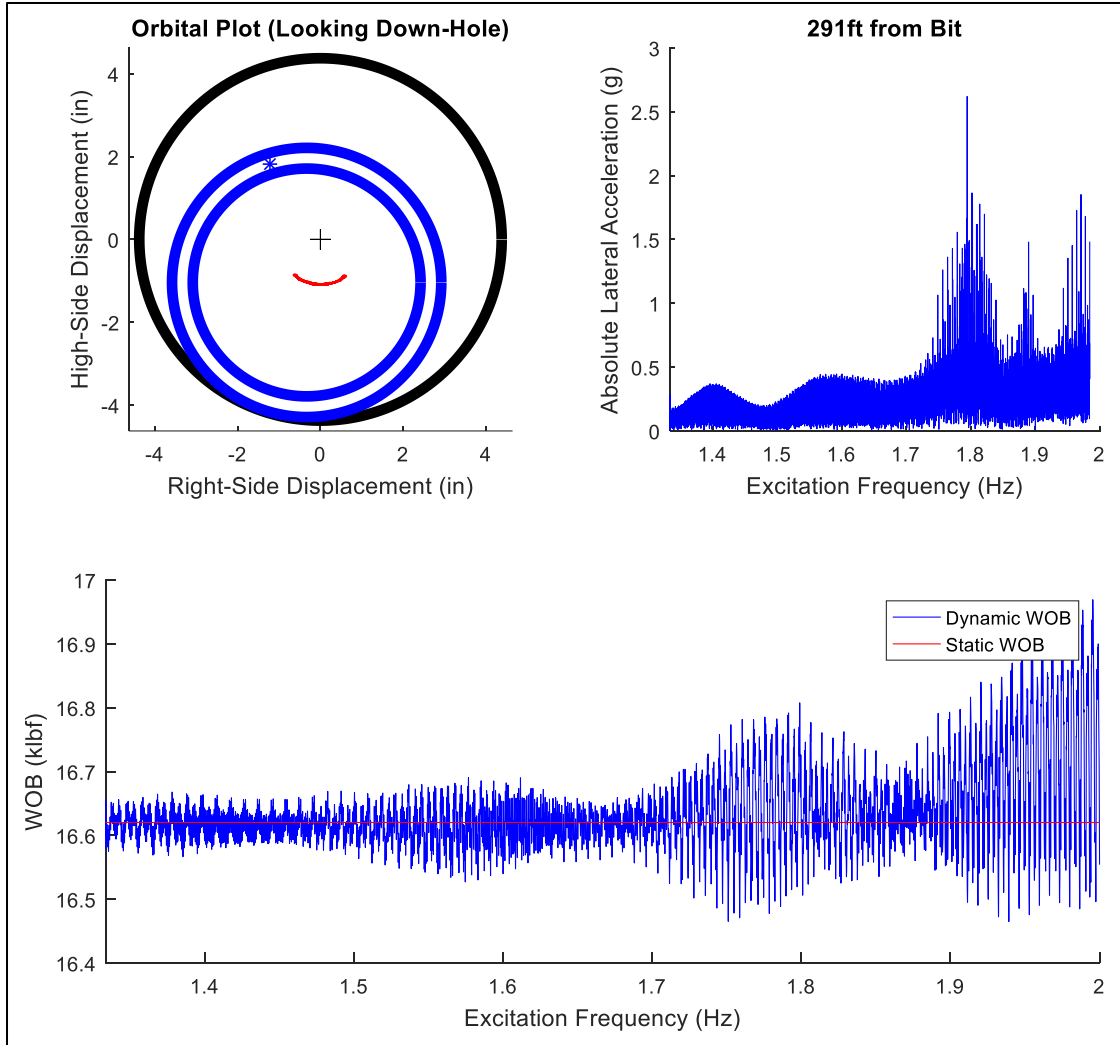


Figure 6.6: Results of Original Nonlinear Simulation

Approaching the primary resonant frequency of 1.8 Hz (Figure 6.9) the largest response is seen over the longest length of the drillstring, and is quite similar to the 18th mode in Appendix D. It can be noted that the primary displacement occurs over a length of 150-450 ft from the bit, which is the same as what would be expected from the forced-frequency result in Figure 6.3. Further increasing the excitation frequency into the 1.9-2.0 Hz range (Figure 6.10) results in the “localized LET resonance” that was also indicated from the forced-frequency response (Figure 6.3) and the free-vibration response (21st mode shape in Appendix D).

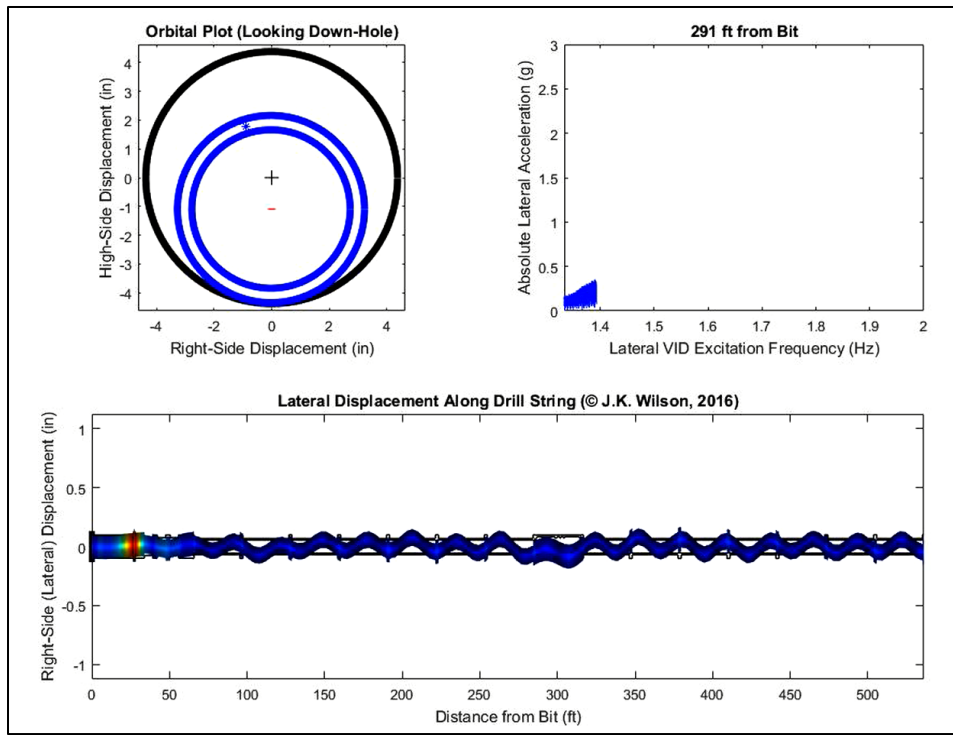


Figure 6.7: Animation “Snap-Shot” of Original Simulation near 1.4 Hz Excitation Frequency

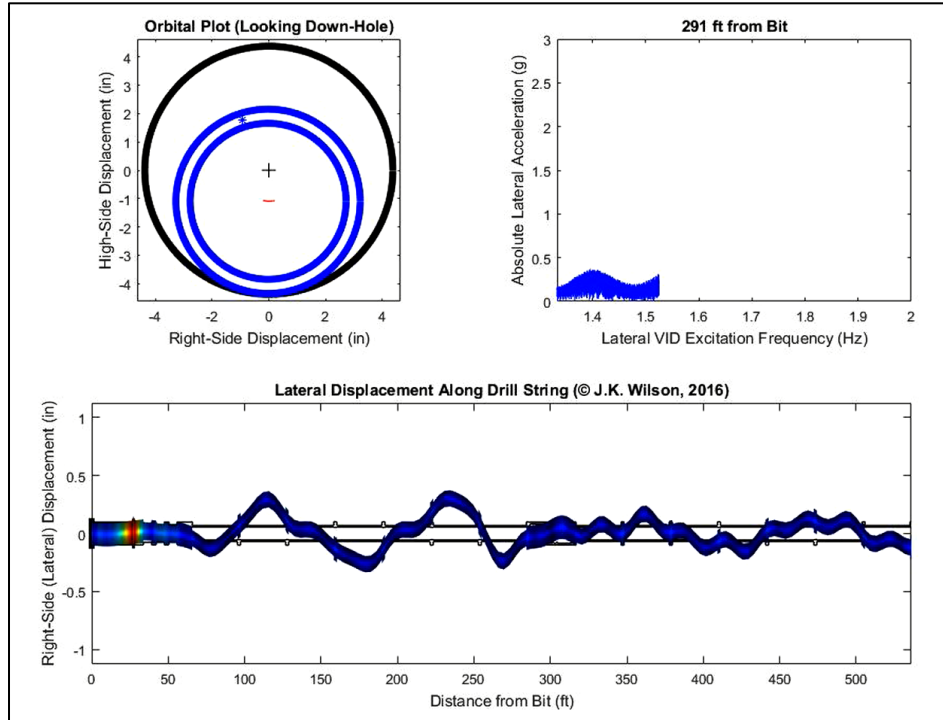


Figure 6.8: Animation “Snap-Shot” of Original Simulation near 1.5 Hz Excitation Frequency

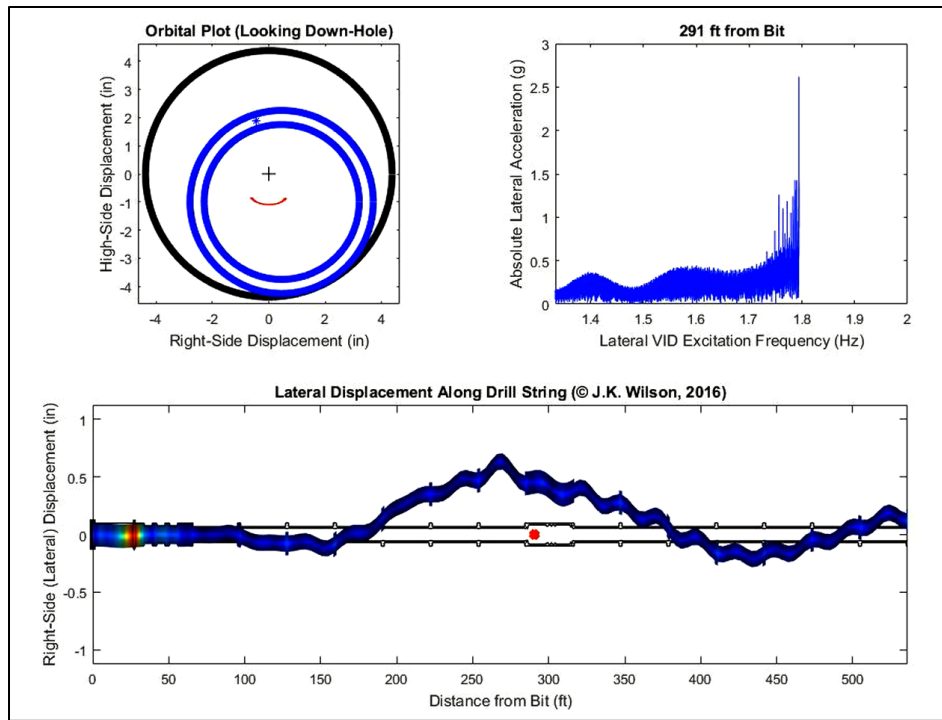


Figure 6.9: Animation “Snap-Shot” of Original Simulation near 1.8 Hz Excitation Frequency

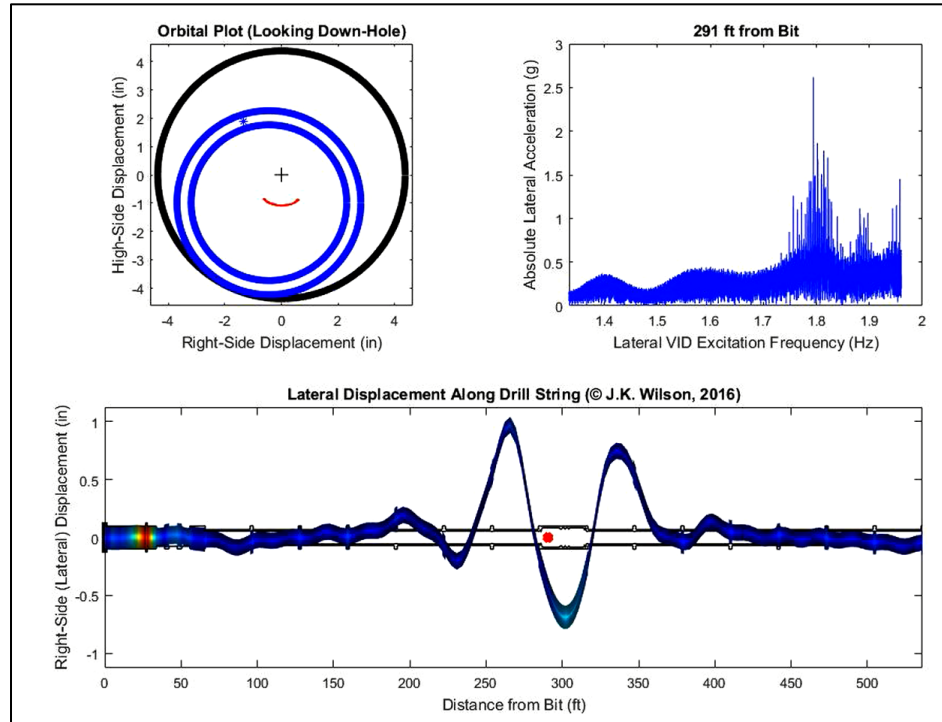


Figure 6.10: Animation “Snap-Shot” of Original Simulation near 1.9-2.0 Hz Excitation Frequency

While the nonlinear resonant behavior of the system is as expected from the linearized analysis in Figure 6.3, the WOB does not respond to the induced lateral vibrations in the way that was initially anticipated. Instead of increasing the average WOB to a higher value, at a lateral resonant frequency of 1.8 Hz, the LET appears to only induce a larger dynamic WOB which oscillates around the initial quasi-static value. The primary cause of this dynamic WOB has to do with the coupling between the lateral and axial displacement, as indicated by the strain relationship in Equation (2.58). Perhaps a better explanation of this coupling can be described in the same way as it was by Wilson and Heisig [47], with the aid of Figure 6.11. The illustration shows an idealized drillstring that is fixed at the top, and free at the bottom. As the middle of the drillstring moves from the center of the figure, towards the left, the axial position of Point B moves upwards towards Point C. As the string is then moved back towards the center, Point C moves back to its original position at point B. For the string to make one complete lateral displacement cycle, the center of the string must then move to the right and then back towards its original position in the center of the figure. Thus, for every one cycle of lateral displacement, the drillstring will undergo two cycles of axial displacement. This coupling should result in an axial excitation that is twice the frequency of the lateral excitation.

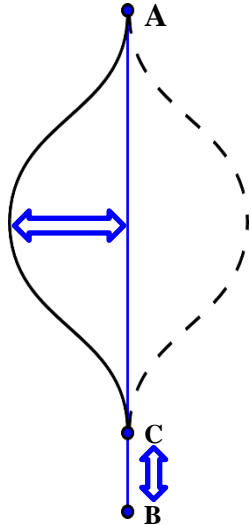


Figure 6.11: Axial Shortening of the Drillstring due to Lateral Displacement (From [47])

This fluctuating WOB can more easily be seen in Figure 6.12, where the plot has been enlarged near an excitation frequency of 1.8 Hz. The figure shows a sinusoidal component to the WOB which has an amplitude of roughly $\pm 150 \text{ lb}_f$, with additional oscillations occurring along the sinusoidal path having approximate amplitudes of 25-50 lb_f . It is suspected that these minor variations are a result of the power section excitation within the LET, however a different presentation of the data is required to validate this. This verification is achieved by generating a constant excitation frequency within the model in order to

observe the steady-state behavior of the nonlinear system. The results of such an excitation, at 1.8 Hz, are shown in Figure 6.13. Here, it can be seen that the steady-state response is shown to occur after about 30 seconds, where a dynamic WOB is still prevalent with an amplitude at around 100 lb_f. The slight reduction in the dynamic WOB value is due to the drillstring operating in a steady-state manner, as opposed to the purely transient behavior in the original simulation. It is unclear exactly how this dynamic WOB will impact the overall ROP, but it certainly suggests that the LET is affecting the axial force transfer to the bit, albeit not in the way that was originally intended. It can be noted that this dynamic WOB effect is being achieved with minimal g-loading on the LET.

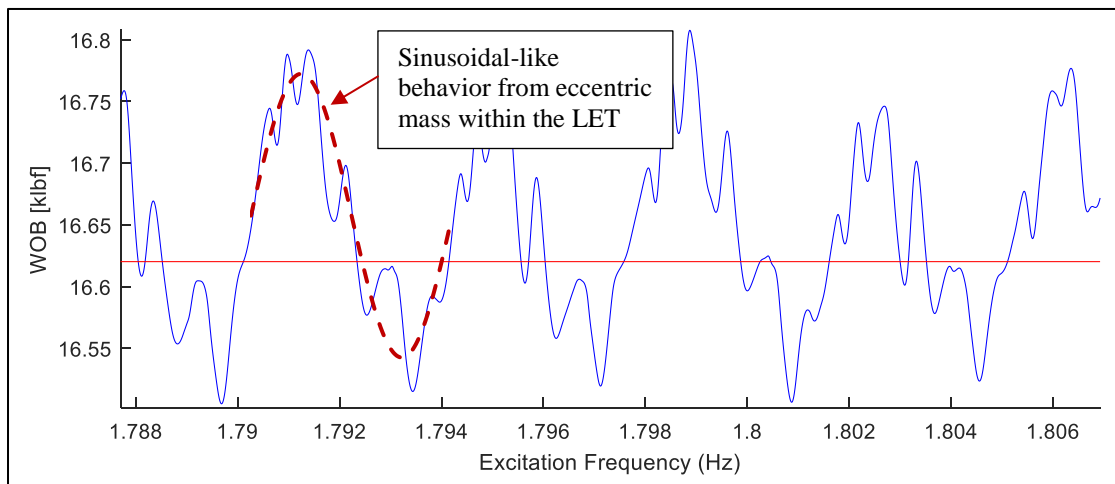


Figure 6.12: WOB Fluctuation in Original Assembly, near 1.8 Hz Excitation Frequency

The WOB data from Figure 6.13 can be enlarged to verify the source(s) of the dynamic axial force. Figure 6.14 and Figure 6.15 show the time between peaks, or the period, of the WOB fluctuations throughout the simulation. Figure 6.14 shows the time-stamps of one cycle of the primary (larger) WOB fluctuation; noting that the frequency is equal to the inverse of the period of oscillation, this excitation frequency can be calculated to be about 3.6 Hz (see (6.2) below), which is twice the frequency of the lateral excitation provided from the eccentric mass in the LET. Thus, the primary cause of the dynamic WOB from the LET excitation is proven to be the axial-lateral coupling of the drillstring displacement.

$$f_{axial} = \frac{1}{T} = \frac{1}{40.94 - 40.66} = 3.57143 \text{ Hz} \approx 3.6 \text{ Hz} = 2(1.8 \text{ Hz}) \quad (6.2)$$

Additionally, a similar calculation can be done for the minor WOB fluctuations, which are called out in Figure 6.15. From the data, these less prominent fluctuations occur at 25 Hz, which is roughly twice the

excitation frequency from the LET's power section when the eccentric mass is operating at 1.8 Hz. This can be seen in equation (6.3).

$$f_{axial} = \frac{1}{T} = \frac{1}{40.94 - 40.9} = 25 \text{ Hz} \approx 25.2 \text{ Hz} = 2(12.6 \text{ Hz}) \quad (6.3)$$

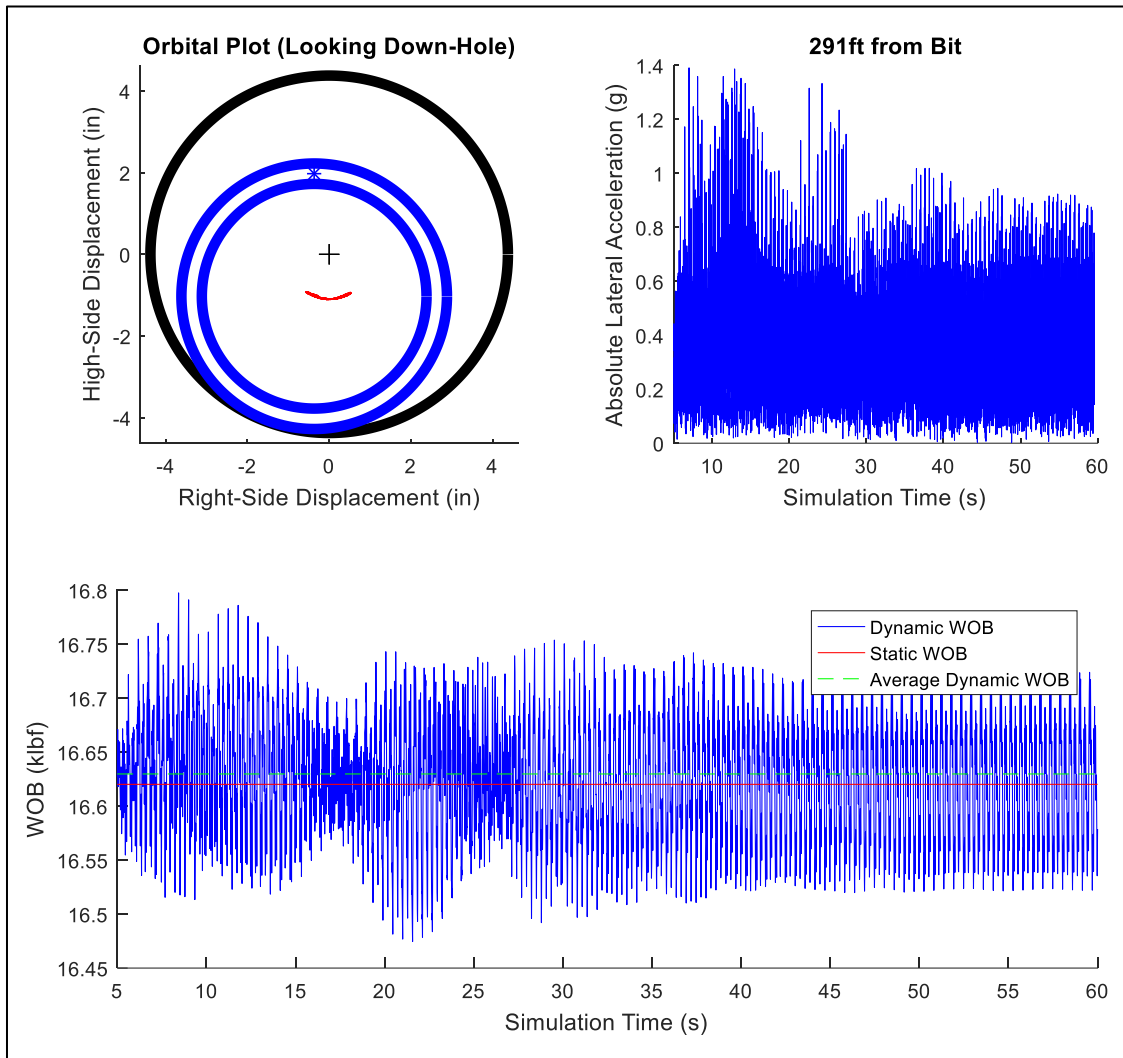


Figure 6.13: Results of Constant Excitation Frequency at 1.8 Hz

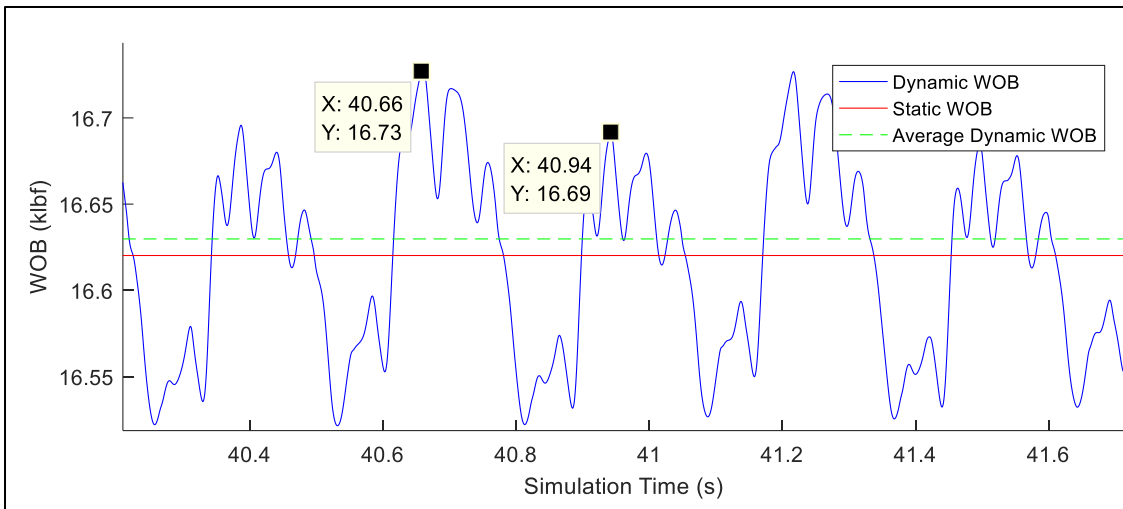


Figure 6.14: Time Stamps of Primary Excitation in WOB Data for 1.8 Hz Excitation Frequency

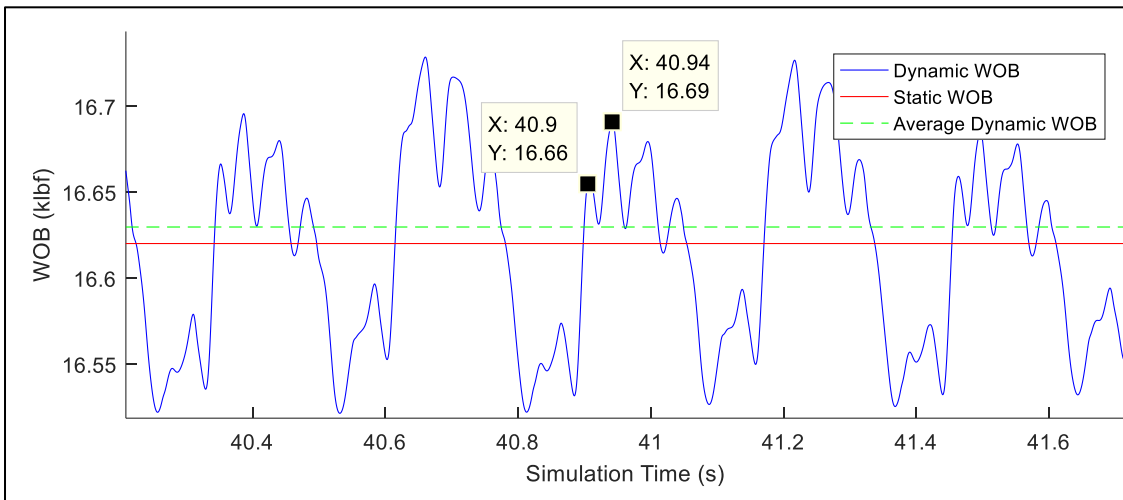


Figure 6.15: Time Stamps of Secondary Excitation in WOB Data for 1.8 Hz Excitation Frequency

Additionally, a slight increase in the average WOB is noticed for the case of a constant 1.8 Hz excitation frequency of the eccentric mass. While the benefit of such an insignificant gain in axial force transfer ($\approx +10$ lb_f) is likely to result in no noticeable benefits, it is interesting to note none the less. This actually suggests that the LET is reducing the frictional drag along the drillstring, although to a much lesser extent than was originally hoped for. Going back to the original simulation (Figure 6.6), while the excitation at 1.8 Hz did not provide a significant increase in the average WOB, further increasing the excitation frequency past 1.9 Hz actually showed a more prominent increase in the average WOB, which suggests a frequency dependence on the axial force transfer along the string. This trend is more visible in Figure 6.16, where the WOB has been enlarged over the 1.9-2.0 Hz region for the original simulation.

Based on the friction relationships (2.70)-(2.72), the only thing that should be contributing to this increase in WOB is a reduction in the friction coefficient due to induced rotational motion. However, when examining the axial and rotational velocity of the drillstring for the original simulation (Figure 6.17) and the constant 1.8 Hz excitation simulation (Figure 6.18), at the LET, the change in both values is so small that it would be unlikely to result in any significant change in the friction coefficient. Additionally, even under quasi-static conditions ($\text{ROP} = 50 \text{ ft/hr}$, $\text{RPM} = 0$, slip velocity $\approx 0.014 \text{ ft/s}$), the friction coefficient is only 0.22. This means that the friction coefficient function is on the left side of the peak in Figure 2.4, which indicates that an increase in slip velocity should only further increase the friction coefficient. Therefore, if the LET was affecting the drillstring as it was originally thought to, then there should have been a decrease in the WOB at a resonant frequency of the drillstring; clearly, there is another mechanism at play which is leading to this increase in average dynamic WOB. This becomes clearer through an observation of a summation of the contact (normal) forces along the drillstring. This value is shown to change significantly over the course of a simulation. Figure 6.19-Figure 6.21 show the summation value of all of the contact forces along the drillstring, as a function of time, for the original simulation case (Figure 6.6). The contact forces do not fluctuate to a great degree until the eccentric mass approaches an excitation frequency of 1.8 Hz. The minor variations at the lower frequencies are due to the drillstring rocking back and forth in the wellbore; as the assembly goes through this motion, the normal contact force is reduced to a minimum every time it “climbs” up the side of the wellbore and is a maximum as it swings down to the low-side of the hole, resulting in the dynamic value shown in Figure 6.19. As can be seen in Figure 6.20, this lower-frequency contact force is relatively smooth and indicates little to no impact loading on the drillstring.

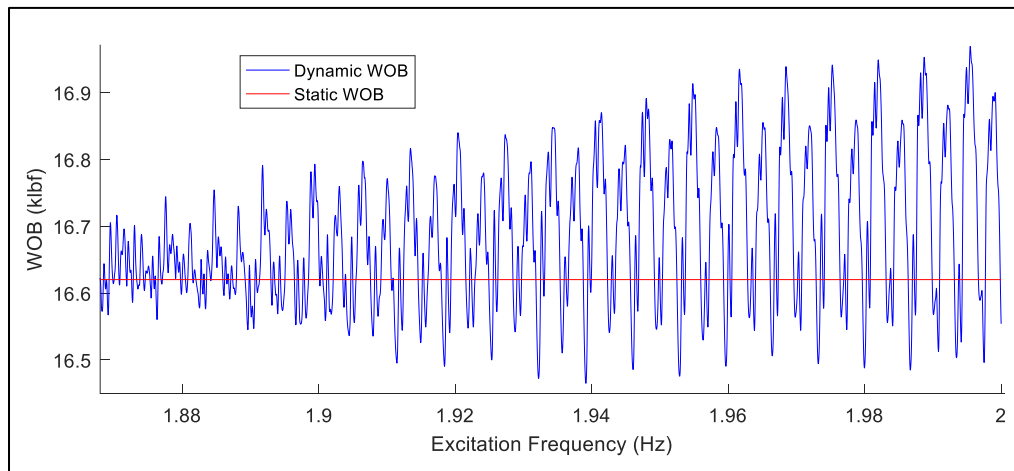


Figure 6.16: WOB Fluctuations near 1.9-2.0 Hz Excitation Frequency for Original Simulation

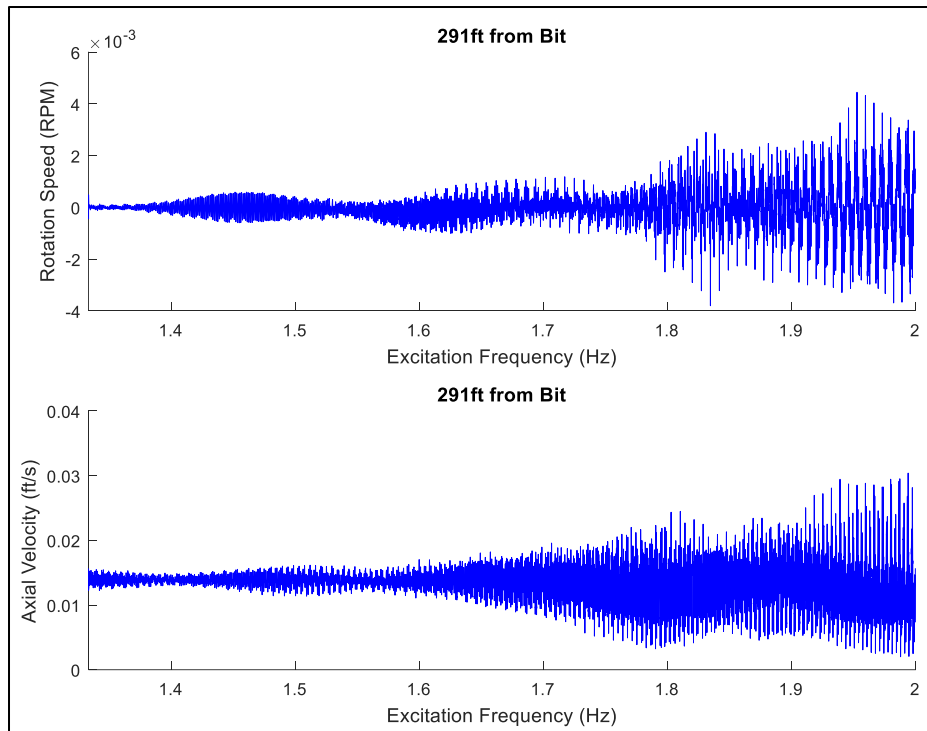


Figure 6.17: Axial and Rotational Velocities from Original Simulation

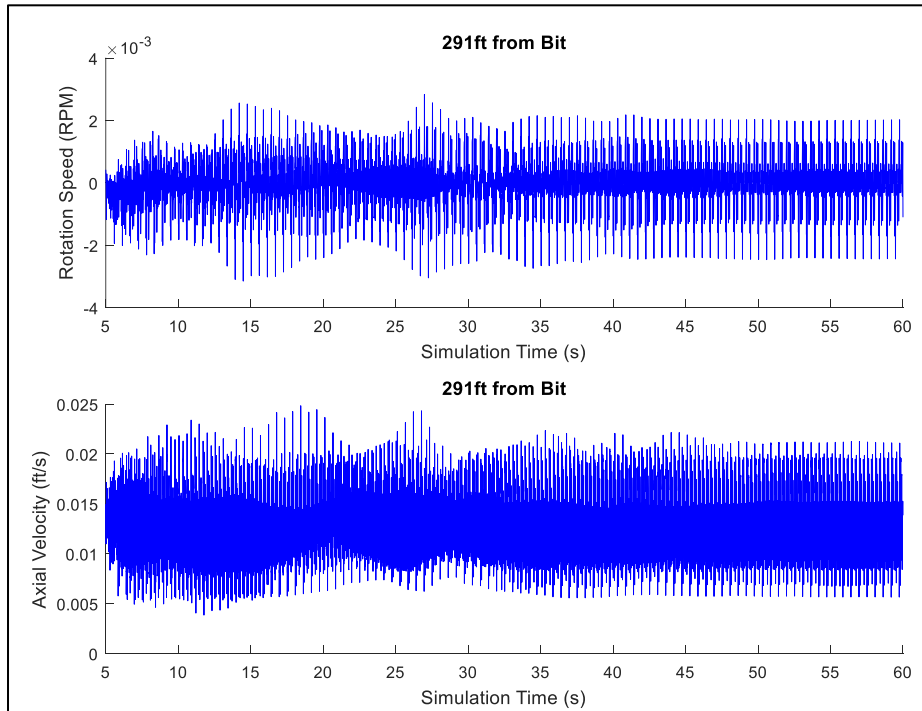


Figure 6.18: Axial and Rotational Velocities from Constant Frequency Simulation (1.8 Hz)

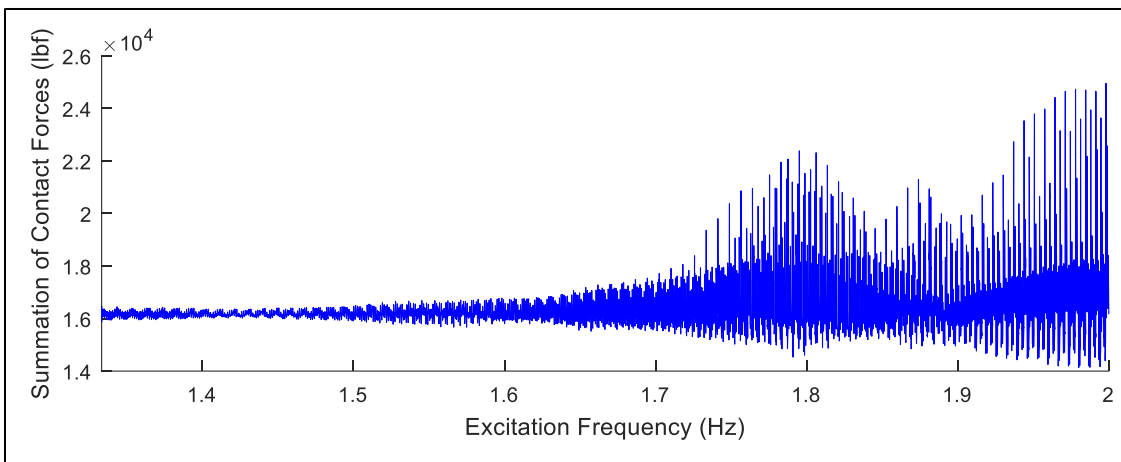


Figure 6.19: Summation of Contact Forces for Original Simulation

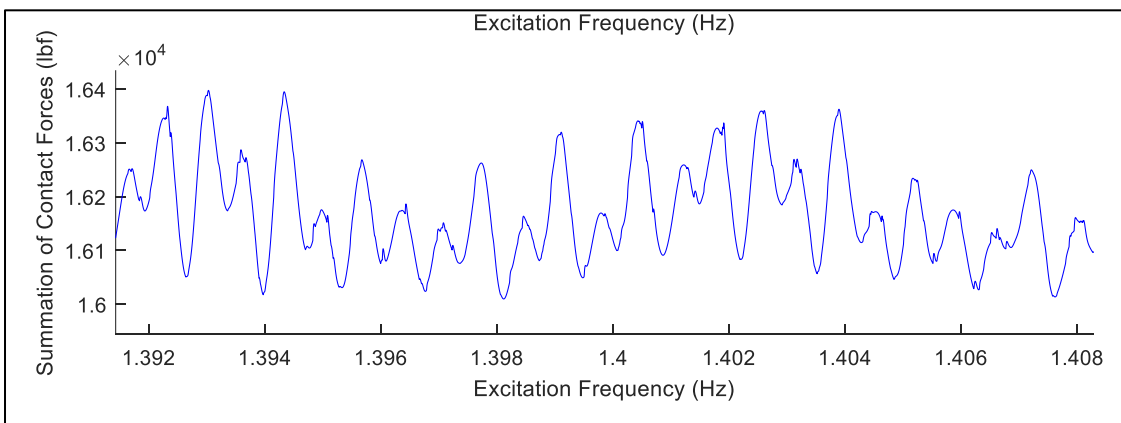


Figure 6.20: Summation of Contact Forces for Original Simulation, near 1.4 Hz Excitation

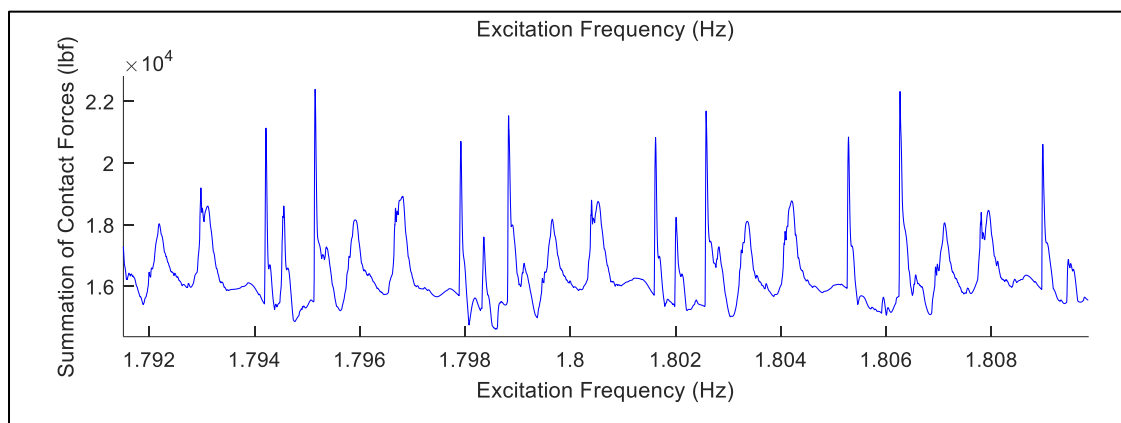


Figure 6.21: Summation of Contact Forces for Original Simulation, near 1.8 Hz Excitation

Figure 6.21 shows the summation of the contact forces along the drillstring as the excitation frequency is increased through 1.8 Hz. This graph indicates sharper, more prominent, peaks as compared to the data in the 1.4 Hz range. These peak values are a result of impacts with the wellbore wall. Intuitively it may seem that the larger contact forces due to impact would increase the frictional drag, but these forces are only momentary and thus would not provide a drastic decrease in the average WOB value. What is more important is that, in order for the impact loading to occur, contact points have to “lift-off” of the wellbore wall. This fact was apparent when conducting the nonlinear validation tests in Section 4 (Figure 4.30-Figure 4.32); the greater the “lift-off”, the greater the resulting impact load. If contact points separate from the wellbore then frictional resistance is temporarily removed from the system. Because the system is under compression, as the frictional resistance is removed, the drillstring will move slightly forward in the wellbore. This “inch-worming” effectively increases the amount of axial force that is transferred to the bit. This trend is also apparent for the constant 1.8 Hz excitation, as can be seen in Figure 6.22. Here, it can be noticed that the periodic spikes in the contact summation are of a slightly lesser value than the original simulation near 1.8 Hz, which again is due to the steady-state nature of the constant frequency excitation.

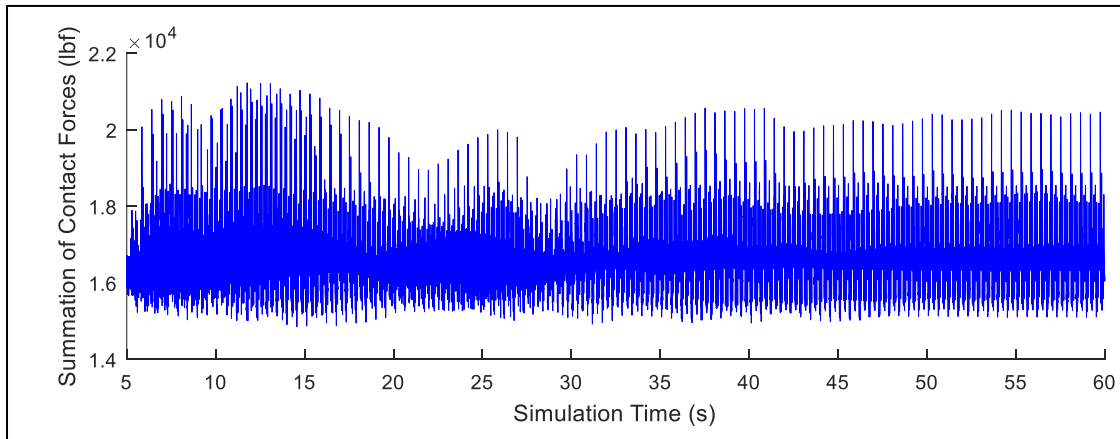


Figure 6.22: Summation of Contact Forces for Constant Excitation Simulation (1.8 Hz)

The manner in which the average dynamic WOB is increased (“inch-worming”) suggests that the specific friction model should not greatly affect the general behavior of the drillstring when subjected to induced lateral vibrations. Therefore, if the friction coefficient in the model is adjusted such that μ_o , in equations (2.70) and (2.71), is a constant value, then this should not change the overall WOB behavior. This conclusion is validated by the results depicted in Figure 6.23. Here the original excitation history is applied (Figure 6.5), using the same simulation parameters, except with the adjusted friction model. It should be noted that the quasi-static friction value for this case is the full static value from the original friction model ($\mu_o = \mu_s = 0.365$). Clearly this is a larger value than the original simulation and ultimately results in a lower value of

the quasi-static WOB ($14,360 \text{ lb}_f$), however it is apparent from the figure that a very similar resonant behavior is present, with peaks in the lateral acceleration and the WOB occurring at 1.8 and 1.9 Hz. Additionally, a slight increase in the average WOB is noticed within the 1.8 Hz frequency range and a larger increase is seen past 1.9 Hz; this was a very similar behavior to what was noted for the simulations using the original friction model. The only real difference between the two is that the adjusted friction model appears to increase the effect of the LET, with a dynamic WOB amplitude of around $\pm 500 \text{ lb}_f$. However, this is a result of the larger friction coefficient and is not a consequence of the difference in the two friction models; a higher friction coefficient results in more lateral displacement (see Figure 2.2), which results in larger axial displacement fluctuations, and ultimately larger WOB variations.

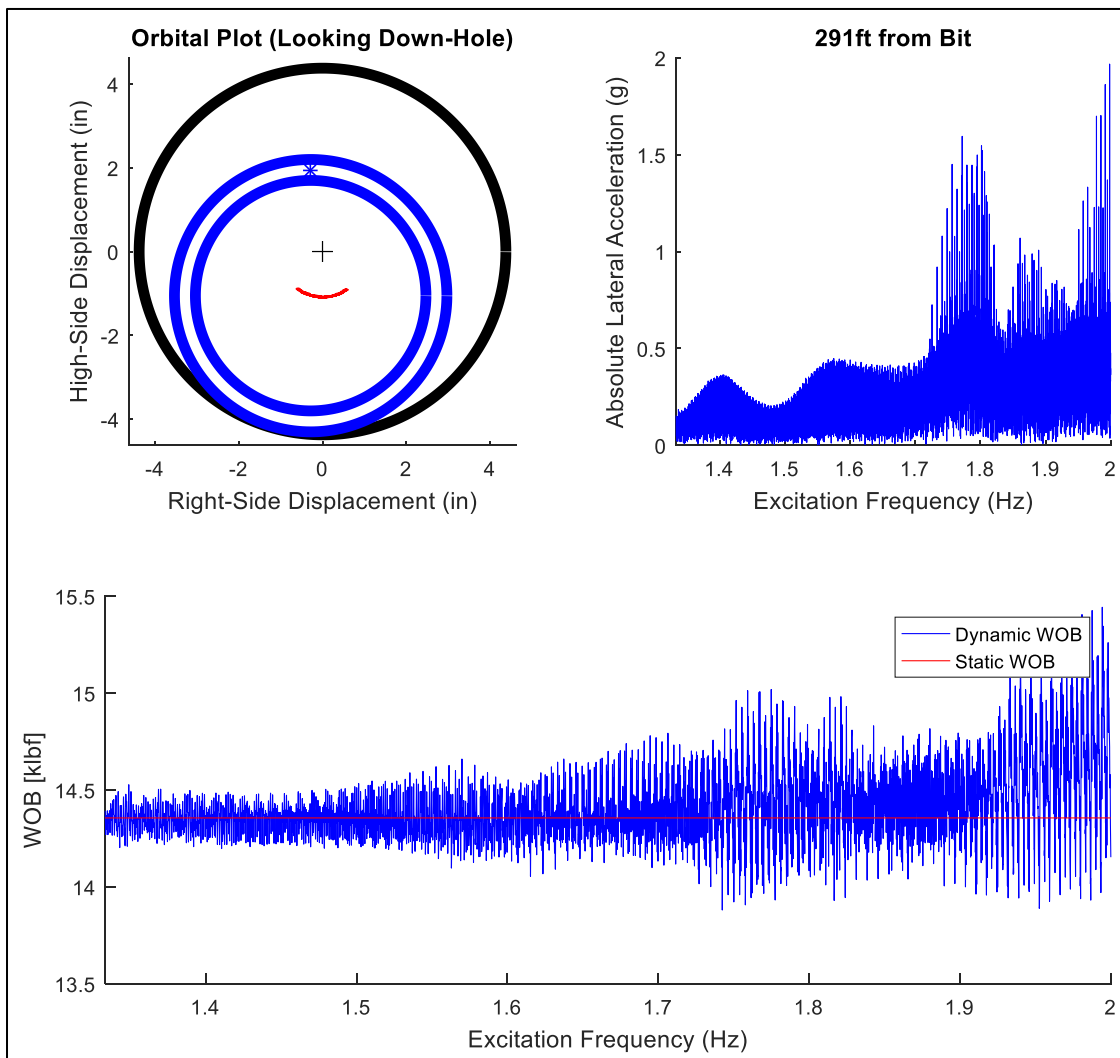


Figure 6.23: Results of Simulation with Alternative Friction Model

At this point it would seem, from the initial two simulation cases, lateral vibration tools do not necessarily “reduce friction”, but provide a dynamic WOB component and allow the drillstring to “inch-worm” itself along the wellbore. This action could potentially assist in working past “stuck points” or ledges in the well, which would give the impression of a reduced friction coefficient during operation. It was also apparent that increasing the excitation frequency above the 1.9 Hz range more definitively increased the average WOB. Therefore, simulations are conducted for a constant excitation frequency at both 1.9 Hz and 2.0 Hz in order to better understand this behavior.

Figure 6.24 displays the results for the case of a constant 1.9 Hz excitation from the eccentric mass within the LET. The lateral acceleration response appears to be slightly smaller than the case of a constant 1.8 Hz excitation, which was also indicated by the results in Figure 6.6. However, it can be pointed out that, according to the linearized forced-frequency response in Figure 6.3, the largest response should have occurred at 1.9 Hz. The differences between the linearized response and the nonlinear response is attributed to the contact/impact behavior, which cannot be predicted within the linearized analysis, as well as the specific monitoring point for the nonlinear simulations; at 291ft from the bit there is more lateral movement at 1.8 Hz, as compared to 1.9 Hz. Had the measurement point been moved closer to 300 ft, it is likely that the maximum lateral acceleration would have been seen at 1.9 Hz.. The average WOB is shown to be about +60 lbf above the quasi-static value, which is still not a large amount but is more than the case of 10 lbf for the 1.8 Hz excitation. Again, because the axial and rotational velocities are relatively small (Figure 6.25), the increase in WOB is coming from the lift-off behavior of the drillstring. However, the summation of the contact forces for the constant 1.9 Hz excitation (Figure 6.25) is about the same as it was for the case of a contact 1.8 Hz excitation (Figure 6.22). This suggests that the portion of the LET/drillstring that is lifting off of the wellbore wall is not necessarily getting more separation distance from the wellbore, which would have resulted in higher impact forces, but just more of the LET/drillstring is being affected and losing contact with the wellbore. This would make sense due to the fact that the excitation force is around 11% higher for the case of 1.9 Hz excitation, as can be understood from equation (5.3). It is also noticed that the 1.9 Hz excitation provides a dynamic WOB component of approximately +/- 130/170 lbf, which is slightly larger than the 1.8 Hz excitation case. The dynamic WOB magnitude has a larger negative component due to the high impact forces. However, as already discussed, these impact forces are “short-lived” and thus do not provide a strong resistance to axial force transfer over extended periods of time. Therefore, the average WOB increased from the quasi-static value.

When further increasing the excitation frequency of the eccentric mass to 2.0 Hz, as shown in Figure 6.26, the average WOB is even further increased to 150 lbf above the static value. This is likely a combination of larger separation from the wellbore, indicated by the larger contact force summations in Figure 6.27, and

the fact that the excitation force grows another 11%, as compared to the 1.9 Hz excitation force, which may be affecting more of the LET/drillstring. Additionally, the displacement pattern in the 1.9-2.0 Hz range (see Figure 6.10) has a larger maximum lateral movement than the case of 1.8 Hz. This larger displacement may be greatly effecting the “lift-off” dynamics of the drillstring. The dynamic WOB component during this excitation is +/- 260/320. Again, the larger negative component is due to the impact loading which is a “short-lived” occurrence, and therefore contributes less to the average behavior. The 2.0 Hz excitation also generates the most severe acceleration response in the LET, with a maximum value between 2 and 2.5 gs, but these levels are still considered benign in the realm of drillstring dynamics.

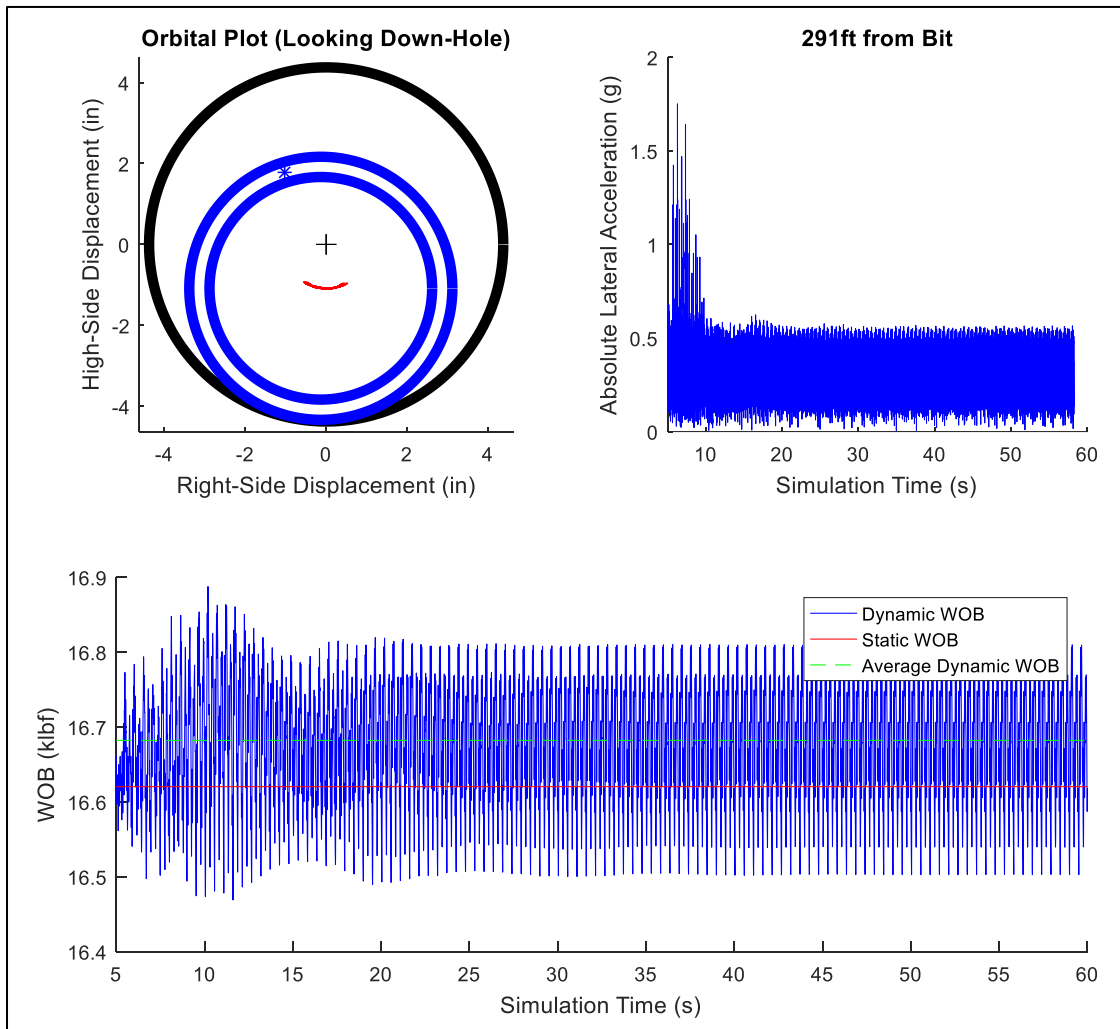


Figure 6.24: Results of Constant Excitation Frequency at 1.9 Hz

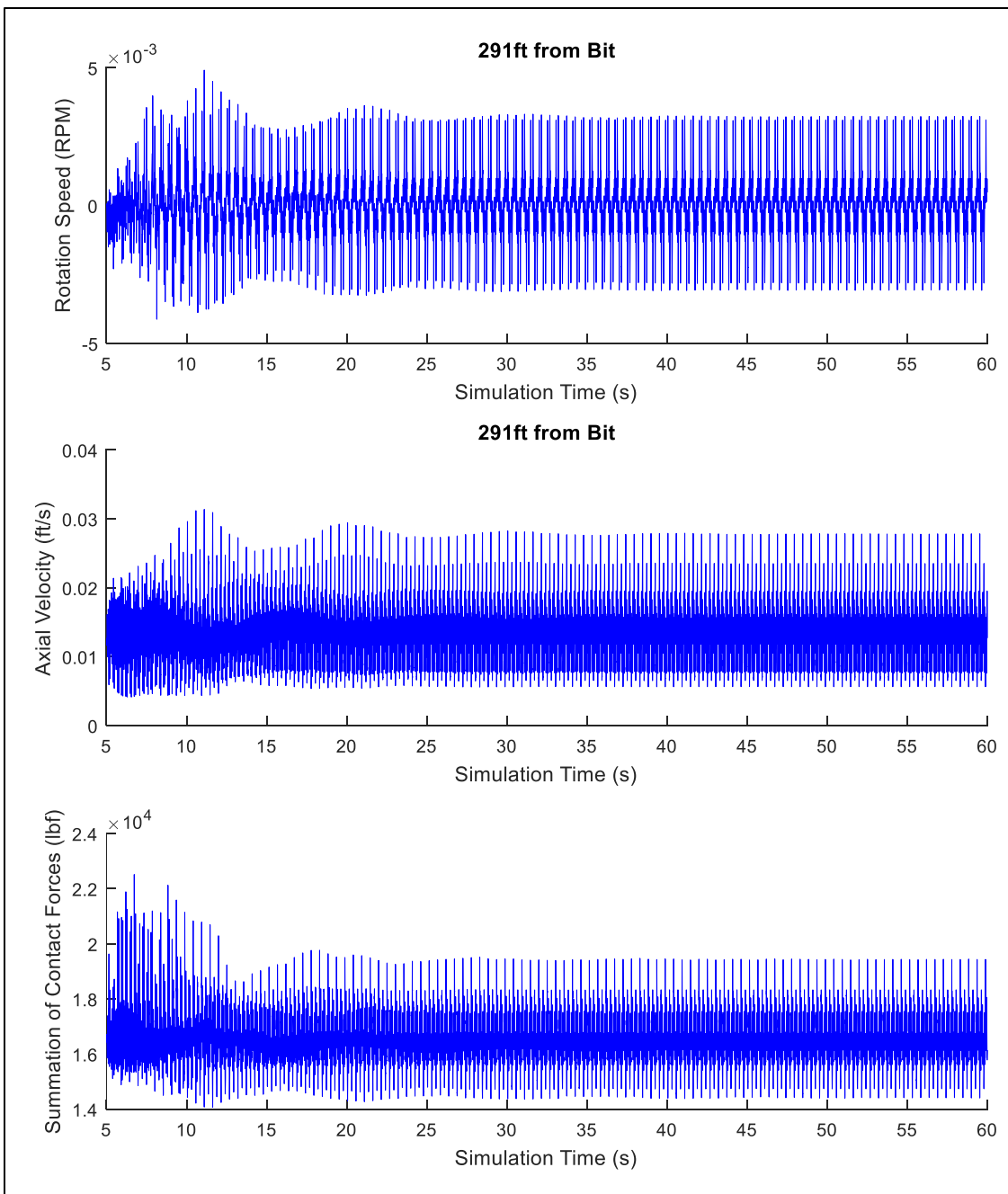


Figure 6.25: Axial and Rotational Velocities, and Summation of Contact Forces for Constant Excitation Simulation (1.9 Hz)

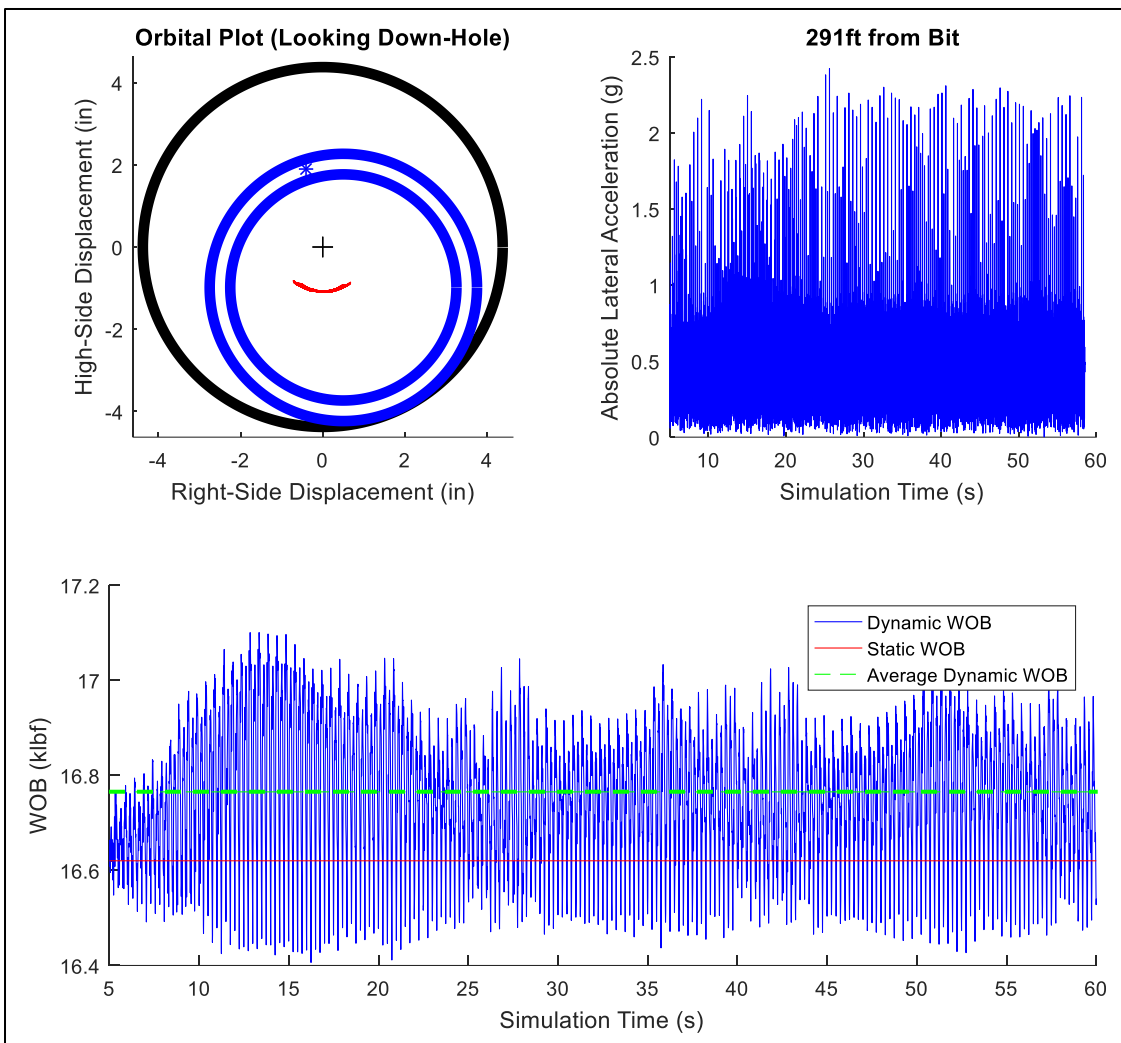


Figure 6.26: Results of Constant Excitation Frequency at 2.0 Hz

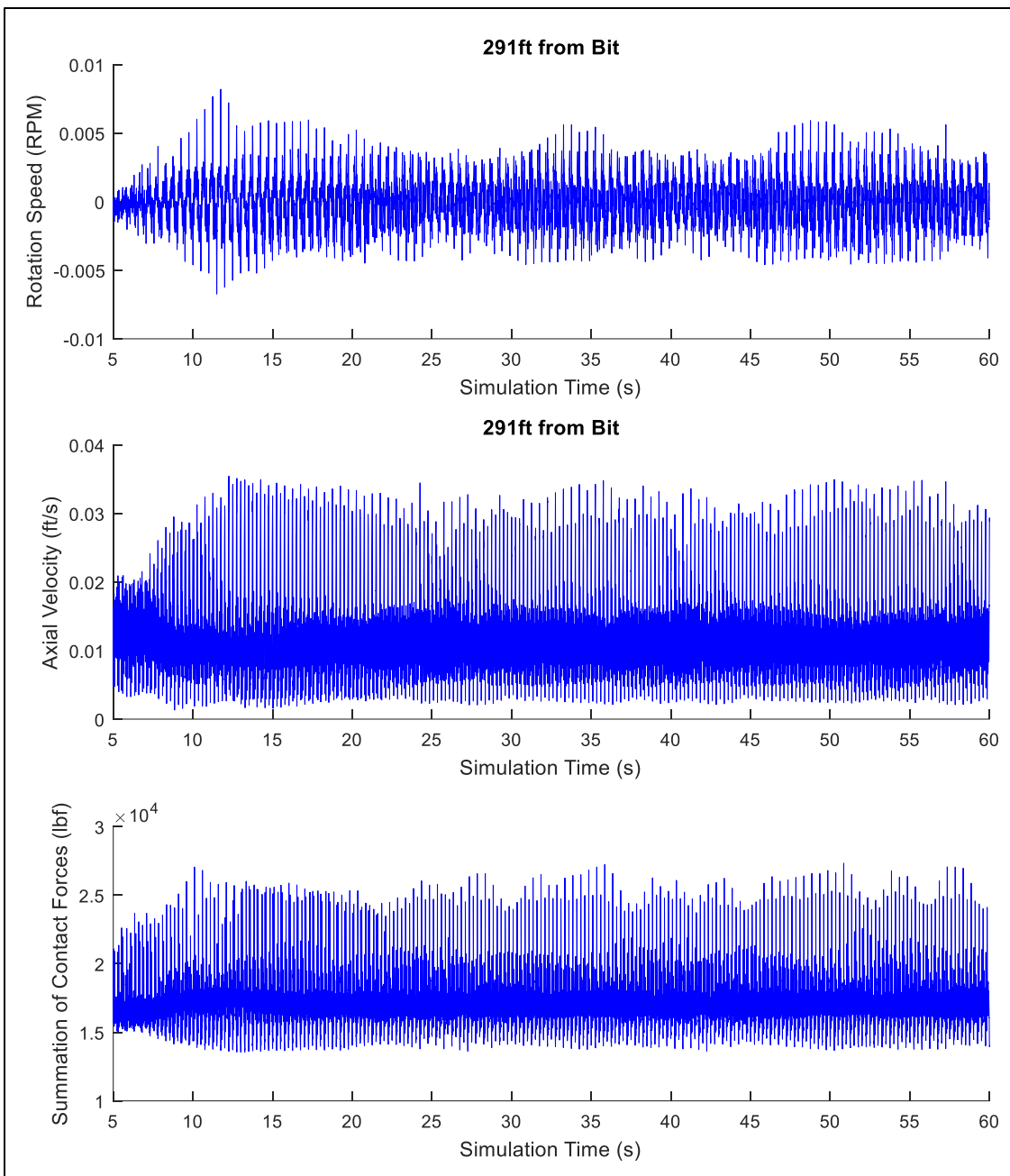


Figure 6.27: Axial and Rotational Velocities, and Summation of Contact Forces for Constant Excitation Simulation (2.0Hz)

6.2.2 Simulations with Fluid Damping

The previous section examined the nonlinear dynamics of the drillstring while ignoring the dissipative effects of the drilling fluid; this is a naive way of thinking about the system, but allows for a fundamental understanding of its behavior. In order to better understand how well the previous simulations represent the “down-hole reality”, the effects of fluid damping are considered. The fluid force model used here is described in Sections 2.4 and 3.2.3.3. Again it should be iterated, that this fluid-damping model is not meant to be a definitive solution to the “fluid-drillstring interaction problem”; it is merely suggested as a possibility that aids in the understanding of what potential factors could contribute to the overall dynamics of the system.

Figure 6.28 shows the results of the original simulation, with the inclusion of the fluid damping model. It is immediately apparent that the average dynamic WOB is smaller than the quasi-static value, which is due to the axial fluid force terms represented by (2.75) and (3.37). This force, which is dependent on fluid flow and axial drillstring velocity, only acts on the outside of the drillstring and is always negative (away from the bit) due to the direction of the annular flow, which effectively reduces the WOB. This effect would likely be balanced by the internal fluid flow on the drillstring, which should be included in the model for a more complete description of the fluid forces acting on the drillstring. However, because the previous section illustrated the fact the induced axial velocity of the drillstring is relatively small, and thus would not contribute much to the axial fluid force term, both the internal and external axial forces due to fluid flow are neglected in the remainder of the simulations.

Apart from the reduction in average dynamic WOB, the results shown in Figure 6.28 have a rather similar trend to the original simulation case (Figure 6.6), with peak responses occurring at the frequencies predicted from the linearized analysis. The magnitudes at these resonant peaks, both in the lateral acceleration plots and the WOB plot, generally have smaller magnitudes due to the fluid-damping. The added fluid forces reduce the amount of lateral displacement in the drillstring and therefore lead to smaller axial displacements due to the coupling effect described earlier. Additionally, there is a less prominent separation between the response levels in the 1.8-2.0 Hz frequency ranges; this may suggest that there is a less strict requirement to achieve a target lateral resonant frequency, i.e. it may not be as important to excite the drillstring exactly at 1.8Hz if this was a target frequency based off of the linearized-dynamic modeling.

Figure 6.29-Figure 6.31 display the results of the constant-frequency-excitation simulations, with the inclusion of fluid damping, for excitation frequencies of 1.8 Hz, 1.9 Hz, and 2.0 Hz. For all cases, the results are quite similar to the simulations without fluid damping, with minor decreases in the response amplitudes. In general, the fluid forces generated as the drillstring moves around within the wellbore do not greatly alter

the response of the system. This, in turn, helps provide confidence in the analysis results presented in Section 5. Table 6.3 summarizes the comparison between the simulations with, and without, the inclusion of fluid damping. In general the fluid damping seems to reduce the level of impact between the drillstring and the wellbore wall, as evident from the smaller difference between positive and negative WOB fluctuations about the average dynamic value. Additionally, the fluid damping smooths the response at the bit; this can very clearly be seen in comparing the WOB between Figure 6.26 and Figure 6.31.

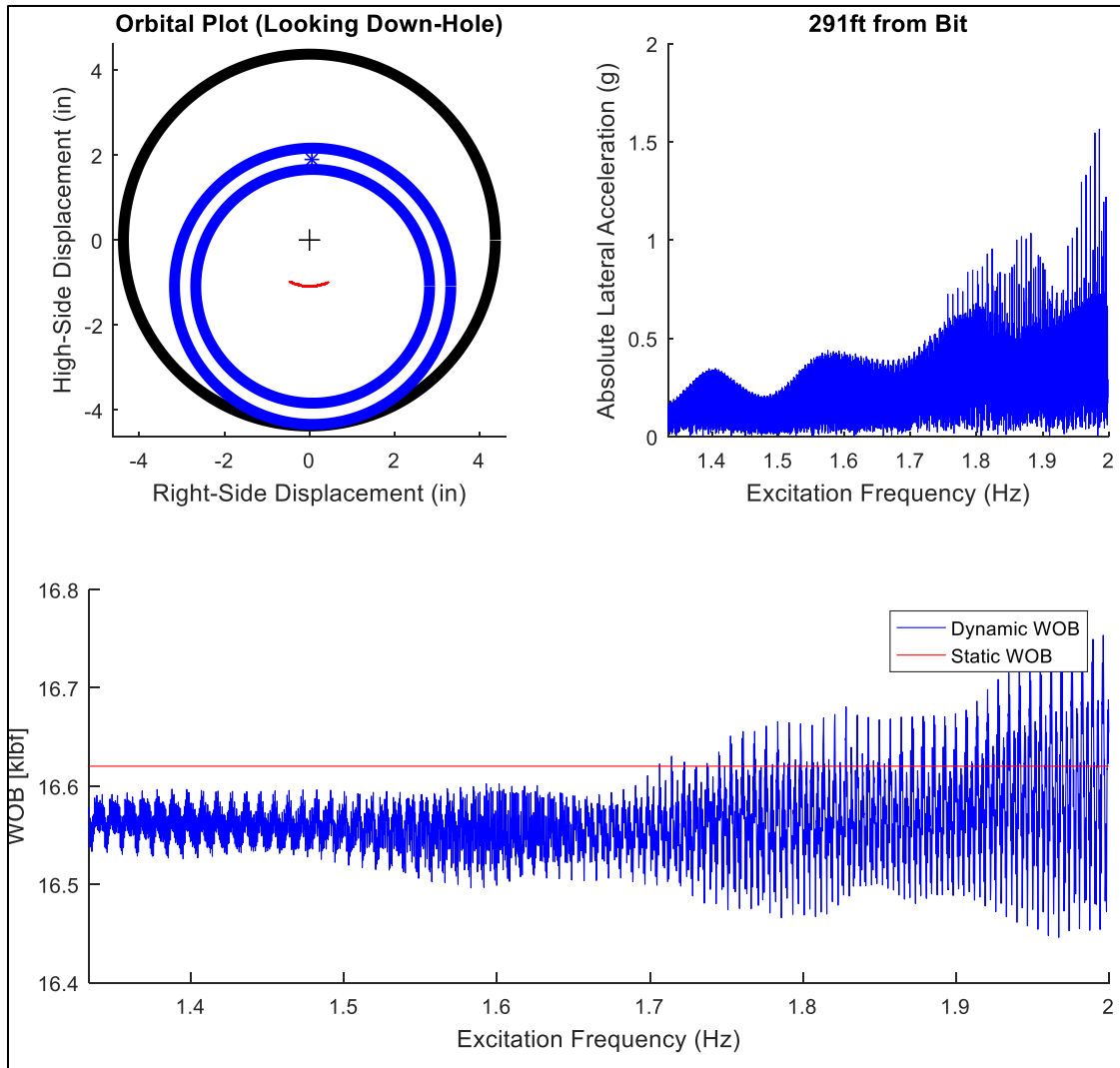


Figure 6.28: Original Simulation with Fluid Damping

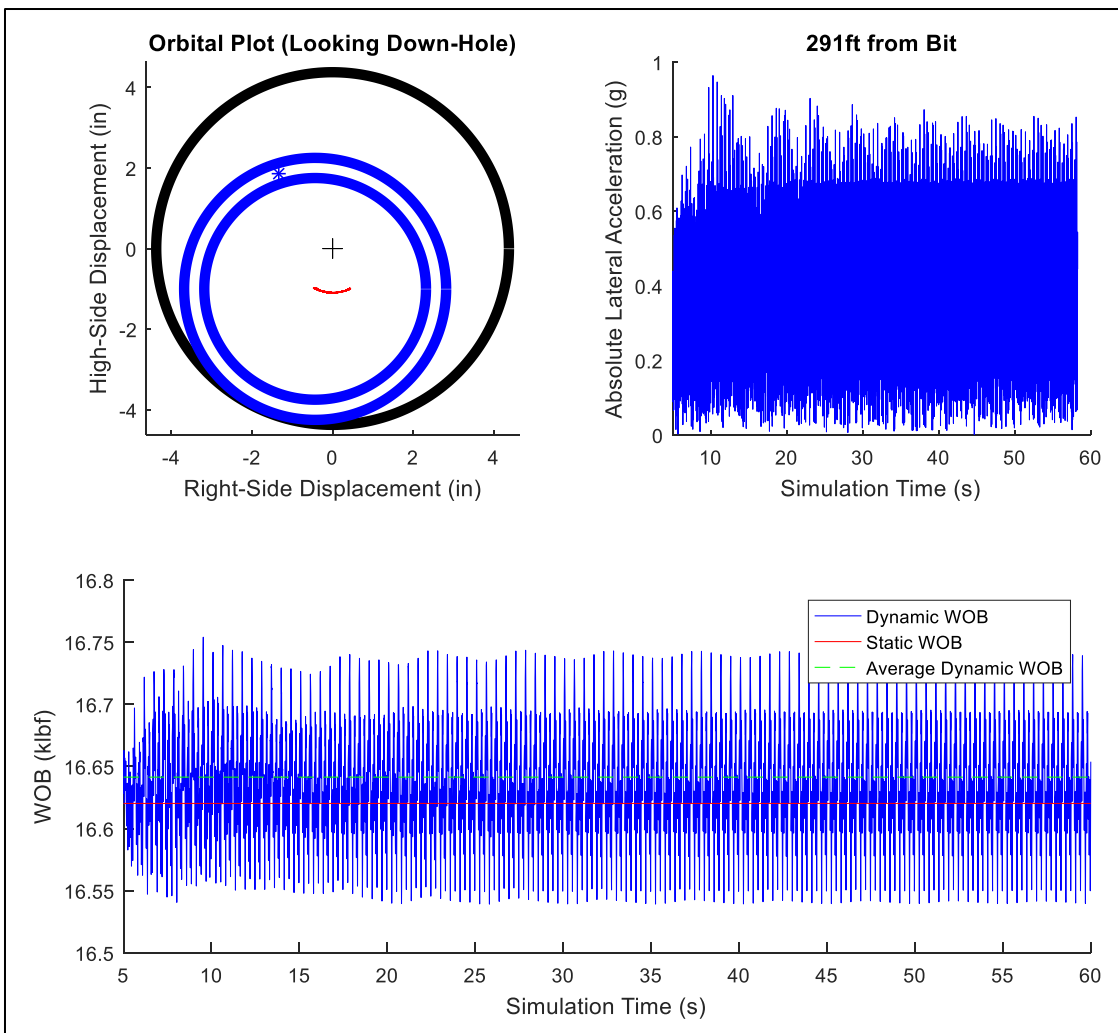


Figure 6.29: Results of Constant Excitation Frequency at 1.8 Hz, with Fluid Damping

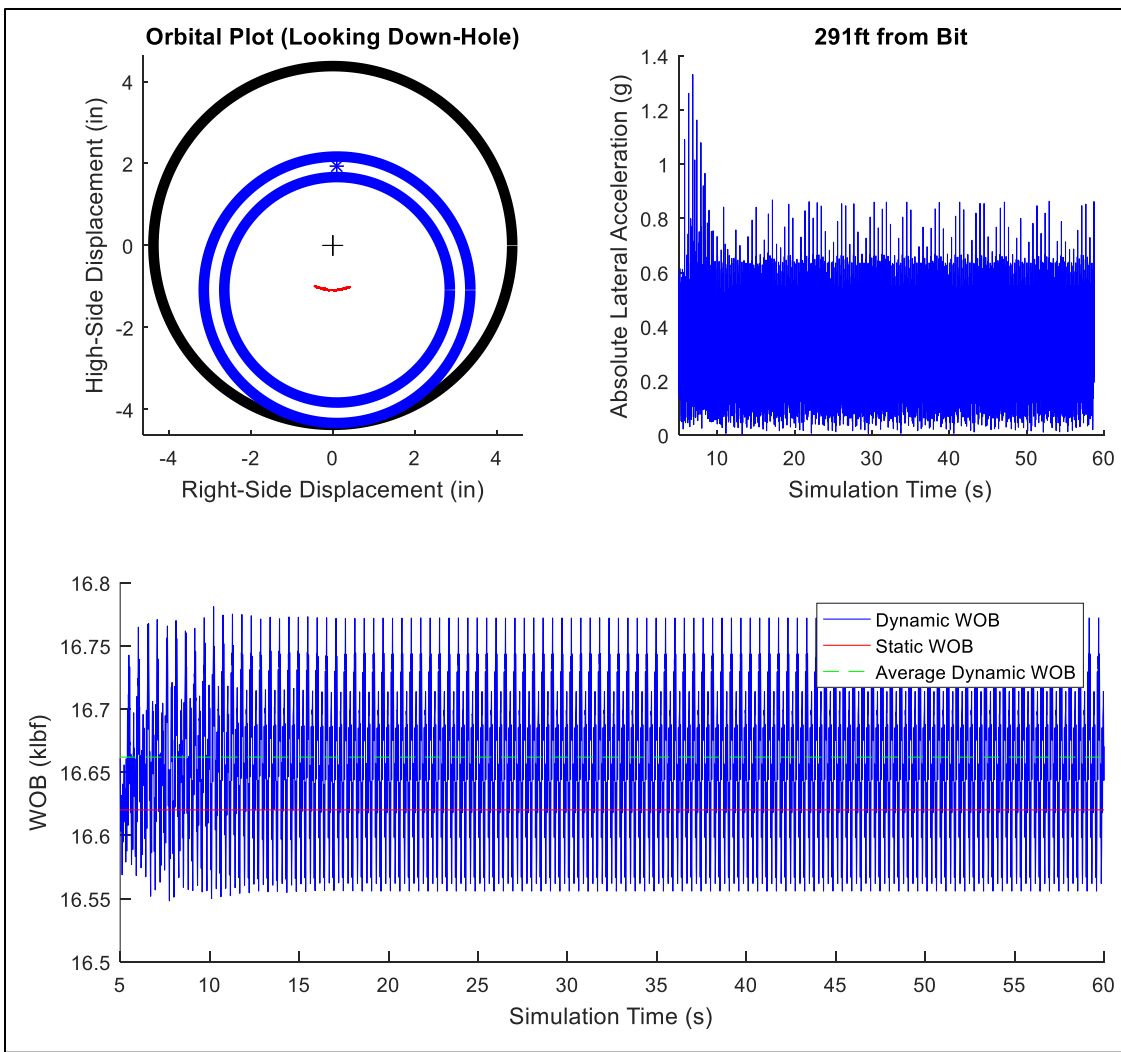


Figure 6.30: Results of Constant Excitation Frequency at 1.9 Hz, with Fluid Damping

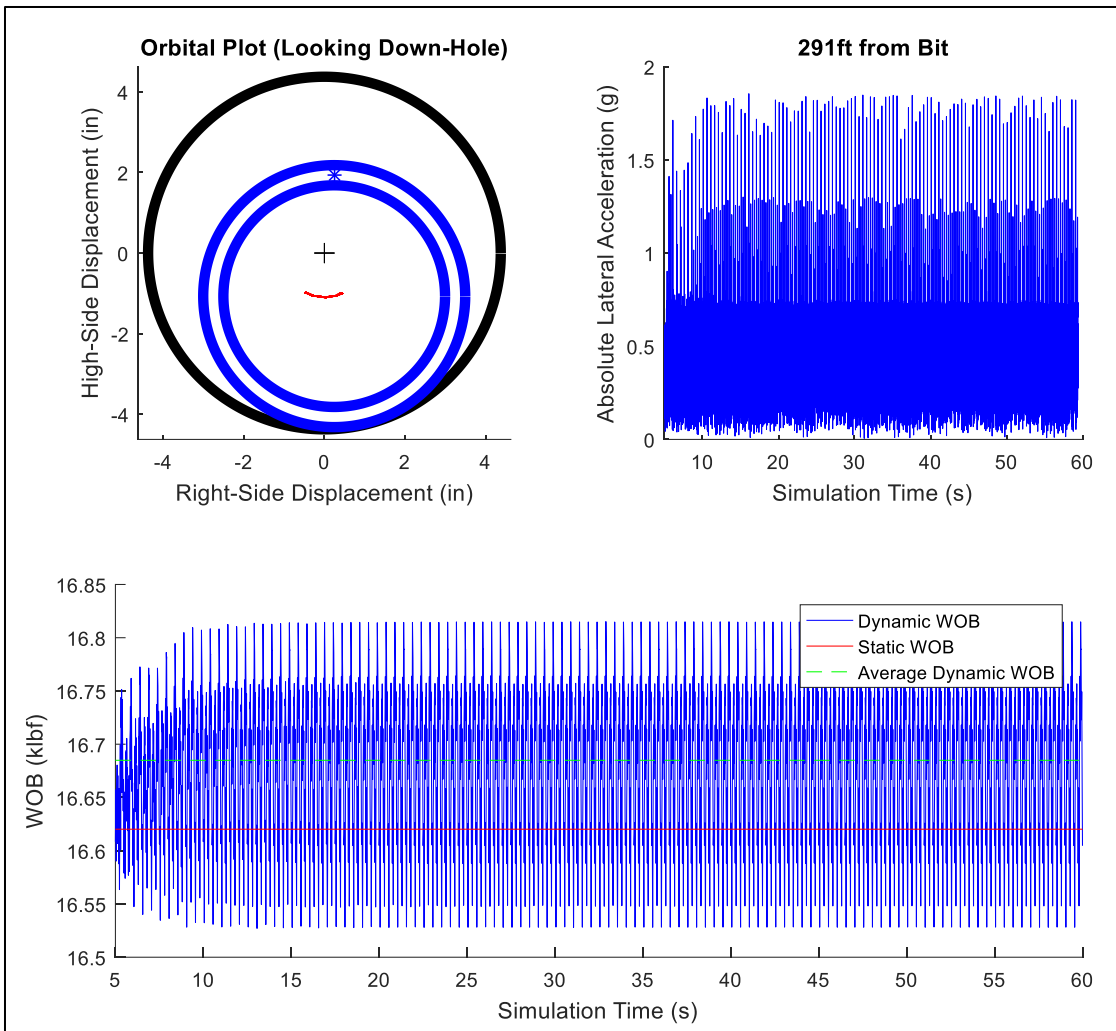


Figure 6.31: Results of Constant Excitation Frequency at 2.0 Hz, with Fluid Damping

Table 6.3: Comparison Summary of Simulations with, and without, Fluid Damping

Excitation Frequency (Hz)	No Fluid Damping		with Fluid Damping	
	Average WOB (klbf)	+/- (lb_f)	Average WOB (klbf)	+/- (lb_f)
1.8	16.63	90/100	16.64	100/100
1.9	16.68	130/180	16.66	110/100
2	16.77	250/320	16.68	130/150

6.2.3 Higher-Frequency Excitations

The previous simulations illustrated the behavior of a lateral excitation tool specifically designed for operation at the lowest predicted lateral resonance frequency of a drillstring. In general, the lowest lateral resonant frequency will be in the 1-3 Hz range for 8 ¾" Horizontal wells; this is fundamentally different than how other LETs have been designed to operate. Tools, like the one outlined by Thorpen and Sanders [3], usually generate a lateral excitation frequency between 10 and 30 Hz. This frequency spectrum, similar to axial excitation tools, is rather arbitrary and based on no scientific reasoning. In order to quantify how operation within this higher frequency range may differ from the lower frequency excitations presented here, a comparative analysis is performed.

To investigate the higher frequency excitation, again, thought must be given to how the excitation is generated within the tool. For a higher rotational speed of the eccentric mass within the LET, a higher output speed from the power section is required. Using a 1:2 lobe configuration power section (1.2 rev/gal), the rotating eccentric mass can produce a 12 Hz lateral excitation frequency at 600 gpm. It should also be kept in mind that, because there is only one lobe on this rotor, the power section will also generate a 12 Hz excitation based on equation (5.12). Thus, not only has the excitation frequency been greatly increased but, the length of the primary excitation source has been nearly doubled. Applying the excitation in the same manner as before (quickly ramping up the frequency for the first five seconds of the simulation, and then holding it constant), with fluid damping included in the model, the WOB response due to the 12 Hz excitation can be seen in Figure 6.32; note that the simulation cut off at 16 seconds due to memory limitations of the workstation on which the simulations were conducted.

The 12 Hz excitation frequency shows the most prominent gain in average WOB out of all the previous simulations, with an increase of 500 lb_f. While this is certainly a more significant increase than the 1.8 Hz case, it is still not a significant increase in comparison to the base WOB level ($\approx 3\%$ of quasi-static WOB). The dynamic WOB component is also the largest seen in the simulations with fluid damping, with a value of about +/- 170/150 lb_f (Figure 6.33). This is different than the previous simulations in that the WOB now goes higher above the average value, than it does in the opposite direction. This is most likely a consequence of the complex whirling motion taking place as a result of the excitation. This motion, which has been enlarged in Figure 6.34, keeps the LET off of the wellbore wall for the majority of the simulation; consequently, this also results in rather severe impact loading which is apparent in the large contact summation forces (Figure 6.35) and the resulting lateral acceleration shown in Figure 6.32. These acceleration levels, which are shown to be in the 40-50 g range, have the potential of causing excessive wear on the housing of the LET as well as the internal components of the tool. This level of dynamic loading also has the potential to result in damage to the borehole wall itself, which could cause hole-enlargements and

wellbore stability issues [147, 148]. Figure 6.35, again, reveals little to no real fluctuation in the rotational velocity during the 12 Hz excitation. However, there are a few larger spikes seen in the data as opposed to the previous simulation. This is direct result of the whirling, and induced impact behavior, seen in Figure 6.32; the large impact loads cause a brief “catch” on the LET as it impacts the wellbore wall, leading to a sudden change in the rotation of the tool.

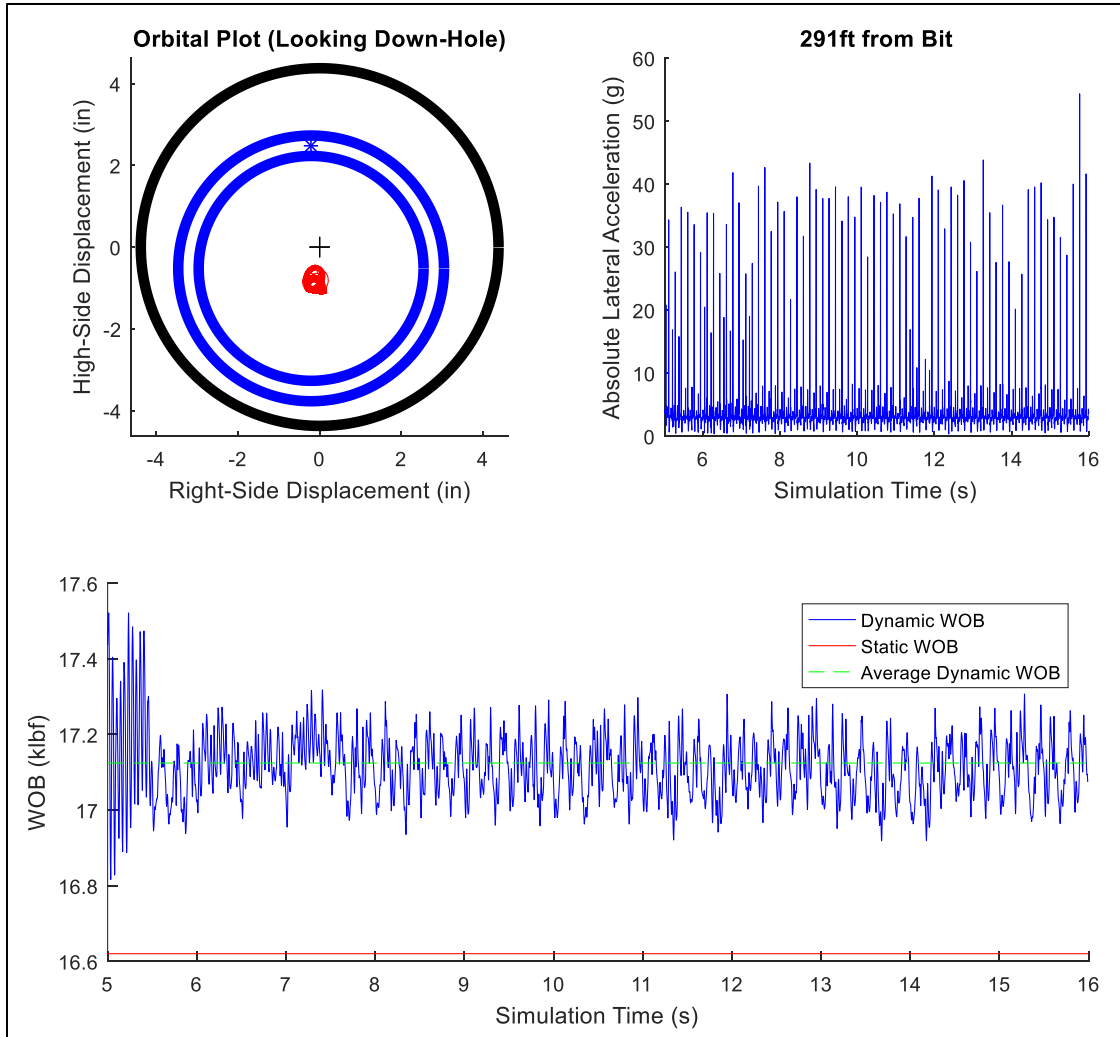


Figure 6.32: Results of Constant Excitation Frequency at 12 Hz, with Fluid Damping

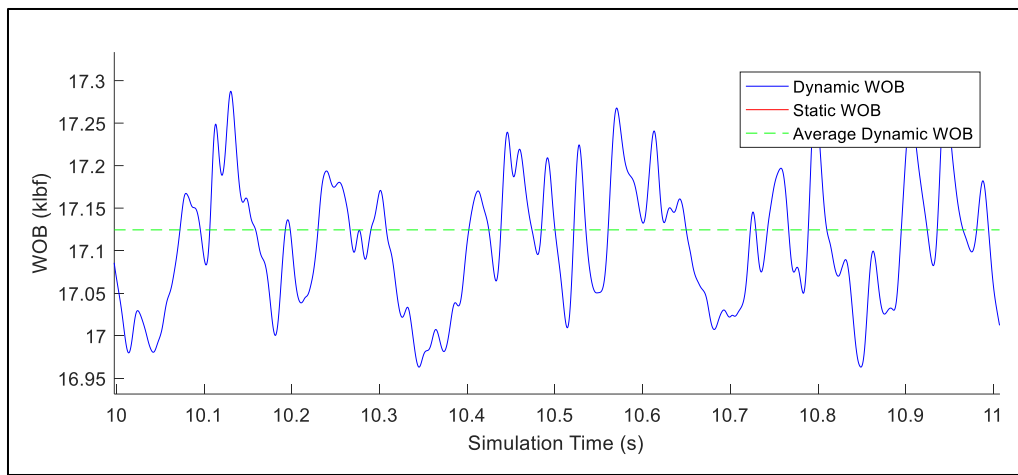


Figure 6.33: WOB Fluctuation of 12 Hz Excitation, between 10 and 11 Seconds Simulation Time

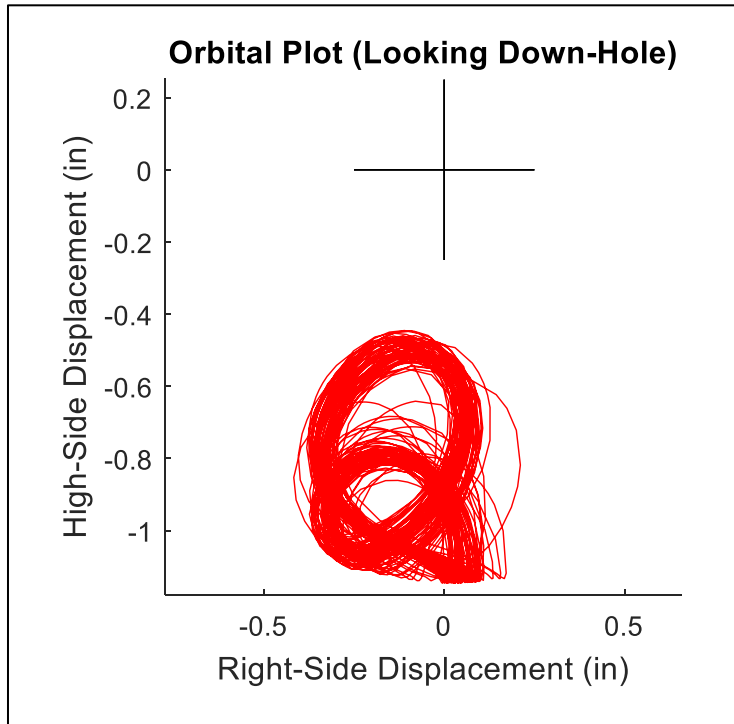


Figure 6.34: Orbital Displacement of Cross-Section for Constant Excitation (12 Hz) Simulation

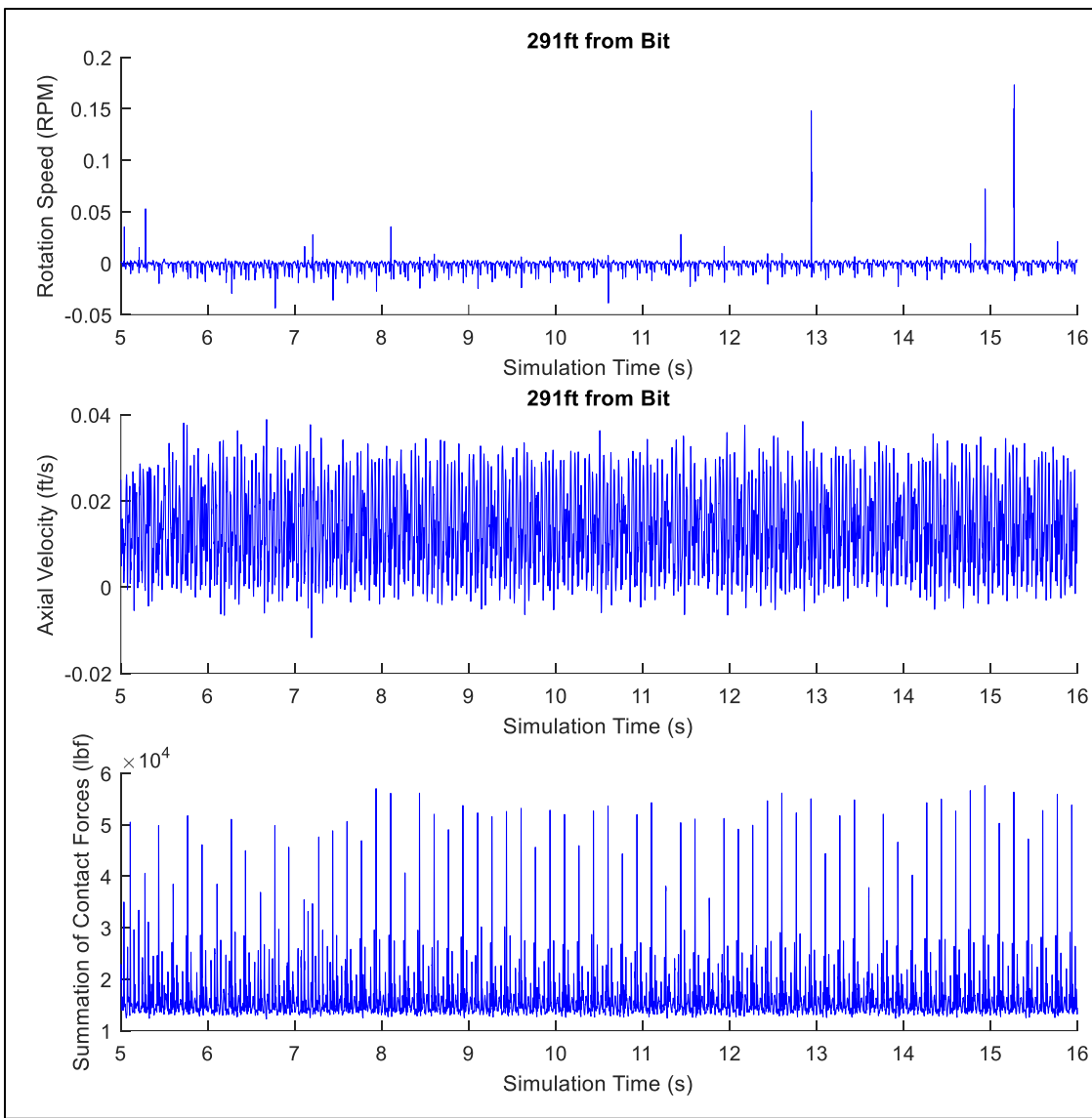


Figure 6.35: Axial and Rotational Velocities, and Summation of Contact Forces for Constant Excitation Simulation (12 Hz)

The results indicated in Figure 6.32-Figure 6.35 do not necessarily suggest that higher frequency excitations (10-30 Hz) are a poor frequency choice, but the excitation force generated from such a frequency range should be thoroughly considered before implementation. For example, at 1.8 Hz, the eccentric mass component of the LET being examined here generates an excitation force of about 8.35 lb_f/ft (note that 2 lb_m/in = 0.745944 slugs/ft, and 1 lb_f = 1 slug*ft/s²), as can be seen in Equation 6.4.

$$F_o = \left(0.7459 \frac{\text{slug}s}{\text{ft}}\right) \left(\frac{1.05 \text{ in}}{12 \frac{\text{in}}{\text{ft}}}\right) (2\pi 1.8)^2 = 8.35 \frac{\text{lb}_f}{\text{ft}} \quad (6.4)$$

This excitation force is about 15% of the weight of the eccentric mass section of the LET ($\approx 56 \text{ lb}_f/\text{ft}$); a moderate force to be generating. When the excitation frequency is increased to 12 Hz (6.5), this excitation force jumps to 371.05 lb_f/ft ; a 4,444 % increase from 1.8 Hz! Obviously, this is a rather dramatic excitation force in relation to the linear weight of the LET. Additionally, as mentioned before, because the eccentric mass is driven by a 1:2 lobe configuration power section, the primary excitation source has roughly doubled in length. Ultimately it seems as though the excitation force, and length, should be properly matched to the chosen excitation frequency so as to avoid harmful vibrations.

$$F_o = \left(0.7459 \frac{\text{slug}s}{\text{ft}}\right) \left(\frac{1.05 \text{ in}}{12 \frac{\text{in}}{\text{ft}}}\right) (2\pi 12)^2 = 371.05 \frac{\text{lb}_f}{\text{ft}} \quad (6.5)$$

6.2.4 Investigating Multiple LETs in the Drillstring

Due to the minimal increase in average WOB with the use of a single LET in the drillstring, it is worth exploring how multiple tools in the drillstring may impact the overall behavior of the system. Similar to the previous simulations, an initial forced-frequency calculation is shown in Figure 6.36 using roughly 1,000 ft of drill pipe. Again, all the same operational parameters were used and friction was omitted for the sake of the linearized calculation. Just as before, the response is identical to what it has been for the all of the calculations thus far, with the primary resonance peak occurring at 1.8 Hz, only now there are multiple peaks; one for each LET in the drillstring. With the same excitation history that was provided in Figure 6.5, a similar result to the original simulation (without fluid damping) can be seen in Figure 6.37 and Figure 6.38. (Note that the simulation terminates before it reaches 2 Hz due to memory limitations of the workstation used for the simulation studies.)

Intuition would suggest that two LETs should produce twice the effect. However, based on the WOB response in Figure 6.37, the overall effect on the WOB is actually about the same as it was for the case of using one LET in the string. This may suggest that the LET needs to be located within a certain distance from the bit in order to be effective, i.e. the WOB results depicted in Figure 6.37 may only be an effect of the LET that is closer to the bit, and the effect of the upper-most LET may be dissipated along the drillstring before it can reach the bit. Unfortunately, due to time constraints, further simulations could not be performed in order to verify this. The simulations contained within this section required between 1 and 2 weeks of CPU time on the workstation used for this study, with the simulation involving two LETs taking the longest to run.

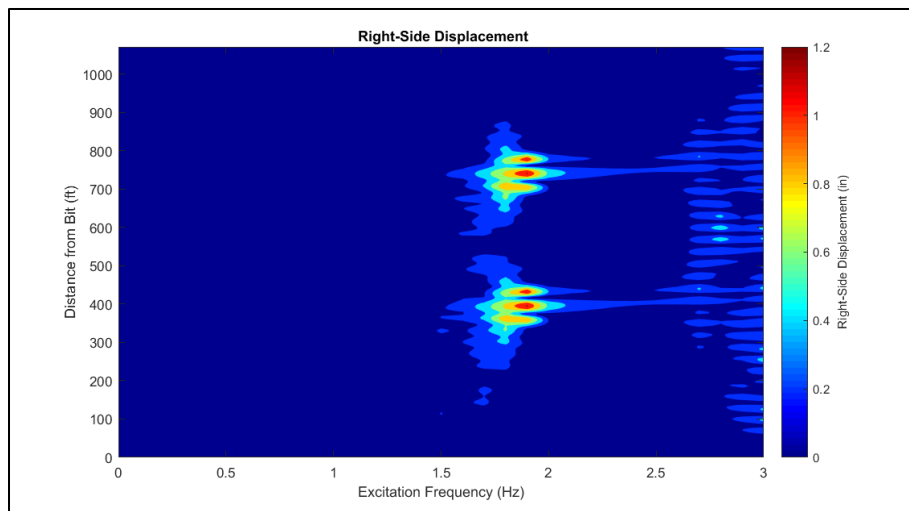


Figure 6.36: Forced-Frequency Response of Assembly with Multiple LETs

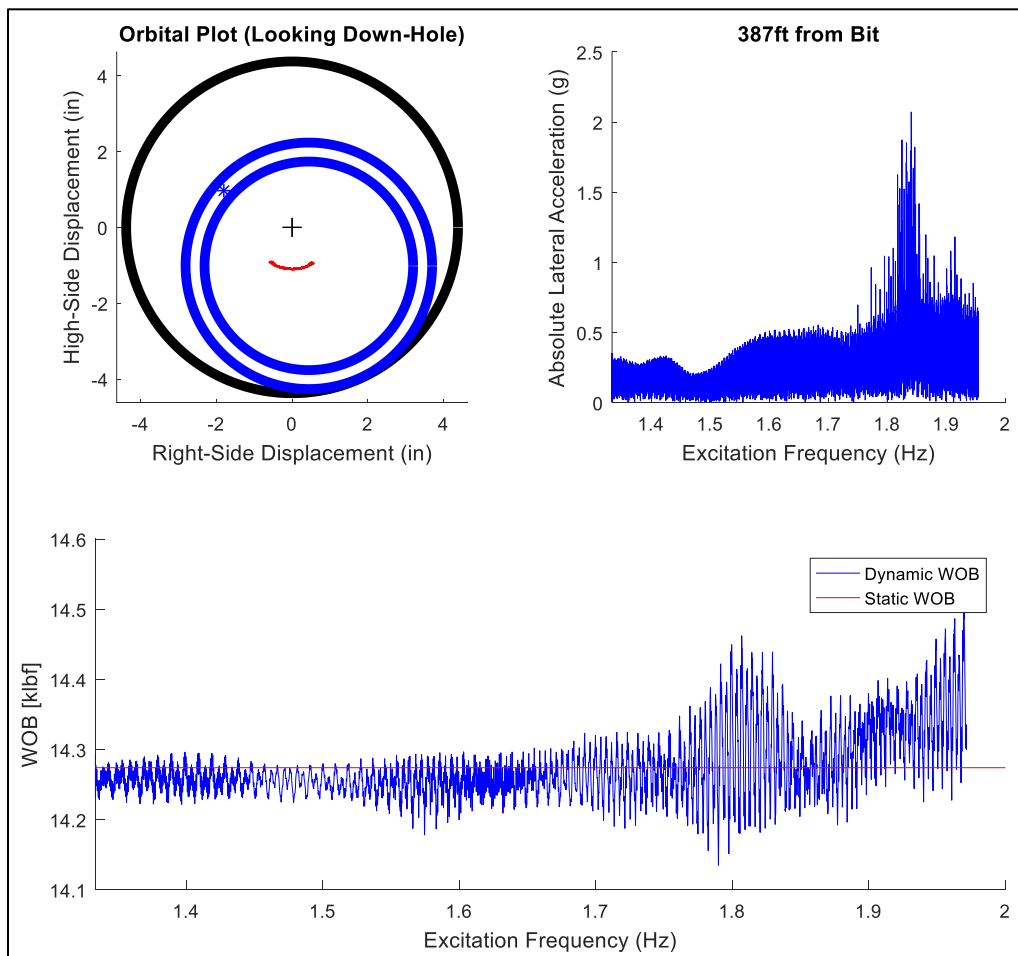


Figure 6.37: Results of Simulation with Multiple LETs in the Drillstring

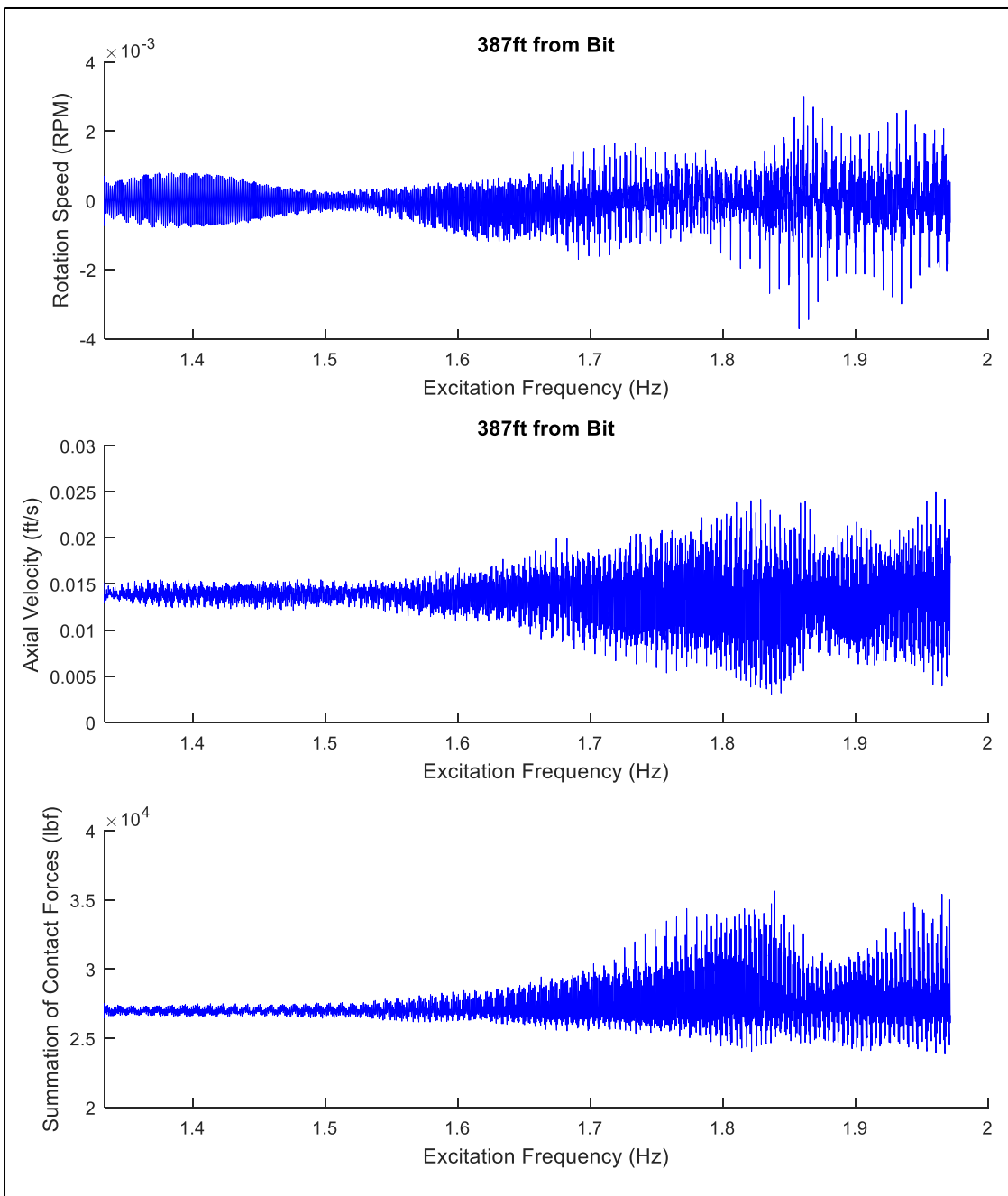


Figure 6.38: Rotational Velocity, Axial Velocity, and the Summation of Contact Forces for the Case of using Multiple LETs in the Drillstring

7. CONCLUSIONS AND FUTURE WORK

7.1 Conclusions

7.1.1 Newly-Developed Drillstring Model

Within the scope of this research study, a new drillstring model has been developed which can perform nonlinear-static, linearized-dynamic, and fully nonlinear-dynamic analysis of drillstrings in three-dimensional wellbores. The model is the most comprehensive to date and accounts for various intricacies associated with the drilling process. Following, and expanding upon, the approach taken by Heisig [34], the drillstring model was derived in a way that incorporates the following aspects of the drillstring and drilling process:

- Fully coupled flexibility. The lateral, axial, and torsional deflections of the drillstring are interdependent on one another; this has been captured in the model via the nonlinear strain-displacement relationships derived in Section 2.
- Geometric nonlinearity. The drillstring can undergo large displacement, but the strain at any given point remains small so as to only allow for elastic deformation. Plastic deformation of any component is considered a “tool failure” and thus does not have any practical benefit for general operations.
- Automatic determination of wellbore contact points. The algorithms calculate where the drillstring comes into contact with the wellbore wall based on the geometry, weight, and flexibility of the various assembly components and the clearance between the drillstring and the borehole. Because of this, the model can readily handle variations in borehole diameter along the length of the wellbore.
- Lateral acting friction between the drillstring and the wellbore. This generates a lateral force which pushes the drillstring up the side of the wellbore when rotation is present (see Figure 2.2), and adds additional torque to the drillstring at the various contact points.
- Arbitrary three-dimensional wellbore profiles. Because the curvature of the well has been imbedded in the strain-displacement relationships of the drillstring, the model can readily account for changes in wellbore curvature and general trajectory variations.
- Added fluid mass. As the drillstring moves within the wellbore, drilling fluid inside the various tubular components is forced to move with the pipe. This effectively adds mass to the system and will greatly affect the dynamic characteristics of the drillstring. Additionally, as the drillstring moves laterally within the wellbore, it must push fluid out of its way; this hydro-dynamic effect generates another added mass term which is accounted for within the present model.

- Fluid forces acting on the drillstring. As the drillstring moves within the wellbore, the fluid will generate resistance and slow the tubulars down. This is a damping effect generated by the fluid-drillstring interaction.
- Axial frictional forces. The axial friction force is specified such that it acts along the longitudinal axis of the drillstring; this is a necessary component of the model in order to properly quantify how friction affects the WOB
- Complex tool geometry. This includes things such as steerable mud motors, rotary steerable systems, and eccentric stabilizers/components.
- Shear beam deformations. This is the “Timoshenko Assumption”, which removes the requirement that the cross-sections of the drillstring must remain perpendicular to its central axis.
- Lateral rotary inertias. The lateral inertia of a cross-section of the drillstring provides resistance to dynamic bending.
- Gyroscopic effects. These are destabilizing moments which act on a rotating shaft.

The last six features listed above are notable advancements over Heisig’s original formulation. This new model was numerically validated through a broad comparison with analytical formulas and previous numerical approaches. Through this evaluation, it has been shown that the “traditional drillstring assumptions” (Neglecting shear deformations, lateral rotary inertias, and gyroscopic effects) are sufficient for modeling drilling operations in modern horizontal wellbores within the typical operational range of drillstrings. Additionally, it has been shown that the developed model, and associated algorithms, are robust enough to handle a wide variety of drilling engineering problems and, in fact, showed a favorable correlation to two initial case studies with actual surface and down-hole measurements.

7.1.2 Analysis of Lateral Excitation Tools in Horizontal Drilling Operations

It was originally suggested that inducing lateral vibrations, in sections of the drillstring that are in contact with the wellbore wall, would help to increase the axial force transfer along the drilling assembly. This idea is based on the concept of a velocity-dependent friction relationship; the more movement/induced-velocity along the drillstring, the greater the potential increase in axial force transfer. With this understanding, it was suspected that inducing a lateral resonance would provide the greatest movement over the longest length of drillstring, and ultimately provide the greatest increase in axial force transfer. Using the developed model, the resonant behavior associated with these induced lateral vibrations was examined in detail. A linearized forced-frequency approach was taken to examine how the lateral resonance of the drillstring, under the action of induced lateral vibrations, changes as various parameters within the model are adjusted. The variables that have been investigated are the wellbore diameter, WOB, mud rheology, inclination, and the wellbore curvature.

The results of the forced-frequency sensitivity study revealed that the model can adequately capture how the various environmental and operational parameters will affect the system, and that the behavior of the LET in an actual wellbore trajectory is reasonably predicted by an “ideal” (straight) well path. Through the study it was shown that three types of resonant behavior patterns are known to occur: contact resonance, pipe-body resonance, and localized LET resonance. The first of these resonant behaviors is associated with a rocking-like motion of the drillstring, back-and-forth along the low-side of the wellbore wall; this is called a contact resonance because it induces this rocking motion at the contact points. Similarly, the pipe-body resonance is primarily associated with movement of the drill pipe segments in between the tool joints; this type of behavior may still produce slight lateral movement of the contact points, but the majority of the response will be isolated to the pipe body. The localized LET resonance is just what it sounds like; a large dynamic response within a localized region ($\approx \pm 75$ ft) around the lateral excitation tool. In general, the forced-frequency analysis can sufficiently capture how these resonant behaviors of the drillstring change, under the action of induced lateral vibration from an LET, in modern horizontal well configurations. As such, this analysis approach is ideally suited for optimizing horizontal drilling operations when using an LET. It should be noted that, while an LET could be run through a curved wellbore section, the forced-frequency modeling indicated that LETs may not provide as strong of a response in highly curved wellbores. The curvature of the well is shown to induce a “secondary stabilization” effect, in which drill pipe that is adjacent to the LET bows downward and is forced against the wellbore wall. The resulting contact forces, generated at the drill pipe, effectively reduce the drillstring’s response to the vibration from the LET.

While the linearized forced-frequency analysis provided tremendous insight into how the lateral resonant behavior of the drillstring changed with varying environmental and operational parameters when using an LET, it could not directly quantify the effect such a tool has on the WOB; for this reason, nonlinear-dynamic analysis was used. The robustness of the nonlinear simulations definitively showed that the linearized results were capturing the generalized resonant behavior of the nonlinear system and predicting the proper frequencies of the drillstring that resulted in the largest response. This is quite reassuring considering the fact that friction was completely ignored for the linearized analysis; thus, also proving that friction is not a critical parameter for estimating the linearized-dynamic resonant behavior of drillstrings when subjected to induced vibrations from LETs. More importantly, the nonlinear simulations showed that the induced lateral vibrations do, in fact, have a noticeable effect on the WOB. However, this effect is not a simple increase in the average dynamic WOB as was originally thought. The primary result of inducing lateral vibration with an LET is a dynamic WOB which oscillates about the initial static value. This dynamic WOB component has a direct dependency on the excitation frequency of the drillstring, with the largest values occurring within the resonant frequencies predicted from the linearized analysis; up to ± 260 lb_f in some cases. It is

unclear how this dynamic WOB may affect the ROP, but it does suggest that the induced axial waves in the drillstring may help in overcoming “stuck points” along the wellbore such as ledges and cuttings deposits.

An increase in the average dynamic WOB, which was thought to be the primary effect of LETs, was actually shown to be a rather minor secondary result of the induced lateral vibrations. What’s more, the increase in average WOB is not due to an increase in the slip-velocity at the contact points along the drillstring; the axial velocity and rotational velocities generated by the LET’s vibration are simply too small to provide an appreciable increase in the slip-velocity, and subsequent decrease in the friction coefficient (See Section 2). The slight increase in the average WOB was determined to be the result of sections of the drill pipe, near the LET, losing contact with the wellbore. This momentary, and repetitive, loss of contact along the drillstring appears to result in an “inch-worming” behavior, where the drillstring is building up axial compressive force that is released upon separation from the wellbore. This pushes the drillstring slightly forward, resulting in an almost skipping-like behavior. This further supports the idea that the LET may be very beneficial at working past “tight” spots in the wellbore. This result also suggest that the general response from the LET shouldn’t be directly dependent on the friction model being used, which was also verified via a simulation using only the friction relationships given by equations (2.70) and (2.71), i.e. no velocity-weakening effect. However, it can be noted that the dynamic WOB, induced by the LET, increases in magnitude with larger friction coefficients. This is because higher friction values will result in a larger lateral displacement which, due to the axial-lateral coupling along the drillstring, results in more axial displacement. Therefore, the tool should be more effective at inducing a dynamic WOB in wellbores with more drag.

It should be kept in mind that the LET explored in this work was intentionally designed to operate below 2.5 Hz. However, as was noted in Section 1, there are commercial tools similar to this that are meant to operate within the 10-30 Hz range. In order to compare how the two frequency ranges may affect the response of the system, a simulation was performed within this higher frequency range, at an excitation of 12 Hz. It was quickly apparent that the higher excitation frequency resulted in adverse dynamics surrounding the LET; the tool generated a whirling motion that resulted in severe impact loading with the wellbore (\approx 40-50g). However, it must be realized that the eccentric mass within the LET was not adjusted for the higher frequencies. At 12 Hz, the excitation force provided from the eccentric mass was around 370 lb_f/ft, as compared to around 8.5 lb_f/ft at an excitation frequency of 1.8 Hz. For a tool (the LET) that weighs approximately 56 lb_f/ft, the 12 Hz excitation is clearly excessive. If higher excitation frequencies are desired from an LET, the excitation force should be matched accordingly. Perhaps there is even an optimum value of the excitation force that would provide the greatest benefit without generating severe impact with the wellbore.

Although operation at a lateral resonant frequency of the drill pipe did not greatly increase the average WOB, and more so provided only a dynamic WOB component, the lateral displacement along the drillstring is still thought to provide a benefit for improving hole-cleaning in high-inclination wells. This observation is based purely on the nature of the motion of the drillstring, but it cannot be definitively proven without proper verification. Therefore, future work is necessary in order to understand the practicality of this idea.

7.2 Future Work

The most obvious, and likely the most critical, next step would be validating that the model is predicting the actual dynamics taking place down-hole. While a similar model [34] has been validated on multiple occasions [102-105], and compares quite favorably with the current model, it has not been applied to the specific situation of inducing lateral vibrations in horizontal wellbores. Verifying this modeling approach would require specific testing considerations in order to answer three primary questions: How well does the predicted resonant frequency match reality? How well does the model estimate the actual response in both acceleration magnitude and longitudinal reach? And how does the LET affect the WOB? These could all potentially be answered with a single test, with multiple vibration measurement devices in the drillstring. Ignoring cost limitations for the moment, an ideal testing procedure may have the following form:

- 1) Obtain high-frequency measurement devices that can be run every joint, or every stand (3 joints), which have a minimal profile. Ideally, these would be devices that could be run in a specialized drill pipe connection so as to not significantly alter the structure of the drillstring, and the devices should continuously record data at a minimum of 100 Hz. This minimum frequency requirement is desired so that the frequency signatures from the eccentric mass and power section rotor within the LET can be adequately detected. As a general rule, data should be recorded at a minimum of twice the frequency that is hoped to be observed (Nyquist Frequency); in a practical sense, it is always good to have data recorded at 4 or more times the anticipated down-hole frequencies.
- 2) Obtain a down-hole WOB measurement device that can continuously record data at the same frequency as the vibration logging devices. Care should be taken to make sure that the WOB measurement device is appropriately compensated for down-hole pressure and temperature variations.
- 3) Position the WOB recording device relatively close to the bit; within 50 ft should be sufficient.
- 4) Place the vibration recording devices in the drillstring such that the lateral vibration levels will be recorded at the LET, throughout the expected “contact resonance” peak, and beyond the expected longitudinal reach of the LET’s vibration (see Figure 5.4). This will determine how far along the drillstring the lateral vibrations from the LET are “felt”, which will be a direct indicator of the tool’s reach, and it will help to quantify the level of damping within the system.

- 5) While slide drilling, the flow rate can be increased in a step-wise manner so as to perform a frequency-sweep of the excitation from the eccentric mass within the LET. This frequency-sweep should increase all the way through the anticipated contact resonance peak, and then decrease back through the same frequencies in order to achieve some repeatability in the experiment.

The data from this type of test should be able to verify the resonant frequency predicted from the linearized modeling, quantify the dynamic down-hole WOB during this resonant excitation, and show the level of vibration along the drillstring due to the LET's excitation. Of course, these testing procedures are very generalized and will need to be refined based on the specific testing environment as well as the funding of the experiment. Regardless of the limitations, properly planned field tests would be the greatest indicator of practicality in using these types of tools as well as the suggested modeling approach.

Other field tests can also be done to explore additional applications of the LET. One of these possibilities, which was briefly discussed in previous sections, is using an LET to improve hole-cleaning efficiencies. The nature of the vibrations generated from the LET provide a continuous side-to-side motion of the drillstring in highly-inclined wellbores. This induced motion could very well assist in lifting the cuttings off of the low-side of the wellbore and pushing them into the higher flow velocities on the high-side of the hole, or the continuous movement could prevent cuttings from accumulating in the first place. Additionally, the gentle lateral motion generated from the LET may serve as a stabilizer “de-sticker”. Oftentimes stabilizers run in the BHA are blamed for “hanging-up” during various drilling operations; it may be worth investigating if the LET could be used near such a stabilizer to help prevent this “hanging-up” at different points along the wellbore. Another potential of field testing, which may be more of a “tortuosity-indexing” exercise, would be to quantify the level of wellbore deviation that would result in the “ideal” forced-frequency calculations (straight wellbore) no longer being valid. This potentially could be done as a post-well analysis, if the data is available, by comparing the planned well paths to the “as-drilled” surveys. A measure of “tortuosity severity”, similar to those that have been presented recently [114], could then be used as a go/no-go indicator for the applicability of the ideal LET analysis on the “ideal” wellbore.

From a modeling perspective, one could also explore the theoretical potential for increasing the ROP. The results in Section 6 showed that the LET should generate a dynamic WOB that has a magnitude on the order of a couple hundred pounds, at a frequency of twice the lateral excitation frequency generated from the LET. By incorporating an appropriately complex bit-formation interaction model, the effect that this dynamic WOB has on the ROP can be better understood. Additionally, similar modeling approaches could be applied to the case of axial excitations tools; the present model could easily be expanded to account for these types of devices, and their effects on the WOB could be determined just as they were for the present case of LETs.

The fluid-damping is another aspect of the modeling that deserves further investigation. As discussed in Section 6, ignoring the frictional effects of the internal fluid flow through the drillstring, while including the effects of the external annular flow, resulted in a decrease in the WOB. It was not crucial in the present study to include both contributions, therefore they were neglected. However, if the damping model were to be applied to other scenarios, say for the case of induced axial vibrations, then both the internal and external frictional flow effects should be accounted for. Additionally, the nonlinear damping coefficient (C_d), which was defined as part of the proposed nonlinear fluid-drillstring interaction, is rather arbitrary. The underlying physics behind this assumption should be verified and/or refined before the damping model can be considered an accurate representation of the true fluid-drillstring interaction. It may also be worth considering how cuttings loading scenarios may, or may not, be affecting the damping of the nonlinear system.

As a final thought, this work has generated a very powerful analysis tool for examining the nonlinear behavior of drilling assemblies, however it is limited by the computational requirements of the algorithms. Nonlinear-static and linearized-dynamic calculations of short/small assemblies ($< 1,000$ ft, $< 300\text{--}400$ elements) are reasonably managed on a standard engineering-grade mobile workstation (laptop). Therefore, the developed model is ideally suited for general BHA analysis which could easily support operations in optimization or failure-analysis applications. Unfortunately, when looking at the nonlinear-static/linearized-dynamic behavior of entire drillstrings, or the nonlinear-dynamic behavior of any assembly, the computation time required is simply too demanding for practical “day-to-day” analysis. For this reason, it would be beneficial to develop a more efficient way of solving the nonlinear system. Computationally, this could be done with an alternative approach to the finite element method; this was done by Belaid [94] for Torque and Drag analysis, although the specific algorithm/method was not revealed so it is of little use to the research community. Alternatively, perhaps there is a way of further parallelizing the process of solving the matrix equations that result as part of the finite element procedure. Matlab’s built in matrix algebra operators already utilize parallel processing in order to achieve a high degree of efficiency on CPUs. However, if the process could be extended such that the calculations could be run on a cluster of GPUs, which could be as many as 500-1000 GPUs on a single graphics card, then it may be possible to further speed up the computations. This may be easier said than done, but is certainly worth investigating.

REFERENCES

1. Hubbert, M.K., *Nuclear Energy and the Fossil Fuels*, in *The API Spring Meeting of the Southern District*. 1956: San Antonio, TX, USA.
2. Weaver, D.K., *Practical Aspects of Directional Drilling*, in *Drilling and Production Practice*. 1946: New York, NY, USA.
3. Thorpen, P. and M. Sanders, *Shedding New Light on Downhole Vibration Tools*, in *Oilfield Technology: Exploration, Drilling, Production*. 2015, Palldian Publications Ltd. p. 27-29.
4. Al-Ali, A., S. Barton, and A. Mohanna, *Unique Axial Oscillation Tool Enhances Performance of Directional Tools in Extended Reach Applications (SPE 143216)*, in *Brasil Offshore Conference and Exhibition*. 2011: Macaé, Brazil.
5. Azike-Akubue, V., et al., *Agitation Tools Enables Significant Reduction in Mechanical Specific Energy (SPE 158240)*, in *Asia Pacific Oil and Gas Conference*. 2012: Perth, Australia.
6. Barton, S., F. Baez, and A. Alali, *Drilling Performance Improvements in Gas Shale Plays using a Novel Drilling Agitator Device (SPE 144416)*, in *SPE North American Unconventional Gas Conference and Exhibition*. 2011: The Woodlands, TX, USA.
7. Newman, K.R., *Vibration and Rotation Considerations in Extending Coiled-Tubing Reach (SPE 106979)*, in *SPE/ICoTA Coiled Tubing and Well Intervention*. 2007: The Woodlands, TX, USA.
8. Rasheed, W., *Extending the Reach and Capability of Non Rotating BHAs by Reducing Axial Friction (SPE 68505)*, in *SPE/ICoTA Coiled Tubing Roundtable*. 2001: Houston, TX, USA.
9. Skyles, L.P., Y.A. Amirasiani, and J.E. Wilhoit, *Converting Static Friction to Kinetic Friction to Drill Further and Faster in Directional Holes*, in *IADC/SPE Drilling Conference and Exhibition*. 2012: San Diego, CA, USA.
10. Angona, F.A., *Drill String Vibration Attenuation and Its Effect on a Surface Oscillater Drilling System*. Journal of Engineering for Industry, 1965. **87**(2): p. 110-114.
11. Chin, W.C., *Wave Propagation in Drilling, Well Logging and Reservoir Applications*. Advances in Petroleum Engineering. 2014, Hoboken, NJ, USA: Scrivener Publishing, LLC/ John Wiley & Sons, Inc.
12. Macpherson, J.D., J.S. Mason, and J.E.E. Kingman, *Surface Measurement and Analysis of Drillstring Vibrations While Drilling (SPE 25777)*, in *SPE IADC Drilling Conference*. 1993: Amsterdam, The Netherlands.
13. Payne, M.L., *Drilling Bottom-Hole Assembly Dynamics. Ph.D. Dissertation*. 1992, Rice University: Houston, TX, USA. p. 328.
14. Dykstra, M.W., *Nonlinear Drill String Dynamics. Ph.D. Dissertation*, in *Petroleum Engineering*. 1996, University of Tulsa: Tulsa, OK, USA.

15. Centala, P., et al., *Unlocking Two-Cone-Bit Potential: Technology, People, and Planning Make it Possible and Lessons Learned* (SPE 99017), in IADC/SPE Drilling Conference, SPE, Editor. 2006: Miami, FL, USA.
16. Franca, L.F., *Drilling Action of Roller-Cone Bits: Modeling and Experimental Validation*. Journal of Energy Resources Technology, 2010. **132**(4): p. 9.
17. Murphy, D., et al., *Deepwater Drilling in Both Hard and Abrasive Formations: The Continuing Challenge of Bit Optimization* (SPE 151787), in North Africa Technical Conference and Exhibition. 2012: Cairo, Egypt.
18. Pessier, R. and M. Damschen, *Hybrid Bits Offer Distinct Advantages in Selected Roller Cone and PDC Bit Applications* (IADC/SPE 128741), in IADC/SPE Drilling Conference and Exhibition. 2010: New Orleans, LA, USA.
19. Aadnoy, B., et al., *Advanced Drilling and Well Technology*. 2009, Richardson, TX, USA: Society of Petroleum Engineers.
20. Mitchell, R.F. and L.W. Lake, *Petroleum Engineering Handbook, Volume II: Drilling Engineering*. 2006, Richardson, TX, USA: Society of Petroleum Engineers.
21. Mitchell, R.F., Miska, S.Z., *Fundamentals of Drilling Engineering*. 2011, Richardson, TX, USA: Society of Petroleum Engineers.
22. McDermott, J.R., et al., *Extended Reach Drilling (ERD) Technology Enables Economical Development of Remote Offshore Field in Russia* (SPE/IADC 92783), in SPE/IADC Drilling Conference. 2005: Amsterdam, The Netherlands.
23. Sonowal, K., et al., *How Continuous Improvement Lead to the Longest Horizontal Well in the World* (SPE/IADC 119506), in SPE/IADC Drilling Conference and Exhibition. 2009: Amsterdam, The Netherlands.
24. Lahee, F.H., *Problem of crooked holes*. AAPG Bulletin, 1929. **13**(9): p. 1095-1162.
25. Anderson, A., *Underground Surveys of Oil Wells*. Transactions of the AIME, 1929. **82**(1): p. 30-40.
26. Gleason, S., *Slanted oil wells work new marvels*. Popular Science, 1934. **124**(5): p. 40-49.
27. Allen, R.E., *Theory and Practice of Directed Drilling*. Transactions of the AIME, 1933. **107**(1): p. 31-41.
28. Eastman, H.J. *The Latest Developments and Achievements of Directional Drilling in the Exploitation of Oil Fields*. in 3rd World Petroleum Congress. 1951. The Hague, the Netherlands.
29. Hughes, J.D., *Value of Oil-Well Surveying and Applications of Controlled Directional Drilling*, in *Drilling and Production Practice*. 1935: New York, NY, USA.
30. Joshi, S.D., *A Review of Horizontal Well and Drainhole Technology* (SPE 16868), in 62nd Annual Technical Conference and Exhibition. 1987: Dallas, TX, USA.

31. Menand, S., *A New Buckling Severity Index to Quantify Failure and Lock-up Risks in Highly Deviated Wells* (SPE 151279), in *SPE Deepwater Drilling and Completions Conference*. 2012: Galveston, TX, USA.
32. Schaaf, S., C.R. Mallary, and D. Pafitis, *Point the-Bit Rotary Steerable System: Theory and Field Results* (SPE 63247), in *SPE Annual Technical Conference and Exhibition*. 2000: Dallas, TX, USA.
33. Andreassen, E., et al., *Rotary Steerable System Improves Reservoir Drilling Efficiency and Wellbore Placement in the Statfjord Field* (IADC/SPE 39329), in *IADC/SPE Drilling Conference*. 1998: Dallas, TX, USA.
34. Heisig, G., *On the Static and Dynamic Behaviour of Drill Strings in Spatially Curved Boreholes*. Ph.D. Thesis, in *Mechanical Engineering*. 1993, Technische Universität Braunschweig: Braunschweig, Germany.
35. Augustine, N., et al., *Utilizing Short Bit-to-Bend Motor Technology Enables Monobore Wells to be Drilled in the Niobrara Unconventional Shale Play with a Single Drilling Assembly* (IADC/SPE 178867), in *IADC/SP Drilling Conference and Exhibition*. 2016: Fort Worth, TX, USA.
36. Duan, M., et al., *Transport of Small Cuttings in Extended-Reach Drilling* (SPE 104192). SPE Drilling and Completions, 2008. **23**(3): p. 258-265.
37. Sanchez, R.A., et al., *Effect of Drillpipe Rotation on Hole Cleaning During Directional-Well Drilling* (SPE 56406). SPE Journal, 1999. **4**(2): p. 101-108.
38. Ozbayoglu, M.E., et al. *Effect of Pipe Rotation on Hole Cleaning for Water-Based Drilling Fluids in Horizontal and Deviated Wells* (SPE 114965). in *IADC/SPE Asia Pacific Drilling Technology Conference and Exhibition*. 2008. Jakarta, Indonesia.
39. Rocha, L.Z.S., R. Andrade, and K. Soffried, *How Water Depth Affects Extended Reach Drilling*, in *Offshore Technology Conference*. 2003: Houston, TX, USA.
40. Heisig, G. and M. Neubert, *Lateral Drillstring Vibrations in Extended-Reach Wells* (IADC/SPE 59235), in *IADC/SPE Drilling Conference*. 2000: New Orleans, Louisiana, USA.
41. Heisig, G., *Postbuckling Analysis of Drillstrings using the Finite-Element Method*, in *ASME Energy Sources Technology Conference and Exhibition*. 1995: Houston, TX, USA.
42. Cameron, C., *Drilling Fluids Design and Management for Extended Reach Drilling* (IADC/SPE 72290), in *IADC/SPE Middle East Drilling Technology*. 2001: Bahrain.
43. Patel, A., et al., *Lubricants and Drag Reducers for Oilfield Applications - Chemistry, Performance, and Environmental Impact* (SPE 164049), in *SPE International Symposium on Oilfield Chemistry*. 2013: The Woodlands, TX, USA.

44. Balandin, I.Y., *Buoyant Aluminum Drill Pipes for Extended-Reach Drilling (SPE 135677)*, in *SPE Russian Oil & Gas Technical Conference and Exhibition*. 2010: Moscow, Russia.
45. Jellison, M.J., et al., *Drillstring Technology Vanguard for World-Class Extended-Reach Drilling*, in *Offshore Technology Conference*. 2007: Houston, TX, USA.
46. Maidla, E., et al., *Field Proof of the New Sliding Technology for Directional Drilling (SPE/IADC 92558)*, in *SPE/IADC Drilling Conference*. 2005: Amsterdam, The Netherlands.
47. Wilson, J.K. and G. Heisig, *Nonlinear Drillstring-Dynamics Modeling of Induced Vibrations in Unconventional Horizontals (SPE 173049)*. SPE Drilling and Completions, 2015. **30**(3): p. 243-256.
48. Bodine, A.G., *Sonic Drill Versatile*. Oil and Gas Journal, 1955. **54**: p. 74-74.
49. Ishikawa, K.-i., et al., *A study on combined vibration drilling by ultrasonic and low-frequency vibrations for hard and brittle materials*. Precision Engineering, 1998. **22**: p. 196-205.
50. Jahan, M.P., Y.S. Wong, and M. Rahman, *Evaluation of the effectiveness of low frequency workpiece vibration in deep-hole micro-EDM drilling of tungsten carbide*. Journal of Manufacturing Processes, 2012. **14**: p. 343-359.
51. Pujana, J., et al., *Analysis of ultrasonic-assisted drilling of Ti6Al4V*. International Journal of Machine Tools & Manufacture, 2009. **49**: p. 500-508.
52. Yin, S. and T. Shinmura, *Vertical vibration-assisted magnetic abrasive finishing and deburring for magnesium alloy*. International Journal of Machine Tools & Manufacture, 2004. **44**: p. 1297-1303.
53. Aguiar, R.R. and H.I. Weber, *Development of a Vibroimpact Device for the Resonance Hammer Drilling*. in *XII International Symposium on Dynamic Problems of Mechanics*. 2007. Rio de Janeiro, Brazil.
54. Cobb, J.B., *Percussion tool increases drilling rate, cuts costs*. World Oil, 1962. **155**(5): p. 116-120.
55. Ghasemloo, A., et al., *Elastodynamic and finite element vibration analysis of a drillstring with a downhole vibration generator tool and a shock sub*. Journal of Mechanical Engineering Science, 2015. **229**(8): p. 1361-1384.
56. Ledgerwood, J., L.W., *Efforts to Develop Improved Oilwell Drilling Methods (SPE 1458)*. Journal of Petroleum Technology, 1960. **12**(4): p. 61-74.
57. Li, H., *Experimental Investigation of the Rate of Penetration of Vibration Assisted Rotary Drilling*. M. Eng. Thesis. 2011, Memorial University of Newfoundland: Newfoundland and Labrador, Canada.

58. Samuel, R., *Friction Factors: What are they for torque, drag, vibration, bottom hole assembly and transient surge/swab analyses?* Journal of Petroleum Science and Engineering, 2010. **73**: p. 258-266.
59. Zifeng, L., L. Xisheng, and Z. Daqian, *A Steady Tension-Torque Model for Drillstring in Horizontal Wells (SPE 26295)*, S.o.P. Engineers, Editor. 1993.
60. Brett, J.F., *The Genesis of Torsional Drillstring Vibrations (SPE 21943)*. SPE Drilling Engineering, 1992. **7**(3): p. 168-174.
61. Kumar, V.C. and I.M. Hutchings, *Reduction of the sliding friction of metals by the application of longitudinal or transverse ultrasonic vibration*. Tribology International, 2004. **37**(10): p. 833-840.
62. Mason, C.J. and D.C.-K. Chen, *Step Changes Needed to Modernize T&D Software (SPE/IADC 104609)*, in *SPE/IADC Drilling Conference*. 2007: Amsterdam, The Netherlands.
63. Clausen, J.R., et al., *Drilling with Induced Vibrations Improves ROP and Mitigates Stick/Slip in Vertical and Directional Wells (SPE 168034)*, in *IADC/SPE Drilling Conference and Exhibition*. 2014: Fort Worth, TX, USA.
64. McCarthy, J.P., et al., *A Step Change in Drilling Efficiency: Quantifying the Effects of Adding an Axial Oscillation Tool Within Challenging Wellbore Environments (SPE/IADC 119958)*, in *SPE/IADC Drilling Conference and Exhibition*. 2009: Amsterdam, The Netherlands.
65. Robertson, L., et al., *Dynamic Excitation Tool: Developmental Testing and CTD Field Case Histories (SPE 89519)*, in *SPE/ICoTA Coiled Tubing Conference and Exhibition*. 2004: Houston, TX, USA.
66. Jones, S., et al., *A New Friction Reduction Tool with Axial Oscillation Increases Drilling Performance: Field-Testing with Multiple Vibration Sensors in One Drill String (IADC/SPE 178792)*, in *IADC/SPE Drilling Conference and Exhibition*. 2016: Fort Worth, TX, USA.
67. Forster, I. and R. Grant, *Axial Excitation and Drill String Resonance as a Means of Aiding Tubular Retrieval - Small Scale Rig Testing and Full Scale Field Testing (SPE 151096)*, in *IADC/SPE Drilling Conference and Exhibition*. 2012, SPE: San Diego, CA, USA.
68. Gee, R., et al., *Axial Oscillation Tools vs. Lateral Vibration Tools for Friction Reduction - What's the Best Way to Shake the Pipe? (SPE/IADC 173024)*, in *SPE/IADC Drilling Conference and Exhibition*. 2015: London, UK.
69. Newman, K., et al., *Modeling the Affect of a Downhole Vibrator (SPE 12175)*, in *SPE/ICoTA Coiled Tubing and Well Intervention Conference and Exhibition*. 2009: The Woodlands, Texas, USA.
70. Liu, Y., et al., *Modeling friction-reducing performance of an axial oscillation tool using dynamic friction model*. Journal of Natural Gas Science and Engineering, 2016. **33**: p. 397-404.

71. Shor, R.J., et al., *For Better or Worse: Applications of the Transfer Matrix Approach for Analyzing Axial and Torsional Vibration (SPE/IADC 173121)*, in *SPE/IADC Drilling Conference and Exhibition*. 2015: London, UK.
72. Wicks, N., et al., *Modeling of Axial Vibrations to Allow Intervention in Extended Reach Wells (SPE 156017)*, in *SPE Deepwater Drilling and Completions*. 2012, SPE: Galveston, TX, USA.
73. Voghell, M., et al., *Downhole Vibration Analysis: Fishing Agitation Tool Efficiency in Stuck Pipe Recovery (SPE 163516)*, in *SPE/IADC Drilling Conference and Exhibition*. 2013: Amsterdam, The Netherlands.
74. Bailey, J.J. and I. Finnie, *An Analytical Study of Drill-String Vibration*. Journal of Engineering for Industry, 1960. **82**(2): p. 122-127.
75. Finnie, I. and J.J. Bailey, *An Experimental Study of Drill-String Vibration*. Journal of Engineering for Industry, 1960. **82**(2): p. 129-135.
76. Paslay, P.R. and D.B. Bogy, *Drill String Vibrations Due to Intermittent Contact of Bit Teeth*. Journal of Engineering for Industry, 1963. **52**(2): p. 187-194.
77. Bradbury, R.E. and J. Wilhoit, J.C., *Effect of Tool Joints on Passages of Plane Longitudinal and Torsional Waves Along Drill Pipe*. Journal of Engineering for Industry, 1963. **85**(2): p. 156-162.
78. Graham, R.D., M.A. Frost III, and J. Wilhoit, J.C., *Analysis of the Motion of Deep-Water Drill String - Part 1: Forced Lateral Motion*. Journal of Engineering for Industry, 1965. **87**(2): p. 137-144.
79. Frost III, M.A. and J.C. Wilhoit Jr., *Analysis of the Motion of Deep-Water Drill Strings - Part 2: Forced Rolling Motion*. Journal of Engineering for Industry, 1965. **87**(2): p. 145-149.
80. Hsu, F.-H. and J. Wilhoit, J.C., *Lateral Vibration of Drill Pipe Including Wall Reaction (SPE 1046)*, in *SPE Conference on Drilling and Rock Mechanics*. 1965: Austin, TX, USA.
81. Burgess, T.M., G.L. McDaniel, and P.K. Das, *Improving BHA Tool Reliability with Drillstring Vibration Models: Field Experience and Limitations (SPE/IADC 16109)*, in *SPE/IADC Drilling Conference*. 1987: New Orleans, LA, USA.
82. Huang, T. and D.W. Dareing, *Predicting the Stability of Long Vertical Pipe Transmitting Torque in a Viscous Medium*. Journal of Engineering for Industry, 1966. **88**(2): p. 191-199.
83. Frohrib, D.A. and R. Plunkett, *The Free Vibrations of Stiffened Drill Strings with Static Curvature*. Journal of Engineering for Industry, 1967. **89**(1): p. 23-29.
84. Dareing, D.W. and B.J. Livesay, *Longitudinal and Angular Drill-String Vibrations with Damping*. Journal of Engineering for Industry, 1968. **90**(4): p. 671-679.
85. Nicholson, J., R.W., *Analysis of Constrained Directional Drilling Assemblies. Ph.D. Dissertation*, in *Petroleum Engineering*. 1972, University of Tulsa: Tulsa, OK, USA.

86. Eronini, I.E., *A Dynamic Model for Optimization and Control of Rock Drilling. Ph.D. Dissertation*. 1978, University of California, Berkeley: Berkeley, CA, USA.
87. Dykstra, M.W., et al., *Drillstring Component Mass Imbalance: A Major Source of Downhole Vibrations (SPE 29350)*. SPE Drilling and Completions, 1996. **11**(4): p. 234-241.
88. Millheim, K., S. Jordan, and C.J. Ritter, *Bottom-Hole Assembly Analysis Using the Finite-Element Method (SPE 6057)*. Journal of Petroleum Technology, 1978. **30**(2): p. 265-274.
89. Millheim, K.K. and M.C. Apostal, *The Effect of Bottomhole Assembly Dynamics on the Trajectory of a Bit (SPE 9222)*. Journal of Petroleum Technology, 1981. **33**(12): p. 2324-2338.
90. Brakel, J.D., *Prediction of Wellbore Trajectory Considering Bottom Hole Assembly Dynamics. Ph.D. Dissertation*, in *Petroleum Engineering*. 1986, University of Tulsa: Tulsa, OK, USA.
91. Shyu, R.-J., *Bending Vibration of Rotating Drill Strings. Ph.D. Dissertation*, in *Ocean Engineering*. 1989, Massachusetts Institute of Technology: Cambridge, MA, USA.
92. Apostal, M.C., G.A. Haduch, and J.B. Williams, *A Study to Determine the Effect of Damping on Finite-Element-Based, Forced-Frequency-Response Models for Bottomhole Assembly Vibration Analysis (SPE 20458)*, in *65th Annual Technical Conference and Exhibition*. 1990: New Orleans, LA, USA.
93. Jansen, J.D., *Nonlinear Dynamics of Oilwell Drillstrings, Ph.D Dissertation*, in *Civil Engineering*. 1993, Technische Universiteit Delft: Delft, The Netherlands. p. 221.
94. Belaid, A., *Modélisation tridimensionnelle du comportement mécanique de la garniture de forage dans les puits à trajectoires complexes : application à la prédiction des frottements garniture-puits. Ph.D. Dissertation* 2005, École Nationale Supérieure des Mines de Paris: Paris, France.
95. Mongkolcheep, K., *A Lyapunov Exponent Approach for Identifying Chaotic Behavior in a Finite Element Based Drillstring Vibration Model. M.S. Thesis*, in *Mechanical Engineering*. 2009, Texas A&M University: College Station, TX, USA.
96. Ritto, T.G., *Numerical Analysis of the Nonlinear Dynamics of a Drill-String with Uncertainty Modeling. DOCTEUR DE l'UNIVERSITÉ PARIS-EST*, in *Engineering*. 2010, Université Paris-Est: Paris, France. p. 152.
97. Cunha, J., A., C. Soize, and R. Sampaio, *Computational modeling of the nonlinear stochastic dynamics of horizontal drillstrings*. Computational Mechanics, 2015. **56**(5): p. 849-879.
98. Mongkolcheep, K., A. Ruimi, and A. Palazzolo, *Model Reduction Technique for Predicting the Onset of Chaotic Behavior due to Lateral Vibrations in Drillstrings*. Journal of Vibration and Acoustics, 2015. **137**(2): p. 11.
99. Pabon, J., et al., *Modeling Transient Vibrations While Drilling Using a Finite Rigid Body Approach (SPE 137754)*, in *SPE Deepwater Drilling and Completions Conference*. 2010: Galveston, TX, USA.

100. Silveira, M., *A Comprehensive Model of Drill-String Dynamics using Cosserat Rod Theory*. *Ph.D. Dissertation*. 2011, University of Aberdeen: Aberdeen, Scotland.
101. Al Dushaishi, M.F., *Numerical and Field Data Analysis of Drill Stem Vibration*. *Ph.D. Dissertation*, in *Petroleum Engineering*. 2015, Missouri University of Science and Technology: Rolla, MO, USA.
102. Heisig, G., et al., *Continuous Borehole Curvature Estimates While Drilling Based on Downhole Bending Moment Measurements (SPE 90794)*, in *SPE Annual Technical Conference and Exhibition*. 2004: Houston, TX, USA.
103. Neubert, M., et al., *Verification of an Advanced Analysis Model With Downhole Bending Moment Measurements (SPE 93864)*, in *Asia Pacific Oil & Gas Conference and Exhibition*. 2005: Jakarta, Indonesia.
104. Hohl, A., et al., *Investigation of Lateral & Torsional Vibrations of Drillstrings Based on Simulations, Laboratory Modal Analysis and Field Tests*, in *Oil and Gas European Magazine*. 2014: Hamburg, Germany. p. 18-19.
105. Jogi, P.N., J.D. Macpherson, and M. Neubert, *Field Verification of Model-Derived Natural Frequencies of a Drill String*. Transactions of the ASME, 2002. **124**: p. 154-162.
106. Dykstra, M.W., et al., *Improving Drilling Performance by Applying Advanced Dynamics Models (SPE 67697)*, in *SPE/IADC Drilling Conference*. 2001: Amsterdam, The Netherlands.
107. Janwadkar, S.S., et al., *BHA and Drillstring Modeling Maximizes Drilling Performance In Lateral Wells of Barnett Shale Gas Field of N. Texas (SPE 100589)*, in *SPE Gas Technology Symposium*. 2006: Calgary, Alberta, Canada.
108. Jogi, P., et al., *Visualization of BHA Dynamics Improves Understanding of Downhole Drilling Conditions, Speeds Up Learning Curve*, in *IADC/SPE Drilling Conference*. 2006: Miami, FL, USA.
109. Schmalhorst, B. and M. Neubert, *Dynamic Modeling Software*, in *National Technology Conference "Practical Solutions for Drilling Challenges"*. 2003: Houston, TX, USA.
110. Rincon, D.M. and A.G. Ulsoy, *Complex Geometry, Rotary Inertia and Gyroscopic Moment Effects on Drill Vibrations*. Journal of Sound and Vibration, 1995. **188**(5): p. 701-715.
111. Pai, P.F., X. Qian, and X. Du, *Modeling and Dynamic Characteristics of Spinning Rayleigh Beams*. International Journal of Mechanical Sciences, 2013. **68**: p. 291-303.
112. Stoykov, S. and P. Ribeiro, *Nonlinear forced vibrations and static deformations of 3D beams with rectangular cross section: The influence of warping, shear deformation and longitudinal displacements*. International Journal of Mechanical Sciences, 2010. **52**: p. 1505-1521.
113. Sadd, M.H., *Elasticity: Theory, Applications, and Numerics*. 2009, Oxford, UK: Elsevier.

114. Abughaban, M.F., et al., *Advanced Trajectory Computational Model Improves Calculated Borehole Positioning, Tortuosity and Rugosity* (IADC/SP 178796), in *IADC/SPE Drilling Conference and Exhibition*. 2016: Fort Worth, TX, USA.
115. Paidoussis, M.P., D. Mateescu, and W.-G. Sim, *Dynamics and Stability of a Flexible Cylinder in a Narrow Coaxial Cylindrical Duct Subjected to Annular Flow*. Journal of Applied Mechanics, 1990. **57**(1): p. 232-240.
116. Schmalhorst, B., et al., *Drilling Dynamics in the Presence of Mud Flow* (IADC/SPE 59236), in *IADC/SPE Drilling Conference*. 2000: New Orleans, LA, USA.
117. Pressley, A., *Elementary Differential Geometry, 2nd Edition*. 2010, New York, NY, USA: Springer Undergraduate Mathematics Series.
118. Novozhilov, V.V., *Foundations of the nonlinear theory of elasticity*. 1953, Rochester, NY, USA: Graylock Press.
119. Da Silva, M.R.M.C., *Non-linear Flexural-Flexural-Torsional-Extensional Dynamics of Beams - I. Formulation*. Int. J. Solids Structures, 1988. **24**(12): p. 1225-1234.
120. Jeffryes, B., *Drilling Dynamics (US Patent Application - US 2011/0301924 A1)*, U. States, Editor. 2009, Schlumberger Technology Corporation: USA.
121. Gorelik, I., et al. *Model and Method for a Time-Efficient Analysis of Lateral Drillstring Dynamics*. in *ASME Turbo Expo: Turbine Technical Conference and Exposition*. 2015. Montréal, Canada: ASME.
122. Wilson, J.K. and S.F. Noynaert, *A New Damping Model for Nonlinear Drillstring Dynamics: Understanding the Effects of Rotation, Eccentricity, and Confined Fluid Flow and Their Impact on Unconventional Drillstring Design (SPE 178817 MS)*, in *IADC/SPE Drilling Conference and Exhibition*. 2016: Fort Worth, TX, USA.
123. Paidoussis, M.P., T.P. Luu, and S. Prabhakar, *Dynamics of a long tubular cantilever conveying fluid downwards, which then flows upwards around the cantilever as a confined annular flow*. Journal of Fluids and Structures, 2008. **24**: p. 111-128.
124. Erge, O., et al., *The Effects of Drillstring-Eccentricity,-Rotation, and -Buckling Configurations on Annular Frictional Pressure Losses While Circulating Yield-Power-Law Fluids (SPE 167950)*. SPE Drilling and Completions, 2015. **30**(3): p. 257-271.
125. Reddy, J.N., *An Introduction to Nonlinear Finite Element Analysis*. 2004, New York, NY, USA: Oxford University Press.
126. Fried, I., *Finite-Element Analysis of Time-Dependent Phenomena*. AIAA Journal, 1969. **7**(6): p. 1170-1173.
127. Hu, H.-c., *Variational Principles of Theory of Elasticity with Applications*. 1984, New York, NY, USA: Gordon and Breach.

128. Nachbagauer, K., *State of the art of ANCF elements regarding geometric description, interpolation strategies, definition of elastic forces, validation and the locking phenomenon in comparison with proposed beam finite elements*. Archives of Computational Methods in Engineering, 2014. **21**(3): p. 293-319.
129. Cowper, G.R., *The Shear Coefficient in Timoshenko's Beam Theory*. Journal of Applied Mechanics, 1966. **33**(2): p. 335-340.
130. Luo, Y., *An Efficient 3D Timoshenko Beam Element with Consistent Shape Functions*. Adv. Theor. Appl. Mech., 2008. **1**(3): p. 95-106.
131. Newmark, N., *Computation of Dynamic Structural Response in the Range Approaching Failure*, in *Structural Research Series*, D.o.C.E. University of Illinois, Editor. 1952.
132. Subbaraj, K. and A. Dokainish, *A Survey of Direct Time-Integration Methods in Computational Structural Dynamics - II. Implicit Methods*. Computers and Structures, 1989. **32**(6): p. 1387-1401.
133. Zhang, Q. and T. Hisada, *Analysis of fluid-structure interaction problems with structural buckling and large domain changes by ALE finite element method*. Comput. Methods Appl. Mech. Engrg., 2001. **190**: p. 6341-6357.
134. Mathworks, *MATLAB Software*. 2016.
135. DrillScan, *WellScan Software*. 2016.
136. Carrera, E., G. Giunta, and M. Petrolo, *Beam Structures: Classical and Advanced Theories*. 2011, Chichester, West Sussex, UK: John Wiley & Sons, Ltd.
137. Ho, H.-S., *Prediction of Drilling Trajectory in Directional Wells Via a New Rock-Bit Interaction Model (SPE 16658)*, in *62nd Annual Technical Conference and Exhibition*. 1987: Dallas, TX, USA.
138. Menand, S., et al., *How Bit Profile and Gauges Affect Well Trajectory (SPE 82412)*. SPE Drilling and Completions, 2003. **18**(1): p. 34-41.
139. Menand, S., H. Sellami, and C. Simon, *PDC Bit Classification According to Steerability (SPE 87837)*. SPE Drilling and Completions, 2004. **19**(1): p. 5-12.
140. NCEES, *FE Supplied-Reference Handbook, 8th Edition, 2nd Revision*. 2011, Clemson, SC, USA: NCEES.
141. Timoshenko, S.P., *On the Correction for Shear of the Differential Equation for Transverse Vibrations of Prismatic Bars*. Philosophical Magazine, 1921. **6**: p. 744-746.
142. Ginsberg, J.H., *Mechanical and Structural Vibrations: Theory and Applications*. 2001, New York, NY, USA: John Wiley & Sons, Inc.
143. Chevallier, A., *Nonlinear Stochastic Drilling Vibrations. Ph.D. Dissertation*. 2000, Rice University: Houston, TX, USA.

144. Heisig, G., J. Sancho, and J.D. Macpherson, *Downhole Diagnosis of Drilling Dynamics Data Provides New Level Drilling Process Control to Driller (SPE 49206)*, in *SPE Annual Technical Conference and Exhibition*. 1998: New Orleans, LA, USA.
145. Gabolde, G. and J.-P. Nguyen, *Drilling Data Handbook, 9th Edition*. 2014, Paris, France: Editions Technip.
146. Kinsler, L.E., et al., *Fundamentals of Acoustics, 4th Edition*. 1999, Hoboken, NJ, USA: John Wiley & Sons.
147. Placido, J.C.R., H.M.R. Santos, and Y.D. Galeano, *Drillstring Vibration and Wellbore Instability*. Journal of Energy Resources Technology, 2002. **124**(4): p. 217-222.
148. Zhu, X. and W. Liu, *The Effects of Drill String Impacts on Wellbore Stability*. Journal of Petroleum Science and Engineering, 2013. **109**: p. 217-229.
149. Sawaryn, S.J. and J.L. Thorogood, *A Compendium of Directional Calculations Based on the Minimum Curvature Method (SPE 84246)*. SPE Drilling and Completions, 2005. **20**(1): p. 24-36.
150. Sawaryn, S.J. and M.A. Tulceanu, *A Compendium of Directional Calculations Based on Minimum Curvature Method: Part 2*, in *SPE Annual Technical Conference and Exhibition*. 2007: Anaheim, CA, USA.

APPENDIX A.

MINIMUM CURVATURE RELATIONSHIPS AND TRAJECTORY CALCULATIONS

**Note: All of the concepts and formulas in this section can be found, or derived from, the information found in the work of Mitchell and Miska [21], Sawaryn and Thorogood [149], or Sawaryn and Tulceanu[150].*

A.1 Units Vectors Along a Well Path

The minimum curvature method assumes that the path between two survey points forms a circular arc, whose path is contained entirely within a single plane. The orientation of any point along this path can be determined with the following relationship.

$$\hat{v}_n = [D_3(\gamma_n)][D_1(\varphi_n)]^T \left[D_3\left(\frac{\pi}{2} - \alpha_n\right)\right]^T [I] \quad (\text{A.1})$$

Where n represents a “node” along a given well path (which could represent a single survey point from a particular well), α is the azimuth (clockwise angle measurement with respect to North on a geographical map), φ is the inclination (angle measurement with respect to the true vertical depth direction), and γ is called the tool face angle. The calculation of A.1 results in set of three orthogonal unit vectors that are referred to the tangent vector (\hat{v}_3), the normal vector (\hat{v}_2), and the bi-normal vector (\hat{v}_1). The orientation of these vectors is illustrated via Figure A.1. The figure also helps to explain what the tool face angle is; it is a measure, with respect to the high-side of the hole, of the rotation of the well path coordinates about the central axis of the wellbore. Essentially, the tool face angle aligns the normal unit vector in the direction of the curvature of the wellbore. Thus, the “plane of constant curvature” for a given section of a wellbore is determined by the tangent and normal vectors.

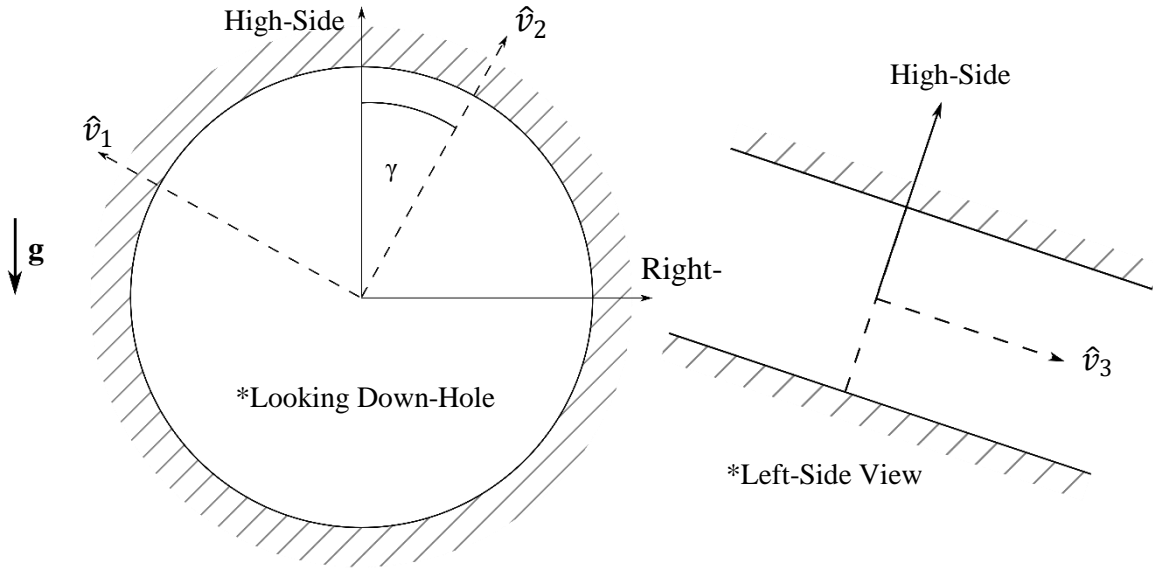


Figure A.1 Orientation of Wellbore Axes Relative to High-Side and Right-Side Vectors.

The inclination and azimuth are routinely measured at specified depth intervals while a well is being drilled, and are readily available. The tool face angle is not measured directly and must be calculated. In order to perform this calculation, the span angle between two survey points must be defined. This is a measure of the angle of the circular arc joining two survey points, and is called the Dog-Leg Angle, or simply “Dog-Leg” as it is frequently referred to in the industry. Knowing that the tangent vector of a wellbore cross-section can be easily computed with (A.2),

$$\hat{t} = (\sin \varphi \cos \alpha) \hat{i} + (\sin \varphi \sin \alpha) \hat{j} + (\cos \varphi) \hat{k} \quad (\text{A.2})$$

the Dog-Leg Angle (β_{DL}) for a wellbore section between two survey points can be calculated as

$$\hat{t}_1 \cdot \hat{t}_2 = \cos \beta_{DL} \quad (\text{A.3})$$

$$\beta_{DL} = \arccos[\sin \varphi_1 \sin \varphi_2 \cos(\alpha_1 - \alpha_2) + \cos \varphi_1 \cos \varphi_2] \quad (\text{A.4})$$

It can be noted that the curvature of a wellbore section is typically normalized over a reference course length (usually 100 ft or 30 m) in order to provide direct comparisons between the severity of curvatures between different wellbores and wellbore sections. This reference curvature is called the Dog-Leg Severity (DLS) and is generally expressed as a degree per normalize course length ($^{\circ}/100\text{ft}$ or $^{\circ}/30\text{m}$).

Additionally, the high-side and right-side vectors of a well need to be defined. These were also shown in Figure A.1 and can be mathematically expressed as

$$\hat{hs} = (\cos \varphi \cos \alpha) \hat{i} + (\cos \varphi \sin \alpha) \hat{j} - (\sin \varphi) \hat{k} \quad (A.5)$$

$$\hat{rs} = -(sin\alpha) \hat{i} + (cos\alpha) \hat{j} \quad (A.6)$$

Noting that the normal vector can also be expressed as

$$\hat{v}_2 = \frac{1}{\kappa_o} \left[\cos \varphi \cos \alpha \frac{d\varphi}{ds} - \sin \varphi \sin \alpha \frac{d\alpha}{ds} \right] \hat{i} + \frac{1}{\kappa_o} \left[\cos \varphi \sin \alpha \frac{d\varphi}{ds} + \sin \varphi \cos \alpha \frac{d\alpha}{ds} \right] \hat{j} + \frac{1}{\kappa_o} \left[\sin \varphi \frac{d\varphi}{ds} \right] \hat{k} \quad (A.7)$$

**Note: The κ_o term is the relative curvature of the wellbore, $\kappa_o = \frac{\beta_{DL}}{\Delta s}$. Multiplying this number by a normalized course length (100 ft or 30m) will give the DLS.*

The tool face angle can readily be determined from vector relationships

$$\hat{hs} \cdot \hat{v}_2 = \cos \gamma \quad (A.8)$$

$$\hat{rs} \cdot \hat{v}_2 = \cos \left(\frac{\pi}{2} - \gamma \right) = \sin \gamma \quad (A.9)$$

$$\tan \gamma = \frac{\hat{rs} \cdot \hat{v}_2}{\hat{hs} \cdot \hat{v}_2} \quad (A.10)$$

Through some slight algebra, and utilizing trigonometric relationships, (A.10) can be reduced to

$$\gamma = \text{atan} \left(\frac{\Delta \alpha}{\Delta \varphi} \frac{\sin \varphi}{\sin^2 \varphi + \cos^4 \varphi \cos^4 \alpha} \right) \quad (A.11)$$

It should be noted that the *atan* function is only valid on the interval from $-\frac{\pi}{2} \leq \gamma < \frac{\pi}{2}$. Because the tool face angle is always a positive number ranging from 0 to 2π , (A.11) must be properly adjusted in order to determine the appropriate angle. This adjustment can be made by checking the scalar projection of the normal vector onto the high-side vector.

$$\gamma = \pi - \gamma \quad \text{if } \hat{v}_2 \cdot \hat{hs} < 0 \quad (A.12)$$

**Note: In performing calculations with the arc tangent function, it is generally recommended to find a more reliable coding implementation. For example, using the “ $\gamma = \text{atan2}(y,x)$ ” function in MATLAB, if the 2*

required inputs are known; or, alternatively, using equation (A.8) to determine γ , and adjusting the output angle based on the limitations of the arc cosine function.

A.2 Trajectory Calculations

The global coordinates of a well can be successively calculated, starting from the surface location (x_0 , y_0 , z_0), by using the inclination, azimuth, and calculated dogleg angle.

$$\Delta x = [\sin \varphi_1 \cos \alpha_1 + \sin \varphi_2 \cos \alpha_2]R \quad (\text{A.13})$$

$$\Delta y = [\sin \varphi_1 \sin \alpha_1 + \sin \varphi_2 \sin \alpha_2]R \quad (\text{A.14})$$

$$\Delta z = [\cos \varphi_1 + \cos \varphi_2]R \quad (\text{A.15})$$

$$R = \frac{\Delta s}{\beta_{DL}} \tan\left(\frac{\beta_{DL}}{2}\right) \quad (\text{A.16})$$

Where Δs is the course length between two survey points in the well.

A.3 Interpolation between Survey Points

Occasionally, such as the case of applying the minimum curvature method to the finite element model presented in this work, it is necessary to interpolate between survey points. This is required for determining the proper vector orientation of each node within the finite element model. Knowing the dogleg angle, the course length, and the initial inclination and azimuth of a given wellbore section, the inclination and azimuth of a point along a constant curvature wellbore section can be calculated as

$$\varphi = \arccos \left[\cos \varphi_1 \cos(\kappa_o \Delta s) + \frac{\cos \varphi_2 - \cos \varphi_1 \cos \beta_{DL}}{\sin \beta_{DL}} \sin(\kappa_o \Delta s) \right] \quad (\text{A.17})$$

$$\alpha = \arccos \left(\frac{\hat{t} \cdot \hat{i}}{\sin \varphi} \right) = \arccos \left\{ \frac{1}{\sin \varphi} \left[\sin \varphi_1 \cos \alpha_1 \cos(\kappa_o \Delta s) + \frac{\sin(\kappa_o \Delta s)}{\sin \beta_{DL}} (\sin \varphi_2 \cos \alpha_2 - \sin \varphi_1 \cos \alpha_1 \beta_{DL}) \right] \right\} \quad (\text{A.18})$$

In this case Δs is the distance along the wellbore section, with respect to the initial position of that particular section, to the point of interest. Similar to (A.11), the \arccos function is only valid over a specified interval such that $0 \leq \alpha < \pi$. Understanding that the azimuth ranges from 0 to 2π , it is necessary to correct this angle based on the orientation of the tangent vector. This can be done via (A.19).

$$\alpha = 2\pi - \alpha \quad \text{if } \hat{t} \cdot \hat{j} < 0 \quad (\text{A.19})$$

APPENDIX B.

DERIVATION OF TIME-INTEGRATION EQUATIONS

The nonlinear system of equations representing the drillstring within a wellbore are written as

$$[\underline{M}_\rho + \widetilde{\underline{M}}_F] \ddot{\underline{u}} + \underline{C} \dot{\underline{u}} + \underline{F}_{M_{Gyro}}(\underline{u}, \dot{\underline{u}}, \ddot{\underline{u}}) + \underline{F}_B(\underline{u}) + \underline{F}_W(\underline{u}, \dot{\underline{u}}) + \underline{F}_f(\underline{u}, \dot{\underline{u}}) = \underline{Q} + \underline{F}_{Exc}(t) \quad (3.43)$$

Assuming the values are known at time t and $t + \Delta t$, the system can be represented as a Taylor series expansion (with respect to \underline{u} , and neglecting higher order terms) as

$$\begin{aligned} [M]\ddot{\underline{u}}^{t+\Delta t} + [C]^{t+\Delta t}\dot{\underline{u}}^{t+\Delta t} + [K]^{t+\Delta t}\underline{u}^{t+\Delta t} &= \underline{Q} + \underline{F}_{Exc}^t - \underline{F}_{M_{Gyro}}^{t+\Delta t} - \underline{F}_B^{t+\Delta t} - \underline{F}_W^{t+\Delta t} - \underline{F}_f^{t+\Delta t} \quad (B.1) \\ [K]^{t+\Delta t} &= \left[\frac{\partial \underline{F}_{M_{Gyro}}}{\partial \underline{u}} \right]^{t+\Delta t} + \left[\frac{\partial \underline{F}_B}{\partial \underline{u}} \right]^{t+\Delta t} + \left[\frac{\partial \underline{F}_W}{\partial \underline{u}} \right]^{t+\Delta t} + \left[\frac{\partial \underline{F}_f}{\partial \underline{u}} \right]^{t+\Delta t} \\ [C]^{t+\Delta t} &= \beta_D[M] + \gamma_D[K]^{t+\Delta t} \\ [M] &= \underline{\underline{M}}_\rho + \widetilde{\underline{\underline{M}}}_F \end{aligned}$$

The superscript, $t + \Delta t$, signifies that the vector or matrix is evaluated at the current displacement iteration with the velocities and accelerations from the previous time step. Ultimately, the velocities and the accelerations remain constant through each time step, as shown by (B.2).

$$\begin{aligned} \left[\frac{\partial \underline{F}_{M_{Gyro}}}{\partial \underline{u}} \right]^{t+\Delta t} &= \frac{\partial \underline{F}_{M_{Gyro}}}{\partial \underline{u}}(\underline{u}^{t+\Delta t}, \dot{\underline{u}}^t, \ddot{\underline{u}}^t) & \underline{F}_{M_{Gyro}}^{t+\Delta t} &= \underline{F}_{Gyro}(\underline{u}^{t+\Delta t}, \dot{\underline{u}}^t, \ddot{\underline{u}}^t) \\ \left[\frac{\partial \underline{F}_B}{\partial \underline{u}} \right]^{t+\Delta t} &= \frac{\partial \underline{F}_B}{\partial \underline{u}}(\underline{u}^{t+\Delta t}) & \underline{F}_B^{t+\Delta t} &= \underline{F}_B(\underline{u}^{t+\Delta t}) \\ \left[\frac{\partial \underline{F}_W}{\partial \underline{u}} \right]^{t+\Delta t} &= \frac{\partial \underline{F}_W}{\partial \underline{u}}(\underline{u}^{t+\Delta t}, \dot{\underline{u}}^t) & \underline{F}_W^{t+\Delta t} &= \underline{F}_W(\underline{u}^{t+\Delta t}, \dot{\underline{u}}^t) \\ \left[\frac{\partial \underline{F}_f}{\partial \underline{u}} \right]^{t+\Delta t} &= \frac{\partial \underline{F}_f}{\partial \underline{u}}(\underline{u}^{t+\Delta t}, \dot{\underline{u}}^t) & \underline{F}_f^{t+\Delta t} &= \underline{F}_f(\underline{u}^{t+\Delta t}, \dot{\underline{u}}^t) \end{aligned} \quad (B.2)$$

Newmark's [131] method assumes that displacement and velocity, at a given time-step, can both be expressed as

$$\dot{\underline{u}}^{t+\Delta t} = \dot{\underline{u}}^t + (1 - \delta_N)\Delta t \ddot{\underline{u}}^t + \delta_N \Delta t \ddot{\underline{u}}^{t+\Delta t} \quad (B.3)$$

$$\underline{u}^{t+\Delta t} = \underline{u}^t + \Delta t \dot{\underline{u}}^t + \left(\frac{1}{2} - \alpha_N \right) \Delta t^2 \ddot{\underline{u}}^t + \alpha_N \Delta t^2 \ddot{\underline{u}}^{t+\Delta t} \quad (B.4)$$

Where δ_N and α_N are constants that dictate the integration scheme. Noting that Equation (B.1) is a function of Δu , it is beneficial to rewrite (B.4) as

$$\underline{\Delta u}^{t+\Delta t} = \Delta t \dot{\underline{u}}^t + \left(\frac{1}{2} - \alpha_N \right) \Delta t^2 \ddot{\underline{u}}^t + \alpha_N \Delta t^2 \ddot{\underline{u}}^{t+\Delta t} \quad (\text{B.5})$$

Solving (B.5) for the acceleration at time $t + \Delta t$, it can be rewritten as

$$\ddot{\underline{u}}^{t+\Delta t} = \frac{1}{\alpha_N \Delta t^2} \underline{\Delta u}^{t+\Delta t} - \frac{1}{\alpha_N \Delta t} \dot{\underline{u}}^t - \left(\frac{1}{2\alpha_N} - 1 \right) \ddot{\underline{u}}^t \quad (\text{B.6})$$

Now, Plugging (B.6) into (B.3)

$$\dot{\underline{u}}^{t+\Delta t} = \frac{\delta_N}{\alpha_N \Delta t} \underline{\Delta u}^{t+\Delta t} + \left(1 - \frac{\delta_N}{\alpha_N} \right) \dot{\underline{u}}^t + \Delta t \left(1 - \frac{\delta_N}{2\alpha_N} \right) \ddot{\underline{u}}^t \quad (\text{B.7})$$

And plugging (B.7) and (B.6) into (B.1) the relationship for incremental displacements at time $t + \Delta t$ is found to be

$$[M] \left\{ \frac{1}{\alpha_N \Delta t^2} \underline{\Delta u}^{t+\Delta t} - \frac{1}{\alpha_N \Delta t} \dot{\underline{u}}^t - \left(\frac{1}{2\alpha_N} - 1 \right) \ddot{\underline{u}}^t \right\} + [C]^{t+\Delta t} \left\{ \frac{\delta_N}{\alpha_N \Delta t} \underline{\Delta u}^{t+\Delta t} + \left(1 - \frac{\delta_N}{\alpha_N} \right) \dot{\underline{u}}^t + \Delta t \left(1 - \frac{\delta_N}{2\alpha_N} \right) \ddot{\underline{u}}^t \right\} + [K]^{t+\Delta t} \{ \underline{\Delta u}^{t+\Delta t} \} = \underline{Q}^t + \underline{F}_{Exc}^t - \underline{F}_{Mgyro}^{t+\Delta t} - \underline{F}_B^{t+\Delta t} - \underline{F}_W^{t+\Delta t} - \underline{F}_f^{t+\Delta t} \quad (\text{B.8})$$

(B.8) can be rewritten in a “friendlier” form as

$$\begin{aligned} & \left[\frac{1}{\alpha_N \Delta t^2} [M] + \frac{\delta_N}{\alpha_N \Delta t} [C]^{t+\Delta t} + [K]^{t+\Delta t} \right] \underline{\Delta u}^{t+\Delta t} = \underline{Q}^t + \underline{F}_{Exc}^t - \underline{F}_{Mgyro}^{t+\Delta t} - \underline{F}_B^{t+\Delta t} - \underline{F}_W^{t+\Delta t} - \underline{F}_f^{t+\Delta t} + \\ & [M] \left\{ \frac{1}{\alpha_N \Delta t} \dot{\underline{u}}^t + \left(\frac{1}{2\alpha_N} - 1 \right) \ddot{\underline{u}}^t \right\} + [C]^{t+\Delta t} \left\{ \left(\frac{\delta_N}{\alpha_N} - 1 \right) \dot{\underline{u}}^t + \Delta t \left(\frac{\delta_N}{2\alpha_N} - 1 \right) \ddot{\underline{u}}^t \right\} \end{aligned} \quad (\text{B.9})$$

(B.9) can be further reduced in a condensed manner, as was shown in Section 3.

$$[K_{eff}]^{t+\Delta t} \underline{\Delta u}^{t+\Delta t} = \underline{Q}_{eff}^{t+\Delta t} \quad (\text{B.10})$$

$$[K_{eff}]^{t+\Delta t} = \frac{1}{\alpha_N \Delta t^2} [M] + \frac{\delta_N}{\alpha_N \Delta t} [C]^{t+\Delta t} + [K]^{t+\Delta t}$$

$$\underline{Q}_{eff}^{t+\Delta t} = \underline{Q} + \underline{F}_{Exc}^t - \underline{F}_{M_{gyro}}^{t+\Delta t} - \underline{F}_B^{t+\Delta t} - \underline{F}_W^{t+\Delta t} - \underline{F}_f^{t+\Delta t} + [M] \left\{ \frac{1}{\alpha_N \Delta t} \dot{\underline{u}}^t + \left(\frac{1}{2\alpha_N} - 1 \right) \ddot{\underline{u}}^t \right\} + \\ [C]^{t+\Delta t} \left\{ \left(\frac{\delta_N}{\alpha_N} - 1 \right) \dot{\underline{u}}^t + \Delta t \left(\frac{\delta_N}{2\alpha_N} - 1 \right) \ddot{\underline{u}}^t \right\}$$

B.6, B.7, and B.10 represent the incremental equations, in time, that are solved for the nonlinear simulations.

APPENDIX C.
SURVEY DATA FROM NORTHEAST WELL

MD	INC	AZI	831	7.96	306.75
0	0	0	856	8.77	308.57
106	0.41	88.72	881	9.47	310.55
131	0.4	92.53	906	10.14	311.32
156	0.38	100.87	931	10.92	312.05
181	0.41	100.09	956	11.34	312.65
206	0.4	101.52	981	11.81	312.11
231	0.36	102.14	1006	12.14	311.64
256	0.28	107.95	1031	12.45	311.19
281	0.37	89.58	1056	12.53	310.6
306	0.33	104.97	1081	12.75	310.65
331	0.28	93.65	1106	12.88	309.82
356	0.36	92.23	1131	13.1	308.89
381	0.32	78.98	1156	13.37	308.49
406	0.2	70.35	1181	13.74	308.06
431	0.2	58.74	1206	14.4	306.9
456	0.08	6.3	1231	15.03	306.11
481	0.16	320.66	1256	15.29	306.76
506	0.24	345.62	1281	15.54	307.08
531	0.43	311.15	1306	15.98	309.09
556	1.2	292.46	1331	16.39	309.67
581	1.76	288.67	1356	16.53	309.88
606	2.41	287.51	1381	16.93	311.1
631	2.9	286.66	1406	17.26	315.01
656	3.66	288.74	1431	17.55	316.92
681	4.47	289.74	1456	17.81	317.2
706	5.17	292.12	1481	18.04	317.17
731	5.51	295.65	1506	18.39	317.19
756	5.94	298.42	1531	18.65	317.11
781	6.56	301.29	1556	18.93	317.36
806	7.37	304.5	1581	19.26	317.32

1606	19.67	316.94	2456	19.29	303.48
1631	19.99	316.91	2481	19.09	302.24
1656	20.17	316.8	2506	19.02	301.96
1681	19.91	314.91	2530.99	18.68	301.98
1706	19.56	312.47	2555.99	18.75	301.72
1731	19.86	312.66	2580.99	18.08	300.76
1756	19.94	313.16	2605.99	17.96	300.28
1781	20.28	314.67	2630.99	17.57	298.94
1806	20.59	315.53	2655.99	17.18	295.41
1831	20.96	316.04	2680.99	16.91	293.5
1856	21.35	316.21	2705.99	16.59	291.96
1881	21.83	316.61	2730.99	16.71	290.5
1906	22.37	316.86	2755.99	17.01	288.22
1931	22.85	316.98	2780.99	17.12	287.72
1956	22.85	316.44	2805.99	16.78	286.22
1981	22.01	314.92	2830.99	16.91	285
2006	21.96	314.46	2855.99	16.94	284.25
2031	21.99	313.52	2880.99	17.31	282.93
2056	21.9	313.35	2905.99	17.56	280.38
2081	21.94	313.38	2930.99	17.72	279.43
2106	22.02	313.38	2955.99	17.36	278.02
2131	21.88	314.12	2980.99	17.35	276.88
2156	22.03	314.01	3005.99	17.08	275.78
2181	22.19	314.29	3030.99	17.46	274.39
2206	22.22	314.5	3055.99	18.08	271.51
2231	22.02	314.07	3080.99	18.75	268.48
2256	21.04	312.01	3105.99	19.58	265.63
2281	20.62	310.74	3130.99	20.1	263.2
2306	20.65	309.65	3155.99	20.44	260.78
2331	20.43	308.77	3180.99	20.71	258.45
2356	19.84	307.41	3205.99	20.79	255.72
2381	19.76	306.9	3230.99	21.08	253.05
2406	19.85	306.18	3255.99	21.27	251.27
2431	19.49	304.7	3280.99	21.91	250.19

3305.99	22.62	249.48	4155.99	28.51	237.13
3330.99	22.91	248.8	4180.99	29.46	237.39
3355.99	23.44	247.27	4205.99	30.03	236.92
3380.99	24.1	245.58	4230.99	30.47	236.75
3405.99	24.35	243.99	4255.99	30.28	235.58
3430.99	24.92	242.73	4280.99	29.72	234.76
3455.99	25.45	242.08	4305.99	29.39	234.37
3480.99	26.11	241.4	4330.99	29.51	234.31
3505.99	26.4	240.16	4355.99	29.2	234.48
3530.99	26.82	239.06	4380.99	29.11	234.75
3555.99	26.97	238.06	4405.99	28.97	234.94
3580.99	27.48	237.69	4430.99	28.59	235.35
3605.99	27.89	237.04	4455.99	28.87	235.17
3630.99	28.34	236.56	4480.99	28.97	235.36
3655.99	28.46	236.18	4505.99	28.92	235.62
3680.99	28.03	235.27	4530.99	29.23	236.57
3705.99	27.7	234.75	4555.99	29.56	237.28
3730.99	27.22	233.77	4580.99	29.48	237.64
3755.99	27.08	232.82	4605.99	29.75	237.67
3780.99	27.03	231.98	4630.99	29.47	237.73
3805.99	26.26	231.26	4655.99	29.18	237.84
3830.99	26.06	230.72	4680.99	29.62	237.97
3855.99	26.16	230.89	4705.99	29.75	238.39
3880.99	25.77	231.14	4730.99	29.76	238.73
3905.99	25.31	230.28	4755.99	29.96	239.38
3930.99	24.95	230.67	4780.99	30.08	239.81
3955.99	25.18	231.4	4805.99	30.04	240.01
3980.99	25.32	232.3	4830.99	29.8	240.45
4005.99	25.24	232.81	4855.99	29.77	240.89
4030.99	25.32	233.18	4880.99	29.55	241.22
4055.99	25.71	233.99	4905.99	29.78	241.59
4080.99	26.27	235.45	4930.99	29.87	241.58
4105.99	27.05	236.24	4955.99	29.84	241.45
4130.99	27.73	236.92	4980.99	29.8	240.91

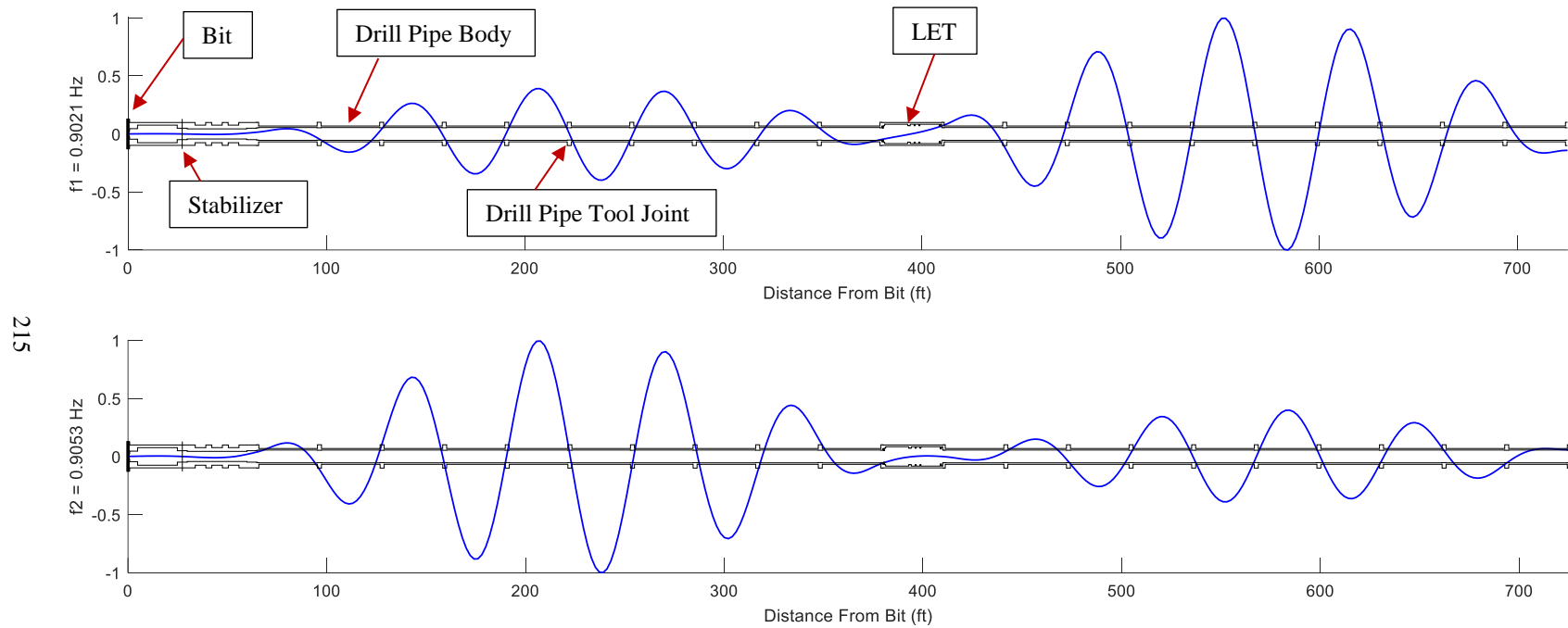
5005.99	29.94	240.73	5855.99	27.83	237.33
5030.99	29.76	240.06	5880.99	27.55	236.94
5055.99	29.55	239.89	5905.99	27.08	236.19
5080.99	29.01	239.83	5930.99	26.67	235.43
5105.99	28.9	239.82	5955.99	26.35	235.06
5130.99	29.14	239.78	5980.99	26.64	235.36
5155.99	28.88	239.22	6005.99	26.92	236.33
5180.99	28.92	239.46	6006.44	26.92	236.34
5205.99	28.95	239.39	6037	27.49	236.08
5230.99	28.89	238.69	6067	27.2	235.06
5255.99	28.63	238.27	6097	26.9	235.5
5280.99	28.57	238.34	6127	26.54	234.85
5305.99	28.6	238.77	6157	26.03	233.42
5330.99	28.15	238.68	6187	25.95	232.4
5355.99	28.1	238.67	6217	26.24	236.15
5380.99	28.18	238.92	6247	26.42	238.55
5405.99	28.15	239.14	6276	26.51	237.77
5430.99	27.88	238.98	6306	26.49	237.37
5455.99	27.87	238.75	6336	26.46	237.04
5480.99	27.78	238.33	6366	25.98	237.14
5505.99	27.31	237.68	6396	27.29	233.24
5530.99	27.24	237.26	6426	29.14	224.4
5555.99	26.88	236.81	6455	31.6	217.39
5580.99	26.48	236.54	6485	33.88	212.66
5605.99	26.11	235.96	6515	35.77	208.14
5630.99	26.69	235.72	6545	37.57	202.61
5655.99	27.18	235.62	6575	39.8	197.94
5680.99	27.26	235.73	6605	41.89	193.97
5705.99	27.42	235.47	6635	44.04	189.89
5730.99	27.4	235.23	6665	46.81	187.77
5755.99	27.31	235.1	6695	48.9	185.71
5780.99	27.3	235.6	6724	51.23	184.03
5805.99	27.74	236.35	6755	54.34	182.9
5830.99	27.93	237.23	6785	56.82	181.84

6815	59.55	179.07	9321	89.93	161.19
6845	62.36	174.91	9410	89.66	159.82
6875	63.72	173.23	9500	89.66	159.44
6904	67.06	170.87	9590	89.9	159.93
6934	71.78	167.65	9679	89.1	157.82
6964	75.73	167.26	9769	89.9	160.96
6994	78.3	166.45	9859	89.7	160.33
7024	81.18	165.27	9948	89.6	158.78
7054	86.27	164.32	10037	89.73	161.78
7088	89.46	164.28	10127	89.66	161.74
7171	89.6	164.02	10216	89.23	160.43
7261	88.33	160.65	10306	89.77	160.61
7350	88.96	161.97	10396	90.2	161
7440	90.37	161.83	10485	89.39	160.53
7530	89.8	159.56	10575	89.23	160.24
7619	89.09	158.19	10664	90.1	160.59
7709	89.4	158.59	10754	89.5	159.62
7798	88.63	158.48	10843	88.7	157.31
7888	89.56	160.42	10933	89.63	159.93
7978	88.93	158.52	11023	89.5	159.85
8067	90.57	160.49	11112	89.16	158.89
8157	90.13	160.57	11202	90.23	160.06
8246	89.5	160.39	11291	89.6	159.3
8336	89.4	159.53	11381	90.1	162.59
8425	88.86	159.97	11471	90.57	163.42
8515	89.6	161.83	11560	90.71	162.89
8604	89.43	160.84	11650	88.32	161.67
8694	89.9	161.69	11739	89.23	160.8
8784	89.93	161.15	11829	88.83	160.87
8874	89.93	160.77	11919	89.63	160.04
8963	89.46	160.06	12008	89.63	160.69
9052	90.37	160.94	12098	88.79	159.83
9142	89.53	158.54	12187	89.66	160.72
9231	89.5	159.28	12277	89.5	159.07

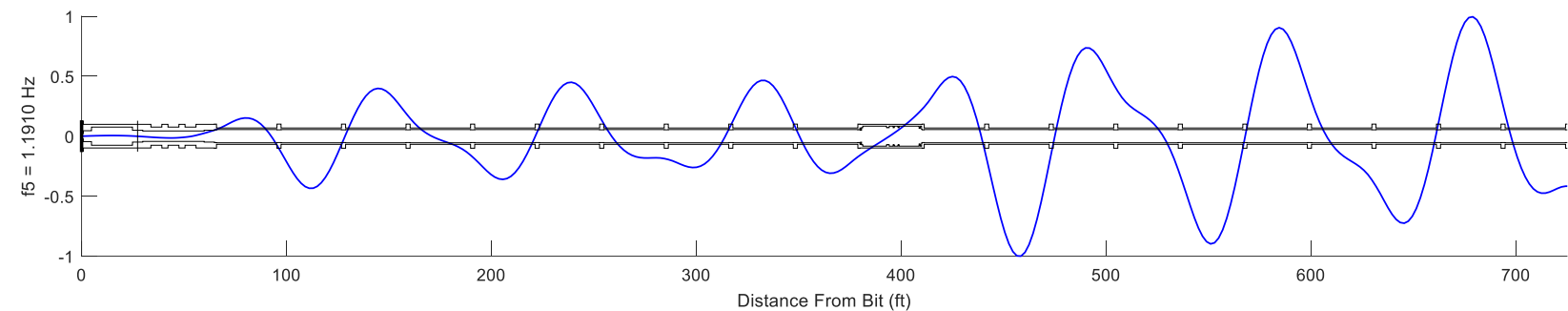
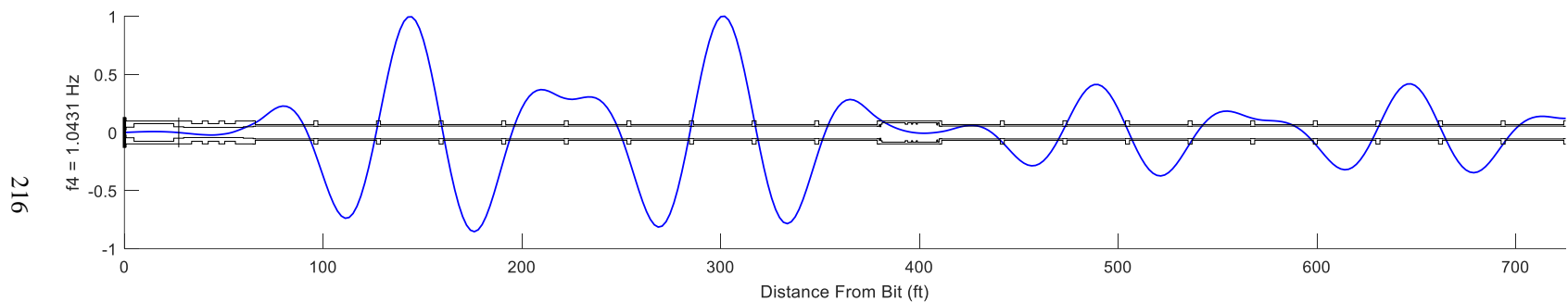
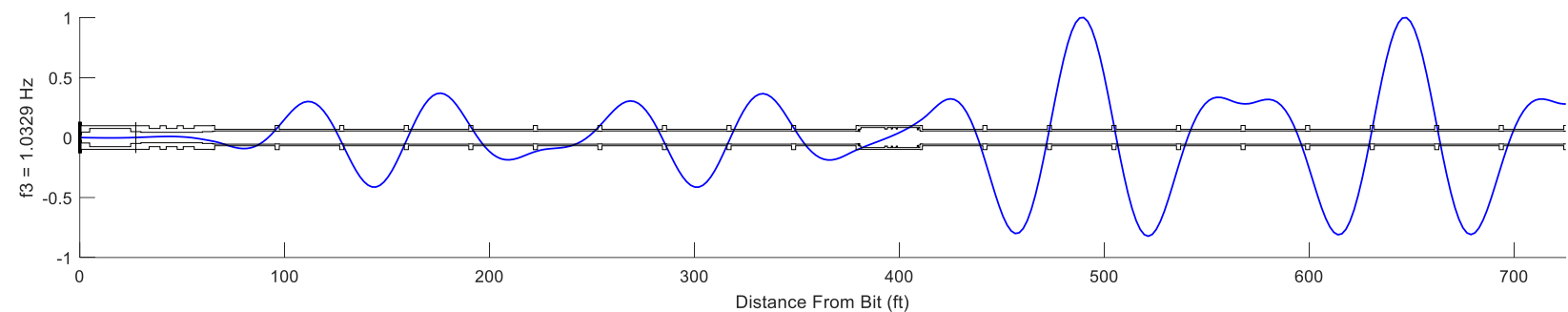
12366	89.5	158.89	15412	90.27	160.37
12456	88.56	159.24	15502	89.83	161.88
12545	89.77	161.14	15591	90.07	161.54
12635	89.56	161.91	15680	89.43	162.17
12724	89.77	159.78	15770	89.66	160.5
12814	89.66	160.16	15860	89.93	160.81
12904	90.13	160.98	15949	89.56	160.14
12993	89.7	159.5	16039	89.19	159.68
13083	88.76	160.51	16128	89.46	160.06
13173	88.96	160.44	16217	89.56	159.73
13262	89.23	160.84	16307	89.2	160.76
13352	89.16	160.54	16397	88.62	160.62
13442	88.82	160.18	16486	88.38	159.87
13531	89.46	160.28	16575	89.66	159.54
13621	90.03	160.5	16665	90.13	159.59
13710	89.33	158.82	16754	88.22	159.16
13800	89.5	158.67	16844	89.67	159.69
13890	90.13	158.37	16933	90.2	159.57
13979	88.8	158.07	17023	88.72	159.25
14069	88.09	160.21	17112	89.26	160.14
14158	89.23	161.18	17202	89.43	160.66
14248	88.59	160.97	17291	89.76	159.47
14338	88.62	160.55	17381	89.56	161.2
14427	88.82	161.18	17471	89.8	160.08
14517	90	160.11	17560	89.16	161.22
14606	90.24	160.36	17650	88.96	160.95
14696	89.06	160.31	17739	90.03	161.8
14785	88.82	159.55	17829	89.97	161.53
14875	89.66	160.83	17919	89.5	160.79
14965	89.83	161.08	18008	90.07	160.45
15054	89.53	160.01	18098	88.72	159.53
15144	89.26	159.74	18187	89.5	160.89
15233	88.83	158.45	18277	89.23	160.03
15323	90.37	160.67	18367	88.79	156.94

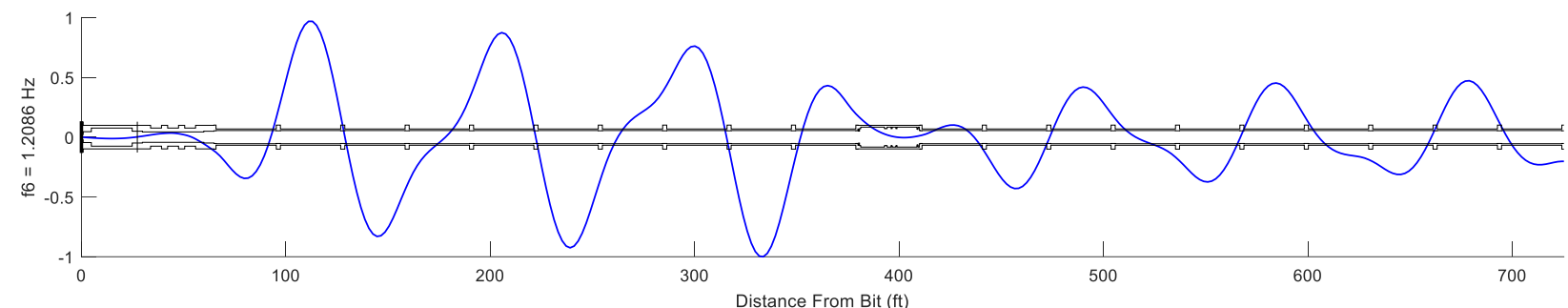
18456	90.37	161.02	18993	91.24	159.29
18546	89.76	158.16	19082	91.74	159.55
18635	89.63	160.36	19171	92.31	159.79
18725	89.46	159.57	19221	92.32	158.75
18814	90.77	161.14	19277	92.32	158.75
18903	91.01	160.8			

APPENDIX D.
FREE VIBRATION PLOTS FOR SECTION 5

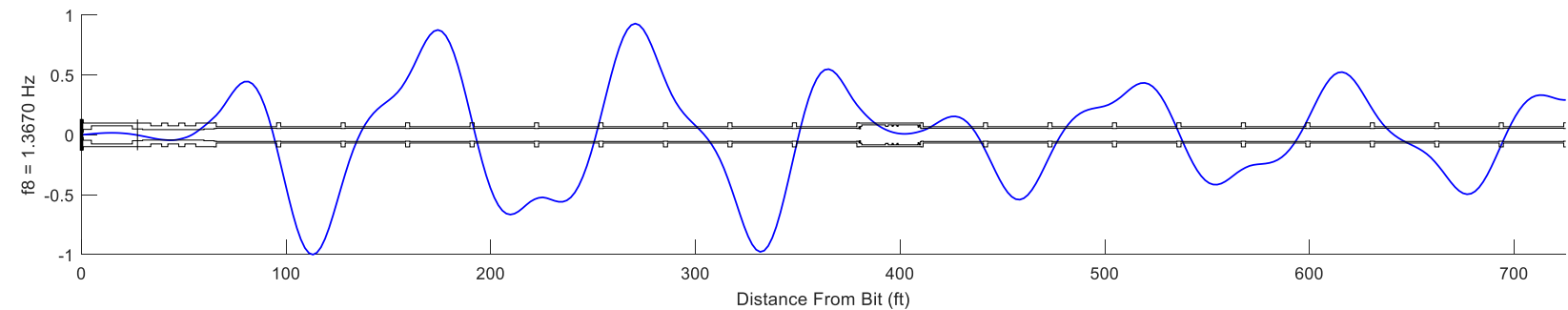
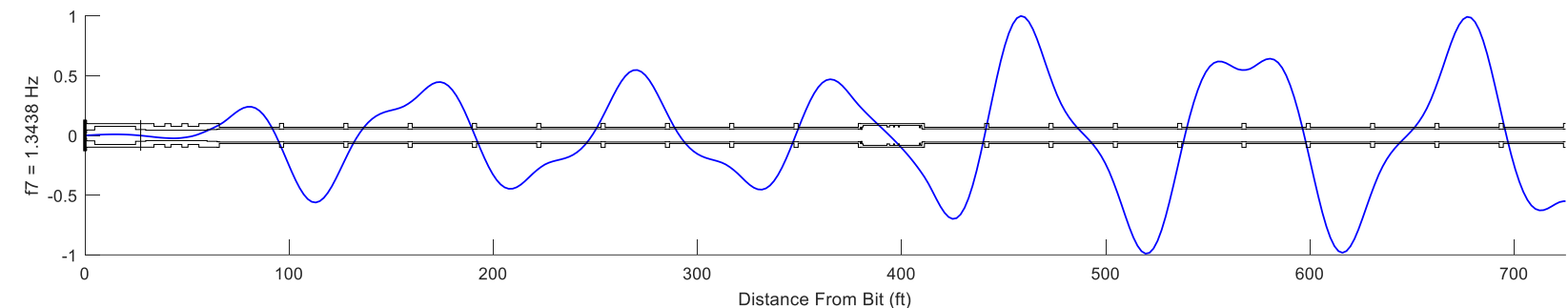


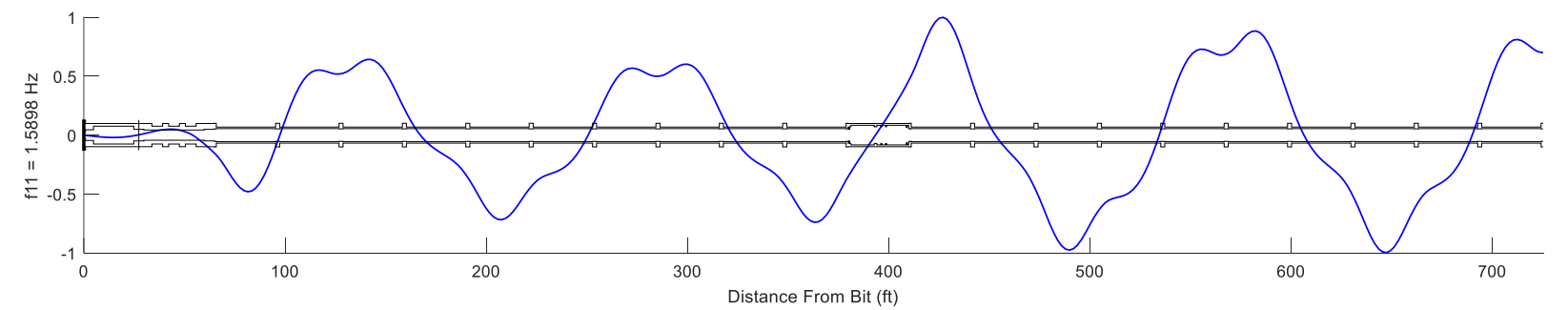
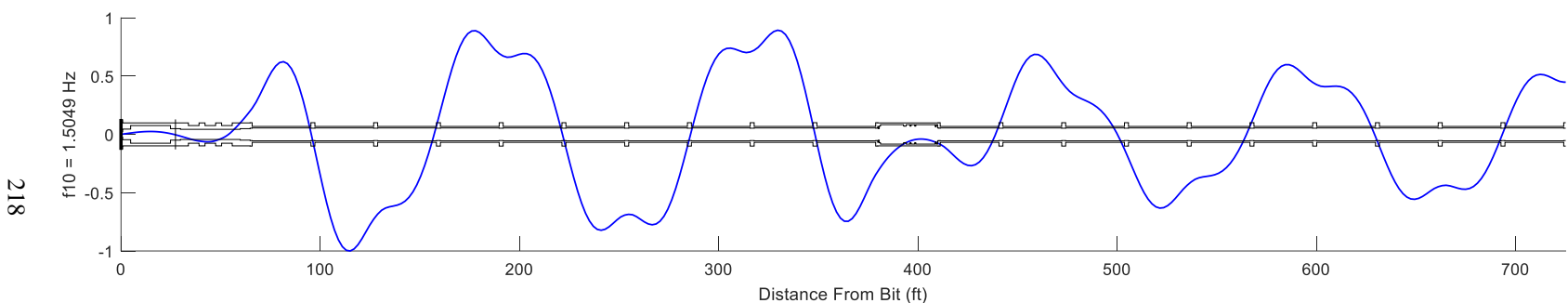
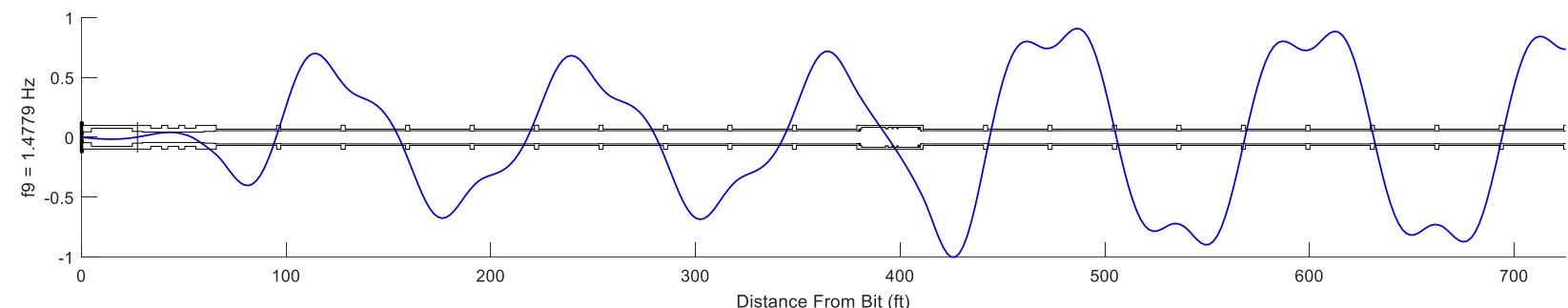
*Note: Figures show the right-side mode shapes (shapes in the horizontal-plane, i.e. looking down on top of the drillstring in a horizontal well) of the assembly examined in Section 5. The displacement patterns are modal displacements, which do not have an actual magnitude associated with them. Essentially, these plots indicate the vibration pattern that is likely to occur at a given frequency.

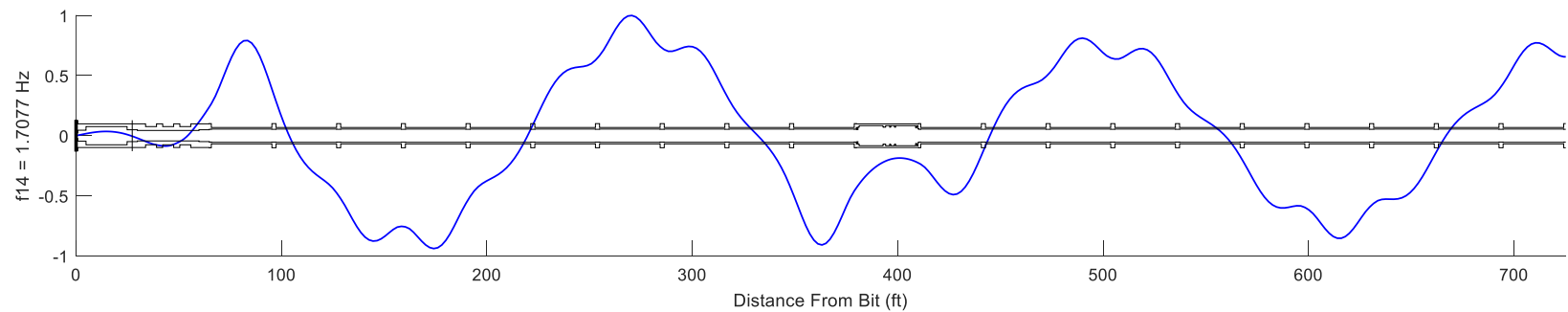
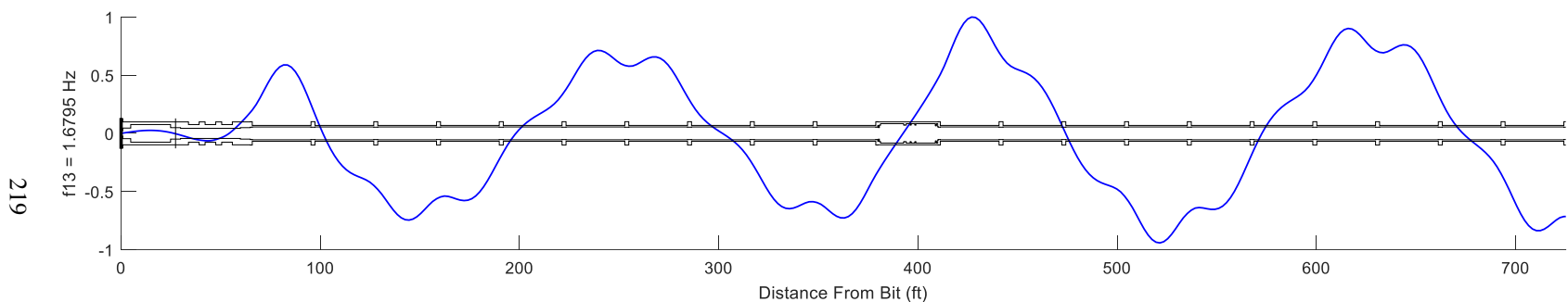
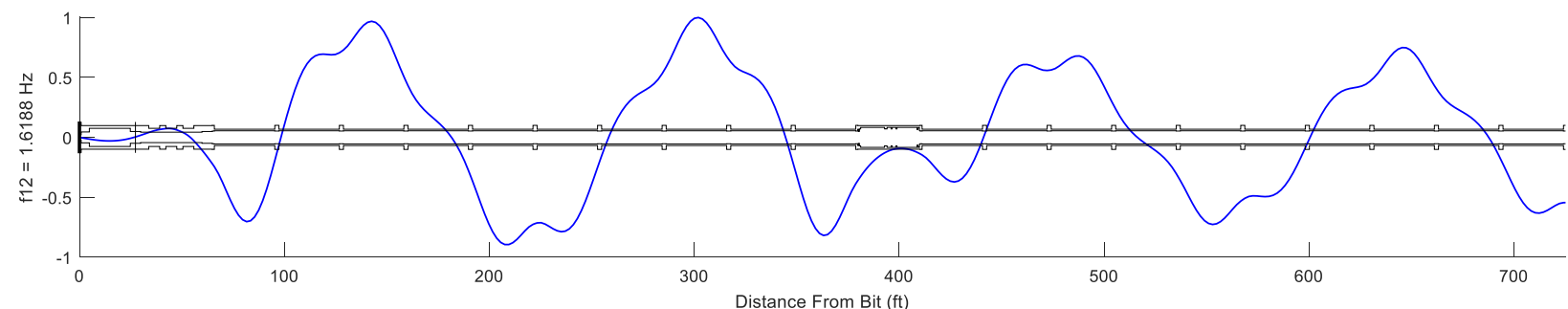


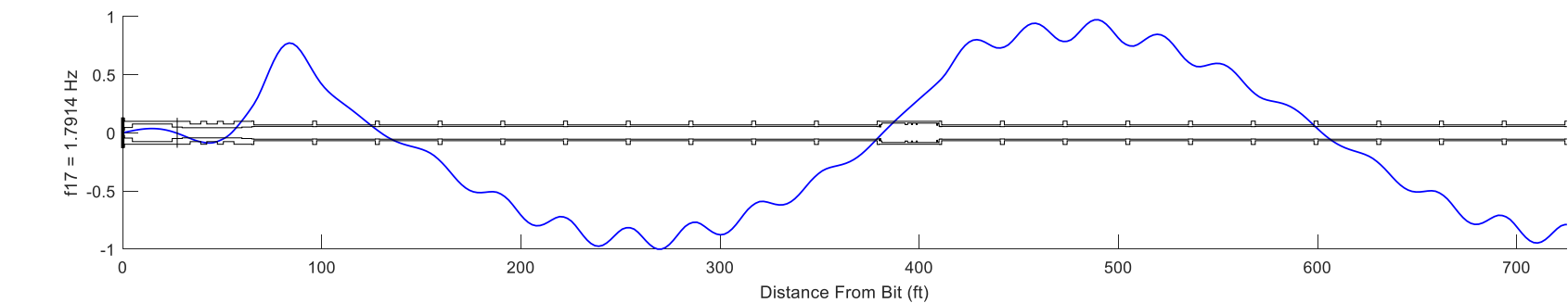
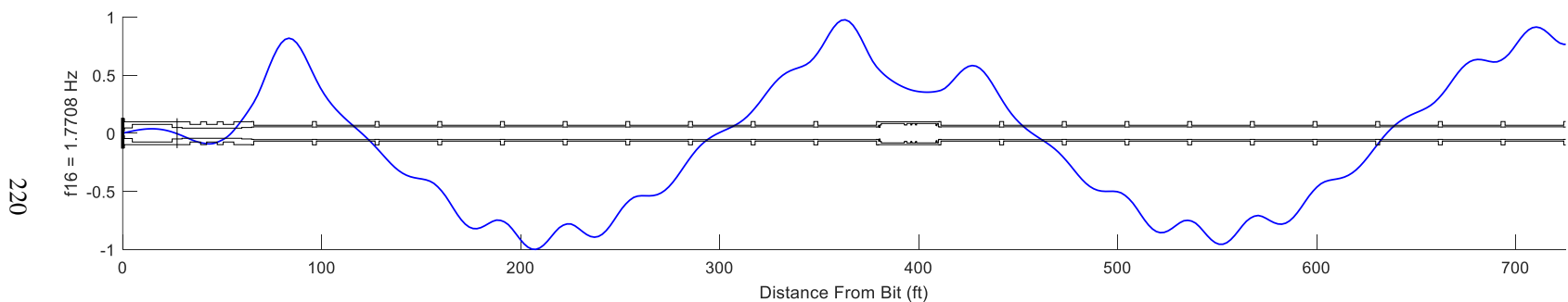
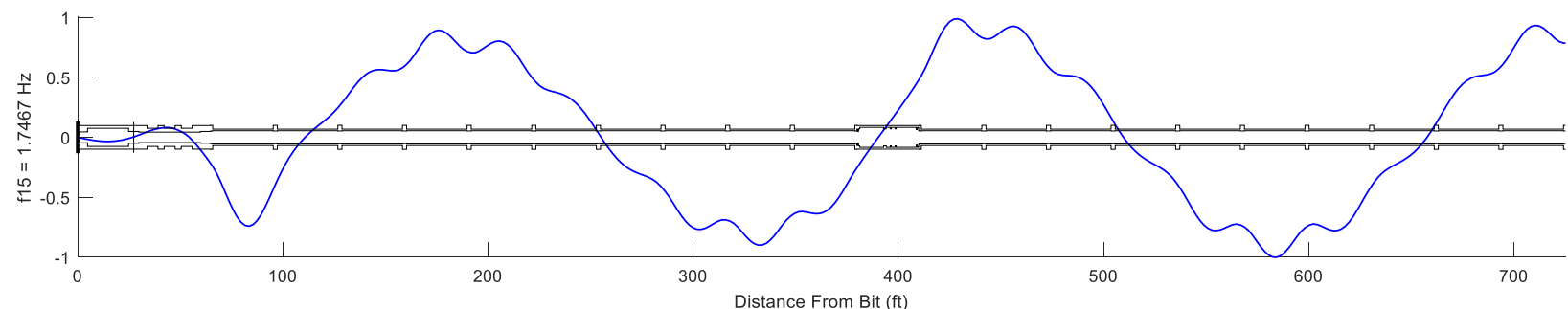


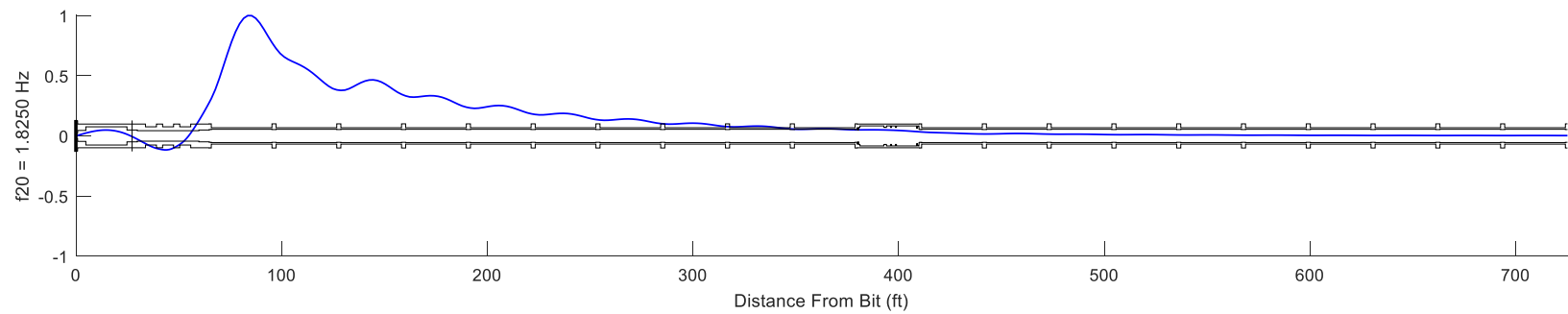
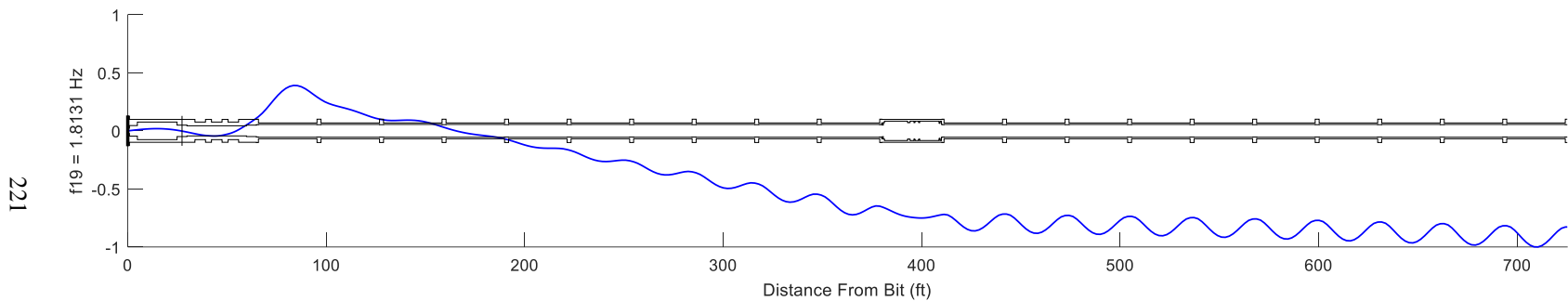
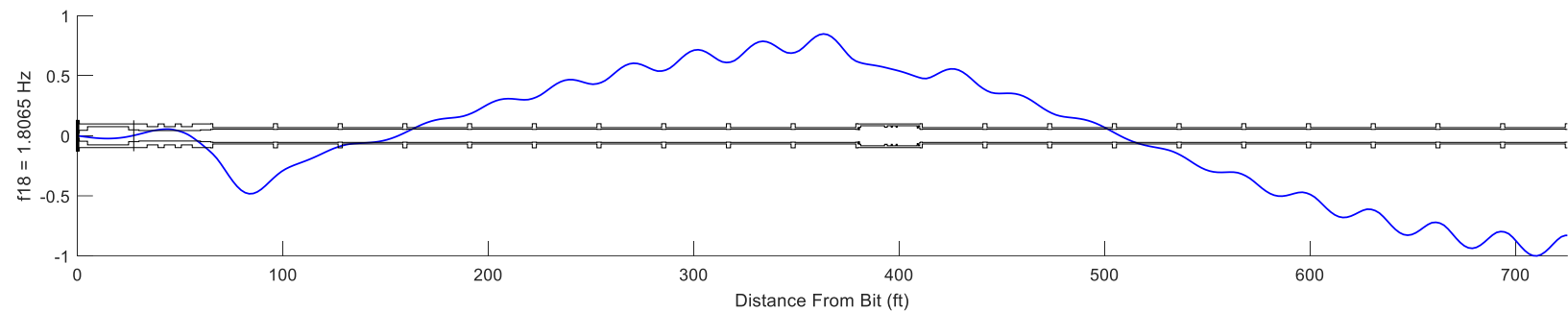
217

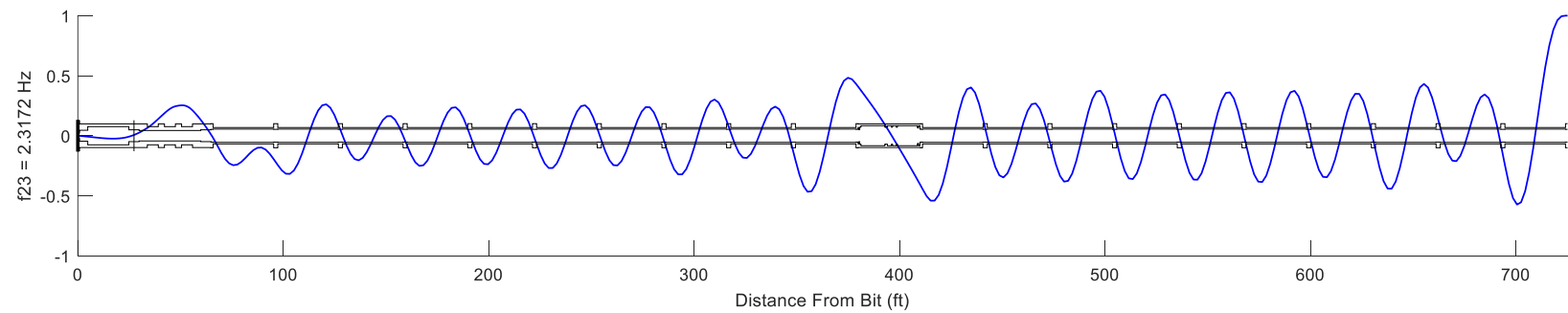
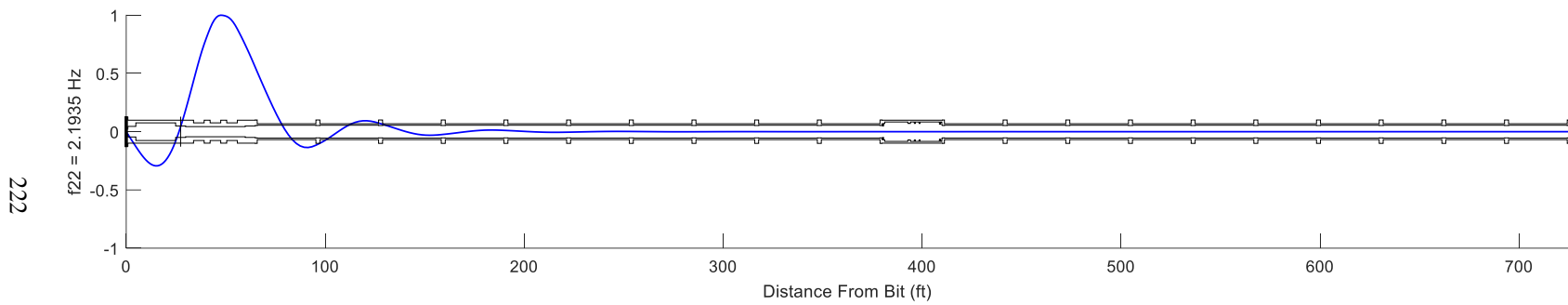
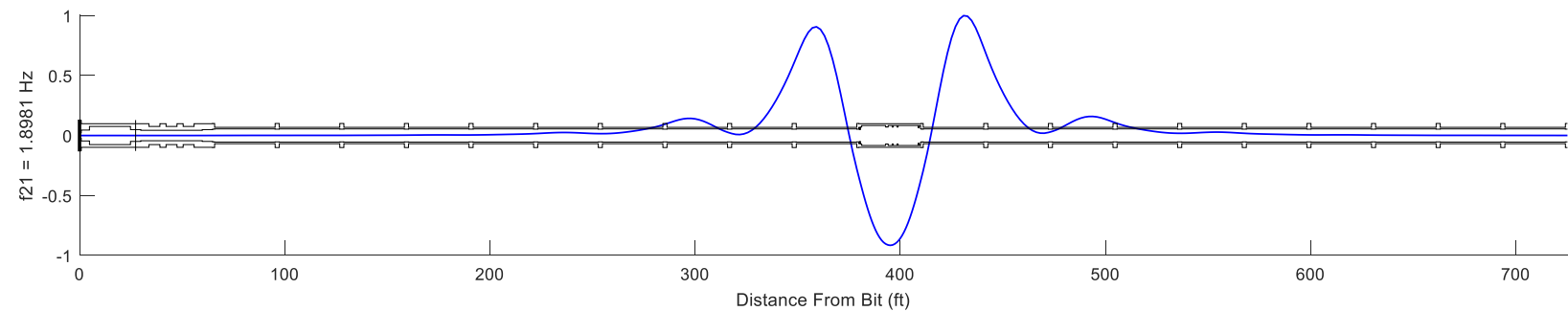


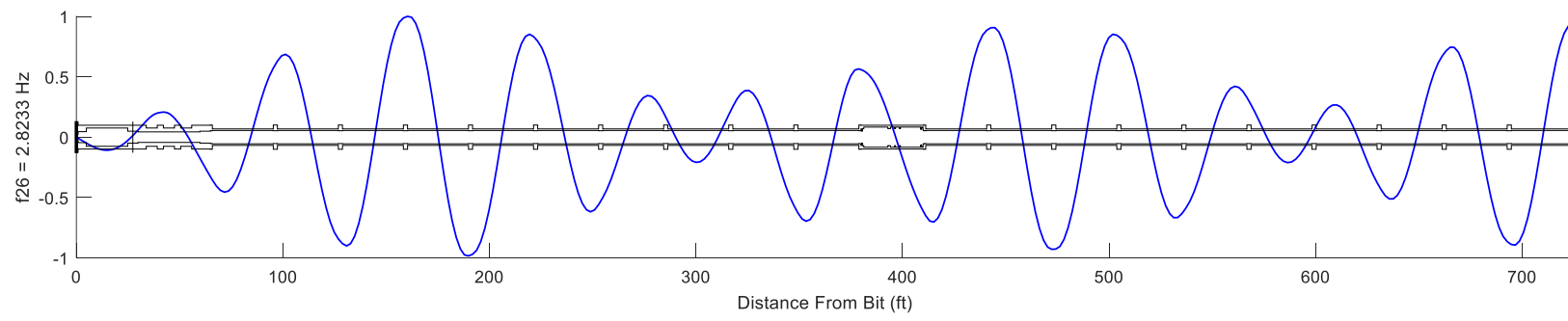
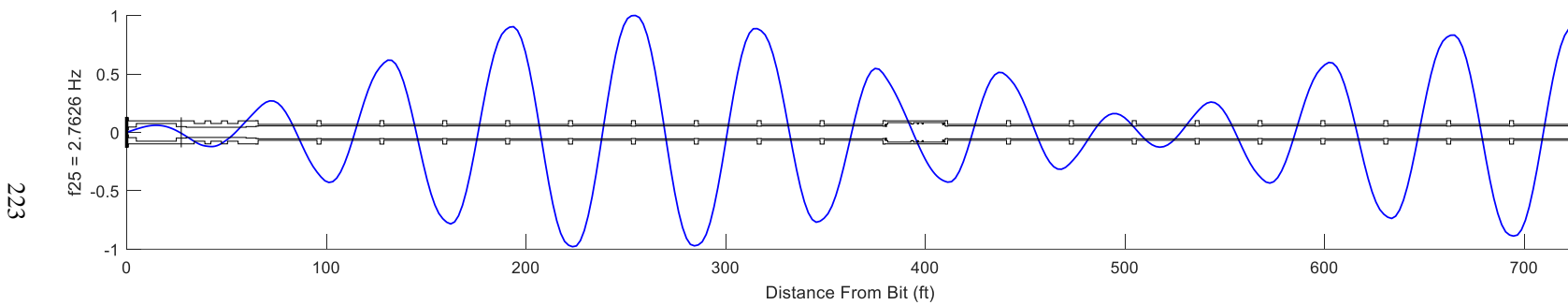
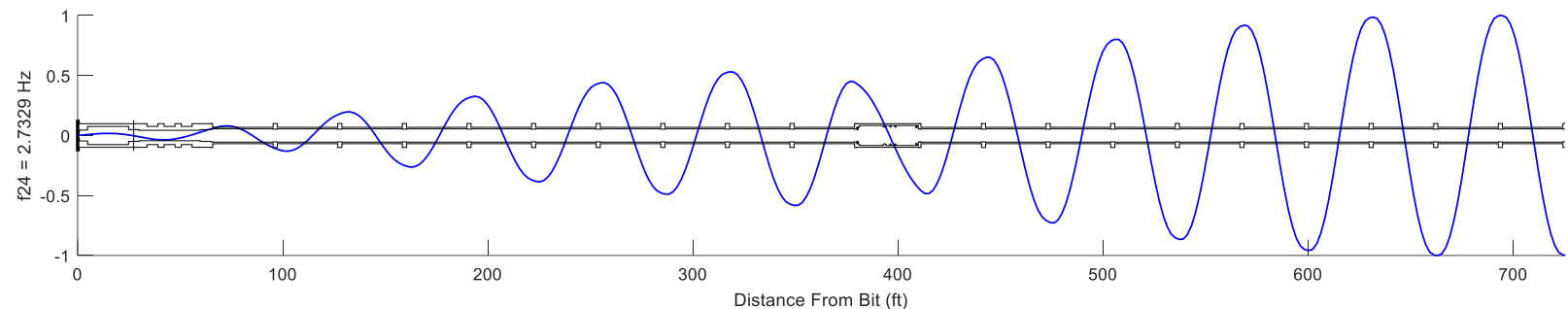


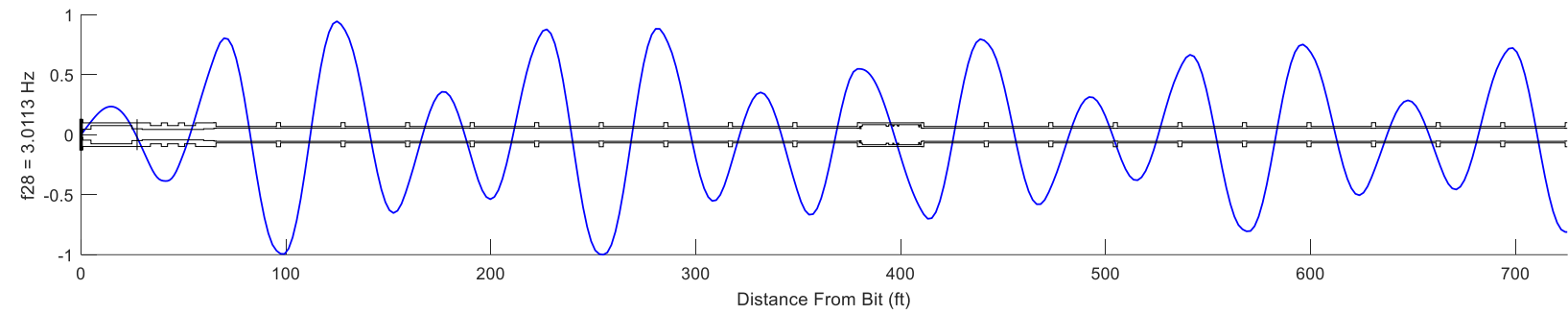
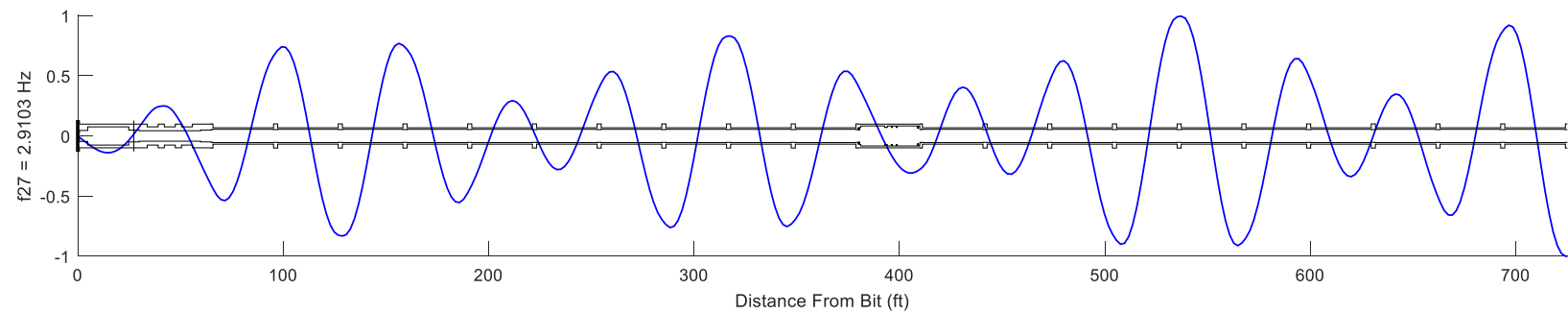












APPENDIX E.
FORCED VIBRATION PLOTS FOR SECTION 5

E.1 - Variations in Hole Size

7 7/8" Wellbore

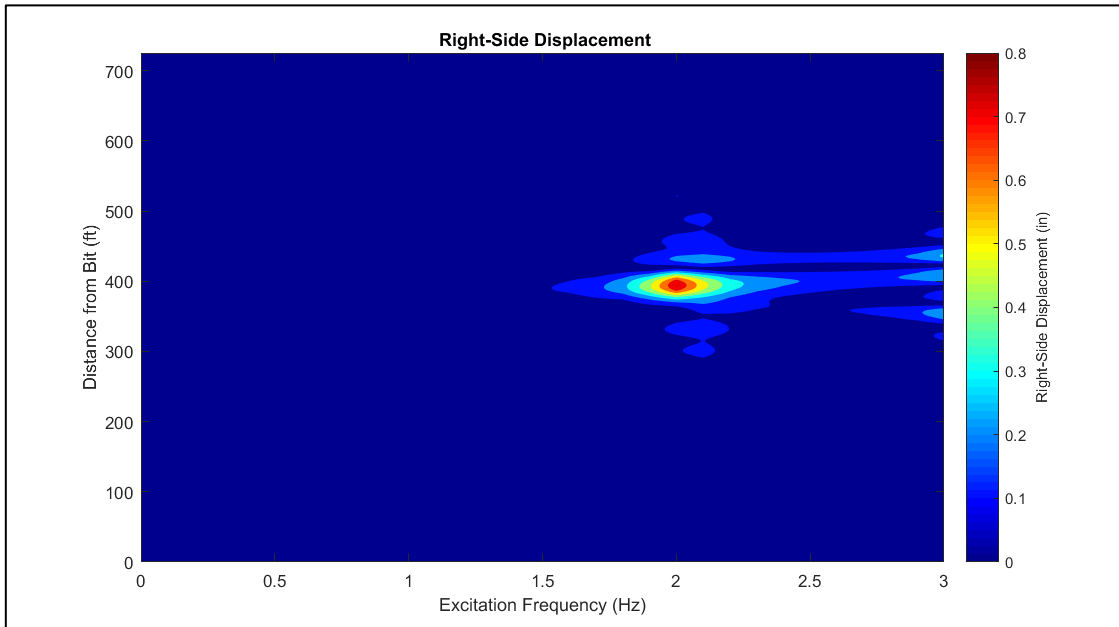


Figure E.1: Right-Side Displacement for a 7 7/8" Wellbore

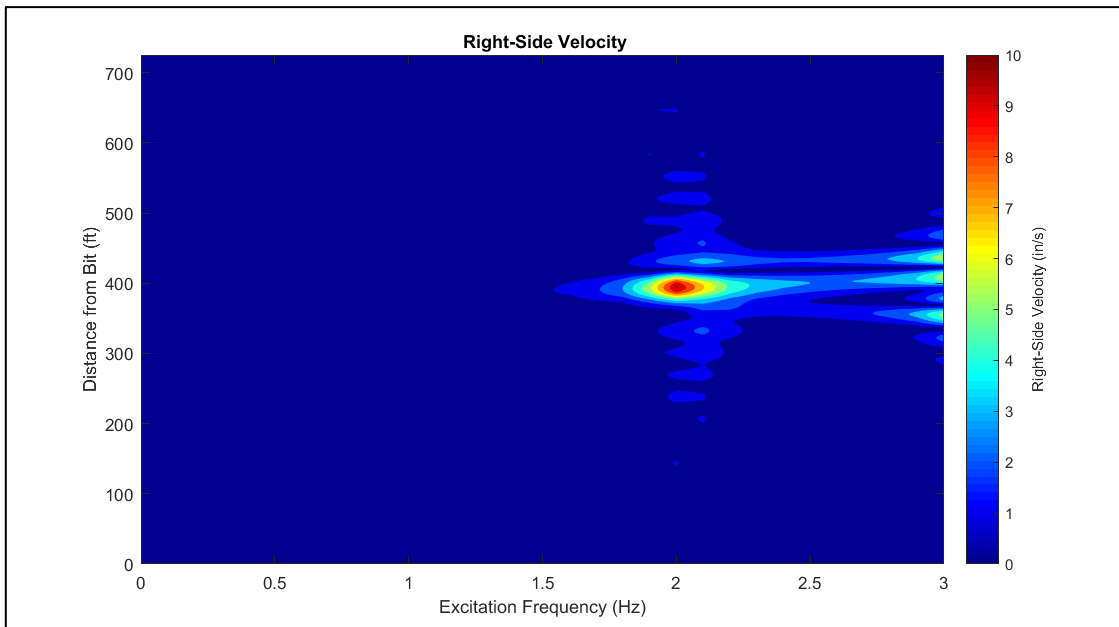


Figure E.2: Right-Side Velocity for a 7 7/8" Wellbore

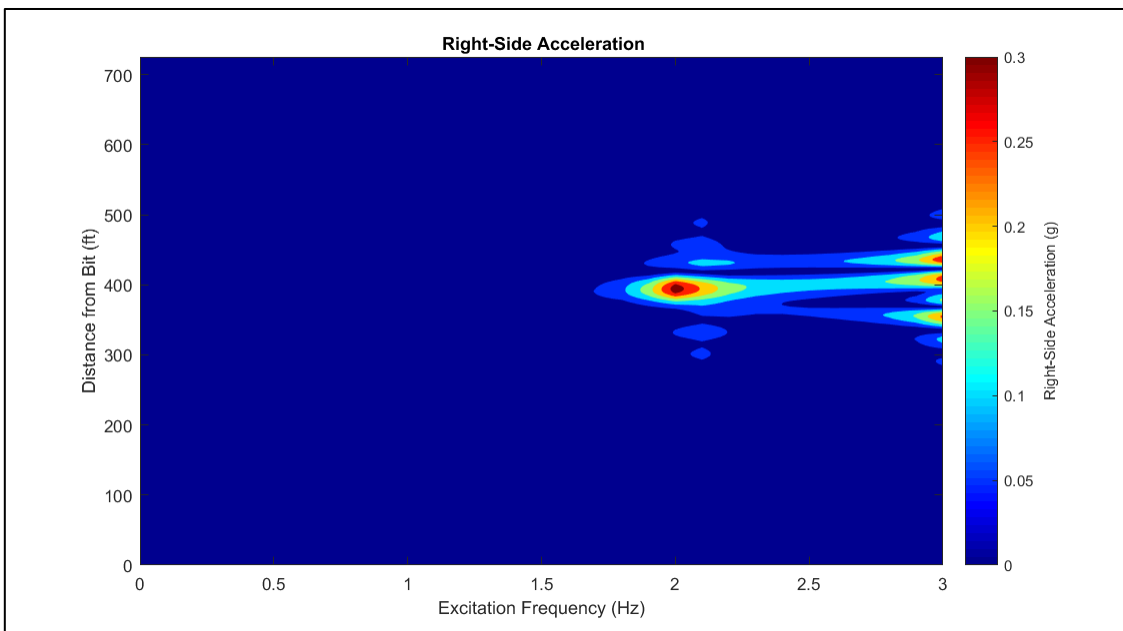


Figure E.3: Right-Side Acceleration for a 7 7/8" Wellbore

8 ½" Wellbore

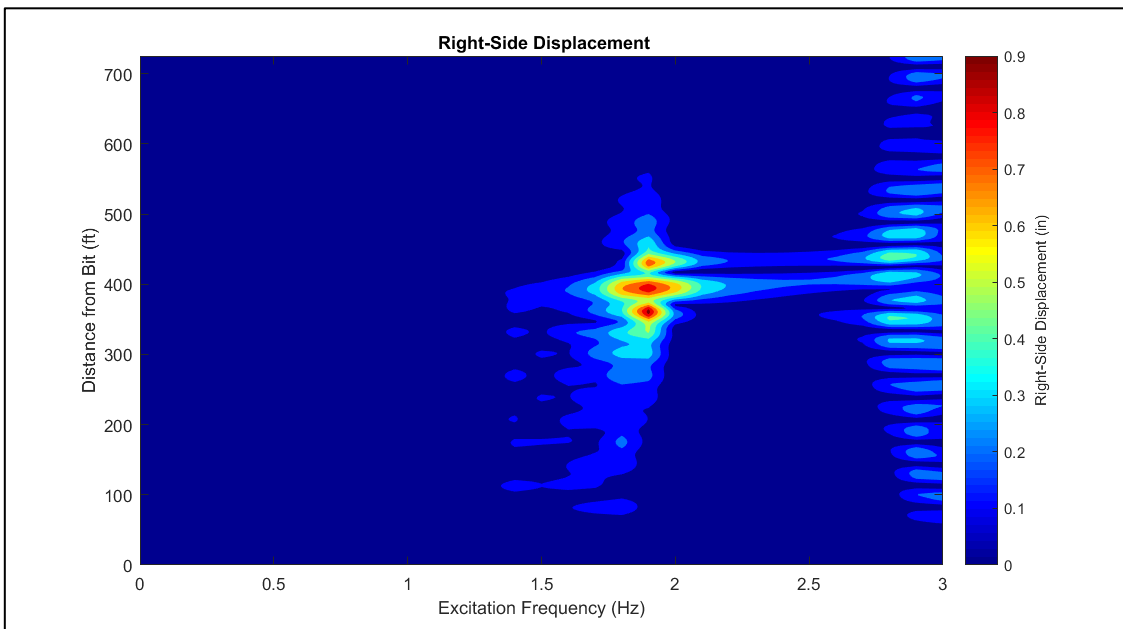


Figure E.4: Right-Side Displacement for an 8 1/2" Wellbore

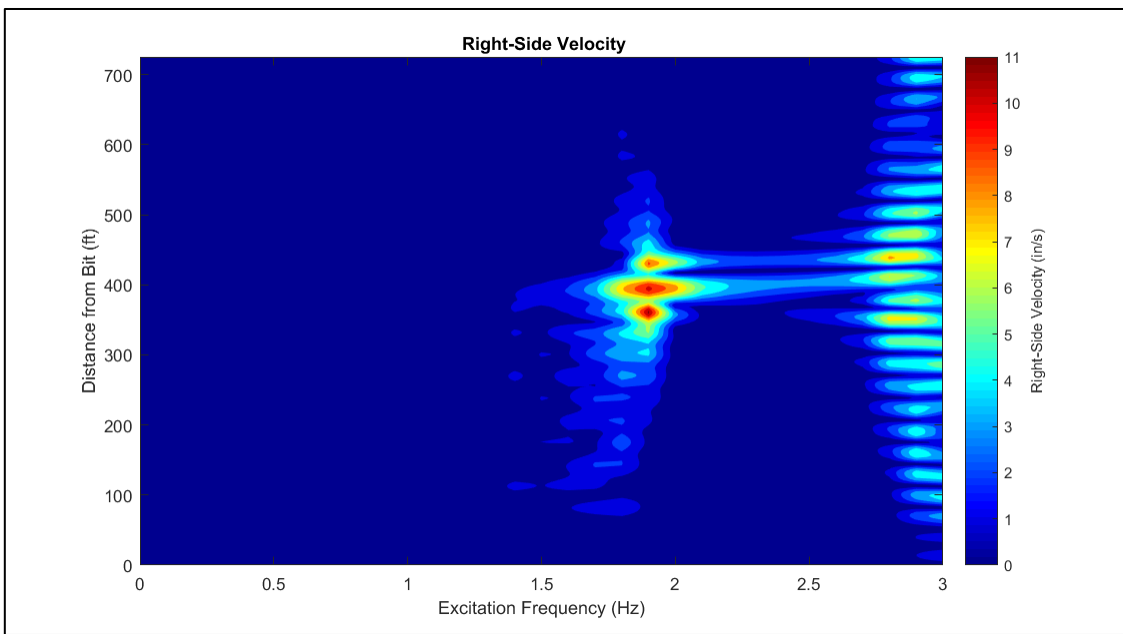


Figure E.5: Right-Side Velocity for an 8 1/2" Wellbore

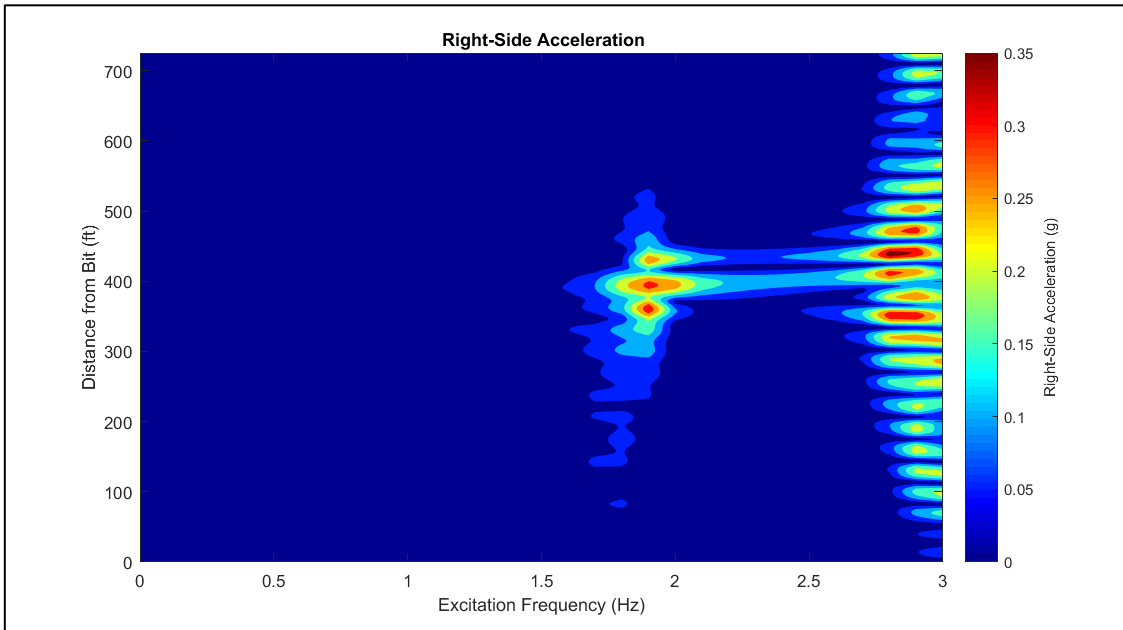


Figure E.6: Right-Side Acceleration for an 8 1/2" Wellbore

8 3/4" Wellbore

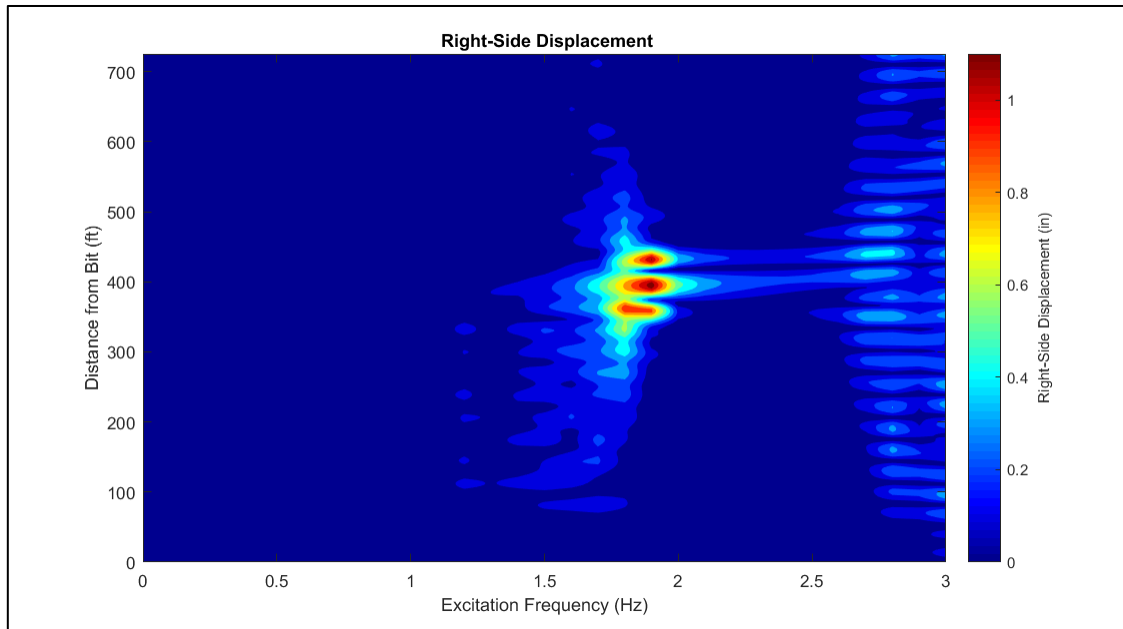


Figure E.7: Right-Side Displacement for an 8 3/4" Wellbore

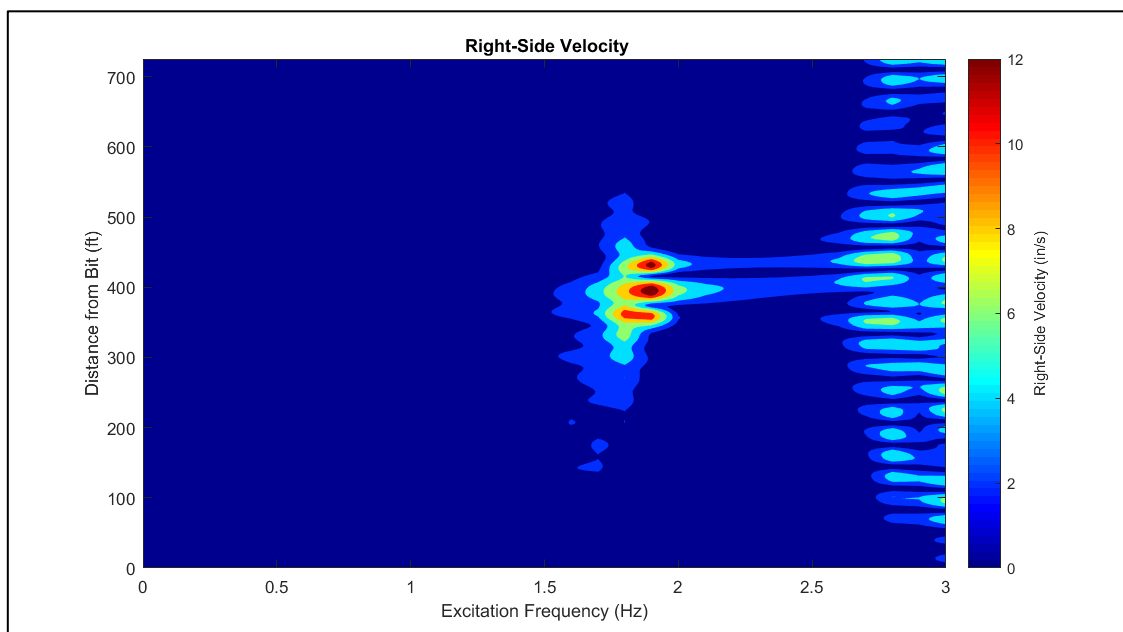


Figure E.8: Right-Side Velocity for an 8 3/4" Wellbore

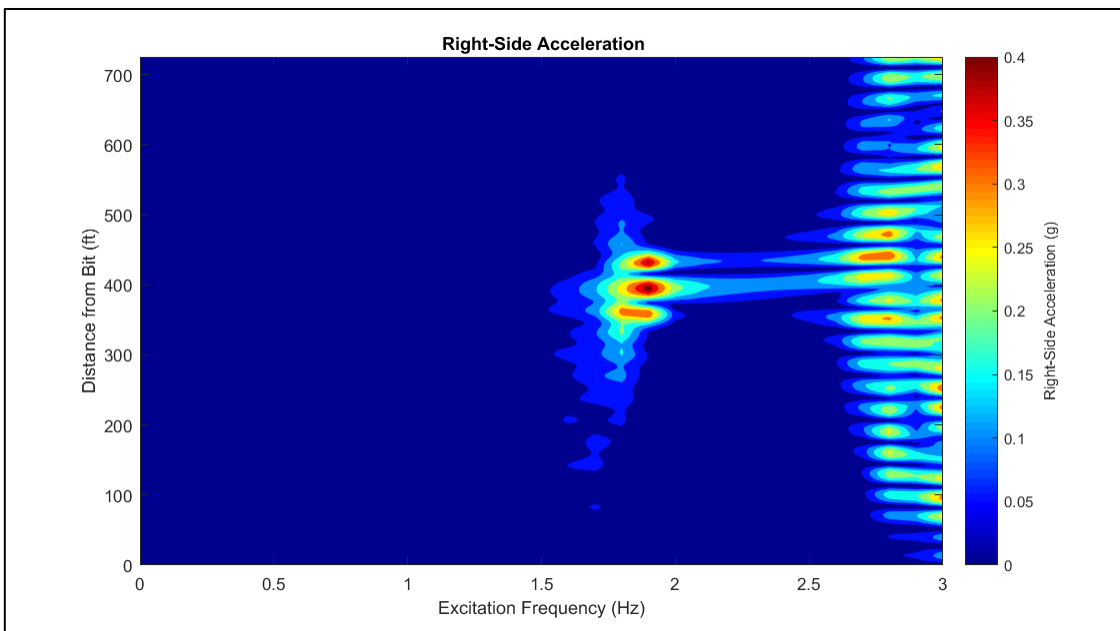


Figure E.9: Right-Side Acceleration for an 8 3/4" Wellbore

E.2 - Variations in WOB

$$WOB = 5 \text{ klb}_f$$

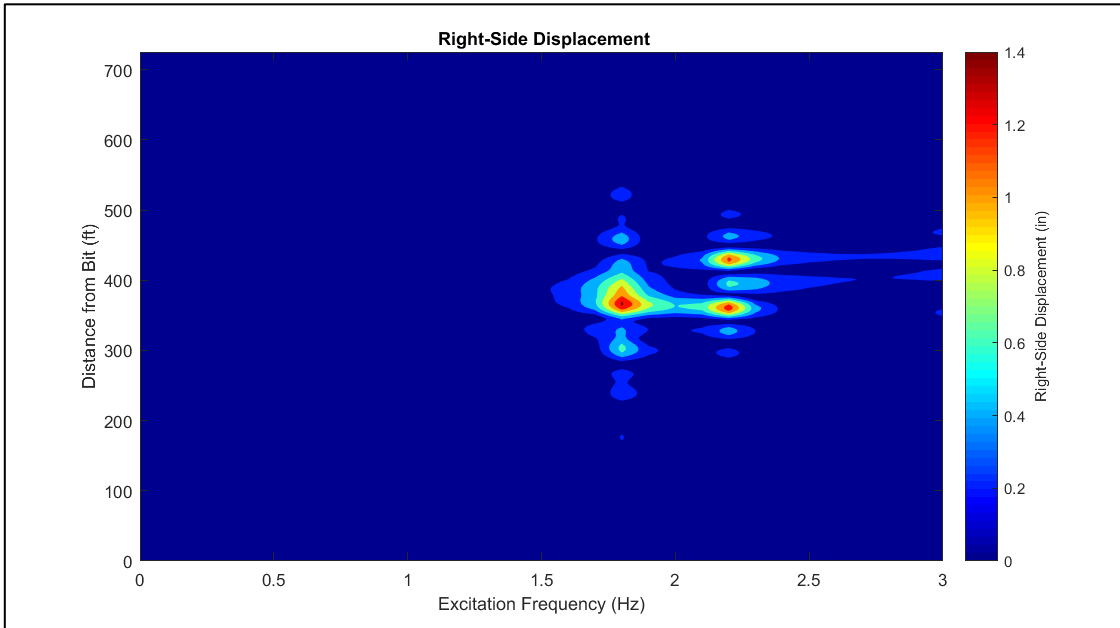


Figure E.10: Right-Side Displacement for 5 klb_f WOB

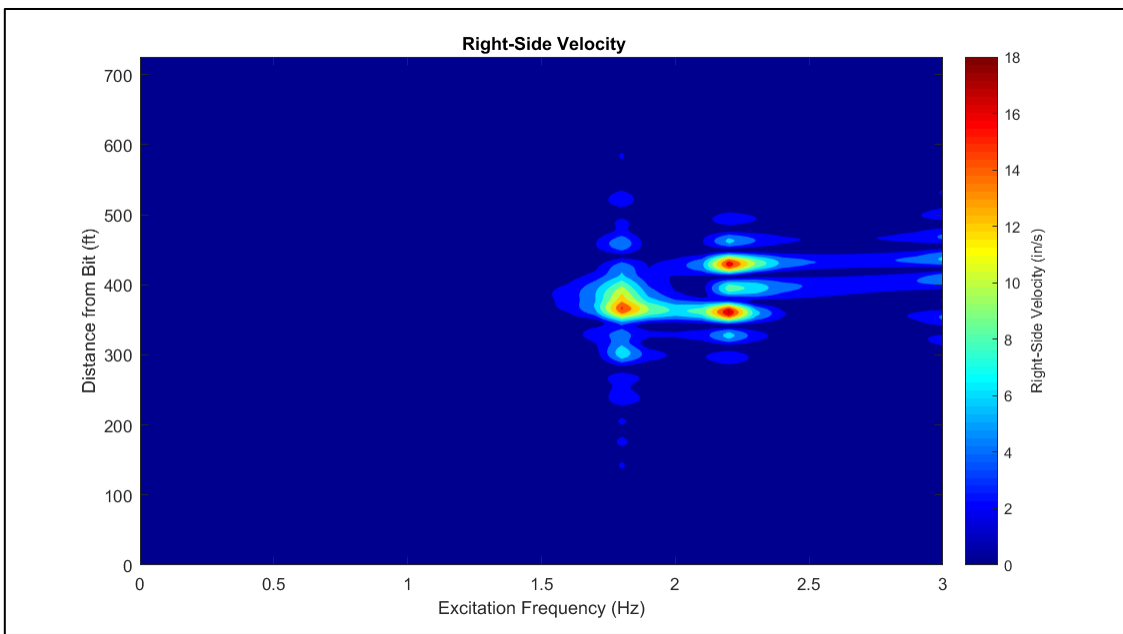


Figure E.11: Right-Side Velocity for 5 klb_f WOB

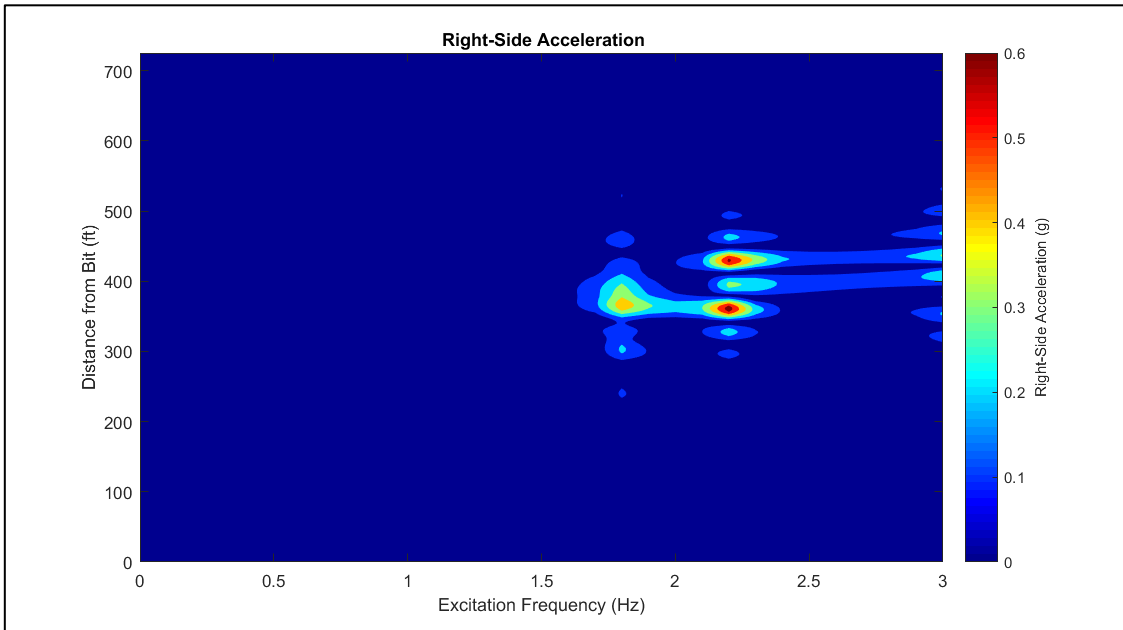


Figure E.12: Right-Side Acceleration for 5 klb_f WOB

$WOB = 10 \text{ klb}_f$

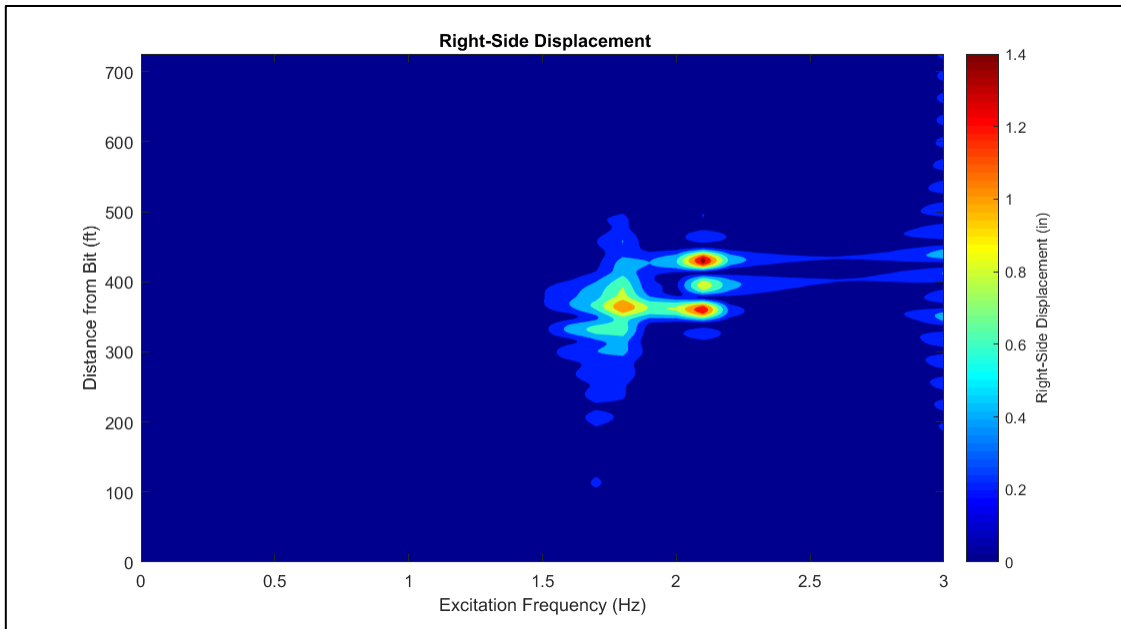


Figure E.13: Right-Side Displacement for 10 k lb_f WOB

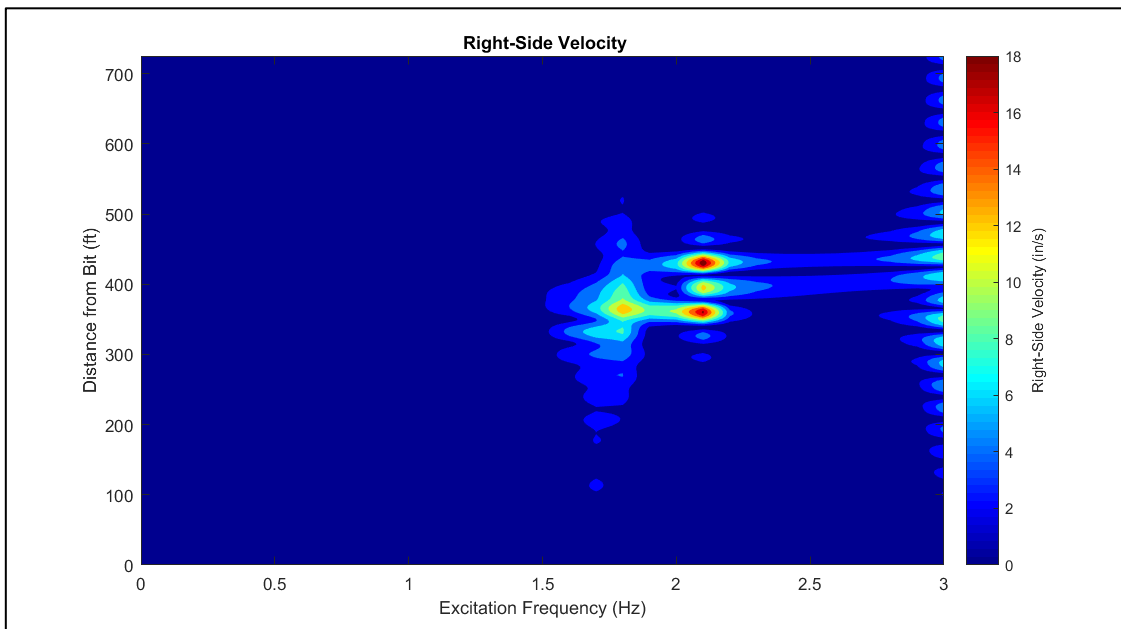


Figure E.14: Right-Side Velocity for 10 k lb_f WOB

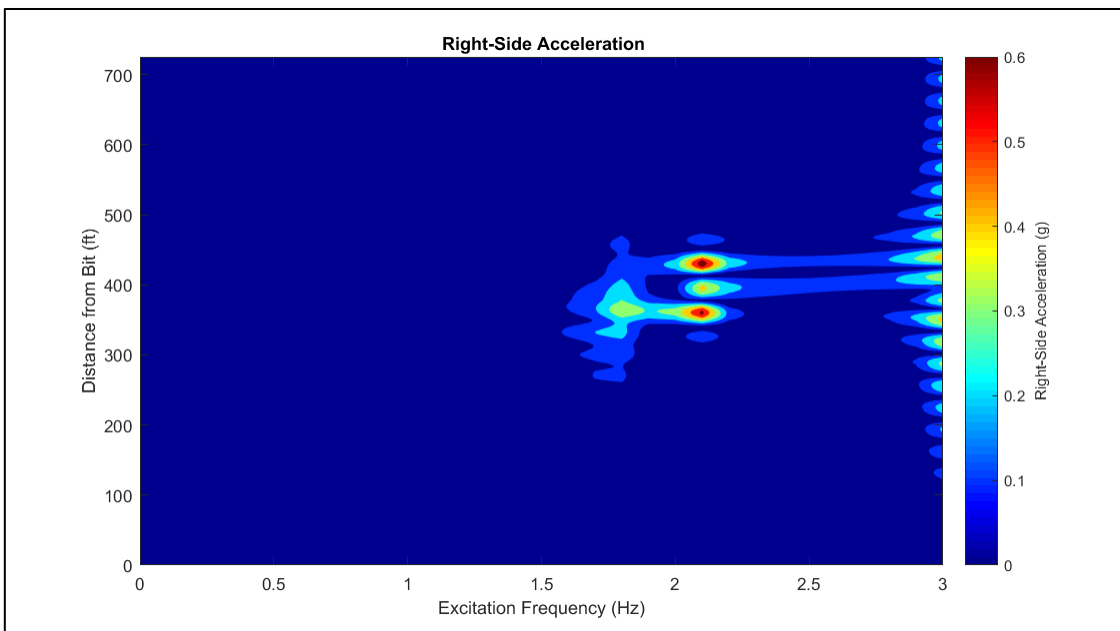


Figure E.15: Right-Side Acceleration for 10 klb_f WOB

$WOB = 15 \text{ klb}_f$

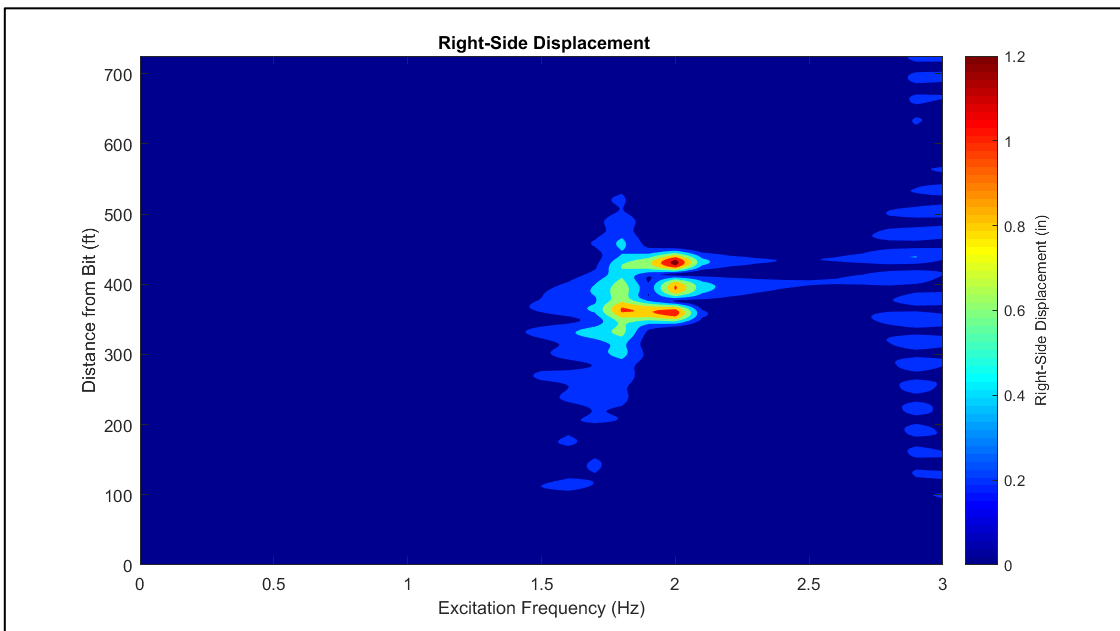


Figure E.16: Right-Side Displacement for 15 klb_f WOB

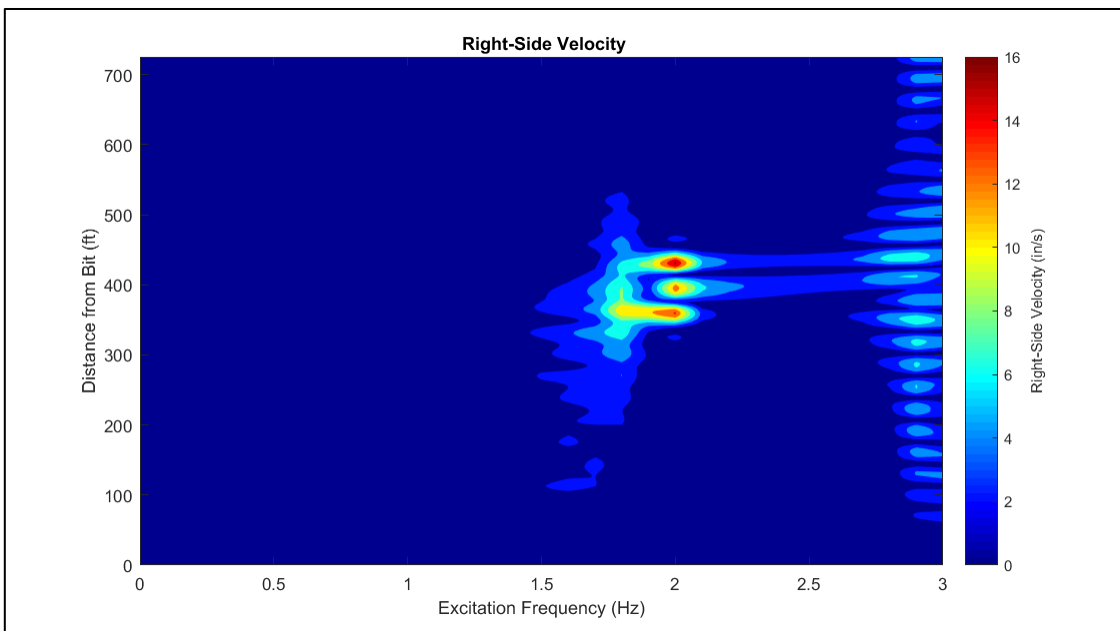


Figure E.17: Right-Side Velocity for 15 klf WOB

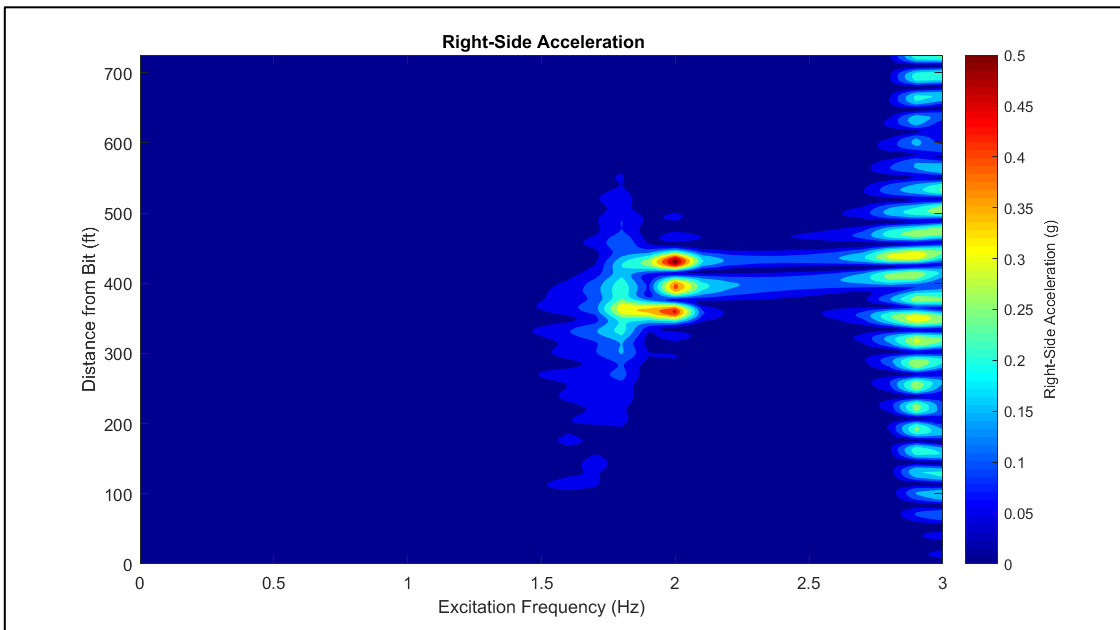


Figure E.18: Right-Side Acceleration for 15 klf WOB

E.3 - Variations in Mud Density

$MW = 8\text{ppg}$

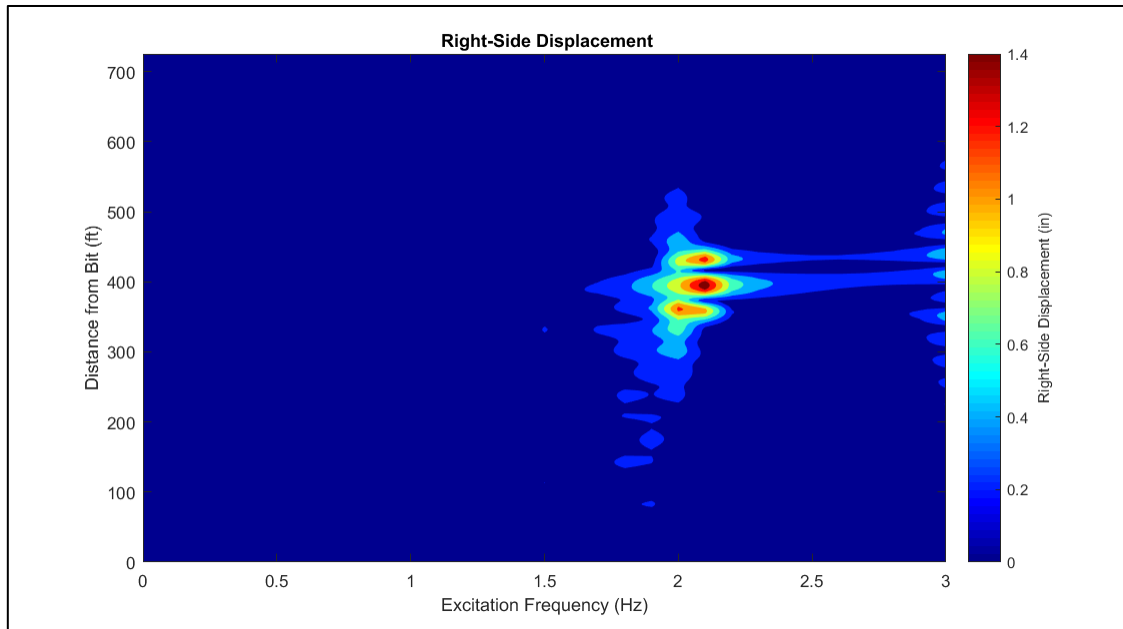


Figure E.19: Right-Side Displacement for 8ppg MW

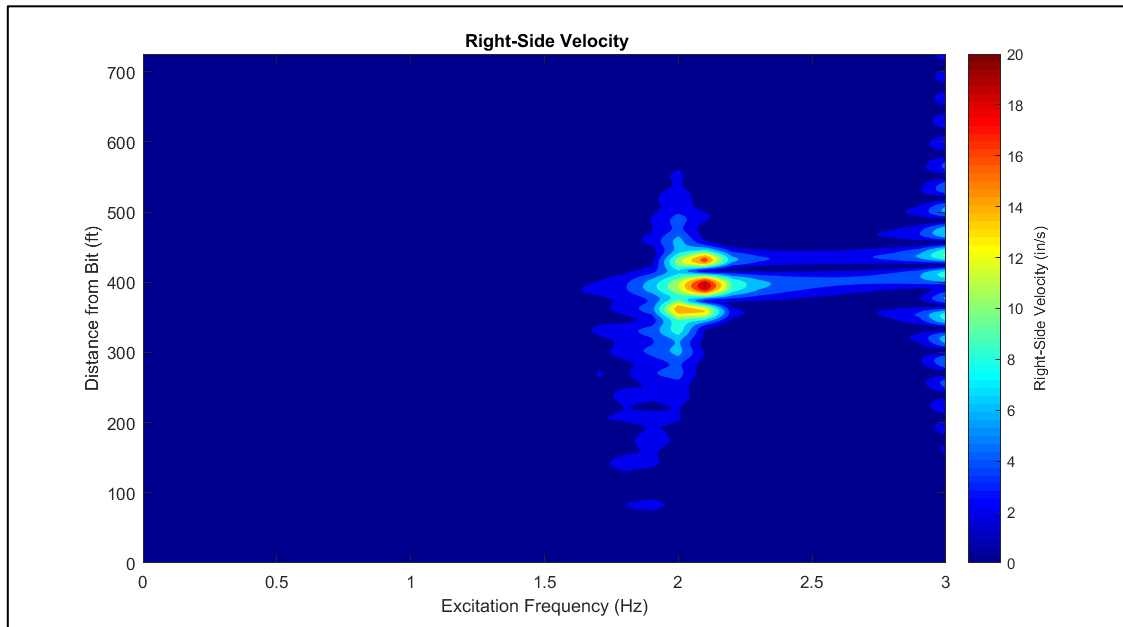


Figure E.20: Right-Side Velocity for 8ppg MW

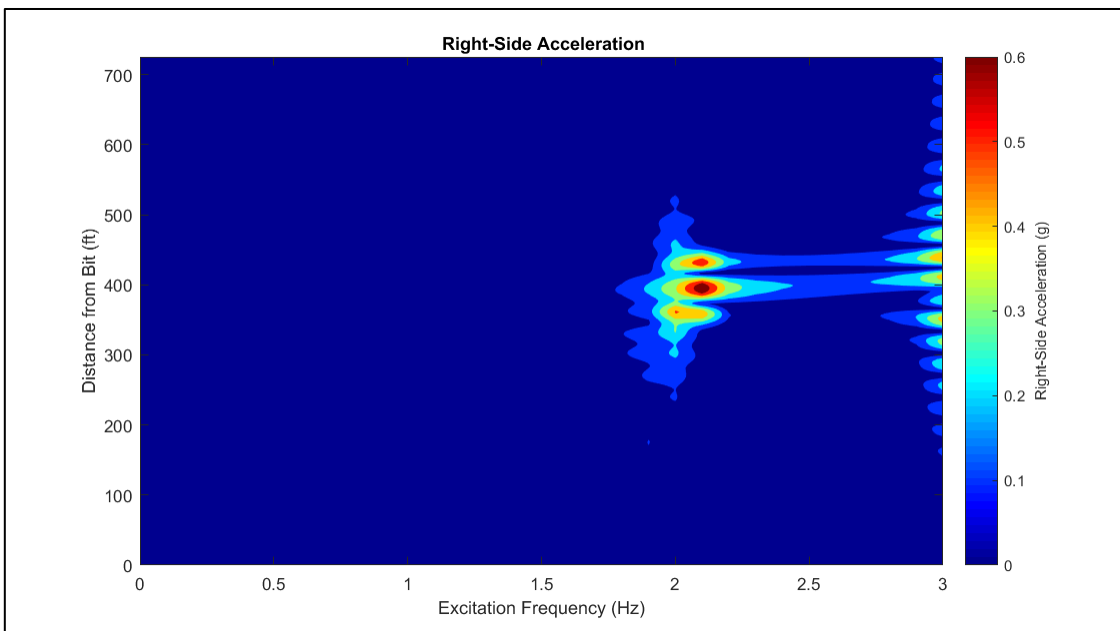


Figure E.21: Right-Side Acceleration for 8ppg MW

$MW = 10\text{ppg}$

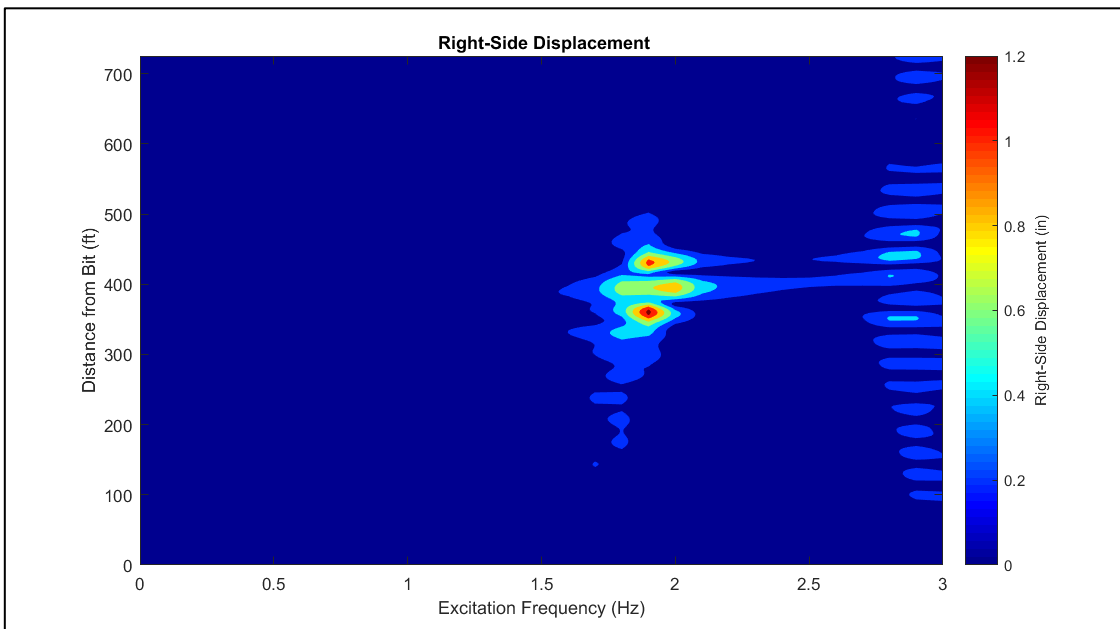


Figure E.22: Right-Side Displacement for 10ppg MW

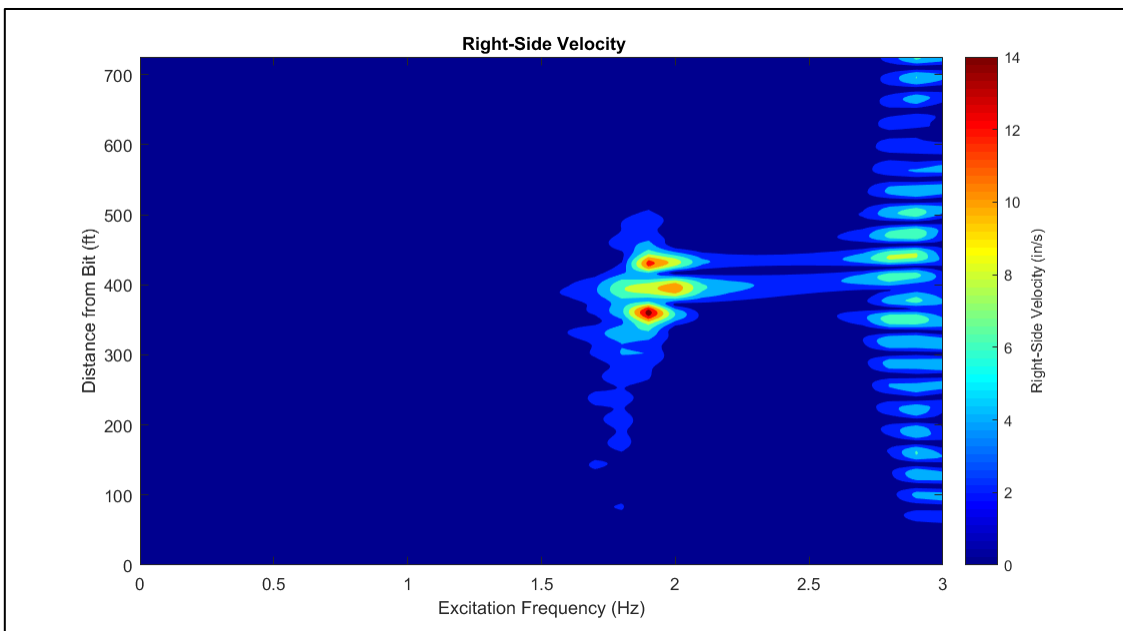


Figure E.23: Right-Side Velocity for 10ppg MW

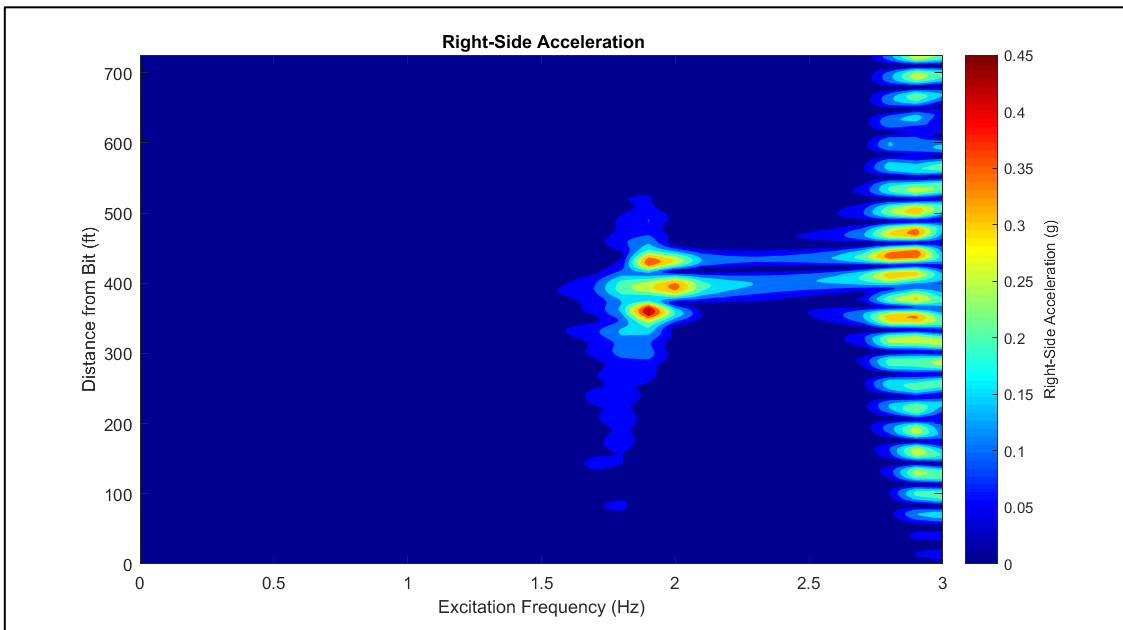


Figure E.24: Right-Side Acceleration for 10ppg MW

$MW = 12\text{ppg}$

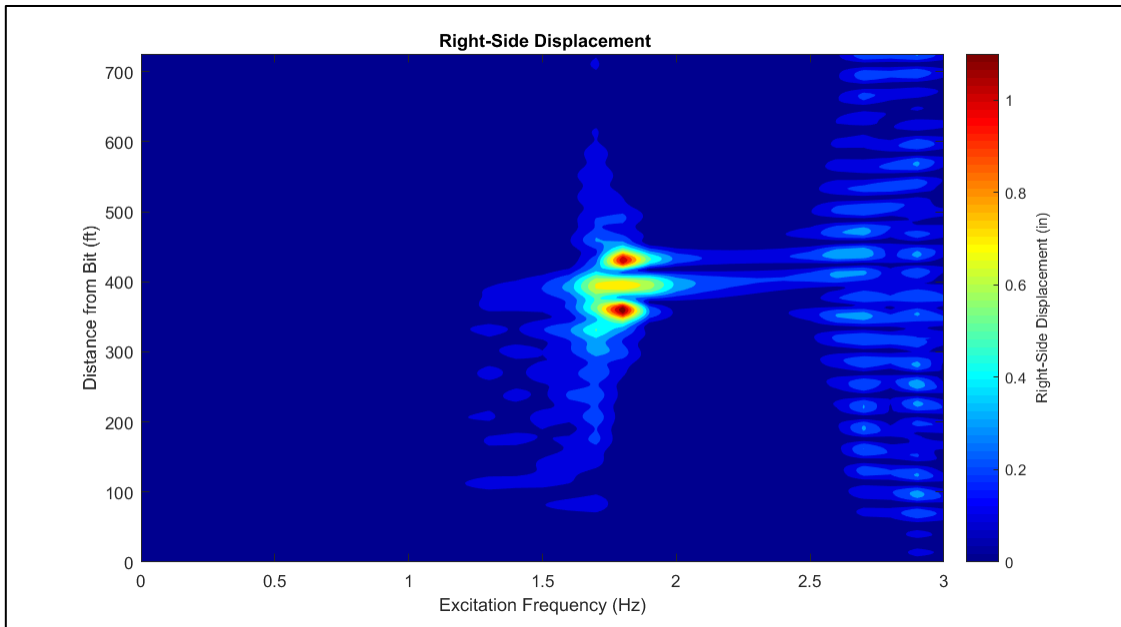


Figure E.25: Right-Side Displacement for 12ppg MW

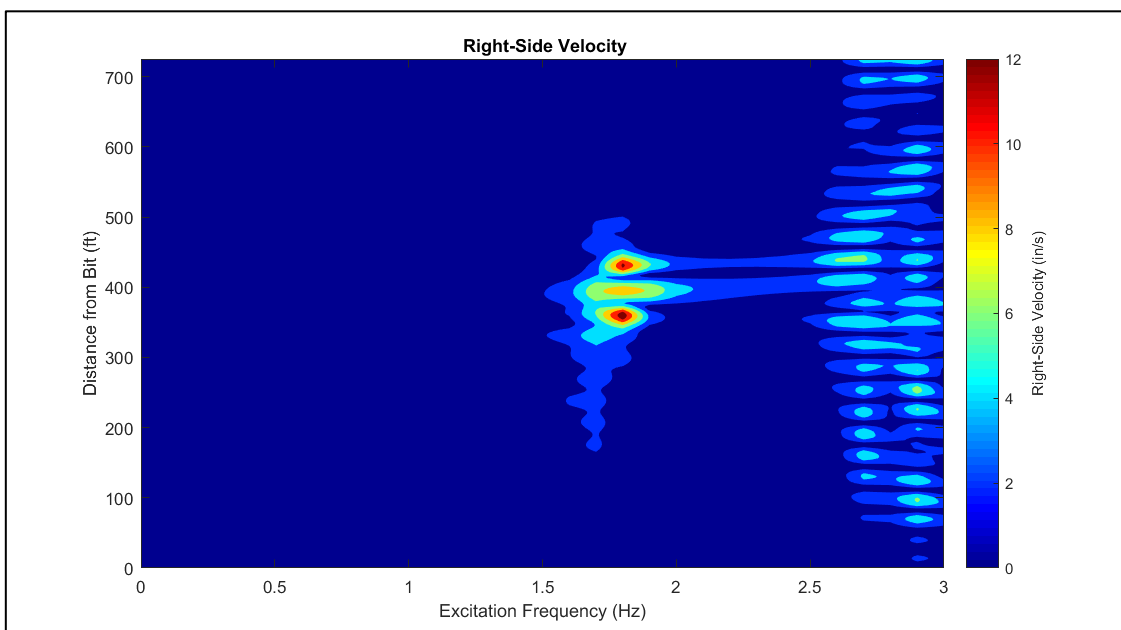


Figure E.26: Right-Side Velocity for 12ppg MW

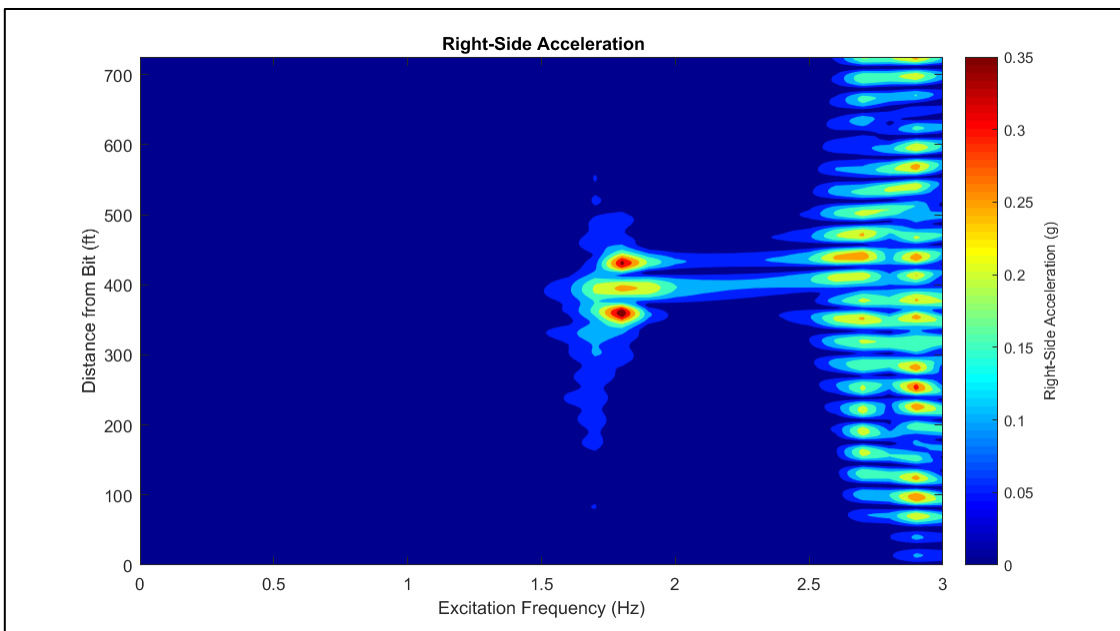


Figure E.27: Right-Side Acceleration for 12ppg MW

E.4 - Variations in Plastic Viscosity

$PV = 12cp$

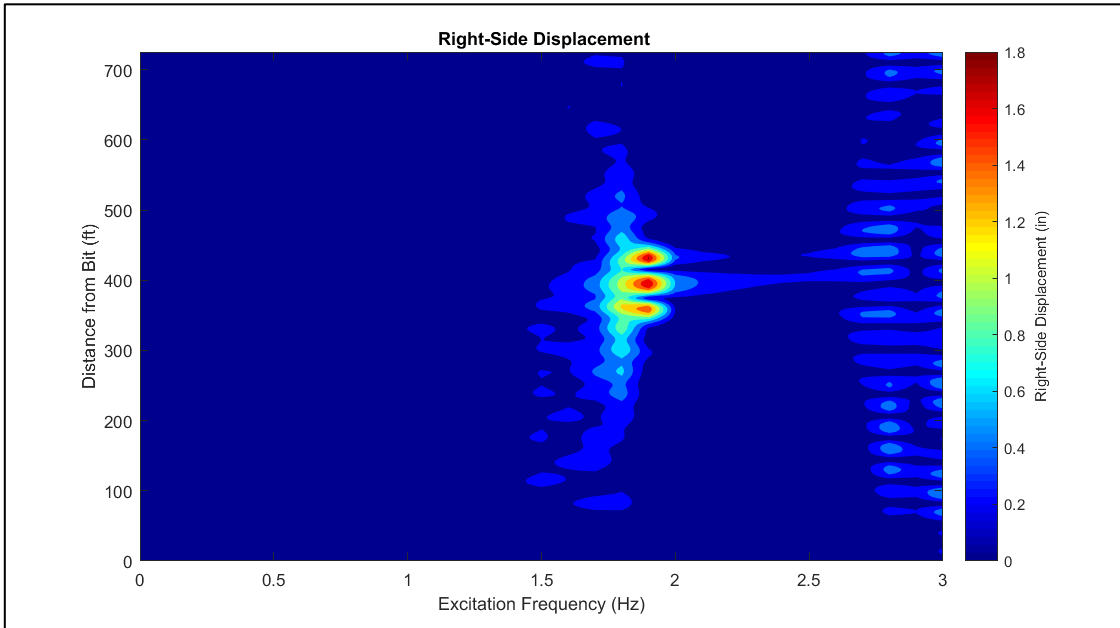


Figure E.28: Right-Side Displacement for 12cp PV

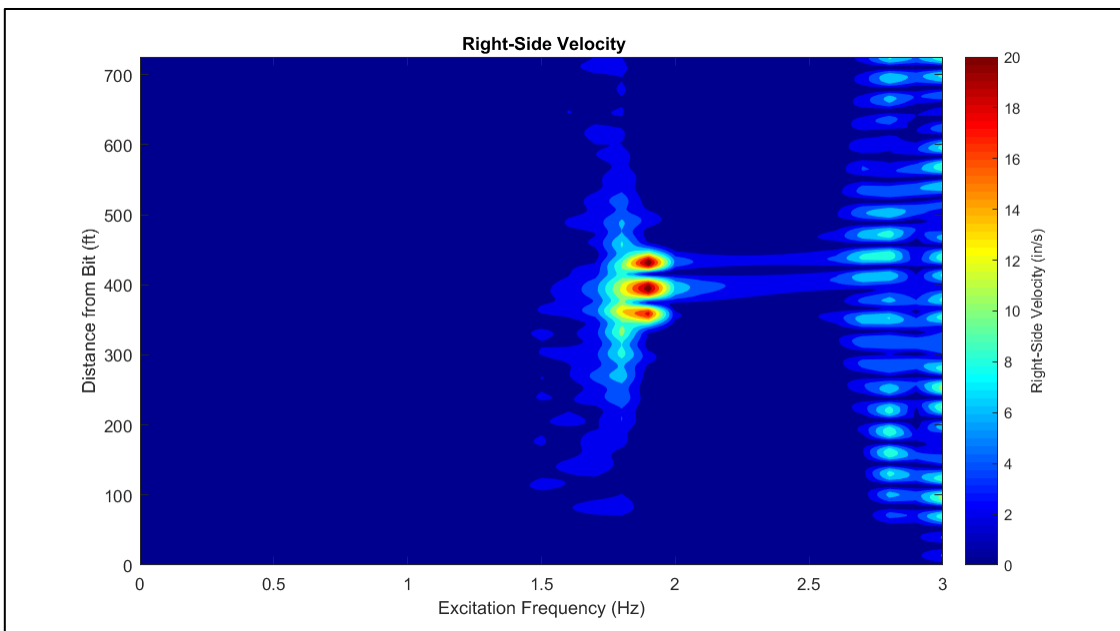


Figure E.29: Right-Side Velocity for 12cp PV

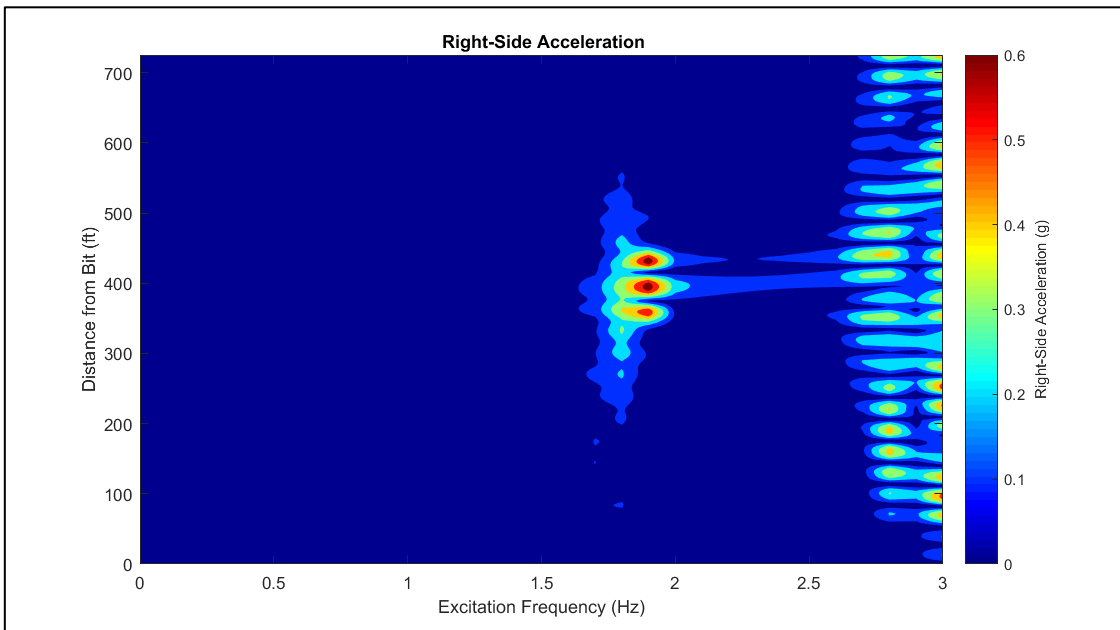


Figure E.30: Right-Side Acceleration for 12cp PV

$PV = 24cp$

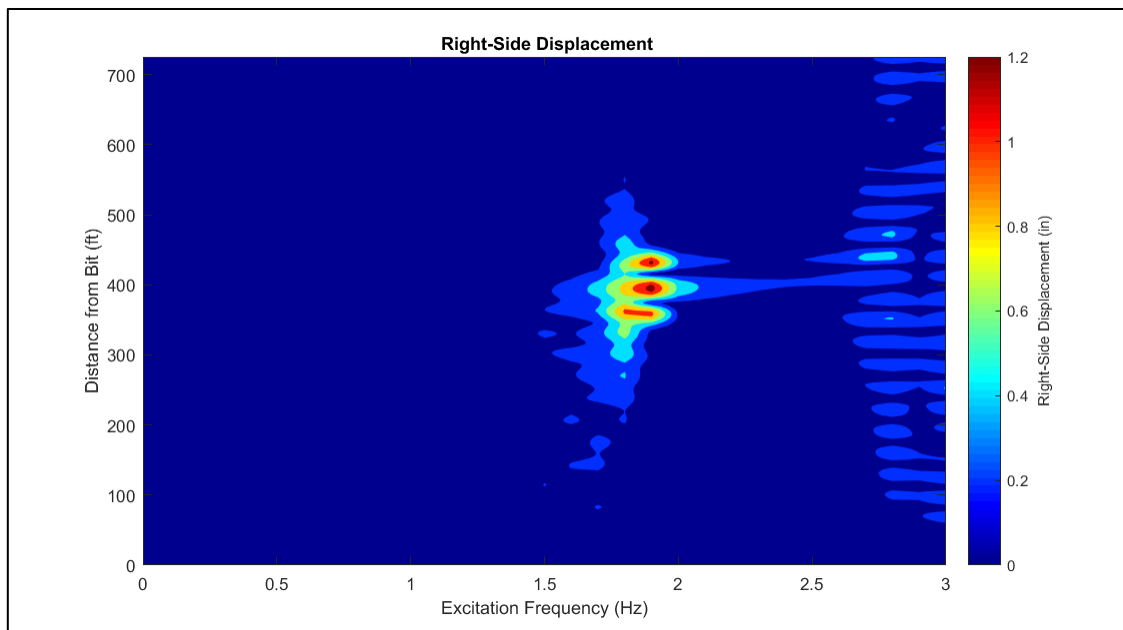


Figure E.31: Right-Side Displacement for 24cp PV

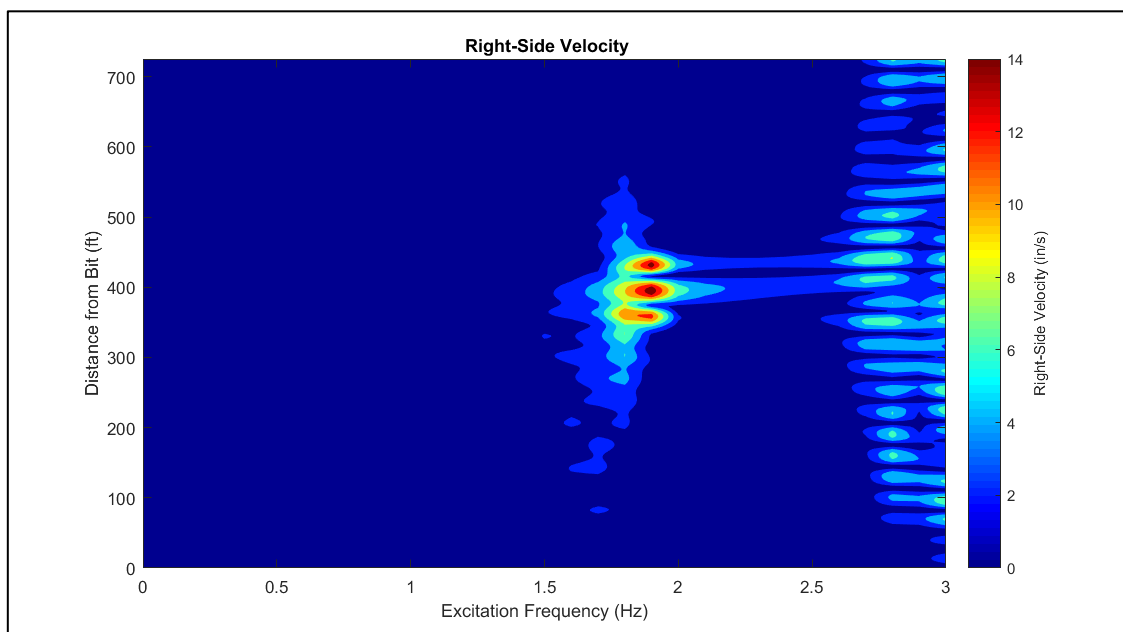


Figure E.32: Right-Side Velocity for 24cp PV

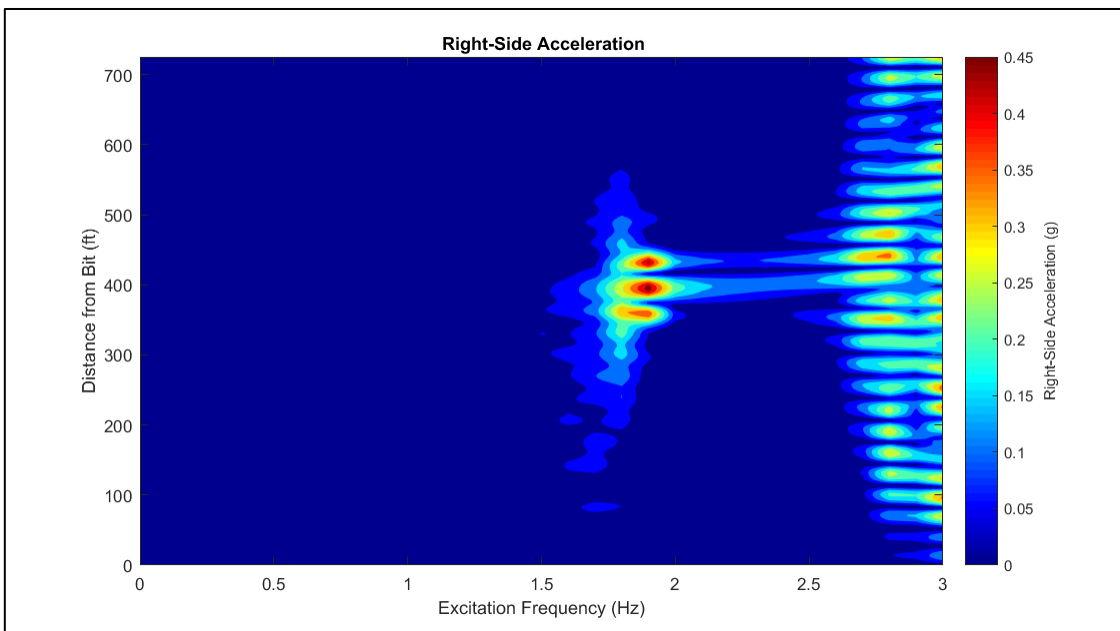


Figure E.33: Right-Side Acceleration for 24cp PV

PV = 36 cp

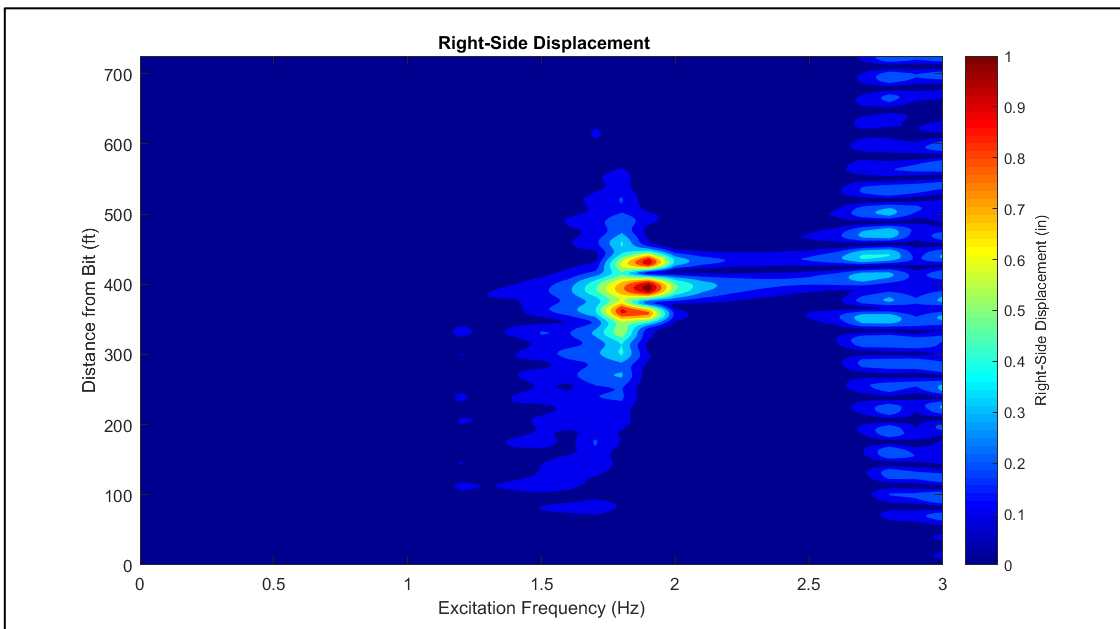


Figure E.34: Right-Side Displacement for 36cp PV

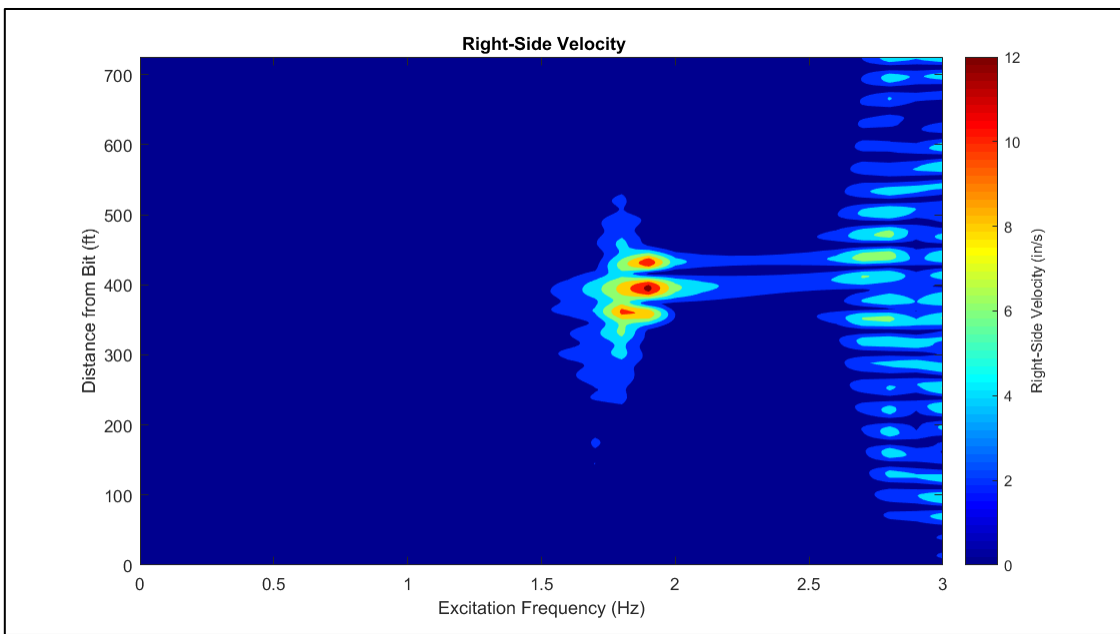


Figure E.35: Right-Side Velocity for 36cp PV

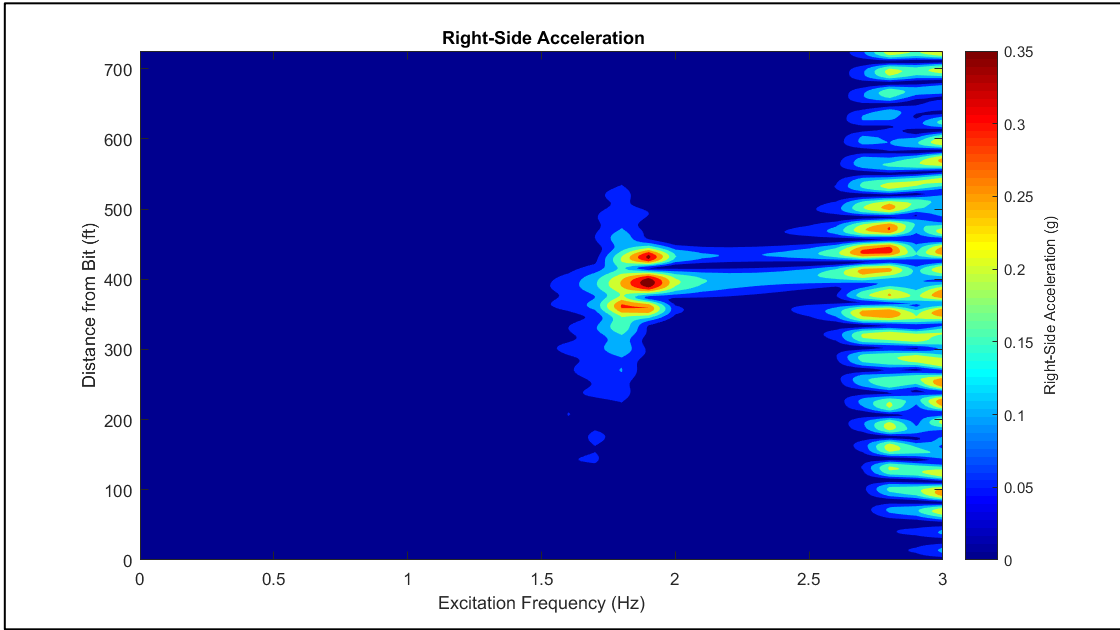


Figure E.36: Right-Side Acceleration for 36cp PV

E.5 - Variations in Inclination

Inclination = 30°

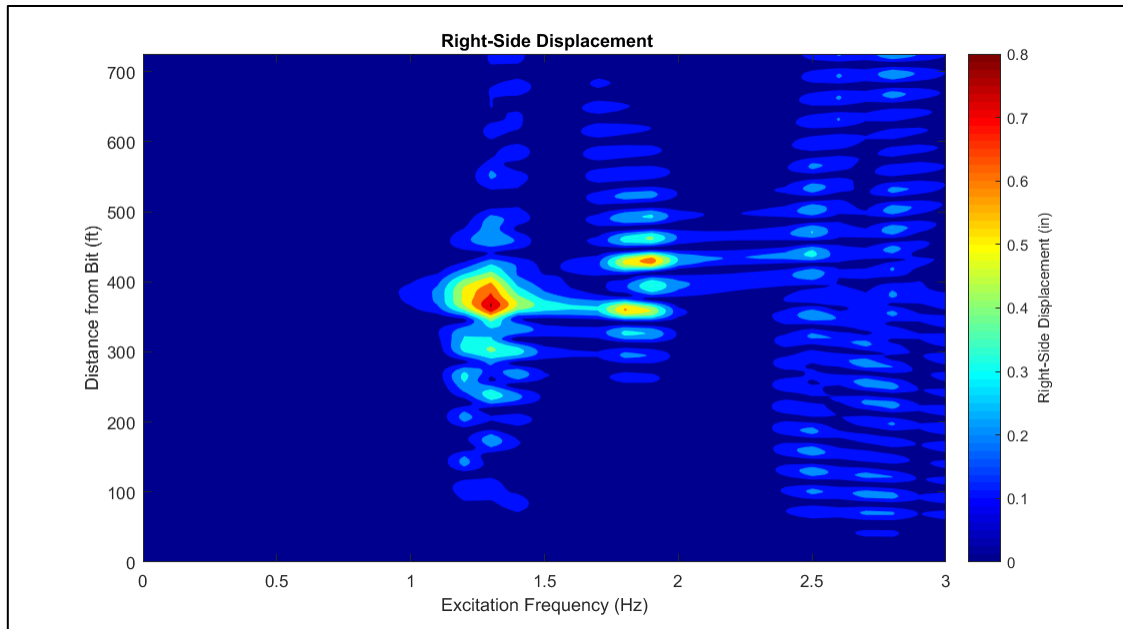


Figure E.37: Right-Side Displacement for $\varphi = 30^\circ$

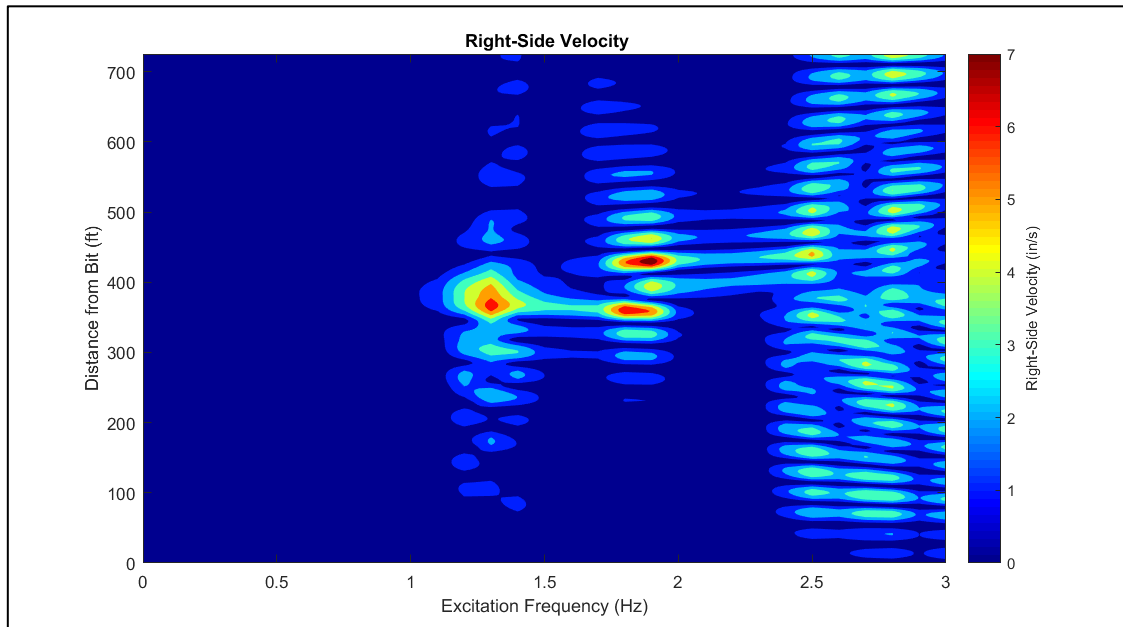


Figure E.38: Right-Side Velocity for $\varphi = 30^\circ$

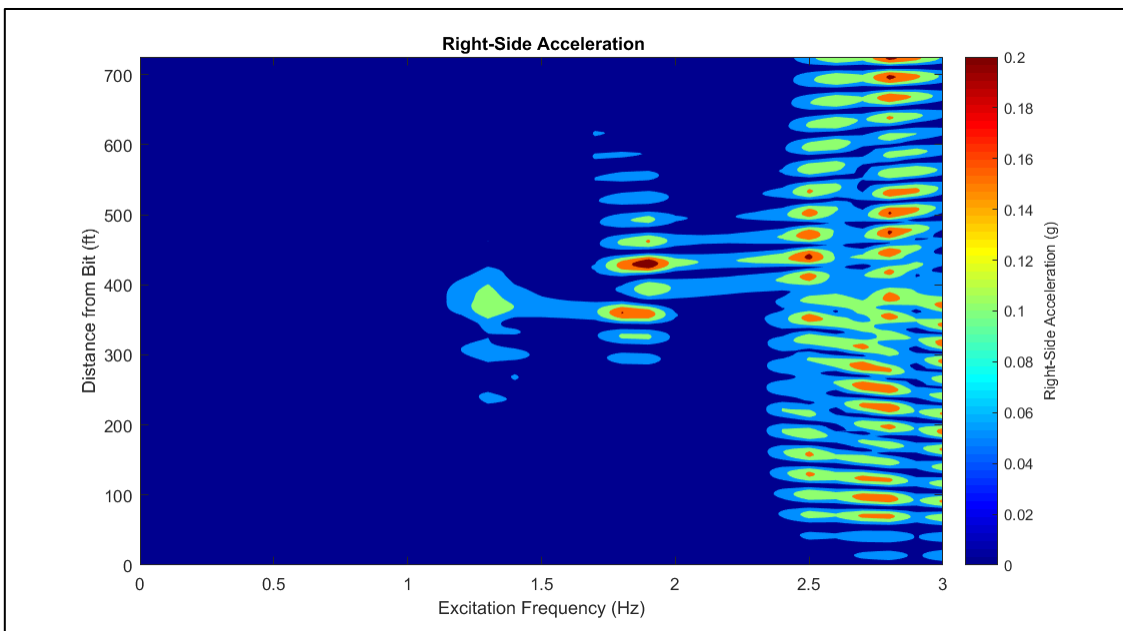


Figure E.39: Right-Side Acceleration for $\varphi = 30^\circ$

Inclination = 45°

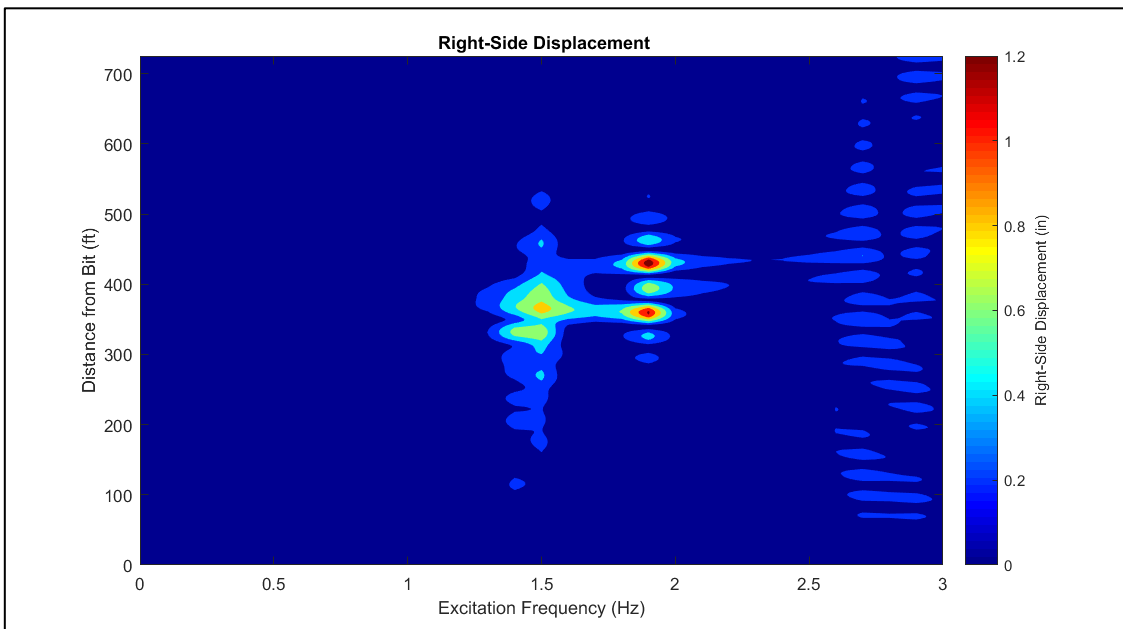


Figure E.40: Right-Side Displacement for $\varphi = 45^\circ$

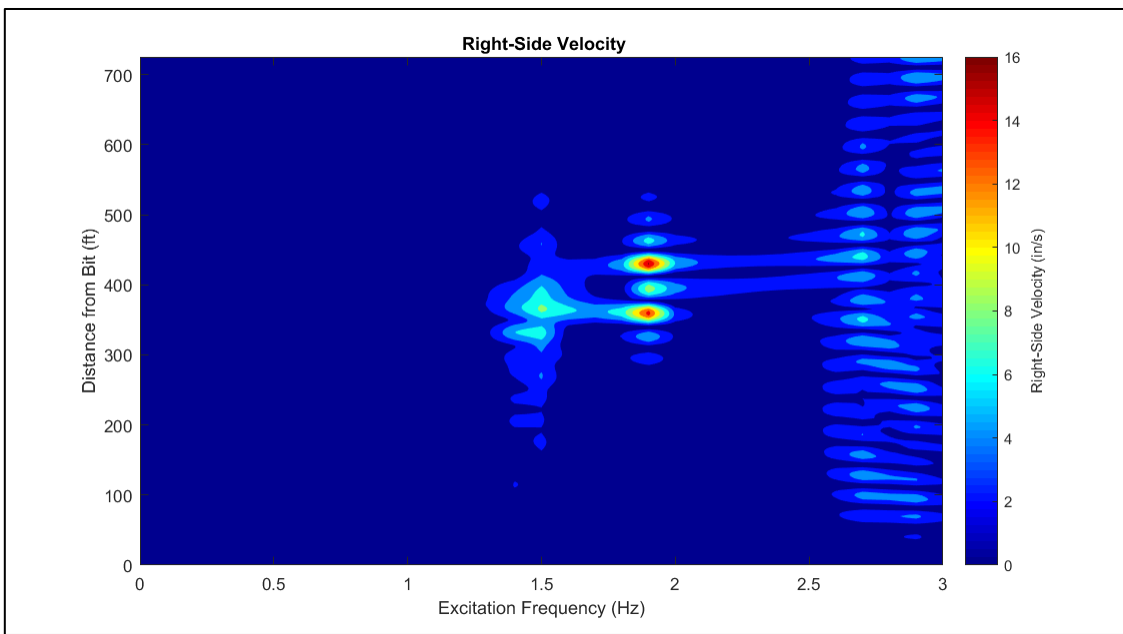


Figure E.41: Right-Side Velocity for $\varphi = 45^\circ$

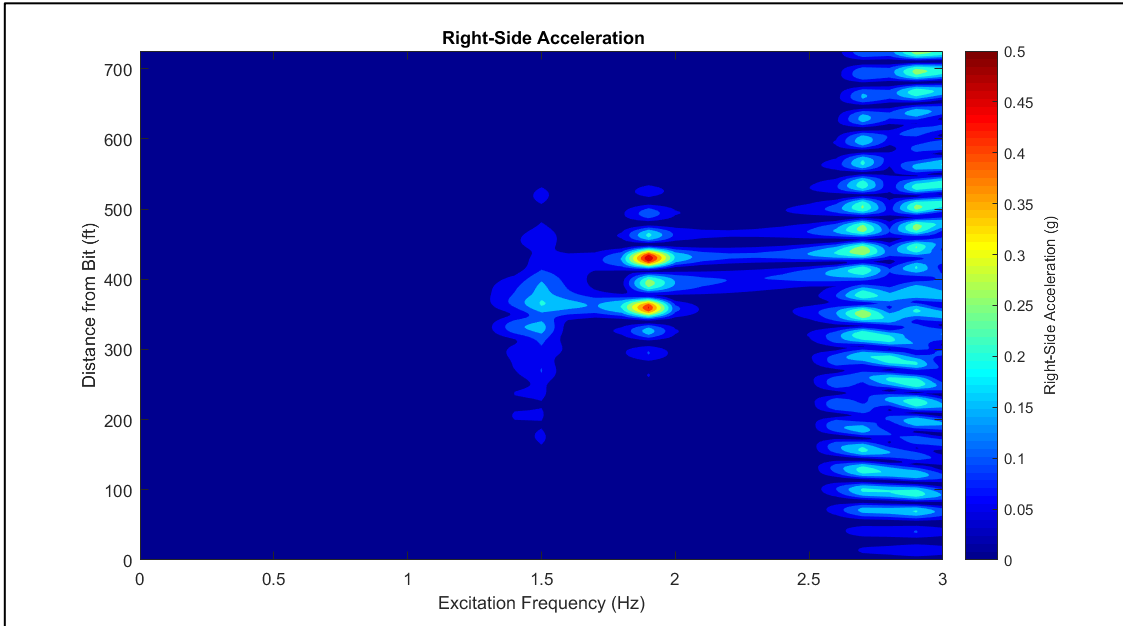


Figure E.42: Right-Side Acceleration for $\varphi = 45^\circ$

Inclination = 60°

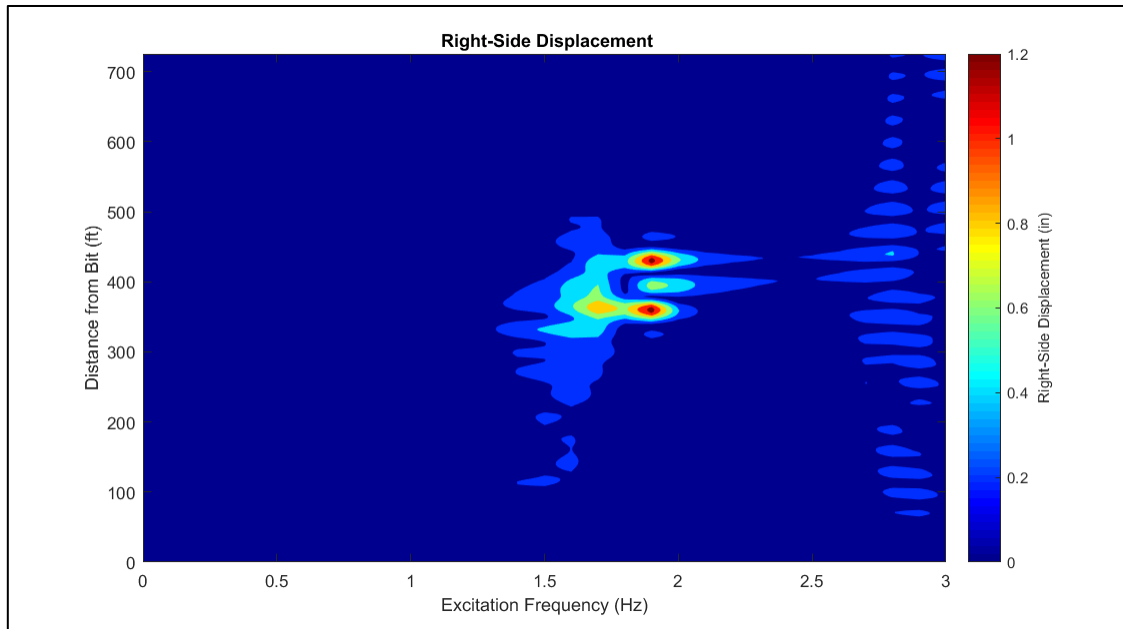


Figure E.43: Right-Side Displacement for $\varphi = 60^\circ$

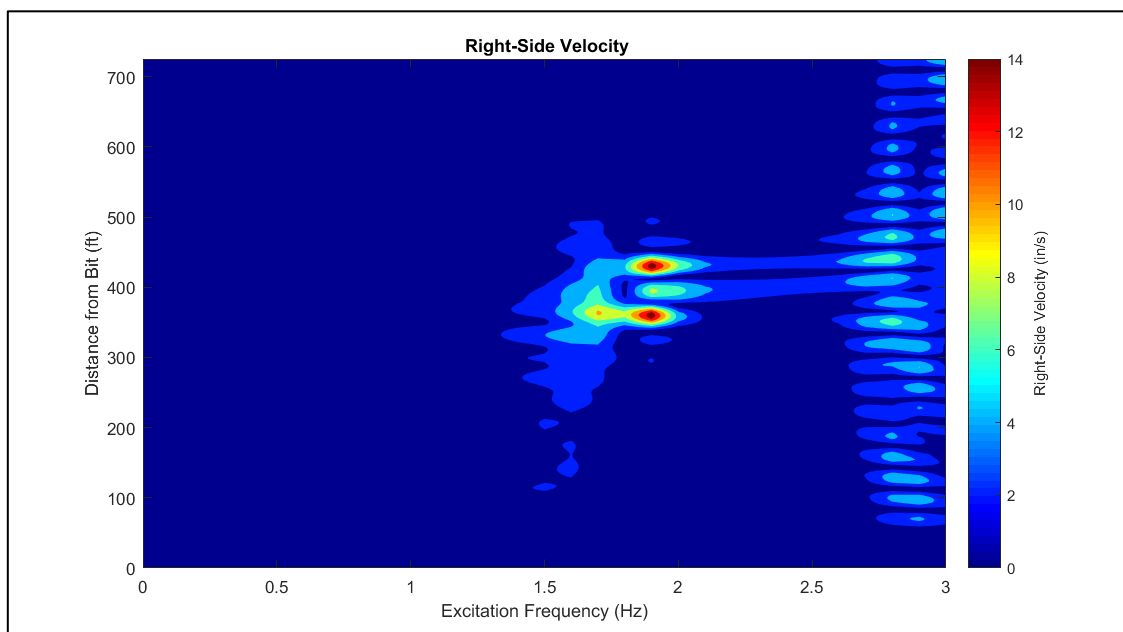


Figure E.44: Right-Side Velocity for $\varphi = 60^\circ$

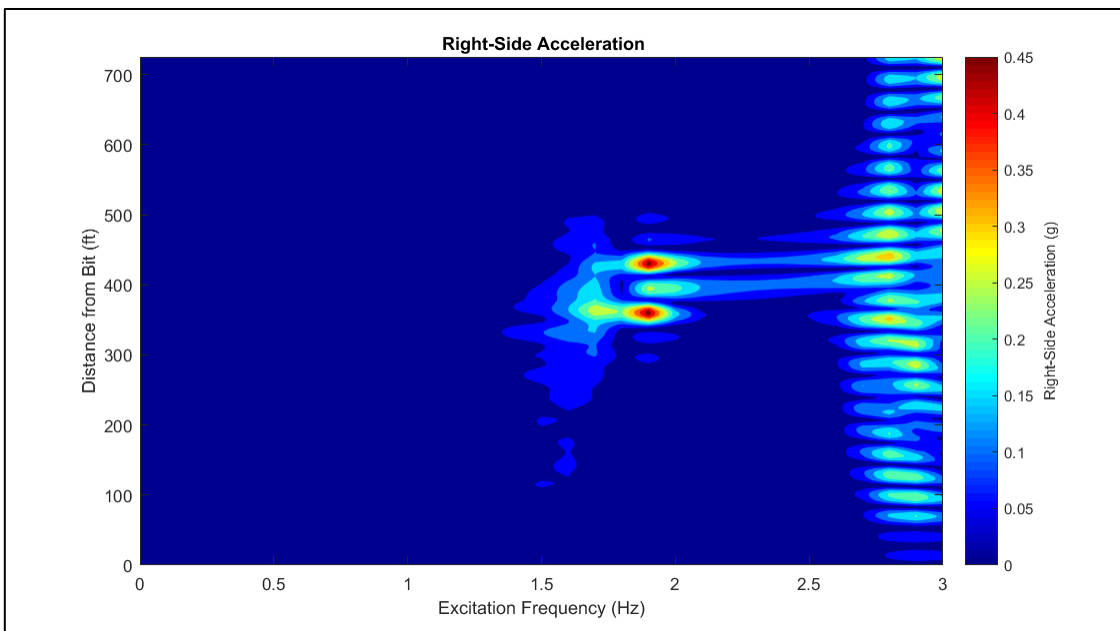


Figure E.45: Right-Side Acceleration for $\varphi = 60^\circ$

E.6 - Variations in Wellbore Curvature

$DLS = 5^\circ/100 \text{ ft}$

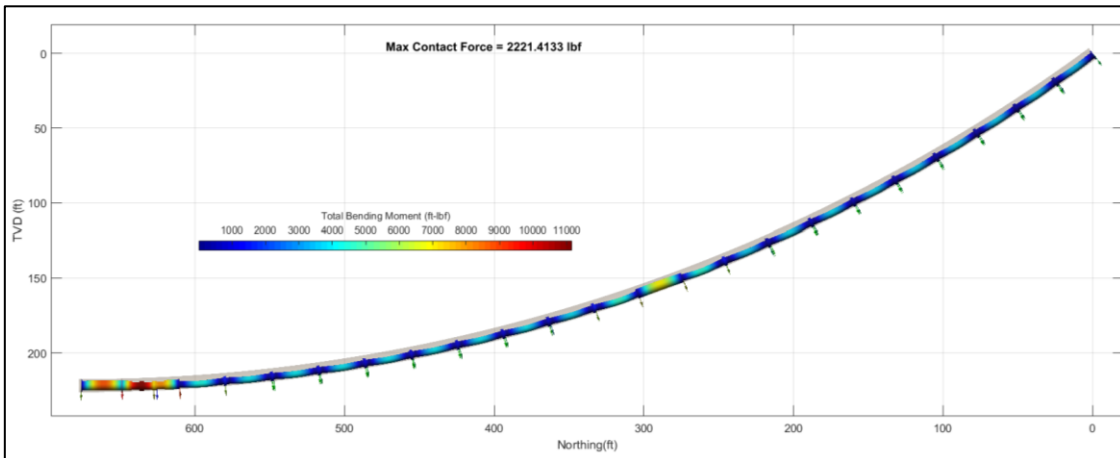


Figure E.46: Drillstring Mechanics Plot for $DLS = 5^\circ/100 \text{ ft}$, Landing at 90° Inclination

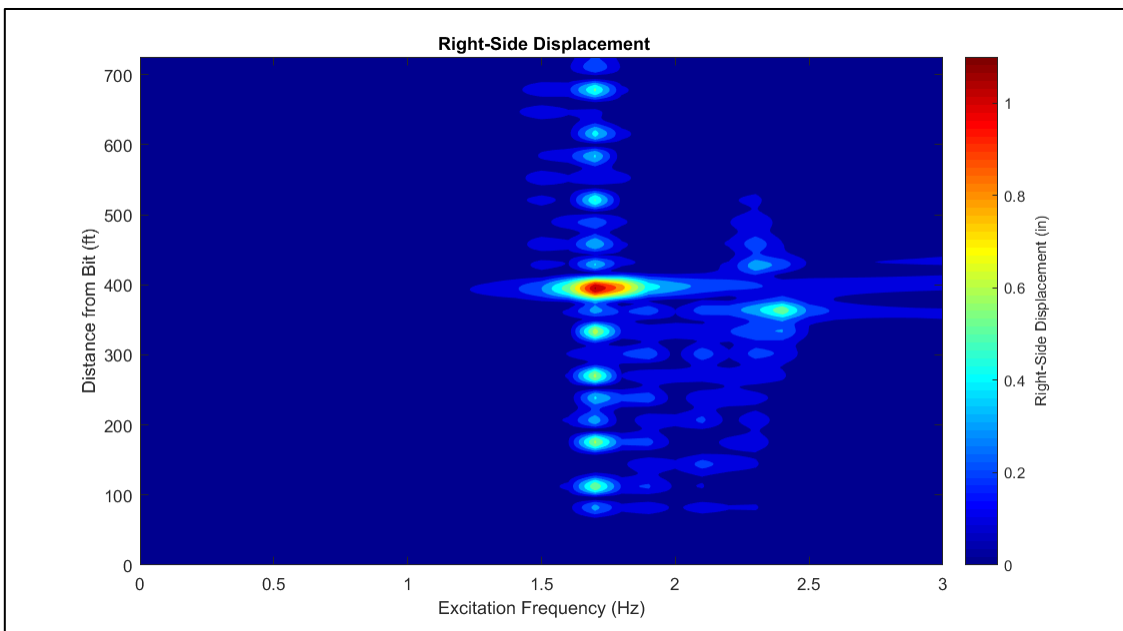


Figure E.47: Right-Side Displacement for DLS = 5°/100ft

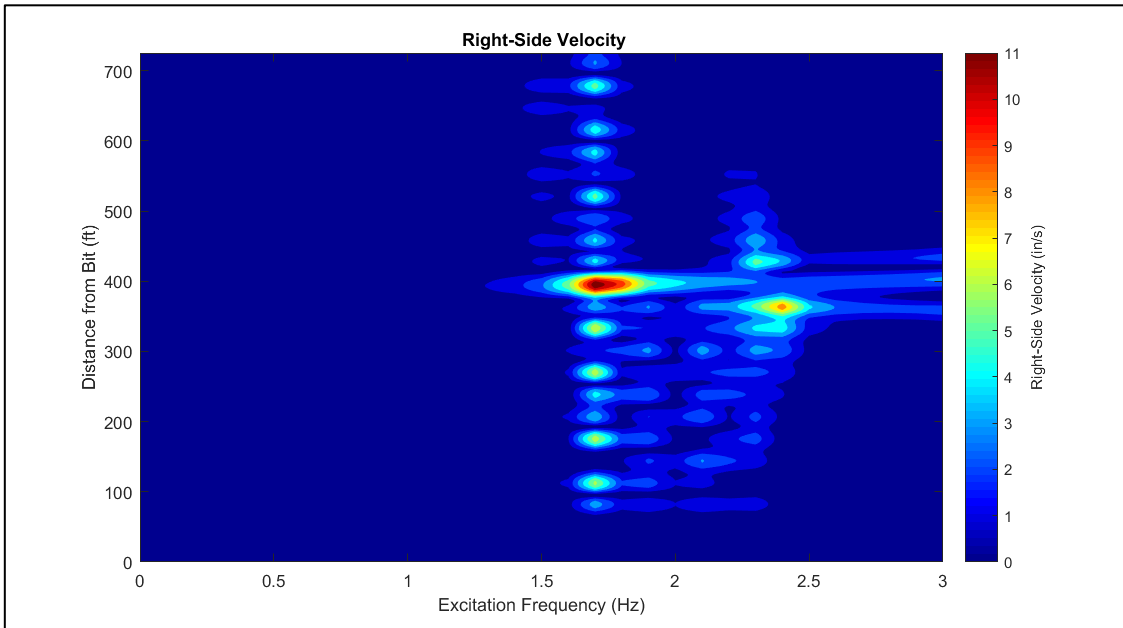


Figure E.48: Right-Side Velocity for DLS = 5°/100ft

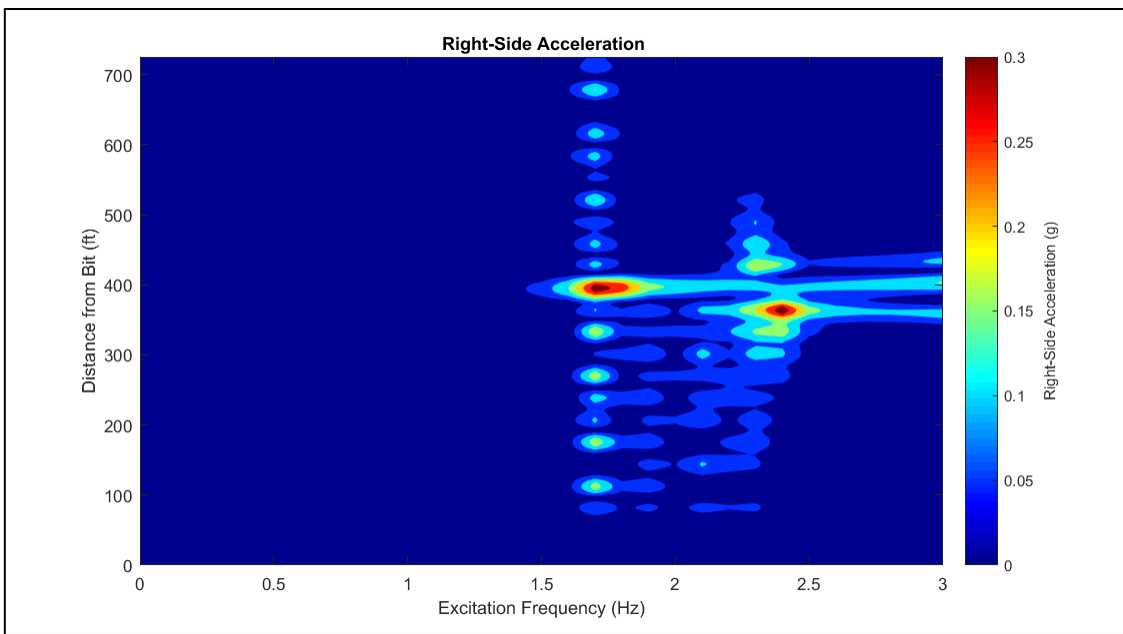


Figure E.49: Right-Side Acceleration for DLS = 5°/100ft

$$DLS = 10^\circ/100 \text{ ft}$$

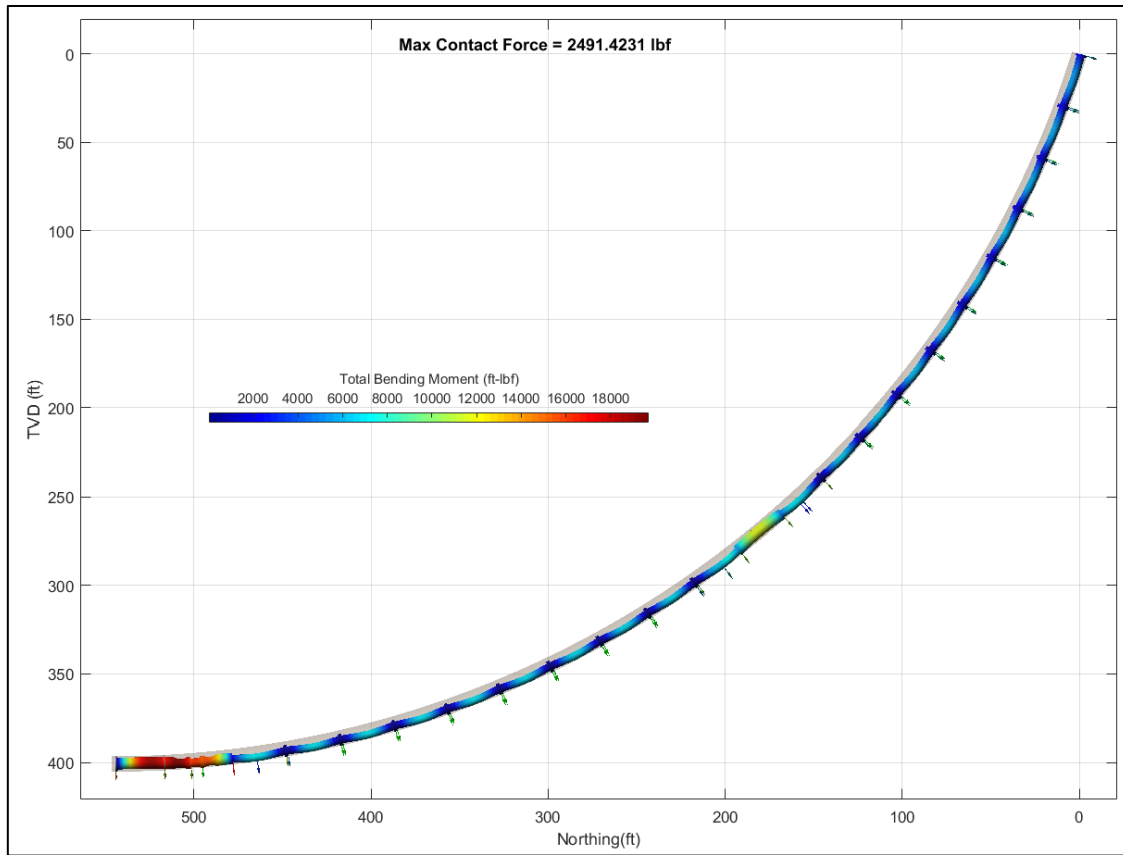


Figure E.50: Drillstring Mechanics Plot for $DLS = 10^\circ/100 \text{ ft}$, Landing at 90° Inclination

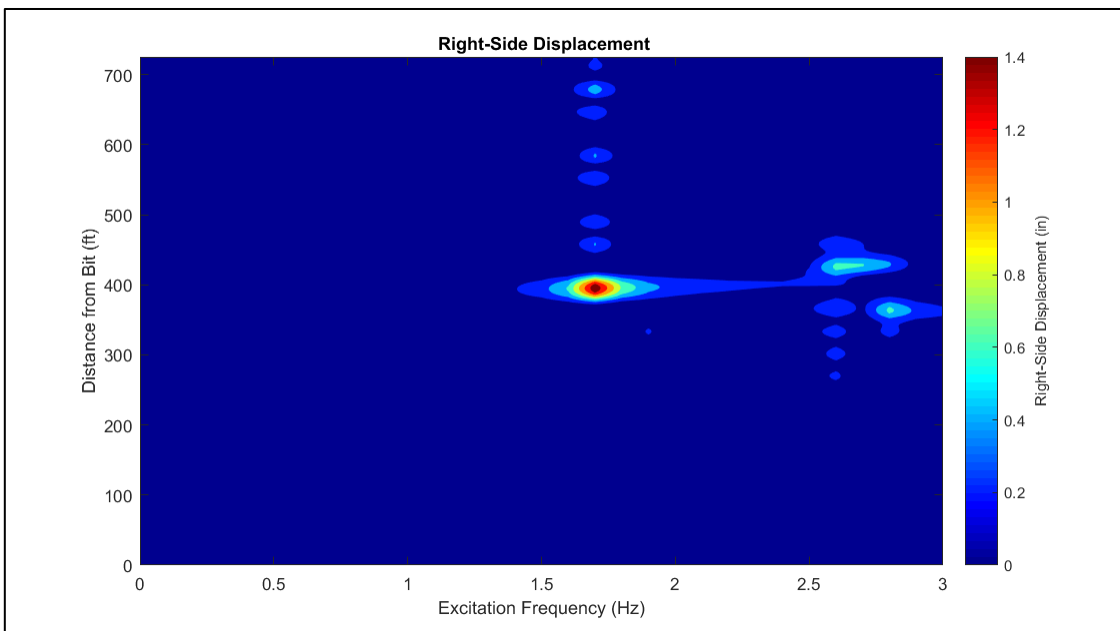


Figure E.51: Right-Side Displacement for DLS = $10^\circ/100\text{ft}$

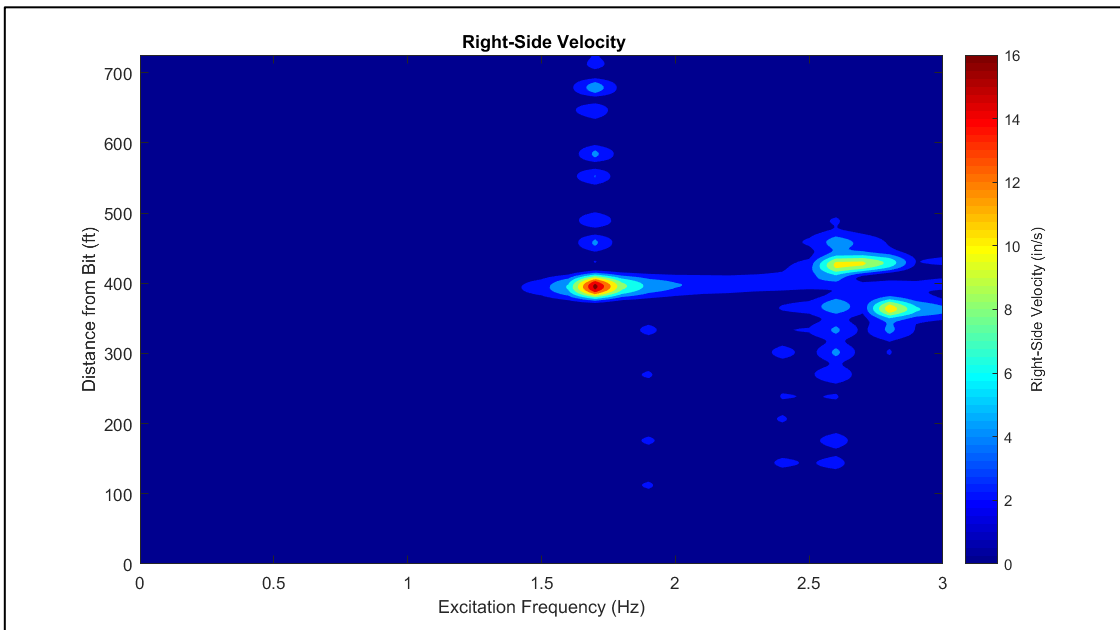


Figure E.52: Right-Side Velocity for DLS = $10^\circ/100\text{ft}$

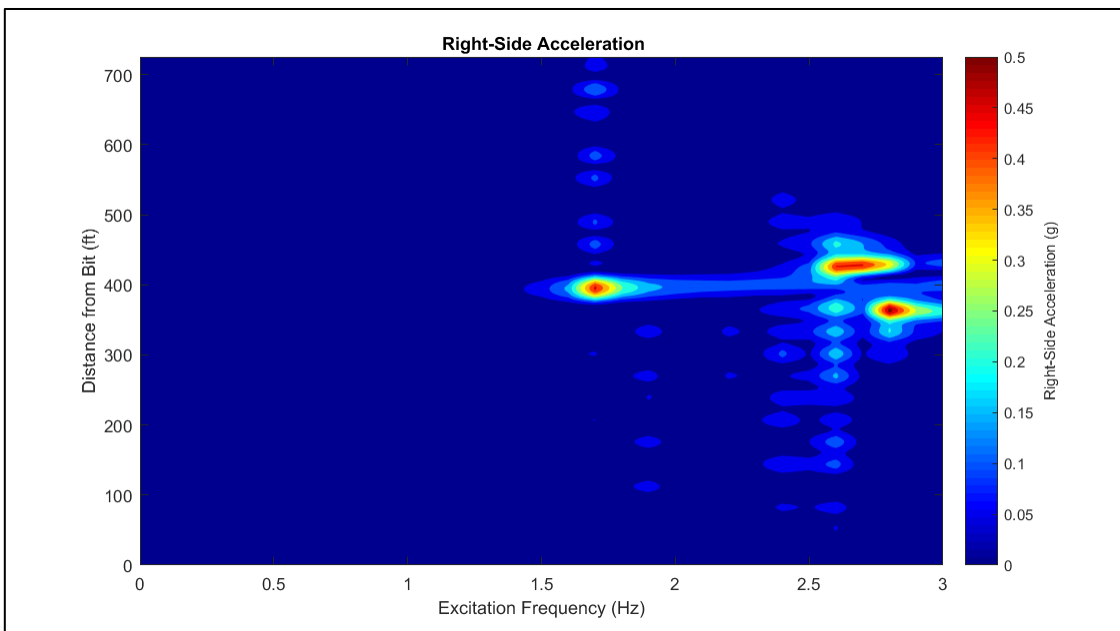


Figure E.53: Right-Side Acceleration for DLS = 10°/100ft

E.7 - Variations in DP and Tool Joints

Drill Pipe Body: 4 ½" 16.6 ppf S – 135 (ID:3.826)

- Tool Joint: NC50 (OD: 6.375, ID: 3.5, 18.63 ppf)

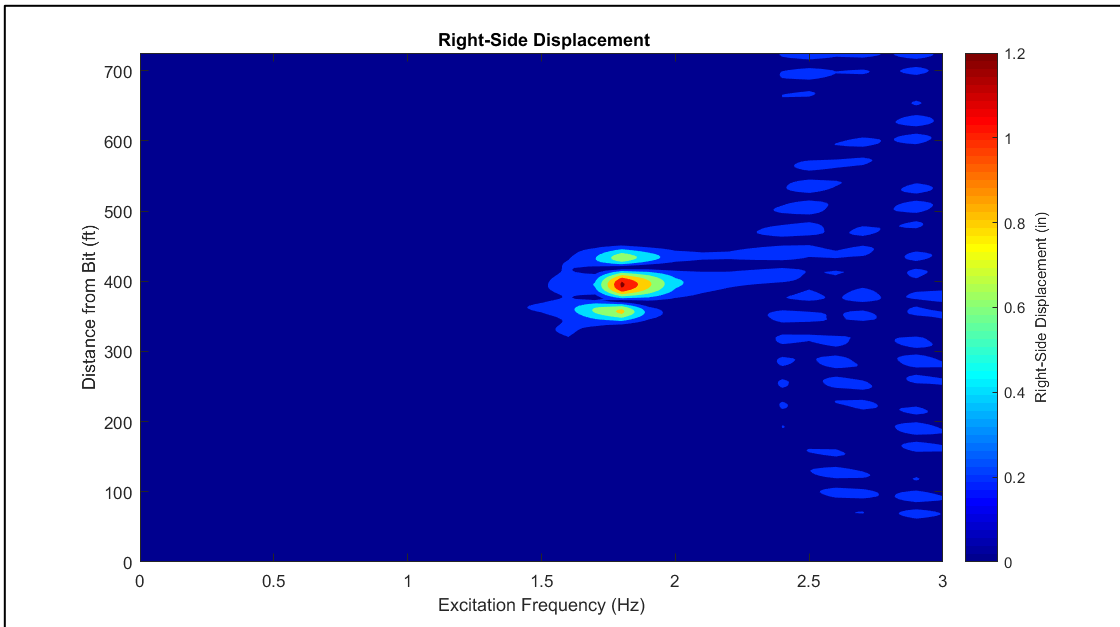


Figure E.54: Right-Side Displacement for Tool Joint: NC50 (OD: 6.375, ID: 3.5, 18.63 ppf)

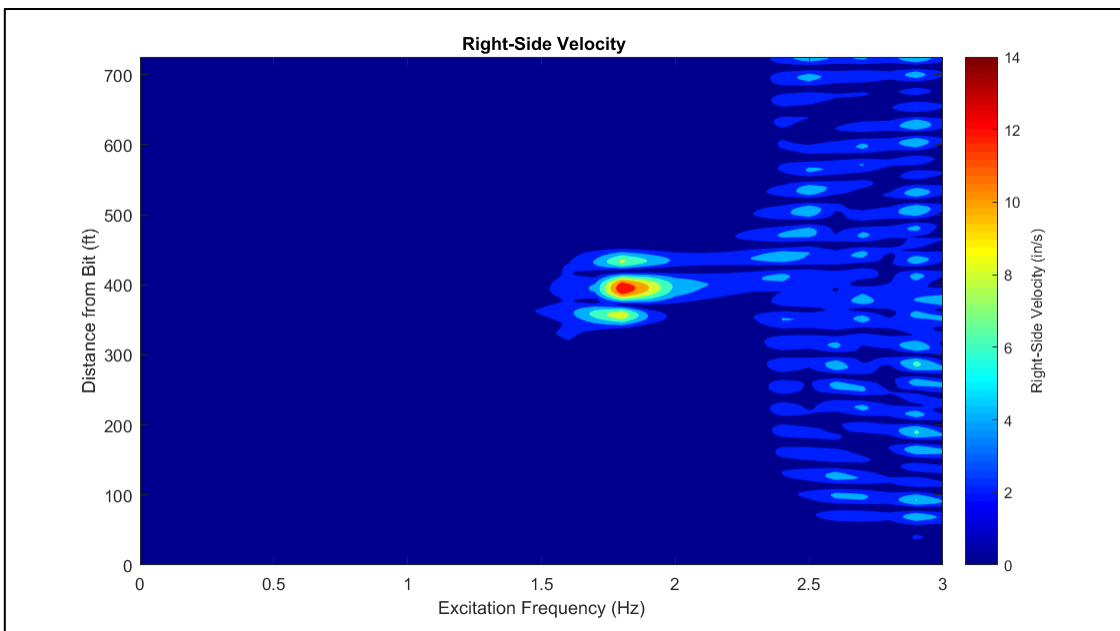


Figure E.55: Right-Side Velocity for Tool Joint: NC50 (OD: 6.375, ID: 3.5, 18.63 ppf)

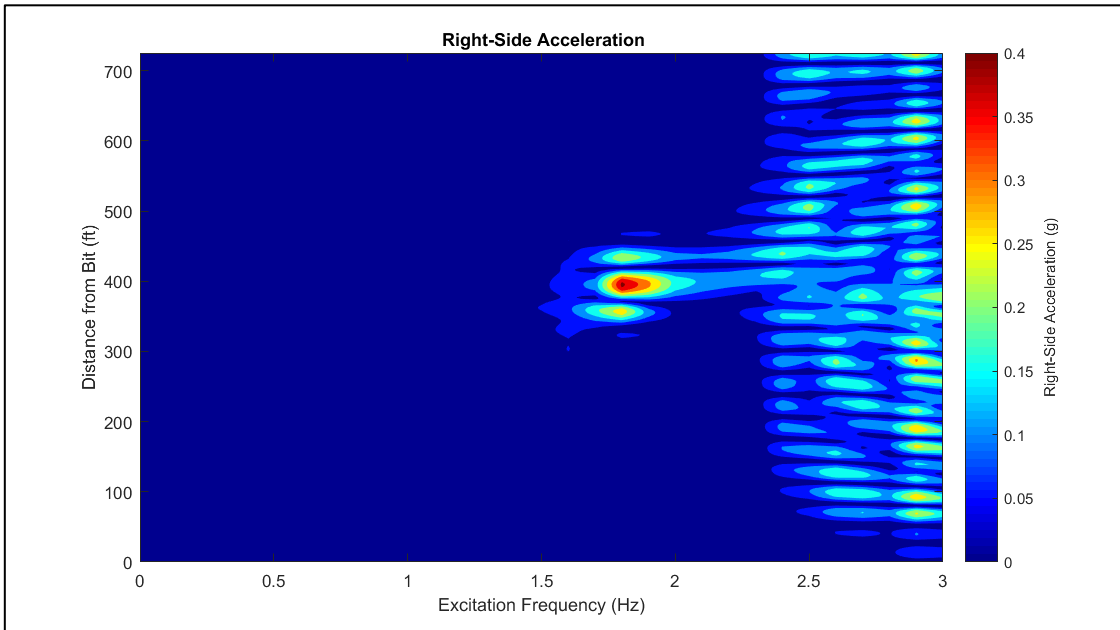


Figure E.56: Right-Side Acceleration for Tool Joint: NC50 (OD: 6.375, ID: 3.5, 18.63 ppf)

- Tool Joint: NC50 (OD: 6.625, ID: 3.5, 19.11 ppf)

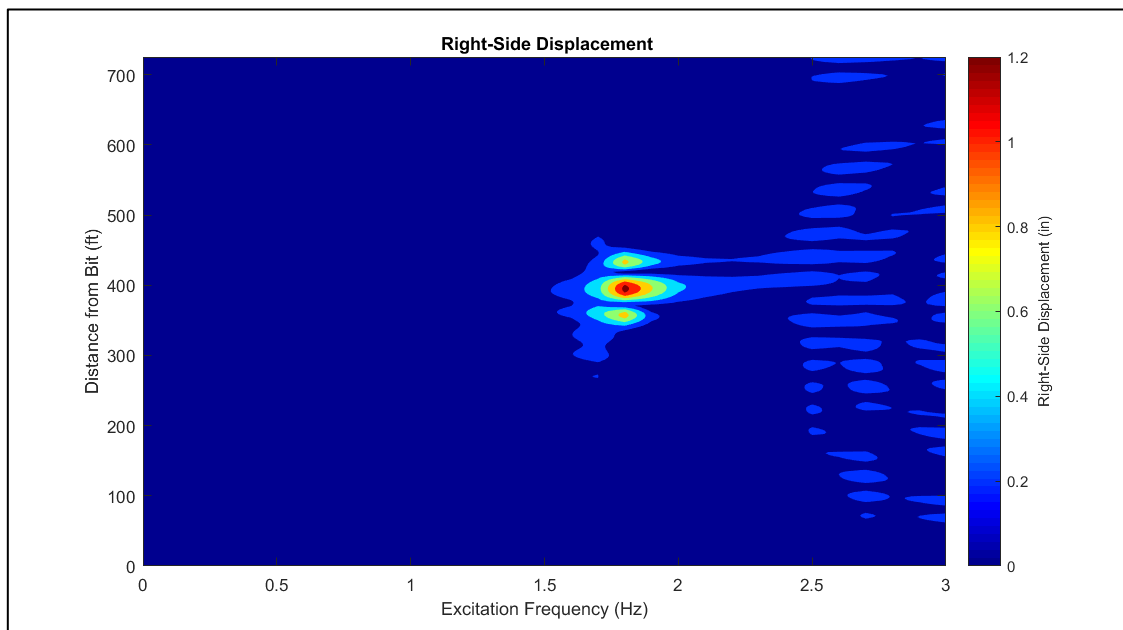


Figure E.57: Right-Side Displacement for Tool Joint: NC50 (OD: 6.625, ID: 3.5, 19.11 ppf)

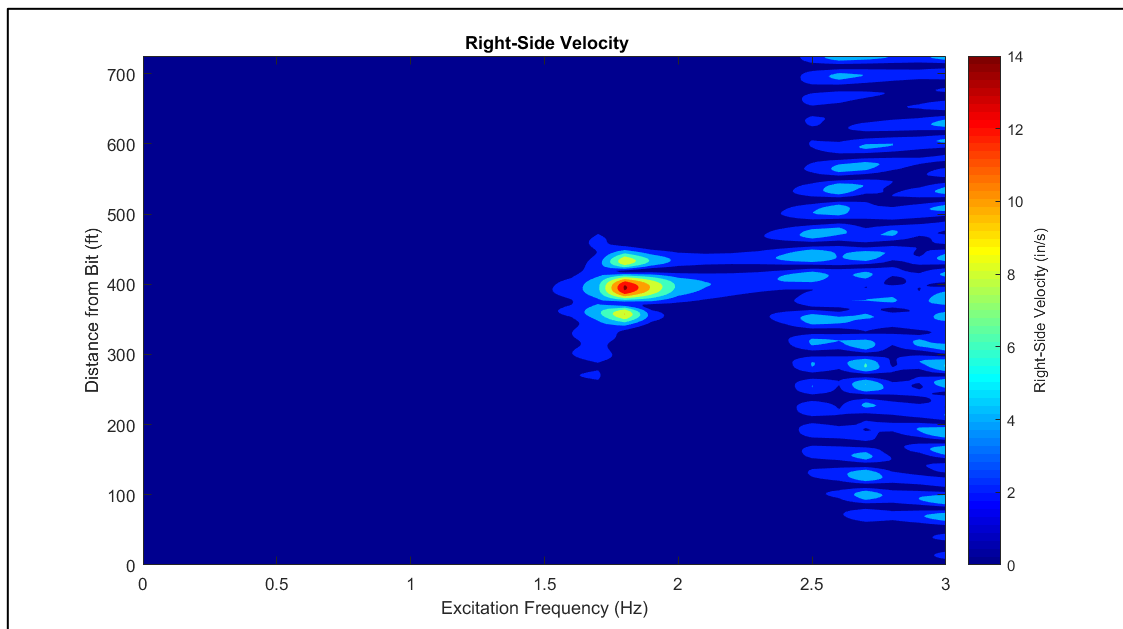


Figure E.58: Right-Side Velocity for Tool Joint: NC50 (OD: 6.625, ID: 3.5, 19.11 ppf)

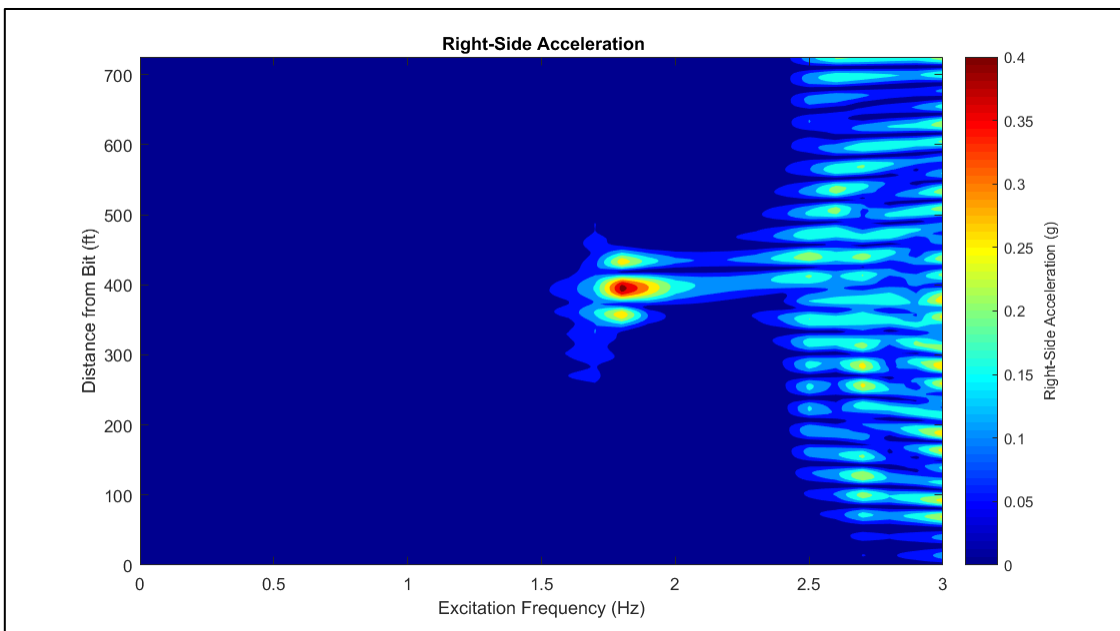


Figure E.59: Right-Side Acceleration for Tool Joint: NC50 (OD: 6.625, ID: 3.5, 19.11 ppf)

- Tool Joint: NC46 (OD: 6.252, ID: 2.752, 18.83 ppf)

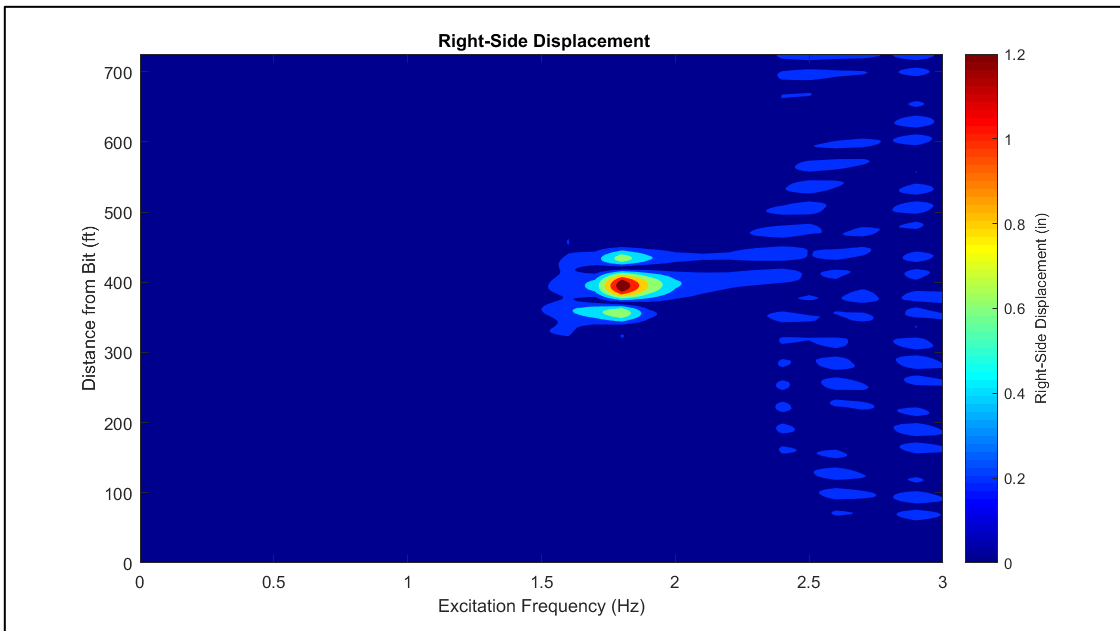


Figure E.60: Right-Side Displacement for Tool Joint: NC46 (OD: 6.252, ID: 2.752, 18.83 ppf)

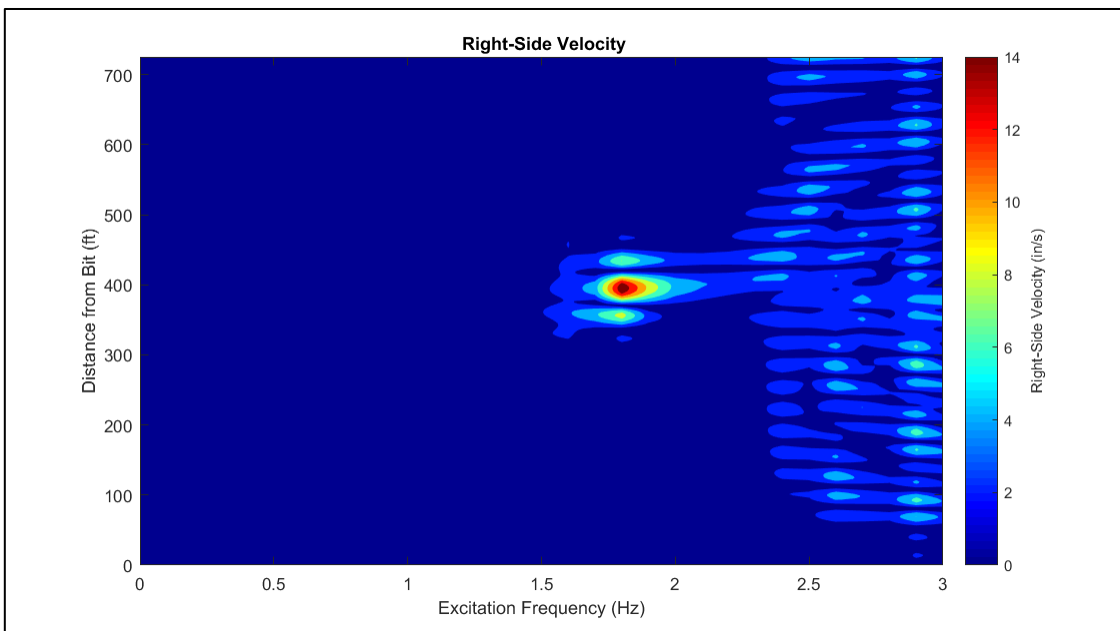


Figure E.61: Right-Side Velocity for Tool Joint: NC46 (OD: 6.252, ID: 2.752, 18.83 ppf)

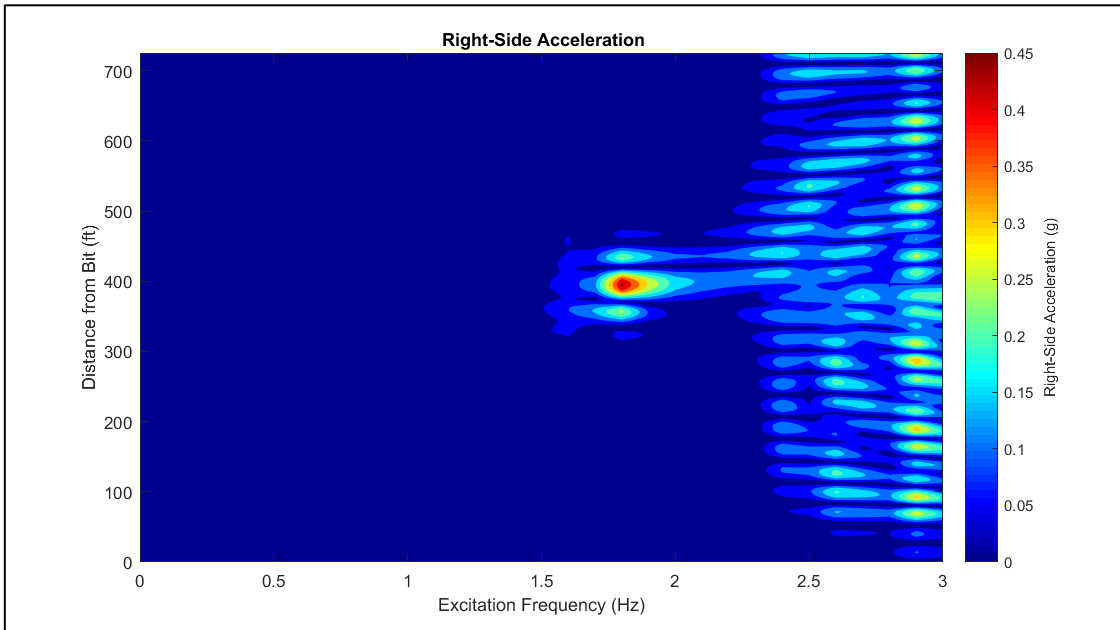


Figure E.62: Right-Side Acceleration for Tool Joint: NC46 (OD: 6.252, ID: 2.752, 18.83 ppf)

- Tool Joint: FH (OD: 6.252, ID: 2.5, 19.02 ppf)

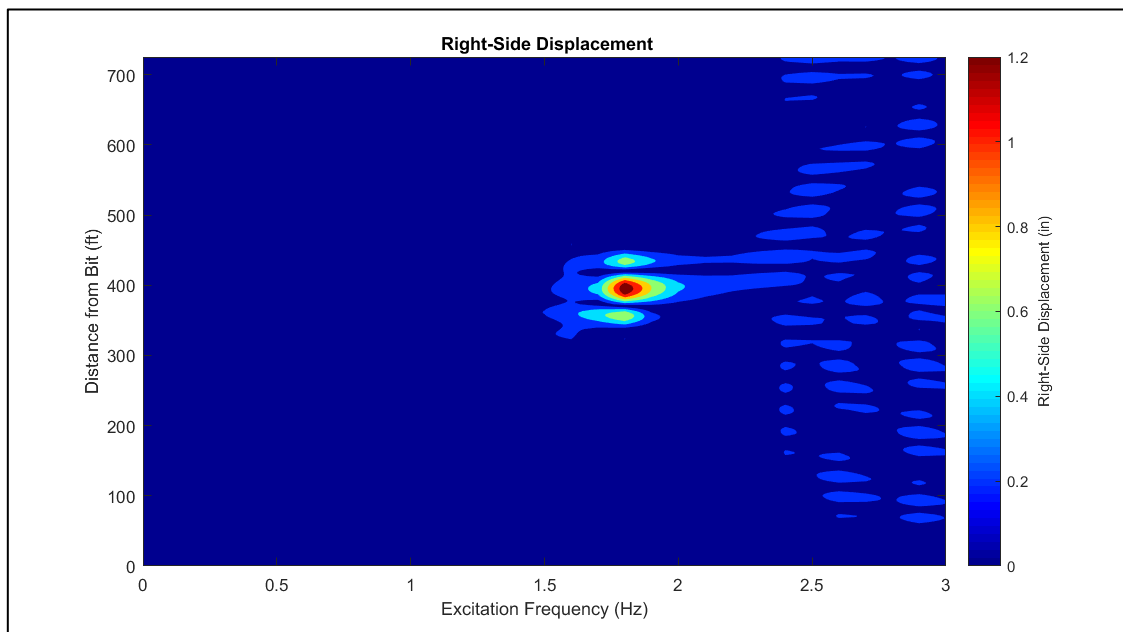


Figure E.63: Right-Side Displacement for Tool Joint: FH (OD: 6.252, ID: 2.5, 19.02 ppf)

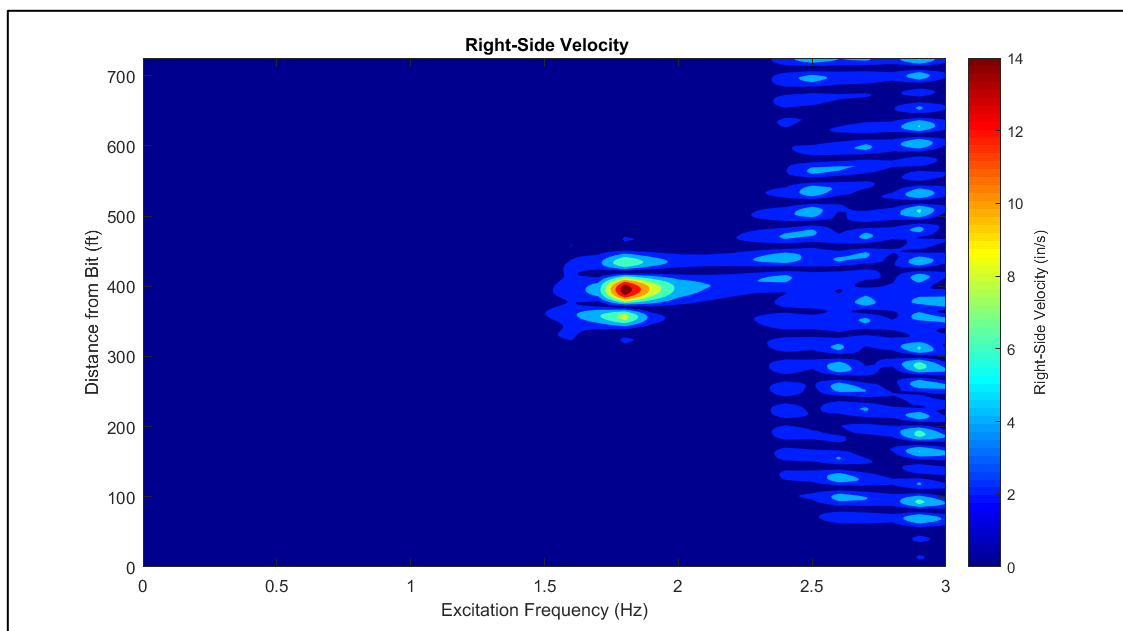


Figure E.64: Right-Side Velocity for Tool Joint: FH (OD: 6.252, ID: 2.5, 19.02 ppf)

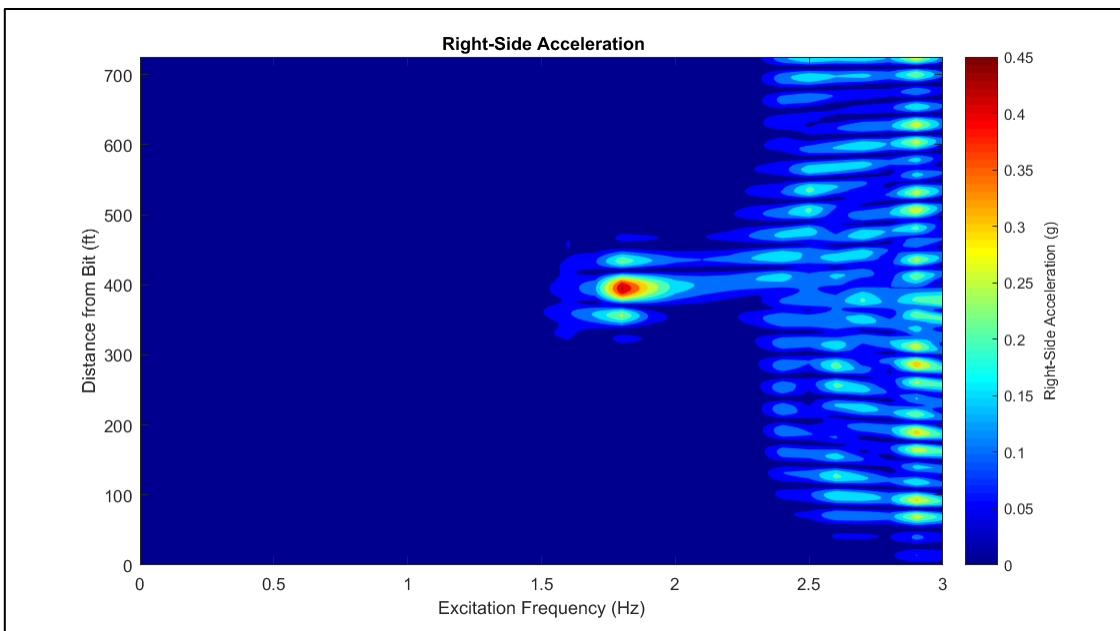


Figure E.65: Right-Side Acceleration for Tool Joint: FH (OD: 6.252, ID: 2.5, 19.02 ppf)

- Tool Joint: H90(OD:6.00, ID: 3, 18.16ppf)

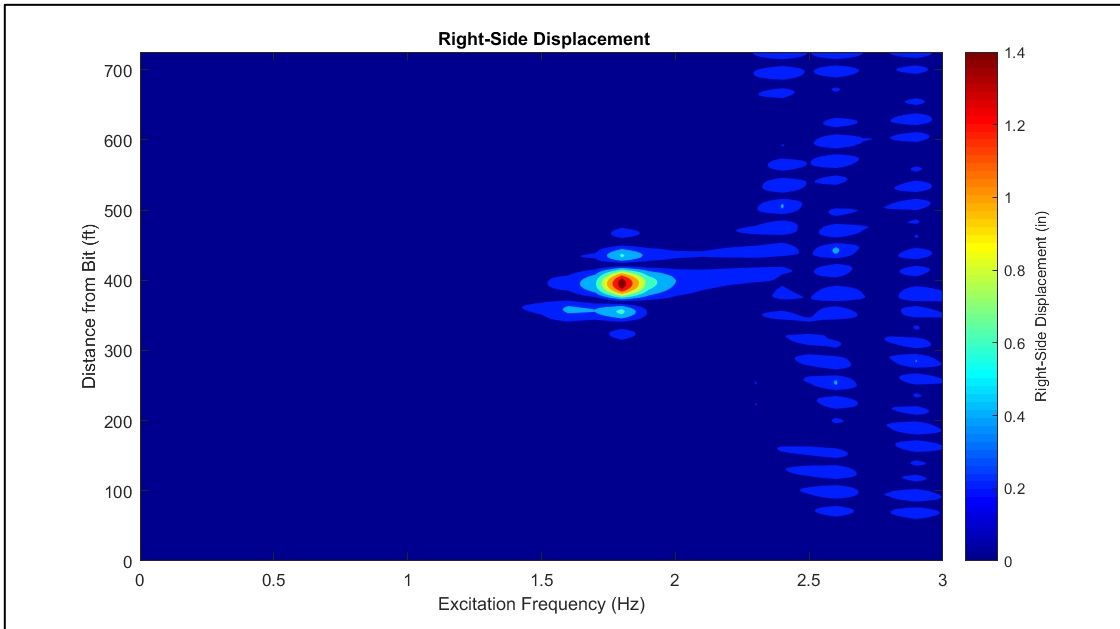


Figure E.66: Right-Side Displacement for Tool Joint: H90(OD:6.00, ID: 3, 18.16ppf)

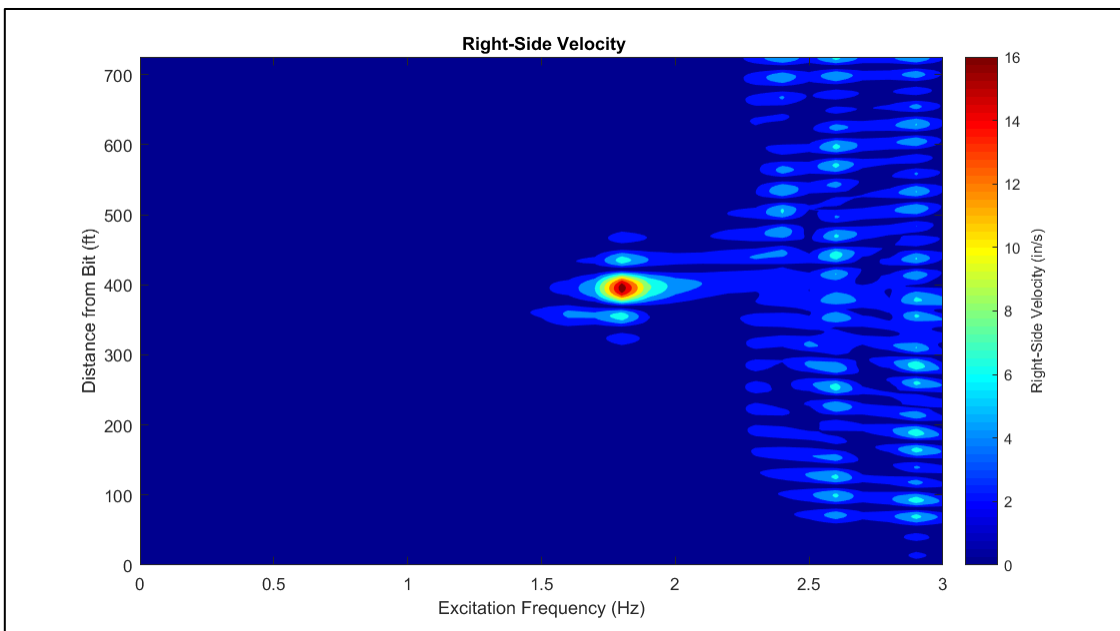


Figure E.67: Right-Side Velocity for Tool Joint: H90(OD:6.00, ID: 3, 18.16ppf)

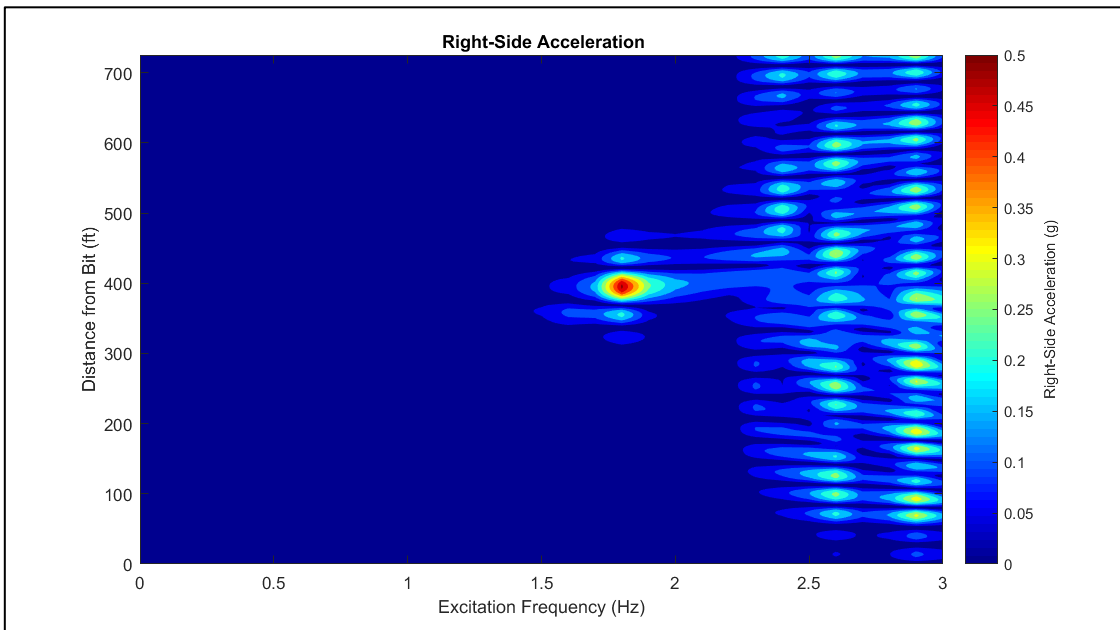


Figure E.68: Right-Side Acceleration for Tool Joint: H90(OD:6.00, ID: 3, 18.16ppf)

Drill Pipe Body: 4 ½" 20 ppf, S-135 (ID:3.64)

- Tool Joint: NC50 (OD = 6.625", ID = 3", 23.06ppf)

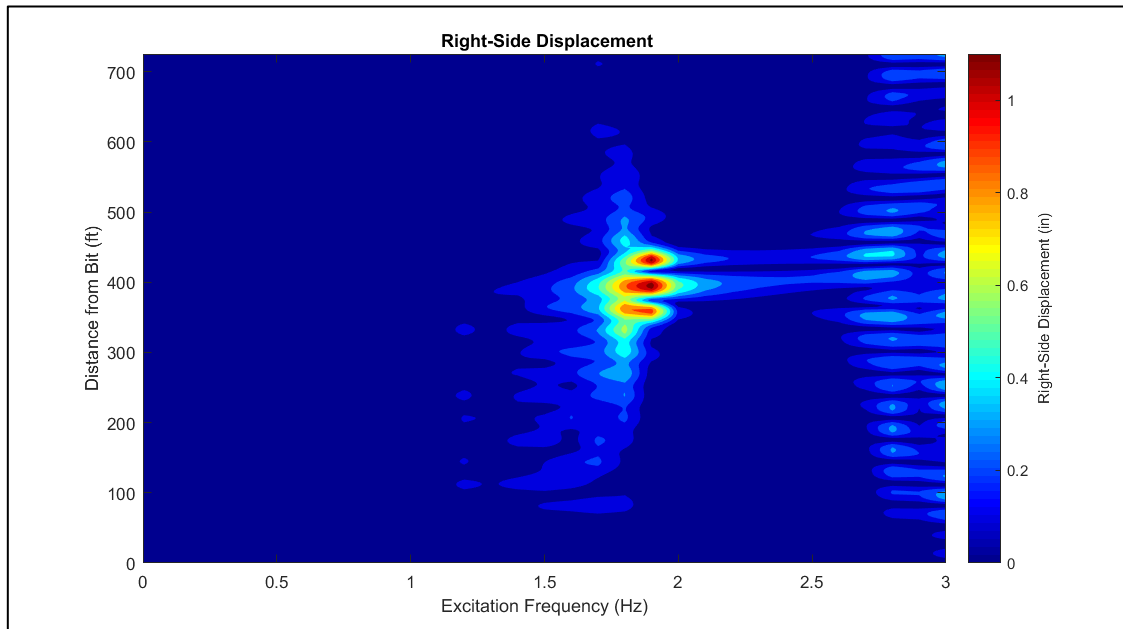


Figure E.69: Right-Side Displacement for Tool Joint: NC50 (OD = 6.625", ID = 3", 23.06ppf)

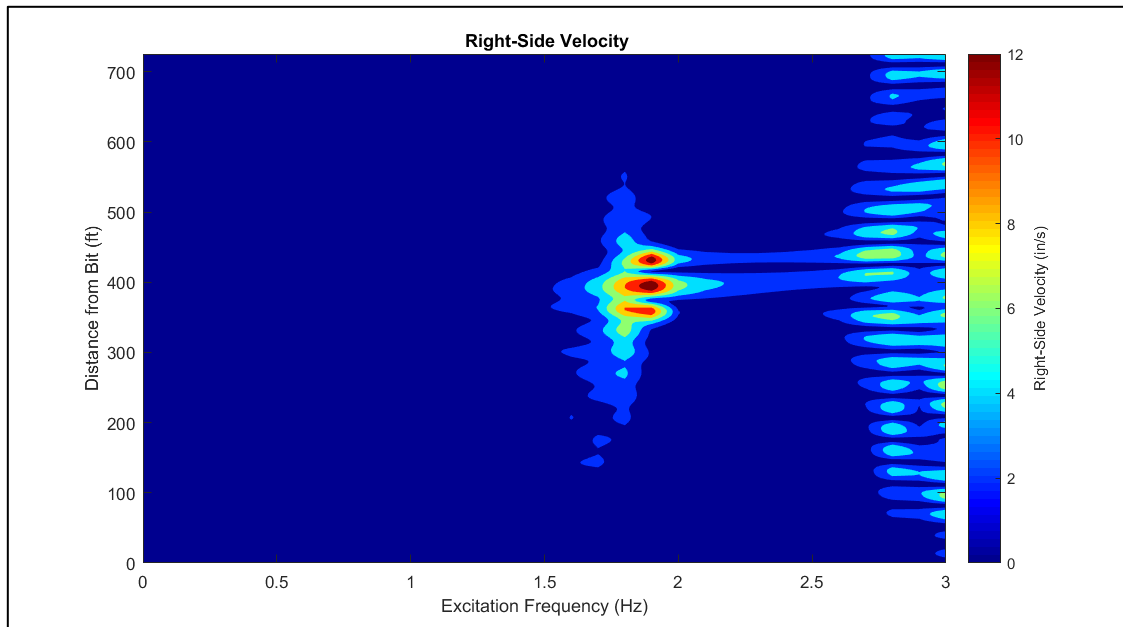


Figure E.70: Right-Side Velocity for Tool Joint: NC50 (OD = 6.625", ID = 3" , 23.06ppf)

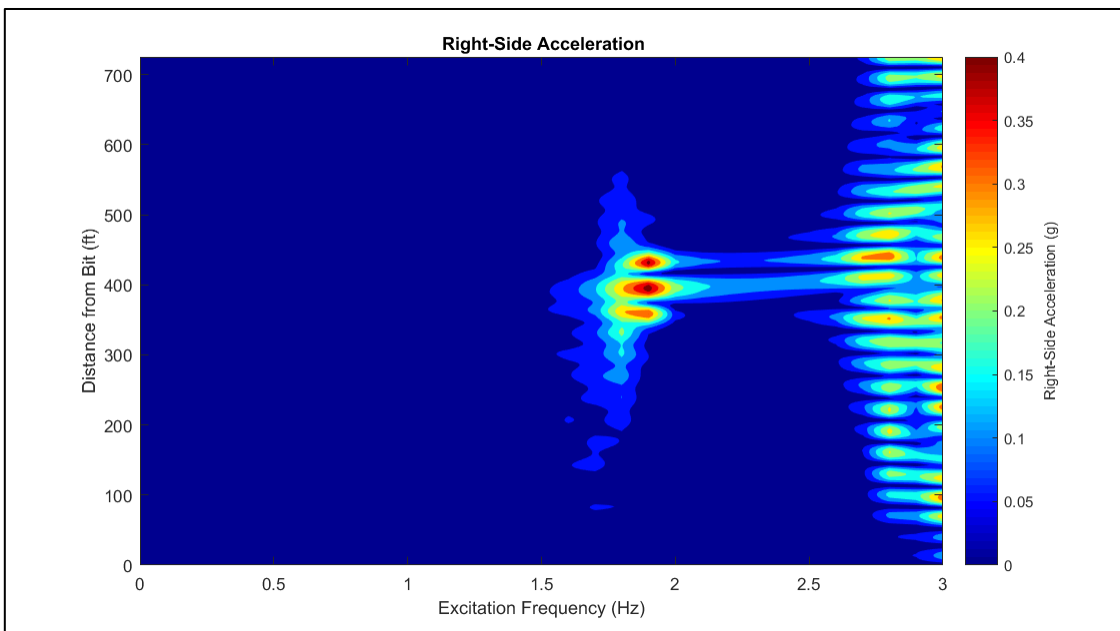


Figure E.71: Right-Side Acceleration for Tool Joint: NC50 (OD = 6.625", ID = 3", 23.06ppf)

- Tool Joint: NC46 (OD = 6.25", ID = 2.25", 22.98ppf)

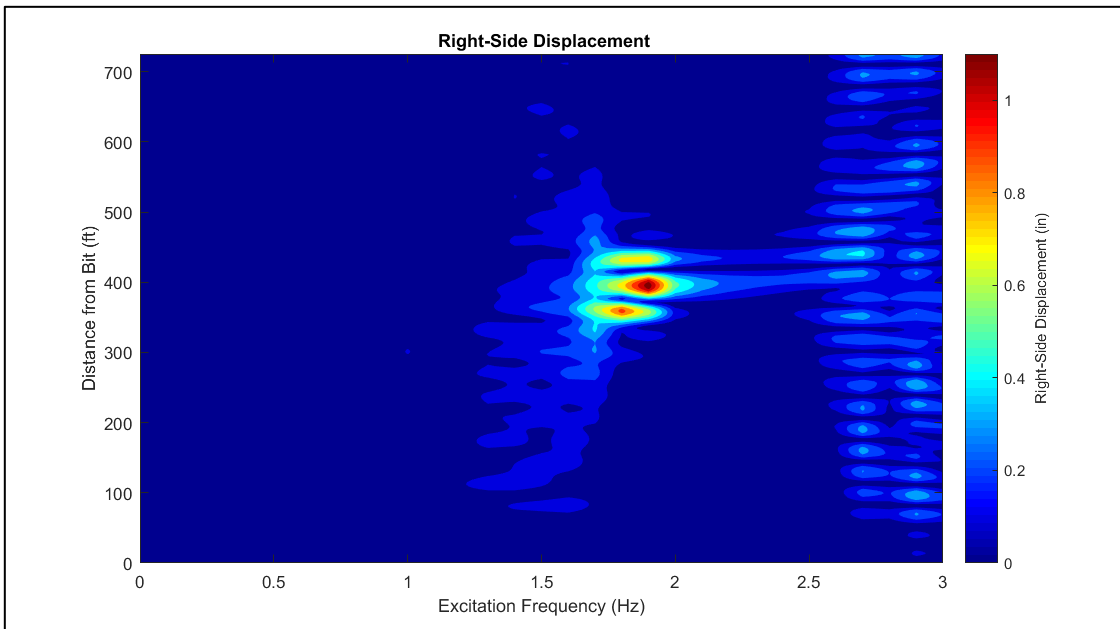


Figure E.72: Right-Side Displacement for Tool Joint: NC46 (OD = 6.25", ID = 2.25", 22.98ppf)

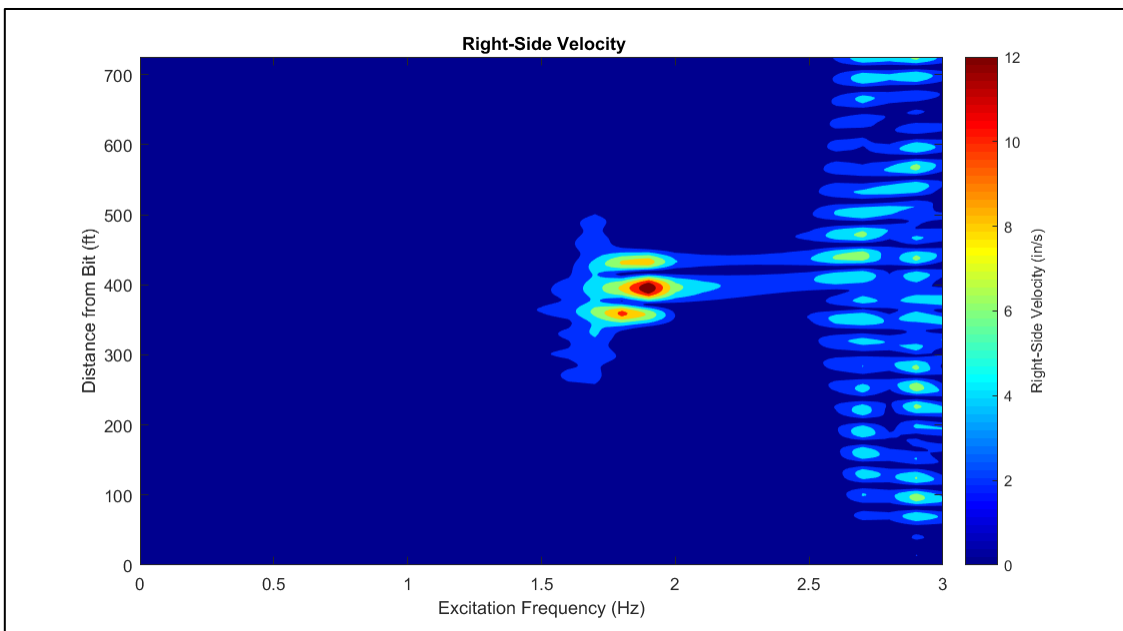


Figure E.73: Right-Side Velocity for Tool Joint: NC46 (OD = 6.25", ID = 2.25", 22.98ppf)

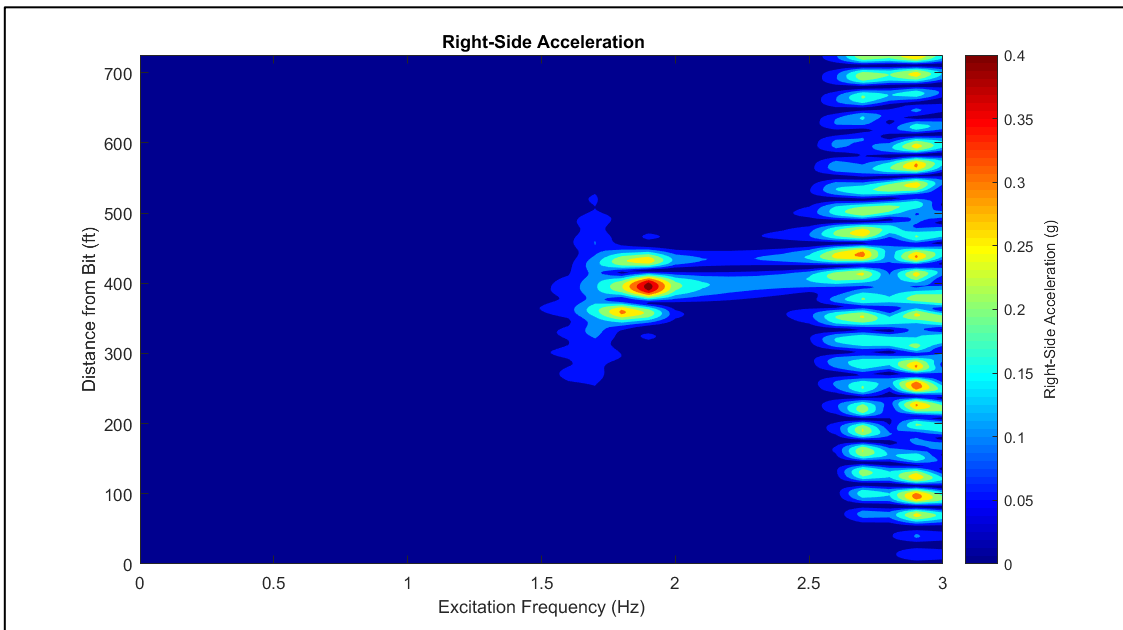


Figure E.74: Right-Side Acceleration for Tool Joint: NC46 (OD = 6.25", ID = 2.25", 22.98ppf)

Drill Pipe Body: 5" 19.5 ppf, S-135

- Tool Joint: NC50 (OD = 6.625", ID = 2.75", 22.56ppf)

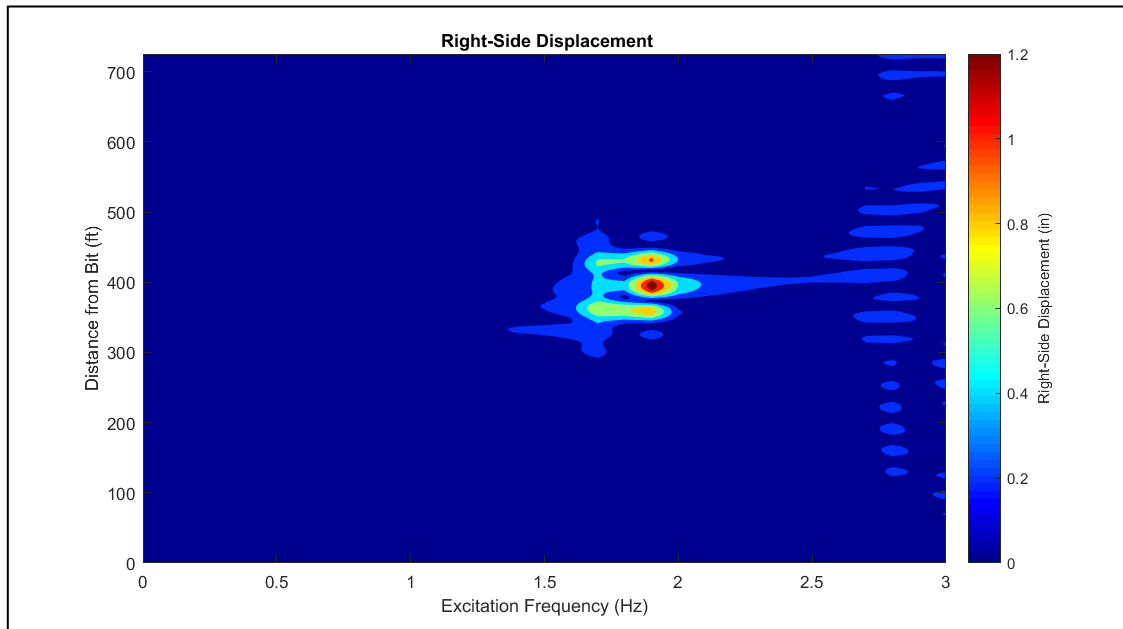


Figure E.75: Right-Side Displacement for Tool Joint: NC50 (OD = 6.625", ID = 2.75", 22.56ppf)

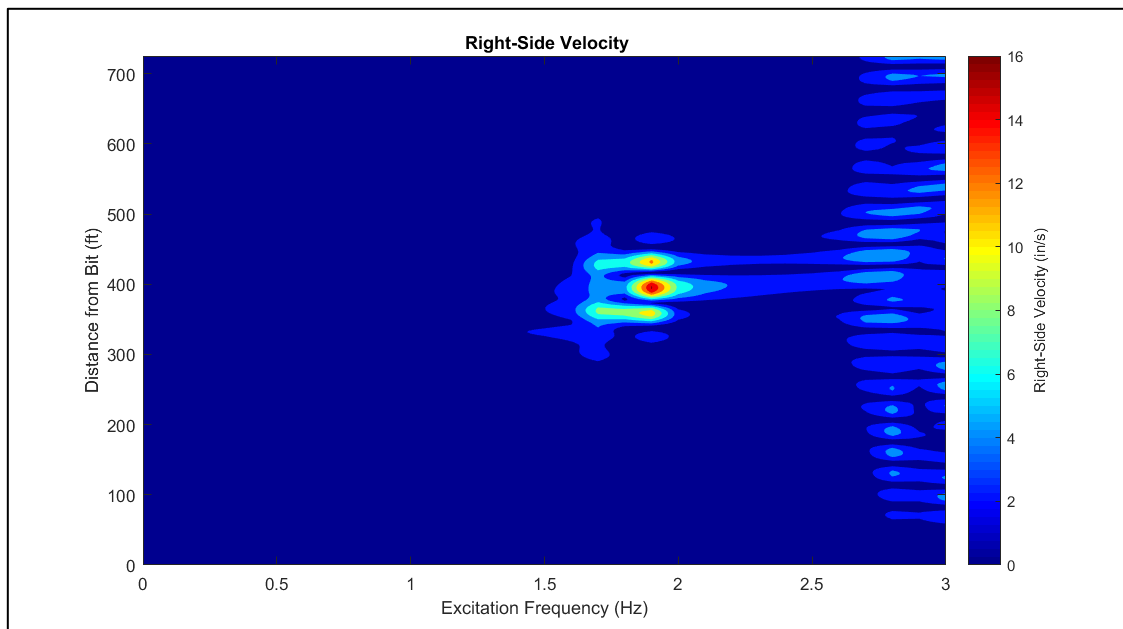


Figure E.76: Right-Side Velocity for Tool Joint: NC50 (OD = 6.625", ID = 2.75", 22.56ppf)

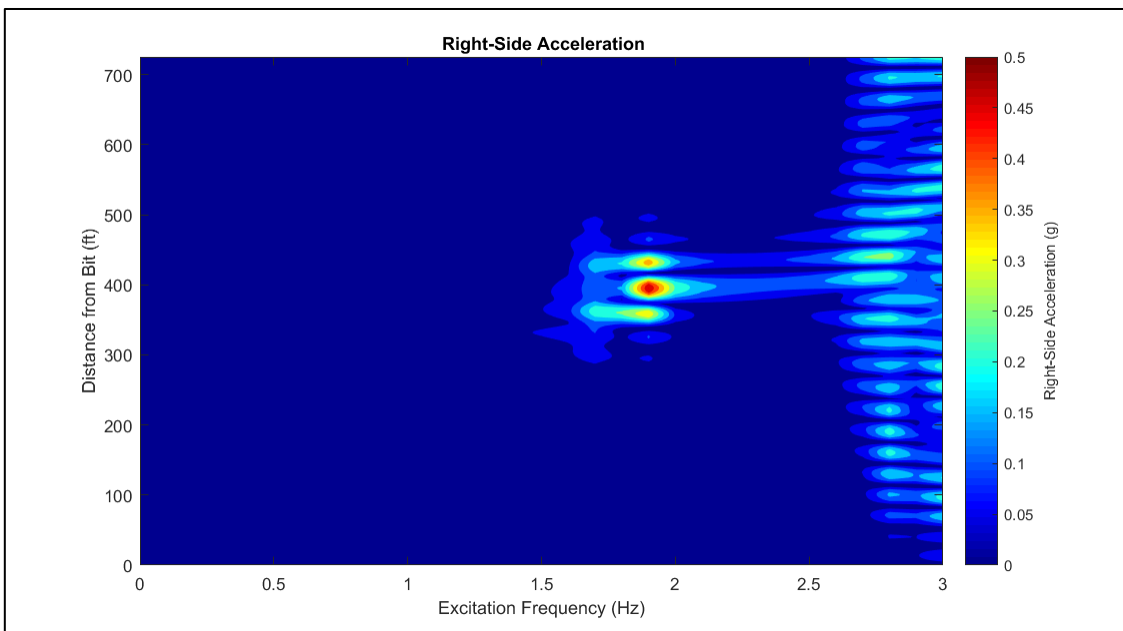


Figure E.77: Right-Side Acceleration for Tool Joint: NC50 (OD = 6.625", ID = 2.75", 22.56ppf)

- Tool Joint: 5 ½ FH (OD = 7.25", ID = 3.5", 23.42ppf)

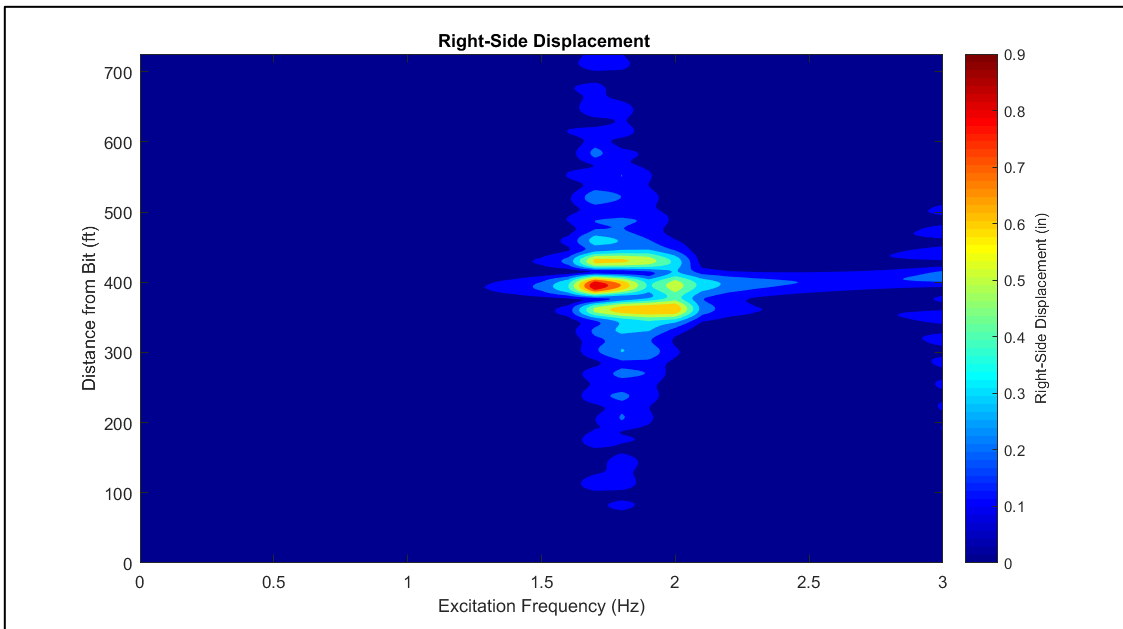


Figure E.78: Right-Side Displacement for Tool Joint: 5 ½ FH (OD = 7.25", ID = 3.5", 23.42ppf)

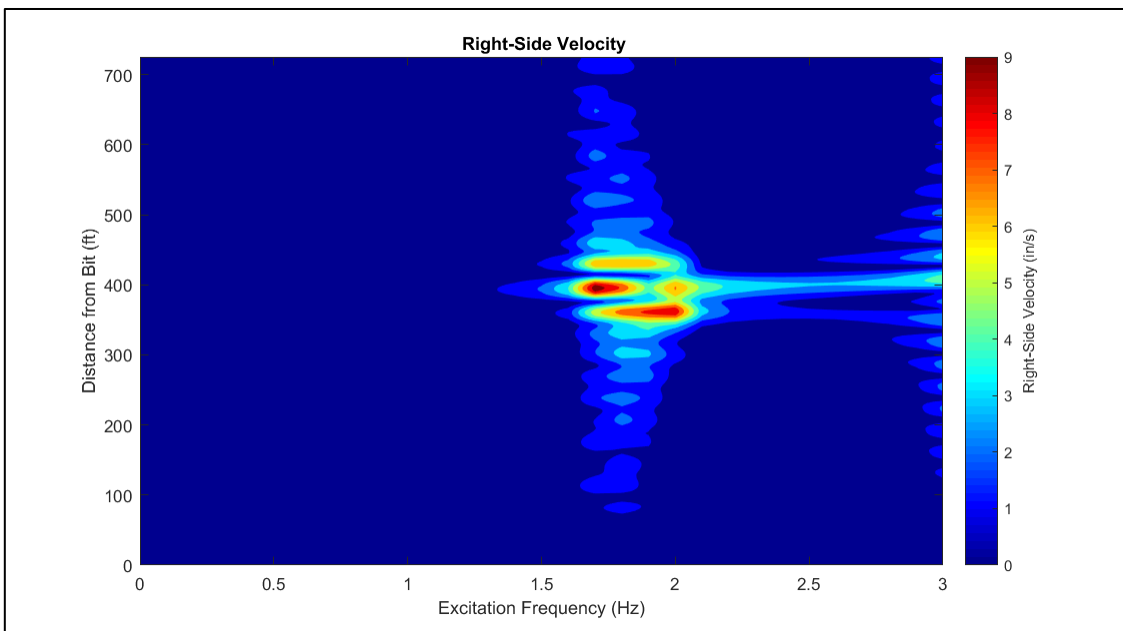


Figure E.79: Right-Side Velocity for Tool Joint: 5 ½ FH (OD = 7.25", ID = 3.5", 23.42ppf)

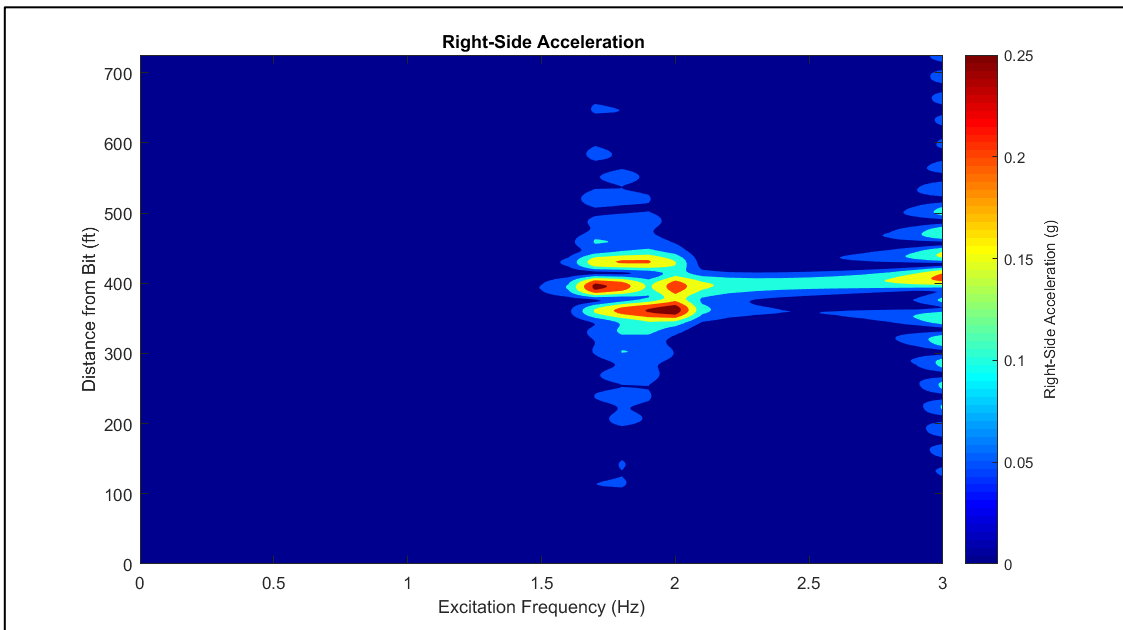


Figure E.80: Right-Side Acceleration for Tool Joint: 5 ½ FH (OD = 7.25", ID = 3.5", 23.42ppf)